Titles of Related Interest—
Other CIM Proceedings
Published by Pergamon

Bickert REDUCTION AND CASTING OF ALUMINUM
Chalkley TAILING AND EFFLUENT MANAGEMENT
Closset PRODUCTION AND ELECTROLYSIS OF LIGHT METALS
Dobby PROCESSING OF COMPLEX ORES
Jaeck PRIMARY AND SECONDARY LEAD PROCESSING
Jonas DIRECT ROLLING AND HOT CHARGING OF
  STRAND CAST BILLETS
Kachaniwsky IMPACT OF OXYGEN ON THE PRODUCTIVITY
  OF NON-FERROUS METALLURGICAL PROCESSES
Macmillan QUALITY AND PROCESS CONTROL IN REDUCTION AND
  CASTING OF ALUMINUM AND OTHER LIGHT METALS
Plumpton PRODUCTION AND PROCESSING OF FINE PARTICLES
Rigaud ADVANCES IN REFRACTORIES FOR THE
  METALLURGICAL INDUSTRIES
Ruddle ACCELERATED COOLING OF ROLLED STEEL
Salter GOLD METALLURGY
Thompson COMPUTER SOFTWARE IN CHEMICAL AND
  EXTRACTIVE METALLURGY
Twigge-Molecey PROCESS GAS HANDLING AND CLEANING
Tyson FRACTURE MECHANICS
Wilkinson ADVANCED STRUCTURAL MATERIALS

Related Journals
(Free sample copies available upon request)

ACTA METALLURGICA
CANADIAN METALLURGICAL QUARTERLY
MINERALS ENGINEERING
SCRIPTA METALLURGICA

PROCEEDINGS OF THE INTERNATIONAL SYMPOSIUM ON
ADVANCES IN PROCESSING OF CERAMIC AND METAL MATRIX
COMPOSITES, HALIFAX, AUGUST 20-24, 1989

Processing of Ceramic and Metal Matrix Composites

Editor
H. Mostaghaci
Atlantic Research Laboratory
National Research Council
Halifax, Nova Scotia

Symposium organized by the Materials Engineering Section of
The Metallurgical Society of CIM

28th ANNUAL CONFERENCE OF METALLURGISTS OF CIM
28ᵉ CONFÉRENCE ANNUELLE DES MÉTALLURGISTES DE L'ICM

*In order to make this volume available as economically and
as rapidly as possible, the authors' typescripts have been
reproduced in their original forms. This method
unfortunately has its typographical limitations but it is
hoped that they in no way distract the reader.*

Foreword

With the growing interest in the use of ceramics as structural components, and the need to use them in combination with metals (both for joining purposes and as the reinforcement material for metallic matrices), it has become important to re-evaluate ceramic-metal compatibility and properties of cermet products. The goal is to combine the advantageous properties of both metals and ceramics.

The suggestion that a symposium on Advances in Ceramic and Metal Matrix Composites would be an excellent forum within the Annual Conference of Metallurgists of CIM arose out of discussions with colleagues in the General Organizing Committee of the 28th Annual Conference of Metallurgists in early 1988. There was no doubt that such a meeting would be both very valuable and timely. Scientific and technological achievements in the field of both ceramic and metal matrix composites have become quite considerable in recent years. For a subject of this nature having both an academic and a strong technological content, close contact with relevant ongoing work in research institutes, and university, industrial and government laboratories was required.

As a result of this effort, the present book was compiled. It contains the papers presented at the First International Symposium on Advances in Processing and Application of Ceramic and Metal Matrix Composites, held in conjunction with the 28th Annual Conference of Metallurgists of CIM, Halifax, August 20-24, 1989. It represents the current achievements of two of the most important fields in materials research, and serves as an indicator of the interactions between ceramics and metals.

Now it is time to say thanks to all whose help has made the program and the proceedings a success. Many people come to mind. I am very grateful to Dr. Roger Foxall, Director of the Atlantic Research Laboratory, for his permission to use the facilities, and clerical assistance at ARL, and to Dr. Stirling Whiteway for invaluable assistance in reviewing the papers. I have also to acknowledge my deep indebtedness to Miss Michelle Lamontagne, ably assisted by Miss Vicky Wagner, Mrs. Dian Marciniak, Mrs. Debbie MacDonald and Mrs. Beth Garside at the Atlantic Research Laboratory, for their calm efficiency in dealing with a very large volume of correspondence and paper-work, and in the typing of many sections of this proceedings. I also extend my thanks to all the authors, without whom this volume could not have materialized.

Hamid Mostaghaci
Halifax, August 1989

Si₃N₄ whisker synthesis and effect of gas phase composition on Si₂N₂O formation

Harue Wada

Department of Materials Science and Engineering, University of Michigan, Ann Arbor, Michigan 48109, U.S.A.

ABSTRACT

Single crystal Si_3N_4 whisker was synthesized by the carbothermal reduction of SiO_2 under N_2 gas flow. The Si_3N_4 whisker was formed through the VS mechanism. Si_3N_4 was first formed as a granule, typically a polycrystalline, and then grown as a single crystal whisker from the {100} plane of the granule along the <210> direction. Lattice parameters measurements and microanalysis of Si/Al ratio both identified the Si_3N_4 whisker as β'-Sialon with Z value ranging from 0.8 to 1.1. Increasing N_2 gas flow rates increased yield of Si_3N_4 whisker, but Si_2N_2O was also formed during the Si_3N_4 whisker synthesis. The Si_2N_2O formation was limited to a bottom area of the charged powders. The formation of Si_2N_2O phase is closely related to the $[p_{SiO}/p_{N_2}]$ ratio and p_{O_2} in the gas phase. Stability of phases among $Si_3N_4/Si_2N_2O/SiC$ is calculated as a guideline to control the Si_2N_2O formation. To suppress Si_2N_2O, the $[p_{SiO}/p_{N_2}]$ ratio must be lower than that of the phase boundary in the Si_3N_4/Si_2N_2O equilibrium, whereas it must be higher than that of the phase boundary in the SiC/Si_2N_2O equilibrium. The formation of Si_2N_2O was caused most likely due to a fluctuation in the $[p_{SiO}/p_{N_2}]$ ratio in the gas phase surrounding the lower area of the charged materials.

INTRODUCTION

Ceramic whiskers, offering the advantages of high melting points, low densities and high moduli, have become important reinforcing materials in both ceramic-matrix composites [CMC] and metal-matrix composites [MMC]. A single step process has been developed for ceramic whiskers synthesis based on the phase stability of the Si-C-N-O system and reported [1,2]. In this report, the synthesized single crystal Si_3N_4 and β'-sialon whiskers are analyzed. Localized formation of Si_2N_2O phase is discussed based on the $[p_{SiO}/p_{N_2}]$ ratio in the gas phase.

EXPERIMENTAL WORK

About 3 grams of silica, carbon and halide ($3NaF \cdot AlF_3$ or NaF) mixture with an atomic ratio of Si/C/Na = 1/3/1 was charged to a graphite tube inside a horizontal graphite reaction chamber, which was directly connected to a gas inlet at one end and an outlet at the other end. The graphite reaction chamber was placed in a mullite tube. A high purity (N_2 + 3% H_2) gas mixture was further purified through a $Mg(ClO_4)_2$ column, then introduced directly into the graphite reaction chamber. The gas flow rate was controlled by a Matheson 602 type flow meter, which had been calibrated by the bubble method against Ar and (Ar + H_2) gases. Four levels of flow rate were applied in this study: 25, 50, 75 and 100 cc/min.

All the reactions were carried out at 1623 K for 10 hours. The temperature was measured by a Pt/Pt-10% Rh thermocouple calibrated against the melting point of Au. Upon the completion of reaction, the remaining carbon was evaluated by oxidizing in air at 973 K to determine approximate reaction yield. For the purpose of comparisons, one run was carried out with pure Si instead of silica as the starting material.

The reaction products were identified by X-ray diffraction. Pure silicon was used as an internal standard to determine the lattice constants. The morphology and composition of whiskers were investigated by SEM (Hitachi-S-520) and TEM (Jeol 2000-FX), respectively. The growth direction and the composition of whiskers were analyzed by electron diffraction and micro analysis, respectively. The exhaust was led into a bubbler containing a saturated $PbCl_2$ solution and the fluorine in the exhaust was collected as PbClF precipitate.

In selected runs, the oxygen partial pressure was measured continuously during the reaction by a ZrO_2(CaO) solid electrolyte [2]. The exhaust gas in these runs was also collected at certain time intervals for CO/CO_2 analysis by gas chromatography.

RESULTS AND DISCUSSIONS

Synthesis

Whiskers were formed at the original powder bed and around the wall of graphite tube. Figure 1 shows a typical product before carbon burning. White wool-like whiskers had formed at the upper part, while the lower part was a mixture of short whiskers and powders containing approximately 40 wt% of carbon. The letter B shown in Fig. 1 is an area between them and locates at the lower end of the upper whiskers.

Figure 2 is a TEM micrograph of the whiskers grown at the upper part. These whiskers are transparent and identified by XRD as β'-sialon. The diameters of the whiskers are in a range from 0.5 to 1.2 μm, and the lengths are on the order of millimeters. The bottom part comprises short whiskers and powders, and was identified as a mixture of β'-sialon and Si_2N_2O. Figure 3 shows the cross section of a whisker. Most of the whiskers have rectangular cross sections. The fact that no droplets were ever observed at whisker tips suggests that the whisker growth was through the gas/solid (VS) mechanism and the liquid phase was not involved. Typically, a polycrystalline was found at the root from which the whisker grew along the <210> direction as shown in Fig. 4. Sometimes a whisker stemmed from a single crystal, and both the whisker and the single crystal have the same orientation, with <210> as the growth direction. It can be concluded that Si_3N_4 was first formed as a granule (either polycrystalline or single crystal), and then grew in a whisker form from the {100} plane of the granule along the <210> direction.

Figure 5 shows a typical X-ray energy spectrum of a β'-sialon whisker. The Si K_a and Al K_a peaks are clearly seen but no sodium peaks were detected. The Si/Al ratio was determined by using the equation, $C_{Si}/C_{Al} = K_{Si-Al} \cdot I_{Si}/I_{Al}$, where C is element wt%, I is characteristic X-ray intensity and K is Cliff-Lorimer factor. A K_{Si-Al}=1.002 was used in
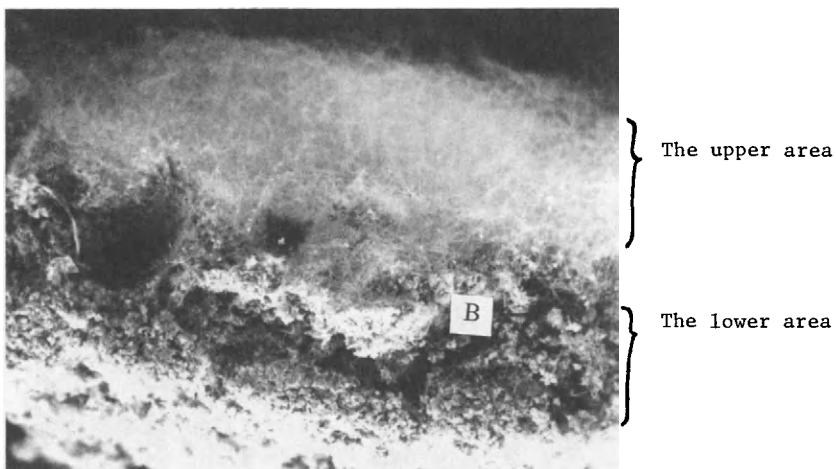
Figure 1. Reaction products before carbon removal.
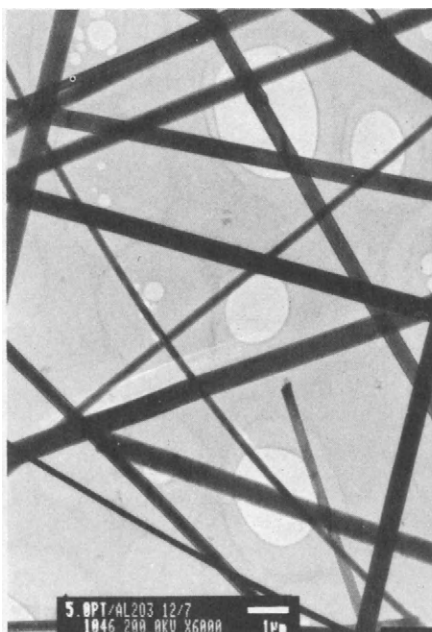
Figure 2. TEM micrograph of β'-sialon upper whiskers.
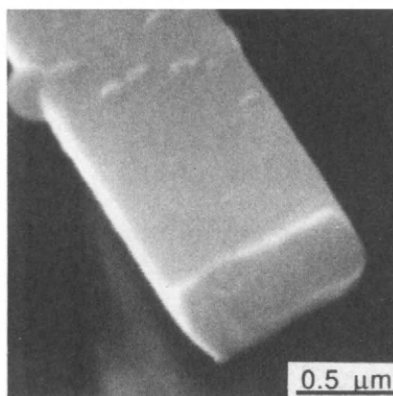
Figure 3. SEM micrograph of cross section of β'-sialon whisker.

Figure 4. SEM micrograph of β'-sialon whisker with polycrystalline root.
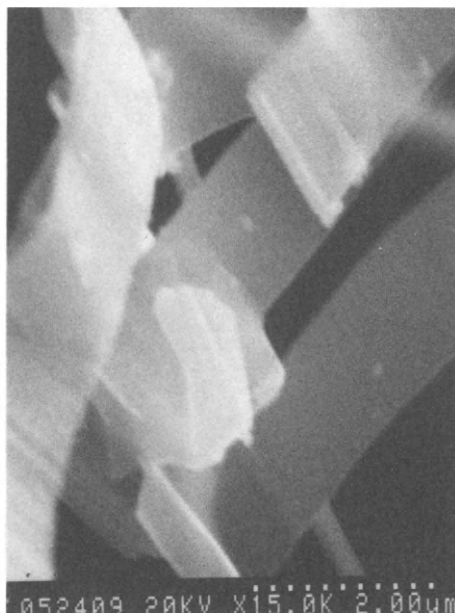
Figure 6. SEM micrograph of α-Si3N4 whiskers.
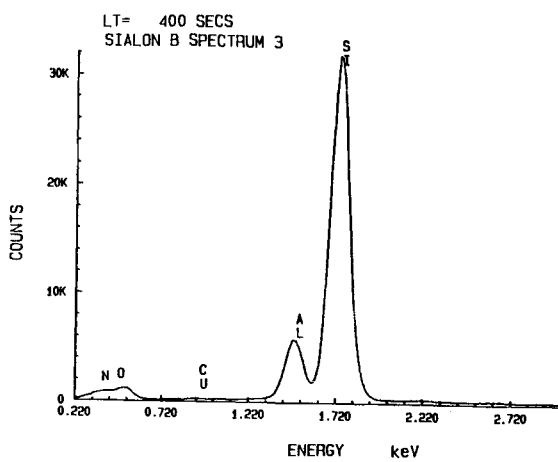
Figure 5. Typical X-ray spectrum from β'-sialon whisker.

this study. Based on the measured Si/Al atomic ratio, the Z value of β'-sialon ($Si_{6-Z}Al_ZO_ZN_{8-Z}$) was determined to be in the range from 0.8 to 1.1. The lattice parameters of β'-sialon are closely related to the Z value, as demonstrated by Jack [3] and Hohnke and Tien [4]. Our results are in reasonable agreement with these studies.

With [3NaF•AlF3] as the molten bath, β'-sialon was the main product; however, when [NaF] substituted for [3NaF•AlF3], α-Si_3N_4 became the dominant phase. The α-Si_3N_4 whisker is easily distinguished by the ribbon-like morphology, as shown in Fig. 6, with about 1 μm in width and less than 0.1 μm in thickness. The growth direction of the α-Si_3N_4 whisker is <211>. The same morphology of α-Si_3N_4 whiskers was also reported by other studies [5,6].

Reaction Mechanism

As discussed previously, the whisker formation is most likely through the VS mechanism. There are three possible reaction routes that could be responsible for the Si_3N_4 whisker formation:

$$3SiO(g) + 3CO(g) + 2N_2(g) = Si_3N_4(\beta) + 3CO_2(g) \qquad (1)$$
$$\Delta G°_1 = -1437.972 + 0.942T, \qquad kJ/mole \text{ of } Si_3N_4 \qquad (1-1)$$

$$3SiO(g) + 3C(s) + 2N_2(g) = Si_3N_4(\beta) + 3CO(g) \qquad (2)$$
$$\Delta G°_2 = -952.356 + 0.438T, \qquad kJ/mole \text{ of } Si_3N_4 \qquad (2-1)$$

$$3SiF_4(g) + 2N_2(g) = Si_3N_4(\beta) + 6F_2(g) \qquad (3)$$
$$\Delta G°_3 = 3920.19 + 0.018T, \qquad kJ/mole \text{ of } Si_3N_4 \qquad (3-1)$$
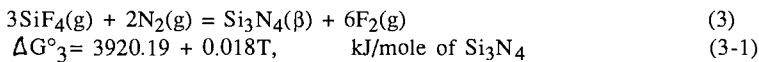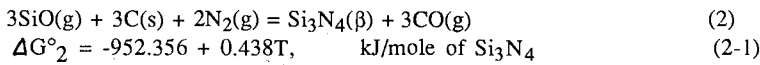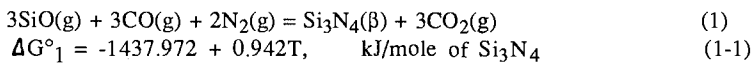
All the standard free energies of formation used in this study were obtained from JANAF Tables [7], except that of β-Si_3N_4 and $Si_2N_2O(s)$, which were from the same source as described in Ref. [1]. The contribution from Eq. (3) is considered to be insignificant for the following reasons: (1) $\Delta G°_3$ =3,949 kJ at 1623 K which is much higher than those of Eq. (1) and Eq. (2), 91 kJ and -241 kJ, respectively, and (2) the fluorine recovery as the PbClF precipitate was always about 40% despite the fact that the Si yield changed as reaction conditions were changed. However, the evolution of SiF_4 from the melt, even small, may enhance the evolution of SiO(g). The necessary presence of solid carbon at the reaction site, i.e., the whisker tip, rules out the possibility of the gas-solid reaction of Eq. (2) as the major reaction, especially when the whiskers were as long as millimeters; furthermore, α-Si_3N_4 whiskers have been found on an alumina substrate where solid carbon is absent. Therefore, Eq. (1) is the most probable reaction for the Si_3N_4 whiskers formation. For the crystal grown from the vapor phase, it is generally believed that the growth form is closely related to the supersaturation of gaseous components. In general, a lower supersaturation favors the formation of whiskers, whereas a higher supersaturation ratio would results in powders. Since the gas-phase reaction of Eq. (1) is the route for Si_3N_4 formation, the growth form of Si_3N_4 is closely related to the partial pressures of N_2, SiO and CO/CO_2.

Figure 7 is a SEM micrograph of whiskers grown in the area B of Fig. 1. Some whiskers have knuckles. A SEM/EDX analysis showed that both whiskers and knuckles are β'-sialon. The knuckles were polycrystalline, while the whisker portions between knuckles were single crystals. It seems that the anisotropic whisker growth and the isotropic polycrystalline growth have occurred alternately in these particular whiskers. The fact that these whiskers were found only in the area B, suggests that the formation of these whiskers is location-related. The gas composition is expected to fluctuate during the

formation of whiskers in this area, and it was probably responsible for the change of growth form, i.e., from whisker to knuckle and vice versa.

The importance of SiO gas for Si_3N_4 whisker formation was clearly demonstrated by replacing SiO_2 with Si as the starting material: no whiskers were formed and the carbon consumption was only one-third of that in the SiO_2 cases of the same reaction conditions. The major morphology of the product was the hexagonal particulate of a mixture of α-, β- Si_3N_4 and Si which was unreacted remaining Si.

The formation of β'-sialon can be expressed as the following reaction [8],

$$(6-Z)SiO(g) + (4-Z/2)N_2(g) + (6-2Z)CO(g) + ZAl(g)$$
$$= Si_{(6-Z)}Al_ZO_ZN_{(8-Z)} + (6-2Z)CO_2(g) \qquad (4)$$
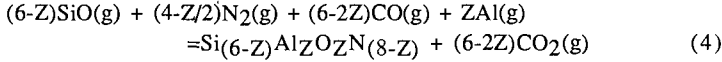
Effect of [p_{SiO}/p_{N_2}] Ratio on Phase Stability

As shown in Fig 1, a localized formation of silicon oxynitride was observed even under low oxygen partial pressures.   The formation of Si_2N_2O phase was limited to the lower area of charged materials.   The upper area, on the other hand, showed wool yarn-like β- Si_3N_4 or sialon whiskers.   Formation of Si_2N_2O is observed not only in the whisker synthesis but also in other Si_3N_4 ceramic processings, such as reaction bonding and sintering. When $a_C=1$, β-Si_3N_4 and Si_2N_2O are in equilibrium from 1400 to 1650 K under $p_{N_2} = 0.1$ MPa and $p_{O_2} = 10^{-21}$ -10^{-22} MPa range[1]. The β-Si_3N_4 phase becomes a stable phase with lower oxygen partial pressures, whereas Si_2N_2O is a stable phase with higher oxygen partials pressures [1].   There were two possibilities that causes the Si_2N_2O formation in the lower area in the present study: (1) the flowing nitrogen gas might have had less accessibility to the lower area than the upper area, or (2) SiO partial pressure was higher in the lower area compared to that in the upper area.   In either case, the [p_{SiO}/p_{N_2}] ratio might not be the same in these two areas.

Effect of the [p_{SiO}/p_{N_2}] ratio on the phase stability was calculated for β-Si_3N_4, Si_2N_2O and β-SiC phase, while SiO_2 was not included because it is not an equilibrium phase when β- Si_3N_4 is a stable phase [1,2]. The main components of the gas phase assumed as N_2, O_2, SiO and CO/CO_2. The standard states of activities are pure solids components for all the solid phases, and 1 atm pure gases for all the gases and temperature is 1623 K.

β-Si_3N_4/Si_2N_2O Equilibrium

Since the CO/CO_2 ratio has been found very close to its equilibrium value in the whisker synthesis [2], an overall reaction of β-Si_3N_4 formation from SiO(g) can be expressed as Eq. (5) by combining the following two reactions, $3SiO (g) + 3CO (g) + 2N_2 (g) = Si_3N_4(\beta) + 3 CO_2 (g)$ and $CO_2 (g) + C = 2CO (g)$,

$$3 SiO (g) + 2N_2 (g) + 3C = Si_3N_4(\beta) + 3 CO (g) \qquad (5)$$
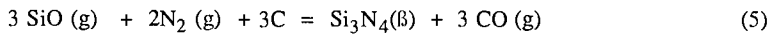
$$\log K_5 = \log \{ a_{Si_3N_4} p_{CO}^3 / p_{SiO}^3 p_{N_2}^2 a_C^3 \} = 49,747/T - 22.88$$

where p_X's and a_X's are the partial pressures and the activities of X, respectively. When Si_3N_4 is a stable solid phase, $a_{Si_3N_4} =1$, then p_{SiO} can be obtained from Eq. (5) as,

$$\log p_{SiO} = -1/3 \log K_5 - 2/3 \log p_{N_2} + \log p_{CO} - \log a_C \qquad (5-1)$$

The same calculation is applied to the Si_2N_2O formation as,

$$2 \; SiO \; (g) \; + \; N_2 \; (g) \; + \; C \; = \; Si_2N_2O \; (s) \; + \; CO \; (g) \qquad\qquad (6)$$
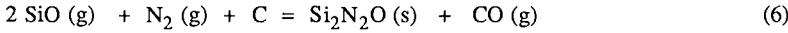
$$\log K_6 \; = \; 29{,}211/T \; - \; 10.81$$

and $\log p_{SiO}$ is expressed by the following equation for $a_{Si_2N_2O} = 1$,

$$\log p_{SiO} = 1/2[\; - \log K_6 \; - \log p_{N_2} \; + \; \log p_{CO} \; - \log a_C] \qquad\qquad (6\text{-}1)$$

There is a pair of p_{SiO} and p_{N_2} with the known values of a_C and p_{CO} for each reaction, Eq. (5) and Eq.(6). Figure 8 shows the calculated pairs of $\log p_{SiO}$ and $\log p_{N_2}$ at $a_C = 1$ for both Si_3N_4 and Si_2N_2O formations. When Si_3N_4 and Si_2N_2O are in equilibrium, the two lines share the same p_{N_2} and p_{SiO} values. From Eqs.(5-1) and (6-1), the equilibrium p_{N_2} is obtained as a function of p_{CO} and a_C as,

$$\log p_{N_2} \; = \; 6 + 3 \log p_{CO} \; - \; 3 \log a_C \qquad\qquad (7)$$

Figure 8 shows that the Si_3N_4/Si_2N_2O are in equilibrium at $p_{N_2}=10^3$ when $p_{CO}=10^{-1}$, while it changes to $p_{N_2}=10^{-3}$ when p_{CO} is 10^{-3}, i. e., Si_3N_4 becomes more stable with decreasing p_{CO} if the carbon activity is kept constant. Because one of the controllable variables in the experiment is oxygen pressure, the equilibrium p_{O_2} is calculated as follows,

$$Si_3N_4 \; (\beta) \; + \; 3/2 \; O_2 \; (g) \; = \; 3 \; SiO \; (g) \; + \; 2N_2 \; (g) \qquad\qquad (8)$$
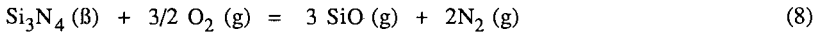
$$\log K_8 \; = \; \log \{ \; p_{SiO}^3 \; p_{N_2}^2 / \; a_{Si_3N_4} \; p_{O_2}^{3/2} \; \} \; = -31{,}382/T + 36.04$$

$$\log p_{O_2} \; = \; -2/3 \log K_8 \; + \; 4/3 \log p_{N_2} \; + \; 2 \log p_{SiO} \qquad\qquad (8\text{-}1)$$

Figure 9 shows $\log p_{N_2}$ and corresponding p_{CO} and p_{SiO}. The Si_3N_4 phase is stable on the upper side of the $\log p_{N_2}$, while Si_2N_2O is the stable phase on the other side of the line. The Si_3N_4/Si_2N_2O are in equilibrium on the $\log p_{N_2}$ line which can be written as,

$$Si_3N_4 \; (\beta) \; + \; O_2 \; (g) \; = \; Si_2N_2O \; (s) \; + \; SiO \; (g) \; + \; N_2 \; (g) \qquad\qquad (9)$$
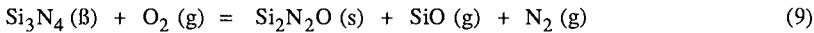
$$\log K_9 = \log\{ \; a_{Si_2N_2O}/a_{Si_3N_4} \; \} + \log \; \{p_{SiO} \; p_{N_2}/p_{O_2}\} \qquad\qquad (9\text{-}1)$$

Since Si_3N_4 and Si_2N_2O form practically no solid solution, there are only three possibilities for the first term of Eq. (9-1) : (a) If the two phases are in equilibrium, $\log\{a_{Si_2N_2O}/a_{Si_3N_4}\}= 0$; (b) if Si_2N_2O is the only stable phase, $\log\{a_{Si_2N_2O}/a_{Si_3N_4}\} > 0$; and (c) if Si_3N_4 is the only stable phase, $\log\{a_{Si_2N_2O}/a_{Si_3N_4}\} < 0$. To suppress the Si_2N_2O formation, which corresponds to the case (c), the second term must be higher than that of the Si_3N_4/Si_2N_2O equilibrium, either by lower p_{O_2} or higher $[p_{SiO} \; p_{N_2}]$, which
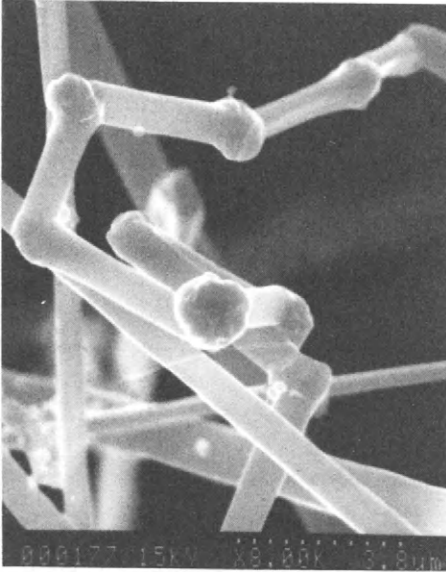
Figure 7.   SEM micrograph of whiskers
            with knuckles.
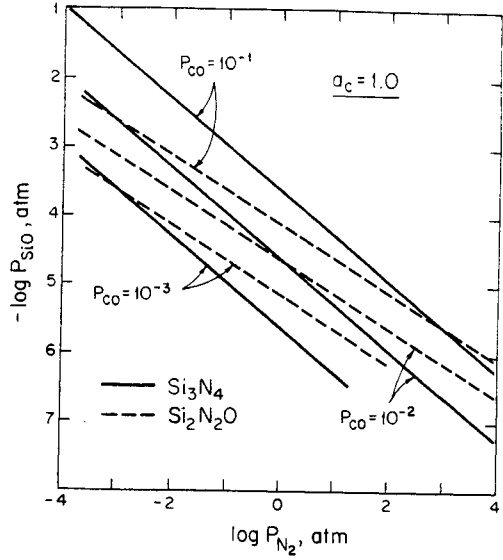
Figure 8. Log p_{N_2} and log p_{SiO} for
          β-Si_3N_4/ Si_2N_2O at 1623K.
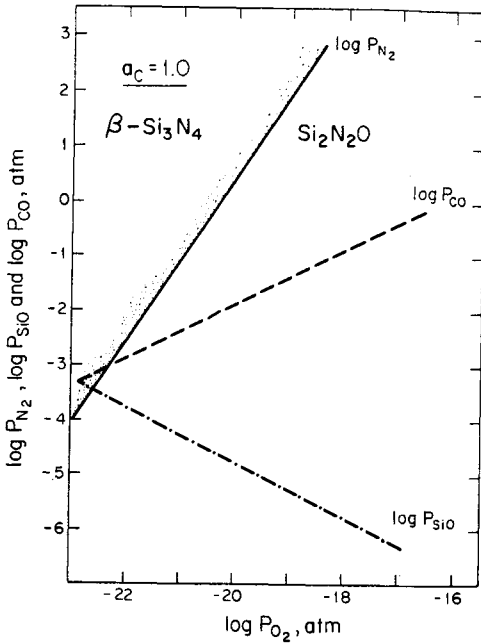
Figure 9.   Equilibrium p_{N_2} and corres-
            ponding p_{CO} and p_{SiO} for
            β-Si_3N_4/Si_2N_2O.
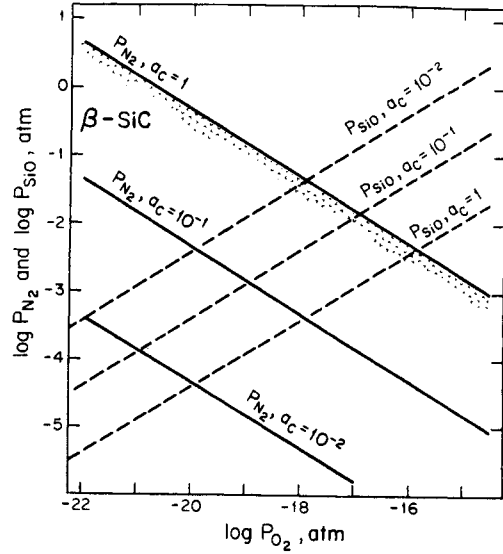
Figure 10. Equilibrium p_{N_2} and corres-
           ponding p_{SiO} for SiC/Si_2N_2O.

implys   lower $[p_{SiO}/p_{N_2}]$ ratios as seen in Fig. 9.   The carbon activity has no direct effect on that.   Therefore, to suppress the Si_2N_2O phase formation, the $[p_{SiO}/p_{N_2}]$ ratio must be maintained in adequately low as well as keeping the oxygen pressure low.

SiC/ß-Si₃N₄ Equilibrium

A SiC formation can be expressed by the following reaction:

$$SiO\ (g)\ +\ 2C\ =\ SiC\ (\beta)\ +\ CO\ (g) \tag{10}$$

$$\log K_{10} = \log\ \{\ a_{SiC}\ p_{CO}/p_{SiO}\ a_C^2\ \}\ =\ 4{,}277/T\ -\ 0.16$$

When SiC is a stable solid phase, $a_{SiC} = 1$, and $\log p_{SiO}$ is calculated as,

$$\log p_{SiO} = -\log K_{10} + \log p_{CO} - 2 \log a_C \tag{10-1}$$

When both the Si_3N_4 and SiC phases are coexisting, $a_{SiC} = a_{Si_3N_4} = 1$. By combining Eqs. (5-1) and (10-1), the equilibrium p_{N_2} is obtained as,

$$\log p_{N_2} = -0.17 + 3/2 \log a_C \tag{11}$$

A pair of equilibrium p_{N_2} and p_{SiO} is determined for each set of a_C and p_{CO}.
The oxygen partial pressure is calculated as follows:

$$SiC\ (\beta)\ +\ O_2\ (g)\ =\ SiO\ (g)\ +\ CO\ (g) \tag{12}$$
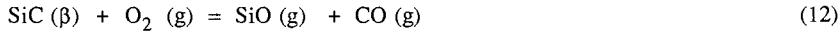
$$\log K_{12} = \log\ \{\ p_{SiO}\ p_{CO}/a_{SiC}\ p_{O_2}\ \}\ =\ 7{,}966/T\ -\ 8.93$$

The equilibrium p_{O_2} can be calculated for each pair of equilibrium p_{SiO} and p_{CO} as,

$$\log p_{O_2} = -13.69 + \log p_{SiO} + \log p_{CO} \tag{12-1}$$

The Si_3N_4/SiC equilibrium can be expressed by the following equation,

$$Si_3N_4\ (\text{ß})\ +\ C\ +\ O_2\ (g)\ =\ SiC\ (\beta)\ +\ 2SiO\ (g)\ +\ 2N_2\ (g) \tag{13}$$
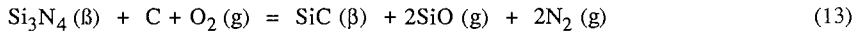
$$\log K_{13} = \log\ \{\ a_{SiC}/a_{Si_3N_4}\ \} + \log\ \{\ p_{SiO}^2\ p_{N_2}^2/p_{O_2}\ a_C\ \}$$

Because log $\{\ a_{SiC}/a_{Si_3N_4}\ \}$ < 0 when Si_3N_4 is a stable phase, the values of $[p_{SiO}^2\ p_{N_2}^2/a_C]$ must be higher than those at the Si_3N_4/SiC equilibrium at a known p_{O_2}. The $\{p_{SiO}^2$ $p_{N_2}^2/a_C\ \}$ is basically controlled by a_C: it is higher with the lower a_C, while the $[p_{SiO}/p_{N_2}]$ ratio decreases.

SiC/Si₂N₂O Equilibrium

The same calculation is carried out for the SiC/Si_2N_2O equilibrium.   A pair of equilibrium p_{SiO} and p_{N_2} are calculated by combining Eqs. (6-1) and (10-1), while log p_{O_2} is calculated by Eq. (12-1) for these p_{SiO}'s.   The equilibrium p_{N_2} is a function of both p_{CO} and a_C,

$$\log\ p_{N_2}\ =\ -2.23\ +\ 3\log a_C\ -\ \log p_{CO} \tag{14}$$

The final result is summarized in Fig. 10. The SiC is a stable solid phase along the lower side of the $\log p_{N_2}$ line at each carbon activity, while the Si_2N_2O phase is stable along the upper side of the line. The equilibrium can be expressed as,

$$SiC\ (\beta)\ +\ N_2\ (g)\ +\ SiO\ (g)\ =\ Si_2N_2O\ (s)\ +\ C \tag{15}$$
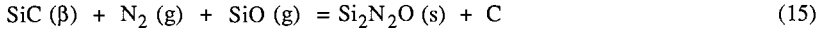
$$\log K_{15} = \log\ \{\ a_{Si_2N_2O}/a_{SiC}\}\ +\ \log\ \{\ a_C/p_{SiO}\ p_{N_2}\ \} \tag{15-1}$$

When SiC is the only stable solid phase, the first term of Eq. (15-1) must be $\log \{a_{Si_2N_2O}/a_{SiC}\} < 0$, which requires that either a_C must be higher or $[p_{SiO}/p_{N_2}]$ ratios must be lower than those at the SiC/Si_2N_2O equilibrium. Figure 10 shows that $[p_{SiO}\ p_{N_2}] =$ constant as far as a_C = constant and decreases with decreasing a_C, while $[p_{SiO}/p_{N_2}]$ ratio increases with the decresing a_C. Therefore, to suppress the Si_2N_2O formation, the $[p_{SiO}/p_{N_2}]$ ratio must be higher than that in the SiC/Si_2N_2O equilibrium, but keeping a_C higher is more effective in ensuring the formation of only ß-SiC phase.

$[p_{SiO}/p_{N_2}]$ Ratio

A calculation of gas phases has shown that the solid phase stability is closely related to the $[p_{SiO}/p_{N_2}]$ ratio. Logarithms of $[p_{SiO}/p_{N_2}]$ ratios in the gas phase which is in equilibrium with either Si_3N_4/Si_2N_2O, Si_3N_4/SiC or Si_2N_2O/SiC are plotted against $\log p_{O_2}$ in Fig. 11 for three a_C levels. The values of the $[p_{SiO}/p_{N_2}]$ ratio are increased more than 100 times when a_C decreases 10 times. The Si_3N_4 phase is a stable phase in lower sides of the lines at all levels of carbon activity. At a_C= 1 and $\log p_{O_2}$ = -20, the Si_3N_4 phase is a stable phase below the solid line, and the Si_2N_2O phase becomes a stable phase until $\log [p_{SiO}/p_{N_2}]$ reaches to the next solid line at about $\log [p_{SiO}/p_{N_2}]$ = -4, above which the SiC phase is the most stable phase.

In our nitride whisker formation, SiO (g) is produced by the decomposition of SiO_2(s). A value of p_{SiO} is estimated as $\log p_{SiO}$ = -2.53 atm at 1623 K by substituting $\log p_{CO}$ = -1.7 [2], and a_C= 1 into the following equation:

$$SiO_2\ (s)\ +\ C\ =\ SiO\ (g)\ +\ CO\ (g) \tag{16}$$

$$\log K_{16}\ =\ -35,261/T\ +\ 17.50$$

There are two possible causes for the Si_2N_2O formation in the lower area of charged material: p_{N_2} and p_{SiO}. The nitrogen pressure in the lower area can be one of the following: the same p_{N_2} as flowing gas, or the same with the equilibrium p_{N_2} of the Si_3N_4/Si_2N_2O two solid phase equilibrium, or the same with the equilibrium p_{N_2} of the Si_2N_2O single solid phase formation. The values of p_{N_2} are calculated as $\log p_{N_2}$ = -0.013 for the first case, and $\log p_{N_2}$= 0.9 for the second case and $\log p_{N_2}$= -3.8 for the third case. Since the N_2 gas pressure was $\log p_{N_2}$= -0.013 atm, all three cases were possible, but the first and second cases were more likely occurred than the third case because the mixture of Si_3N_4 + Si_2N_2O was always obtained in the lower area.

The $[p_{SiO}/p_{N_2}]$ ratios are estimated for each case as $\log [p_{SiO}/p_{N_2}]$ = -2.5, -3.4 and 1.3, reasectively. From Fig. 11, it can be concluded that either the first and second cases can
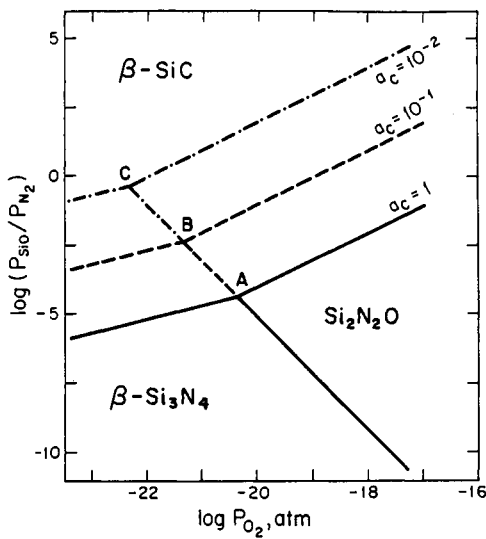
Figure 11. Effect of $[p_{SiO}/p_{N_2}]$ ratio on the phase stability of Si_3N_4, Si_2N_2O and SiC at 1623 K.

probably occur in the lower area depending on a fluctuating SiO (g) evolution.   It might not be caused only by the fluctuation in SiO(g) but possibly affected by a fluctuation in p_{CO} as well.   In the the third case, the estimated $[p_{SiO}/p_{N_2}]$ ratio is far beyond the Si_2N_2O stable area when log p_{N_2}= -3.8, and SiO_2 must remain as a stable phase in this $[p_{SiO}/p_{N_2}]$ ratio.   However, solid SiO_2 phase was never found at the end of the whisker formation. The higher $[p_{SiO}/p_{N_2}]$ ratio consequently increases p_{O_2} in the lower area.   In Fig. 11, the lowest oxygen pressures, which correspond to the log $[p_{SiO}/p_{N_2}]$ = -2.5 and -3.4, are in the range of log p_{O_2}= -18.5 to -19.5 atm.

To confirm the effect of gas phase composition on the phase stability, a mixture of ß'-sialon and o'-sialon (= Al containing Si_2N_2O) powders formed at the lower area was transferred to a graphite boat and spreaded thinly.   The mixture then was heat treated at 1623 K for 7 hours under 1 atm nitrogen gas.   All oxynitride powders were converted to nitride after the annealing.   Analyses of these powders are being continued.

References
1) H. Wada, M. J. Wang and T. Y. Tien, J. Am. Ceram. Soc.,**71**(1988), p. 837.
2) H. Wada and M. J. Wang, Proceedings of International Conference on Whisker- and Fiber-Toughened Ceramics, Oak Ridge, ASM International, 1988, p. 63.
3) K. H. Jack, J. Mater. Sci.,**11**(1976), p. 1135.
4) H. Hohnke and T. Y. Tien, "Progress in Nitrogen Ceramics", Ed. by F. L. Riely, Martinus Nijhoff Publishers,1983, p.101.
(5) V. N. Gribkov, V. A. Silaev, B. V. Schetanov, E. L. Umantsev and A. S. Isaikin, Soviet Physics-Crystallography, **16** (1972), p. 852.
(6) A. Szweda, A. Hendry and K. H. Jack, "Special Ceramics", **7**, Ed. by J. Taylor and P. Popper, British Ceramics Society, 1981, p.107.
7) JANAF Thermochemical Tables, 3rd Edition, Am. Chem. Soc., Am. Inst. Phy. and NBS, 1986.
8) H. Wada, In press, Proceedings of International Sym. Advanced Structural Materials-Structural Ceramics, CIM, 1988.
9) H. Wada and M. J. Wang, Submitted to J. Mater. Sci., 1988; To be presented at the Amer. Cer. Soc. Annual Meeting, 1989.

The effects of surface treatment of SiC whiskers on rheological properties of their aqueous suspensions

I. Melluish
Department of Materials Science and Engineering, McMaster University,
Hamilton, Ontario, Canada, L8S 4L7

K.J. Konsztowicz
Atlantic Research Laboratory, National Research Council Canada,
Halifax, Nova Scotia, Canada, B3H 3Z1

ABSTRACT

Casting from suspension is an important technique for making dense ceramic matrix composites. However, the tendency of short fibres and whiskers to agglomerate is a major difficulty in preparing dense (over 50 vol % solids), yet homogenous, suspensions of such fibers with ceramic matrix powders. In the technique of preparing composite suspensions by mixing two or more independent slurries, the rheological properties of whisker (fiber) suspensions became of primary importance.

In this study SiC whiskers were given a variety of surface treatments, and aqueous suspensions of a wide range of pH then were prepared. Viscosity and sedimentation measurements were performed. With proper surface treatment, stable aqueous suspensions of at least 15 vol % could be prepared without deflocculants at both pH 3 and 11. Values of the electrophoretic mobility of SiC suspensions are related to the spatial arrangement of the whiskers in suspensions, as assessed by SEM examination.

KEYWORDS

SiC whiskers, dense suspensions, homogeneity, surface impurities, viscosity, sedimentation, electrophoretic mobility, agglomeration.

INTRODUCTION

Increasing interest in application of new types of whiskers and fibres in advanced ceramic technology introduces many unusual problems due to the particular nature of these components, related mainly to their elongation and extraordinary specific surface development (Milewski, 1986).

Dispersion properties of fine particles in liquids rely on a complex balance between the Van der Waals forces of attraction of particles, electrostatic repulsion of ions adsorbed on their surfaces, and the forces of gravity (Roosen, Hausner, 1988). Since the chemistry of solid/liquid interface affects the dispersion properties to a large extent, experimental work has been carried out recently on SiC whisker suspension with the aim of improving whisker surface properties and, by these means, their dispersability.

Two basic approaches to the problem of removal of surface impurities can be described:

1. Oxidation, proposed by Adair et al (1988) based on the assumption that poor dispersion is mainly due to the presence of an excessive number of oxygen ions on $SiC_{(w)}$ surfaces.
2. Chemical treatment, used by Sacks and co-workers (1988), in order to remove leachable impurities, mainly Ca ions, believed to be the main reason for poor dispersability of $SiC_{(w)}$ in water.

According to Whitman and Feke (1986) the oxidation of fine SiC powders removes only the physisorbed species from exposed surfaces, and is not capable of removing the chemisorbed ones. These authors suggest that the chemisorbed impurities can be eliminated only by repeated dilution in acidic aqueous electrolytes. They defined the apparent point of zero-charge for fine SiC powders at pH $\approx$ 5.5 - 7.0.

The similar value of pH $\approx$ 7 has been given by Sacks et al for the isoelectric point (IEP) of SiC whiskers washed in HNO_3 and then in NH_4OH, followed by rinsing in deionized water. The zeta-potential values presented by these authors indicate that successful dispersion of SiC whiskers in water can be achieved either in acid (below pH = 4) or base range of pH (over pH = 11). The highest values of Z-potential can be found at even lower acidity, about pH = 2.5, but the increase of ionic strength of the solution destabilizes the whiskers.

Since the dispersion of SiC whiskers in the acidic range of water solutions carries many advantages, in particular when the whiskers subsequently have to be mixed with alumina powder suspension, the purpose of this work was to study in detail the conditions of dispersion of SiC whiskers in H_2O of the narrow acid pH range, between 2.5 and 4.4.

EXPERIMENTAL PROCEDURE

As-received SiC whiskers[1] were examined for sedimentation and viscosity in water suspensions with 10% and 20% solids content, and pH varying in the acid range. The pH values have been adjusted only by small additions of 0.1N HNO_3. Similar tests have been performed on SiC whiskers washed for 12h in acid (0,18N HNO_3) and base (0,15 N NH_4OH). Another batch of whiskers was processed in a similar way, by washing in acid and base, but additionally these whiskers have been rinsed in deionized H_2O several times until constant pH of their suspension was reached. Out of this latter batch, samples with solids content = 31 w/o were prepared by careful additions of small amounts of 0,1 N HNO_3 which brought the pH values to 2.5; 3; 3.5; 3.9; 4.4 respectively.

---

[1]Tateho, SCW 1

These samples were then centrifuged and small amounts were re-diluted (with pH adjustment) to the level of ∿300 p.p.m. in their respective supernatants for the measurement of electrophoretic mobility. Tenfold decrease of dilution, to ∿30 p.p.m. and subsequent vacuum filtering on a microporous membrane enabled the preparation of samples for SEM observations of dispersion of SiC whiskers at different pH values.

RESULTS AND DISCUSSION

<u>Sedimentation</u>

Measurements of sedimentation heights on as-received and washed-only (rinsed once) whiskers with solids contents 3 and 7 vol % and sedimentation times typical for ceramic powders (up to 300 min) did not give consistent results, irrespective of pH value. applied. Fig. 1 shows that these whiskers practically do not sediment at all, producing large lumps across the heights of the cylinders.
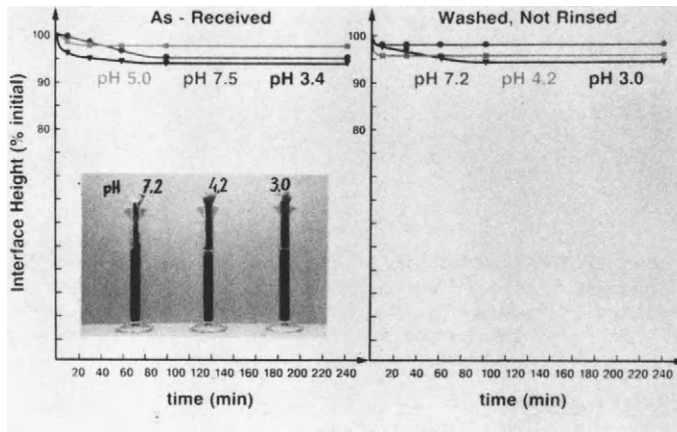
<u>**Figure 1**</u> Sedimentation test for SiC whiskers in water suspensions
left: as-received (solids content ∿ 3v/o); right: washed (solids
content ∿ 7v/o), at selected pH values.

Whiskers washed in HNO$_3$ acid and in NH$_4$OH base, then properly rinsed in deionized water to constant pH value show quite different sedimentation behaviour. Although it is rather difficult to determine sedimentation heights in normal times since there is no clear supernatant over the whiskers' cake, Fig. 2 shows that after a relatively long time approaching ∿1000 min, the interfaces can be seen in samples at pH 3 and 4. It is remarkable that only these suspensions with pH 3 and 4 (also pH 11 to some extent) are fluid and homogenous enough to be easily handled.
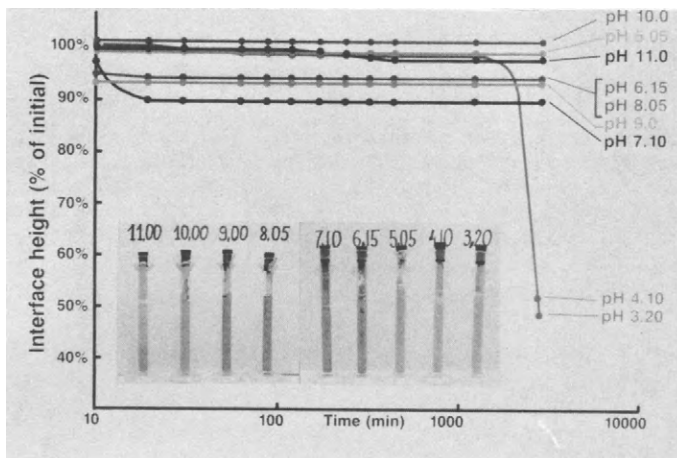
Figure 2 Sedimentation test of SiC whiskers washed in HNO_3 and NH_4OH, and
rinsed in deionized water to constant pH. The values of pH in
testing cylinders adjusted by small additions of O.1N HNO_3 or O.1N
NH_4OH only, in their respective ranges.

Fig. 3 indicates a dramatic change in the appearance of sedimentation samples
with pH 3 to 5. Suspension at pH 5 (left) is completely lumped, sample of pH 4
(middle) shows some heterogeneities and only the suspension at pH 3 (right) is
really homogenous.

The detailed sedimentation test of water suspensions of SiC (whiskers) in the
acid pH range between pH = 2.5 and pH = 4.4 confirms previously discussed
results and also the results of Sacks et al (1988), indicating that the longest
times of sedimentation, and the greatest sediment density can be obtained in
the acid range of water suspension.
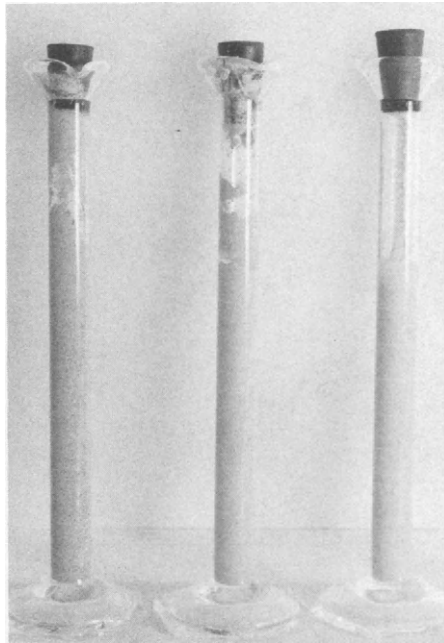
Figure 3 SiC whiskers in water (5.2v/o solids) after 1500 min of
         sedimentation, left: pH = 5.1; middle: pH = 4.1; right: pH = 3.2

Viscosity and Electrophoretic Mobility

Fig. 4 shows the results of viscosity measurements[2] for $SiC_{(whiskers)}$ water
suspensions with 15.4% solids content. These data prove that the samples with
pH=3 and 4 have the best dispersion, in particular the sample with pH=3.
Viscosity of water suspension with pH=4 is of the same order as that with
pH=11.

---

[2] Brookfield, model LVTD

10000

pH 6 →   □← pH 8

pH 10 →

η[mPa·s]

1000

pH 7 →   ← pH 5

100   ○ ←pH 11

                       ■ ←pH 4

                       ←pH 3

10

1   10   100   1000

SHEAR RATE [rad·s^{-1} x 10^2]
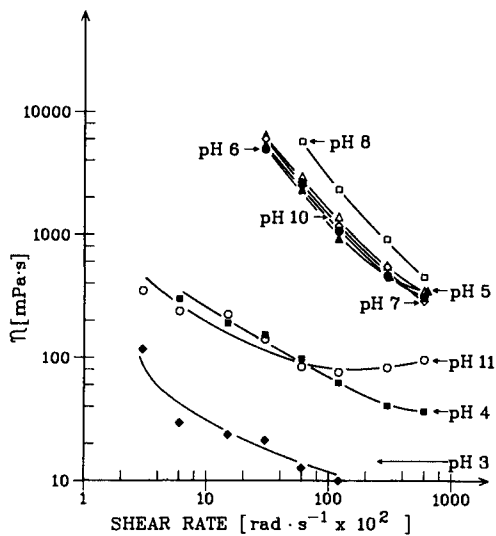
Figure 4 Viscosity of water suspensions of washed and rinsed SiC whiskers
          (15.4v/o solids) with different pH values.

The difference in viscosity between SiC$_{(w)}$ water suspension of pH 4 and 5 is
quite striking, as can be observed from the plot of viscosity vs. pH, Fig. 5.
This figure indicates also the dispersion compatability of SiC whiskers and
fine alumina powder[3] in acid pH range.

[3] Reynolds, RCHP-DBM
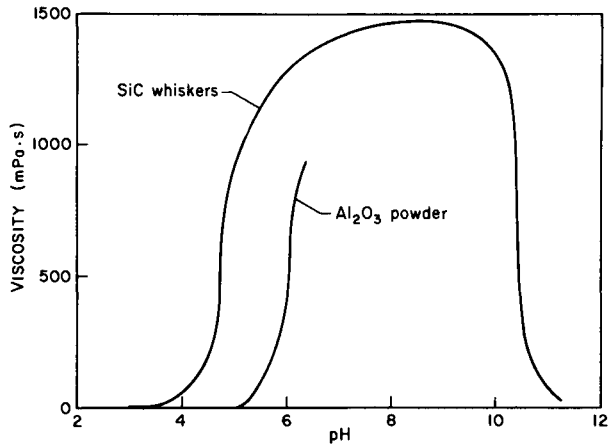
Figure 5 Compatability of dispersion of SiC whiskers and Al_2O_3 water suspensions in acid range of pH.

The results of the measurements of electrophoresis mobility[4] of SiC (whiskers) in water suspensions as a function of pH indicate their strong tendency to agglomerate with increasing pH (Fig. 6). It has to be noted, however that these data can not be considered unequivocally, since there is a substantial difference in behaviour of the particles in very diluted suspensions such as those used in electrophoretic mobility tests, and real suspensions with high solids content. In this latter case, the increase of ionic strength of the suspension with larger acid additions would lead to overlapping and deformation of electrostatic double layers on particle surfaces and loss of stability against flocculation.

---

[4] Rank Brothers, Mark III. Monoresearch Labs.
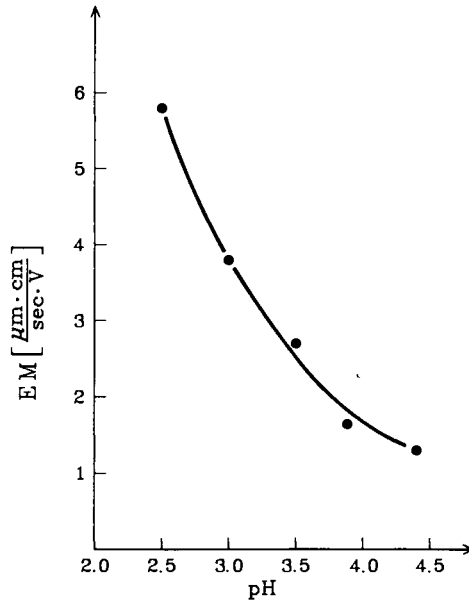
Figure 6 Electrophoretic mobility of diluted water suspensions (300 ppm) of SiC whiskers vs pH in acid range.

This tendency is very well confirmed by the values given on "Viscosity vs pH" plot (Fig. 7) for dense (31.4% of solids) SiC whiskers water suspensions in acid range. Despite the highest measured value of electrophoretic mobility (see Fig. 6) at pH 2.5, dense whisker suspension shows the viscosity much higher than that of pH=3. Further increase of viscosity follows the decrease of electrophoretic mobility, leaving a narrow "window" of practically useful pH values between 3 and 4 for the acceptable dispersion of SiC whiskers in water suspensions.
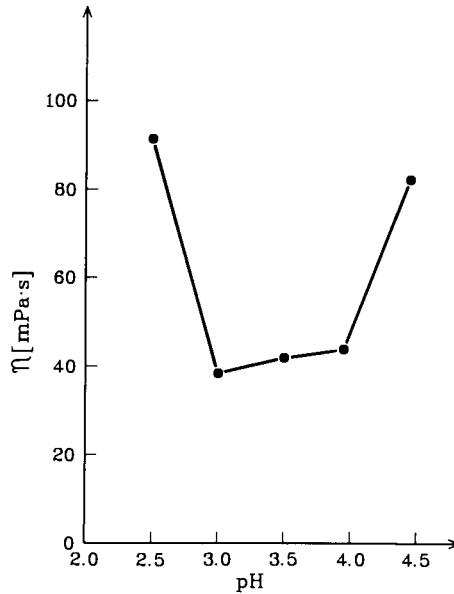
<u>Figure 7</u> Viscosity of dense water suspensions of SiC whiskers (31.3v/o) **in**
          acid range of pH.

<u>Microscopic Observations</u>

The SEM[5] study of dispersed powders confirms previously **described results.**
Fig. 8a is the image of the sample dispersed at pH=2.5. **Despite the good**
overall dispersions, the tendency to re-flocculation **due to the increased ionic**
strength seems to be obvious with whisker agglomerates of 10-20 μm of
diameter.

Fig. 8b proves that the lowest viscosity combined **with still good values** of
electrophoretic mobility results in the best **dispersion of SiC whiskers** at
pH=3. With only a slight increase of pH up to **3.5, the SiC whiskers** show the
tendency to agglomerate, in particular the **smallest ones (Fig. 8c).** There is
much less "free" whiskers of small size filtered **from diluted solution** at
pH=3.9. Most of them form "balls" of remarkable **size of dozens** of microns
(Fig. 8d). The increase of pH of water suspension to the value of 4.4 brings
about almost complete agglomeration of the whiskers (Fig. 8e).

---

[5] Jeol 2XA 35C
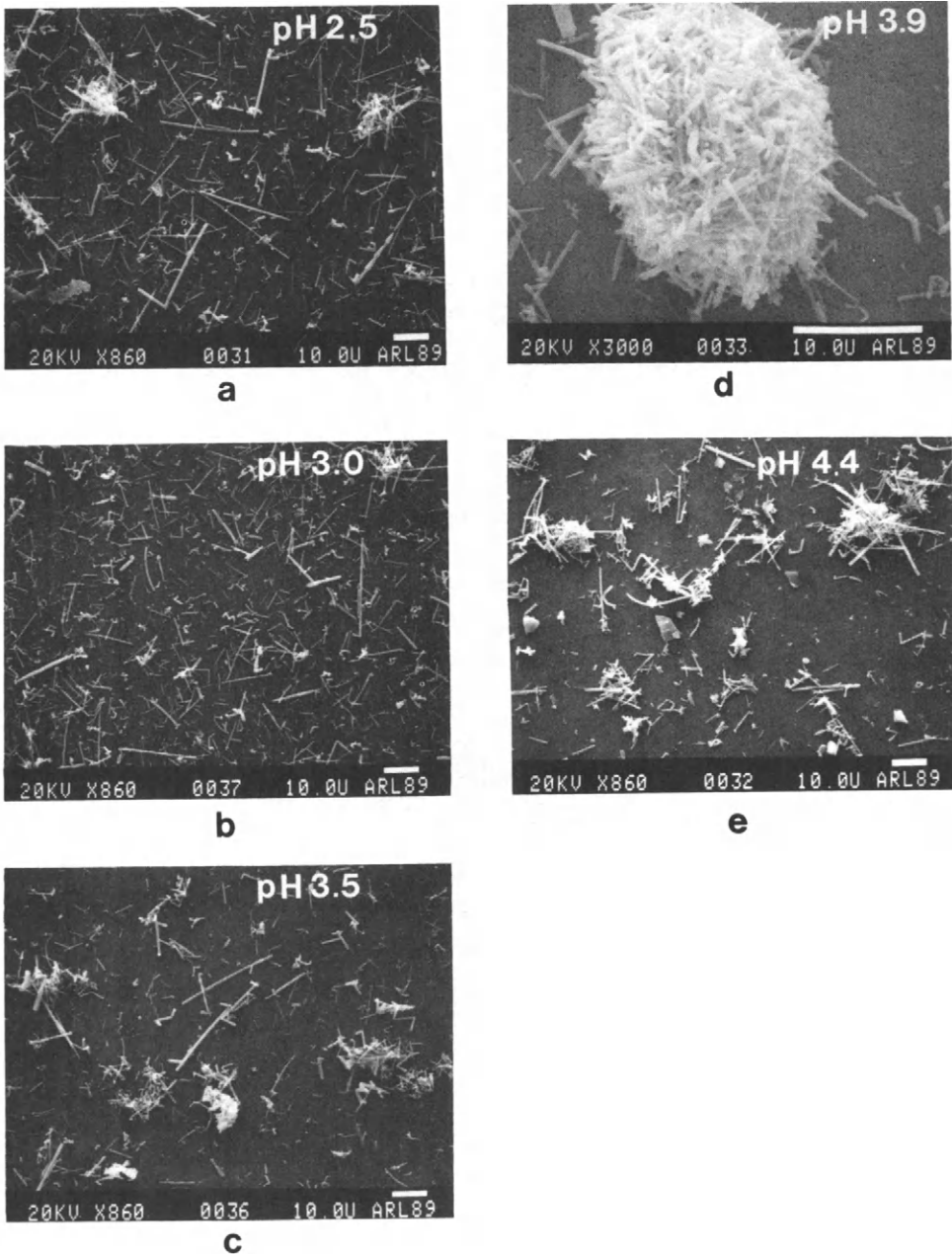
Figure 8 SEM micrographs of SiC whiskers strongly dispersed in water (30 ppm) a) pH = 2.5; b) pH = 3.0; c) pH = 3.5; d) pH = 3.9 "ball"-like agglomerate of small whiskers; e) pH = 4.4
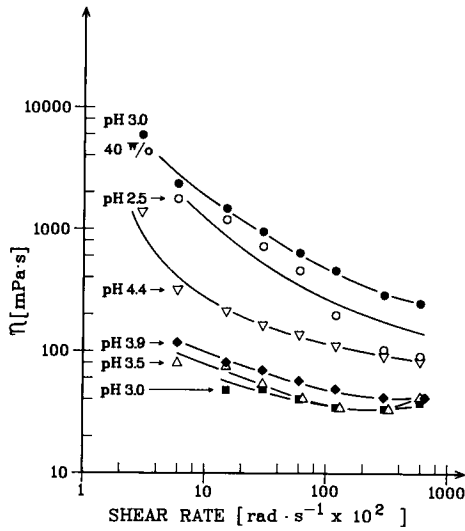
Figure 9   Viscosity of dense water suspension of SiC whiskers
(40w/o solids) at pH = 3 compared to less dense slurries
(31.3%) with different pH values.

Experience acquired with the use of the above described combination
of experimental techniques enabled the optimization of SiC whiskers
dispersions in water and led to development of dense SiC$_{(w)}$
suspension with 17.5 % solids (40 w/o) without the use of organic
deflocculants, having fairly good viscosity (Fig. 9) and ready to
mix with a dense suspension of the matrix powders.

SUMMARY AND CONCLUSIONS

- Dispersion properties of SiC whiskers in aqueous suspensions have been examined over a wide range of pH, from 3-11.
- Washing in HNO_3 with following neutralization in NH_4OH significantly enhances dispersability of SiC whiskers in water suspensions. Subsequent intensive rinsing to constant pH, removing products of chemical reactions from whisker surfaces and a final solution, additionally increases their dispersability.
- The lowest viscosities and highest solid loadings have been achieved in acid range of pH of aqueous suspension.
- The values of measured electrophoretic mobility combined with those of viscosity, and related to SEM observation prove that the best dispersion of SiC water suspensions appears at a very narrow pH range, from 3 to 3.5.

ACKNOWLEDGEMENTS

REFERENCES

1. J.H. Adair, B.C. Mutsuddy, J. Drauglis, (1988) "Stabilization of Silicon Carbide Whisker Suspensions: I, Influence of Surface Oxydation in Aqueous Suspensions". Advanced Ceramic Materials, 3 [3] 231-234.

2. J.V. Milewski, (1986) "Efficient Use of Whiskers in the Reinforcement of Ceramics", Advanced Ceramic Materials, 1 [1] 36-41.

3. A. Roosen, H. Hausner, (1988) "Techniques for Agglomeration During Wet-Chemical Powder Synthesis". Advanced Ceramic Materials, 3 [2] 131-137.

4. M.D. Sacks, Hae-Weon Lee, O.E. Rojas, (1988) "Suspension Processing of Al_2O_3/SiC Whisker Composites". J. Am. Ceram. Soc., 71 [5] 370-379.

5. P.K. Whitman, D.L. Feke, (1986) "Colloidal Characterization of Ultrafine Silicon Carbide and Silicon Nitride Powders". Advanced Ceramic Materials, 1 [4] 366-370.

Rheological behaviour of injection moldable ceramic-ceramic composites

I. Tsao, S.C. Danforth
Center for Composite Manufacturing Science and Engineering,
Department of Ceramic Engineering, Rutgers, The State University,
Piscataway, New Jersey 08855-0909, U.S.A.

A.B. Metzner
Chemical Engineering Department, University of Delaware, Spencer Labs,
Newark, Delaware 19716, U.S.A.

EXTENDED ABSTRACT

The potential of ceramic-ceramic composites as engineering materials is outstanding. However, new, net shape processing methods must be developed to yield uniform, controlled microstructures. Injection molding and extrusion are two such processing routes; however, very high solids loadings of ceramic powder and whisker fillers must be incorporated into the molten polymer system, which results in an extremely high viscosity. Understanding and successfully modeling the flow behavior of these materials is necessary in order that filler content, ratio, and size can be manipulated to yield optimized flow as well as final ceramic-ceramic composite mechanical properties. This research will strongly contribute to that understanding.

There is currently great interest in the potential for whisker reinforced ceramic-ceramic composites to revolutionize the structural ceramics area. These materials offer increased strength, toughness, and thermal shock resistance over monolithic ceramic materials. For this potential to be realized, however, new methods of processing complex shapes in an automated, reliable fashion are needed. One such approach is injection molding. There are several key issues which are to be addressed in this work, including: mixing, dispersion, and analysis and modeling of the rheological properties of the polymer melts with very high ceramic powder and whisker solids loading.

All compounds investigated were mixed in a torque rheometer. The mixer has a 215 cm^3 capacity, with two counter rotating roller blades. The mixing conditions were fixed at 125°C and 100-60 rpm in order to achieve optimum mixing. Compounding time was 50 minutes at 100 rpm and another 50 minutes at 60 rpm. Instron Capillary Viscometry was used to characterize the rheological properties of the ceramic filled polymer systems simulating the injection molding process. Different capillary tubes were applied to study the end, slip and non-Newtonian fluid effects.

Highly filled Si powder and SiC whiskers in the molten polyethylene and stearic acid were characterized by capillary viscometry

simulating the injection molding process. Three corrections were applied to obtain true wall stress, shear rate and viscosity (at steady state) under the assumption of laminar flow. Results showed that the end effect ($|L/D|_{excess}$) is relatively tube diameter and temperature independent. Typical end effects vary from 1.5 to 0.5 for SiC whisker containing systems for shear rates >10^2 sec^{-1}. Generally, the excess pressure needed increased with SiC whisker content, however $|L/D|_{excess}$ shows the opposite trend. The slip effect is difficult to resolve, and appears to be small, <15%. Power law indexes (n) of all investigated systems vary from 0.718 to 0.958, which indicates shear thinning behavior. The degree of shear thinning increases as total solids loading and SiC whisker content increases. Up to 50% error will be introduced by use of a single tube measurement without making these three corrections. Viscosities increased dramatically with increased solids loading and powder to whisker volume ratios. (See Figs. 1 and 2.) Velocity profiles were constructed using the power law index n. All investigated systems showed nearly parabolic flow patterns, although a tendency toward plug flow is shown for increasing solids loading and SiC whisker contents. Finally, SEM pictures showed that a high degree of whisker alignment occurred in areas adjacent to the capillary wall and that the whiskers are randomly oriented in the central area of the extrudate.
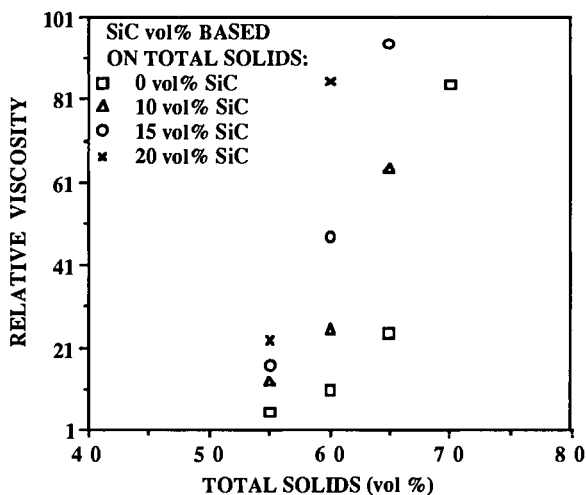
Fig. 1.   Relationship between system relative viscosity and total solids loading for powder and whisker filled injection molding formulations for ceramic-ceramic composites, measured at 140°C, and 100 sec^{-1}.
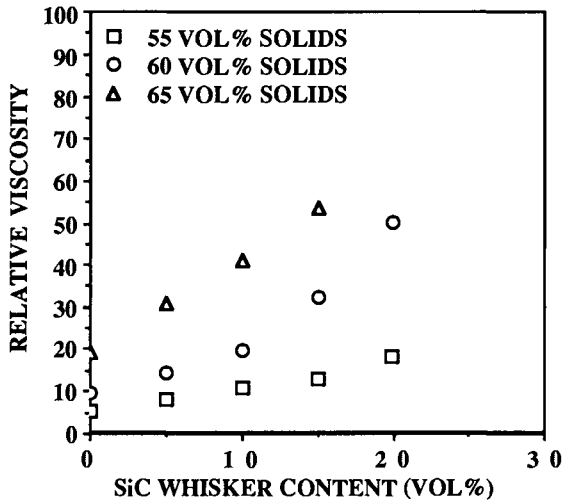
Fig. 2. Relative viscosity of composite compositions as a function of SiC whisker content. Measurements were made at 140°C and 1000 sec^{-1}.

Coated powders for uniform microstructure and fabrication easiness of composites

S. Dallaire and B. Champagne
Industrial Materials Research Institute, National Research Council Canada,
75 de Mortagne Blvd., Boucherville, Québec, Canada, J4B 6Y4

ABSTRACT

A new, inexpensive and simple method for agglutinating fine powder on bare particles or cores has been developed. This process allows to coat various kinds of cores with different types of coatings (metal, ceramic, cermet, polymer, etc.). In this work, the advantages of the technique are exemplified by a specific application: the fabrication of wear-resistant composites. Thick iron powder coatings were agglutinated on WC-Co particles. These coated particles were compacted by powder metallurgy techniques and thereafter the compact was infiltrated with copper in order to make them wear-resistant composite parts. The use of coated particles leads to major improvements in the WC-Co particle dispersion. It also provides a material suitable for feeding commercial compacting presses and thus greatly facilitates the production of composites on an industrial scale.

KEYWORD

Coating of particle; metal-matrix composite; wear-resistant cermet; agglutination coating process; uniform dispersion.

INTRODUCTION

Over the past years, the production of metal-matrix composites has attracted considerable attention. By selecting specific constituents, composites can be produced with unique properties adapted to resist more aggressive environments. In the fabrication of particulate composites, a uniform dispersion of particles and a strong adhesion of these particles to the matrix are of primary concern. The degree of dispersion is far from being perfect due to segregation during composite fabrication and powder handling. The cohesion of ceramic particles within the metallic matrix is also dramatically affected when clusters are formed. The use of particles adequately coated is practically the only way to overcome both the global and local segregation during composites fabrication (Chaklader and Linger, 1976; Lavendel, 1974).

Indeed the techniques that have been reported for the metal coating of ceramic particles:- 1) chemical plating from the aqueous solutions of metal salts (Chaklader and Linger, 1976; Horie and co-workers, 1987; Kunda, 1971; Meddings, Kunda and Mackiw, 1961; Vijayan and co-workers, 1985); 2) physical vapour deposition (Pavlov and co-workers, 1984); and 3) chemical vapour deposition (Pleass and Schimmel, 1972) are limited in terms of coating homogeneity, material and thickness.

A new coating method based on an agglutination process has been developed to coat different kinds of ceramic particles with various metallic elements. This method is described and its advantages are exemplified with the fabrication of a wear-resistant composite consisting of WC-Co particles dispersed in a copper-infiltrated steel matrix.

WEAR-RESISTANT COMPOSITES CONTAINING WC-Co PARTICLES

Even though the wear resistance is a system property, it is generally admitted that the wear resistance greatly depends on the hardness of the material compared to that of the abrasive. The toughness is also of tremendous importance, particularly in applications involving large stresses. Thus, wear-resistant materials generally consist of different amounts of hard phase materials in a metallic matrix. The hard phase constituent provides the hardness whereas the metallic matrix improves thoughness.

Previous investigations (Angers and co-workers, 1982) concerning the properties and wear behaviour of a composite material made of WC-Co particles in a steel matrix yielded a favourable combination of wear resistance and thoughness. The method used to produce these composites has been reported previously (Angers and co-workers, 1982). It consists in consolidating mixtures of WC-Co cemented carbide particles, steel powder and powder of alloying elements by powder metallurgy techniques. After the preparation of the mixture containing the elements, specimens are cold pressed at 550 MPa to about 80% of the theoretical density. These green compacts are then sintered and simultaneously infiltrated at 1120°C for 1800 s with a copper alloy. After completing the fabrication steps summarized in Fig. 1, a dense composite whose typical microstructure is shown in Fig. 2 is obtained.
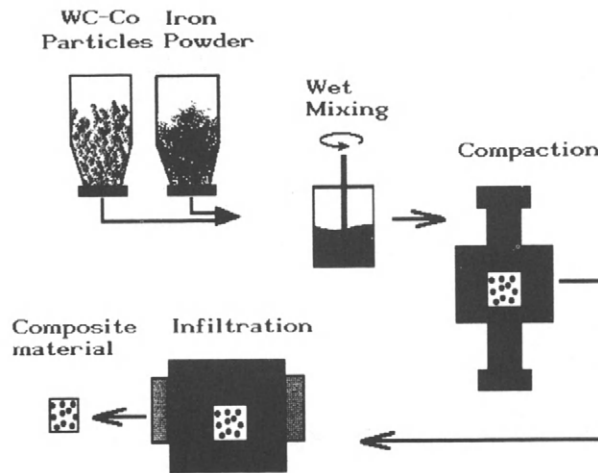
Fig. 1 - Fabrication steps of WC-Co composites.

DRAWBACKS OF THE CONVENTIONAL P/M PROCESSING

A severe technical limitation is encountered in the conventional P/M processing of these composites. Mixing of WC-Co particles with iron powder leads to segregation. Indeed, even if the WC-Co ceramic and the metal powder (steel) are mixed thoroughly, separation of the phases due to the difference in density cannot be avoided during storage, transport and handling. It leads to a non-uniform dispersion of the hard phase and segregation of the metallic phase in such a way that optimum properties are not maintained throughout the structure. Only the wet mixing of constituents could improve dispersion. However the wet mixing is hardly practicable in process automation.

Moreover, the processing described above limits the proportion of ceramic hard phase to a certain extent. Indeed, for volume proportion above 35%, compaction problems arise in maintaining an adequate shape and in preserving the edges and corners of compacts. Moreover, the density of green

matrix is very sensitive to a non-uniform distribution of a second phase at a higher volume content. A large decrease in matrix density occurs with an increase in the amount of the second phase when it is non-uniformly dispersed. It has been pointed out in the laboratory testing of hese wear-resistant composites (Champagne and Angers, 1985) that wear losses are mainly caused by the erosion of the matrix and the reduction of the bonding interface area between the WC-Co particles and the matrix. The WC-Co particles are easily pulled out when the bonding between WC-Co particles and the matrix is reduced.

Without taking into account the economics, the wear performance of these composites can be considerably increased if the proportion of the hard phase is raised. Therefore, high wear-resistant composites should be composed of a metallic continuous skeleton surrounding the particles and the volume content of particles should be maximized.
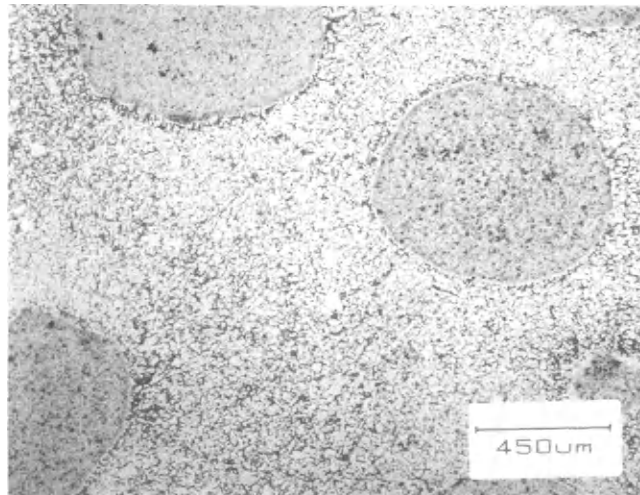
Fig. 2 - Microstructure of the WC-Co composite done by mixing powders.

PACKING OF PARTICLES AND COMPOSITES PRODUCTION

It is known that monosized spherical particles can be packed in an array close to one of those predicted by the classic theory on particle packing (Beddow, 1980). Equally sized spheres packed in one of four different ways lead to specific volume values as shown in Table 1.

Table 1 - SYSTEMATIC ASSEMBLAGES OF SPHERES

Assemblages	Volume occupied %
Cubic	52.4
Orthorhombic	60.5
Tetragonal	69.8
Rhombohedral	74.0

ᵗIn practice, the set formed by the particles depends upon the impulses and forces that are transmitted during handling. Though an array as those proposed in Table 1 is difficult to obtain in the present case, nevertheless the volume of hard phase is expected to be significantly increased. Typically,one can expect that many of these types of assemblages are locally possible and the volume occupied by monosized particles could be about 63%. Therefore,this constitutes the upper limit in particle content within a composite if each particle touches another. The amount of powder coating should represent at least 37 vol. % for filling the voids. Such a high content of hard particles is actually impossible to reach by compaction of mixed powder due to segregation. However, with powder-coated particles it is possible to obtain composites containing a high volume of hard phase. Moreover, coated particles also make possible tailored and ideal composites.

COATING OF CERAMIC PARTICLES WITH METAL POWDER

An agglutination technique (Hojo, Dallaire and Champagne, 1988) is proposed to circumvent the above-mentioned drawbacks. The process which consists in agglutinating fine metal powder on ceramic particles with the help of a binder for producing composite particles with a thick metal coating has been described before (Dallaire and Champagne, 1989).

This coating method that has been found very effective for coating ceramic particles with various kinds of metal powders is partly derived from the tumbling agglomeration of powders (Classen and Petzow, 1971). Binder-coated ceramic particles and fine metal powder are loaded in a brass cylinder internally coated with teflon and tilted at an angle to the horizontal axis of rotation as shown in Fig. 3. The tumbling ensures a good mixing and a uniform movement of the ceramic particles and of the
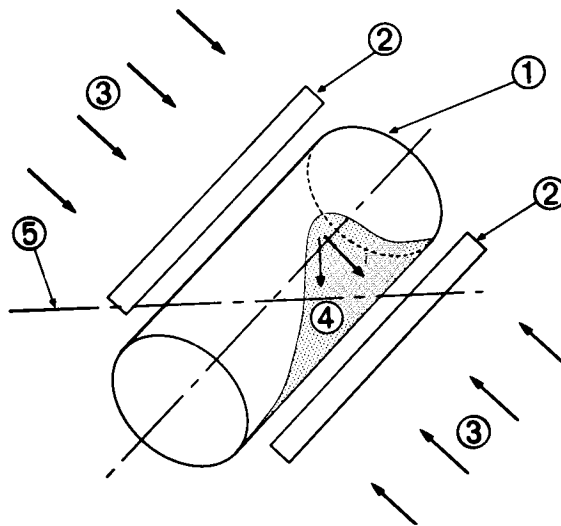
Fig. 3 - Schematic representation of the agglutination apparatus:
1, tilted cylinder; 2, heating elements; 3, cooling medium; 4, load; 5, rotation axis.

metal powder. Upon heating the cylinder, the binder reaches a viscous state under conditions effective to provide a fine powder coating on the ceramic particles. After cooling, it results in a layer of metal powder agglutinated around ceramic particles (Fig. 4). In a subsequent step, a heat treatment can be carried out to remove the binder and at the same time to slightly sinter the powder layer which is then coherently bonded to the ceramic particles.
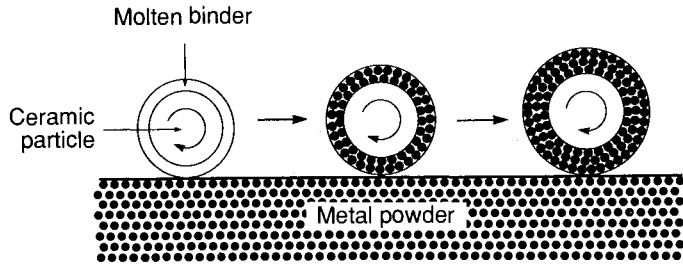
Fig. 4 - Mechanism of Agglutination Coating.

EXPERIMENTAL DETAILS

WC-Co particles (-20 Mesh) were coated with iron powder in a metal cylinder heated by electric bands as shown in Fig. 5. To avoid binder overheating, a temperature controller regulated precisely the power delivered to the bands. The procedure used to coat ceramic particles with metal powder can be described as follows:

The first step consists in covering ceramic cores with the binder by introducing both the cores and the binder into the cylindrical container. The container is then rotated and heated until the binder (Polyethylene glycol, m. wt 3350, melting range comprised between 54 and 58°C) becomes viscous. After a period of 15 minutes, the binder coating operation is completed and the cylinder is allowed to cool to room temperature. The resulting binder-coated ceramic particles are slightly sieved to separate those that have stuck together.
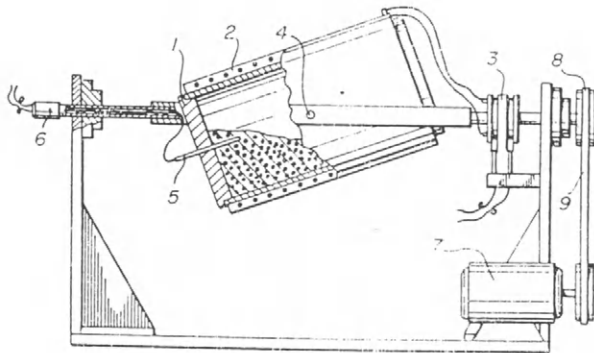
Fig. 5 - Agglutination coating apparatus

The second step consists in agglutinating metal powder to these binder-coated cores. Binder-coated WC-Co particles, the fine iron powder and a lubricant are put into the cylinder. The cylinder is then simultaneously heated and rotated leading to the agglutination process itself. The process parameters used in this study are listed in Table 2. After cooling, iron-coated WC-Co particles are separated from minute residue by sieving.

Iron-coated WC-Co particles are then dewaxed at a temperature comprised between 350 and 600°C and specimens are uniaxially compacted and copper/infiltrated at 1125°C.

Table 2 - PROCESS PARAMETERS USED FOR COATING WC-Co PARTICLES

Binder content	7.75 g/100 g WC-Co
Metal powder load	155 g Fe/255 g WC-Co
Filling of cylinder	9%
Rotation speed	8 rpm
Tilt angle	22°C
Temperature	51-51.5°C (for covering particles with binder)
Heating time	1200 s

RESULTS AND DISCUSSION

Because the amount of iron powder that ought to be agglutinated around WC-Co particles is high (37.5 wt%), a large amount of binder must be deposited on the surface of cores. This step consisting in covering WC-Co particles with the binder is of prime importance. Heating up to a maximum temperature range of 51-51.5°C (the softening temperature of PEG) for 15 minutes is the most appropriate cycle to coat WC-Co particles with a fairly large amount of binder and to avoid the sticking of particles together.

Even if WC-Co particles are large enough to agglutinate coarse metal powders, the as-received Atomet 95 iron powder was found inappropriate to obtain an uniform coating. As shown in Fig. 6, the as-received iron powder contains spheres and agglomerates larger than 40 μm. After sieving at -400 Mesh, this iron powder is more suitable for the agglutination purpose (Fig.7). It has been observed that a general rule of thumb consists in maintaining the ratio between the ceramic particle diameter and the metal powder diameter below 10 depending on the coating density that should be reached.

Though the metal powder was almost coarse, a thick and uniform metal powder coating was obtained by using the agglutination process (Figs. 8 and 9). The composite powder is a free-flowing material particularly convenient for composite fabrication purposes. Die filling operations can be actually performed without any particular care, procedure (wet mixing) or equipment.

By repeating the same fabrication steps involving mixtures of WC-Co particles with iron powder, a different composite was made. In comparison with the composite made by powder mixing, the new composite contains a larger amount of hard phase more uniformly distributed within the ductile matrix as shown in Fig. 10. As mentioned before, this composite would possess a better abrasion resistance than that of a composite made in a conventional manner
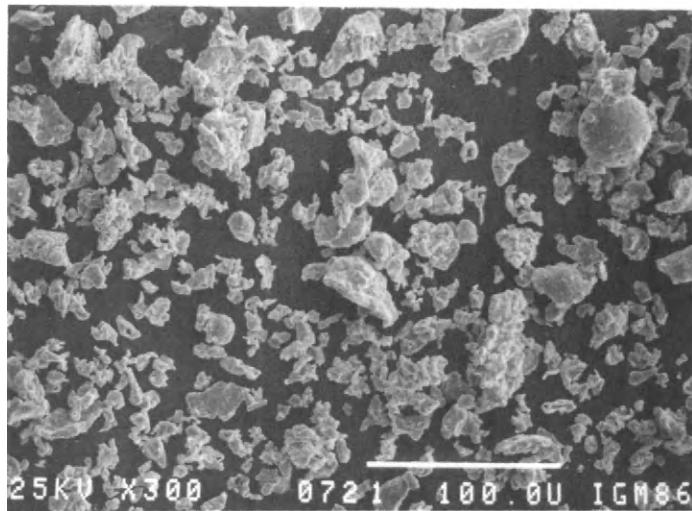
Fig. 6 - As-received iron powder.
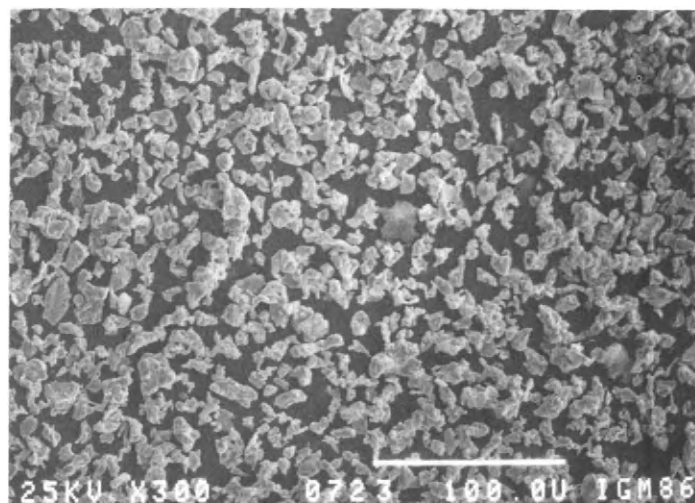
Fig. 7 - Iron powder sieved at - 400 Mesh.
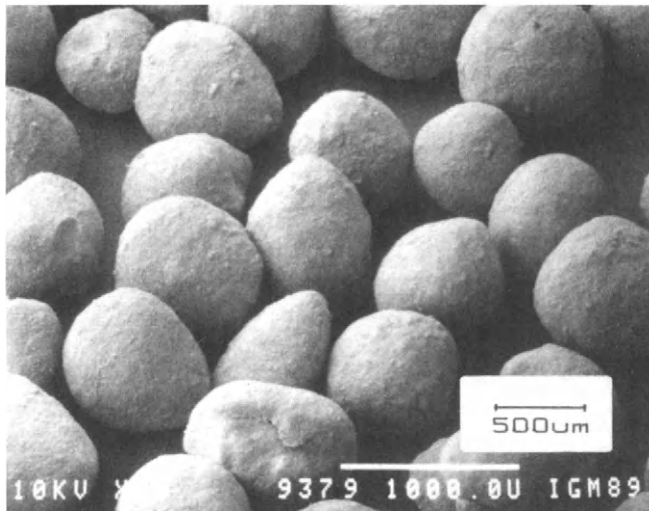
Fig. 8 - Uncoated WC-Co particles.

Fig. 9 - Iron-Coated WC-Co particles.
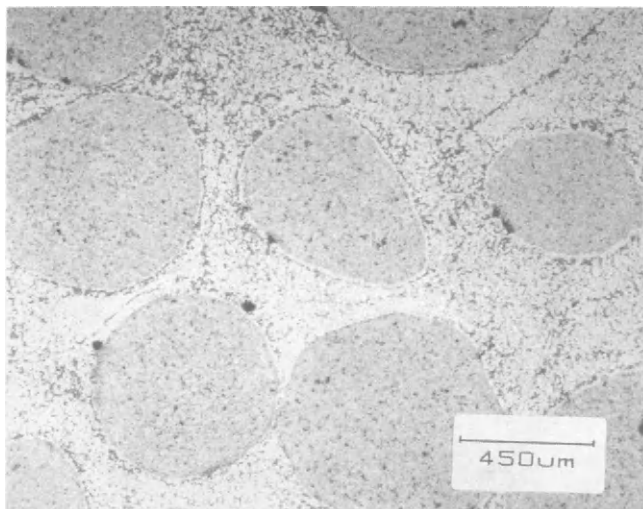
Fig. 10 - Microstructure of the WC-Co composite done with coated particles.

CONCLUSION

In the fabrication of composites containing a dispersion of particles, a uniform dispersion of particles and a strong adhesion of these particles to the matrix can be achieved by the use of powder-coated particles. This dispersion responsiblefor the composite performance is not deteriorated during storage or handling. Moreover, the dispersion can be carried to obtaining composites with a higher volume content of particles.

The proposed powder coating method is flexible and simple. To achieve an uniform and dense powder coating it only requires fine powders whose particle size depends on the size of particles to be coated.

ACKNOWLEDGEMENT

REFERENCES

Angers, R., B. Champagne, M. Fiset and P. Chollet (1982). Progress in Powder Metallurgy, Vol. 38, Metal Powder Industries Federation, Princeton, pp.159-175.

Beddow, J.K. (1980). Particulate Science and Technology, Chemical Publishing Co. Inc., New York.

Champagne, B., and R. Angers (1985). Wear of Materials 1985, American Society of Mechanical Engineers, New York, pp. 142-148.

Chaklader, A.C.D., and K.R. Linger (1976). Composites, 53, 239-243.

Claussen, N., G. Petzow (1971). Proc. 3rd European Powder Metallurgy Conf., Suppl., pp.225-248.

Dallaire, S., Champagne, B., and J. Hojo (1989). Surface and Coating Technology. Accepted publication.

Hojo, J., S. Dallaire and B. Champagne (1988). U.S. Pat. 4, 788,080.

Horie, Y., T. Kanbe, Y. Kumagaya and S. Isobe (1987). <u>Bosei Kanri</u>, <u>31</u>, 162-169.

Kunda, W. (1971). <u>7th Plansee Seminar Preprints</u>, Reutte, Austria, pp. 1-13.

Lavendel, H.W. (1974). <u>Bull. Am. Ceram. Soc.</u>, <u>53</u>, 797-799,808.

Meddings, B., W. Kunda and V.N. Mackiw (1961). <u>Proc. Int. Conf. Powder Metallurgy</u>, Interscience Publishers, New York, pp.775-798.

Pavlov, Yu.A., I.V. Blinkov, K.A. Myagkov and A.V. Manukhin (1984). <u>Paroshk. Metall.</u>, <u>8</u>. 1-4.

Pleass, C.M., and D.G. Schimmel (1972). <u>Proc. Int. Conf. Chem. Vap. Dep.</u>, American Nuclear Society, Hinsdale, pp.513-535.

Vijayan, C.P., J. Hojo, J.J. Hechler, B. Champagne and S. Dallaire (1985). <u>Electroless Nickel Conference IV</u>, Gardner Publications Inc., Cincinnati, pp. 3.1-3.17.

Fabrication and properties of zirconia-ceria ceramics

V.C. Pandolfelli, N.J. Ali, S. Bradwell, M. Rainforth and S.J. Milne

School of Materials, University of Leeds, Leeds LS2 9JT, England

ABSTRACT

Wet chemical precipitation routes have been used to prepare ZrO_2-CeO_2 powders of different purity levels. The powders have been processed into ceramics, and the influence of chemical composition on sintering behaviour observed.

KEYWORDS

Zirconia-ceria ceramics, powder synthesis, impurity effects.

INTRODUCTION

Ceria stabilised tetragonal zirconia ceramics (Ce-TZP) have been reported to exhibit higher toughness and better thermal ageing behaviour than the more established yttria-zirconia (Y-TZP) system (Sato, 1985). Consequently there is growing interest in studying the processing characteristics of ZrO_2-CeO_2 compositions in order to better understand and exploit the properties of these tough ceramics. As with other TZP materials, wet chemical routes for synthesising starting powders are an attractive means of achieving a high level of chemical homogeneity in the ceramic (Duh, 1988).

By contrast to yttria stabilised zirconia, there is a wide range of dopant compositions in the ceria system for which the tetragonal crystal structure may be retained to room temperature (Tani, 1983). Compositions around 10-12 mol % CeO_2 appear to offer a favourable compromise between high toughness and high strength (Tsukuma, 1985).

Information on the effect of dopants and impurities is limited. However some results imply that rare earth impurities, originating in the cerium starting reagent produce significant differences in fracture toughness and mechanical strength compared to higher purity materials (Tsukuma, 1985, 1986).

In the present study a range of ZrO_2-CeO_2 powders prepared by chemical methods are being evaluated: preliminary results are now reported for compositions in the range 10-12 mol %.

EXPERIMENTAL

Starting reagents used were zirconium tetrachloride (Aldrich 99.5% purity), zirconium (n) propoxide (Aldrich) and cerium III nitrate hexahydrate (Aldrich 99.9% purity).

Two synthesis routes were examined. In the first, the zirconium propoxide starting material was converted to a hydroxide and dissolved in nitric acid. To this, the cerium salt was introduced and the solution simply evaporated to dryness whilst stirring. The dried cake was then milled (see later). The other route involved co-precipitation of high purity cerium nitrate and zirconyl chloride solutions. Careful washing and drying procedures, including freeze drying, were carried out in order to minimise particle agglomeration in the product.

Silica was introduced to selected samples by suspending the ceria-zirconia powders in an aqueous suspension of colloidal silica, followed by freeze drying. Other dopants were introduced via their water soluble salts.

Where appropriate, powders were milled using a propanol/zirconia grinding system. Powder characterisation was carried out using scanning and transmission electron microscopy (SEM/TEM), X-ray sedimentation (Micromeritics 5000 ET) and BET gas adsorption techniques (Perkin-Elmer 212D). Chemical analysis for zirconium and cerium was performed using Inductively Coupled Plasma (ICP) emmission spectroscopy (ARL 3580B).

For sintering studies, powders were die-pressed at 100 MPa and fired in air at 1450°C for 3 hours. The powders were first calcined at 900°C to reduce surface area and improve die-packing behaviour. Fired densities were measured using a water displacement technique, having ensured maximum wetting of exposed porosity.

Microstructures were examined by means of SEM.

An indentation technique was adopted for assessing fracture toughness (Vickers hardness testing machine).

RESULTS AND DISCUSSION

Powders produced by simple evaporation of mixed solutions are, for convenience, labelled ZC-A; the coprecipitated products are denoted ZC-B. The properties of the powders are summarised in Table 1.

TABLE 1   Summary of Powder Properties

Powder code	ZC-A	ZC-B
Synthesis route	Solution-evaporation + milling	Co-precipitation
Average crystallite size	~20 nm	~50 nm
Agglomerate maximum size	~3 µm	~6 µm
Purity level	~96%	≥99.5%

Both powders were composed of small crystallites only a few tens of nanometers in size, Fig. 1. These clustered into agglomerates with an upper size of ~3 µm, and ~6 µm for ZC-A and ZC-B respectively, Fig. 2. However TEM revealed a relatively open structure within the agglomerates, Fig. 1, and compaction behaviour was typical of a weakly aggregated powder.
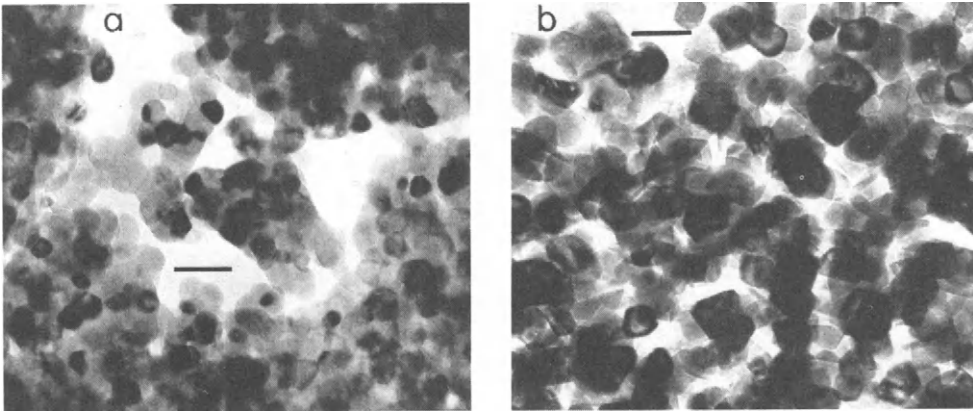
Fig. 1.   Transmission electron micrograph of a) ZC-A and b) ZC-B
          Bar represents 50 nm.
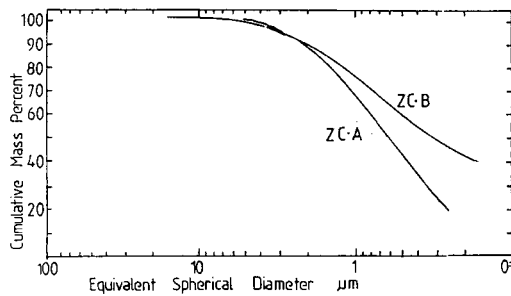
Fig. 2.   X-ray sedimentation data.

Despite their similar physical properties ZC-A and ZC-B exhibit quite different sintering characteristics.

Pellets of ZC-A powders reach densities of 6.1 gcm^{-3} after firing at 1450°C for 3 hours. Under similar conditions ZC-B reaches only 5.2 gcm^{-3}. Assuming a theoretical density of 6.2 gcm^{-3} for each powder[1], calculated from unit cell lattice parameters, ZC-A and ZC-B pellets correspond to densities of ~98% and ~83% theoretical respectively.

_____

[1]Slight errors arise for ZC-A due to its significant level of impurity elements.

Chemical analysis by ICP techniques provided an explanation for the dissimilar sintering characteristics.

ZC-A contained approximately 4 wt % of impurity elements, whilst the co-precipitated ZC-B powders are of approximately 99.5% purity. In addition to the differences in composition, ZC-B also contains slightly larger particles, and had not been milled. In order to investigate the effects of these parameters, samples of ZC-B were milled under similar conditions to those used for ZC-A. Agglomerate size was consequently reduced to < 3 µm; in addition some chemical contamination would have probably occurred. The corresponding ceramic density increased from ~83% to ~94.5% theoretical, a value some 4% below the maximum density of ZC-A. To study the importance of impurity elements, one of the species known to be present in ZC-A, SiO_2, was now added to base compositions of ZC-B which had undergone milling. A significant increase in density to ~98% theoretical, similar to that obtained for ZC-A, resulted for SiO_2 levels of 0.5 wt %, Fig. 3.
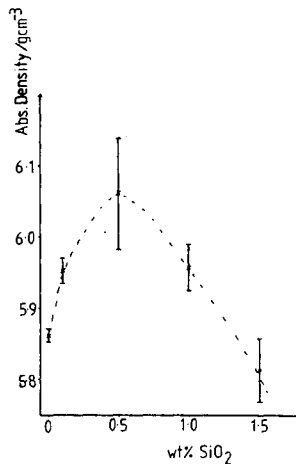
Fig. 3. Plot of sintered density versus wt % of added SiO_2, for ZC-B (12 mol %).

Doping unmilled powders (with SiO_2 and Al_2O_3) increased the density to only ~90% theoretical. Hence milling and dopant additions were both required in order to sinter co-precipitated ZC-B powders to near theoretical density. Milling was beneficial in reducing the agglomerate particle size of ZC-B, but the initial agglomerates had appeared to be relatively weakly bound and milling was not expected to have such a dramatic effect on densification behaviour; the improved sintering may therefore also have been related to contamination, and homogenisation effects.

Silica additions probably promoted the formation of a liquid phase during sintering and so aided the densification process. Microstructural evidence is as yet inconclusive; a typical fracture surface of a ZC-B ceramic is shown in Fig. 4. Confirmation of the influence of impurity elements was obtained from studies of two commercially available Ce-TZP powders[2]. Again the low purity product,

[2]Supplied by Unitec Ceramics, U.K., and Toya Soda, Japan.

containing ~3 wt% of impurities, exhibited superior densification characteristics.
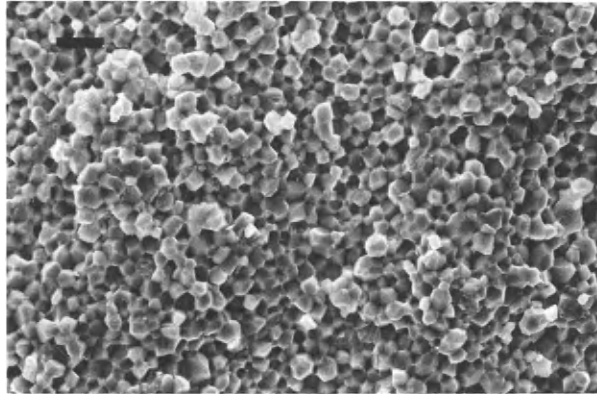
Fig. 4. Fracture surface of a ZC-A ceramic after firing at
1450°C for 3 hours. Bar represents 5 μm

Other additives have proved to be even more effective for ZC-A and ZC-B; it has
thus been possible to sinter ZC-B powders to over 98% theoretical density. Indeed
similar high density values may be achieved for Ce-TZP powders made by con-
ventional mixed oxide processing, if selected dopants ($\leq$ 1 wt%) are introduced.
These results shall be reported elsewhere.

Clearly the mechanical properties of the ceramic are the most important criteria
for assessing the merits of any Ce-TZP powder. Measurements of fracture toughness
using an indentation technique proved inconclusive. No cracks could be observed
extending from the indent of ceramics made from the 'in-house' or commercial
powders even under the highest loads, 1.1 kN. This suggests the materials are all
of very high toughness, but an accurate measure of their fracture toughness must
await the results of tests using a Chevron notch method.

CONCLUSIONS

The results of the preliminary work reported here emphasise the important influence
of impurities on the densification behaviour of ceria-zirconia ceramics. Silica is
one oxide which has been shown to have a beneficial effect, but extensive research
coupled to accurate multi-element analysis is required in order to clarify the
precise role of specific dopants. The reward for such an approach shall be a
better understanding of the critical processing parameters for producing Ce-TZP
ceramics of optimum mechanical performance.

ACKNOWLEDGEMENTS

REFERENCES

Duh, J.G., Dai, H.T. and Chiou, B.S. (1968). Sintering, Microstructure, Hardness and Fracture Toughness Behaviour of Y_2O_3-CeO_2-ZrO_2. J. Am. Ceram. Soc., 71, [10] 813-19.

Sato, T. and M. Shimada (1985). Transformation of Ceria Doped Tetragonal Zirconia Polycrystals by Annealing in Water. Am. Ceram. Soc. Bull., 64, 1302-1384.

Tami, E., Yashimura, M. and Somiya, S. (1983). Revised phase diagram of the system ZrO_2-CeO_2 bellow 1400°C, J. Am. Ceram. Soc., 66, 506-510.

Tsukuma, K. and Shimada, M. (1985). Strength, fracture toughness and Vickers hardness of CeO_2-Stabilized tetragonal ZnO_2 polycrystals (Ce-TZP), J. Mat. Sci., 20, 1178-1184.

Tsukuma, K. (1986). Mechanical Properties and Thermal Stability of CeO_2 containing Tetragonal Zirconia Polycrystals, Am. Ceram. Soc. Bull., 65, 1386-1389.

Alumina/zirconia composites produced from alumina and zirconyl chloride

A.S. Rao, M.R. Krishnadev
Department of Materials Science and Engineering, University of Cincinnati, Cincinnati, Ohio 45221, U.S.A.

A. Purohit
Argonne National Laboratory, Argonne, Illinois 60439, U.S.A.

ABSTRACT

Alumina and zirconia were coprecipitated in a gel form from boehmite alumina and zirconyl chloride. After calcination, ball milling and dry pressing the powder, the boehmite alumina / zirconia composite green bodies were sintered in the temperature range 1480 - 1600°C. The gel route derived powder density upon sintering was in the range 84 - 96 %. The flexural strength increased with an increase in the sintering temperature; however, the composite strength did not increase significantly due to an increase in the concentration of zirconia particles. X-ray diffraction analysis of the sintered composites suggest that the dispersed zirconia did not coarsen even after sintering at 1600°C. This is thought to account for the much lower composite strength.

Key Words

Processing alumina / zirconia composites via. gel synthesis density strength

Introduction

Transformation toughened zirconia / alumina ceramic component fabrication requires the uniform distribution of zirconia particles throughout the alumina matrix. Better dispersion of zirconia into alumina can only be achieved when the agglomeration of fine particles is kept at a minimum. It has been suggested in the literature [1 - 2] that a proper mixing of both alumina and zirconia under proper pH conditions would produce a better ceramic. Another alternate method of homogenizing alumina and zirconia is to precipitate the zirconia phase onto alumina [3 - 5]. The aim of the present investigation is to study the effect of coprecipitation of both alumina and zirconia species in a gel form, prior to sintering and to study the resulting microstructure, composite density and strength.

Materials

Commercially available boehmite alumina powder (Vista Chemical Company, Ponca City, OK), zirconyl chloride octa hydrate and analytical grade ammonium hydroxide were used in the preparation of alumina / zirconia composites.

Experimental Procedure

Processing of alumina and zirconia composites

Figure 1. illustrates the flow diagram of the zirconia / alumina
composite processing. The coprecipitation was carried out as follows : First
boehmite slips were prepared in distilled water by dispersing the powder using
an ultrasonic probe for 10 minutes. Concentrated HCl acid was added drop by
drop to the suspension being stirred continuously till most of the powder is
dissolved. It was always found that a small fraction of the boehmite alumina
powder remained undissolved. No special attention was given to remove the
undissolved precipitate. Later the pH of the boehmite (alumina) solution was
slightly increased by the addition of ammonium hydroxide. Aqueous zirconyl
chloride solution was added to the acidified alumina (boehmite) solution.
The mixture was heated slowly at 60°C for 6 hours while continuously being
stirred. Later the thick gel was dried at 200°C. The dry gel was calcined at
600°C for 6 hours. The calcined zirconia / alumina gel was ball milled for 12
hours using zirconia balls. The concentration of zirconyl chloride was
estimated in such a way that after complete decomposition, zirconia would have
a composition in the composite in the range 0 - 15 %(vol).Green ceramic plates
were dry pressed at ~ 50 mPa and were sintered at different temperatures in
the range 1480 - 1600°C.

DISSOLVE BOEHMITE ALUMINA
IN ACID SOLUTION, PH ~ 2.0

DISSOLVE ZIRCONYL CHLORIDE
IN DISTILLED WATER, PH ~3.0

MIX BOTH SOLUTIONS AND ADJUST
PH ~ 3.5 BY ADDING AMMONIUM
HYDROXIDE.   KEEP STIRRING THE
SOLUTION AND HEAT GENTLY AT
60°C FOR 6 HOURS.

HEAT THE GEL AT 200°C OVERNIGHT
UNTIL THE GEL BECOMES HARD.
CALCINE THE GEL AT 600°C FOR
6 HOURS.   BALL MILL THE GEL
OVERNIGHT.

DRY PRESS AT 50 MPa AND SINTER
SAMPLES AT DIFFERENT TEMPERATURES
IN THE RANGE 1480 - 1600°C FOR
2 HOURS.

Fig. 1. Flow Diagram of the Processing of Alumina/Zirconia Composites

Measurements

The particle size analysis, powder density and surface area of both alumina and zirconia powders were determined using dynamic light scattering, helium pycnometer, and nitrogen adsorption BET apparatus respectively. In order to determine the optimum pH values for the coprecipitation of both alumina and zirconia and form a gel, microelectrophoresis experiments were carried out using as synthesized alumina, zirconia and alumina zirconia powder mixtures. The calcination conditions for alumina / zirconia gel were determined from differential scanning calorimetry experiments. The density of the sintered composite samples was determined using the Archimedes principle. The flexural strength of the composites was measured using four point bending method and the structural changes in the zirconia particles was investigated using X-ray diffraction technique. The microstructure of the composites was analyzed using scanning electron microscopy.

Results

For the purpose of characterization, the zirconia powders were precipitated as before, with the exception that alumina was not present in solution. Similarly alumina was also precipitated in the absence of zirconia. The particle size, surface area and density of the as synthesized and / or calcined powders and gels are given in Table 1. These results suggest that boehmite alumina separates from the solution phase as large particle while zirconia forms in a small crystallite form. The density of both as synthesized alumina and / or zirconia is low. However, upon calcination at 600°C, the density of these powders increases and achieves a density value that is comparable to the density of crystalline alumina or zirconia. Calcination temperature was chosen to be 600°C, because, the differential scanning calorimetry, and thermo gravimetry analysis results obtained on our gel samples indicated that for a near complete removal of the network building water of hydration, the gels have to be heated at ~400°C. The differential scanning calorimeter studies

also indicate that around 580°C, the fine zirconia crystallites undergo a phase change.

Figure 2 shows the zeta potential versus pH profiles of as synthesized alumina, and alumina / zirconia gel powders. These results suggest that the addition of zirconia to the boehmite powders tend to shift the iep (isoelectric point) of alumina towards the acidic side of the pH scale. At high zirconia concentrations (~ 15 %(vol)),alumina and zirconia particles flocculate even at pH 3. We found that this type of information was very useful in our gel synthesis process, because, only the zeta potential data has provided the optimum pH condition for coprecipitation of boehmite and zirconia, that can form a stable gel.

The density of sintered alumina / zirconia composites, represented as a percentage of its theoretical density value, is given in Figure 3 as a function of zirconia concentration and sintering temperature of the composites. The results suggest that as the zirconia concentration in the composite increases the composite density decreases. The density of the composite increases with an increase in the sintering temperature. The compositional analysis of the zirconia / alumina composites determined by the chemical analysis is given in Table 2. These results suggest that the concentration of zirconia in our composites is in good agreement with the predicted values. This suggests that a complete and effective gelation and / or precipitation of alumina and zirconia can be achieved using the above processing method given in Figure 1.

Table 1. Surface Area, Density, Mean Particle Diameter and Crystallite Size of As Precipitated Boehmite Alumina, Zirconia Powder and Powdered Alumina/Zirconia Gel

Powder Characteristics	Boehmite* Alumina		Zirconia[#]		Powdered Aluminia/Zirconia** Gel	
	AS	Cal	As	Cal	Dry	Cal
Surface Area (m^2/g)	26.4		80	92	6	32.1
Density (g/c·c)	3.76	3.92	4.32	5.86	3.81[%]	4.06[%]
Mean Diameter (microns)	1.2		<0.2	<0.2		1.0
Crystallite Size (nm)			20	11		

* precipitation by acid neutralization in solution
\# spray atomization synthesis of $ZrOCl_2$ solution into NH_4OH
** coprecipitation and simultaneous gelation
AS: As synthesized powder
Cal: calcined powder; calcination temperature: 600^oC
Dry: dried gel; drying temperature: 200^oC
%: density of gel containing 10% (vol.) zirconia

The structural morphology of the sintered composites differed considerably. While alumina / zirconia composites containing zirconia $\leq$ 10 %(vol.) showed very broad peaks at low 2 theta values (small angle scattering), samples containing ~15 %(vol.) zirconia showed very little small angle scattering. In order to derive some semi quantitative trends in the structural morphology, we estimated the fraction of fine crystallite structure retained in the sintered composites using the relative height of the X - ray intensity for low angle scattering peaks and peak heights of the monoclinic and tetragonal zirconia peaks. Thus the error in the estimation of fine crystallite structure could be $\pm$ 50 %. However, the accuracy in the measurements of the monoclinic and tetragonal phases of zirconia in our samples is ~95 %.The semi quantitative results of the estimation of the crystallinity of zirconia from X- ray diffraction, analysis results for sintered composite samples (sintering temperature 1600^oC), is given in Table 3 as a function of zirconia concentration in the composites.

These results suggest that fine crystallite form of zirconia was retained in the sintered composites even after sintering at high temperature ($\leq 1600^oC$). In addition, these results also suggest that for a given temperature, both fine crystallite concentration and the tetragonal zirconia crystal phase in alumina / zirconia composites decreases with an increase in the zirconia concentration. The X-ray results are in good agreement with the density measurements shown in Figure 3. Since the transformation of tetragonal to monoclinic crystal phase involves an increase in volume, zirconia in less
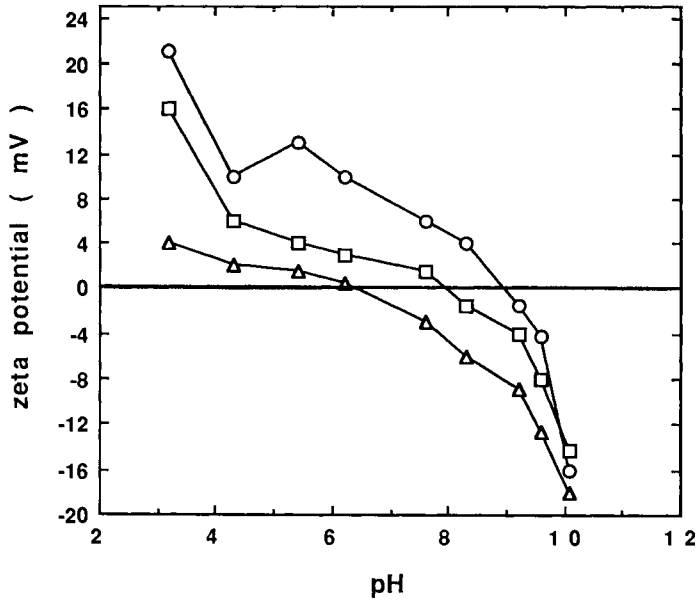
Fig. 2. Zeta Potential of (◯) Alumina, (☐ ,△) Alumina/Zirconia Mixture
         Measured in 10^{-3} M KNO_3 Solution. Zirconia Concentration (☐) 10
         and (△) 15% (Vol.).

Table 2. Zirconia Concentration in Sintered Zirconia/Alumina Composites As
          Was Estimated From Chemical Analysis

Theoretical Concentration % (Vol.)	Actual Analysis Value in the Composite % (Vol.)
10	8.9
12.5	12.3
15	16.0

dense composites can freely transform from tetragonal to monoclinic structure
upon cooling. For example the density of alumina / zirconia composites
sintered at 1600°C containing 10 and 15 %(vol) zirconia is 96 and 94 %
respectively. The % of monoclinic phase of zirconia in these composites is 12
and 58 % respectively.
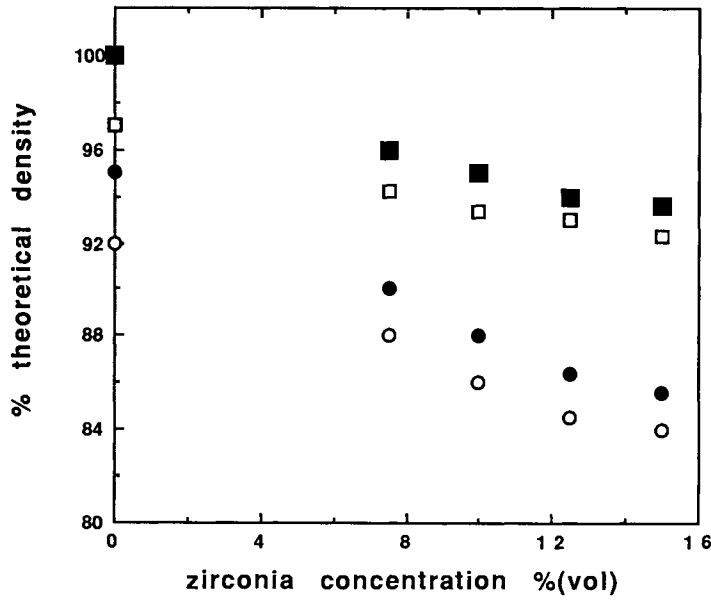
Fig. 3. Density of Sintered Zirconia and Alumina Composites Represented as a Percentage of the Theoretical Density Versus Zirconia Concentration. Sintering Temperature (◯) 1480, (●) 1500, (☐) 1550 and (■) 1600°C.

Table 3. Semiquantitative Estimate of the Nature of Zirconia Particle Crystal Structure as was Determined from the X-ray Diffraction Patterns of the Sintered Zirconia/Alumina Composites. Sintering Temperature 1600°C

Zirconia Concentration % (Vol.)	Zirconia Crystal Structure % of the Total Composition		
	Fine Crystallites	Monoclinic	Tetragonal
10	40	12	48
12.5	22	36	32
15	14	58	28

The flexural strength of all the zirconia toughened alumina composite samples produced from boehmite and zirconyl chloride is shown in Figure 4. These results suggest that as the sintering temperature is increased, the sintered composite strength also increases. Addition of zirconia to the alumina although, improves the composite strength, the actual magnitude of increase in the composite strength is low. Figure 5 shows typical scanning electron micrographs of sintered alumina and 10 %(vol.) zirconia / alumina composite surface. From Figure 5 (A - B), it can be suggested the addition of zirconia to the alumina matrix has inhibited the grain growth of alumina particles. Similar observations were noticed for all composite samples. For quantitative analysis on the grain size and size distribution,scanning electron micrographs with back scattered image contrast were obtained. The results on the microstructural examination of 10, 12.5 and 15 %(vol) zirconia alumina composites sintered at 1550°C is shown in Figure 6. These results suggest that the distribution of zirconia in the composites is uniform. For quantitative deter- mination of the zirconia or the alumina grain size, and size distribution, a number of scanning electron micrographs were taken of random from different parts of the test sample. The grain size and the histograms representing the grain size as a function of the fraction measured in a class were plotted. Table 4 illustrates typical mean size values obtained for zirconia and alumina grains in composites as a function of zirconia concentration. These results suggest that the alumina and zirconia mean grain size decreases with an increase in the zirconia concentration of a composite. It can also be noticed that the grain size increases with an increase in the sintering temperature.
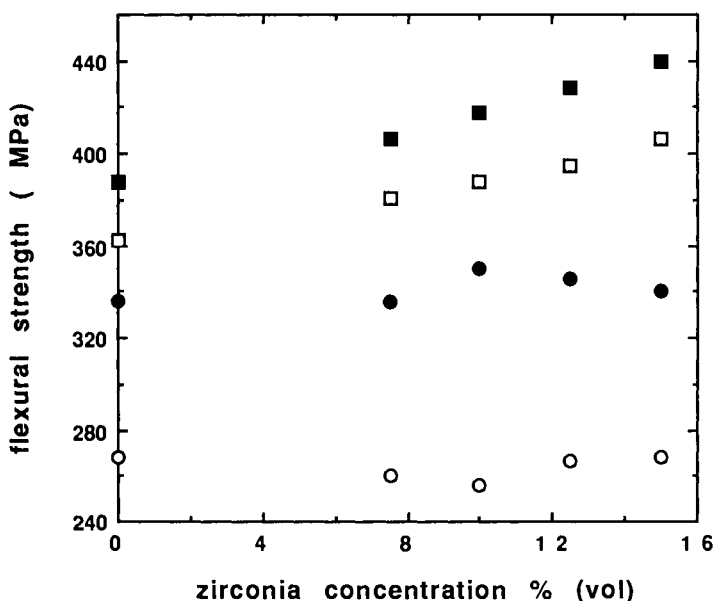
Fig. 4. Flexural Strength of Sintered Zirconia and Alumina Composites as a Function of Zirconia Concentration. Sintering Temperature (○) 1480, (●) 1500, (☐) 1550 and (■) 1600°C.
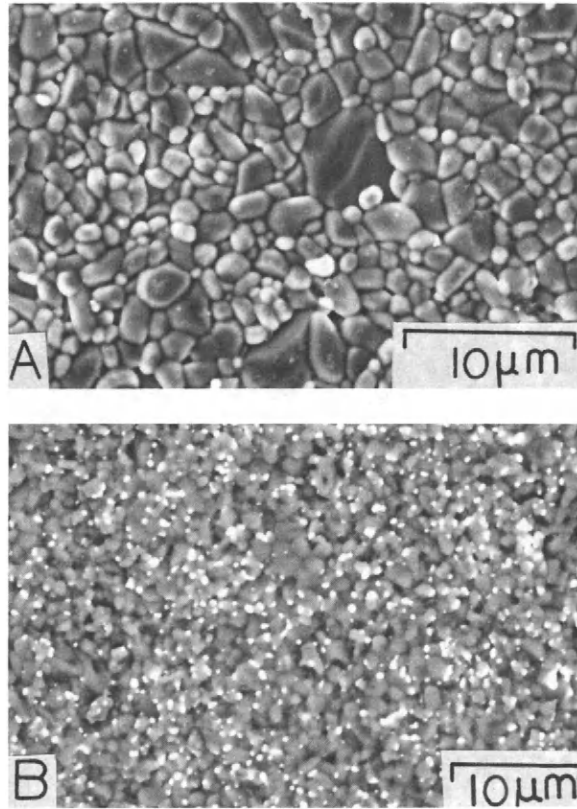
Fig. 5. Secondary Electron Image of the Microstructure of Sintered (A)
Alumina and (B) 10% (Vol.) Zirconia/Alumina Composite.

Note : It has to be emphasized that although the ziconia and alumina grain
size seen from the micrographs shown in Figure 5 and 6 appears to be 100 %
larger than the actual size, the results shown in Table 4 are the actual size.
These discrepancies arise from the fact that the electron microscope
conditions were very different. While obtaining the micrographs for grain
morphology, the contrast and brightness levels were equal. For quntitative
analysis, the micrographs were obtained under very high contrast conditions.
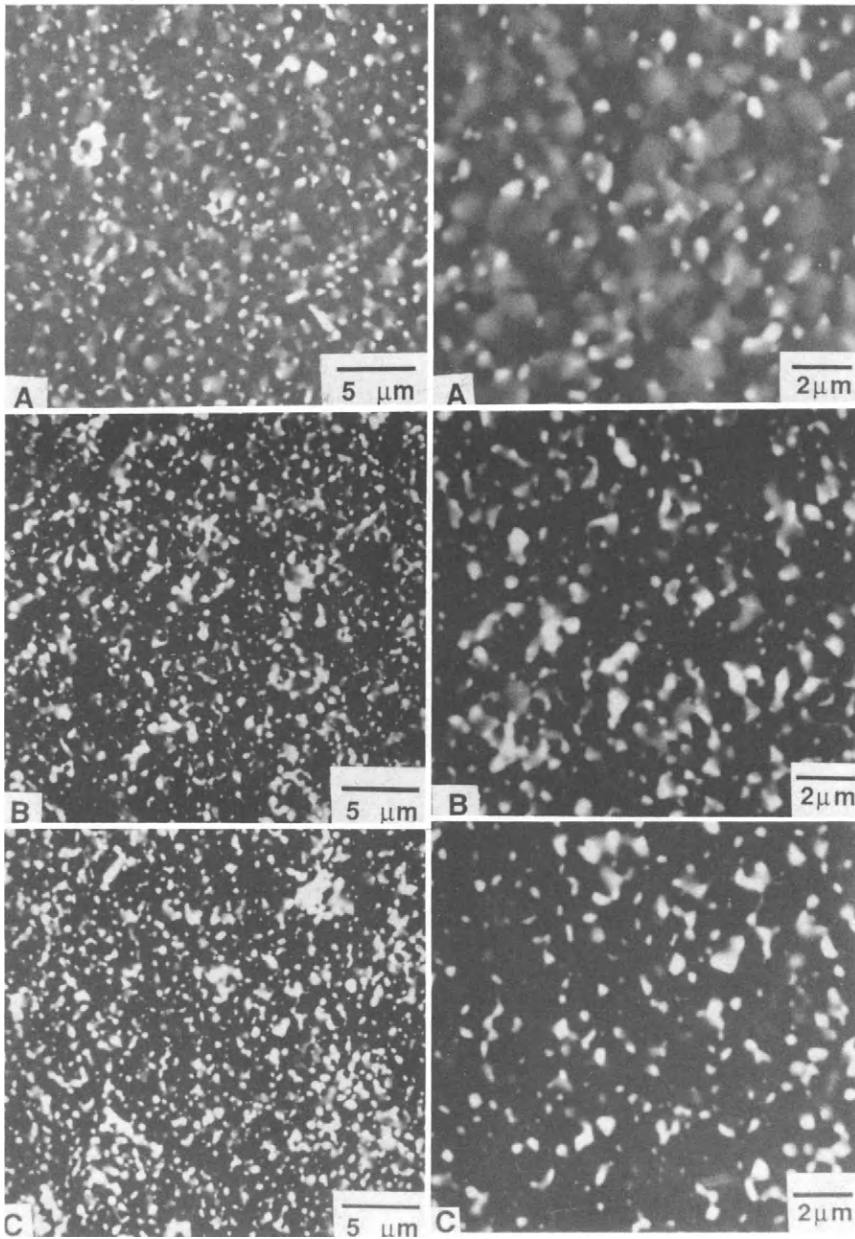
Fig. 6. Back Scattered Electron Image of the Microstructure of Sintered (A) 10, (B) 12.5 and (C) 15% (Vol.) Zirconia/Alumina Composites. Sintering Temperature 1550°C.

Table 4. Alumina and Zirconia Particle Mean Grain Size in Sintered Composites
as a Function of Zirconia Concentration

Sintering Concentration % (Vol.)	Sintering Temperature (^{o}C)	Grain Size (microns)	
		Alumina	Zirconia
0		3.2	---
10	1480	2.3	0.4
12.5		2.0	0.35
15		1.8	0.3
0		3.5	---
10	1500	2.4	0.45
12.5		2.2	0.4
15		2.0	0.35
0		3.8	---
10	1550	2.6	0.5
12.5		2.3	0.45
15		2.1	0.4
0		4.2	---
10	1600	2.8	0.6
12.5		2.4	0.6
15		2.2	0.5

NOTE: 10% (Vol.) ZrO_2 Composites show a narrow size distribution.
Standard deviation Al_2O_3: $\pm$ 0.4μm; ZrO_2: $\pm$ 0.2μm
12.5 and 15% (Vol.) ZrO_2 composites show broad distribution.
12.5% (Vol.) standard deviation: Al_2O_3: $\pm$ 0.8μm; ZrO_2: $\pm$ 0.2μm
15% (Vol.) standard deviation: Al_2O_3: $\pm$ 0.6μm; ZrO_2: $\pm$ 0.2μm

Discussion

The above results clearly demonstrate that coprecipitation of boehmite alumina
and zirconia in gel form prior to the sintering process would improve the
dispersibility of zirconia phase into the alumina phase. However, the sintered
composites are not dense, as a result their flexural strength is very low.
Therefore, it is essential to understand various steps that are involved in
the sintering process of the gel derived powders. It is known that during
hydrolysis and / or gelation, the water molecules are retained in the zirconia

or alumina crystals as network builders. Although, most of the crystal bound water can be removed by the calcination process below 600°C, it is possible that some trapped water or residual water of hydration may require still higher temperature for their removal. As a result, during the heating of the green ceramic to reach the sintering temperature, volatiles, such as the water vapor leaving the green ceramic may induce microcracks in the bulk. Such a microcracking process will impede the densification process.

Another alternate sequence of events involved in the sintering of zirconia in composites containing fine crystallite zirconia and crystalline alumina powders that was suggested in the literature [5] is as follows :

First, the fine crystallite zirconia particles will tend to coat the much larger alumina particles. During the sintering process fine zirconia coalesce into larger particles depending upon the state of agglomeration before sintering and their concentration on the surface of alumina. Both crystallite concentration and the state of agglomeration are important because, at low zirconia concentrations, fine crystallites have to migrate sufficiently over a long distance along the grain boundary into the vicinity of another zirconia particles inorder to aggregate and coalesce. The increase in the concentration of the zirconia particles, not only decreases the particle - particle separation distance in the green state, but also increases the probability of one fine crystallite reaching the other zircinia particle or the agglomerate very easily during sintering.

If the presence of only large agglomerates can contribute to the growth of the fine crystallites into large grains, fine crystallites that were bound together by the water molecules in the green ceramic processed using the gel route should also grow during sintering. Since our results suggest that a large fraction of the zirconia crystallites remain as fine crystallites, it is possible that the sintering mechanism for gel derived powder is different from the other processes. Qualitatively, it is reasonable to suggest that both microcracking of the green ceramic during heating as a results of the removal residual volatile products and the inability of the fine crystallite migration into the vicinity of another particle during sintering are responsible for the observed low density and mechanical strength of the sintered composites.

Since it is known that oxide surface polarizes in water, it is possible that the electrostatic repulsive forces on the surface of zirconia crystallites inhibit the zirconia crystal growth process during sintering. However, the application of an external mechanical driving force during migration and sintering of fine crystallites should counteract the effects of the surface repulsive forces of the fine zirconia particles. Therefore it would be interesting to examine the density and flexural strength of the sintered composites produced under hot press conditions. We intend to investigate the effects of sintering methods on structure and properties of these zirconia alumina composites and the results will be reported at a later date.

Conclusion

The following conclusions can be derived from the present investigation :

1. Fine zirconia particles produced in a gel along with boehmite particles dominate the electrophoresis process. At low pH values both alumina and zirconia can be precipitated and the mixture can be gelated very easily.

2. Zirconia particles in the composites retain their fine crystallite structure even after sintering at 1600°C.

3. The density and the flexural strength of the sintered composites increases with an increase in the sintering temperature. However, the effect of zirconia concentration on the strength of sintered composite is not very significant.

4. Zirconia particles can be dispersed very effectively into the alumina matrix using the gel process.

Acknowledgment

References

1. S.Baik, A. Blier and P. R. Becher, "Preparation of Al2O3 - ZrO2 Composites by Adjustment of Surface Chemical Behavior,"Mater. Res. Soc. Symp.Proc.,73, 791-800 (1986).

2. E. M. DeLiso, W. R. Cannon and A. S. Rao, "Dilute Aqueous Dispersions of ZrO2 and Al2O3," Mater. Res. Soc. Symp. Proc., 60, 43-50 (1986).

3. T. Kosmac, R. Wagner and N. Claussen, "X-ray Determination of Transformation Depths in Ceramics Containing Tetragonal ZrO2," J. Amer. Ceram. Soc., 64, C72-73 (1981).

4. M. Ezoe, Y. Murse, K. Daimon and E. Kato,"Formation and Thermal Changes of monoclinic Zirconia Polycrystalline Thin Films by Sol-Gel Process," Yogyo Kyohaishi, 94, 82-86 (1986).

5. A. Srinivasa Rao and W. R. Cannon, "Alumina / Zirconia Composites Produced from Commercial Alumina and Syntheiszed Hydrous Zirconia," Ceramics International (in Print).

Effects of agglomeration on the casting behaviour of dense aqueous suspensions of Al₂O₃/ZrO₂

K.J. Konsztowicz, S.G. Whiteway and D. Glennie

*Atlantic Research Laboratory, National Research Council Canada,
Halifax, Nova Scotia, Canada, B3H 3Z1*

ABSTRACT

Water suspensions of Al_2O_3/ZrO_2 were made containing 50 vol% of solids, the solids being of from 5 to 30 vol% of 3Y-PSZ. No deflocculants were used, and the zirconia was sub-micron in size. Viscosities and castabilities of suspensions, and green densities of castings, were measured. These properties were related to electrophoretic mobilities and particle/agglomerate size distributions of the suspensions. The spatial arrangement of microstructural features in cast bodies was examined by SEM. It is suggested that the microcracks in sintered ZTA composites originate with hetero-flocculation in the suspensions, leading to the formation of crack-like voids in the green body during casting.

KEYWORDS: zirconia-toughened alumina; aqueous suspensions; agglomeration; microcrack-toughening.

I INTRODUCTION

The toughening role of zirconia in ZTA composites is well established due to intensive research over the past 15 years. Various effects of zirconia have been described, for example transformation toughening (1), microcrack toughening (2) and hindering of grain growth of the alumina matrix (3). These mechanisms have the common characteristic that they provide microstructural features which effectively reduce the chance of initiating cracks, and/or can halt their disastrous propagation.

There are a number of parameters which affect particular processing stages of ceramic materials and which may serve to incorporate toughening features in the final sintered bodies. An example is agglomeration/flocculation of powders in liquid suspensions used for slip-casting. Baik, Bleier and Becher (4) have shown that hetero-flocculation is likely to occur in water suspensions of mixtures of alumina and zirconia powders. DeLiso, Cannon and Rao found (5) that an increasing degree of flocculation decreases the density of a green body of ZTA. Such porosity may, if properly controlled, lead to toughening of the sintered body.

The purpose of this work was to assess the effects of hetero-flocculation, in dense aqueous suspensions of alumina and zirconia powders, on the properties of the slurries. In addition, the microstructure of the green slip-castings was examined. The results suggest that hetero-flocculation of the suspended powders is the main reason for the appearance of crack-like voids in green bodies. Upon sintering these voids become multiple microcracks, with length and amount depending on the fraction of zirconia added to the mixture of powders.

II EXPERIMENTAL PROCEDURES

1. Materials

Partially stabilized zirconia[#] was attrition-milled for 4 hours and the size fraction under 1 μm recovered by centrifugation. The alumina[##] was of 0.5 μm

average particle size. Separate dense suspensions of 77 wt.% solids were prepared at pH 5 by blending these powders with deionized water and HNO_3.

The two slurries prepared this way were mixed together in appropriate proportions to give compositions of 5, 10, 20 and 30 vol % of zirconia with respect to the total content of solids. (In subsequent discussion the composition of suspensions will be denoted simply in %, the definition being as given above). Each composite suspension was homogenized for 12 hours in a planetary mixer[@] and then subjected to ultrasonication[@@] for 10 min at 90% of power before examination and use.

2. Characterization

(a)Water Suspension. The viscosity of the dense composite slurries was measured at room temperature using a digital viscometer[<>]. Electrophoretic mobility was determined[$] on diluted samples (300 ppm) prepared by high-speed centrifugation of the dense suspensions and remixing small amounts of the sediments with appropriate quantities of their respective supernatants at pH 5. A centrifuge-type instrument[$$] was used to determine the median size and particle size distribution of the grains/agglomerates, at pH 5, for dilute suspensions of the separate alumina and zirconia and all the composites. Samples for SEM studies were prepared from 30 ppm suspensions in deionized water at pH 5 by vacuum filtering, drying and carbon coating. The observations were performed in the backscattered-electron mode[*] and images processed by an image analyser[**] in order to enhance phase contrast.

(b)Consolidated Bodies. Slip-casting rates for all compositions were determined from the wall thicknesses (6) of cylindrical crucibles (5 cm in both outside dia. and height) cast into standard plaster molds[&] for a time of 1200 seconds. The densities of the dried green bodies were measured by a standard mercury displacement technique[&&]. From these measurements a casting constant was calculated. After these measurements the samples were broken and their fresh fracture surfaces were carbon coated and observed under the SEM for the presence of crack-like defects. In addition to the crucible shapes, rectangular plates of the composites, 10 x 7 cm, were cast onto plaster surfaces. Plates and crucibles were dried in air and sintered at 1500 C for 2 hours to a density of 99% of theoretical. Zirconia was retained completely in tetragonal form after sintering as well as after grinding and polishing.

[#] 3Y-PSZ from Toyo Soda
[##] Reynolds RCHP-DBM
[@] Turbula, type 2TC
[@@] Heat Systems, model W-385
[<>] Brookfield, model LVTD
[$] Rank Brothers, Mark III
[$$] Horiba, model Capa 700

[*] JEOL 2XA 35C
[**] Kevex 8005
[&] The molds were made from U.S Gyspum #1 Pottery Plaster, mixed with water in the proportion 2000g plaster to 1460g water.
[&&] The mercury densitometer was from Fairey Tectramics.

III RESULTS

The viscosity of the dense suspension, at pH 5, is shown as a function of composition in Fig. 1. The viscosity exhibits a minimum at 10% of ZrO_2.
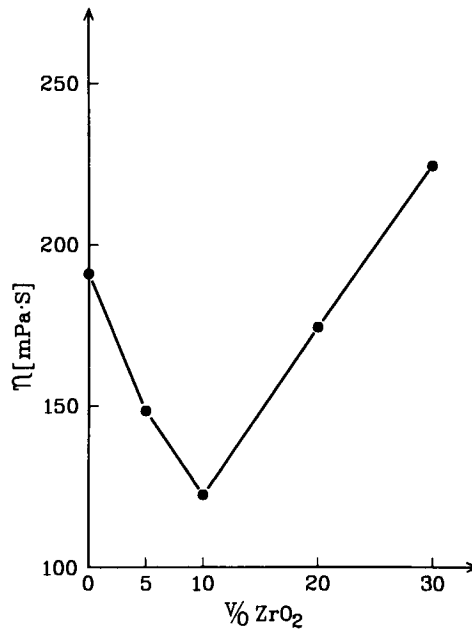
Figure 1 Effects of composition changes on viscosity of zirconia/alumina dense suspensions.

The initial sizes of the alumina and zirconia particles/agglomerates differed from the values given by the manufacturers and also differed from the values measured for the mixtures made here. A plot (Fig. 2) of the median grain/agglomerate size vs. the composition shows a slight minimum at a concentration 10% ZrO_2.
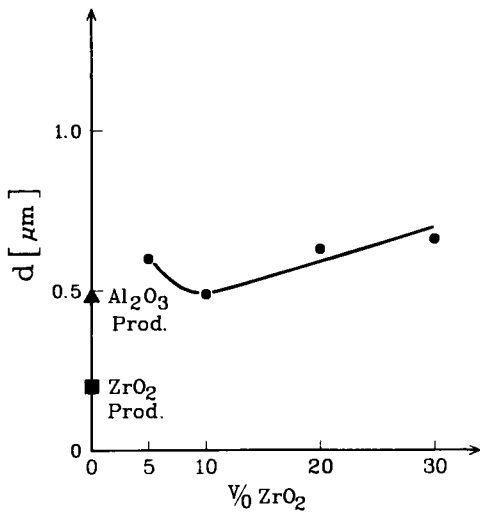
Figure 2 Changes of median zirconia particle/agglomerate size in dense suspensions with increasing zirconia content.
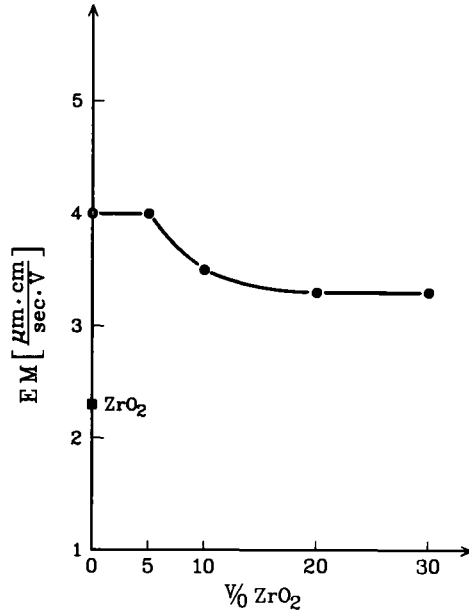
Figure 3 Effects of increasing content on electrophoretic mobility of powder mixtures in diluted (300 ppm) water suspensions.

Figure 3 shows the electrophoretic mobility of the suspensions at pH 5 as a function of composition. The addition of 5% zirconia does not affect the mobility, relative to pure alumina. With further addition of zirconia to 20% the mobility is decreased, but is not lowered further at a concentration of 30%. The electrophoretic mobility of pure zirconia is about half that of alumina.
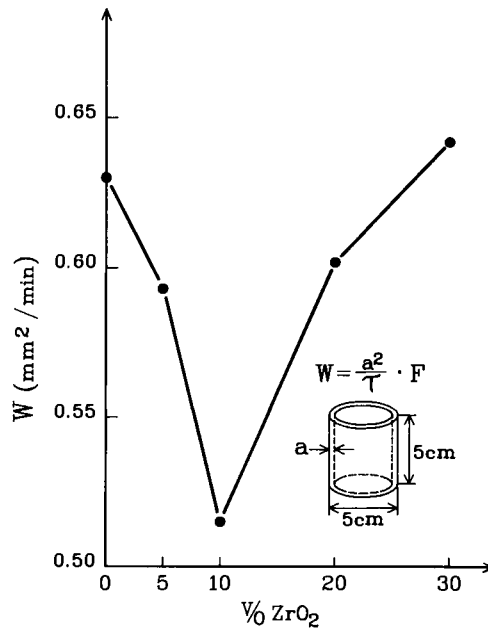
Figure 4 Casting kinetics of dense water slurries of zirconia/alumina
composites as a function of zirconia content. Casting constant "W"
calculated from wall thickness ("a") of crucibles cast with the same
time "τ".

The curve of the casting constant vs. the composition (Fig. 4) also shows a
minimum at 10%. The density of the green body is affected by the casting
constant, although the plot of green density vs composition (Fig. 5) does not
show an inflection like some of the other plots presented here. Instead, the
density of the green bodies decreased steadily with increasing amount of
zirconia in a composition.
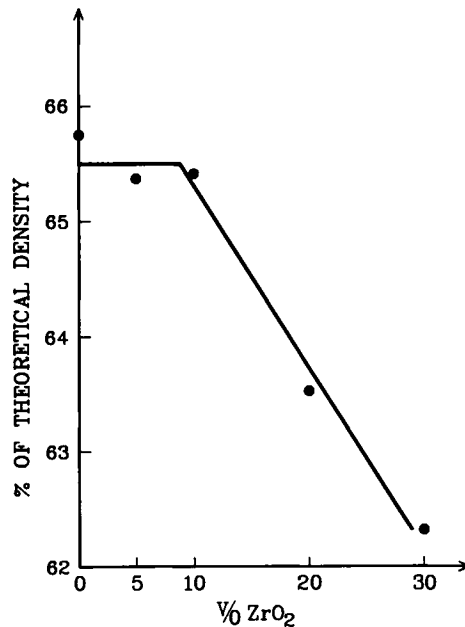
Figure 5 The bulk density of green zirconia/alumina composites (measured by
mercury displacement technique) as a function of increasing zirconia
amount.

Observations from SEM

A series of figures (Fig. 6, a-e) shows images of powder suspensions diluted to
30 ppm, observed in the backscattered-electron mode, and processed by the image
analyser. Zirconia shows as the white phase and alumina as the gray. These
micrographs clearly show the effect of the amount of zirconia on the degree of
flocculation in composite suspensions. The distribution of grains in pure
alumina as shown in Fig. 6a is quite regular, although a few evenly distributed
flocs several microns in size are visible. In contrast (Fig. 6b) the grains of
pure zirconia powder have a stronger tendency to flocculate; this is not
surprising considering that the electrophoretic mobility of zirconia is about
half that of alumina at pH 5. At a composition of 5% (Fig. 6c) almost all the
zirconia grains preferentially join with alumina grains to form flocs a few
microns in size.

At a concentration of 10% (Fig. 6d) the zirconia grains become quite evenly
distributed in flocs with alumina. It is notable that these flocs of mixed
grains are the smallest and the most regular in size compared to all other
compositions.
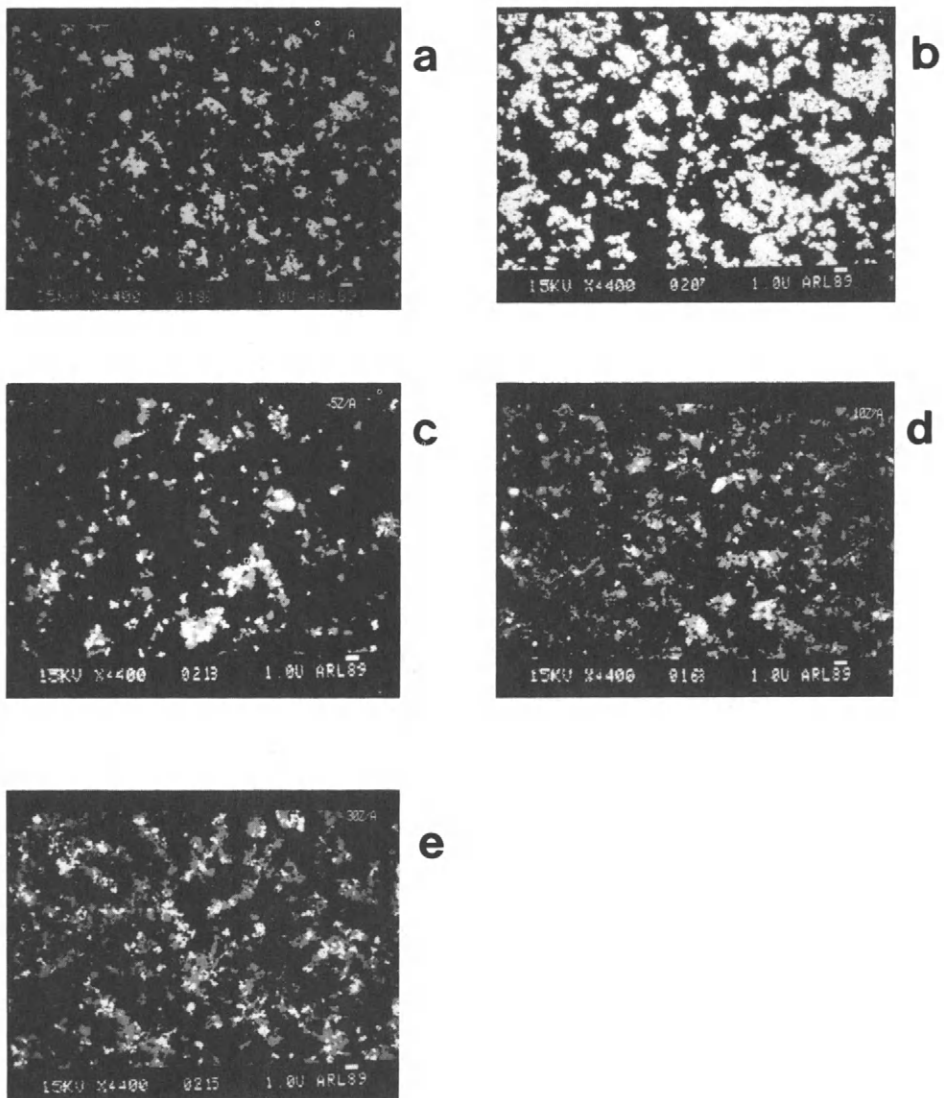
Figure 6 Dispersed powders of alumina (a) zirconia (b) and their mixtures: (c) 5v/o ZrO_2/Al_2O_3; (d) 10v/o ZrO_2/Al_2O_3; (e) 30v/o ZrO_2/Al_2O_3. Backscattered electron images processed by image analyser to give uniform white color to zirconia and gray to alumina.

Further increases of zirconia produce large flocs of mixed grains, which even become interconnected at a composition of 30% (Fig. 6e). The above images do not necessarily represent the size of alumina/zirconia flocs in the dense water slurries, since they were of samples obtained from very diluted suspensions deposited on a microfilter. However these 2-dimensional images should reasonably reflect the mechanisms acting in casting suspensions.
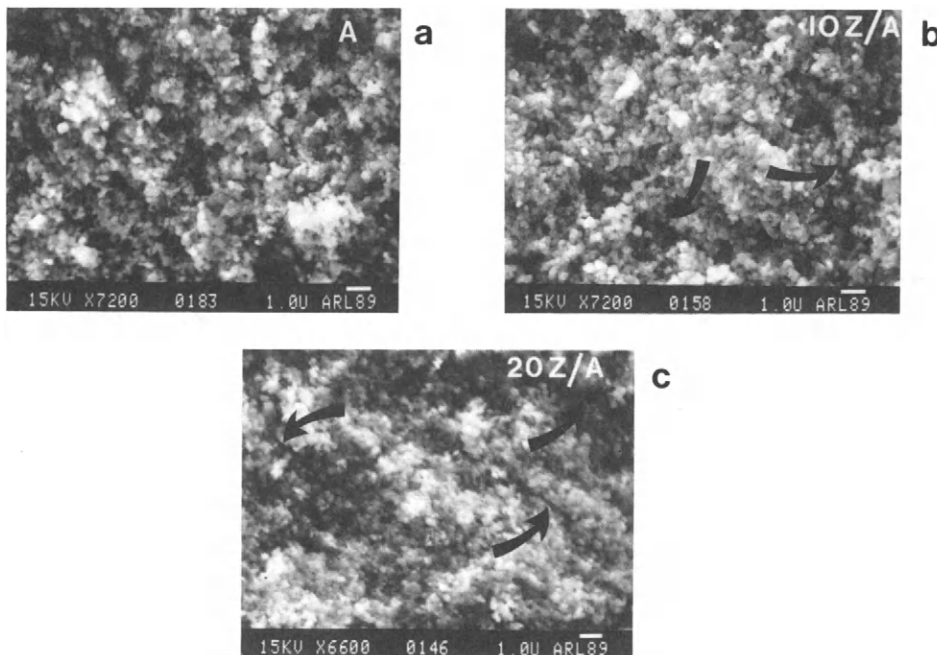
Figure 7 Fracture surfaces of green bodies of alumina (a); 10v/o ZrO_2/Al_2O_3 (b); and 20v/o ZrO_2/Al_2O_3 (c).

The next series of SEM images are of the fracture surfaces of actual green castings, dried and with density about 65% that of theoretical. They too indicate the development of flocs of different sizes as the concentration of zirconia is changed. Figure (7a) is for pure alumina, and shows that the microstructure is built from small units which would have been flocs in the water suspension. Some small pores can be observed, as well as another type of microstructural feature - defects of crack-like aspect which originated in the separations between the flocs of the casting suspension. At a composition of 10% (Fig. 7b) the microstructure reveals more pronounced separation lines between the (relatively small) flocs and the crack_like voids do not exceed 20 microns in length. These crack-like voids surrounding the zirconia/alumina flocs become quite large in the case of the 20% composition, Fig. (7c).

These observations of cracklike voids in the microstructures of green bodies of these composites, together with the previous observations of the mechanism of flocculation, suggest that the microcracks found in sintered ZTA materials originate with the voids surrounding flocs of the mixed powders. This suggestion is reinforced by the observation that the size of the flocs changes with the concentration of zirconia in water suspensions.

IV DISCUSSION

Microcracks have been observed often in ZTA composites and their presence, considered necessary for the occurence of toughening, is usually ascribed to (t-m) phase transformation of zirconia under stress (transformation toughening) or during sintering (microcrack toughening). Green (7) found that the size of microcracks scaled with the zirconia grain size, about 1 micron. Lange (8) found crack-like voids around large agglomerates, elimination of which increased the strength to 1 GPa, although some other microcracks of the size 10μm were sill observed, particularly in compositions with more than 10% zirconia. Ruhle et al. (9), in their study of process-zone thinning, defined the length of microcracks growing in a stress field as being up to 10μm. However, despite the very careful processing they used, they found also much larger cracks in ZTA material, the presence of which was difficult to explain and which were finally defined as "processing defects", responsible for lowering the strength of the ZTA composite. Wilfinger and Cannon (10) found many cracks in their ZTA materials processed from dense slurries. Recently Tomaszewski (11) quantitatively assess the average length of cracks in ZTA materials obtained by pressureless sintering of the mixtures of sedimented and chemically processed powders. He found the minimum value of about 100 microns not only in those ZTA composites that contained zirconia transformed to the monoclinic phase but also in materials with the tetragonal phase completely retained.

Considering the general lack of agreement about the time they appear and the length of the microcracks, it is possible that they not only originate with the phase transformation of ZrO_2 particles under stress or during sintering, but in addition might be due to powder processing before consolidation. The results of the present work show that crack-like voids surrounding powder flocs already exist in a green body of ZTA composite. The size and number of these defects depends on the zirconia content.

Pask (12) has shown that the addition of SiO_2 to Al_2O_3 changes strongly its Z-potential. The work of Kagawa et al (13) with several oxide systems shows that the iso-electric point (and thus also the electrophoretic mobility at a given pH) changes significantly when two different ceramic powders are mixed in aqueous suspension. Results given here confirm that the electrophoretic mobility changes upon the addition of zirconia to alumina. The viscosities of the mixtures, which are sensitive to the occurence of flocs (14), indicate that there is an optimum floc size corresponding to the addition of about 10% of zirconia. These observations are strongly supported by the microscopic evidence of flocculation. The occurence of hetero-flocculation of zirconia/alumina water suspensions has been indicated by Baik et al (4). The density measurements show that the porosity of the green casts increases as the proportion of zirconia increases. Some of this porosity occurs as crack-like voids and have been observed here directly using the SEM. Recent results of DeLiso et al (5) also confirm the decrease of density of ZTA composite green bodies with increase of the measured floc size.
Thus it might be postulated that microcracks in ZTA materials are formed during powder mixing, due to hetero-flocculation of zirconia and alumina grains. Crack-like voids appear around the flocs during formation of the microstructure of the green body and they do not close completely upon consolidation.

The better the processing technique used the better the homogeneity and the

smaller the floc size, thus the smaller the cracks in the green and the sintered body. In particular HIP and HP can reduce significantly the size of crack-like voids. Tomaszewski (11) observed cracks up to 100 microns in length for pressureless sintered material. The measured fracture toughness in this case was about 7 MPa•m$^{1/2}$ (typical for ZTA materials containing microcracks), while the bending strength was strongly affected by the length of cracks and was only about 300 MPa. At the other extreme examples of completely dense ZTA microstructures can be found in the literature, such as in the work of Rajendran and Rossel (15) using co-precipitation. Their material had a fracture toughness of only 4 MPa•m$^{1/2}$ but a strength as high as 2,4 MPa. This material had no flocs at the powder-mixing stage so that without microcracks having been introduced in this way its toughness remained low. The zirconia particles were too small to cause transformation microcracking and their only role was in hindering grain growth of the alumina; this helped to provide the high strength.

In case of well processed ZTA materials containing microcracks of size between 1 to 10 microns after sintering, the mechanism of microcrack toughening usually gives values of K_{1c} in the range of 6 to 8 MPa•m$^{1/2}$. Additionally, when these materials contain zirconia grains of appropriate size (16) enabling the retention of tetragonal phase after sintering, values of toughness of the order of 10 MPa•m$^{1/2}$ have been reported.

It is suggested here that the structured voids introduced at the mixing stage of composite processing, by hetero-flocculation of powders, is the primary cause of microcrack toughening. It is felt that the presence of crack-like voids in the green body helps to reduce the transformation strain energy during sintering. An increase in zirconia results in an increase in floc size and length of the crack-like void in the green body, making it easier for tetragonal zirconia to transform into monoclinic in the final stages of sintering. For this reason the ZTA composites processed from water suspensions containing more zirconia have increasing amounts of the monoclinic phase.

CONCLUSIONS

The primary feature of the explanation thus is that microcracks originate with the separation voids between the powder flocs. Transformation either follows or does not, depending on the size of tetragonal zirconia grains. Due to particular features of hetero-flocculation the ZTA composites always have the optimum fraction of zirconia defining optimum floc size. This has to be related to the density/length ratio for microcracks which, in conjunction with residual stresses, might be the primary reason for the existence of a maximum at fracture toughness values found for ZTA materials containing particular amounts of zirconia.

ACKNOWLEDGEMENTS

REFERENCES

1. N. Claussen, "Stress-Induced Transformation of Tetragonal ZrO_2 Particles in Ceramic Matrices ", J. Am. Ceram. Soc., 61 [1-2] 85-86 (1978).

2. N. Claussen, "Fracture Toughness of Al_2O_3 with an Unstabilized ZrO_2 Dispersed Phase", J. Am. Ceram. Soc., 59 [1-2] 49-51 (1976).

3. F.F. Lange and Margaret M. Hirlinger, "Hindrance of Grain Growth in Al_2O_3 - ZrO_2 Inclusions", J. Am. Ceram. Soc. 67 [3] 164-168 (1984).

4. S. Baik, A. Bleier and P.F. Becher, "Preparation of Al_2O_3 - ZrO_2 Composites by Adjustment of Surface Chemical Behaviour", in "Better Ceramics Through Chemistry, II", MRS Proceedings (1987).

5. E.M. DeLiso, A.S. Rao and W.R. Cannon, "Electrokinetic Behaviour of Al_2O_3/ZrO_2 Powders in Dilute and Concentrated Aqueous Dispersions", Advances in Ceramics, 21 (1987).

6. G.N. Babini, C. Galassi, R. Lapasin and E. Lucchini, "Rheological Properties of Aqueous Suspensions of SiN_3 - Si - Al_2O_3 - ZrO_2 Powders", Journal de Physique C1, 47, 73-78 (1986).

7. D.J. Green, "Critical Microstructures for Microcracking in Al_2O_3 - ZrO_2 Composites", J. Am. Ceram. Soc., 65 [12] 610-614 (1982).

8. F.F. Lange, "Processing-Related Fracture Origins". J. Am. Ceram. Soc. 66 [6] 396-408.

9. M. Ruhle and N. Claussen, "Transformation and Microcrack Toughening as Complementary Processes in ZrO_2 - Toughened Al_2O_3", J. Am. Ceram. Soc. 69 [3] 195-197 (1986).

10. K. Wilfinger and W.R. Cannon, "Processing of Transformation-Toughened Alumina", Cer. Eng. Sci. Proc., 7, 1169-1181 (1986).

11. H. Tomaszewski, "Toughening Effects in Al_2O_3-ZrO_2 System", Ceramics International 14, 117-125 (1988).

12. J.A. Pask, "Ceramic Processing-A Ceramic Science", Bull. Am. Ceram. Soc. 58, 1163 (1979).

13. M. Kagawa, Y. Syono, Y. Imamura and S. Usui, "Surface Characterization of Ultrafine ZrO_2-SiO_2 Powders by Electrophoretic Mobility Measurements", J. Am. Ceram. Soc. 69 [3] C50-51 (1986).

14. E.M. DeLiso, W.R. Cannon and A.S. Rao, "Dispersion of Alumina-Zirconia Powder Suspensions", Advances in Ceramics Vol. 24: Science and Technology of Zirconia III, 335-341 (1988).

15. S. Rajendran and H.J. Rossell, "High Strength Alumina-Zirconia Composites", pp. 549-553 in Ceramic Developments, Materials Science Forum Volumes 34-36 (1988). Trans Tech Publications Ltd., Switzerland.

16. R.C. Garvie, "Critical Size Effects in Alumina-Zirconia Alloys", Advances in Ceramics Vol. 24: Science and Technology of Zirconia III, 55-69 (1988).

Science of sintering ceramic matrix composites

Mohamed N. Rahaman
*Department of Ceramic Engineering, University of Missouri-Rolla,
Rolla, Missouri 65401, U.S.A.*

ABSTRACT

Critical issues in the conventional, pressureless sintering of ceramic matrix
composites containing particulate or whisker-type inclusions are examined.
Current work in the search for processing improvements which will allow the
attainment of high density and controlled microstructure by pressureless
sintering is illustrated with examples that exploit the use of sintering aids,
colloidal techniques and viscous sintering.

KEYWORDS

Ceramic matrix composites; processing; sintering; colloidal processing; sintering
aids; viscous sintering.

INTRODUCTION

Ceramic matrix composites are required to meet the demands of many technological
applications ranging from advanced heat engines to electronic substrates. The
most recognized path to the formation of advanced ceramics involves powder
compaction into a porous body that is made dense by heat treatment. In the
formation of composites, however, the presence of second phase inclusions (i.e.
particles, whiskers or fibers) is found to lead to a drastic reduction in the
densification rate of the porous matrix. Thus considerable difficulties are often
encountered in the formation of ceramic matrix composites by conventional
sintering.

In order to enhance the densification rate of composites and to achieve the high
density normally required, techniques such as hot-pressing (Becher and Wei, 1984;
Wei and Becher, 1985; Gadkaree and Chyung, 1986; Porter, Lange and Chokshi,
1987), hot isostatic pressing (Lundberg and coworkers, 1987) and liquid phase
sintering (Tiegs and Becher, 1987) have been employed. These techniques,
however, suffer from a number of severe disadvantages. Hot pressing and hot
isostatic pressing are relatively expensive forming methods and they also have
size limitations. Sintering aids can lead to a deterioration of properties.

Because of the considerable benefits of finding solutions to the problems
encountered in the sintering ceramic matrix composites, numerous efforts have
been made within the past five years, both theoretically and experimentally, to
understand the problems at a fundamental level so that the conventional sintering
process can be better applied to the fabrication of ceramic matrix composites. In
identifying the current issues, it is important to consider the advances that
have been made in theoretical modelling, the quantitative testing of theoretical
predictions by model experimental investigations, the search for processing
improvements, and the results of the exploitation of any processing improvements.
These issues are now examined.

CURRENT ISSUES

Theoretical Modelling

Transient stresses are developed during sintering when one region in a
powder compact shrinks differently from its surroundings. Deviatoric creep
will always seek to relieve the stresses. The calculation of the stresses
therefore requires a viscoelastic solution to the problem where differential
shrinkage generates internal stresses in the body and the internal stresses
are relaxed by creep. Several authors have attempted to determine analytically
the magnitude of the transient stresses and their effect on densification (Evans,
1982; Raj and Bordia, 1984; Hsueh and coworkers, 1986; Scherer, 1987; De Jonghe
and Rahaman, 1988). A convenient model is the "composite sphere" consisting of a
spherical domain (i.e. the inclusion) which can shrink faster or slower than the
surrounding spherical cladding (i.e. the matrix). For the case where the domain
does not sinter as fast as the matrix (i.e. inert, rigid inclusion), a
compressive stress, σ_i, arises within the inclusion and radial compressive and
tangential tensile stresses arise within the matrix. The stresses in the matrix
could be resolved into a shear stress, dependent on the distance from the
inclusion/matrix boundary and a hydrostatic tensile stress, σ_m, independent of
position but dependent on the volume fraction of inclusion, v_i; σ_m is usually
referred to as a "backstress" since it opposes the sintering stress due to
reduction in surface area. The stresses σ_i and σ_m satisfy a "force balance"
condition and are related by the equation

$$\sigma_m(1 - v_i) + \sigma_i v_i = 0 \qquad\qquad (1)$$

An important aspect of the theories of Raj and Bordia (1984) and Hsueh and
coworkers (1986) is that they predict large backstresses. Scherer (1987) has
shown that the large stresses predicted by these authors result from
incompatible expressions for the shear and bulk viscosities of the matrix.
Further, the analysis of Scherer showed that the densification rate of the
matrix phase of the composite can be expressed as

$$\dot{\epsilon}_{m\rho} = (\Sigma/\eta_{mb})/[1 + 4v_i\eta_{ms}/(3\eta_{mb})] \qquad\qquad (2)$$

where Σ is the sintering stress, v_i is the inclusion volume fraction, and η_{mb}
and η_{ms} are the bulk and shear viscosities of the matrix, respectively. A
different treatment of the problem by De Jonghe and Rahaman (1988) has yielded
an expression similar to Eqn. (2). According to this equation, the matrix
densification rate of the composite is equal to that of the unreinforced
matrix, (Σ/η_{mb}), times a factor that depends on v_i and the ratio η_{ms}/η_{mb} only.
Since this ratio is approximately constant within the density and temperature
ranges of the experiments (De Jonghe and Rahaman, 1988; Chu, De Jonghe and
Rahaman, 1989), the benefits that may result from changes in the processing
parameters or the heating schedules would be those that are obtained in the
improved sintering or microstructure development of the unreinforced matrix.

Model Experimental Studies

Although many experimental studies have been made over the past twenty years
to understand the sintering of bimodal and agglomerated powders, the first
model experiments in which the densification of a two-phase powder compact
containing controlled amounts of an inert, particulate phase was measured as a
function of time or heating schedule were performed by De Jonghe, Rahaman and

inclusions; the matrix phase was a polycrystalline oxide (ZnO) or an amorphous glass (soda-lime) and the inclusion phase was SiC.

For the amorphous matrix composite, the densification rate obeyed the rule of mixtures when the inclusion volume fraction, v_i, was less than 0.1, and could be well described by the theory of Scherer (1987) for $v_i < 0.15$. At higher inclusion content, network formation, which was not taken into account in Scherer's theory, appeared to be the main cause of the deviation from theory. In contrast, the inclusions drastically reduced the densification rate of the polycrystalline matrix composite even at quite low inclusion content (< 5 v%). Similar data for polycrystalline matrices have been obtained recently by Bordia and Raj (1988) and Tuan, Gilbart and Brook (1989). The effect of the inclusions on densification is illustrated in Fig. 1 where the matrix densification rate of the composite relative to that of the unreinforced material is plotted as a function of the matrix density for both the glass matrix composite and the polycrystalline matrix composite; the inclusion content of the samples are approximately the same ($\approx$ 10 v%) and the same technique was used to form the green composite samples.

An important current issue is understanding the difficulties in densifying polycrystalline matrix composites. As pointed out earlier, the earlier explanation in terms of high backstresses due to mismatch in densification rates between the matrix and the inclusions has been seriously undermined by the theory of Scherer (1987). In addition, network formation between the inclusions appears to be unimportant for the low inclusion volume fraction at which the drastic reduction in the densification rate is clearly seen. Two suggestions that are currently receiving serious attention are due to Lange (1988) and Bordia and Scherer (1989). Lange attributed the drastic reduction in the densification rate to "damage" (e.g. voids) in the matrix produced by differential densification that result from non-uniform packing or from the powder compaction process. Bordia and Scherer suggested that the different stress fields in the radial and hoop directions experienced by the shrinking matrix can lead to anistropies in the densification rate and the shear and bulk moduli and these, in turn, cause a reduction in the densification rate.

Recently Rahaman and De Jonghe (1989) utilized the technique of loading dilatometry to investigate the effect of the inclusions on both the shear deformation (creep) and densification processes. In this technique, a low uniaxial stress is applied to the compact during sintering; measurement of the axial and radial strain rates allows the determination of the creep strain rate and the volumtric densification rate. The system that was studied consisted of a fine-grained matrix of ZnO reinforced with 10 v% of coarse SiC inclusions. It was found that the time dependence of the creep rate is unaffected by the inclusion phase. The densification rate was, however, drastically reduced by the presence of the inclusions. In the context of expressions for densification and for creep of particulate composite systems, this observation restricts the number of possible causes that may lead to the strong lowering of the densification rate by a relatively low volume fraction of inclusions. For a powder compact creeping under a low uniaxially applied stress, σ_z, the creep rate may be expressed as (Rahaman and De Jonghe, 1987b, De Jonghe and Rahaman, 1988)

$$\dot{\epsilon}_c = \sigma_z/\eta_c \tag{3}$$

where η is the creep viscosity. Similarly, defining the sintering stress, Σ, as an equivalent externally applied stress, then the densification rate may be expressed as

$$\dot{\epsilon}_\rho = \Sigma/\eta_\rho \tag{4}$$

where η_ρ is the bulk (or densification) viscosity.
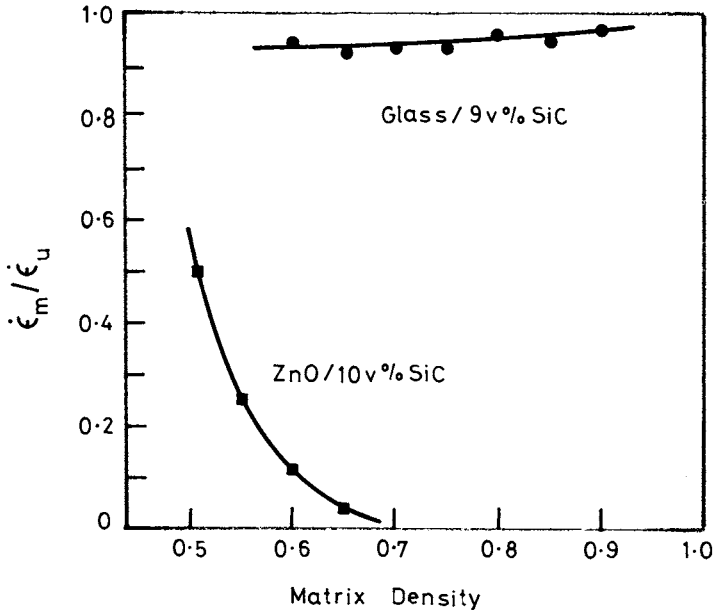
Fig. 1.   Matrix densification rate for a composite with a glass
          matrix or a polycrystalline matrix.

Model considerations as well as experiments (Scherer, 1987; De Jonghe and
Rahaman, 1988) suggest strongly that the creep viscosity and the bulk
viscosity are intimately related. It is plausible to assume that the
indifference of the creep viscosity to the presence of the inclusion phase
will be similarly reflected in the bulk viscosity. It can therefore be argued
that the relative decrease in the densification rate resides in the decrease
of the sintering stress, Σ, rather than in an increase in the bulk viscosity.
Such a decrease must then be due to an effect that can be expressed as a
quasi-hydrostatic backstress, σ_{qb} opposing Σ. The matrix densification rate of
the composite can then be expressed as

$$\dot{\epsilon}_{m\rho} = (\Sigma/\eta_\rho)(1 - \sigma_{qb}/\Sigma). \tag{5}$$

While a number of factors can lead to a reduction in Σ, it should be pointed
out at this stage that the backstress due to mismatch in the densification
rate between the matrix and the rigid inclusions (i.e. σ_m) cannot be proposed
as the main component of σ_{qb}; model considerations indicate clearly that σ_m is
small.

The experiments of Rahaman and De Jonghe (1989) also show that the reduction
in the densification rate (due to the inclusion phase) is present from the
earliest stages of densification, as shown in Fig. 2 where the ratio of the
densification rate to the creep rate is plotted as a function of density for
the reinforced and unreinforced samples. This observation indicates that the
causes of the reduction are also present from the beginning and have to be

sought in differences in matrix microstructure caused in the compaction process or in the spacial distribution of the dispersed phase, along the lines proposed by Lange (1988).

Search for Processing Improvements

An important issue becomes the search for processing improvements which will allow optimization of the composite densification rate during conventional sintering. In terms of Equation (5), these include increasing the sintering stress, reducing the matrix viscosity and reducing the quasi-hydrostatic backstress. For inclusion contents > ≈ 15 v% network formation between the inclusion particles (Lange, 1987) leads to a severe reduction in the densification rate and must be considered. The processing improvements will now be addressed in the following sections:
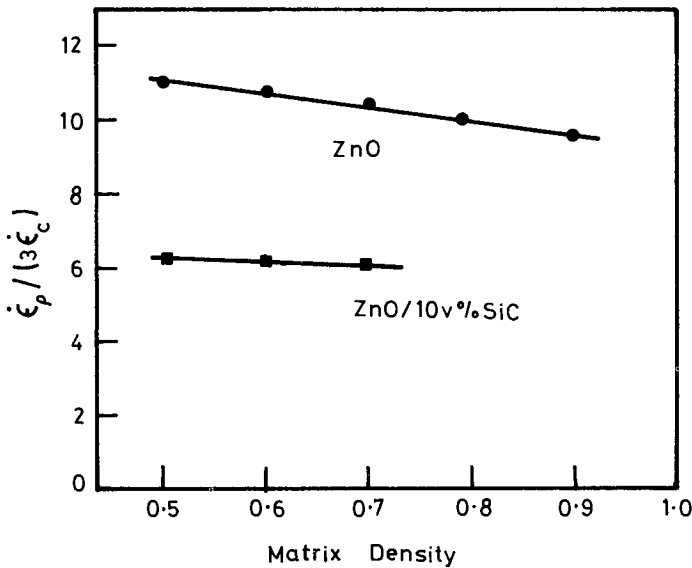
Fig. 2. The reduction in the densification rate occurs from the earliest stages of sintering for a polycrystalline matrix composite.

(a) Increase in the sintering stress, Σ. Since the sintering stress scales inversely as the mean pore radius, the use of fine, active powder as the matrix material would be beneficial.

(b) Reduction in the matrix viscosity, η_ρ. For polycrystalline materials where matter transport occurs by diffusion, the viscosity can be expressed by the equation:

$$\eta_\rho = G^n kT/(AD\Omega) \tag{6}$$

where G is the matrix grain size, n is an integer that depends on the

diffusion mechanism (i.e. n = 2 for volume diffusion and n = 3 for grain boundary diffusion), k is the Boltzmann constant, T is the temperature, A is a numerical constant, D is the diffusion coefficient, and Ω is the atomic volume. Consequently, small particle size and high temperature would be desired.

Benefit may also be achieved through selection of the matrix material. The use of glass-ceramic matrices that permit densification prior to crystallization would be effective in reducing the matrix viscosity during the densification stage. The effectiveness of the lower matrix viscosity for enhancing densification is illustrated for the glass and ZnO matrix composites discussed earlier (Fig. 1); the viscosity of the glass matrix is approximately 2 orders of magnitude lower than that of the ZnO as shown in Fig. 3. The use of controlled heating schedules in which the matrix viscosity is continuously decreasing during sintering is also expected to be beneficial for glass-ceramic matrix composites.
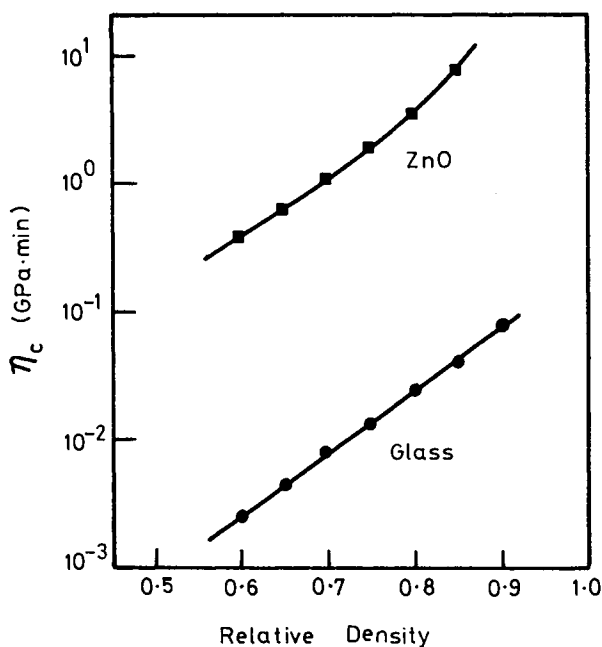
Fig. 3. Difference in matrix viscosity for a glass matrix and a polycrystalline zinc oxide matrix.

Additives that form a liquid phase at the sintering temperature are also effective in reducing the matrix viscosity. However, these sintering aids would be useful only if the presence of the second phase does not lead to a severe degradatin in properties. In this context, a better objective would be the development of sintering with a transient liquid phase.

(c) Reduction in the quasi-hydrostatic backstress, σ_{qb}. The techniques outlined above for reducing the matrix viscosity would also be expected to be

effective for reducing the the backstresses developed during sintering since they cause an increase in the stress relaxation rate. Since the major component of σ_{qb} appears to be the backstress due to differential densification within the matrix phase, the use of colloidal processing techniques to produce ordered distributions of the dispersed phase and to eliminate heterogeneities (e.g. density variations and microcracks) from the matrix phase of the green composite would be beneficial. The reduction in the minor component of σ_{qb} due to the mismatch in densification rate between the matrix and the inclusion phase has to be found in additional treatments; one technique that has been suggested is the use of fugitive coatings on the inclusions.

(d) Reducing the constraints of network formation between the inclusions. The inclusion particles will initially interfere and later come into contact and may stop densification at some critical volume fraction, f^*. For inclusions of uniform size, percolation theory indicates that the inclusions will form a contiguous network when $f \approx 0.16$. Although the densification rate will be reduced, appreciable densification will still occur above this critical volume fraction if the inclusion network is not stiff enough to resist the sintering stress (Rahaman and De Jonghe, 1987). Therefore reducing the matrix viscosity would also be beneficial for reducing the constraints of network formation.

Exploitation of Processing Improvements

Three techniques have shown good promise for achieving high densities with controlled microstructure by conventional, pressureless sintering. They involve the use of sintering aids that form a liquid phase at the sintering temperature, colloidal processing and viscous sintering prior to crystallization. These techniques are discussed in the following sections.

(a) Liquid phase sintering. In terms of Equation (5), the use of liquid phase sintering promotes densification through a reduction in the matrix viscosity which, in turn, can lead to a reduction in the quasi-hydrostatic backstresses that arise from differential densification. Tiegs and Becker (1987) used conventional processing techniques to fabricate green composites consisting of a polycrystalline Al_2O_3 matrix containing SiC whiskers and studied the sintering of these composites with or without liquid phase sintering additives (0.5 wt% MgO + 2 wt% Y_2O_3). For a sample containing 15 v% whiskers (aspect ratio $\approx$ 40), the use of the liquid phase sintering additives produced a final relative density of 0.82, compared to a value of 0.70 for the sample sintered without a liquid phase. Milling the whiskers to reduce their aspect ratio to $\approx$ 15-20 (thereby reducing the severity of network formation) produced a further increase in the final density ot 0.92.

(b) Colloidal processing. This technique is capable of producing green composite samples with uniform distributions of the inclusion phase in addition to unifrom, controlled packing of the matrix phase. Consequently it promotes densification through the reduction of the quasi-hydrostatic backstress. The technique was used recently by Sacks, Lee, and Rojas (1988) to prepare polycrystalline Al_2O_3 matrix composites containing whiskers of SiC (aspect ratio $\approx$ 20). For a whisker loading of 15 v%, the green and sintered relative densities of the composite prepared by colloidal processing were 0.69 and 0.83, respectively, compared to values of 0.52 (green) and 0.70 (sintered) for the dry processed sample.

(c) Viscous sintering prior to crystallization. The lower viscosity of glass or amorphous materials (relative to polycrystalline materials) which in turn

leads to a reduction in the quasi-hydrostatic backstress is exploited in this technique. The attainment of high sintered density is dependent on maximizing both the uniformity of the green composite and the amount of densification prior to crystallization. After sintering it will be necessary to control the nucleation and growth of the crystalline phase to obtain the required microstructure. Rahaman and Jeng (1989) used a sol-gel technique to prepare a uniformly mixed powder of amorphous mullite containing 15 v% SiC whiskers (average aspect ratio ≈ 35). Conventional compaction of the powder in a die produced a green composite with a relative density of 0.45 and after sintering for 1 hour at 1550°C the final density was 0.85. The shrinkage kinetics of the ureinforced mullite and the composite sample are shown in Fig. 4 as a function of temperature.

The techniques outlined in this section show good promise for the formation of composites with high density and controlled microstructure by conventional, pressureless sintering. With further optimization of the processing variables, it is expected that composites containing < 20 v% particulate or whisker-type inclusions can be sintered to densities > 0.9 of the theoretical.
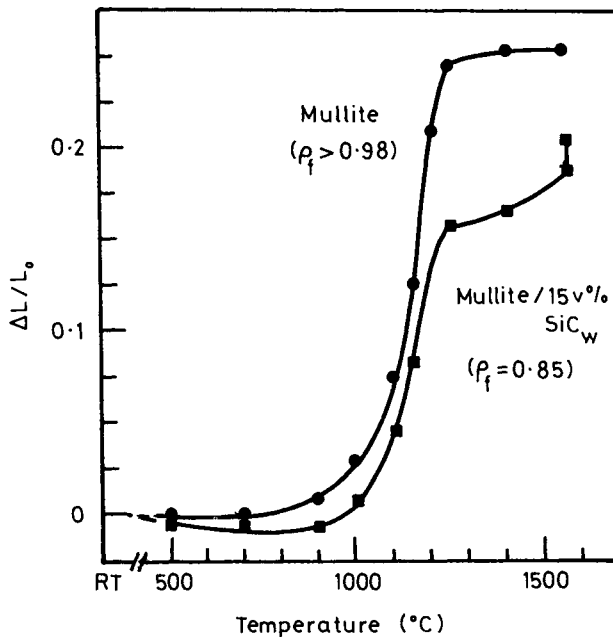
Fig. 4.   Viscous sintering prior to crystallization leads to high
          density composites.

CONCLUSIONS

Although some progress has been made in understanding the sintering of ceramic particulate composites, much work still remains to identify unambiguously the causes of the drastic reduction in the densification rate of polycrystalline

matrix composites. Current suggestions point in a direction that would predict considerably less effects on densification with uniform, ordered distributions of the dispersed phase compared to those distributions that result from imperfect or random mixing.

REFERENCES

Becher, P. F., and G. C. Wei (1984). Toughening behavior of SiC-whisker reinforced alumina. J. Am. Ceram. Soc., 67, C-267--C-269.

Bordia, R. K., and R. Raj (1988). Sintering of TiO_2-Al_2O_3 composites: a model experimental investigation. J. Am. Ceram. Soc., 71, 302-310.

Chu, M-Y., L. C. De Jonghe, and M. N. Rahaman (1989). Effect of temperature on the densification/creep viscosity during sintering. Acta Metall., in press.

De Jonghe, L. C., M. N. Rahaman, and C-H. Hsueh (1986). Transient stress in bimodal compacts during sintering. Acta Metall., 34, 1467-1471.

De Jonghe, L. C., and M. N. Rahaman (1988). Sintering stress of homogeneous and heterogeneous powder compacts. Acta Metall., 36, 223-229.

Evans, A. G. (1982). Considerations of inhomogeneity effects in sintering. J. Am. Ceram. Soc., 65, 497-501.

Gadkaree, K. P. and K. Chyung (1986). Silicon carbide whisker-reinforced glass and glass-ceramic composites. Am. Ceram. Soc. Bull., 65, 370-376.

Hsueh, C-H., A. G. Evans, R. M. Cannon, and R. J. Brook (1986). Viscoelastic stresses and sintering damage in heterogeneous powder compacts. Acta Metall., 34, 927-936.

Lange, F. F. (1988). Densification of powder rings constrained by cylindrical cores. Paper presented at the 90th Annual Meeting of the American Ceramic Society, Cincinnati, Ohio, May 1-5.

Lundberg, R., L. Kahlman, R. Pompe, R. Carlsson, and R. Warren (1987). SiC-whisker-reinforced Si_3N_4 composites. Am. Ceram. Soc. Bull., 66, 330-333.

Porter, J. R., F. F. Lange, and A. H. Chokshi (1987). Processing and creep performance of SiC-whisker-reinforced Al_2O_3. Am. Ceram. Soc. Bull., 66, 343-347.

Rahaman, M. N., and L. C. De Jonghe (1987a). Effect of rigid inclusions on the sintering of glass powder compacts. J. Am. Ceram. Soc., 70, C-348--C-351.

Rahaman, M. N., and L. C. De Jonghe (1987b). Creep-sintering of zinc oxide. J. Mater. Sci., 22, 4326-4330.

Rahaman, M. N., and D-Y. Jeng (1988). Sintering of mullite aerogels and mullite matrix composites. Advances in Ceramics, in press.

Rahaman, M. N., and L. C. De Jonghe (1989). Sintering of particulate composites under a uniaxial stress. Submitted to J. Am. Ceram. Soc.

Raj, R., and R. K. Bordia (1984). Sintering behavior of bi-modal powder compacts. Acta Metall., 32, 1003-1019.

Sacks, M. D., H-W. Lee, and O. E. Rojas (1988). Suspension processing of Al_2O_3/SiC whisker composites. J. Am. Ceram. Soc., 71, 370-379.

Scherer, G. W. (1987). Sintering with rigid inclusions. J. Am. Ceram. Soc., 70, 719-725.

Tiegs, T. N., and Becher, P. F. (1987). Sintered Al_2O_3-SiC-whisker composites. Am. Ceram. Soc. Bull., 66, 339-342.

Tuan, W. H., E. Gilbart, and R. J. Brook (1989). Sintering of heterogeneous ceramic compacts, Part 1: Al_2O_3-Al_2O_3. J. Mater. Sci., 24, 1062-1068.

Wei, G. C., and P. F. Becher (1985). Development of SiC-whisker-reinforced ceramics. Am. Ceram. Soc. Bull., 64, 298-304.

Whisker-reinforced silicon nitride matrix composites ; USING using pressureless sintering

D. Muscat, M. Pugh and R.A.L. Drew

Department of Mining and Metallurgical Engineering, McGill University, Montreal, Quebec, Canada, H3A 2T5

ABSTRACT

The acicular nature of β-Si_3N_4 gives it outstanding mechanical properties. It also has exceptional thermal properties, and is therefore seen as a suitable material for high temperature, structural applications. One way of enhancing its toughness is by reinforcing the matrix with whiskers. In this work, β-Si_3N_4 whiskers were dispersed in Si_3N_4 using two methods, namely, Attrition Milling/Ultrasonic dispersing and pH adjustment. Samples were compressed and sintered at 1800°C and the green and sintered densities were measured. SEM was used to study the fractured and polished surfaces to determine the densification problems and investigate the effect of the whiskers on microstructural development. There was clear evidence of increased acicularity in the β grains due to the presence of whiskers. However high densities were not achieved; the reasons for which are discussed.

KEYWORDS

Silicon Nitride, Ceramic Matrix Composites, Whisker Reinforced Ceramics, Silicon Nitride Whiskers, Sintering.

INTRODUCTION

Structural Ceramic materials have proven to be potential materials for many high temperature applications. However, the brittle nature of ceramics limits their use due to their catastrophic mode of failure. Fiber reinforcement has been successfully applied in polymer and, to a certain extent, metal matrices. The idea is currently being applied to ceramics, with the aim of increasing the toughness, strength and high-temperature creep resistance of the material. Work on continuous fiber and whisker reinforcement is very active at present (Mah and others, 1987), and fabrication technology of these composites is rapidly growing (Cornie and others, 1986).

The outstanding high temperature properties of Silicon Nitride makes it a possible substitute for superalloys in heat engines (Richardson, 1985). This is due to its acicular crystal structure which forms and is stable at temperatures of about 1700°C (Lange, 1973). The aspect ratio of the crystals has a direct effect on the mechanical properties of the material (Ziegler, Heinrich and Wötting, 1987). Some researchers (Buljan, Baldoni and Huchabee, 1987; Lundberg and others, 1987; Shalek and others, 1986; Singh and others, 1988) have added high aspect ratio crystals to reinforce Si_3N_4 using SiC whiskers. An increase of up to 40% in fracture toughness (K_{1c}) was reported.

Most whisker reinforced ceramic-matrix-composites (CMC) are sintered using hot pressing techniques, which have limitation. With uniaxial

hot pressing, only shapes of simple geometry may be formed. The
alternative to this is hot isostatic pressing (HIP). However this
method is expensive and not feasible for high production rates. Hot
pressing techniques may also cause damage to the whiskers in the
matrix. A cheaper alternative allowing uniform shrinkage is low
pressure sintering.

Whiskers are included in the material when the ceramic is still in
powder form. The dispersion of whiskers and powder has been the
subject of research work by a number of authors (Sacks, Lee and Rojas,
1988). The problems that arise include agglomeration of the powders
due to their sub-micron dimensions, and non-uniform mixing of the
different powders. Colloidal suspension techniques seems to be the
path to follow in processing the powders.

In this work, ß-Si_3N_4 whiskers were dispersed in Si_3N_4 powder using
two different techniques. Low pressure sintering (0.1 MPa) was used
in an attempt to form a composite. The objective of this work was to
obtain a microstructure with a large volume fraction of acicular
crystals and an aspect ratio comparable to that of the original
whiskers.

EXPERIMENTAL PROCEDURE

The Si_3N_4 powder used in these experiments was UBE-SN-E10. Table 1
shows the specifications of the as-received powder. Si_3N_4 whiskers
used were UBE-SN-WB (Fig. 1). Typically the diameter was 1 µm, with
an aspect ratio of 10-50.

TABLE 1   UBE-SN-E10 Powder Specification

Particle Size	:	0.1-0.3 µm
Specific Surface Area	:	10-14 m^2/g
Purity	:	N>38.0%; O<2.0%; C<0.2%
		Cl<100ppm; Fe<100ppm;
		Ca<50ppm; Al<50ppm.

Sintering additives of Y_2O_3, AlN and Al_2O_3 were added to the powder in
the proportions shown in Table 2. Whisker mixes of 5, 15 and 30 wt.
percent were made for each dispersion method. In each case a powder
having no whisker additives was processed in the same manner for base-
line comparison.

TABLE 2   Proportion of Sintering Additives

Si_3N_4	:	88.74%
Al_2O_3	:	4.97%
Y_2O_3	:	4.56%
AlN	:	1.72%

Dispersion

Two methods of dispersion were used. In the first method, The powder,
sintering additives and whiskers were mixed together in iso-propyl
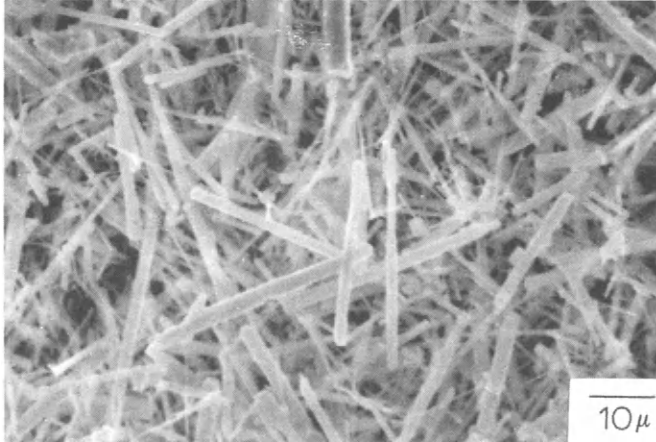
Fig. 1.   UBE-SN-WB Whiskers

alcohol as a liquid medium, in an attrition mill for 30 minutes, using Si_3N_4 balls as a grinding medium. The slip was then ultrasonicated for 30 minutes, and later attrition milled again for another 30 minutes. The alcohol was then dried off (Fig. 2).

In the second method, the powders, additives and whiskers were mixed in deionized water. NH_4OH was then added to adjust the pH to 10.0. The suspension was blended in a high speed homogenizer and ultra-sonicated for 5 minutes. The pH was then readjusted to 7.0 and the water was boiled off (Fig. 3).

Powder Processing

The powder mixes were granulated through a sieve with an opening of 212 µm. Uniaxial pressing was used to form bars of equal dimensions (42mm x 7.5mm x 4mm). An average of 10 bars were made for each powder mix. The bars were then cold isostatically pressed up to a pressure
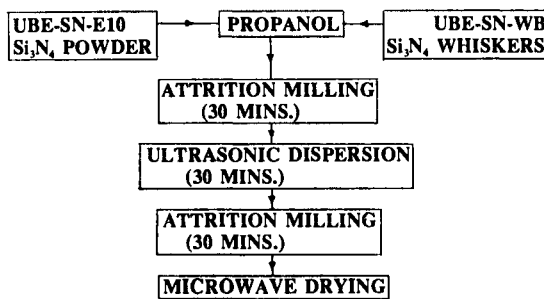
Fig. 2.   Attrition Milling/Ultrasonic dispersion
          process

```
┌─────────────┐   ┌─────────────┐   ┌─────────────┐
│ UBE-SN-E10  │──▶│  DEIONIZED  │◀──│  UBF-SN-WB  │
│ Si₃N₄ POWDER│   │    WATER    │   │Si₃N₄ WHISKERS│
└─────────────┘   └─────────────┘   └─────────────┘
                         │
                         ▼
                  ┌─────────────┐
                  │pH ADJUSTMENT│
                  │   (NH₄OH)   │
                  └─────────────┘
                         │
                         ▼
                   ┌──────────┐
                   │ BLENDING │
                   └──────────┘
                         │
                         ▼
                  ┌─────────────┐
                  │ NEUTRALIZE  │
                  │   (HNO₃)    │
                  └─────────────┘
                         │
                         ▼
                    ┌─────────┐
                    │ DRYING  │
                    └─────────┘
```
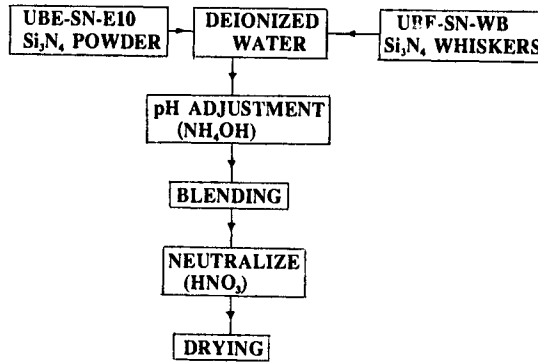
Fig. 3.   pH Adjustment dispersion process

of 342 MPa. Green densities of the bars were obtained by measuring the dimensions and the weight. The bars were then placed in a boron nitride crucible and covered with a BN/Si_3N_4 powder bed to reduce decomposition of the powder. Sintering was carried out at 1800°C for 1 hour in a nitrogen atmosphere at a pressure of 0.1 MPa. The sintered density of the bars was measured using Archimedes' method, in water.

The bars were machined using a diamond grinding wheel (240 grit) to make the faces parallel. They were then tested for fracture strength in a 4-point bending test machine. The fractured surfaces of green and sintered bars, together with polished surfaces of the sintered bars were analysed using a Scanning Electron Microscope (SEM).

RESULTS & DISCUSSION

To obtain a good composite, it is important to have a homogenous dispersion of the reinforcing phase inside the matrix. The nature of
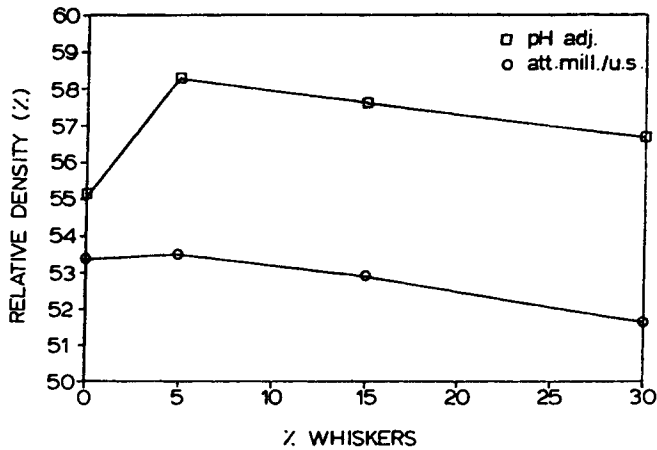
Fig. 4.   Relative green densities
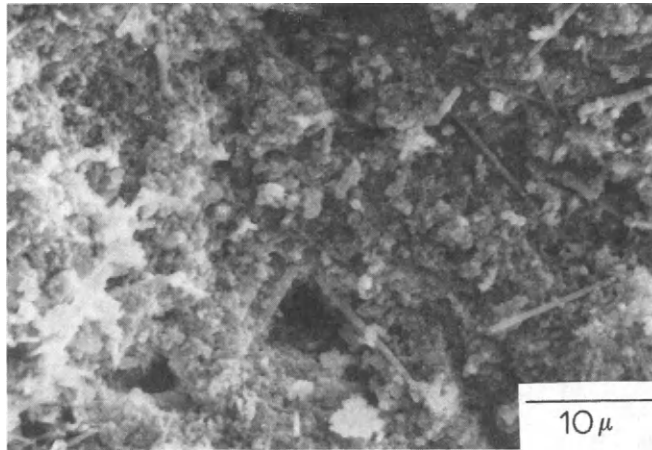
Fig. 5.   Green compact showing bridging (15%
          whiskers)

the dispersion is reflected in the manner in which the powder and the
whiskers pack to form green bodies (Milewski, 1986). Figure 4 shows
a plot of the green densities of the bars as whisker content was
increased. Density decreased as more whiskers were added to the
powder. This may be attributed to the fact that, as the whiskers start
to touch one another, they cause bridging. This leaves large pores in
the green microstructure (Fig. 5) which are not filled by the powder
during isostatic pressing. These pores will not close during sintering
and hence contribute to the poor densification.

The method using pH adjustment gave higher densities than attrition
milling plus ultrasonic dispersion. The dispersion of whiskers was
homogenous. However agglomerates of whiskers were occasionally
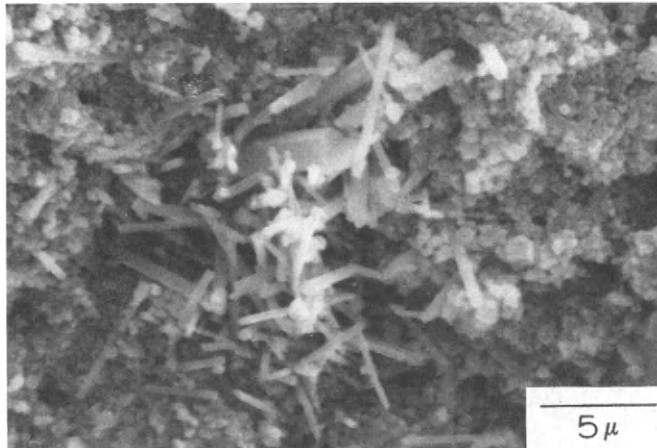
Fig. 6.   Whisker agglomerate (15% whiskers)
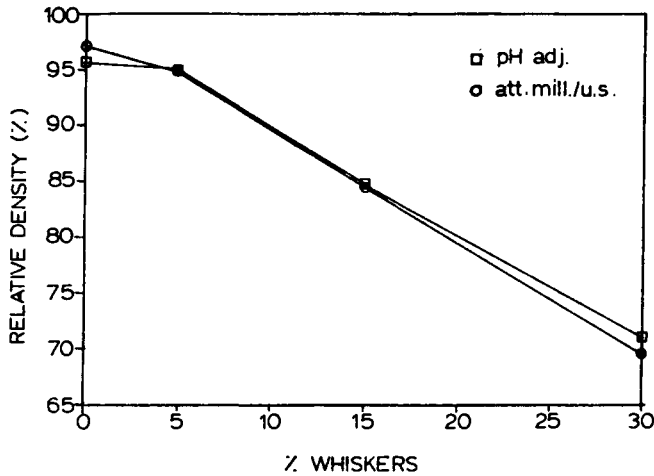
Fig. 7.   Relative sintered densities

observed (Fig. 6). In both cases, the green density increased after additions of small fraction of whiskers. This may be attributed to a bimodal size distribution caused by the introduction of whiskers with relatively large dimensions compared to the matrix powder (d_{50} = 0.2µm).

The improved green densities obtained by the pH adjustment method over the attrition milling/ultrasonication method, was not reproduced in the sintered density results. Figure 7 is a plot of sintered relative density versus whisker content. It can be seen that the values were identical for both methods. The addition of whiskers hindered densification and, at high whisker volume content, they formed a skeletal network, thus jamming the densification mechanism.
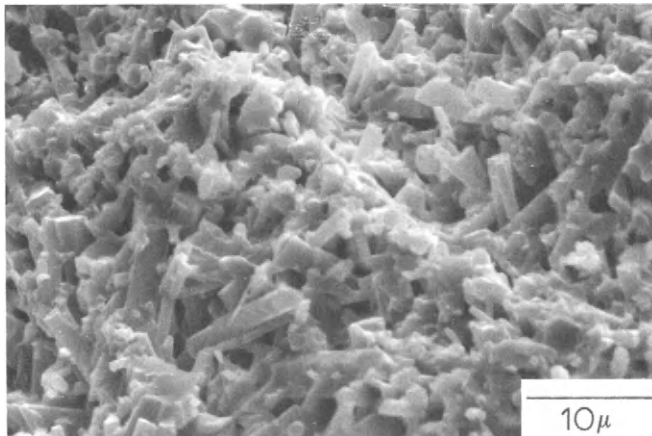
Fig. 8.   Sintered microstructure (30% whiskers)
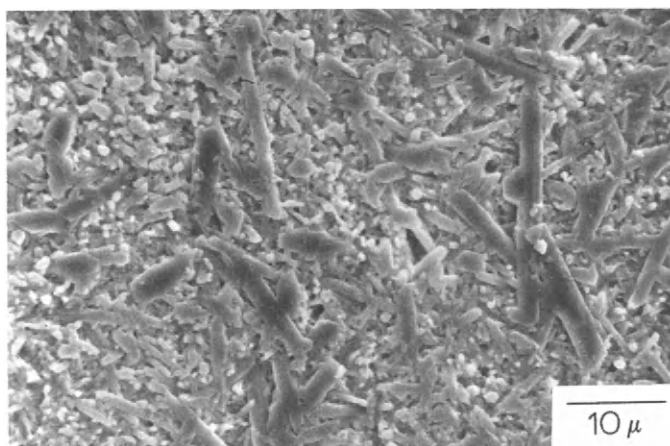
Fig. 9.   Polished sintered surface (5%
          whiskers)

The liquid phase formed did not aid the rearrangement of the whiskers
during the initial stages of sintering, and the capillary pressure
created when the particles were wet by the liquid was not sufficient
to overcome the bridging effect of the whiskers. As a result, large
pores remained in the microstructure. In addition, because of the
phase transformation of Si_3N_4 into an acicular microstructure (the
stable phase at the sintering temperature), vapour–liquid–solid growth
occurred into these pores. The final matrix is a fully transformed
acicular structure (Fig. 8).

One of the main objectives of this work was to increase the acicul-
arity of the overall microstructure by employing whiskers. Although
the matrix was not fully densified, it was still possible to observe
the nature of the grains. Figure 9 shows a polished surface of a 5%
whisker content sintered surface where large acicular grains are
present in the microstructure. These are the initial whiskers which
were added to the powder and is clear evidence that ß whiskers remain
stable throughout the sintering process. However crystal growth
appears to have occurred, thus increasing the diameter of the original
whiskers. In the high whisker content samples (Fig. 10), besides
having a large volume of high aspect ratio whiskers present, the pores
in the microstructure allowed the matrix ß grains to grow to an
equivalent size as the original whiskers. This formed a relatively
uniform matrix of acicular crystals composed of whiskers and
transformed ß grains.

The plot of Modulus of Rupture (M.O.R.) versus whisker content shows
the strength decreasing with increasing whisker content (Fig. 11).
The drop in strength was expected as this was a result of the
increased porosity present in the material. However, it may also be
seen that the values for the samples processed by pH adjustment were
lower than the ones for the attrition milling/ultrasonicating method.
This difference may be attributed to the different processing used.
A possible explanation might be a result of not having a uniform
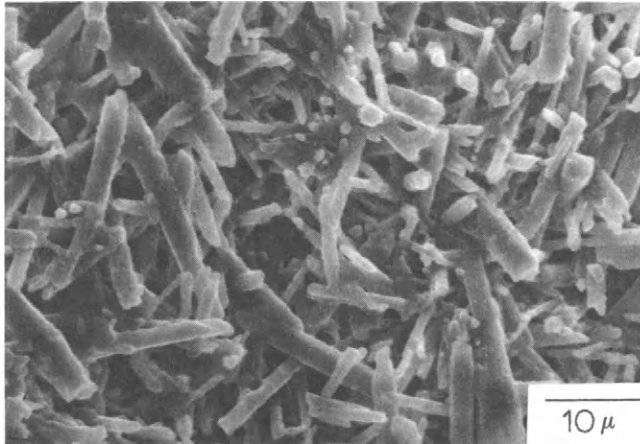
Fig. 10.   Polished sintered surface (30%
           whiskers)

dispersion of the sintering additives. In the pH adjustment method,
the additives were never actually dispersed with the Si_3N_4 powder by
milling and hence may have been agglomerated. This may give rise to
uneven sintering and areas of varying density. Areas of low density
would have a significant effect on the strength, as indicated in
Fig. 11.
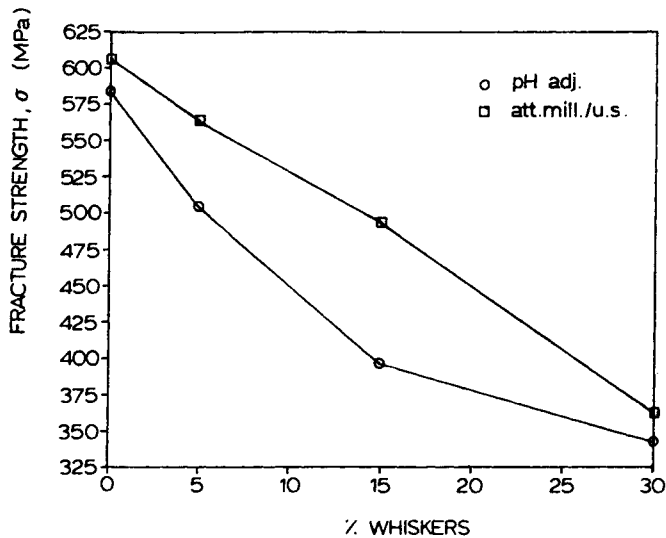
Fig. 11.   M.O.R. values from a
           4-Point Bending Test

CONCLUSIONS

1. Green density was improved using pH adjustment.
2. Bridging of whiskers, at higher volume fraction, was observed, and this hinders efficient packing.
3. The improved green density using pH adjustment was not reproduced in the values of sintered density after firing. Sintered density decreased as whisker volume content was increased. Whiskers formed a skeletal network and jammed the densification mechanism. Thus porosity increased with whisker content.
4. The M.O.R. also decreased as a result of porosity. However the M.O.R. values of the attrition milled samples were seen to be higher than the samples processed by pH adjustment.
5. The original ß whiskers were retained in the final microstructure, which shows that the reinforcement of Si_3N_4 with $ß-Si_3N_4$ whiskers is a promising method for increasing toughness of these materials.

REFERENCES

Buljan, S.T., J.G. Baldoni, and M.L. Huckabee (1987). Si_3N_4-SiC Composites. Am. Ceram. Soc. Bull., 66, 347-352.

Cornie, J.A., Y. Chiang, D.R. Uhlmann, A. Mortensen, and J.M. Collins (1986). Processing of Metal and Ceramic Matrix Composites. Am. Ceram. Soc. Bull., 65, 293-304.

Homeny, J., W.L. Vaughn, and M.K. Ferber (1987). Processing and Mechanical Properties of SiC-Whisker-Al_2O_3-Matrix Composites. Am. Ceram. Soc. Bull., 66, 333-338.

Lange, F.F. (1973). Relation between Strength, Fracture Energy and Microstructure of Hot Pressed Si_3N_4. J. Amer. Carem. Soc., 56, 518-522.

Lundberg, R., L. Kahlman, R. Pompe, R. Carlsson, and R. Warren (1987). SiC-Whisker-Reinforced Si_3N_4 Composites. Am. Ceram. Soc. Bull., 66, 330-333.

Mah, T., M.G. Mendiratta, A.P. Katz, K.S. Mazdiyasni (1987). Recent Developments in Fiber-Reinforced High Temperature Ceramic Composites.

Milewski, J.V. (1986). Efficient use of Whiskers in the Reinforcement of Ceramics. Advanced Ceramic Materials, 1, 36-41.

Porter J.R., F.F. Lange, and A.H. Chokshi (1987). Processing and Creep Performance of SiC-Whisker-Reinforced Al_2O_3. Am. Ceram. Soc. Bull., 66, 343-347.

Sacks, M.D., H. Lee, and O.E. Rojas (1988). Suspension Processing of Al_2O_3/SiC Whisker Composites. J. Am. Ceram. Soc., 71, 370-379.

Shalek, P.D., J.J. Petrovic, G.F. Hurley, and F.D. Gac (1986). Hot-Pressed SiC Whisker/Si_3N_4 Matrix Composites. Am. Ceram. Soc. Bull., 65, 351-356.

Singh, J.P., K.P. Goretta, D.S. Kupperman, and J.L. Routbort (1988). Fracture Toughness and Strength of SiC-Whisker-Reinforced Si_3N_4

Composites. <u>Advanced Ceramic Materials</u>, <u>3</u>, 357-360.

Richardson, D.W. (1985). Evolution in the U.S. of Ceramic Technology for Turbine Engines. <u>Am. Ceram. Soc. Bull.</u>, <u>64</u>, 282-286.

Tiegs, T.N., P.F. Becher (1987). Sintered Al_2O_3-SiC-Whisker Composites. <u>Am. Ceram. Soc. Bull.</u>, <u>66</u>, 339-342.

Wei, G.C., P.F. Becher (1985), Development of SiC-Whisker-Reinforced Ceramics. <u>Am. Ceram. Soc. Bull.</u>, <u>64</u>, 298-304.

Ziegler, G., J. Heinrich, and G. Wötting (1987). Review: Relationships between Processing, Microstructure and Properties of Dense and Reaction-Bonded Silicon Nitride. <u>Journal of Materials Science</u>, <u>22</u>, 3041-3086.

Gas pressure sintering of Si₃N₄-based composites

H. Mostaghaci
Atlantic Research Laboratory, National Research Council Canada,
Halifax, Nova Scotia, Canada, B3H 3Z1

ABSTRACT

Silicon nitride composites containing 10wt% of both Y_2O_3 and Al_2O_3 as
densification aids and up to 30 wt% TiN as reinforcement material can be
reproducibly sintered to relative densities of >99% by a gas-pressure sintering
process. Compacts with high density are produced by first sintering to the
close-pore stage (~92%T.D.) in 0.2 MPa of N_2 pressure at 1850°C and then
increasing the N_2 to 5 MPa where rapid densification proceeds. The experimental
results are interpreted in terms of a theoretical argument concerning gas-filled
pores and gas solubility effects.

KEYWORDS

Silicon nitride, gas pressure sintering, composites

INTRODUCTION

Efforts to prepare a dense pressureless-sintered form of silicon nitride
initially had only limited success[1,2], e.g. a maximum density of 80% (based on
a theoretical density of 3.18 Mg m⁻³) was achieved by Kazakov[2], but only when a
large quantity (60 mol%) of MgO was added. Continued attempts throughout the
early 1970's to pressureless-sinter Si_3N_4 with oxide additives led to new
achievements[3,4], but the sintered densities remained around 90%. To improve
further this sinterability higher temperatures (>1800°C) may be used, but this
introduces the problem of thermal decomposition of Si_3N_4[4]. The pore formation
due to thermal decomposition of Si_3N_4 prevents further shrinkage. A number of
recent studies have shown[5-8], however, that thermal decomposition can be
minimized or controlled by using increased N_2 pressures up to about 7 MPa, and
Si_3N_4 ceramics with densities >99% can be developed[8]. The present study
involves the application of a two-step gas-pressure sintering process for the
preparation of particulate-reinforced Si_3N_4 composites with relative densities
>99%. Small amounts of Y_2O_3 (2-8 Wt%) and Al_2O_3 (2-8 Wt%) are used as
densification aids for sintering a high purity, α-Si_3N_4 powder under N_2 pressure.
Observations on densification behaviour and microstructure developments are
presented for Si_3N_4 composites sintered in P_{N_2} up to ~6MPa and temperatures up
to 1900°C.

EXPERIMENTAL PROCEDURE

The as-received Si_3N_4 powder (UBE, SN-E10) had oxygen and chlorine contents of
1.47 wt% and 100 ppm respectively, and a specific surface area of ~11m²g⁻¹. This
powder was composed of >99% α-Si_3N_4. The starting Si_3N_4 powder plus 10 wt% of
both Y_2O_3 (Aldrich Chemical Co.) and Al_2O_3 (Reynolds, RC-HP-DBM), and up to
30 Wt% TiN (ICD Chemicals) were processed by attritor milling in an alumina lined
container with Si_3N_4 balls in iso-propanol for 3 hours, and dried in a microwave
oven. Samples in the form of rectangular bars were fabricated by isostatic
pressing at 140 MPa.

The powder compacts then were embedded in a powder bed consisting of Si_3N_4+BN, and sintered in an electrically heated graphite furnace capable of operating up to 2200°C in 10 MPa of inert gas pressure. The temperature was measured using a W5Re/W26Re thermocouple installed close to the sample in the hot zone of the furnace.

Density of powders and sintered samples were measured using gas pycnometry and Hg immersion techniques respectively. Sintered samples also were characterized by weight loss and shrinkage, and the distribution of phases present were determined from polished sections and fracture surfaces using SEM.

RESULTS AND DISCUSSION

1) Single-step sintering

In this technique, which has been a common practice for sintering nitride ceramics, the Si_3N_4 compacts are sintered at temperatures of >1800°C under a certain overpressure of N_2. Experimental observation on the effects of N_2 pressure, at constant temperature on the densification of Si_3N_4 compositions, indicated that there is a continuous drop in sintered density for an increasing N_2 pressure during single-step sintering. To help explain this phenomenon, the following theoretical argument will give guidance for the expected changes in the average equilibrium size of pores filled with an insoluble gas of a given pressure and the corresponding maximum relative density expected at equilibrium.

An isolated, closed pore containing an insoluble gas of low diffusivity (e.g.: N_2) in the solid will continue to shrink after pore closure until the following equilibrium condition is attained:

$$r_e = \frac{2\gamma}{P_e - P_a}$$

where: r_e – Equilibrium pore size
P_e – Pressure inside a closed spherical pore
γ – Solid-vapor surface energy
P_a – External applied pressure

It is clear from the above equation that there is a continuous increase in pore size, and hence a drop in sintered density, for increasing N_2 pressure during single-step sintering at a constant T. This is due to the fact that the driving force for pore closure ($2\gamma/r_{pore}$) is opposed by the applied gas pressure, P_a, which builds up in the pore. Assuming an equilibrium pore radius at the time of pore closure (ρ=92% T.D.), and that the gas in the pore does not dissolve into the matrix phases, the density and pore size variation as a function of applied gas pressure can be illustrated in Fig. 1. As can be seen, increasing the applied gas pressure causes an increase in equilibrium pore radii and consequently a decrease in density. This indicates that, if the closed-pore condition is reached under a low applied gas pressure, and the external pressure is subseqently increased, near theoretical densities can be achieved.

2) Two-step sintering

The gas-pressure sintering process described here is used primarily for its effectiveness during the final stages of the sintering process, i.e. when the pore phase transforms into discrete, disconnected pores that are filled with gas pressure at the seal-off conditions. Experimentally, in this work, the fabricated Si_3N_4 compacts were sintered to the closed-pore stage, which is

typically achieved by firing for 1/2 h at 1850°C under 0.2 MPa of N_2 pressure. After completion of this step and while the samples remained in the furnace, the second step consisted of increasing N_2 pressure to a higher P_N value, typically 5 MPa, for rapid densification. The pressure-temperature-time cycle used during the gas-pressure sintering process is illustrated in Fig. 2.
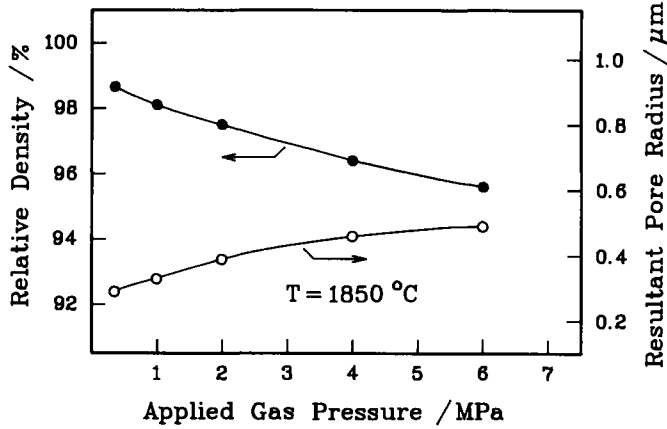
Figure 1 - Theoretical estimation of density and equilibrium pore pressure as a function of gas pressure during a single-step sintering cycle.
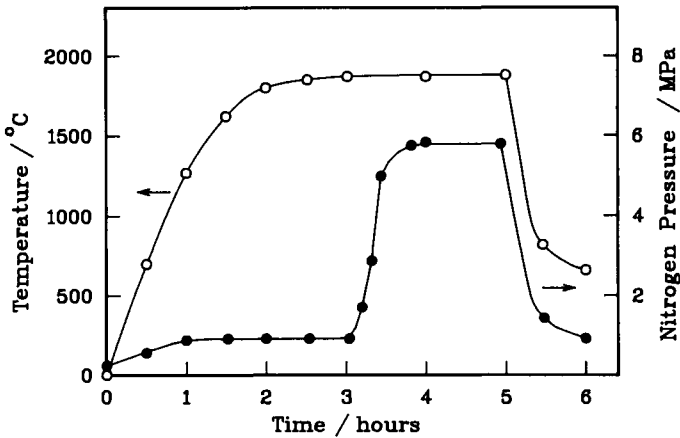
Figure 2 - A typical temperature-time-pressure profile of a two-step gas pressure sintering cycle.

A summary of some of the sintering results is given in Fig. 3. As can be seen
samples of Si_3N_4 containing up to 30 wt%. TiN were densified to ∿99% of
theoretical density by the two-step gas pressure sintering. However,
densification of Si_3N_4 composites during the two-step gas pressure sintering was
found to be independent of the TiN content of the composite. A typical
microstructure of sintered Si_3N_4 containing 30 wt% TiN having a relative density
of ∿ 99% is illustrated in Fig. 4. The microstructure is indicative of a dense
body having a few small (<0.5μm) intergranular pores.
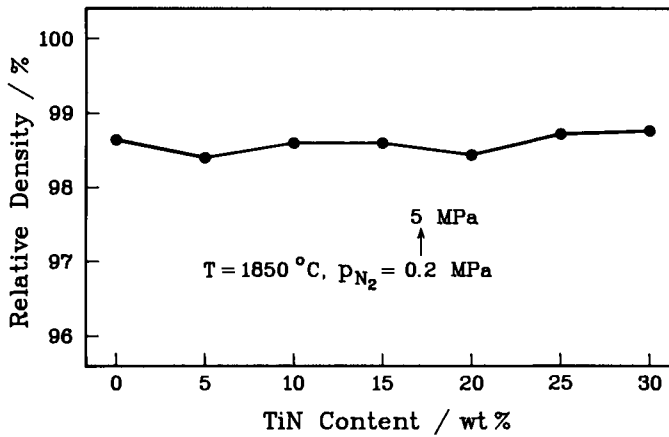
Figure 3 - Sintered densities as a function of TiN content in Si_3N_4 composite
           materials after a two-step sintering cycle.
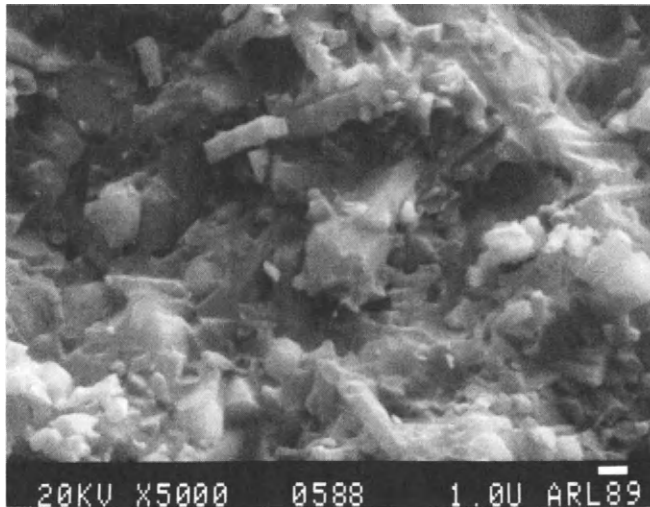
Figure 4 - SEM micrograph from the fracture surface of a Si_3N_4-based composite
           containing 30 wt% TiN.

CONCLUSIONS

1. Silicon nitride-titanium nitride composites containing up to 30 wt% TiN can be fabricated to densities >99% by gas-pressure sintering.

2. Microstructural observations show that pore growth due to the gas pressure building up within the pores during one-step sintering does not occur in two-step sintering process.

3. Densification of Si_3N_4-TiN compositions is found to be independent of the TiN contents of these compositions.

ACKNOWLEDGEMENTS

REFERENCES

1) Aito, S. Somiya, S. and K. Kato, (1966) J. Jap. Soc. Powder Met. 13, 186.
2) Kazakov, V. K. (1967) Trans. Izvest. Akad, Nauk SSSR. Neorganisch Materialy 3, 1661.
3) Terwilliger, G. R. (1974) J. Am. Ceram. Soc., 57, 48.
4) Terwilliger, G. R. and Lang, F. F. (1975), J. Mat. Sci., 10, 1169.
5) Mitomo, M. (1976) J. Mat. Sci., 11, 1103.
6) Mitomo, M. (1978) PP. 539-544 in: Proceedings of the International Symposium on Factors in Densification and Sintering of Oxide and Non-Oxide Ceramics, Eds. S. Somiya and S. Saito, Gakujutsu Bunken Fuky-kai, Tokyo, Japan .
7) Mitomo, M. and K. Mizuno, (1986), PP. 263-270 in Proceedings of the Second International Symposium on Ceramic Materials and Components for Engines, Eds.: W. Bunk and H. Hausner, Verlag Deutsch Keramishe Gesellschaft.
8. Greskovich, C. D. and J. A. Palm, AMMRC TR 80-46, September 1980, SRD-80-111.

The effect of oxygen partial pressure on densification of zirconia-chromia mixtures

G.R. Doughty
Atlantic Research Laboratory, National Research Council Canada,
Halifax, Nova Scotia, Canada, B3H 3Z1

R.J. Brook
Max Planck Institut, Stuttgart, Federal Republic of Germany

ABSTRACT

An investigation has been made of the effect of sintering atmosphere on the densification in the system zirconium oxide - chromium oxide. Mixtures of unstabilized zirconia and chromia with compositions from 100% ZrO_2 to 100% Cr_2O_3 have been fired in air and in an atmosphere generated over graphite. All the chromia-containing materials sintered to a higher density in the low oxygen partial pressure than in air.

3 mol.% yttria-doped zirconia with 0-5 mol.% Cr_2O_3 additions were fired in a controlled atmosphere dilatometer in air and in Ar-CO-CO_2 gas mixtures. The maximum densification rates of chromia-doped materials occurred at low oxygen partial pressures close to that corresponding to the Cr-$Cr_2O_3$3 equilibrium. At these low oxygen partial pressures, Cr_2O_3 acted as a densification aid for zirconia with maximum effect at around 0.7 mol.% Cr_2O_3. Doping of a fully stabilized zirconia with 1.5 mol.% chromia was not beneficial for densification whether fired in air or in a low oxygen partial pressure.

KEYWORDS: zirconia, chromia, sintering, densification, oxygen partial pressure.

INTRODUCTION

In spite of the widespread research activity in the zirconia field, the system chromia-zirconia has received scant attention. An examination of the literature shows a predominance of references to patents for specific compositions, applications and processing methods rather than to scientific investigations. Chromia has been used as an additive to pre-sintered zirconia for improved wear properties (1). Zirconia has been used as an additive for chromia-based materials to improve strength and toughness (2). It has been suggested (3) that zirconia-chromia ceramics have not been widely used owing to the low densities of air fired mixtures.

The majority of references to the sintering of chromia- containing materials have come from the work of Yamaguchi (3,4,5,6,7) which has included some results of sintering of chromia-zirconia mixtures (3, 7). This work has compared the effect of a reducing atmosphere generated by carbon with that of air on the sintering of mixtures of chromium oxide and pure (unstabilized) zirconia containing > 30 mol.% chromia at 1500°C. The findings were that although firing in air for 2 hours at 1500°C resulted in little or no densification, the fired samples being only ~ 53% of the theoretical density, when specimens were placed in a carbon powder bed, they sintered to > 98 % of the theoretical density. The later more detailed description of the work (7) also added the fact that specimens containing 10 wt.% chromia sintered to 95 % of the theoretical density when sintered at 1500°C in a reducing atmosphere for 3 hours.

Leistner and Elstner (8) have studied the effect of oxygen partial pressure on the densification of various alumina-chromia-zirconia mixtures and a 60 % zirconia- 40 % chromia material. The highest density zirconia-chromia mixture was obtained after firing in an oxygen partial pressure close to that corresponding to the $Cr-Cr_2O_3$ equilibrium.

Jayaratna et. al. (9) have investigated the effect of the addition of between 0 and 3 mol.% chromia on the densification of an 8 mol.% yttria fully stabilized zirconia during hot pressing. Both alumina and graphite dies were used for the hot pressing though little mention is made of the results using the alumina dies. The results using graphite dies showed that chromium oxide was a densification aid for the zirconia.

The aim of this work is to further quantify densification in the system zirconium oxide - chromium oxide.

EXPERIMENTAL

The first set of sinterings were undertaken using chromia[1]-zirconia[2] mixtures prepared by dry mixing of the oxides. The required quantities of powder were dry mixed in a Spex mixer mill M280 supplied by Glen Creston for twenty minutes using three perspex balls. ZrO_2 -Cr_2O_3 mixtures containing up to 5 mol.% chromia were prepared by doping the zirconia powder using a solution of chromium nitrate, $Cr(NO_3)3.9H_2O$. The chromium nitrate was dissolved in ethanol, then poured over the ZrO_2 powder in a plastic beaker and stirred under an infra-red heat lamp until it had dried. The powder produced was then calcined at 500°C for 1hr to decompose the nitrate to the oxide. Undoped powders were also dispersed in ethanol, dried and calcined using the same procedures.

The 3.0 mol.% yttria-doped zirconia used here was TZ3Y supplied by Toyo Soda[4]. One set of sinterings was carried out on undoped and chromia doped 10 mol.% yttria doped fully stabilized zirconia (10Y-FSZ). These powders were prepared by doping an unstabilized zirconia (TZ0Y from Toyo Soda[4]) with a standard solution of yttrium nitrate together with chromium nitrate, if chromia doping was required, to give a powder of final composition, 98.5 mol.% $(0.90ZrO_2$ -$0.10Y_2O_3$) - 1.5 mol.% Cr_2O_3 . Doping, drying and calcination was performed as above.

Samples to be fired in crucibles were prepared as 10g pellets which were pressed at 40 MPa in a 25.4 mm diameter die to approximately 50 % of the theoretical density. Specimens for air firing were placed in an alumina crucible which was assembled in such a way as to have two lids with calcined alumina between them. This was to avoid contamination of the furnace due to volatilisation of higher oxides of chromium such as CrO_3. The alumina was present to react with any volatiles. Those specimens to be fired in graphite had graphite packed into the crucible though not in contact with the specimen.

A controlled atmosphere sintering dilatometer was used to measure the densification kinetics of some of the powders in different oxygen partial pressures. Specimens for use in the dilatometer were made up of ~1.5 g of powder, pressed at 127 MPa in a one centimetre steel die. It was calculated that this amount of powder, if sintered from a green density of ~40 % of theoretical to full density would require almost the complete range of the transducer.

The oxygen partial pressure during sintering in the dilatometer was controlled by the use of various $CO-CO_2$ gas mixtures. The gases consisted of ~95% Ar and 5% $CO-CO_2$. The compositions used are listed below in table 1. These gases were supplied by BOC Special Gases[5], and had been analysed

1. Accrox C, British Chrome and Chemicals Ltd. Urlay Nook, Eaglescliff, Stockton on Tees, England.
2. MEL SC10, Magnesium Elektron Ltd. Regal House, London Rd., Twickenham, England.
3. Koch-Light Laboratories Ltd., Colnbrook, Bucks, England.
4. Toyo Soda Manufacturing Co, Ltd. Tonda, Shin-Nanyo 746 Japan
5. BOC Special Gases Ltd., 24 Deer Park Road, London SW19 3UF, England.

(HY-line Standard : +- 0.02% accuracy quoted) to check the composition. The oxygen partial pressure was calculated using the data given by Turkdogan (10).

$CO-CO_2$ ratio	Log Oxygen Partial Pressure	
	a) at 1400C	b) at 1500C
10.04 : 1	-10.6	-9.6
93.5 : 1	-12.5	-11.6
1210 : 1	-14.8	-13.8
6262 : 1	-16.2	-15.2

Table 1. $CO-CO_2$ ratios and corresponding oxygen part- ial pressures at 1400 and 1500C for the gases used.

While the furnace was cold, it was twice pumped out using a rotary vacuum pump to ~1 kPa then purged through with the controlled atmosphere gas. A flow rate of 4 ml min^{-1} was used throughout the sinterings, maintaining a slight positive pressure. This gave a change of furnace atmosphere approximately every 5 minutes.

RESULTS

Table 2 lists the results of firing at 1500°C for 4 hrs in an artificial graphite generated atmosphere and in air. These results are shown graphically in figure 1.

mol.% Chromia	Air Fired		Fired in graphite powder	
	Density / Mg.m^{-3}	% Theoretical Density	Density / Mg.m^{-3}	% Theoretical Density
100.0	3.30	63.4	4.30	82.6
75.0	3.25	61.4	5.13	96.7
50.0	3.26	60.3	5.35	98.9
25.0	3.63	66.2	5.46	99.3
10.0	4.11	74.1	5.48	98.5
5.0	4.18	74.9	5.56	99.6
2.0			5.21	93.1
1.0			4.97	88.8
0.5			4.86	86.9
0.0	4.57	81.6	4.69	83.8

Table 2. Final densities and percentage of theoretical density of zirconia- chromia mixtures fired at 1500C for 4 hours in air and in graphite.

X-ray diffraction analysis of these specimens showed only the characteristic lines for chromium sesquioxide and/or monoclinic zirconia.

It can be seen that more results were collected at the zirconia rich range of compositions in order to investigate how far towards 100% zirconia did the plateau of almost theoretical density that starts at between 75 and 50 % chromia extend for materials fired in graphite.
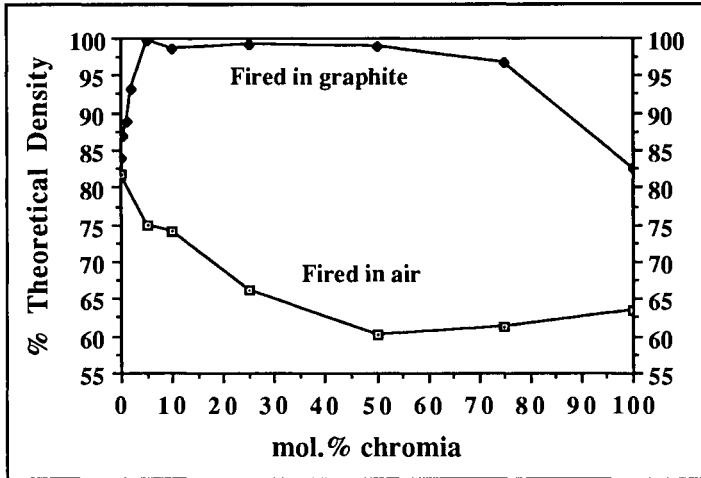
Figure 1. % of theoretical densities of chromia-zirconia mixtures fired
in air and in graphite at 1500C for 4 hours.

Figure 2 shows the fracture surface of a ZrO_2 / 0.5 mol.% chromia sample fired in artificial graphite
for 4 hrs at 1500C. It can be seen that the material is highly densified but with cracks running along
grain boundaries. This highlights a problem in the use of unstabilized zirconia, namely the cracking of
specimens on cooling arising from the tetragonal-monoclinic transformation. In this work, samples
containing up to 100% unstabilized zirconia were fabricated which made the structural integrity of
sintered pellets rather poor, particularly those with high proportions of zirconia which were of high
relative density.
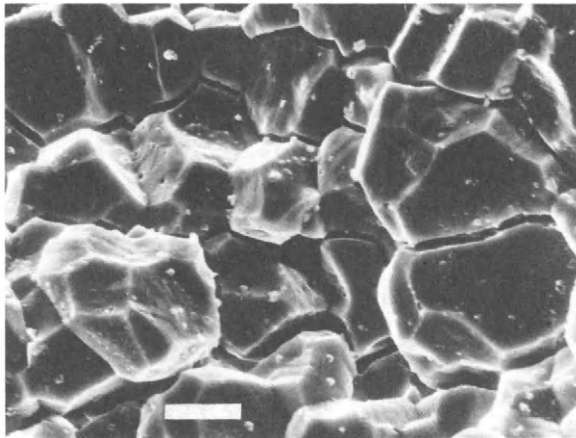
Figure 2. Fracture surface of 0.5 mol.% chromia doped zirconia fired in artificial graphite for
4 hrs at 1500C. Bar = 5μm.

This means that although the high density plateau extends to at least 5% chromia or less after firing in a reducing atmosphere, because of the high density of these materials, the degree of cracking will be very severe on cooling from the sintering temperature. Hence the measured final densities of samples fired in low oxygen partial pressures would not represent the corresponding high density at temperatures above the tetragonal - monoclinic transformation temperature because of the presence of a large amount of both micro- and macro-cracking of specimens on cooling The density measurements do not differentiate between intrinsic porosity resulting from incomplete densification and porosity caused by cracking of the specimens on transformation. Specimens containing high proportions of zirconia were found to be severely cracked after sintering and great care was needed while handling them.

To avoid the problems of transformation and to investigate the extent of the high density plateau at low chromia contents, it was decided to investigate the effects of composition and oxygen partial pressure in the range 0 - 5% chromia doped zirconia, using a 3% yttria-zirconia TZP material as the base.

Log (Oxygen Partial Pressure)	Chromia Content / mol.%	Final Density / Mg.m^{-3}	Log Densification Rate at a density of 5.3 Mg.m^{-3}
-0.07	0.0	5.94	-3.172
	0.4	5.96	-3.447
	0.7	5.91	-3.529
	1.0	5.90	-3.510
	2.0	5.92	-3.903
	5.0	5.31	-5.487
-10.6	0.0	5.74	-4.711
	0.4	5.98	-2.630
	0.7	5.97	-2.472
	1.0	5.92	-3.125
	2.0	5.87	-3.626
	5.0	5.69	-4.789
-12.5	0.0	5.76	-4.533
	0.4	5.98	-2.548
	0.7	5.97	-2.328
	1.0	5.98	-2.409
	2.0	5.92	-3.126
	5.0	5.79	-4.438
-14.8	0.0	5.73	-4.621
	0.4	5.99	-2.610
	0.7	5.79	-2.514
	1.0	5.85	-2.508
	2.0	5.81	-3.508
	5.0	5.78	-4.453
-16.2	0.0	5.73	-4.659
	0.4	5.96	-3.013
	0.7	5.98	-2.753
	1.0	5.94	-2.754
	2.0	5.95	-3.655
	5.0	5.77	-4.586

Table 3. Final density and densification rate (at a density of 5.3 Mg.m^{-3}) of chromia doped 3Y-TZP, fired at 1400C.

Because the TZP zirconia used was already highly sinterable as a consequence of its fine particle size, the monitoring of sintering kinetics would provide a fuller account of the relative sinterability than would be possible solely from the comparison of final densities after firing.

The densification kinetics of the various samples were measured in a controlled atmosphere sintering dilatometer. The green densities of the pellets were all approximately 2.6 Mg m^{-3}, which is about 43 % of the theoretical density of tetragonal zirconia. Final density and densification rate at density = 5.3Mg.m^{-3} (densification rates were calculated from density time data using a mainframe Amdahl computer) are listed in table 3.

There are differences in densification rate which are not mirrored in similar variations in final density. This shows the importance of monitoring the densification kinetics during sintering in determining differences in densification behaviour. In this particular case, measurement of final density after isochronal sinterings would not have revealed the differences in densification with as great a clarity as was possible by using the dilatometer.

Figure 3 shows the effect of oxygen partial pressure on densification rate for the chromia-doped materials. For all of these samples, there is a maximum in densification rate at oxygen partial pressures between 10$^{-12.5}$ and 10$^{-14.8}$. This corresponds to the oxygen partial pressure at which the densification of pure chromium oxide is at a maximum, ie. close to the Cr - Cr$_2$O$_3$ equilibrium (11,12).
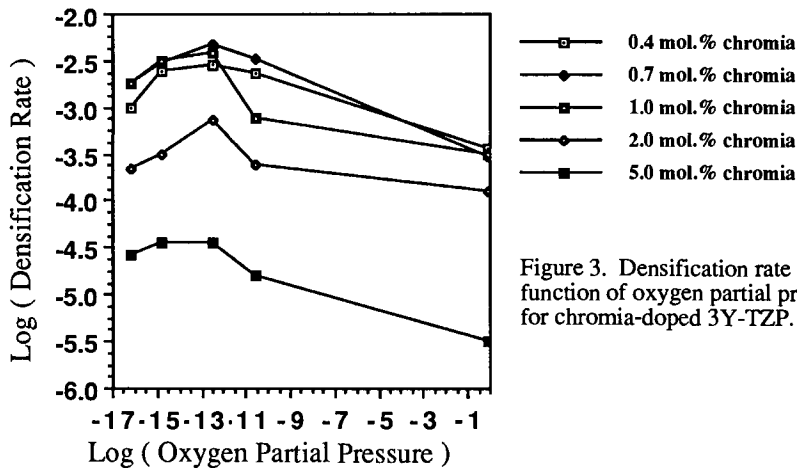
Figure 3. Densification rate as a function of oxygen partial pressure for chromia-doped 3Y-TZP.

Figure 4 shows the variation of densification rate with chromia content for samples fired in an oxygen partial pressure of 10$^{-12.5}$ at 1400C.

When fired in a low oxygen partial pressure, the densification of the TZP was increased with chromium oxide additions with a maximum at around 0.7 mol.% chromia. Densification rates gradually decreased with further additions. The addition of chromium oxide coupled with firing in air is not beneficial to the densification of this TZP material. As the quantity of chromium oxide is increased, so the densification rate decreases.
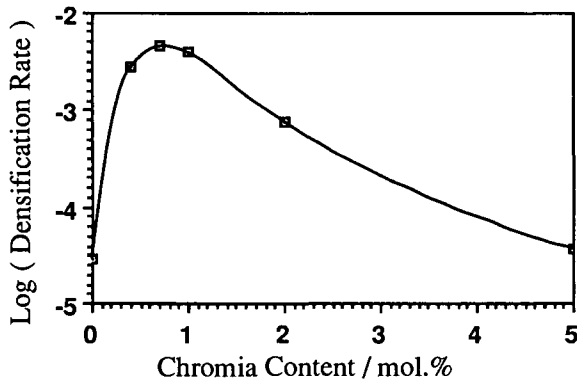
Figure 4. Influence of chromia content on the densification
rate (at a density of 5.3 Mg.m^{-3}) of chromia-doped 3Y-TZP
fired in an oxygen partial pressure of 10$^{-12.5}$.

Figure 5 shows polished and thermally etched sections from a) air fired TZP with no chromia addition
and b) 0.7 mol.% chromia-doped TZP fired in an oxygen partial pressure of 10$^{-14.8}$. The grain size of
air fired samples shows no significant variation with chromia content, being approximately 0.5 μm.
The average grain size of materials fired in the low oxygen partial pressure increased with increasing
chromia content to ~0.75 μm at 0.7 mol.% chromia addition and then remained constant. The increase
in grain size correspond to the increase in number of relatively large cubic grains in the microstructure.
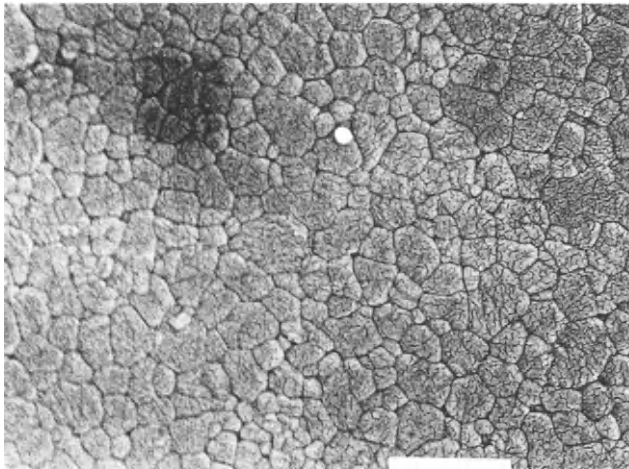
Figure 5.a. Polished and thermally etched section of air fired TZP with no chromia addition.
Bar = 1 μm.
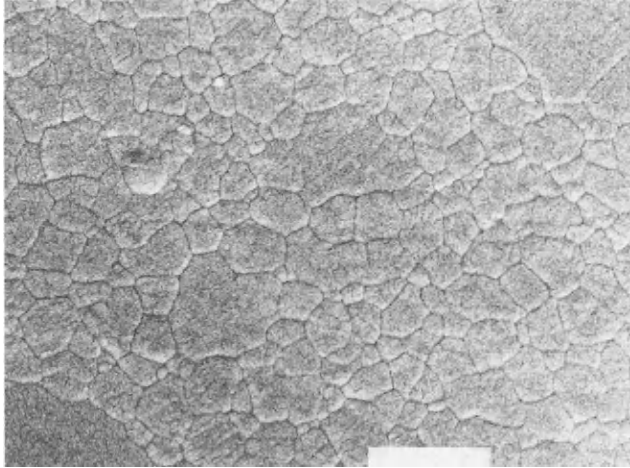
Figure 5 b. Polished and thermally etched section of 0.7 mol.% chromia-doped TZP fired at an oxygen partial pressure of $10^{-14.8}$. Bar = 1 μm.

Specimens of $90.ZrO_2,10.Y_2O_3$, doped and undoped with 1.5 mol.% chromia were prepared and sintered in the controlled atmosphere sintering dilatometer, at 1500°C, in air and in an oxygen partial pressure of 10-13.8 (which corresponds to the equilibrium oxygen partial pressure for the reaction 4/3 Cr + O_2 = 2/3 Cr_2O_3, at 1500°C (158)). Final densities are listed in table 4. Density - time data are plotted in figure 6.

Material[1]	Final Density (Mg. m^{-3})
TZ10Y-A	4.689
TZ10Y-R	4.657
TZ10Y.1.5C-A	4.380
TZ10Y.1.5C-R	4.435

1. A = Fired in air, R = fired in an oxygen partial pressure of $10^{-13.8}$,
1.5C = contains 1.5 mol.% chromia.

Table 4. Final densities of 10% Yttria doped fully stabilized zirconia with no additive and with 1.5 mol.% chromia addition.

These results show that atmosphere has very little effect on the densification of materials undoped with chromia. In samples containing 1.5 mol.% Cr_2O_3, densification is slower than for the 10Y-FSZ, air firing giving a greater decrease in densification rate than firing in an oxygen partial pressure of $10^{-13.8}$.
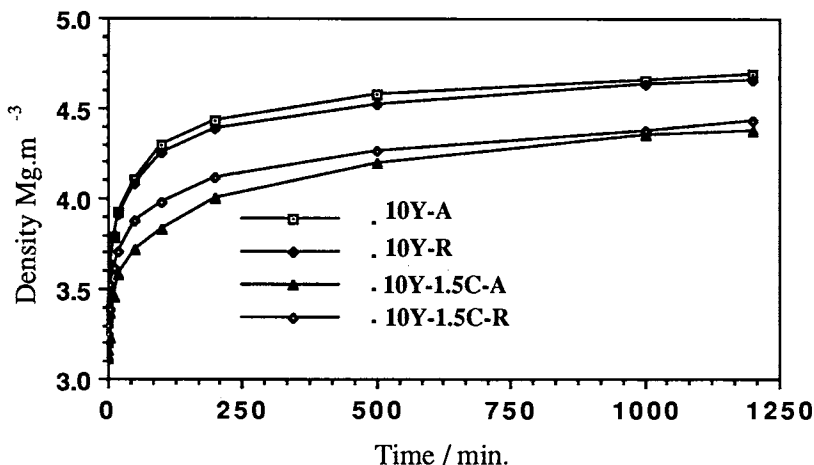
Figure 6. Density - time data for isothermal sintering of 10 mol.% yttria-doped zirconia, with and without 1.5 mol.% chromia addition, in air and in a low oxygen partial pressure at 1500C.

CONCLUSIONS

1) In the system ZrO_2-Cr_2O_3, over virtually the whole composition range, a low oxygen partial pressure during sintering is necessary to achieve any significant densification.

2) Only at low chromia contents does densification of air fired materials take place.

3) For all chromia-containing materials densification is faster in a low oxygen partial pressure than in air and maximum densification rates occur at oxygen partial pressures close to that corresponding to the Cr-Cr_2O_3 equilibrium.

4) In low oxygen partial pressures, chromium oxide is a densification aid for undoped and 3 mol.% yttria-doped zirconia, but not for the 10 mol.% yttria-doped zirconia.

ACKNOWLEDGEMENTS

REFERENCES

1   R.Kamo. "Ceramics for advanced heat engines." Industrial Ceramics 7 (3) 161-166 1987.
2   T.Y.Tien, T.K.Brog, A.K.Li. "Toughened ceramics in the system Al_2O_3:Cr_2O_3 / ZrO_2 :HfO_2
."   Int. J. High Technology Ceramics 2 207-219 1986.
3   A.Yamaguchi. "Densification of Cr_2O_3 -ZrO_2 ceramics by sintering." J. Am. Ceram. Soc.
        64(4)
        C-67 1981.

4   A.Yamaguchi. "Chromium oxide based sintering bodies." U.S. 4,374,897 (Cl 428-446;B329B9/04) 22 Feb. 1983. J.P.Appl. 80/26,863, 4 Mar. 1980.

5   A.Yamaguchi. "Sintering of compounds of chromium oxide-titanium oxide under high reduction." Toyoda Kenkyu Kokoku 37 23-31 1984.

6   A.Yamaguchi. "Sintering of Cr_2O_3 in carbon powder." Yogyo Kyokai Shi 88(4) 184-190 1980.

7   A.Yamaguchi. "Sintering of compositions in the system Al_2O_3 -Cr_2O_3 -SiO_2." Ceram. Int. 12. 19-24 1986.

8   H.Leistner, I.Elstner. "Sintering behaviour of refractories in the ternary system ZrO_2- Al_2O_3 - Cr_2O_3 in dependence of the firing atmosphere." Bundesministerium fur Forschung und Technologie Report BMFT-FB-T-83-105 1983.

9   M.Jayaratna, M.Yoshimura, S.Somiya. "Hot pressing of Y_2O_3 -stabilized ZrO_2 with Cr_2O_3 additions." J. Mat. Sci. 21 591-596 1986.

10   E.T.Turkdogan. Table 1.2 in Physical Chemistry of High Temperature Technology. Academic Press, 1980.

11   P.D.Ownby, G.E.Jungquist. "Final sintering of Cr_2O_3." J. Am. Ceram. Soc. 55(9) 433-436 1972.

12   J.W.Halloran, H.U.Anderson. "Influence of O_2 partial pressure on initial sintering of α–Cr_2O_3 ." J. Am. Ceram. Soc. 57(3) 150 1974.

Processing of ceramic-ceramic composites

S.C. Danforth

Center for Composite Manufacturing Science and Engineering,
Department of Ceramic Engineering, Rutgers,
The State University, Piscataway, New Jersey 08855-0909, U.S.A.

ABSTRACT

Ceramics show great promise as high temperature structural materials.
Ceramic composites offer numerous advantages over monolithic
ceramics, especially increased toughness and decreased flaw
sensitivity. If net shape manufacturing methods can be developed
which produce predictable and controllable microstructures, these
ceramic-ceramic composites will rapidly realize their full potential
as engineered materials. This paper describes some of the current
techniques used to manufacture ceramic matrix composites.

INTRODUCTION

In the past fifteen years, high-performance engineering ceramics have
demonstrated outstanding potential to replace and improve upon high
temperature metals in many demanding applications. Ceramics
possesses many attractive attributes for advanced engine, aerospace,
and other structural applications, such as low density, high
stiffness, high hardness and high temperature properties, especially
chemical inertness. In spite of these very promising
characteristics, monolithic ceramics suffers from defects which are
intimately related to the specific processing methods used in
manufacturing. Such defects, be they pores, cracks, inclusions,
etc., can severely limit the mechanical strength of the ceramic
material. Due to the nature of the atomic bonding (ionic/covalent)
in ceramic materials, they possess an inherently low resistance to
propagation of existing cracks. Such cracks are often associated
with defects as cited above. While metals have critical fracture
toughnesses in the range of 30 to 50 MPa $m^{0.5}$, most monolithic
glasses and ceramics have K_{Ic}'s in the range of 0.5 to 6 MPa $m^{0.5}$. It
is only in recent years that advances have allowed development of
toughened ceramic materials with K_{Ic}'s in the range of 6 to 20 MPa
$m^{0.5}$, and in some cases even higher. Thus the promise exists to
overcome the main drawback of ceramic materials, i.e., low fracture
toughness.

There are generally three accepted methods to overcome the problem of
high sensitivity to defects associated with engineering ceramic
materials. These include the following: 1) Improved control over
starting ceramic powders, dispersion, and consolidation methods. Yet
this has been shown to improve strength and reliability but not
toughness. 2) Utilization of NDE techniques combined with proof

testing (as with currently available commercial Japanese turbine
rotors). Yet currently this approach is too costly and time
consuming, and NDE is incapable of detecting flaws of required
critical size. 3) The use of second phases to toughen the ceramic
matrix, i.e., ceramic-ceramic composites. Significant increases in
toughness of ceramics can be obtained through appropriate toughening
methods. These include the incorporation of second phase particles,
whiskers, platelets and fibers, which have led to increased strength,
toughness, creep, and wear resistance as well as thermal shock
resistance.[1 - 11] To date, the most thoroughly studied ceramic-
ceramic composites are materials such as glass or glass-ceramics
reinforced with carbon or SiC fibers, and Al_2O_3 reinforced with SiC
whiskers (SiC_w). The use of SiCw to reinforce Al_2O_3 has resulted in
increases in strength by a factor of 2, as well as increases in
toughness by a factor of 2-2.5, to ~10 MPa m^{05}. These materials are
now being used commercially as cutting tools for special metal
machining applications. While glass ceramics generally have modest
toughnesses, the incorporation of uni-directional (0°, aligned) SiC
fibers can result in significant increases in toughnesses to the
range of 25 to 50 [7]. (See Fig. 1.)

The mechanisms by which such dramatic increases in toughness occur in
ceramic-ceramic composites depend upon the nature and orientation of
the reinforcing phase [4]. These toughening mechanisms include:
transformation toughening, crack deflection, bridging, pinning,
microcracking, and fiber/whisker pull-out, plastic deformation (for
cermets) and depend upon the reinforcement geometry. In general, for
ceramic composites to be used in place of monolithic ceramic
materials, the advantages in mechanical properties and performance
must outweigh the disadvantages due to increased processing
difficulties (see Fig. 2). While significant improvements are needed
in such areas as new, more thermo-chemically stable reinforcements,
the most significant limiting step to further progress for ceramic-
ceramic composites is the lack of intelligent, net shape
manufacturing methods. There is an urgent need to develop
manufacturing systems for ceramic-ceramic composites which establish
a sound scientific and technological base for modeling and control of
the manufacturing processes. Only then can microstructures and in
turn properties be reliably manufactured.

OVERVIEW OF EXISTING MANUFACTURING METHODS

Manufacturing of ceramic-ceramic composites generally involves two
stages: 1) the incorporation of the reinforcement into the
(unconsolidated or pre-) ceramic matrix material, followed by 2)
final densification. In some instances these steps may be combined
into one. The specific manufacturing steps employed depend upon the
final part geometry required and the nature of the reinforcing phase,
i.e., whether it is discrete particles, whiskers, platelets, long-
chopped fibers, or continuous fibers (see Table I).[8] One of the
most critical requirements in manufacturing these two-phase material
systems is control over the degree of dispersion/mixing of the second
phase in the matrix, and especially the orientation and spatial
distribution of the second phase. Additional manufacturing issues
that must be controlled are the following: flow, residual stresses,
heating and cooling rates, degradation of the reinforcing phase
during processing, as well as the high temperature thermo/chemical

stability and resultant mechanical strength of the matrix/reinforcing phase interface. The final density required for the matrix phase will largely depend upon the application of interest, but for most high temperature uses, it must exceed 75 to 90%, unless surfaces are protected from excess oxidation by 1) inert environment use, 2) protective coatings, or 3) nanometer scale porosity.
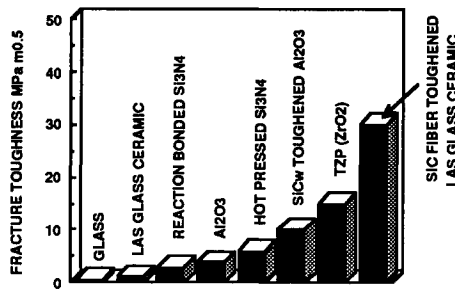
Fig. 1. Fracture toughness, K_{IC} of various ceramics and ceramic-ceramic composites
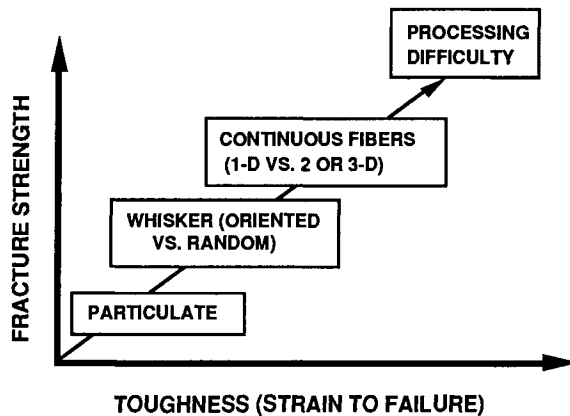
Fig. 2 Relationship between fracture toughness, fracture strength and processing difficulty for ceramic-ceramic composites.

TABLE 1 Manufacturing Processes for Ceramic-Ceramic Composites

PROCESS	EXAMPLES (fiber/matrix)
Viscous glass consolidation	
Ply lay up and hot press	Nicalon/LAS
Matrix transfer mold	Carbon /Glass
Injection mold	
Chemical vapor deposition	
Infiltrate pre-woven	Nicalon/SiC
structures	Carbon/SiC
Polymer conversion	
Infiltrate	Carbon/Carbon
and pyrolysis	Nicalon/SiC
Sol Gel	
Infiltrate and sinter	Carbon/Glass
Powder and hot press	
Traditional ceramic	SiC/Al_2O_3
processing	FP Al_2O_3/Al_2O_3
Gas-Liquid metal reaction	
Lanxide	Nicalon/Al_2O_3

Manufacturing methods used for discrete particle or whisker/platelet/chopped fiber composites offer the promise for low cost, net shape toughened ceramics. In these techniques, the reinforcing phase is mixed with the matrix powder in a dry or wet state and then formed into the desired geometry by die-pressing (simple shapes), isostatic pressing, slip-casting, colloidal filtration, or more recently, injection molding. Densification is carried out either by sintering, hot-pressing, or hot isostatic pressing. The limitations associated with dry manufacturing methods are poor mixing and high levels of agglomeration. Materials manufactured in this manner often have lower strengths than the unreinforced material. Segregation of the matrix and reinforcing phase can be a severe problem with wet or colloidal processing methods unless special precautions (i.e. heterocoagulation) are taken.[10, 11] Whisker/fiber damage can be a problem with plastic forming technologies.

To date, the most promising, automated net shape manufacturing method for ceramic-matrix composites (with discontinuous reinforcements) is injection molding. The evidence for this is the activities of a number of laboratories investigating this manufacturing method.[12,-15] While there is great potential to manufacture ceramic-ceramic composites by injection molding, there are a number of severe problems which need to be overcome before a reliable manufacturing system can be developed for these materials. It has been clear for a number of years, and has recently been shown in the literature, that control over whisker orientation is the single most significant problem in this manufacturing method. It is clear that the whisker orientation is controlled by the following factors: aspect ratio, system rheology, shear rate, slip, and mold geometry.[9, 16-18] The whisker orientation will in turn control sintering stresses (and shrinkages) and ultimately mechanical properties. This is clearly seen in Figs. 3 and 4. Fig. 3 shows the variation in SiC whisker orientation under high and low shear rate conditions respectively,
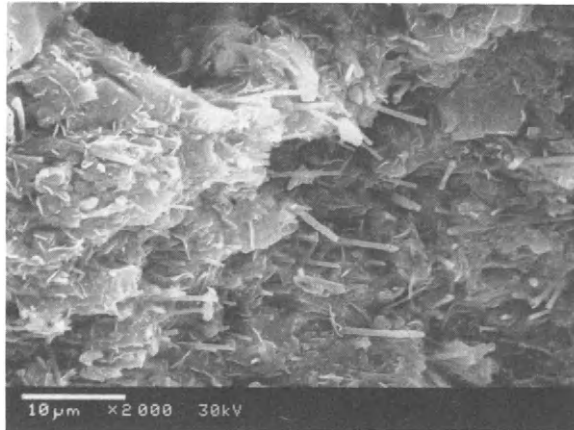
(A)
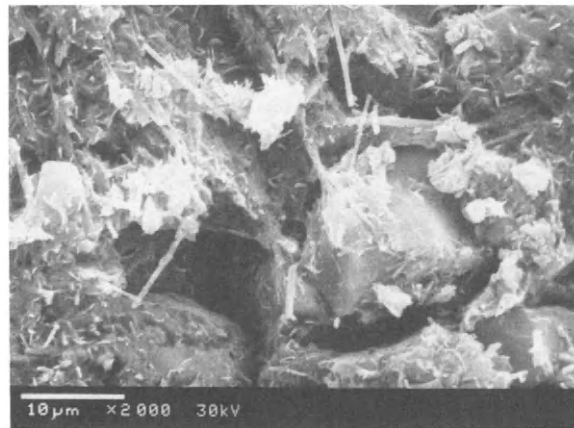
(B)

Fig. 3.   SEM micrographs of as molded fracture surfaces showing
whiskers: aligned to flow (A), and randomly oriented (B). Flow
direction is left to right.

FLOW PATH ALONG TEST BAR LENGTH

GATE

**FLOW
DIRECTION**

SINTERING
SHRINKAGE

SINTERING
SHRINKAGE

**DETAIL OF WHISKER ALIGNMENT
WITH TEST BAR FLOW PATH**

HIP'ed TEST BAR CONFIGURATION
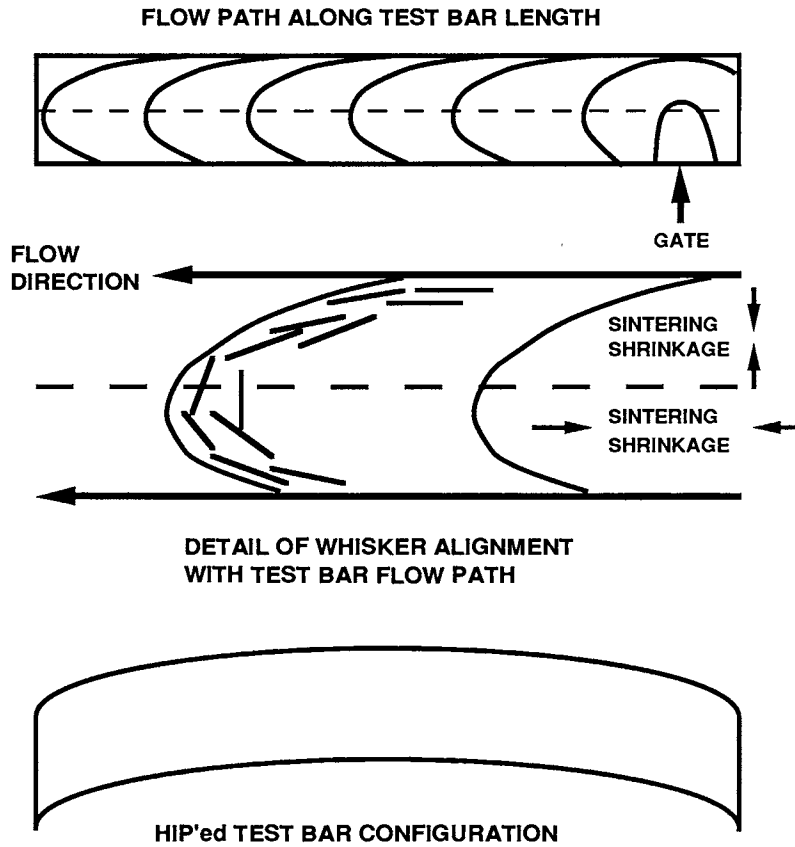
Fig. 4. The strong influence of flow path on reinforcing whisker orientation and sintering shrinkages for injection molded ceramic-ceramic composites.

and Fig. 4 shows the influence of injection mold gate geometry on flow, whisker orientation, and in turn sintering shrinkages.

The second most important issue in injection molding of whisker toughened ceramic-matrix composites is control over whisker length. It has been shown that the ability to toughen a ceramic increases as the acicularity of the reinforcing phase increases, i.e., long fibers are better than short fibers, which are better than plates which are better than equiaxed particles.[4] It is felt, therefore, that processing research should center on problems of whisker (not particulate) toughened composites. Additional work should be done on platelet reinforced materials to examine their toughening abilities and also because of the potential health risks associated with the use of some whisker materials.

The third key area that needs further study is the development of low cost, net shape processing methods for long whisker or chopped fiber ceramic-ceramic composites which will maintain the length and uniform dispersion of the fibers.[1.3,1.4] Present processing methods generally start with a whisker aspect ratio on the order of 50. For whiskers with diameters of 0.5-2 microns, this corresponds to lengths of 25-100 microns. During processing, however, the aspect ratio can be greatly reduced. It is generally not feasible to process materials with final aspect ratios >~25-50[9] This may result in real limitations on the ultimate properties of whisker or chopped fiber ceramic-ceramic composites. Use of long fibers (1000 microns) and maintenance of high aspect ratios (>100) with proper integration and consolidation of the matrix and fiber phase, will lead to the realization of the full potential of toughened ceramics.

Thus for whisker toughened ceramic-matrix composites, there is a very real need for new, automated, net shape manufacturing methods which allow control over whisker length and orientation. Only then can the low cost and high reliability potential of these promising advanced materials be realized.

Manufacturing of continuous fiber ceramic-ceramic composites is accomplished using several techniques. One of the common techniques is for producing simple shapes of continuous fiber (1-D or 2-D) reinforced composites with a glass or glass ceramic or polycrystalline ceramic matrix phase. In this method, fiber tows are drawn through a slurry containing the matrix powder and inorganic binder. Once impregnated, the tows are wound on a mandrel, cut, stacked, and then heated to remove the binder, followed by densification by hot-pressing.[8] Densification generally requires application of pressure to enhance sintering. This is because the presence of the fibers (and also whiskers) at high loadings retards the sintering process. There are two major limitations to this general approach. First, the process is expensive and it is difficult to insure uniform distribution of fibers in the matrix phase. In addition, there are also special requirements for high temperature dies and application of pressure (especially for crystalline ceramic matrices, such as Si_3N_4 or SiC). Complex, net shaped parts can not be manufactured in this manner using glass, glass ceramic, or crystalline ceramic matrices.

A process has been developed recently to allow manufacturing of complex geometries even with 3-D woven fiber reinforcement, provided

the matrix can be processed as a glass.[8] This process is based on
resin transfer molding used for polymer matrix composites. For fiber
reinforced glass composites, the fiber preform is heated in a mold
cavity and the hot molten matrix glass is then forced into the mold
under pressure. This is an exciting new advance for ceramic-matrix
composite manufacturing. Unfortunately, new, automated, net shape
manufacturing methods are still required for non-oxide ceramic
materials with either discrete (particulate, platelet, or whisker)
reinforcement.

There is also interest in using sol gel or inorganic precursors as
matrices for continuous fiber reinforced ceramic matrix
composites.[8, 19] While sol gel shows promise for oxide glass and
glass ceramic matrices, inorganic polymers have the greatest
potential for non-oxide matrices, as well as precursors for ceramic
fibers.[20-23] More research is needed to develop manufacturing
methods using inorganic polymers as precursors to the ceramic matrix.

There are two additional specialized net shape manufacturing
techniques that have been developed for ceramic-matrix composites.
These are the Lanxide process and chemical vapor infiltration (CVI).
In the Lanxide process[24, 25], molten metals are reacted with a gas
to produce oxides or nitrides. As the reaction proceeds, the ceramic
product grows on top of the molten metal, which is wicked up into the
porous oxide or nitride coating. The metal then continues to react
with the gas at the oxide/gas interface and the process continues.
Careful control over reaction conditions, melt chemistry, and pore
structure must be maintained for process optimization. Materials such
as Al_2O_3/Al and AlN/Al, ZrN, Zr, and TiN/Ti have been produced in
this manner. Two unique aspects to this process are the following: 1)
the ability to grow net shape products, and 2) the ability to have
the reaction products grow into a powder, whisker, or fiber preform.
One system with Al_2O_3/Al reinforced with 20 vol% (coated) Nicalon SiC
fibers has four point bend strengths of 997 MPa and fracture
toughnesses of up to 29 MPa $m^{0.5}$. These properties, combined with a
net shape capability make this an attractive manufacturing process.
There may however be upper limits on the use temperature of these
composites due to residual metal phase contents.

The second manufacturing method for ceramic fiber/whisker composites
is chemical vapor infiltration (CVI). In this approach, the
fibers/whiskers are formed into the desired shape (and orientation)
and then placed in a CVD reactor. With the application of heat and
flow of reactant gases, the matrix phase is formed in situ, within
the fiber preform, by CVD reactions [26-31]. This has been used very
successfully to form SiC-SiC composites for high temperature
applications. A recent advance has been introduced [26,27], whereby
the CVI reactor is designed such that a thermal gradient is imposed
across the fiber preform. In this method, the CVI gases enter the
cold side of the fiber preform and exit the hot side. This eliminates
the formation of external surface skins of high density that limit
infiltration densities (without grinding and multiple infiltrations).
With this modification, preforms can be completely infiltrated in
orders of magnitude shorter times than was previously possible.

The advantages to CVI for ceramic-matrix composites include: net
shapes, zero shrinkage, minimum fiber damage, high purity matrices,
and the ability to tailor the CVD chemistry from the beginning to the

end of the process. The major difficulties that have been associated with this technique are: high cost, low production rates, and residual porosity (~10%).

INORGANIC POLYMERS AS PRECURSORS TO CERAMIC FIBERS

The interest in ceramic-ceramic composites has resulted in a large number of investigations into the use of inorganic polymers as precursors to high temperature ceramic fibers.[19-24, 32-37] These inorganic polymers had their origins in the research done for carbon-carbon composites, i.e., the rayon[TM], PAN, and pitch based materials for carbon fibers and carbon matrices.[22, 38] The work by Yajima [22] investigated the use of polycarbosilanes (with Si-C backbones) and polyborosiloxanes (with Si-B-C-O backbones). While there is a great deal of complex chemistry involved in the synthesis of these compounds, it is clearly their processability into fibers or into a matrix and the subsequent crosslinking, pyrolysis, and resultant properties that are of foremost interest to ceramists. For synthesis of SiC fibers, the following general sequence of steps is followed: polycarbosilane synthesis, fiber spinning at ~300°C, curing in air at 190°C, and subsequent pyrolysis in an inert gas at 1200-1300°C. This results in a "SiC" fiber (i.e., Nicalon) with a microcrystalline structure, and a high density. A great deal of work has been done to investigate the use of these fibers as reinforcements for glass and glass ceramic matrices. With appropriate processing and control of matrix/interface bond strength, these materials exhibit extremely good strengths and fracture toughness. The Nicalon fibers generally contain excess carbon and oxygen. The impurities of C and O reduce the high temperature stability of the fibers. High temperature oxidation stability is also a key issue. Yajima points to the possibility of using these inorganics as precursors to a SiC body, by using them as a sintering aid or a source of powder. Others have pointed to the possibility of using these inorganics, not only as the fiber precursor, but also as the matrix precursor.[20, 21, 24, 32, 33, 35, 39]

There have been a wide range of inorganic polymer chemistries investigated as ceramic precursors. These include: polycarbosilane, polyborosiloxane for SiC [22], polyvinylsilane and polysilastyrene for SiC [39-41], polysilazanes from $-[H_2SiNCH_3]-$ monomers for Si_3N_4 [19], phosphorous containing derivatives of decaborane ranging from $B_{10}H_{12}(Ph_2PH)_2$ to $[Ph_2P(CH_2)_3PPh \cdot B_{10}H_{12}]_x$ for B_4C [24, 37], polysilazanes from dichlorosilanes for Si_3N_4 [21], polysilazanes from methyldichlorosilane, CH_3SiHCl_2 for Si_3N_4/SiC [20], and hydridopolysilazane $(SiH)_{39.7}(Me_3Si)_{24.2}(NH)_{37.3}(N))_{22.6}$ for Si_3N_4 [23].

Recent work [36] has addressed the critical issues relevant to converting inorganic polymers into bulk ceramic components (BN). This work points to issues relevant to both fiber and bulk ceramic synthesis. The char or ceramic yield on pyrolysis should be high, on the order of 75 wt%. The residual material should have low levels of impurities such as C and O (for non-carbides and non-oxides respectively). The kinetics of pyrolysis are critical to the development of the microstructure (pore size) of the ceramic material. Through careful control of the pyrolysis process, high

yield ceramic materials should be possible with very fine, uniformly distributed pores. An additional key issue is the ability to stabilize the injection molded parts against deforming during polymer pyrolysis. This problem can be solved by either using a cross linking treatment after molding (HSiCl3), or by using techniques already well established for materials injection molded with organic polymers, i.e., powder beds.[9, 23] The authors [24] have also clearly demonstrated that such materials (reaction bonded Si3N4, RBSN) can have very high fracture strengths and a very high oxidation resistance, provided the residual porosity is on the nanometer scale.

Recent investigations into the use of inorganic precursors for Si3N4 monoliths, binders, and fibers [19, 23] have shown great promise for this approach to manufacturing of advanced ceramics. In one study, - [H2SiNCH3]- monomers were polymerized and pyrolized.[19] Ceramic yields were in the range of 60-85 wt% with purities as high as 98% in terms of Si and N. The authors point out that the low residual C content is a direct result of the absence of SiCH3 groups in the polymer structure. For this material, only alpha and beta Si3N4 were observed after treatment to 1600°C. It was demonstrated that these pre-ceramic inorganic polymers can be used for protective coatings, for fiber spinning, and also as binders for compression molding of powders.

There has been other work done on inorganic polymer precursors to Si3N4 that shows great promise.[23] In this work, hydridopolysilazane polymer (HPZ) was synthesized by reacting trichlorosilane HSiCl3 with hexamethyldisilazane (Me3Si)2NH. After synthesis and distillation, the polymers could readily be processed into fibers. This particular HPZ pre-ceramic inorganic polymer has unique rheological behavior. Once processed, the polymer is cured in HSiCl3 vapor, and pyrolyzed in high purity N2. The authors point out that processing was done in inert atmospheres to prevent oxidation of the product. It is important to note, however, that in TGA experiments conducted in air, weight gains were not observed until temperatures in excess of 290°C were reached. The elimination of an oxidizing curing step significantly increased the purity of the final ceramic material. The final ceramic fibers were not fully dense, and contained up to 20 vol% of very fine (nano-scale) porosity. The fibers had a very low oxygen content and had ~5 wt% microcrystalline carbon. The fibers exhibited brittle failures (from discernible surface defects) with tensile strengths and an elastic modulus up to 3.1 GPa and 260 GPa respectively.

The reported elastic modulus is quite low for Si3N4, yet this is no doubt due to the low density of the pyrolized material. It should be noted, however, that the fracture strength of these materials is extremely high. Conventionally processed, dense, bulk Si3N4 has fracture strengths on the order of 1GPa, at best. There are two main reasons why the HPZ derived polymers have such high fracture strengths in spite of their low density. The first relates to the well known volume sensitivity of strength for ceramic materials, as described by Weibull statistics. The second and most important reason for increased strength is the very fine scale (and presumably uniform distribution) of the residual porosity (20 vol%). Haggerty [36] has clearly shown that materials with high levels of residual porosity

can be very strong (and oxidation resistant) provided the pore sizes are in the nanometer size range.

SUMMARY

It should be clear from the discussion above, that ceramic matrix composites offer a great advantage over many monolithic ceramic materials in terms of strength, toughness, and increased insensitivity to flaws etc. There are however numerous difficulties associated with manufacturing these materials with controlled microstructures. Key microstructural aspects include: reinforcement volume fraction, distribution of the reinforcement in the matrix, reinforcement orientation and distribution, matrix/reinforcement interfacial chemistry, matrix density etc. Only when these aspects of the microstructure can be controlled during manufacturing can ceramic matrix composites be made with reliable and predictable thermo-mechanical properties.

REFERENCES

[1]   S. T. Buljan, J. G. Baldoni, M. L. Huckabee, G. Zilberstein, "MICROSTRUCTURE AND FRACTURE THOUGHNESS OF SILICON NITRIDE COMPOSITES," Proceedings of Whisker and Fiber Toughened Ceramics, Oak Ridge, Tennessee, 113-24, ASM International, 1988.
[2]   T. N. Tiegs, "PROPERTIES OF SiC WHISKER-REINFORCED OXIDE MATRIX COMPOSITES," Proceedings of Whisker and Fiber Toughened Ceramics, Oak Ridge, Tennessee, 105-7, ASM International, 1988.
[3]   K. M. Prewo, J. J. Brennan, and G. K. Layden, "Fiber Reinforced Glasses and Glass-Ceramics for High Performance Applications," Bull. Am. Cer. Soc. 65, 2, 305-313, 322, 1986.
[4]   R. Rice, "Ceramic Matrix Composite Toughening Mechanisms: An Update," Ceram. Eng. Sci. Proc., 7-8, 589-607, 1985.
[5]   J. J. Brennan, and K. M. Prewo, "Silicon Carbide Fiber-Reinforced Glass-Ceramic Matrix Composites Exhibiting High Strength and Toughness," J. Mater. Sci., 17, 2371-82, 1982,
[6]   T. N. Tiegs, and P. F. Becher, "Whisker Reinforced Ceramic Composites," Tailoring Multiphase and Composite Ceramics, Materials Science Research Series, Plenum Press, New York, 639-47, 1986.
[7]   D. Lewis, Office of Naval Research, Personal Communication.
[8]   K. M. Prewo, "Fiber Reinforced Ceramics: New Opportunities for Composite Materials," Bull. Am. Cer. Soc., 68, 2, 395-400, 1989.
[9]   I. Tsao, A. B. Metzner, and S. C. Danforth, "Rheological Behavior of Injection Moldable SiC Whisker Ceramic Composite Formulations: I, Capillary Rheology," Unpublished work to be submitted to J. Am. Cer. Soc., June, 1989.
[10]   M. D. Sacks, H. W. Lee, O. E. Rojas, "Suspension Processing of Al_2O_3/SiC Whisker Composites, J. Am. Cer. Soc., 71, 5, 370-9, 1988.
[11]   P. Huber, E. DeLiso, A. Bleier, and S. C. Danforth, "Processing Parameters for Whisker Reinforced Composites," 13th Annual Conference on Composites and Advanced Ceramics, Cocoa Beach, FL, January, 1989.
[12]   N. D. Corbin, C. A. Wilkins, V. K. Pujari, G. A. Rossi, J. S. Hansen, and K. N. Siebein (Norton Co.), "Development of Toughened Silicon Nitride Composites by Glass Encapsulated Hot Isostatic Pressure," Ceramic Technology for Advanced Heat Engines Project, Semiannual Progress Report for October 1987-March 1988, ORNL/TM-10838, 39-59, December, 1988.

[13]   S. T. Buljan, J. G. Baldoni. J. Neil, and G. Zilberstein, "Dispersoid Toughened Silicon Nitride Composites,", Final Report to Oak Ridge National Labs, ORNL/Sub/85-22011/1, September, 1988.
[14]   M. Janney, Oak Ridge National Labs, Personal Communication
[15]   D. Richerson, C. Griffin, Ceramatec, Personal Communication.
[16]   S. T. Buljan, (GTE Labs), "Silicon Nitride-Metal Carbide Composites," Ceramic Technology for Advanced Heat Engines Project, Semiannual Progress Report for October, 1987-March, 1988, ORNL/TM-10838, 39-59, December, 1988.
[17]   Injection and Compression Molding Fundamentals, A. I. Isayev, ed. Marcel Dekker, New York, 481, 1987.
[18]   O'Brien, K. and J. F. Crincoli, "Improving the Properties of Reinforced Engineering Plastics by Employing Injection Moldable Long Strand Variants," RETEC Meeting, Chicago, IL, Sept. 24, 1987.
[19]   Y. D. Blum, "Polymer Precursors to Silicon Nitride and Other Ceramics: Synthesis and Applications," A Summary of Progress, SRI International, Menlo Park, CA, 1988.
[20]   D. Seyferth, and G. H. Wiseman, "High-Yield Synthesis of Si3N4/SiC Ceramic Materials by Pyrolysis of a Novel Polyorganosilazane," J. Am. Cer. Soc., 67, 7, C-132-3, 1984.
[21]   D. Seyferth, G. H. Wiseman, and C. Prud'Homme, "A Liquid Silazane Precursor to Silicon Nitride," J. Am. Cer. Soc., 66, 1, C-13-14, 1983.
[22]   S. Yajima, "Special Heat Resistant Materials from Organometallic Polymers," Bull., Am. Cer. Soc., 62, 8, 893-903, 1983.
[23]   G. E. Legrow, T. F. Lim, J. Lipowitz, and R. S. Reaoch, "Ceramics from Hydridopolysilazane," Bul. Am. Cer. Soc., 66, 2, 363-67, 1987.
[24]   Y. M. Chiang, J. S. Haggerty, R. P. Messner, and C. Demetry, "Reaction Based Processing Methods for Ceramic Matrix Composites," Bul. Am. Cer. Soc., 68, 2, 420-28, 1989.
[25]   M. S. Newkirk, A. W. Urquhart, and H. R. Zwicker, "Formation of Lanxide[TM] Ceramic Composite Materials," J. Mat. Res., 1, 181-9, 1986.
[26]   C. V. Burkland, W. E. Bustamante, R. Klacka, and J. M. Yang. "Property-Structure Relationships for CVI-Processed Ceramic Matrix Composites", Proceedings of Whisker and Fiber Toughened Ceramics, Oak Ridge, Tennessee, 225-227, ASM International, 1988.
[27]   D. P. Stinton, T. M. Besmann, and R. A. Lowden, Am. Cer. Soc., Bull., 67, 2, 1988.
[28]. D. P. Stinton, R. A. Lowden, T. M. Besmann, and T. L. Starr, "Forced Chemical Vapor Infiltration Fabrication of SiC/SiC Composites,"Proceedings of Whisker and Fiber Toughened Ceramics, Oak Ridge, Tennessee,231-42, ASM International, 1988.CVD
[29]   E. Fitzer and R. Gadow, "Fiber Reinforced Silicon Carbide," Bul. Am. Cer. Soc., 65, 2, 326-35, 1986.
[30]   P. J. Lamicq, G. A. Bernhart, M. M. Dauchier, and J. G. Mace, "SiC/SiC Composite Ceramics," Bul. Am. Cer. Soc., 65, 2, 336-38, 1986.
[31]   P. Reagan, W. Cole, and F. Huffman, "CVD Silicon Carbide Components," Cer. Eng. Sci. Proc., 8, 7-8, 958-67, 1987.
[32]   R. Rice, "Ceramics from Polymer Pyrolysis, Opportunities and Needs--A Materials Perspective," Bull. Am. Cer. Soc., 62, 8, 889-92, 1983,
[33]   R. R. Wills, R. A. Markle, and S. P. Mukherjee, "Siloxanes, Silanes, and Silazanes in the Preparation of Ceramics and Glasses," Bul. Am. Cer. Soc., 62, 8, 904-15, 1983.

[34]   B. E. Walker, Jr., R. W. Rice, P. F. Becher, B. A. Bender, and W. S. Coblenz, "Preparation and Properties of Monolithic and Composite Ceramics Produced by Polymer Pyrolysis," Bull. Am. Cer. Soc., 62, 8, 916-23, 1983.

[35]   R. H. Baney, "Designing Preceramic Polymers," ChemTech., 738-42, December, 1988.

[36]   A. Lightfoot, W. S. Rees, Jr., and J. S. Haggerty, "Boron Containing Ceramic Materials Derived from Polymeric Precursors: Material Characteristics," Cer. Eng. Sci. Proc., 9, 7-8, 1021-30, 1988.

[37]   W. S. Rees, Jr., and D. Seyferth, "High Yield Synthesis of B_4C/BN Ceramic Materials by Pyrolysis of Polymeric Lewis Base Adducts of Decaborane (14)," J. Am. Cer. Soc., 71, 4, C-194-6, 1988.

[38]   J. D. Buckley, "Carbon-Carbon, An Overview," Bul. Am. Cer. Soc., 67, 2, 364-68, 1988.

[39]   R. P. Boisvert, and R. J. Diefendorf, "Polymeric Precursor SiC Matrix Composites," Cer. Eng. Sci. Proc., 9, 7-8, 873-80, 1988.

[40]   B. I. Lee, and L. L. Hench, "Molecular Composites of SiC/SiO_2, SiC/Al_2O_3, and SiC/TiC," Bul. Am. Cer. Soc., 66, 10, 1482-5, 1987.

[41]   R. West, L. D. David, P. I. Djurovich, and H. Yu, "Polysilastyrene: Phenylmethylsilane-Dimethylsilane Copolymers as Precursors to Silicon Carbide," Bul. Am. Cer. Soc., 62, 8, 899-903, 1983.

Ceramic composites by infiltration-processing

Basil R. Marple, S. Jill Glass and David J. Green
Center for Advanced Materials, The Pennsylvania State University,
University Park, Pennsylvania 16802, U.S.A.

ABSTRACT

The infiltration of partially-sintered porous powder compacts at or near room temperature with suitable infiltrants has been used to form multiphase ceramic systems. The infiltration step is normally followed by a heat treatment to bring about such processes as decomposition, solid-state reaction and sintering, depending on the system. Some of the advantages of the process are reviewed and the various design considerations outlined. The fabrication of mullite/alumina and alumina/Y-TZP particulate composites using this technique is discussed and a comparison of the two systems is presented.

KEYWORDS

Infiltration; mullite/alumina; alumina/Y-TZP; particulate composites; surface modification.

INTRODUCTION

The use of composite ceramic bodies for various structural and electronic applications is a well-established concept and the merits of designing with composite materials have been adequately discussed in the literature. The development of new and innovative techniques for fabricating composite bodies is, however, an ongoing process.

The design approach varies from system to system and depends on the application in which a composite component is to be used. For example, in many particulate and whisker ceramic composites, a uniform distribution of the second phase is desired and in the case of fiber-reinforced (and sometimes whisker) materials, a high degree of fiber orientation is often preferred.

Many methods have been used for fabricating composite systems, including the mechanical mixing of the various components, co-precipitation, heterocoagulation and sol-gel techniques. Another method that has been utilized is infiltration. The infiltration of fiber preforms with metal, polymer or ceramic precursors can be used to form fiber-reinforced composites. Metal/ceramic particulate composite bodies can also be formed using a similar process and both room temperature and elevated temperature infiltration processes have been used to form ceramic/ceramic composite materials. Infiltration processing has certain advantages over other processing routes. Included in these is the option of using the process for surface modification or for fabricating bodies with the various infiltrated phases throughout.

In the background section which follows, some of the methods of surface modification currently in use will be discussed and the merits of the infiltration process highlighted. Some of the design considerations required when using the infiltration process for composite fabrication are presented, as well as a discussion of two systems fabricated using this technique.

BACKGROUND

Surface Modification Techniques

The general strategy when modifying the surface of a body is to produce a component with an overall higher level of performance in a particular application than the unmodified component. In some cases, surfaces are modified in such a way so as to introduce compressive surface stresses in a body. Both the chemical (Kistler, 1962; Nordberg and co-workers, 1964) and the physical (Rogers, Rogers and Woo, 1965) tempering of glass are processes which give rise to surface compressive stresses and strengthening. Surface modification has also been carried out by diffusing species into dense bodies at high temperature. For example, chromia has been introduced into alumina in this manner (Kirchner, 1979). Phase transformation in the surface region can be used to affect the surface properties and this has been used in zirconia systems (Green, Hannink and Swain, 1989). Ion implantation by bombardment of surfaces with ions has also been employed to modify the properties of the surface (Polato, Mazzoldi, and Boscoletto, 1987; Hioki and co-workers, 1988).

Protective coatings are sometimes applied to components. This may be accomplished by applying a suitable coating at room temperature followed by heating, or through a process such as chemical vapor deposition (CVD) (Stinton and co-workers, 1984). In addition to CVD techniques being used for depositing additional phases on the surface of dense substrates, porous preforms can be subjected to chemical vapor infiltration (CVI) (Caputo, Lackey, and Stinton, 1985) where material is deposited within the preform forming a composite structure.

Another design approach used in tailoring the surfaces of bodies is tape casting and laminating layers of varying composition. This technique has been used in the SiC/Al_2O_3 system (Kragness, 1988) where the SiC fiber content is higher at the surface and decreases towards the interior.

Other techniques have been used for surface modification as well as for introducing additional phases throughout the body. The above list of surface modification and composite fabrication techniques is not comprehensive but rather represents some of the methods currently available. In addition, with the development of new materials and different combinations of traditional materials, novel fabrication methods continue to be developed.

Infiltration Technique

The infiltration technique is a relatively simple process for fabricating composite bodies. In the present study, porous partially sintered powder compacts were used as preforms but fiber preforms could also be employed. The driving force for the spontaneous infiltration process is the capillary pressure within the network of pores in the preform and infiltration can be enhanced by applying pressure or a combination of vacuum and pressure. As previously mentioned, the control of various parameters including the length of exposure of the preform to the infiltrant, allows the infiltration technique to be used as a surface modification method or as a means of fabricating multiphase composite bodies. Thus, infiltration has the advantage of providing relatively broad control over the depth and composition of the modified zone.

A key step in the design process is the identification and selection of suitable infiltrants. A guide in this respect is the Washburn model of fluid flow in a cylindrical channel (Washburn, 1921) as shown in equation (1)

$$d = (\gamma r t \cos \theta / 2 \eta)^{1/2} \tag{1}$$

which predicts the infiltration depth (d) as a function of various parameters. Based on this relationship, infiltration will be enhanced if the infiltrant possesses a high surface energy, γ, the contact angle, θ, between the infiltrant and solid is small (preferably 0) and the infiltrant viscosity, η, is low. The other parameters in the equation are time, t, and the pore radius, r. In theory, one wishes to increase the pore radius but there is a constraint on this since one must maintain capillarity. It is important to consider the pore radius in the preforms if colloidal suspensions are being used as the infiltrants. If the colloidal particles are too large, they will be trapped at the surface of the preform during the infiltration step.

In the case where the infiltrant must undergo decomposition, following the infiltration step, other factors such as the decomposition temperature must be considered. Decomposition should take place prior to the onset of sintering so as to not interfere with the densification process and should not generate high stresses which could cause preform cracking. To maximize the amount of additional phases incorporated into the body, the density of the infiltrant should be high and the weight loss on decomposition small. The melting temperature of the infiltrant is also important, with infiltrants which are liquid at or near room temperature having an obvious advantage in terms of simplifying the process.

A natural outcome of the infiltration technique is the increase in the pre-sintered density of bodies. This can lead to lower shrinkages during the final densification step and this shrinkage can be further decreased if reactions in the system lead to the formation of phases with a higher specific volume. As will be discussed later, such a reaction occurs in the mullite/alumina system.

The infiltration technique used in this work does have some limitations. Suitable precursors must be available so that the desired phases are formed on heating after infiltration. Since only the porosity in the preform is being used to incorporate extra phases, a limit is placed on the amount of additional phases that can be formed. Multiple infiltrations can, however, be used to more effectively utilize the available porosity and thereby increase the amount of infiltrant introduced into the preform.

Systems Under Study

Mullite/alumina. The incorporation of mullite into alumina is accomplished via an infiltration reaction sintering route. The advantage of this process is that only a silica containing infiltrant needs to be introduced into the pores. The subsequent formation of mullite at high temperatures by the reaction of silica with the alumina already in the preform serves to enhance the amount of second phase formed.

In some applications, the addition of mullite to alumina could lead to an improvement in the performance of the composite over the monolithic material. Mullite has a lower coefficient of thermal expansion (CTE) than alumina ($\alpha_{mullite} \sim 5.3 \times 10^{-6}/°C$, $\alpha_{alumina} \sim 8.8 \times 10^{-6}/°C$) which could lead to an improved thermal shock resistance and may be important when attempting to match the thermal expansion coefficients of various components (Kumar and Niklewski, 1979). The addition of mullite is expected to lower the dielectric constant which is attractive in electronic applications where alumina is often used as a substrate material. The thermal conductivity of mullite is lower than alumina which is a disadvantage for substrate materials or where thermal shock resistance is sought but could be advantageous for applications such as thermal barrier coatings.

For high temperature structural applications mullite/alumina composites offer the potential for improved strength retention (Mah and Mazdiyasni, 1983) and better creep resistance than pure alumina (Penty and Hasselman, 1972). In bodies where mullite is introduced only at the surface, the thermal expansion mismatch between the surface and the bulk could give rise to a surface compressive stress leading to improvements in strength. In both partially and fully modified bodies, higher toughness could result if toughening mechanisms that involve crack-particle interactions, such as crack deflection, are operative.

Alumina/Y-TZP. Some of the potential benefits of adding Al_2O_3 to yttria-tetragonal zirconia polycrystals (Y-TZP) are increased hardness, Young's modulus, toughness and strength. Improvement of these properties is expected to lead to better performance of the composite in structural applications.

Improvements in the hardness and modulus with Al_2O_3 additions are predicted by the rule of mixtures since Al_2O_3 is harder and stiffer than Y-TZP (H=18-23 GPa and E=380 GPa for Al_2O_3, H=10-11 GPa and E=200 GPa for Y-TZP). The addition of Al_2O_3 to Y-TZP has also increased the strength and toughness (Shimada and co-workers, 1988 and Lange, 1982). The source of this toughening effect is not clear. One possibility is that the alumina enhances the transformation toughening effect already present in Y-TZP. Other possibilities are that the second phase Al_2O_3 particles cause crack deflection or that the Al_2O_3 raises the overall toughness of the composite by increasing the grain boundary toughness. Y-TZP materials commonly contain glassy SiO_2-rich grain boundary phases and these could be modified by the Al_2O_3. It has been shown, for example, that the addition of Al_2O_3 can have a significant effect on the grain boundary ionic resistivity (Butler and Drennan, 1982).

Another benefit of Al_2O_3 additions to zirconia is the suppression of the deleterious tetragonal to monoclinic transformation which occurs during low temperature ageing (Sato and co-workers, 1987). This effect is thought to be related to the increasing stability of the tetragonal phase with Al_2O_3 additions (Tsukuma, Ueda and Shimada, 1985).

The addition of Al_2O_3 to Y-TZP may also produce a superior material for some applications since it is expected to lower the CTE. This may lead to improved thermal shock resistance, better expansion matching with other materials and surface compression if the Al_2O_3 is added only to the surface.

The aim of this paper is to compare these two systems in terms of the infiltration behavior and the effect of the second phase on the microstructure and the mechanical properties. This comparison is of interest because, although in many ways the processes in the two systems are similar, there are some distinct differences. The fabrication process for the two systems has been presented.previously (Glass and Green, 1987,1988; Marple and Green, 1988, 1989a) and is shown schematically in Fig. 1. The initial step in both systems is the infiltration of a porous powder preform. In the alumina/Y-TZP system, the infiltration is carried out at ~ 90°C with an aluminum nitrate nonahydrate ($Al(NO_3)_3 \cdot 9H_2O$) melt. Following removal from the infiltrant the aluminum nitrate within the preform resolidifies. For the mullite/alumina system, infiltration takes place at room temperature with an ethyl silicate sol which eventually gels within the preform after removal from the infiltrant.

The second step in the process is the decomposition of the infiltrant. Heating the infiltrated Y-TZP preforms causes the $Al(NO_3)_3 \cdot 9H_2O$ to first remelt and then decompose to alumina. When the infiltrated alumina preforms are heated, the decomposition of the ethyl silicate gel leads eventually to the formation of silica. At this point, in both systems the infiltration and decomposition steps can be repeated to increase the amount of additional phase in the preform.
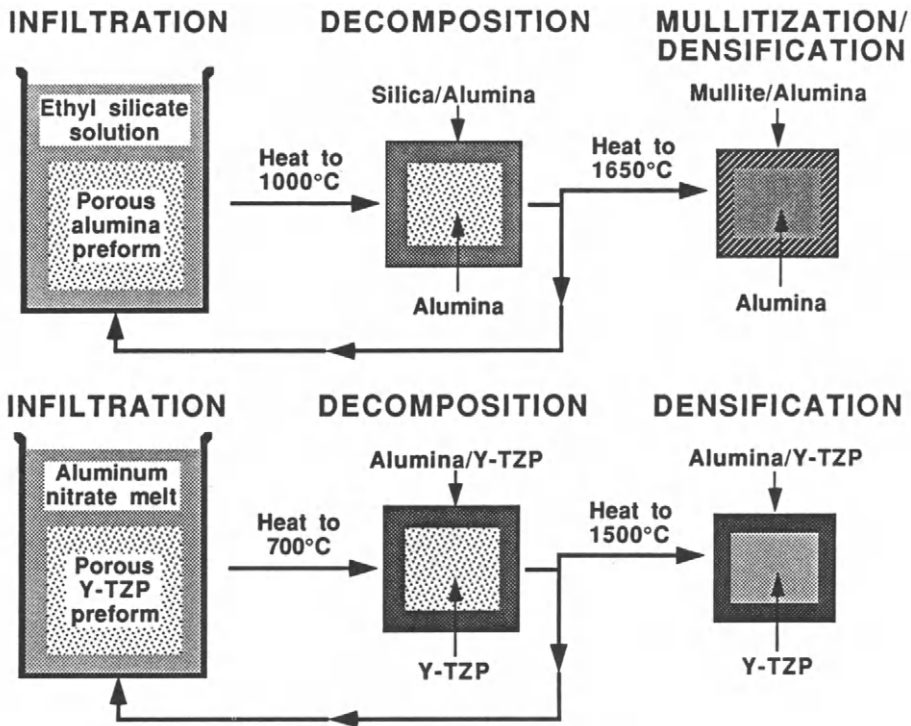
Fig. 1. Schematic of the fabrication process for alumina/mullite and alumina/Y-TZP bodies using the infiltration process.

The last step in the fabrication process is a final firing of the two phase bodies. Alumina/Y-TZP bodies containing 4 - 5 volume% alumina densify to > 99.5% of the theoretical density after heating at 1500°C for 2 h. During the final firing of the silica-containing alumina preforms both the formation of mullite and densification occur. The reaction between the silica, introduced into the preform during infiltration, with the alumina already present serves to enhance the amount of second phase formed in the sample. Bodies containing up to 20 volume% mullite have been densified to > 98.5% after heating at 1650°C for 2 h.

DISCUSSION

Infiltration

The amount of second phase which can be formed in composite bodies is determined by the volume and size of the porosity in the preform, the density of the infiltrant and its weight loss on decomposition as well as on any reactions which occur between the infiltrated phase and the preform material. Plots of the volume percent second phase incorporated into bodies as a function of the preform density for the both systems being studied in this work are shown in Fig. 2. The experimental results are compared to the expected values which were calculated from the densities of the preform and infiltrant and from the expected weight loss of the infiltrant during decomposition. The results indicate a difference in the

way in which the two infiltrants behave. In the alumina/Y-TZP system, the amount of alumina introduced is always slightly lower than the predicted value. This has been discussed previously (Glass and Green, 1988) and it has been suggested that the lower than predicted value is caused by the formation of gas bubbles from the decomposition of the $Al(NO_3)_3 \cdot 9H_2O$ which could be trapped within the preform. It has also been suggested that very fine pores within the preform whose size approach the molecular dimensions of the $Al(NO_3)_3 \cdot 9H_2O$ may not be filled and this would also contribute to a lower than predicted alumina content.
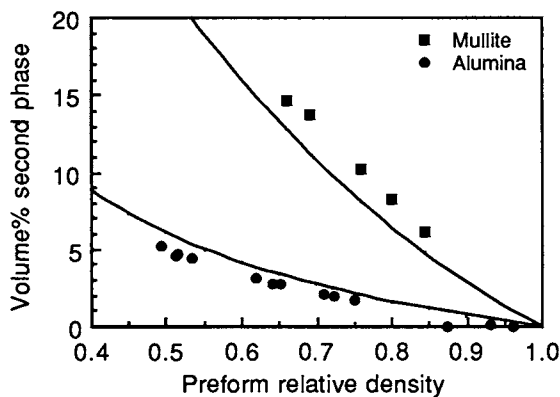
Fig. 2. The observed and predicted volume% second phase formed in composite bodies as a function of the relative density of the preform. The circles and squares represent the observed values. The upper and lower solid lines represent the predicted contents in the mullite/alumina and alumina/Y-TZP systems respectively.

In the mullite/alumina system the mullite content observed experimentally was higher than that predicted. The amount of mullite was calculated from the weight gain (of SiO_2) using densities of 3.19 and 3.98 g/cc for mullite and alumina respectively and assuming mullite was present in stoichiometric proportions (a similar plot based simply on the predicted and observed weight gain of SiO_2 produced a similar result). It has been suggested (Marple and Green, 1989b) that the reason for this result is due to some of the particles of the sol adhering to the pore walls within the preform which gives rise to a concentration gradient between the bulk solution and that within the preform. This concentration gradient leads to a further migration of sol particles into the preform from the bulk solution.

Distribution of Second Phase

Since the infiltration process introduces additional phases in a controlled fashion starting first at the outer surface of a body and proceeding towards the center, it is important to determine the distribution of these additional phases within the sintered body. Results of electron microprobe analysis and neutron diffraction analysis for cases where the infiltration front had reached the center of the body and for partially infiltrated bodies indicate that concentration gradients exist within sintered composite bodies. Figure 3 shows the distribution of SiO_2 (and hence mullite) within sintered mullite/alumina samples infiltrated for varying lengths of time. The profiles were obtained from cross sections of cylindrically-shaped bodies which had been sectioned perpendicular to the cylindrical axis. It is

apparent that the surface concentration of SiO_2 is significantly higher than the concentration in the interior. Even for samples in which the infiltration front has reached the center of the body ($t \geq 4$ h) the SiO_2 concentration in the interior of the body continues to increase with time. This is further indication of a continued migration of sol particles into the preforms with time. Other work has indicated that infiltration proceeds without complete filling of the pores initially, with subsequent back-filling behind the main infiltration front. This would also lead to a concentration profile of the type shown in Fig. 3. Evidence has also been found for liquid redistribution of the infiltrant after the infiltration step. As the liquid phase is removed during drying, infiltrant from further within the preform withdraws into the vacated porosity. Therefore the profiles shown in Fig. 3 could arise from any or all of these effects. Results from X-ray diffraction analysis have confirmed the higher surface concentration of mullite.
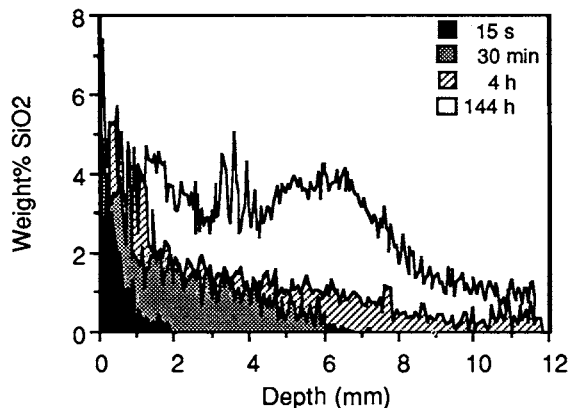
Fig. 3. Concentration profile of SiO_2 in sintered mullite/alumina bodies fabricated using various infiltration times as indicated in the legend. The analysis was carried out using an electron microprobe and the center of the samples was at a depth of 11.8 mm.

In the alumina/Y-TZP system, concentration gradients have also been found to exist. Figure 4 shows the results of the neutron diffraction analysis of composite bodies and the figure indicates a decreasing Al_2O_3 concentration from the surface inward. Since in this system the infiltrant is a homogeneous melt, the proposed mechanism of slow migration of sol particles into the preform due to concentration gradients within the infiltrant, which was presented as one possible explanation for this observation with ethyl silicate sols, could not be operative. Therefore the concentration gradients in this system must be due to back filling behind the main infiltration front, liquid redistribution during the decomposition step or gas entrapment.

The decreasing concentration of second phase from the surface inward found in these two systems is not necessarily an undesirable effect. In cases where the technique is used for surface modification, the higher surface content could be an advantage. For example, if the goal is to form bodies with compressive surface stresses, the higher content at the surface would be beneficial. The gradient in concentration also helps to reduce the abruptness of the interface between the modified and unmodified zones.

The possibility of the existence of a decreasing concentration of the incorporated phases from the surface inward in components fabricated using infiltration processing raises an important design consideration. If the technique is being used to fabricate bodies in which

all phases are uniformly distributed and the phases being incorporated have a higher thermal expansion than those already present, the presence of concentration gradients could give rise to tensile stresses on the surface which would adversely affect the strength. It is therefore important when using the infiltration approach for composite fabrication to use appropriate characterization techniques to determine the distribution of the various phases.

In cases where the goal is to form composite bodies in which the phases are uniformly distributed throughout, processing routes will have to be found to eliminate these concentration gradients. For example, during the infiltration step vacuum and/or pressure might be used to remove air and force the infiltrant into the preform. Also, during the drying and decomposition steps, both the atmosphere and the heating schedule might be closely controlled to try and avoid liquid redistribution.
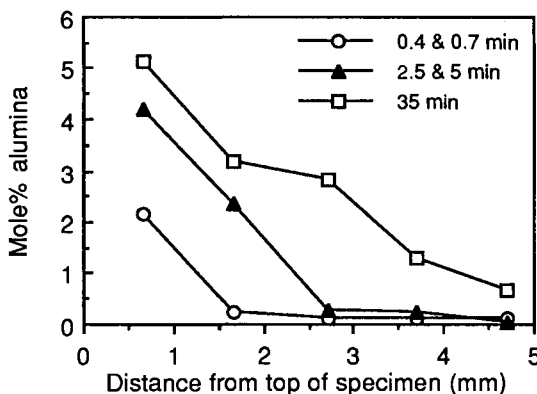
Fig. 4. Concentration of alumina in sintered alumina/Y-TZP bodies as a function of the distance from the surface. The center of the bodies was at 5.5 mm. The legend indicates the length of infiltration. (Sullivan and co-workers, 1988)

Microstructural Analysis

A typical microstructure of an alumina/Y-TZP body containing ~ 5 volume% alumina is shown in Fig. 5. Composite bodies of this composition achieved > 99.5% of the theoretical density after firing at 1500°C for 2 h. Grain size analysis showed no significant difference between the grain size in the infiltrated material and the bulk Y-TZP for the above firing schedule. The mean intercept size of the Y-TZP was approximately 0.34 μm. The alumina phase tends to be found in clusters but the clusters themselves are fairly uniformly distributed within the Y-TZP matrix.

Mullite/alumina composite bodies fabricated by infiltration processing exhibited a relatively uniform distribution of mullite as is shown in Fig. 6 for a composite body containing approximately 13 volume% mullite. The addition of mullite to alumina resulted in a composite body which was more difficult to densify than the monolithic alumina which densified to > 99.5% of the theoretical density after 2 h at 1500°C. Incorporating mullite, however, tended to limit grain growth in alumina. A comparison of the microstructures and a grain size analysis for monolithic Al_2O_3 bodies and composite bodies both sintered at 1650°C have been presented previously (Marple and Green, 1989a) and indicated that the average intercept length of alumina was reduced by greater than an order of magnitude

when 13 volume% mullite was present. The average intercept length of the mullite in the composite bodies was ~ one-half that of the alumina.
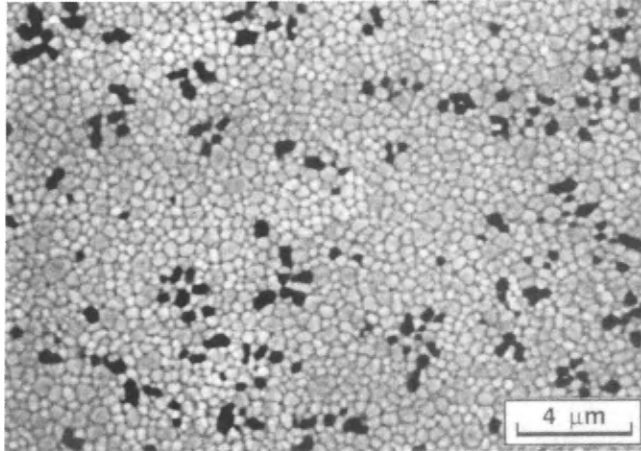
Fig. 5. Micrograph of an alumina/Y-TZP particulate composite fabricated using infiltration processing. (alumina is darker phase)
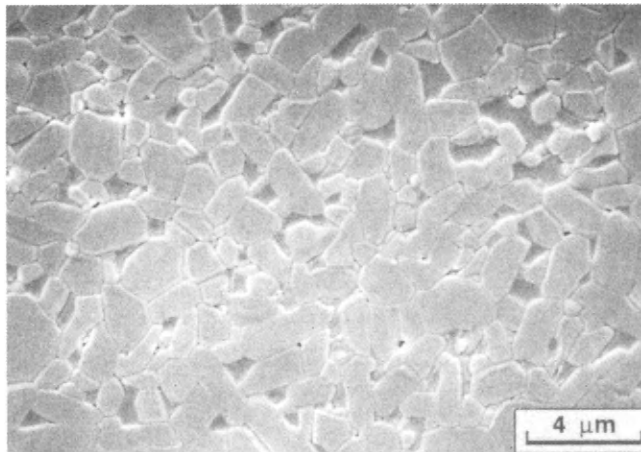
Fig. 6. Micrograph of a mullite/alumina particulate composite fabricated by infiltration processing. (darker phase is mullite)

Mechanical Properties

A comparison of some of the mechanical properties of the Y-TZP and alumina/Y-TZP bodies is shown in Table 1. The results are for samples fabricated using a single infiltration of Y-TZP preforms with a relative density of ~0.58. The bulk alumina content of the

composite bodies was 4 - 5 volume %. The hardness, strength, Young's modulus and fracture toughness all increased when alumina was added to Y-TZP.

TABLE 1 Mechanical Properties of Y-TZP and Alumina/Y-TZP Composites

Property	Y-TZP	Alumina/Y-TZP	%Change
Fracture Toughness (MPa$\sqrt{m}$)	4.8	5.5	+15
Bend strength (MPa)	723	837	+16
Hardness (GPa)	12.9	13.5	+5
Young's Modulus (GPa)	220	250	+14

The mechanical properties of alumina and mullite/alumina bodies are shown in Table 2. The composite bodies were fabricated by subjecting alumina preforms with a relative density of 0.72 to two 4 h infiltrations. Between the two infiltrations, a heating step was used to decompose the infiltrant. The bulk mullite content of the sintered bodies fabricated in this manner was ~ 19.5 volume%. In the monolithic alumina bodies a firing temperature of 1500°C for 2 h was used, to avoid excessive grain growth. The composite bodies were fired at 1650°C for 2 h. The table indicates that the composite bodies had substantially higher values of strength and fracture toughness than the monolithic alumina. As expected, the addition of mullite led to a decrease in the hardness.

TABLE 2 Mechanical Properties of Alumina and Mullite/Alumina Composites

Property	Alumina	Mullite/Alumina	%Change
Fracture Toughness (MPa$\sqrt{m}$)	3.9	6.4	+63
Bend strength (MPa)	355	555	+56
Hardness (GPa)	17.8	16.8	-6

SUMMARY

The infiltration of porous powder compacts is an effective method of fabricating multiphase composites. The technique is relatively simple and allows for broad control over the depth and composition of the modified zone. In the two systems studied, alumina/Y-TZP and mullite/alumina, compositional gradients existed and the near surface content of the added phase was significantly higher than the bulk concentration. The composite bodies formed using the infiltration technique exhibited a relatively uniform distribution of the second phase and in both the alumina/Y-TZP and mullite/alumina systems some of the mechanical properties were substantially enhanced with the addition of the second phase.

REFERENCES

Butler, E. P., and J. Drennan (1982). Microstructural analysis of sintered high-conductivity zirconia with Al$_2$O$_3$ additions. J. Am. Ceram. Soc., 65 [10] 474-478.
Caputo, A. J., W. J. Lackey, and D. R. Stinton (1985). Development of a new faster process for the fabrication of ceramic fiber-reinforced ceramic composites by CVD. Ceram. Eng. Sci. Proc., 6 [7 - 8] 694-706.
Glass, S. J., and D. J. Green (1987). Surface modification of ceramics by partial infiltration. Adv. Ceram. Mater., 2 [2] 129-131.

Glass, S. J., and D. J. Green (1988). Fabrication of multiphase particulate ceramics by infiltration into powder compacts. In G. L. Messing, E. R. Fuller, Jr., and H. Hausner (Ed.) Ceramic Transactions, Vol 1B, Ceramic Powder Science II. The American Ceramic Society, Inc., Westerville, OH. pp. 784-791.

Green, D. J., R. H. J. Hannink, and M. V. Swain (1989). Surface modification of zirconia toughened ceramics (ZTC). In Transformation Toughening of Ceramics. CRC Press, Inc., Boca Raton, FL pp. 199 - 215.

Hioki, T., H. Hasegawa, J. Kawamoto, and O. Kamigaito (1988). Structural and mechanical properties of ion-implanted yttria-stabilized zirconia. In S. Somiya, N. Yamamoto, and H. Yanagida (Ed.) Advances in Ceramics, Vol 24B, Science and Technology of Zirconia III. The American Ceramic Society, Inc., Westerville, OH. pp. 679-690.

Kirchner, H. P. (1979). Coatings and chemical treatments. In Strengthening of Ceramics. Marcel Dekker, Inc., New York. pp. 167-171.

Kistler, S. S. (1962). Stresses in glasses produced by nonuniform exchange of monovalent ions. J. Am. Ceram. Soc., 45 [2] 59-68.

Kragness, E. D., (1988). Processing and Mechanical Behavior of Tape Cast and Laminated Silicon Carbide Whisker/Alumina Composites. M. S. Thesis, The Pennsylvania State University, University Park, PA.

Kumar, A. H., and J. B. Niklewski (1979). Alumina-mullite ceramics for multilayer substrates. Am. Ceram. Soc. Bull., 58 [12] 1179-1181.

Lange, F. F., (1982). Transformation toughening, part 4, fabrication, fracture toughness and strength of Al_2O_3 - ZrO_2 composites. J. Mater Sci., 17 247-254.

Mah, T., and K. S. Mazdiyasni (1983). Mechanical properties of mullite. J. Am. Ceram. Soc., 66 [10] 699-703.

Marple, B. R., and D. J. Green (1988). Incorporation of mullite as a second phase into alumina by an infiltration technique. J. Am. Ceram. Soc., 71 [11] C-471-C-473.

Marple B. R., and D. J. Green (1989a). Mullite/alumina particulate composites by infiltration processing. Accepted for publication in the Journal of the American Ceramic Society.

Marple, B. R., and D. J. Green (1989b). Mullite/alumina particulate composites by infiltration processing II. Manuscript in preparation.

Nordberg, M. E., E. L. Mochel, H. M. Garfinkel, and J. S. Olcott (1964). Strengthening by ion-exchange. J. Am. Ceram. Soc., 47 [5] 215-219.

Penty, R. A., and D. P. H. Hasselman (1972). Creep kinetics of high-purity, ultra-fine grain polycrystalline mullite. Mat. Res. Bull., 7 1117-1124.

Polato, P., P. Mazzoldi, and A. B. Boscoletto (1987). Characterization by nuclear and spectrophotometric analysis of near-surface modifications of glass implanted with heavy ions. J. Am. Ceram. Soc., 70 [10] 775-779.

Rogers, E. H., T. G. Rogers, and T. C. Woo (1965). Residual stresses in a glass plate cooled symmetrically from both surfaces. J. Am. Ceram. Soc., 48 [9] 480-487.

Sato, T., H. Fujishiro, T. Endo, and M. Shimada (1987). Thermal stability and mechanical properties of yttria-doped tetragonal zirconia polycrystal with dispersed alumina and silicon carbide particles. J. Mater Sci., 22 882-886.

Shimada, T., K. Nagata, M. Hashiba, E. Miura, T. Ono, and Y. Nurishi (1988). Strength and fractographic observation of microstructure in Al_2O_3 - ZrO_2 composites. In S. Somiya, N. Yamamoto, and H. Yanagida (Ed.) Advances in Ceramics, Vol 24A, Science and Technology of Zirconia III. The American Ceramic Society, Inc., Westerville, OH. pp. 397-403.

Stinton, D. P., W. J. Lackey, R. J. Lauf, and T. M. Besmann (1984). Fabrication of ceramic-ceramic composites by chemical vapor deposition. Ceram. Eng. Sci. Proc., 5 [7-8] 668-676.

Sullivan, J. D., J. H. Root, B. D. Sawicka, and S. J. Glass (1988). Non-destructive Evaluation of Infiltration-Toughened Ceramics. AECL #9728, Atomic Energy of Canada Ltd.. Chalk River, Ontario, Canada.

Tsukuma, K., K. Ueda, and M. Shimada (1985). Strength and fracture toughness of isostatically hot-pressed composites of Al_2O_3 and Y_2O_3 - partially-stabilized ZrO_2. J. Am. Ceram. Soc., 68 [1] C-4-C-5.

Washburn, E. W. (1921). The dynamics of capillary flow. Phys. Rev., 17 [3] 273-283.

Application of a new ceramic/metal composite technology to form net shape wear resistant pump components

J. Weinstein
ALANX Products L.P., Newark, Delaware 19702, U.S.A.

ABSTRACT

The Lanxide^{TM} ceramic matrix composite process involves the directed oxidation of molten metals to grow reaction product matrix around pre-placed filler or reinforcing materials. This paper will present an overview of the basic process, its net-shaping-making capabilities and the material properties developed, which include excellent erosion resistance. Wear data will be shown from a variety of tests in dry and wet particulate environments. Alanx Products L.P., a joint venture between Lanxide and Alcan, is exploiting and scaling up this process commercially by developing material systems with excellent erosion resistance for use in pumps, valves, and other industrial wear applications, including piston engine components.

KEY WORDS

Alanx Products, Lanxide Corporation, ceramics, composites, wear resistance, CG896, erosion testing, slurry pump testing.

BASIC PROCESS

The Lanxide ceramic matrix composite process is based upon their invention of a completely new way to form ceramic/metal composites. This approach produces wear resistant components through the directed oxidation of molten metals. In the patented process, the oxidation product grows outward from the molten metal to form a ceramic matrix around a formed filler or reinforcing material. The accompanying schematic illustrates the basic process.

silicon carbide filler — preform formation

growth barrier — matrix growth — molten aluminium — alumina/ aluminum alloy matrix growth

finished component shape in ALANX™ CG896 composite
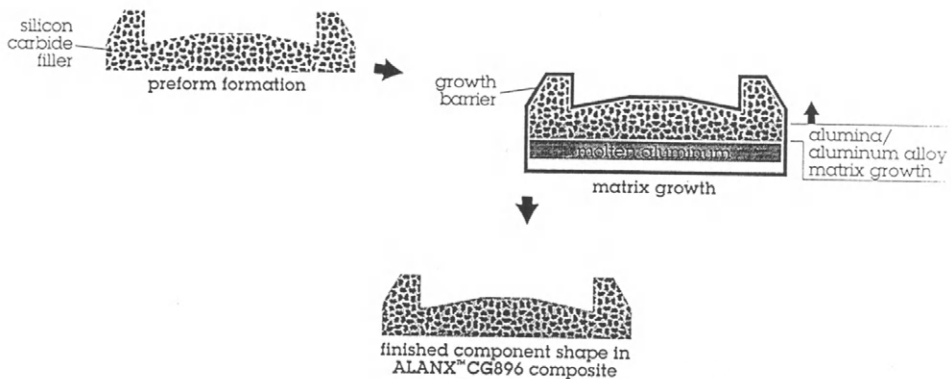
Selected from a wide range of available compositions, filler particles are formed into the final product shape by a fabricating technique such as slip casting, pressing or injection molding. This preform is placed against molten metal in a heated, oxidizing atmosphere. Under special controlled conditions, the matrix grows through the preform, infiltrating the filler without displacing it. Barrier material on the surface of the preform stops the matrix from growing past the desired shape, thus defining the outer surface. In this way, a fully densified composite is obtained with both good surface finish and excellent final dimensional shape - without the shrinkage typically associated with the densification of ceramics. The process is readily scaled up for the production of large and complex shapes.

ALANX PRODUCTS L.P.

Alanx Products L.P., a joint venture between Lanxide and Alcan, is exploiting and scaling up this process commercially by producing its first components in a composite designated Alanx^{TM} CG896, which has exceptional erosive wear resistance. Alanx^{TM} CG896 consists of a three dimensionally interconnected alumina/aluminum alloy matrix grown around a highly loaded particulate silicon carbide filler. The mechanical characteristics of CG896 are dominated by the interconnected ceramic matrix and filler (greater than 90%), thus exhibiting extreme hardness and wear resistance. The brittleness usually associated with ceramics is offset in Alanx Products by the fracture toughness given to Alanx^{TM} CG896 by its ductile metallic alloy matrix component (less than 10%). Alanx^{TM} CG896 is being applied to industrial wear applications such as pumps, valves, hydrocyclones, and material handling equipment, as well as in piston engine components.

WEAR TESTS

Testing of Alanx^{TM} CG896 was done to evaluate its wear resistance in a variety of dry and wet particulate environments.

Laboratory studies were conducted using a standard dry grit blast test done at low angles. Wet testing consisted of both rotating pins and fluted discs in sand-water slurries. Additionally, comparisons were made between Alanx^{TM} CG896 and conventionally used wear resistant ceramics and hard metals.

Alanx^{TM} CG896 has been field tested in a variety of environments with excellent results. Data is presented for accelerated wear tests done on 4" x 3" abrasive slurry pump operated in a sand and water slurry which took place at a pump manufacturer. Total wear was measured for the replaceable wear plate inside the pump which was used to test different materials including hard metal, natural rubber, polyurethanes, and ceramics.

Tetragonal zirconia stabilization in the system ZrO_2-TiO_2-CeO_2

V.C. Pandolfelli, M. Rainforth and R. Stevens
School of Materials, University of Leeds, Leeds LS2 9JT, England

ABSTRACT

To retain zirconia tetragonal at room temperature the optimum composition is close to the eutectoid ratio of the binary mixtures. Fully dense tetragonal zirconia polycrystals (TZP) have been prepared using zirconium and titanium alkoxides, together with cerium nitrate as precursors. A 77.9 ZrO_2.16.5 TiO_2.5.6 CeO_2 mol % composition, sintered in the temperature range 1300-1600°C, has been investigated and the microstructures generated have been characterized in terms of phase composition and by means of quantitative chemical microanalysis. Tetragonal zirconia was formed after sintering at 1350°C for 2 hrs. and showed a high resistance to stress assisted transformation to monoclinic. The stability of this tetragonal phase appears to be associated with the high c/a ratio (1.0327 $\pm$ 0.0001) determined for this material.

KEYWORDS

Zirconia; phase transformation; tetragonal stabilization; titania; ceria.

INTRODUCTION

Both the ZrO_2.CeO_2 and ZrO_2.TiO_2 phase diagram present a large range of tetragonal solid solution. Nevertheless fully dense tetragonal polycrystal ceramics could not be obtained in the ZrO_2.TiO_2 (Pandolfelli, 1989a) or with less than 8 mol % CeO_2 in the ZrO_2.CeO_2 system (Tsukuma, 1985).

Previous investigations of the ZrO_2.TiO_2.CeO_2 ternary system (Longo, 1974) showed that TiO_2 decreases the refractoriness of the ZrO_2.CeO_2 based materials and has no negative effect on the structural stability of the tetragonal and monoclinic solid solution of CeO_2 in ZrO_2. In this ternary system the tetragonal zirconia phase could not be obtained with less than 15 mol % CeO_2, even with the addition of up to 6 mol % of TiO_2.

The best chance of obtaining zirconia tetragonal at room temperature is at the eutectoid composition. In this paper a ternary composition is formulated keeping both the TiO_2/TiO_2 + ZrO_2 and CeO_2/CeO_2 + ZrO_2 eutectoid ratio. The composition 77.9 ZrO_2 .16.5 TiO_2 . 5.6 CeO_2 mol % was prepared and fully dense tetragonal zirconia polycrystalline ceramics were obtained after sintering at 1350°C. A description of the stability of the tetragonal phase and identification of other phases obtained when sintering at higher temperatures is presented.

EXPERIMENTAL PROCEDURE

Powders were prepared by the coprecipitation of zirconium n-propoxide and titanium isopropoxide in a continuously stirred $H_2O/Ce(NO_3)_3.6H_2O$ solution kept at pH = 3 by the addition of acetic acid. Under such conditions the alkoxides co-precipitate whereas the cerium nitrate is retained in solution. On addition of NH_4OH, the pH was adjusted to 10 and the cerous compound was homogeneously precipitated throughout the small zirconium/titanium agglomerates. After separation from the liquid, the precipitates were washed three times with isopropyl alcohol. The powder was calcined at 950°C and then ball milled in alcohol using a zirconia medium.

X-ray diffraction measurements were performed using a Philips PW diffractometer with Ni-filtered CuKα radiation. The volume fraction of monoclinic and tetragonal phase was calculated using Toraya's equation assuming P = 1.31 (Toraya, 1984). Sintering behaviour in air under isothermal conditions was followed using a sintering dilatometer. Electron probe microanalysis was conducted in a Jeol JX 50A equipped with a solid state electron detector (EDX), which allowed simultaneous analyses of the total spectrum. For quantitative studies, high purity ZrO_2, TiO_2 and CeO_2 samples were used as standards. Transmission electron microscopy was performed using a Jeol 200 CX (200 KV) with a Link EDS detector. The average grain size was determined using a linear intercept technique (Mendelson, 1969) on scanning electron (Hitachi S700) micrographs of thermally etched surface of the required samples. A log-normal size distribution of tetrakaidecahedrally shaped grains was assumed and a range of 800 to 1000 grains was considered sufficient to obtain the average. To measure the toughness on a comparative basis the indent-ation technique was used as a function of indentation load (Anstis, 1981).

RESULTS AND DISCUSSION

Comparison of the sintering behaviour of $ZrO_2.TiO_2.CeO_2$ composition at 1300°C and 1350°C (Fig. 1) indicates a possible densification by a liquid phase sintering mechanism. At 1350°C full density was obtained and tetragonal zirconia was the only crystalline phase detected (Fig. 2). At this temperature, strain at grain boundaries and occasional glass at triple points was detected by means of TEM (Figs. 3 and 4). Lattice parameter measurements resulted in a c/a tetragonal ratio of 1.0327 ± 0.0001, which is considerably higher than obtained for the ZrO_2. CeO_2 and $ZrO_2.Y_2O_3$ systems. Although the grain size was relatively large (~ 2.7 µm), the tetragonal phase was very stable. Significant martensitic trans-formation to monoclinic was only achieved by ageing the $ZrO_2.TiO_2.CeO_2$ composition for over 50 hours at 1350°C (Table 1). After ageing the zirconia ceramic (grain size ~ 7.8 µm), its toughness increased considerably due to a contribution from the stress induced transformation (Table 2).

The XRD profile for the sample sintered for 2 hours at 1350°C has also shown additional weak peaks corresponding to the 4.928 Å, 2.338 Å and 2.027 Å inter-planar spacings, which could not be explained on the basis of any of the possible primary phases in this system. This result, associated with the presence of extra spots in the TEM diffraction pattern for the $[112]_t$ direction and their absence from the $[100]_t$, suggested the possible occurrence of short range ordering. The presence of the short range order is believed to contribute to the tetragonal zirconia stabilization and to its considerable resistance to the stress induced transformation.

For this composition in the $ZrO_2.TiO_2.CeO_2$ system, the stability and solid solution is altered by sintering pellets at temperatures over 1400°C (Table 3).

EPMA analysis associated with X-ray diffraction showed the formation of $ZrTiO_4$ above 1400°C and possibly $Ce_2Zr_2O_7$ at higher temperatures. The formation of these new phases is followed by an increase in the monoclinic phase content and the volume fraction of glass present at the grain boundaries.

Although Zr, Ti and Ce were always detected in the glass phase, it became richer in Ti and Ce as the sintering temperature increased (Table 4). Consequently slightly less of the alloying dopants were available to stabilize the tetragonal zirconia.

CONCLUSIONS

Stable tetragonal zirconia polycrystals were obtained in the $ZrO_2.TiO_2.CeO_2$ system. The composition 77.9 ZrO_2 . 16.5 TiO_2 . 5.6 CeO_2 mol % sintered at 1350°C presents a high c/a tetragonal lattice ratio. Stabilization is believed to be related to the possible short range order found in the tetragonal phase (Pandolfelli, 1989b). Strain at the grain boundary and the rare presence of glass at triple points at 1350°C, might be due to a partial redissolution of the glass in the matrix during cooling. On sintering at higher temperatures the stability of the tetragonal phase is altered by an increase in grain size and by migration of Ce and Ti from the matrix, giving rise to $ZrTiO_4$, possibly $Ce_2Zr_2O_7$ and an enrichment of Ti and Ce in the glassy phase.

ACKNOWLEDGMENTS

REFERENCES

Anstis, G.R. and others (1981). A critical evaluation of indentation techniques for measuring fracture toughness: I, Direct crack measurements. J. Am. Ceram. Soc., 64, 533-538.
Longo, V. and Podda, L. (1974). Structural characteristics and refractory properties of $CeO_2.ZrO_2$ mixtures in the presence of impurities: Effect of TiO_2 and Na_2O. Ceramurgia, 4, 3-10.
Mendelson, M.I. (1969). Average grain size in polycrystalline ceramics. J. Am. Ceram. Soc., 52, 443-446.
Pandolfelli, V.C., Nettleship, I. and Stevens, R. (1989a). The influence of titania on stabilization and sintering of tetragonal zirconia, In R. Stevens (Ed.) Proceedings of British Ceramic Society - Complex Microstructures, Vol. 42, British Ceramic Society, Stoke-on-Trent. Accepted publication.
Pandolfelli, V.C., Rainforth, M. and Stevens, R. (1989b). Sintering and micro-structural studies in the system $ZrO_2.TiO_2.CeO_2$. J. Mat. Sci. Submitted publication.
Toraya, H., Yoshimura, M. and Somiya, S. (1984). Calibration curve for quantitative analysis of monoclinic-tetragonal ZrO_2 system by X-ray diffraction. J. Am. Ceram. Soc., 67, C119-C121.
Tsukuma, K. and Shimada, M. (1985). Strength, fracture toughness and Vickers Hardness of CeO_2-stabilized tetragonal ZrO_2 polycrystals (Ce-TZP). J. Mat. Sci., 20, 1178-1184.

TABLE 1   Tetragonal volume fraction (%) for $ZrO_2 \cdot TiO_2 \cdot CeO_2$ composition subjected to different surface treatments

	Tetragonal volume fraction (%)				
	As sintered surface	Ground surface	Fracture surface	Shatter box[+]	Liquid N_2*
1350°C (2 hrs)**	100	100	100	91	100
1350°C (64 hrs)	95	75	70	40	6

[+]XRD after milling for 10 minutes in a WC shatter box.

*XRD of as-sintered surface after being plunged for 5 minutes in liquid nitrogen.

**Dwell time at 1350°C.

TABLE 2   Toughness measurements by indentation technique for the $ZrO_2 \cdot TiO_2 \cdot CeO_2$ composition sintered and aged at 1350°C

	K_{IC} (MPa.m$^{0.5}$)				
	P* = 49 N	P = 73 N	P = 98 N	P = 147 N	P = 196 N
1350°C (2 hrs)	5.8 ± 0.4	4.8 ± 0.5	4.7 ± 0.4	4.6 ± 0.4	–
1350°C (64 hrs)	no cracks	no cracks	8.2 ± 0.4	8.4 ± 0.7	8.6 ± 0.6

*Indentation load

TABLE 3   Density, grain size and tetragonal volume fraction for the $ZrO_2 \cdot TiO_2 \cdot CeO_2$ composition sintered for 2 hours at different temperatures

Temperature (°C)	1300	1350	1400	1450	1500	1600
Density (g/cm^3)	5.40	5.88	5.87	5.81	5.52	5.31
Grain size (μm)	0.9	2.7	5.0	8.0	16.6	36.0
Tetragonal phase (Vol %) (as sintered surface)	100	100	100	97	8	2

TABLE 4   Electron microprobe analysis (EPMA) for the main matrix phase and
intergranular phase for the $ZrO_2.TiO_2.CeO_2$ composition sintered at different
temperatures

	Matrix (mol %)		
Temperature (°C)	ZrO_2	TiO_2	CeO_2
1350	77.22 $\pm$ 0.25	16.96 $\pm$ 0.12	5.80 $\pm$ 0.13
1400	76.87 $\pm$ 0.20	17.08 $\pm$ 0.07	6.05 $\pm$ 0.13
1450	77.67 $\pm$ 0.08	16.51 $\pm$ 0.03	5.82 $\pm$ 0.05
1500	78.50 $\pm$ 0.63	15.91 $\pm$ 0.45	5.60 $\pm$ 0.18
1600	83.30 $\pm$ 0.29	12.20 $\pm$ 0.25	3.95 $\pm$ 0.04
	Intergranular phase (mol %)		
Temperature (°C)	ZrO_2	TiO_2	CeO_2
1400	60.35 $\pm$ 1.22	34.77 $\pm$ 1.07	4.87 $\pm$ 0.15
1450	49.39 $\pm$ 0.15	45.77 $\pm$ 0.15	4.86 $\pm$ 0.01
1500	26.7 - 59.9	32.8 - 57.6	7.3 - 15.7
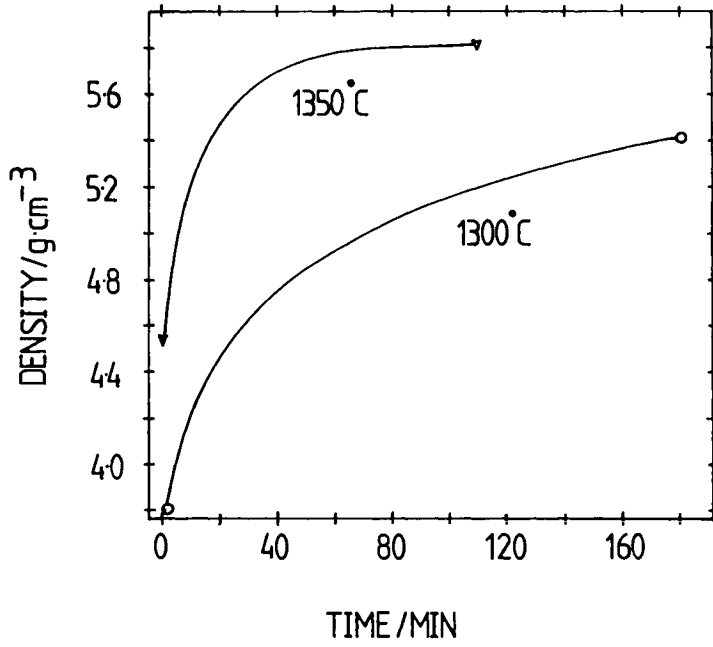
Fig. 1.   Density as a function of time for samples sintered at
           1300 and 1350°C. Curves represent the best fit to 50 data
           points.

5 μm
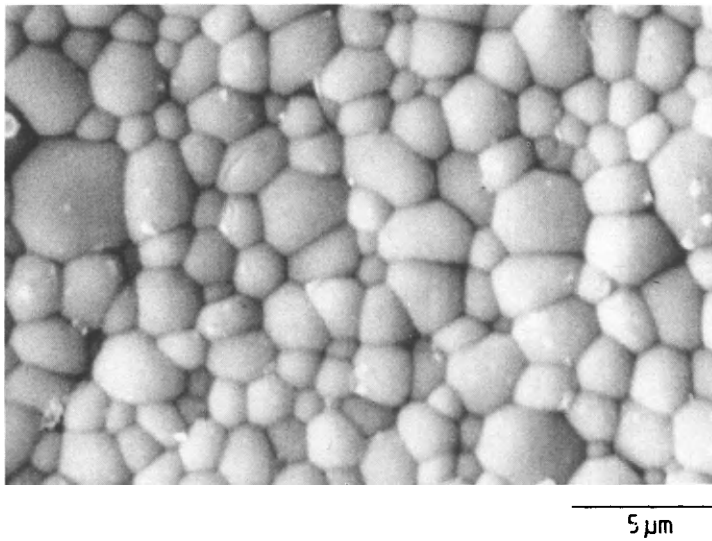
Fig. 2.   SEM micrograph of thermally etched surface from the
           sample sintered at 1350°C.

0·25μm
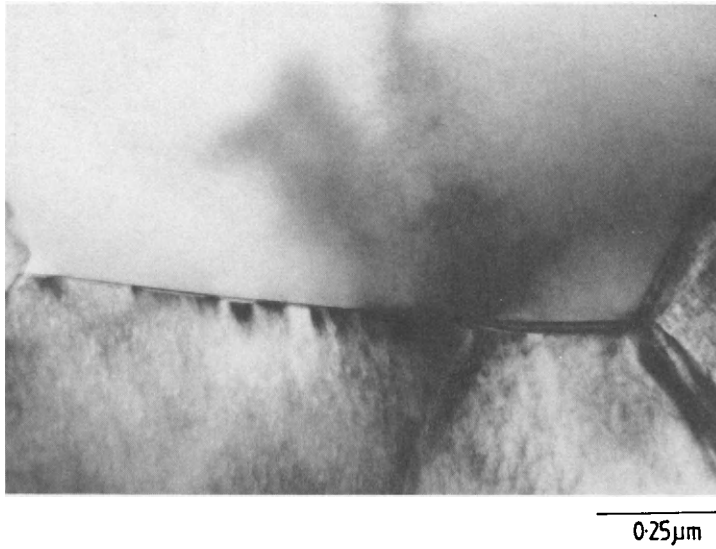
Fig. 3.   TEM micrograph of the sample sintered at 1350°C showing
strain at the grain boundary.

0·25μm
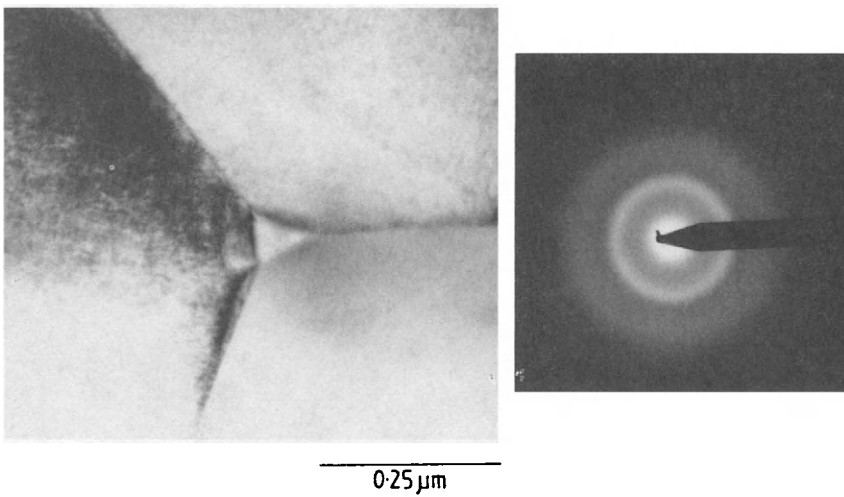
Fig. 4.   TEM micrograph of sample sintered at 1350°C showing
small pocket of an amorphous phase at a triple point.

Development of silicon carbide whisker reinforced silicon nitride composites for heat engine applications

T.B. Troczynski, D. Ghosh
The Electrofuel Mfg. Co. Ltd., Toronto, Ontario, Canada, M6K 1W8

A.K. Kuriakose, T.A. Wheat
CANMET/EMR, Ottawa, Ontario, Canada, K1A 0G1

J. Wright, H. Mostaghaci
Atlantic Research Laboratory, National Research Council Canada, Halifax, Nova Scotia, Canada, B3H 3Z1

M.K. Murthy
M.K.M. Consultants Int., Toronto, Ontario, Canada, M4T 2B7

ABSTRACT

Study of SiC-whisker reinforced Si_3N_4, developed at Electrofuel, reveals little effect of the whisker dispersion on the composite strength and toughness. The room-temperature hardness is increased. Compared to pure matrix material, the composite is more compliant to elevated temperature deformation.

KEYWORDS

Silicon nitride; silicon carbide; whiskers; ceramic/ceramic composites; mechanical properties of ceramics

INTRODUCTION

Increased operational temperature and pressure of the thermodynamic cycle of future heat engine will be beyond the limits of metals currently being used. Accordingly, advanced ceramics developments for reciprocating engines have been underway since the late 1970's in Japan, North America and Europe. Early estimations predicted substantial increases in heat efficiency of the engine through the increase of operating temperature (i.e. "no-cooling" adiabatic cycle) and thus through increase of the compression ratio. The experience gained through the 1980's showed that the increased temperature (achieved through application of insulationg ceramic inserts into existing diesel engines) could improve the heat efficiency by no more than 10% (Dvorak, 1987, Kamo, 1988, Kamigato, 1988). However, a number of other positive consequences of increased operational temperature is expected:
    -less pollution from nitrous oxides, hydrocarbons, carbon
     monoxide and carbon solids;
    -better turbocharging characteristics, higher power;
    -less sensitivity to fuel quality and purity;

Table 1 is a qualitative presentation of the advantages, disadvantages and potential application areas of structural ceramics in heat engines. Two groups of of structural ceramics for heat engine applications involve :
    -thermal insulators : Al_2TiO_5 and ZrO_2-based
    -wear and corrosion resistors : Si_3N_4, SiC, Al_2O_3

TABLE 1   Ceramics for Engine Applications

MATERIAL	ADVANTAGES	DISADVANTAGES	APPLICATION
Al_2O_3	cheap ; easy to densify ; chemically stable ; wear & corrosion resistive	low strength; low thermal cond. high CTE ; low thermal shock resistivity	spark plugs; water pump seals
ZrO_2 (PSZ,TZP AZT)	high strength & toughness; high CTE; low thermal conductivity, easy to shape;	low strength/ density ratio; low hardness; elevated-temp. unstable	insulating plates, liners and heads.
Al_2TiO_5	very low CTE; low thermal conductivity	low strength; unstable > 1000C	insulators under compression;
Si_3N_4	high strength, toughness and hardness;high thermal shock resistivity;	difficult to densify : additives limit applicability to ˜ 1200C	rocker arm insert; swirl chamber;glow plugs;valve seats;turbo charger rotors;
SiC	high hardness, thermal cond., hot strength, corrosion resist., wear resist.	difficult to densify; low toughness and cold strength	water pump seals; abrasive parts;

ZrO_2 and Al_2TiO_5 can double the thermal resistance of cylinder walls and piston head. Si_3N_4, SiC, PSZ and Al_2O_3/TiC offer dramatic improvement of the wear resistivity of components. Their wear against steel is less than 1% of that of steel against steel at the same conditions (Dvorak, 1987). One of the first commercial utilisations of these materials are water pump seals (SiC or Al_2O_3 against carbon), developed for European car manufacturers. Si_3N_4-based components (swirl chamber, turbocharger, glow plugs, valves, rocker arms) are tested by Japanese companies. Ceramic coating, especially plasma-sprayed partially stabilised zirconia, underwent successful road testing in diesel engines in U.S.A. and West Germany. Recently, Toyota reported the use of 34 ceramic components in heat engine (Kamigato, 1987). These are mostly electroceramic sensors and actuators allowing for easier optimisation of the engine performance.

Replacement of metallic parts by reliable structural ceramics will result in less corrosion and wear and thus in higher durability of the engine. However, simple replacement of metallic components by ceramics could give no improvement in the engine performance. Usually design changes are necessary, not only due to different sensitivity of ceramics to thermal and mechanical constrains, but rather for full utilisation of its advantegous properties. Succesful implementation of ceramics in heat engines requires consideration of long term, high-temperature oxidation, creep, corrosion, wear and phase stability effects on mechanical performance and reliability. Finally, the replacement cost at equal or improved performance is a decisive factor for widespread utilisation of structural ceramics in heat engines.

SiC WHISKERS / Si_3N_4 COMPOSITES

In this work Si_3N_4-based ceramics, a leading candidate for engine applications, has been investigated as a matrix of SiC whisker (SiCw) reinforced composite. It is expected that SiCw reinforcement will improve thermal and mechanical stability of the composite without drastic complications of the processing routes. Compilation of the reported room temperature properties of the composites (Shalek, 1986, Hayami, 1986 ,Buljan, 1987, Lundberg, 1987) appears in Table 2 and Fig. 1A (relative fracture toughness normalised to that of pure matrix material) and Fig. 1B (relative strength).

TABLE 2 Reported Relative Room-Temperature Fracture
          Toughness (K,%) and Strength (S,%) for SiCw/Si_3N_4.
          100% = 0 vol% SiCw

Literature Source	Whisker Type & Treatment	Processing & Additives	10%SiC		20%SiC		30%SiC	
			K	S	K	S	K	S
Shalek,1986 (4)	VLS,3-10μm ar=28-40 dry blend	HP 1850°C 5% MgO	135	79	139	76	143	66
Hayami,1986 (5)	Tokai ar=50-300 wet sieve/ sediment	HP 1800°C 40MPa,N_2+CO 10-25mole% Y_2O_3,La_2O_3	132	58	155	60	163	62
Buljan,1987 (6)	Arco ar=33 sonicate/ sediment	HP<1800°C,N_2 6wt%Y_2O_3+1.5 wt% Al_2O_3	96	94	103	100	134	125
Lundberg, 1987 (11)	Tokai surfactant disp.+homo- genized	HIP,1700°C, 200MPa;Si+ 6wt%Y_2O_3+ 2wt%Al_2O_3	90	67	83	62	-	-
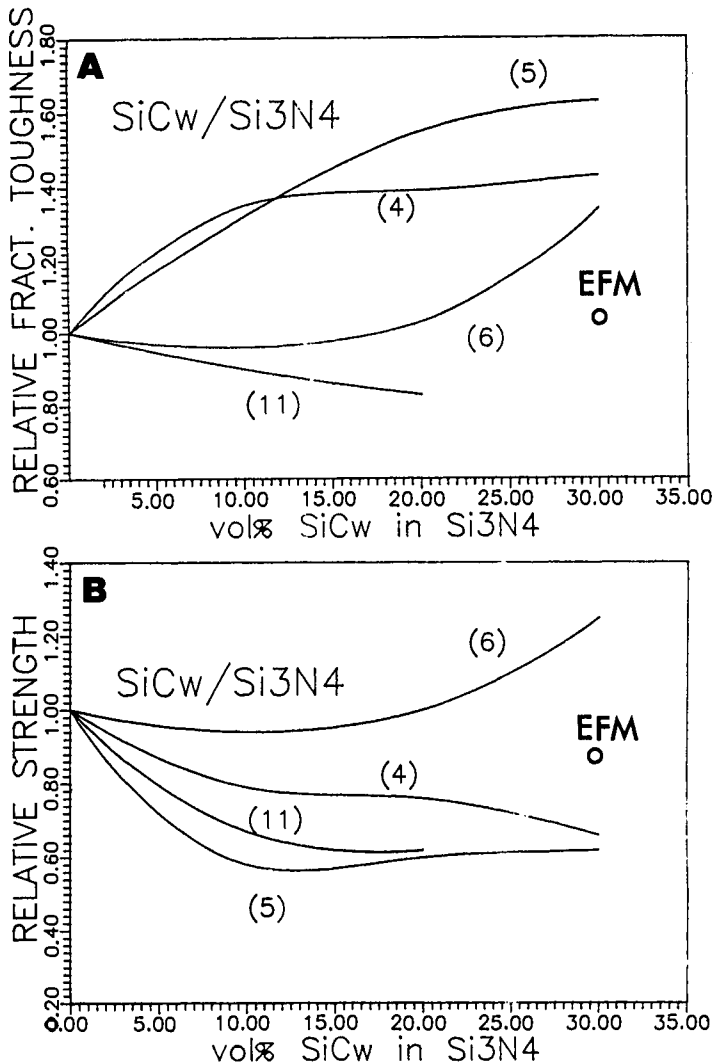
Fig.1 . Compilation of the reported relative values of room-
temperature fracture toughness (A) and bend strength (B) for
SiC/Si$_3$N$_4$ composite. (4) Shalek (1986), (5) Hayami (1986),
(6) Buljan (1987), (11) Lundberg (1987), EFM : this work.

Inconsistency of the reported properties heralds sensitivity of the
system to the type of constituent materials and processing
techniques. Fracture toughness can range between 20% loss (Lundberg,
1987) and 50% gain (Hayami, 1986, Shalek, 1986) for 20 vol% SiC-
composite compared to pure matrix material. Lack of clear correlation
between the fracture toughness and strength of the composites in at
least two cases (Shalek, 1986, Hayami, 1986) indicates difficulties
with whiskers dispersion and/or material densification. As a result,
local-microstructure controlled fracture toughness deviates from
global-flaw population controlled strength.

Investigation of erosion resistivity of SiCw/Si$_3$N$_4$ (Morrison, 1987) showed a lack of the reinforcement effect, up to 20 vol%SiCw. Interestingly, the parent phase microstructure of monolithic Si$_3$N$_4$ had strong effect on the erosion resistivity.

SiCw/Si$_3$N$_4$ composite properties depend on morphology and chemistry of the whiskers as well as the amount and type of the sintering additives. To-date dense SiCw/Si$_3$N$_4$ composites were obtained only by pressure-assisted densification. However, strong bonding between whiskers and glass is particularly detrimental for utilisation of whisker-generated toughening mechanisms (pull-out and crack deflection due to interfacial debonding). It is clear therefore, that the hot pressing schedules (time-temperature-pressure) should be optimised to limit reaction between whiskers and intergranular glassy phase. In this respect, HIP-ping at 200 MPa (Lundberg, 1987) seems to result in toughness deterioration, as opposed to hot-pressing at 20-40 MPa resulting in fracture toughness improvement, Fig. 1A, Table 2.

A high-strength interface between SiCw and Si$_3$N$_4$ is easily achieved for high-oxygen-content whiskers, effectively covered with a layer of silica. This type of whiskers require treatment to decrease their surface reactivity (e. g. acid washing, carbon coating). One of the succesful approaches (Shalek, 1986) utilised exceptionally smooth-surface, VLS-grown whiskers of large diameter (10 μm).

High-temperature creep studies (Porter, 1987, Nixon, 1987) revealed little effect of the whisker phase on material's performance. In fact, pure Si$_3$N$_4$ exhibited lower strain than SiCw/Si$_3$N$_4$ at similar conditions. This unexpected result was explained by greater sensitivity of elevated-temperature deformation to crystallisation of intergranular glass.
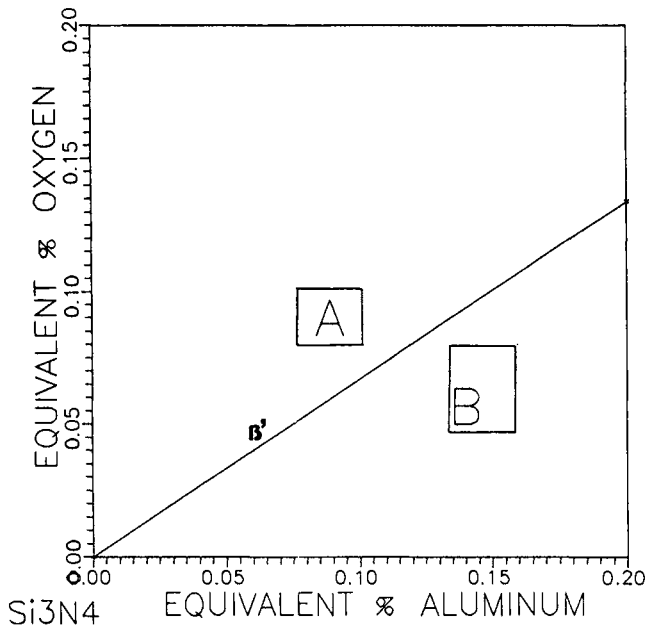
Fig. 2. Compositions of matrix materials type A and B, projected on aluminum/oxygen equivalent plane.

It appears therefore, that a unique feature of the $SiCw/Si_3N_4$ composite system is a lack of a strong effect from SiCw reinforcement. Properties of the composite are more sensitive to microstructure of the parent Si_3N_4 matrix phase than to the SiCw dispersed phase.

EXPERIMENTAL PROCEDURES

Figure 2 presents compositions of the matrix materials for $SiCw/Si_3N_4$ developed in this work. The area A of the Si-Al-O-N-Y system projection presented in Fig. 2 is characterised by higher content of oxygen and sintering additive (~6wt% Y_2O_3) and lower content of aluminum. The area B in Fig. 2 is characterised by lower content of oxygen and sintering additive (~3wt% Y_2O_3) and higher content of aluminum. Pure materials type A exhibit higher fracture toughness and lower hardness than the materials type B . Easier densification of the type A materials was a decisive factor for their choice for processing of the initial series of $SiCw/Si_3N_4$ composites.
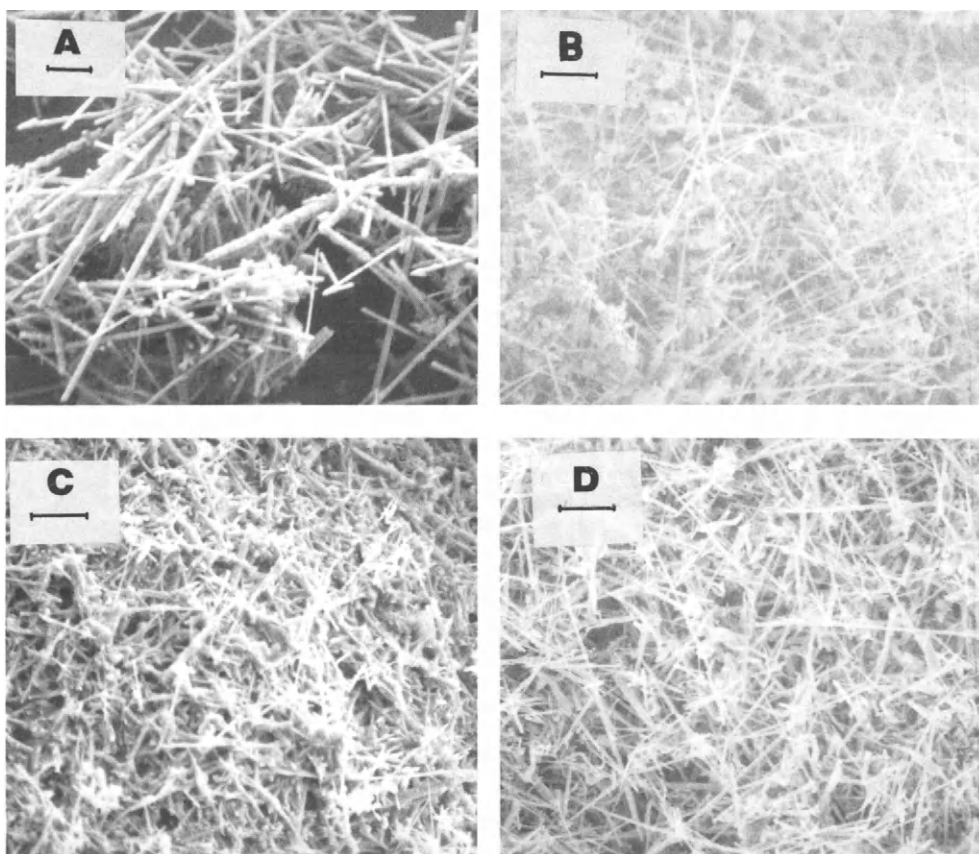
Fig. 3. SEM micrographs of SiC whiskers : (A) American Matrix, (B) Tateho, (C) Arco, (D) Tokai. Bar = 10 μm.

SEM micrographs of candidate SiC whiskers are shown in Fig. 3 and respective characteristics in Table 3. Four types of whiskers were characterised : ARCO (from ARCO Metals Corp., Greer, SC, U.S.A.); Tokai (from Tokai Carbon Co.Ltd., Tokyo, Japan); Tateho (from Tateho Chem. Ind.Co.Ltd., Ako, Japan) and American Matrix (from American Matrix, Knoxville, TN, U.S.A.). The Japanese whiskers are typically of smaller diameter and larger aspect ratio, compared to US products. However, a large aspect ratio could be detrimental for densification kinetics. Values as low as ~10 are sufficient for whisker toughening mechanisms utilisation. Whiskers with high aspect ratio offer more flexibility vs. optimization of the processing time (i.e. deagglomeration by milling).

Critical parameter for processing of $SiCw/Si_3N_4$ composites is the oxygen content in as-received whiskers. Although manufacturers' specifications estimate the oxygen content at ~1wt% level (Tab. 3), the value can vary from batch to batch and should be continuously monitored.

Extreme stiffness and strength of individual whiskers (Young's modulus 400 to 700 GPa and tensile strength 3-14 GPa) favoures them as the dispersed phase in ceramic/ceramic composites. Widespread application of the whisker reinforcement is limited by the involved costs and health hazards.

Considering properties and availability, the American Matrix whiskers were chosen as a dispersed phase for initial study of $SiCw/Si_3N_4$ composites . The processing route for the composite is presented in Fig. 5. The whisker amount was set at 30 vol% as optimum content vs. densification kinetics and the toughening effect. The whiskers were HF-washed to minimise amount of surface silica. Study of the Zeta-potential vs. pH (Fig. 4A) and sedimentation travel for different ultrasonication-dispersion times (Fig. 4B) allowed formulation of optimum treatment routines for whisker/powder/water slurries.

TABLE 3 SiC Whiskers Characteristics.

PROPERTY	AM. MATRIX	TATEHO	TOKAI	ARCO
Diameter, μm	1 - 2	0.4	0.2-0.5	0.7
Length, μm	20 - 100	20-200	40-200	30
Aspect ratio	10 - 100	50-400	50-300	50
Oxygen cont,%	0.9	0.6-1.2	1.0	1.2
Free carbon,%	~ 0.3	~ 0.6	~ 0.4	~ 0.3
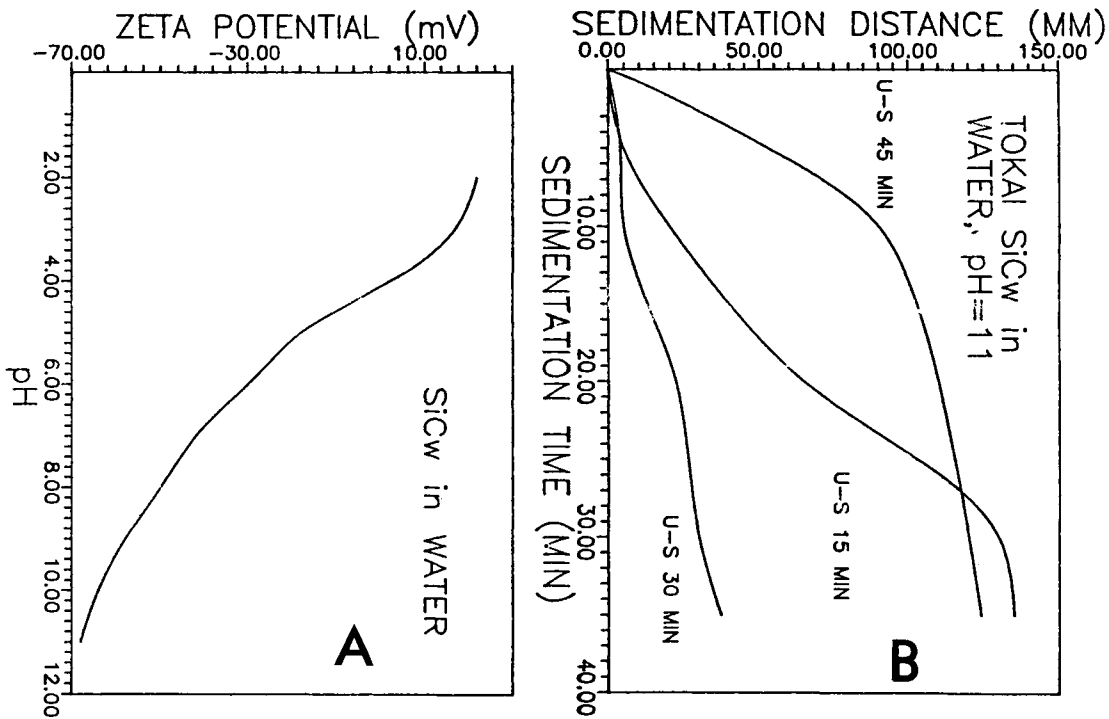
Fig. 4. Characteristics of SiC whiskers in water dispersions :
(A) Zeta-potential vs. pH. (B) Sedimentation travel of the
suspension ultrasonicated for 15, 30 and 45 minutes.
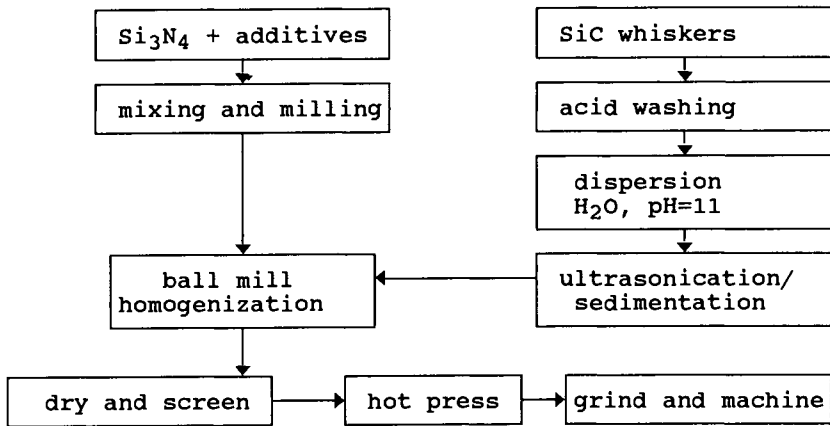
Fig. 5. Processing diagram for SiCw/Si$_3$N$_4$ composite.

Hot pressing at temperatures below 1800°C for less than 200 minutes and pressures of 20 MPa produced 98-99% dense composites. The materials were tested for phase composition (XRD), room-temperature bend strength (bending spans 12.7/25.4 mm, cross-head displacement rate 0.5 mm/min) and Vickers hardness (98 N load). Fracture toughness was measured using an indentation technique (Niihara, 1984). Short-term stress relaxation characteristics at elevated temperatures (1000-1300°C) were determined as described in a companion paper (Troczynski, 1989). The stress-relaxation parameter R [MPA/min] was measured by monitoring the decrease of load at constant strain in four-point-bending, at 900-1350°C. Analysis of R vs. temperature allowed for determination of thermal loss-of-rigidity points in short-term stressing applications.

RESULTS AND DISCUSSION

Table 4 presents compilation of room-temperature composite properties, as compared with that of pure matrix materials. Both ceramics exhibit similar density and indentation fracture toughness (the relative toughness as well as strength for the materials obtained in this work are plotted in Fig. 1A,B as EFM points, for comparison with literature data). Although average bend strength of the two materials is similar within limits of one standard deviation, the strength distribution is wider for the composite. Compilation of the strength test results for the two materials, Fig. 6, gives the Weibull modulus of 5.7 for the composite and 9.8 for the matrix material.

TABLE 4   Room Temperature Properties of 30 vol% $SiCw/Si_3N_4$ Composite and the Si_3N_4 Matrix.

PROPERTY	$SiCw/Si_3N_4$	Si_3N_4
Color	Green	Grey
Density, g/cc	3.22	3.26
Density, % th.	98-99	99
K_{IC}, MPa√m	7.0±0.5	6.5±0.5
Strength, MPa	660±110	740±80
Calculated flaw size, μm	30	20
Weibull Modulus	6	10
Hardness, GPa	17.5±0.2	15.5±0.1
Wear resistivity factor W	18	16

The spread of strength values could indicate presence of flaws introduced during powder processing (especially that of the whiskers dispersion) or the test sample preparation. Extensive examination of the fracture surfaces by optical and scanning electron microscopy (Fig. 7) revealed good dispersion of the whiskers. Moreover, the composites processed in similar way, but based on Al_2O_3 matrix, revealed Weibull modulus of ~9 (Ghosh, 1989). It is concluded accordingly, that machining-generated microcracks rather than agglomerate-originating flaws deteriorated the strength distribution characteristics of 30 vol% SiC/Si_3N_4.
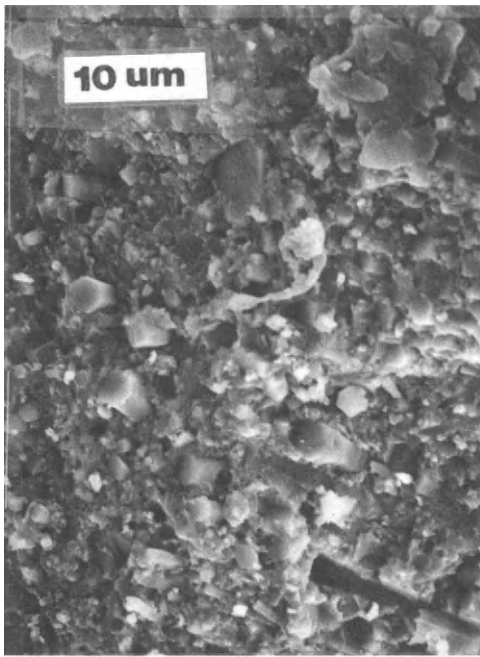
Fig. 7. Room-temperature fracture surface of SiCw/Si_3N_4 composite.
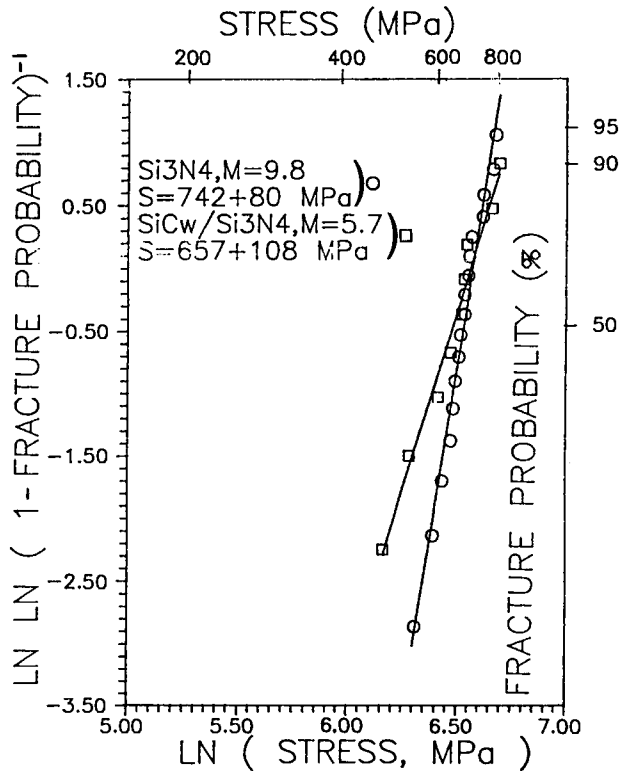
Fig. 6. Bend strength distribution for 30 vol%SiCw/Si_3N_4 composite and Si_3N_4 matrix.

The hardness of the composite material (17.5 GPa) is significantly higher than that of the matrix (15.5 GPa). This is attributed to high hardness of the dispersed SiCw (~26 GPa) and indicates strong interfacial bonding between the dispersed and continuous phases (in agreement with unchanged fracture toughness values). The net effect is increased wear resistivity of the composite. If the average values of hardness H(GPa) and fracture toughness K(MPa√m) are combined into wear-resistivity factor $W = K^{0.75} \cdot \sqrt{H}$ (Baldoni, 1986), W=18 is obtained for 30vol%SiCw/Si_3N_4 composite and W=16 for the matrix material. The improved wear resistivity indicates viability of the material's application in heat engines.

Fracture surface of the composite tested at room temperature is shown in Fig. 7. Majority of the whisker diameters are in the range of 1-3 μm, but some reach 5 μm. The whisker pull-out up to 2-3 diameters is evident. The whiskers are preferentially oriented normal to the hot pressing direction (the micrograph plane is parallel to the hot pressing direction). Occasional debonding of a large part of the whisker surface (upper-right corner of Fig. 7) indicates that the intergranular strength of Si_3N_4 is higher than the interfacial strength of $SiCw/Si_3N_4$.

The elevated-temperature tests involved short-term load relaxation (LR) at 900-1350°C, as described in the companion paper (Troczynski, 1989). The LR results for the composite and matrix material are compared in Fig. 8. It seems that excessive amounts of oxygen introduced into the system with the whiskers accelerates especially intermediate-temperature (900-1100°C) stress relaxation. In the range 1300-1400°C however, the presence of whiskers introduces additional resistance for the composite deformation.

It has been noticed that some specimens exhibited extremly high mechanical compliance during load relaxation tests. Examination of the fracture surfaces of these samples (broken after completion of the test at 1300°C) revealed extensive regions of subcritical crack growth. Figure 9A presents a low-magnification micrograph of the fractured test bar, with the tensile surface on the top. The fracture surface topography change from rough (magnified in Fig. 9B) to smooth (Fig. 9C) is typical for abrupt change of the crack velocity. The micrographs of slow and fast crack growth regions (Fig. 9B and 9C respectively) show layer of glass (resulting from oxidation at 1300°C), with frozen bubbles of nitrogen, originating from decomposition of Si_3N_4. No viscous pull-out of SiCw is visible.
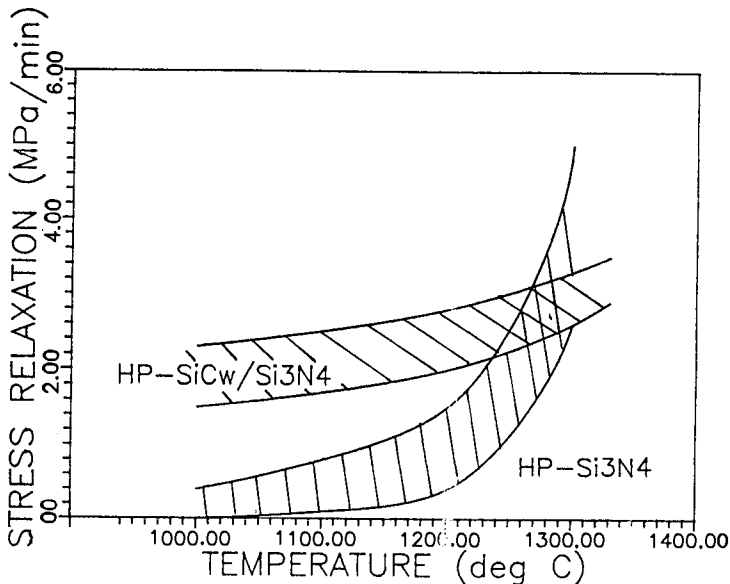
Fig. 8. Compilation of elevated-temperature stress relaxation parameters R for SiCw/Si3N4 composite and Si3N4.
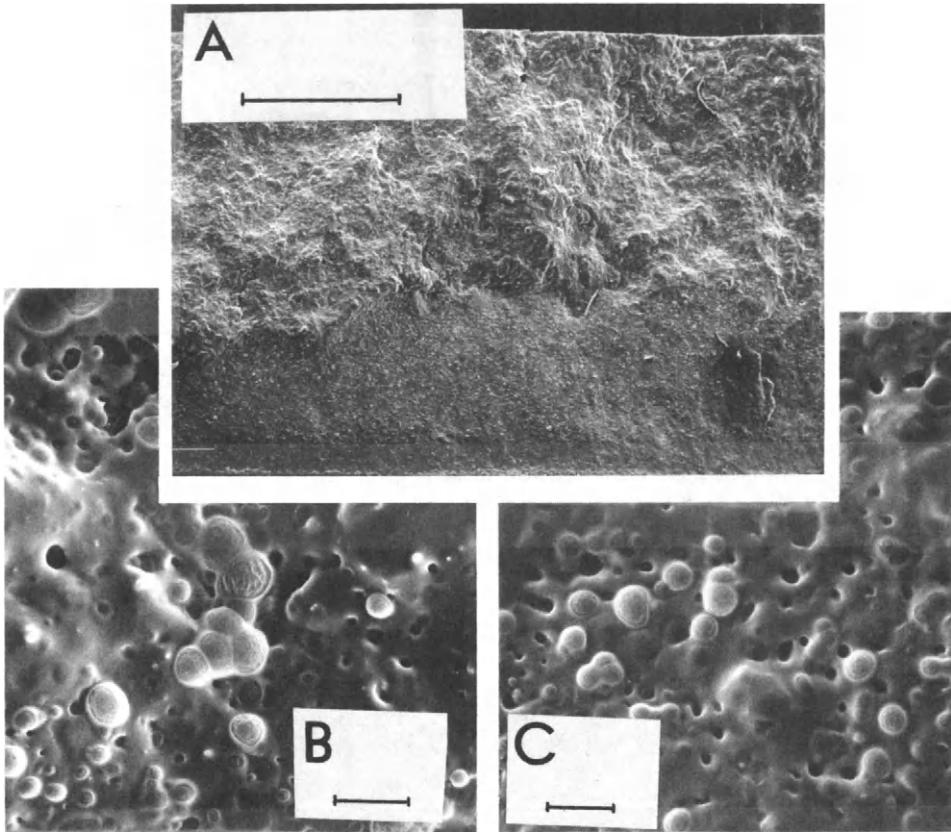
Fig. 9. Fracture surface of SiCw/Si$_3$N$_4$ composite tested at 1300°C :
(A) Macrograph showing slow (top) and fast (bottom) crack
growth regions. Bar = 1 mm. (B) Magnification of Fig. 9A top
(C) Magnification of Fig. 9A bottom. Bar = 10 μm.

The effect of subcritical crack growth was indicated in literature
for high-temperature fracture of SIALON (Fields, 1983). The
decomposition and nitrogen bubbling has been found to be especially
intensive for low-Z sialons (material type A utilised in this work
has Z=0.7). It is expected that the phenomenon could effect long-term
properties of SiCw/Si$_3$N$_4$ composites utilised at high temperatures.

CONCLUSIONS

SiCw/Si$_3$N$_4$ composites were developed with the aim of high-temperature
applications in heat engines. The composite containing 30 vol% SiCw
exhibited an increase in hardness (17.5 GPa) compared to that of the
pure matrix material (15.5 GPa). Other room-temperature properties of
the composite material showed little change as compared to the matrix
(i.e. fracture toughness 7 vs. 6.5 MPa√m, bend strength 657 vs. 742
MPa). The lower Weibull modulus of the composite (5.7 vs. 9.8) is
attributed to the machining flaws introduced during specimen
preparation.

Elevated-temperature load-relaxation tests revealed material's sensitivity to subcritical crack growth. Due to higher oxygen content, the composite deforms faster at intermediate temperatures (900-1100°C). At high temperatures (> 1300°C) presence of the whiskers network results in increased resistance to deformation of the composite.

REFERENCES

Buljan, S. T., J. G. Baldoni and M. L. Huckabee (1987). Si_3N_4-SiC Composites. Am. Ceram. Soc. Bull. 66, 347-352.

Buljan, S. T. and V. K. Sarin (1986). Design and wear resistance of Si_3N_4-based composites. In E. A. Almond, C. A. Brookes and R. Warren (Ed.), Inst. Phys. Conf. Series No. 75, Adam Hogler Ltd., Bristol, UK, pp. 873-882.

Dworak, W. and D. Fingerle (1987). Ceramic materials for engines. Trans. J. Br. Ceram. Soc. 86, 170-178.

Fields, R. J., E. R. Fuller, Jr., T. J. Chuang, L. Chuck and K. Kobayashi. Crack growth in sialons. In R. C. Bradt, A. G. Evans, D. P. H. Hasselman and F. F. Lange (Ed.), Fracture Mechanics of Ceramics, vol. 6, Plenum, New York, pp.463-474.

Hyami, R., K. Ueno, I. Kondou, N. Tamari and Y. Toibana (1986). In E. Tressler, G. L. Messing, C. G. Pantano kand R.E. Newham (Ed.), Tailoring Multiphase and Composite Ceramics, Vol. 20, Plenum, New York, pp. 663-674.

Kamo, R. (1987). Ceramics for advanced heat engines. Industrial Ceramics 7, 161-166.

Kamigaito, O. (1987). Ceramic components for passenger car engines. Industrial Ceramics 7, 207-212.

Lundberg, R., L. Kahlman, R. Pompe, R. Carlsson and R. Warren (1987). SiC-whisker reinforced Si_3N_4 composites. Am. Ceram. Soc. Bull. 66, 330-333.

Morrison, C. T., J. L. Routbord and R. O. Scattergood (1987). Erosion of silicon carbide whisker reinforced silicon nitride. In P.F Becher, M. V. Swain and S. Somiya (Ed.), Advanced Structural Ceramics, Materials Research Society, Pittsburg, Pennsylvania, pp. 207-214

Nixon, R. D., S. Chevacharoenkul, M.L. Buckabee, S. T. Buljan and B. F. Davis (1987). Deformation bechaviour of SiC whisker reinforced Si_3N_4. In P.F Becher, M. V. Swain and S. Somiya (Ed.), Advanced Structural Ceramics, Materials Research Society, Pittsburg, Pennsylvania, pp. 295-302

Porter, J. R., F. F. Lange and A. H. Chokshi (1987). Processing and creep performance of silicon carbide reinforced silicon nitride. In P.F Becher, M. V. Swain and S. Somiya (Ed.), Advanced Structural Ceramics, Materials Research Society, Pittsburg, Pennsylvania, pp. 289-294.

Niihara, K., A. Nakahira and T. Hirai (1984). The effect of stoichiometry on mechanical properties of boron carbide. J. Am. Ceram. Soc. 67, C-13-C-14.

Shalek P.D., J. J. Petrovic, G. F. Hurley and F. D. Gac (1986). Hot-pressed SiC whisker/Si_3N_4 matrix composites. Am. Ceram. Soc. Bull. 65, 351-356.

Troczynski, T.B., D. Ghosh and S. Das Gupta (1989). Mechanical properties of silicon nitride particulate composites. This volume.

Fibre-matrix interface testing of ceramic composites

David C. Cranmer
National Institute of Standards and Technology, Ceramics Division,
Gaithersburg, Maryland 20899, U.S.A.

ABSTRACT

An instrumented indenter technique has been used to measure fiber/matrix
bonding in several ceramic composites including SiC/LAS-III, chemically vapor
infiltrated (CVI) SiC/SiC, and SiC monofilament/Borosilicate Glass. The
indenter measures the load on and displacement of the fiber directly, thus
avoiding the necessity of measuring small indent sizes. Values of fiber/matrix
debond strength (τ_d) and interfacial frictional stress (τ_f) have been measured
in each of these systems. In several instances, no movement of the fiber was
observed. Differences in τ have been ascribed to differences in bonding
between the fibers, coatings, and matrices. Variability in τ within each
sample has been observed and will be discussed.

KEYWORDS

Ceramics, ceramic matrix composites, glass-ceramic composites, glass
composites, mechanical properties, fiber/matrix interfacial strength,
indentation push-in, indentation push-out

INTRODUCTION

Examination of the central issues involved in developing high quality, tough
ceramic matrix composites shows that one of the most important areas involves
the chemistry and properties of the fiber-matrix interface. While determining
an appropriate interface composition is clearly important (Cranmer, 1989;
Hillig, 1986), appropriate test techniques for determining the interfacial
properties, especially the bond strength (mechanical or chemical) must be
available to aid in deciding if a particular interface composition is suitable.

The properties of the interface are primarily responsible for the stress-strain
behavior and damage tolerance of ceramic composites. The interfacial strengths
(τ) of glass and ceramic matrix composites have been measured by at least two
different techniques (Marshall, 1984; Mandell and co-workers, 1986; Marshall
and Oliver, 1987; Coyle, Chan, and Deshmukh, 1988; Deshmukh and co-workers,
1988; Goettler and Faber, 1988) including indentation push-in and single fiber
pull-out. The interfacial strength which can be measured is one of two types:
debond (τ_d) and frictional (τ_f). The debond strength is related to the degree
of chemical bonding between the fiber and the matrix, while the frictional
stress relates to the slippage of the fiber in the matrix.

Single fiber pull-out tests give the most direct measure of the interface
strength (Harris, Morley, and Philips, 1975; Penn and Lee, 1982; Piggott and
co-workers, 1986; Deshmukh and Coyle, 1988; Goettler and Faber, 1988; Griffin
and co-workers, 1988), but the tests performed to date have only been conducted
on monofilaments. The combination of a small fiber diameter (10-20 μm) for

materials such as Nicalon SiC[1], high temperature (>700°C) processing required to obtain an acceptable sample geometry, and handling to set up each experiment makes it extremely difficult to perform the test on a large number of samples, hence it has not and is not likely to be used on small diameter fibers. Depending on the nature of the interaction (chemical and/or mechanical) between the fiber and the matrix, the single fiber pull-out test gives information about both the debonding and frictional processes occurring in composites. For glass matrix systems, the results indicate a clear influence of thermal expansion mismatch on the interfacial properties with higher mismatches resulting in higher mechanical clamping of the fiber by the matrix and residual stresses in the matrix (Deshmukh and Coyle, 1988; Griffin and co-workers, 1988; Goettler and Faber, 1988). Typical results for SiC/borosilicate are shown in Table 1.

TABLE 1 Frictional Shear Stress for SiC Monofilament/Borosilicate Glass
Single Fiber Pull-Out Test
(Numbers in parenthesis represent number of samples averaged)

Analysis	Reference	τ_f (MPa)	
Poisson's Contraction	8	3.6 ± 0.7	(9)
Residual Stress	9	15 - 28	
Residual Stress-Free	9	12.5	
Simple Analysis	13	5 - 6.5	
Simple Analysis		5.6 ± 2.7	(8)

Indentation testing to determine τ_f was first initiated by Marshall (1984). Fiber/matrix frictional stresses of 2.5 ± 0.9 MPa were measured for a SiC-reinforced glass-ceramic[2], but the method requires precise measurement of very small indentation sizes, potentially a significant source of error. The analysis assumes that the elastic depression of the matrix adjacent to the indented fiber, the stress field of the indent and the surface stress concentrations, as well as changes in fiber diameter due to Poisson's expansion can be neglected. For the analysis to be valid, the specimen thickness must be large compared to the diameter of the fiber. The analysis also does not account for non-orthogonal loading of the fiber or misorientation of the fiber from a direction parallel to the applied force. Additional studies by Marshall and Oliver (1987) refined the method by using a pyramidal indenter at ultralow loads (< 0.12 N). In this version, the indenter is instrumented to provide independent determinations of force applied to the fiber and displacement of the fiber in the matrix. The revised method permits examination of both debonding and frictional sliding in a SiC/glass-ceramic composite. Values of τ_f on the order of 3.5 MPa were obtained on this material, in good agreement with the initial measurements using the Vickers diamond. One particular aspect which limits its use is the special apparatus required to apply very small loads. While most of the work on the indentation push-in test has been conducted using a standard Vickers diamond geometry, Mandell and co-workers (1986) have shown that the shape of the indenting diamond can be changed to increase the amount of sliding which can be observed. Another limitation of the indentation push-in test is that the large monofilaments tend to crush

---

[1] Nicalon SiC, Nippon Carbon Co., Ltd., Tokyo, Japan. Trade names and companies are identified in order to adequately specify the materials and equipment used. In no case does such identification imply that the products are necessarily the best available for the purpose.

rather than slide, thus obliterating the indentation impressions and yielding inaccurate displacement measurements.

While the typical indentation push-in test uses the Vickers diamond to push the fiber into the matrix, the indentation push-out test uses the diamond to push the fiber through the matrix. The push-out test requires the use of thinner specimens (< 2-3 mm) than the push-in test. The basic assumptions in the analysis of the push-out test are the same as for the push-in test and also neglects stress concentrations at the bottom surface where the fiber emerges during the test. In the push-out test, three regimes are envisioned: an initial region in which the diamond is in contact with the fiber only and the sliding length is less than the thickness of the sample, a plateau region in which the sliding length is greater than or equal to the thickness of the sample, and a final region in which the diamond makes contact with and deforms the matrix. These regimes are shown schematically in Fig. 1. In principle,
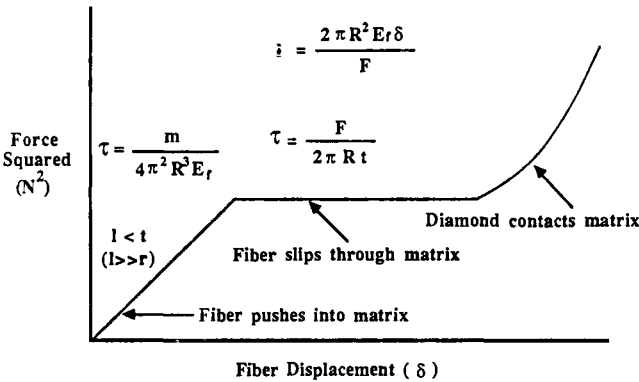
Fig. 1. Schematic of force^2/displacement for indentation push-out test.

the initial regime also represents the behavior of the push-in test; however, the assumption that specimen thickness is much greater than the fiber diameter is not valid if the thickness is too small. In addition, the surface stress concentrations will play a larger role than in thicker samples. In the initial regime, τ is determined from the slope (m) of a plot of the force on the fiber squared (F^2) versus displacement (δ):

$$\tau = m/4\pi^2 R^3 E_f \qquad\qquad (1)$$

where R is the radius of the fiber and E_f is the elastic modulus of the fiber. In the plateau region of the curve, τ is determined from the force at which the plateau occurs:

$$\tau = F/2\pi Rt \qquad\qquad (2)$$

where t is the thickness of the specimen. In the last regime, where the diamond is in contact with the matrix, τ cannot be determined. Which value of τ (debond or frictional) is measured in the plateau region depends on whether or not there is a strong chemical bond between the fiber and matrix and what geometry indenter is being used. In the typical geometry using a standard Vickers diamond, when the fiber debonds, the frictional stress is also exceeded and the fiber slips until either contact with the surrounding matrix occurs or

until friction slows the fiber displacement to a value expected from frictional stresses alone. If no debonding can occur, then only slippage due to friction is present.

For large monofilaments such as the SCS-6 SiC, where the SiC is deposited on a carbon core, two plateaus are expected. The first occurs when the carbon core (33 μm diameter) slips in the SiC; the second when the SiC fiber (about 140 μm diameter) slips in the matrix. The fiber displacements at which each of these events takes place can be calculated from the geometry of the Vickers diamond. The diamond should make contact with the SiC at a displacement of about 5 μm, and it should contact the matrix at a displacement of 20 μm. Thus a plateau occurring prior to 5 μm can be attributed to the slippage of the carbon core, and one occurring prior to 20 μm can be attributed to slippage of the SiC. Whether one or two plateaus occur depends on the debond strength of the interfaces between the core and SiC, and between the SiC and the surrounding matrix.

A series of composite systems were chosen which had reasonably well defined chemistry at the interface. The systems examined include a borosilicate glass matrix reinforced by SiC monofilaments[2], a lithium aluminosilicate glass-ceramic matrix reinforced by SiC fibers[3], and a chemically vapor infiltrated silicon carbide matrix reinforced by SiC fibers[4]. Table 2 shows the nominal interface chemistries of the composites examined.

TABLE 2 Nominal Interfacial Chemistry of Tested Composites

Material	Interface Chemistry
SiC fiber/LAS III matrix	Carbon, NbC[1]
SiC monofilament/Borosilicate glass matrix	Carbon layer on fiber
SiC fiber/CVI deposited SiC matrix	Carbon layer deposited on fiber[2]

[1] Brennan, J. J., "Interfacial Studies of SiC Fiber Reinforced Glass-Ceramic Matrix Composites", Annual Report for Contract N00014-82-C-0096, 30 September 1986.
[2] As reported by Oak Ridge National Laboratory.

EXPERIMENTAL PROCEDURE

The SiC/borosilicate glass material was made by hot pressing at 800°C for 30 minutes at about 14 KPa. The SiC/LAS III was obtained from United Technologies Research Center, and the CVI SiC from Oak Ridge National Laboratory. The specimens were polished to expose the fibers parallel to the direction of indentation. The tests were performed using an instrumented indenter, allowing

[2] SCS-6, Textron Specialty Materials, Lowell, MA.

[3] Nicalon SiC/LAS-III, United Technologies Research Center, East Hartford, CT.

[4] Oak Ridge National Laboratory, Oak Ridge, TN.

for independent determinations of force and displacement. A schematic of the
test apparatus is shown in Fig. 2.
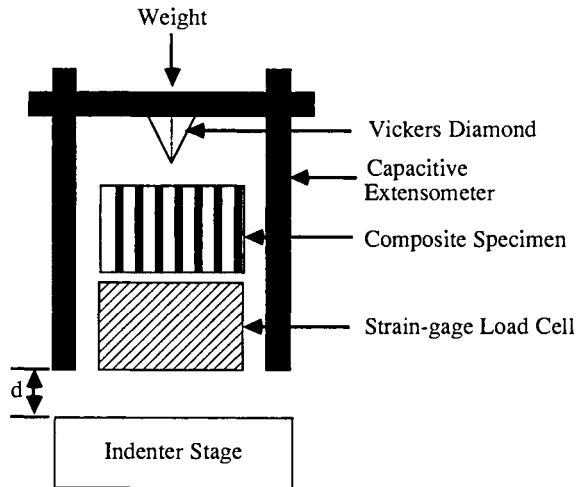
Fig. 2. Schematic of indentation apparatus.

Displacement was determined using a pair of capacitance probes; the change in
capacitance in a probe varies as it approaches a fixed target. Targets were
fixed with respect to the specimen surface, and each probe was initially
calibrated using a laser interferometer. Specimens for indentation included 1
mm and 2 mm thick multifilament SiC/glass-ceramic or CVI SiC and 0.3 mm thick
monofilament SiC/borosilicate glass. A 50-75 g load was used for the SiC/LAS
III and CVI SiC materials, and the loads ranged from 130 to 150 g for the
SiC/borosilicate material. Based on the debond strength of the SiC/glass, as
determined from the single fiber pull-out test ($\approx$9 MPa, Deshmukh and Coyle,
1988), loads < 140 g should exhibit a single plateau of the core slipping in
the SiC while loads > 140 g should exhibit both plateaus.

RESULTS AND DISCUSSION

The value of τ measured depends on the test method employed as well as the
material being tested. The push-out test could measure debond strength or
frictional stress, depending on the material and the indenter geometry. For
the SiC/borosilicate glass system, the push-out test shows either one or two
plateaus (Fig. 3).

As described above, based on the debond strength of SiC/glass, loads < 140 g
should exhibit a single plateau while those > 140 g should exhibit two
plateaus. The first case is shown in Fig. 3a. The force at the plateau gives
a value of τ_d of 38 MPa for the core slipping through the SiC. The second case
is shown in Fig. 3b, where the force at the first plateau gives a value of τ of
36 MPa for the core slipping in SiC and the force at the second plateau gives a
value of τ of 10 MPa for the SiC slipping in the matrix. Tests on additional
fibers gave an average value of τ of 30 $\pm$ 9 MPa for the core in SiC. The value
of τ for SiC in the matrix is in reasonable agreement with τ_d obtained from the
single fiber pull-out test. These results are based on a fairly small number
of fibers and additional verification is required to more firmly establish

SCS-6 SiC/Borosilicate Matrix
Indentation Push-Out Test
Load = 130 g

Plateau yields debond
strength of 38 MPa for
carbon core slipping
in SiC fiber

a)

Second plateau yields debond
strength of 9.9 MPa for
SiC slipping in matrix

First plateau yields debond
strength of 36 MPa for
C core slipping in SiC

SCS-6 SiC/Borosilicate Matrix
Indentation Push-out Test
Load = 150 g

b)
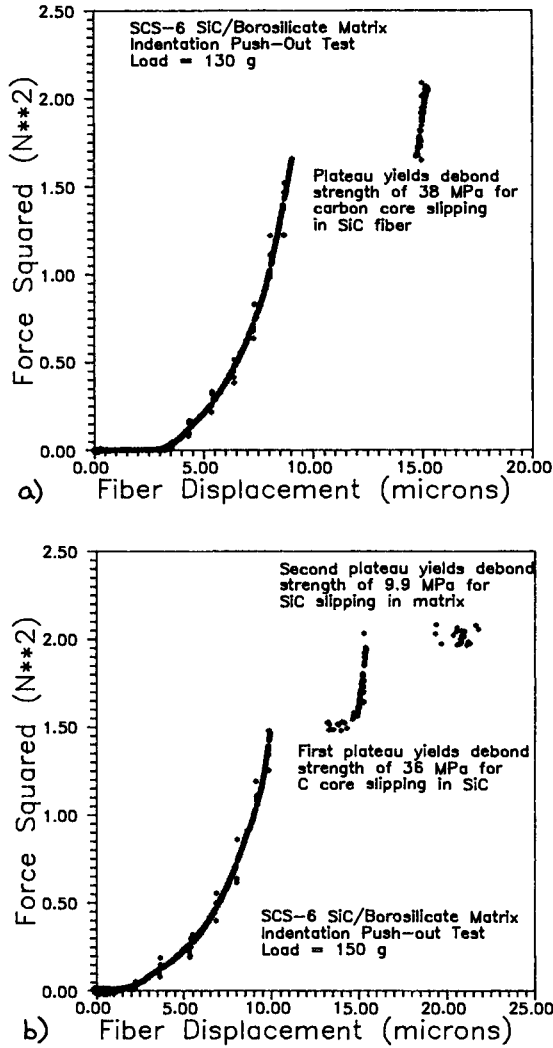
Fig. 3.   Results of indentation of SiC monofilament in borosilicate
glass matrix.
a.   Indentation load = 130 grams.
b.   Indentation load = 150 grams.

these values. In addition to more data, the hardness impressions should be
analyzed according to the method of Marshall (1984) to confirm that the two
methods agree. Examination of the SiC/glass-ceramic system shows that τ is
dependent on the investigator as well as the technique. The indentation push-
in results yield τ's varying from 1 to 10 MPa (Marshall, 1984; Marshall and
Oliver, 1987; Coyle, Chan, and Deshmukh, 1988; Deshmukh and Coyle, 1988) and
from 1 to 100 MPa, depending on the heat treatment (Coyle, Chan, and Deshmukh,
1988). The discrepancy in heat treated materials is due to differences in the

fiber-matrix interface bonding with some fibers being more tightly bound than others. This would lead to differences in both debond strength and frictional pull-out. The discrepancy in various unannealed materials is due to both differences in the fiber-matrix bond and fiber misorientation with respect to the applied force. In a sample which is 2 mm in thickness, the indentation test was either of the push-in or push-out type. Typical results are shown in Fig. 4.
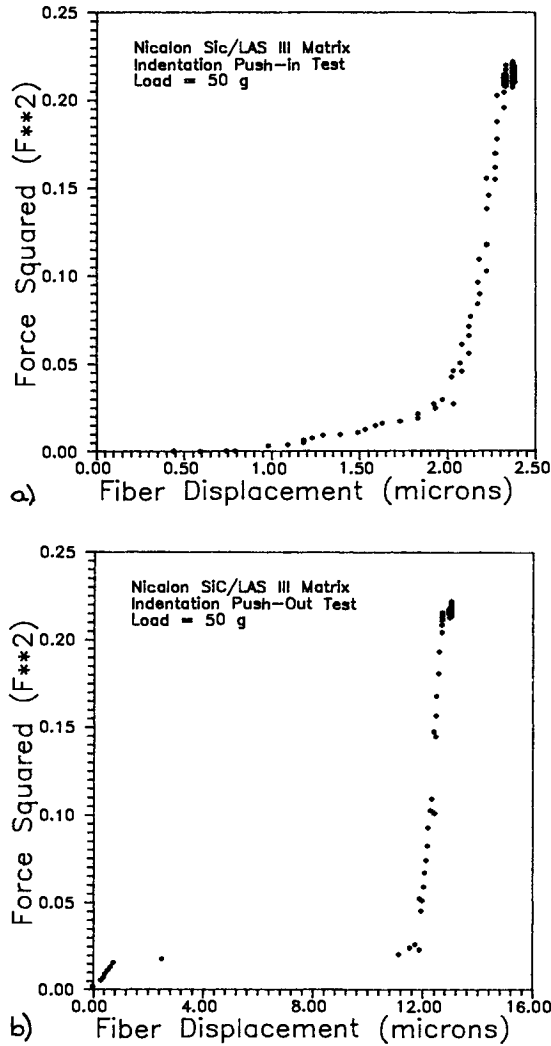
Fig. 4. Results of indentation of SiC in lithium aluminosilicate matrix.
    a. Push-in result (l < t)
    b. Push-out result (l > t)

In Fig. 4a, a push-in type is shown while Fig. 4b shows a push-out result. In both figures, however, τ is on the order of 1-6 MPa for this system, leading to the conclusion that this τ is due to frictional effects. Values of τ as high as 55 MPa, determined on other fibers in the same sample, were also observed, leading to the supposition that there are differences in the bonding between fiber and matrix at different locations in the specimen. This can be confirmed using appropriate transmission electron microscopy techniques. The indentation push-out test results are more difficult to obtain because of the need to use flat and polished samples. For this thickness sample, it is apparent that the assumptions for both types of test are met. For thinner samples, the assumption that the thickness >> fiber diameter may be violated, thus τ_f determined from the plateau region of the push-out test may not agree with that obtained in the initial region where push-in is assumed to take place. The analysis of the push-out test in the plateau region is simpler than that required for the push-in test and is not affected by the assumptions regarding elastic interactions after the force is released and what happens below the slip region during testing.

For the CVI SiC material, a typical push-out test result is shown in Fig. 5.
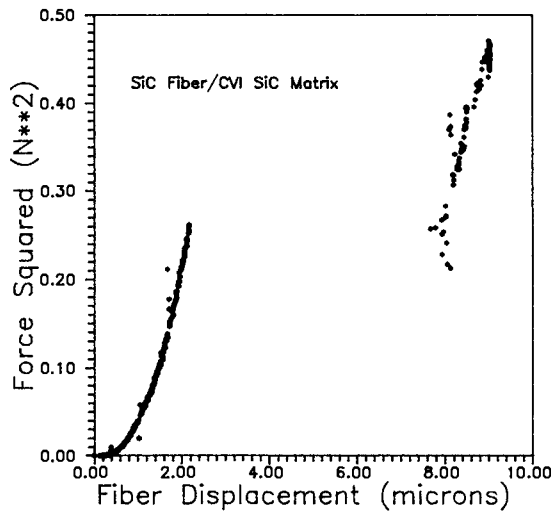
Fig. 5.   Results of indentation of SiC in CVI SiC matrix.

As expected, a plateau is evident at a force of 0.5 N, and in fact exhibits a slightly decreasing force as the fiber moves. The observed decrease is due to the decrease in fiber sliding length as the fiber slides out of the matrix. This type of curve represents the frictional sliding behavior of the material.

The value of τ measured for the SiC/borosilicate system corresponds well with the debond strength determined from the single fiber pull-out test. The interface strengths measured in the SiC/LAS III system could be either debond or frictional. The value determined for the SiC/CVI SiC system is that typical of the frictional stress, and agrees with τ's determined using a nanoindenter (Lowden, 1989). It can readily be seen that although the nominal fiber surface chemistries are very similar, very different results can be obtained. These differences can be ascribed to non-uniformities in the coatings or to small

differences in the actual chemistry at the interface, either due to formation of a phase at the interface (as in the SiC/LAS III) or due to unfavorable chemical reactions at the interface (as is likely the case in the SiC/borosilicate).

CONCLUSION

The indentation tests use a minimal amount of material and can be performed on samples containing either large monofilaments or small diameter multifilament tows. They provide information on either the debond strength (τ_d) for interfacial frictional stress (τ_f), depending on indenter geometry and material characteristics. It is possible that the push-out test can be performed at slower loading rates with a different indenter geometry, thus allowing for separation of the debonding strength from the interfacial friction stress in the force^2-displacement curve. The preparation of indentation push-out samples is no more difficult than for indentation push-in samples but the analysis is simpler. Interfacial strengths determined using the indentation methods agree well with one another and with values measured using the single fiber pull-out test. Debond strengths determined from the indentation push-out test agree with the results obtained using the single fiber pull-out test.

ACKNOWLEDGEMENTS

REFERENCES

Cranmer, D. C. (1989) Fiber coating and characterization, Am. Ceram. Soc. Bull., 68, 415-419.

Coyle, T. W., Chan, H. M., and Deshmukh, U. V. (1988) Effects of heat treatments in air on the microstructure and mechanical behavior of the fiber/matrix interface in an LAS glass-ceramic matrix-SiC fiber composite. In H. Ishida (Ed.) Interfaces in Polymer, Ceramic, and Metal Matrix Composites, Elsevier, Amsterdam., pp. 489-501.

Deshmukh, U. V., and Coyle, T. W. (1988) Determination of interface strength in glass-SiC composites via single fiber tensile testing, Cer. Eng. Sci. Proc., 9, 627-634.

Deshmukh, U. V., Kanei, A., Freiman, S. W., and Cranmer, D. C. (1988) Effect of thermal expansion mismatch on fiber pull-out in glass matrix composites. In F. D. Lemkey, S. G. Fishman, A. G. Evans, and J. R. Strife (Eds.) High Temperature/ High Performance Composites MRS Symp. Vol. 120, Materials Research Society, Pittsburgh.

Goettler, R. W., and Faber, K. T. (1988) Interfacial shear stresses in SiC and Al_2O_3 fiber-reinforced glasses, Cer. Eng. Sci. Proc., 9, 861-870.

Griffin, C. W., Limaye, S. Y., Richerson, D. W., and Shetty, D. K. (1988) Evaluation of interfacial properties in borosilicate-SiC composites using pull-out tests, Cer. Eng. Sci. Proc., 9, 671-678.

Harris, B., Morley, J., and Philips, D. C. (1975) Fracture mechanisms in glass-reinforced plastics, J. Mat. Sci., 10, 2050-2061.

Hillig, W. B. (1986) Prospects for ultra-high-temperature ceramic composites. In R. E. Tressler, G. L. Messing, C. G. Pantano, and R. E. Newnham (Eds.), Tailoring Multiphase and Composite Ceramics, Plenum, New York, pp. 697-712.

Lowden, R. A. (1989) Private communication.

Mandell, J. F., Grande, D. H., Tsiang, T.-H., and McGarry, F. J. (1986) Modified microdebonding test for direct in situ fiber/matrix bond strength determination in fiber composites. In J. M. Whitney (Ed.), Composite Materials: Testing and Design, ASTM STP 893, Philadelphia, pp. 87-108.

Marshall, D. B. (1984) An indentation method for measuring matrix-fiber frictional stresses in ceramic composites, J. Am. Cer. Soc., 66, C259-C260.

Marshall, D. B., and Oliver, W. C. (1987) Measurement of interfacial mechanical properties in fiber-reinforced ceramic composites, J. Am. Cer. Soc., 70, 542-548.

Penn, L. S., and Lee, S. M. (1982) Interpretation of the force trace for Kevler/epoxy single filament pull-out tests, Fibre Sci. Tech., 17, 91-97.

Piggott, M. R., Sanadi, A., Chua, P. S., and Andison, D. (1986) Mechanical interactions in the interphasial region of fiber reinforced thermosets. In H. Ishida and J. L. Koenig (Eds.), Composite Interfaces, Elsevier, Amsterdam, pp. 109-121.

Interfacial mechanical properties in ceramic matrix composites

M.N. Rahaman, S.H. Wang
Department of Ceramic Engineering, University of Missouri-Rolla, Rolla, Missouri 65401, U.S.A.
L.R. Dharani
Department of Mechanical and Aerospace Engineering and Engineering Mechanics,
University of Missouri-Rolla, Rolla, Missouri 65401, U.S.A.

ABSTRACT

Single fiber pullout tests were used to measure the interfacial shear stresses between silicon carbide fibers and cordierite glass-ceramic matrices. The effect of fiber embedded length, processing schedule, and matrix toughening were investigated. An analytical model was developed to predict the interfacial stresses. The calculations show that the stresses are highly dependent on the specimen thickness and the method of testing.

KEYWORDS

Single fiber pullout test; ceramic matrix composites; interfacial shear stress, shear lag.

INTRODUCTION

It is widely recognized that the mechanical and physical properties of composite materials are controlled to a large extent by the structure and properties of the fiber-matrix interface. For ceramic matrix composites in which both the fibers and the matrix are brittle, debonding between the fibers and the matrix and subsequent fiber pullout make an important contribution to increasing the fracture toughness. The interfacial shear strength therfore plays a critically important role in determining the fracture toughness of ceramic matrix composites. Relatively low interfacial shear strength is required to promote the toughening mechanisms and to reduce the level of brittle failure of the fibers.

The realization of the importance of the fiber-matrix interface for developing the mechanical properties of ceramic matrix composites has led to a growing need for test methods that will allow quantitative characterization of the interface. The single fiber pullout test provides one of the most direct methods of measuring interface parameters and has been used extensively for polymer and metal matrix composites (Greszczuk, 1969; Lawrence, 1972; Takaku and Arridge; 1973; Harris, Morley, and Phillips, 1975; Bartos, 1980; Gray, 1984; Chua and Piggott, 1985a). For a variety of reasons, it has not been used for ceramic matrix composites until recently (Deshmukh and Coyle, 1988; Goettler and Faber, 1988, 1989; Griffin and coworkers, 1988). Instead less direct tests, e.g.

measurement of matrix crack spacing and crack opening displacements during loading and unloading of composites (Marshall and Evans, 1985) or indentation methods (Marshall, 1984; Marshall and Oliver, 1987) have been used.

In the present work, the single fiber pullout test was used to measure the interfacial shear stress between single fibers of SiC imbedded in a cordierite (magnesium aluminum silicate) matrix. The effect of fiber embedded length, sample processing conditions (time or temperature), and matrix toughening by the incorporation of SiC whiskers were studied. An analytical model based on a consistent shear lag theory was developed to predict the interfacial stresses.

EXPERIMENTAL PROCEDURE

Samples of cordierite containing single fibers of SiC were fabricated by conventional sintering or hot pressing. The fibers (SCS-6; Avco Specialty Materials, Lowell MA) had a diameter of $\approx$ 140 micron and had a non-stoichiometric, carbon rich layer on the outer surface. The stoichiometric cordierite matrix powder ($2MgO.2Al_2O_3.5SiO_2$) was prepared in the laboratory by a sol-gel process. The relevant properties of the fiber and the matrix material are given in Table I.

TABLE 1:   Properties of the SiC Fiber and the Cordierite Matrix
Used in the Single Fiber Pullout Tests.

	Fiber[*]	Matrix[**]
Density (Mg/m^3)	3.2	2.5
Coefficient of Thermal Expansion ($10^{-6}/^oC$)	4.4	2.0
Young's Modulus (GPa)	430	110
Tensile Strength (MPa)	4100	70

[*]Manufacturer's specifications.
[**]Ceramic Source, Vol. 2, 1986. Published by the American Ceramic Society.

The samples fabricated by conventional sintering were formed by a slip casting process as shown schematically in Fig. 1. After drying, the samples were sintered in air at 950°C for 2.5 hours. In addition, some samples were heated further at 1050°C for 2 hours in order to examine the effect of oxidation. The fabricated samples were $\approx$ 8 mm in diameter and their thickness varied from 2 to 4 mm.

The method used for fabricating the hot-pressed samples is shown schematically in Fig. 2. A special graphite die was constructed to maintain alignment of the fiber; with this arrangement, the embedded length of the fiber was equal to the thickness of the sample. In order to examine the effect of matrix toughening, samples were fabricated with a matrix of cordierite or cordierite containing 15 v% SiC whiskers. Additional samples were fabricated in which the fiber was oxidized under controlled conditions prior to incorporation into the matrix. All samples were hot pressed under identical conditions (1050°C for 25 min under a pressure of 10 MPa) in a high purity argon atmosphere. The samples were 12 mm in diameter and 1-4 mm thick.

Individual samples were loaded in uniaxial tension on an Instron universal testing machine using a 5 kg load cell. The samples were placed freely on

supports that were a fixed distance apart and the fiber was pulled at a rate of 1 mm/min. The fiber pullout length was measured from the thickness of the sample and compared with the value measured from the chart speed.

RESULTS

The single fiber pullout tests gave data for the load as a function of chart length from which the force versus displacement curve were obtained. Figure 3 shows a typical curve for the samples tested in this work. The force increased linearly with displacement until pullout began at which point there was a sharp drop in the force. This was followed by a slight increase in the force after which there was further pullout accompanied by a slight drop in the force. This process continued until the remaining part of the fiber pulled out smoothly. It has been observed by a number of workers and is referred to as "stick-slip" friction (Chua and Piggott (1985b).

As illustrated in Fig. 3, if P_d is the maximum force at which pullout began (referred to as the debond force), and P_f is the force immediately after the sharp drop that followed the initial pullout (referred to as the frictional force), then the debond stress is given by

$$\tau_d = P_d/(2\pi r l_e) \tag{1}$$

where r is the radius of the fiber and l_e is the fiber embedded length. The frictional shear stress is refined by

$$\tau_f = P_f/(2\pi r l_e) \tag{2}$$

In deriving eqs. (1) and (2) it is assumed that the embedded length l_e is very small so that the interfacial shear stress may be treated as constant. The debond force as a function of embedded length is shown in Fig. 4 for the sintered and hot pressed samples; for these samples the fibers were not pretreated prior to incorporation in the matrix and there was no oxidation after the fabrication procedure. The debond force is seen to increase with increasing embedded length. For a fixed embedded length, the debond force force for the sintered samples are approximately twice the value for the hot-pressed sapmles; this can be explained in terms of increased oxidation and chemical bonding for the sintered samples fabricated in air. Within the limits of experimental error, the debond stress is independent of the embedded length.

Average values for the debond stress and the frictional shear stress for the samples studied in this work are given in Table 2. The results for the samples

TABLE 2: Single Fiber Test Results for the Debond Stress, τ_d, and the Frictional Shear Stress, τ_d.

Sample Description	τ_d (MPa)	τ_f (MPa)
1. Hot Pressed Samples:		
(a) cordierite matrix/untreated fiber	11	5
(b) cordierite matrix/oxidized fiber	17	8
(c) composite matrix/untreated fiber	9	6
(d) composite matrix/oxidized fiber	13	8
2. Sintered Samples:		
(a) 950°C, 2.5 h, air	21	8
(b) 950°C, 2.5h, and 1050°C, 2h, air	32	23

with a composite matrix (cordierite/15 v% SiC whiskers) are not significantly different from those for the unreinforced cordierite matrix. An important observation is the drastic effect of processing conditions and oxidation on the interfacial properties.

ANALYSIS OF THE STRESS-DISPLACEMENT DATA

An analytical model based on a consistent shear lag theory was developed for predicting the interfacial stresses as a function of the displacement. The idealized geometry of the single fiber pullout sample considered in the model is shown in Fig. 5. The composite region is sectioned into a number of vertical elements $(1, 2, \ldots, n, \ldots, N)$ of arbitrary width, h. Then the transverse (x) and axial (y) equilibrium equations for a generic element (n) and the free edge elements (1 and N) are written down as

$$\sigma_{x(n+1/2)} - \sigma_{x(n-1/2)} + (h/2)[\tau_{n+1/2),y} + \tau_{(n-1/2),y}] +$$

$$\delta[\sigma_{x(n-1/2)} - (h/2)\tau_{(n-1/2),y}] + \delta_{nN}[-\sigma_{x(n+1/2)} -$$

$$(h/2)\tau_{(n+1/2),y}] = 0 \qquad\qquad (3a)$$

$$\tau_{(n+1/2)} - \tau_{(n-1/2)} + h\sigma_{yn,y} + \delta_{n1}\tau_{(n-1/2)} -$$

$$\delta_{nN}\tau_{(n+1/2)} = 0 \qquad\qquad n = 1,2,\ldots,N \qquad\qquad (3b)$$

where σ_x, σ_y and τ are the transverse normal, axial, and shear stresses respectively, the subscripts $(n+1/2)$ and $(n-1/2)$ indicate the mid-nodes between the elements n and $(n+1)$, and $(n-1)$ and n, respectively, subscript y preceded by a comma indicates differentiation with respect to y, and δ_{mn} is the Kronecker delta ($\delta_{mn} = 0$ for $m \neq n$ and $\delta = 1$ for $m = n$).

In order to make the problem mathematically tractable, a set of approximate constitutive relations were derived based on a consistent shear lag theory and finite difference approximations. When these approximate relations are substituted into Eqs. (3) and (4) the resulting equations in terms of axial and transverse displacements can be written in the following matrix form

$$\{w'\} = [K_w]\{w\} \qquad\qquad (4)$$

where

$$\{w\} = \{u_1, \ldots, u_N, v_1 \ldots, v_N, u_1', \ldots, u_N', \ldots, v_1', \ldots, v_N' \ldots\}^T$$

and

$$[K_w] = \begin{bmatrix} [0] & [0] & [1] & [0] \\ [0] & [0] & [0] & [1] \\ [K_u] & [0] & [0] & [C_u] \\ [0] & [K_v] & [C_v] & [0] \end{bmatrix}$$

with u_n and v_n representing the x and y displacement components of an element n, the tri-diagonal (NxN) matrices $[K_u]$, $[K_v]$, $[C_u]$, and $[C_v]$ are functions of the element orthotropic stiffnesses, (C_{ij}), and the element width, h, and the primes represent differentiation with respect to the non-dimensional variable, η.

The general solution of the equations given above can be written down if the eigenvalues and eigenvectors of the matrix $[K_w]$ are known. Let r_j (with j = 1,2,...,K_1) be the real eigenvalues of the matrix $[K_w]$, $\{A_j\}$ and $\{B_j\}$ be the first 2N components of the corresponding eigenvectors,, and $p_j + iq_j$ (with p_j, q_j > 0, and j = 1,2,...,K_2) be the complex eigenvalues of the matrix $[K_w]$, $\{A_j^R\}$ + $i\{A_j^I\}$ and $\{B_j^R\}$ + $i\{B_j^I\}$ be the first 2N components of the corresponding eigenvectors, where K_1 and K_2 are the number of the real and complex eigenvalues, respectively, so that $K_1 + 2K_2 = 4N$. The eigenvalues can be calculated numerically once the matrix $[K_w]$ is formed. Then the general solution to Eq. (4) can be written in terms of eigenvectors and 4N constants that are determined from the boundary conditions. Once the displacements u_n and v_n are known the stresses can be calculated using the approximate stress-displacement relations mentioned earlier. Further details of the analytical model and the solution scheme are given elsewhere (Dharani, 1988).

DISCUSSION

Using the analytical model, the stresses at the interface were determined as a function of the embedded length, l_e, which is also equal to the sample thickness in this work. The shear stress distribution at the fiber matrix interface before debonding occurs (i.e. the elastic interface) is shown in Fig. 6 for three embedded lengths and for a given applied load on the fiber. The shear stress attains its maximum value, τ_{max}, at a finite distance from the the surface of the sample that is supported on a rigid support. For smaller embedded lengths the stress distribution becomes highly non-uniform. The maximum shear stress depends on the supported length, as shown in Fig. 7 for two typical embedded lengths. The experiments were performed before the analytical results became available; although the same procedure was used in the single fiber pullout tests the exact supported length was not recorded. For moderately thick samples (> ≈ 2.5 mm) the maximum shear stress is less dependent on the support conditions. In addition for very thin samples, the analytival results indicate a large tensile stress at the interface on the pullout end and a large compressive stress at the corresponding point on the opposite surface of the sample, as shown in Fig. 8. Again, for thicker samples the effect is not significant. It is clear from the present discussion that the sample thickness and the method of supporting the sample need to be carefully controlled during the pullout test.

If debonding is assumed to occur at the location of the maximum shear stress (i.e. τ_{max}) and when the maximum shear stress reaches the debond stress, τ_d, of the interface, then

$$\tau_d = C\tau_{max}P_d \qquad (5)$$

where C is a constant for the sample. For the present investigation C = 0.04. The maximum shear stress predicted from the model is shown in Fig. 9 as a function of the embedded length. From the load at the initiation of debonding (measured from the load-displacement curve of the fiber pullout test) and the maximum shear stress predicted by the model for a given embedded length, the debond stress of the interface was calculated from Eq. (5). Since the

model assumed a constant supported length, the calculated debond stress was compared with data obtained by a non-linear regression analysis of the experimental results of P_d versus l_e and the equation (Goettler and Faber, 1988)

$$P_d = A\tanh(\alpha l_e) \tag{6}$$

where A and α are constants; the comparison is shown in Table 3. In light of the assumptions made, the model predictions appear reasonably encouraging.

TABLE 3.   Comparison of the Model Predictions for the Interfacial
Debond Stress (in MPa) with Experimental Data

Sample Description	Experiment	Model
1. Hot Pressed Samples:		
(a) cordierite matrix/untreated fiber	12	15
(b) cordierite matrix/oxidized fiber	25	24
(c) composite matrix/untreated fiber	11	13
(d) composite matrix/oxidized fiber	13	15
2. Sintered Samples:		
(a) 950°C, 2.5 h, air	32.6	29.9
(b) 950°C, 2.5h, and 1050°C, 2h, air	37.4	50.8

CONCLUSIONS

The single fiber pullout test is a viable method for measuring the interfacial mechanical proerites in ceramic matrix composites. For SiC fibers embedded in a cordierite matrix, the debond stress was 11 MPa for samples fabricated by hot pressing in high purity argon. Processing in air or oxidation led to large increases in the debond stress.

An analytical model based on a consistent shear lag theory showed that the sample thickness and the support conditions during testing must be carefully controlled in the single fiber pullout test. For a fixed support condition, the model gave good agreement with the data.

REFERENCES

Bartos, P. (1980). Analysis of pullout tests on fibers embedded in brittle matrices. J. Mater. Sci., 15, 3122-3128.

Chua, P. S. and M. R. Piggott (1985a). The glass fiber-polymer interface: I - theoretical consideration for single fiber pull-out tests. Composites Sci. Technol., 22, 33-42.

Chua, P. S. and M. R. Piggott (1985b). The glass fiber-polymer interface: II - work of fracture and shear stresses. Composites Sci. Technol., 22, 107-119.

Deshmukh, U. V. and T. W. Coyle (1988). Determination of the interface strength in glass-SiC composites via single fiber tensile testing. Ceram. Eng. Sci. Proc., 9, 627-634.

Dharani, L. R. (1988). A micromechanics analytical model for characterizing sublaminate damage. Final Report, NSF Grant No. 8504591.

Goettler, R. W. and K. T. Faber (1988). Interfacial shear stress in SiC and Al$_2$O$_3$ fiber-reinforced glasses. Ceram. Eng. Sci. Proc., 9, 861-870.

Goettler, R. W. and K. T. Faber (1989). Interfacial shear stresses in fiber-reinforced glasses. Composites Sci. Technol., in press.

Gray, R. J. (1984). Analysis of the effect of embedded fiber length on fiber
    debonding and pullout from an elastic matrix, part 1: review of theories.
    J. Mater. Sci., 19, 861-870.
Greszczuk, L. B. (1969). Theoretical studies of the mechanics of the
    fiber-matrix Interface in composites. In Interfaces in Composites. ASTM STP
    452, American Society for Testing and Materials, Philadelphia. pp 42-58.
Griffin, C. W., S. Y. Limaye, D. W. Richerson, and D. K. Shetty (1988).
    Evaluation of interfacial properties in borosilicate-SiC composites using
    pullout tests. Ceram. Eng. Sci. Proc., 9, 671-678.
Harris, B., J. Morley, and D. C. Phillips (1975). Fracture mechanisms in
    glass-reinforced plastics. J. Mater. Sci., 10, 2050-2061.
Lawrence, P. (1972). Some theoretical considerations of fiber pull-out from
    an elastic matrix. J. Mater. Sci., 7, 1-6.
Marshall, D. B. (1984). An indentation method for measuring matrix-fiber
    frictional stresses in ceramic composites. J. Am. Ceram. Soc., 67,
    C-259--C-260.
Marshall, D. B. and A. G. Evans (1985). Failure mechanisms in ceramic
    matrix/ceramic-fiber composites. J. Am. Ceram. Soc., 68, 225-231.
Marshall, D. B. and W. C. Oliver (1987). Measurement of interfacial
    mechanical properties in fiber reinforced ceramic composites. J. Am. Ceram.
    Soc., 70, 542-548.
Takaku, A. and R. G. C. Arridge (1973). The effect of interfacial radial and
    shear stress on fiber pull-out in composite materials. J. Phys. D: Appl.
    Phys., 6, 2038-2047.
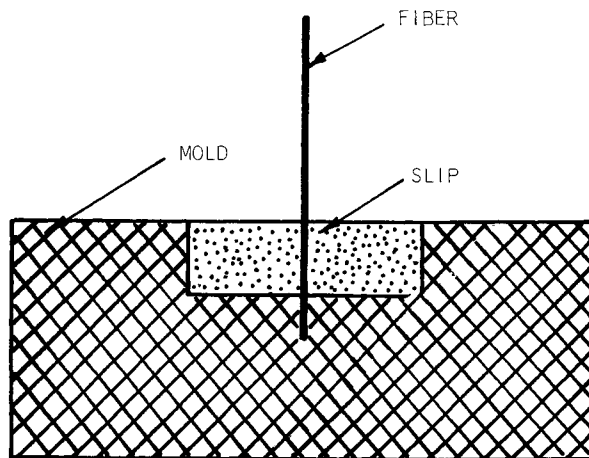
Fig. 1. Slip-casting technique for fabricating
        sintered samples.
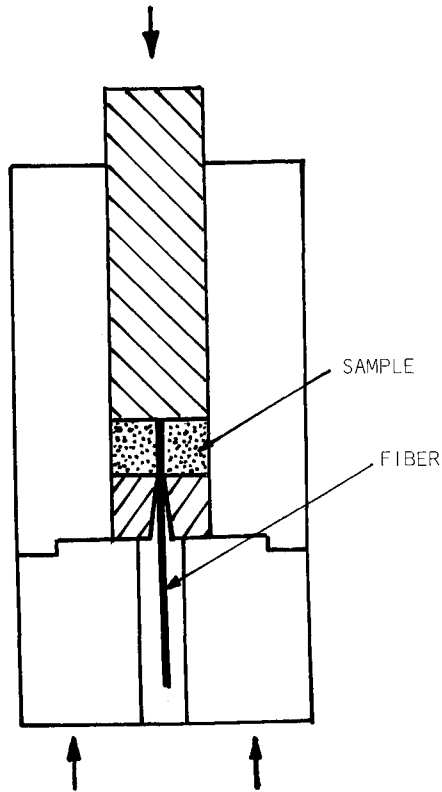
Fig. 2. Graphite die for fabricating
hot pressed samples.

CROSSHEAD DISPLACEMENT (mm)
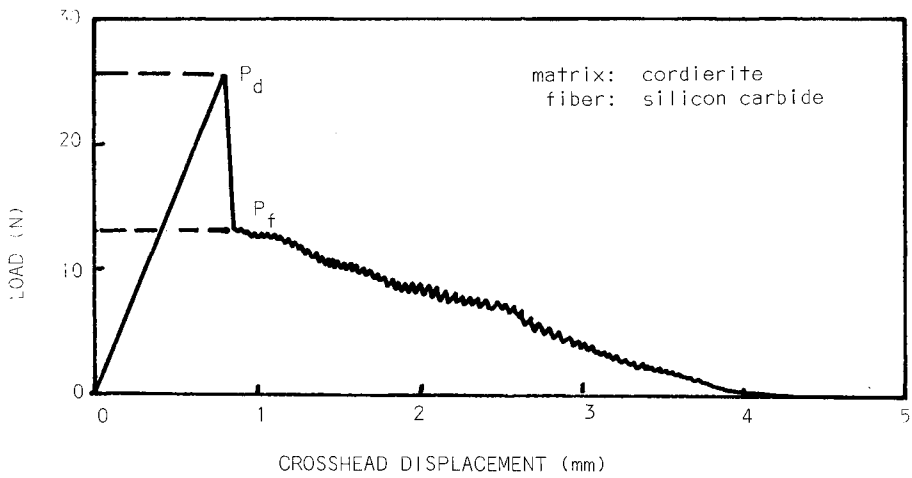
Fig. 3. Typical load-displacement curve.
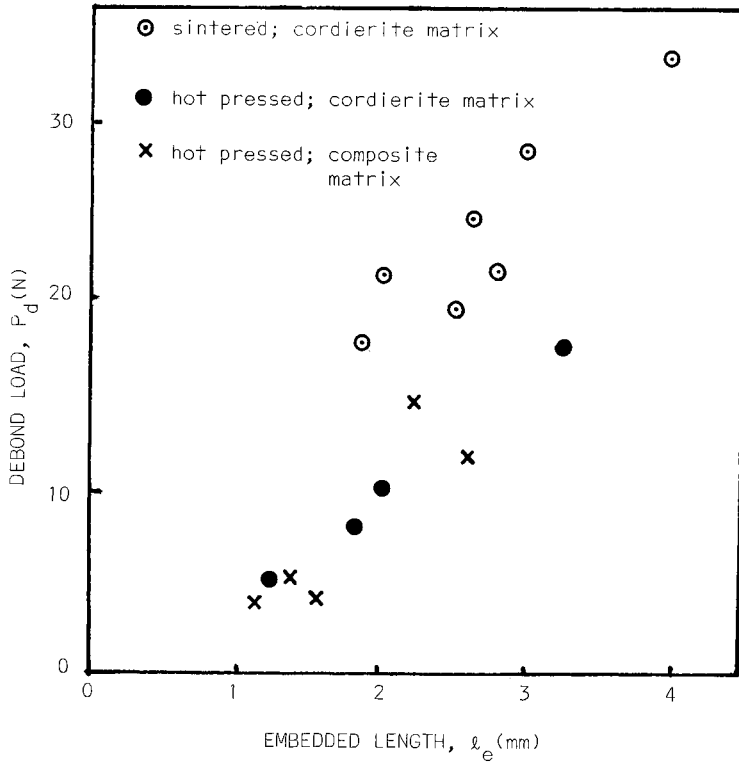
Fig. 4. Debond load as a function of embedded length.
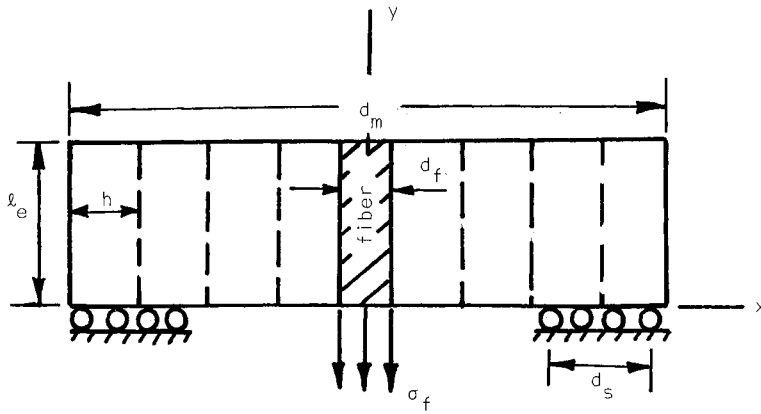
Fig. 5. Schematic of the analytical model of the fiber pullout configuration (ℓ_e-specimen thickness embedded length, d_s-support width, d_m-specimen width, d_f-fiber width)
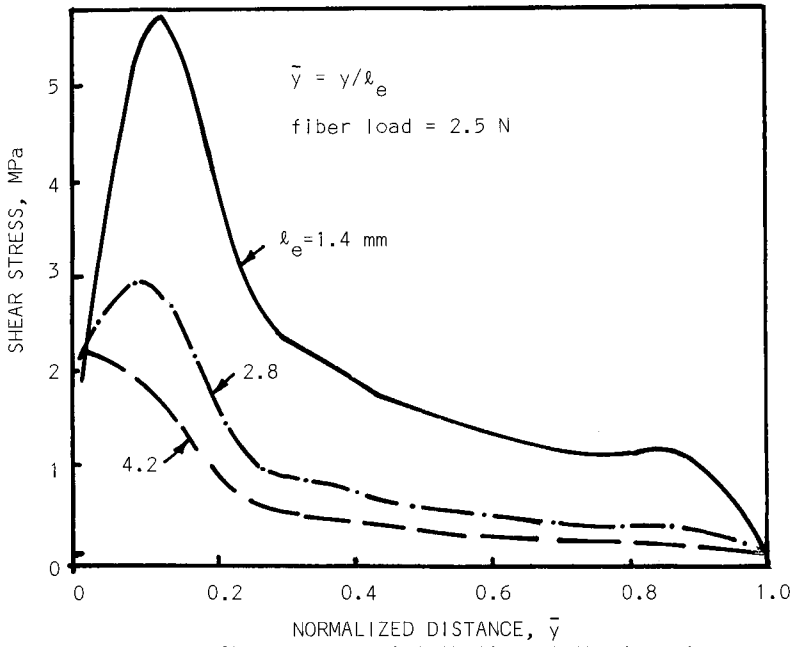
Fig. 6.   Shear stress distribution at the interface.
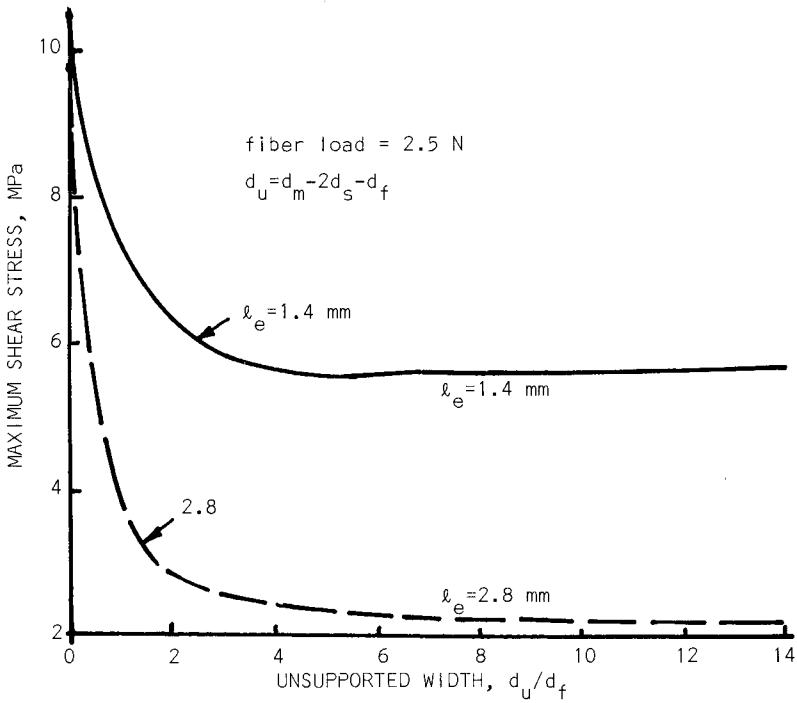
Fig. 7.   Effect of support condition on maximum shear stress.
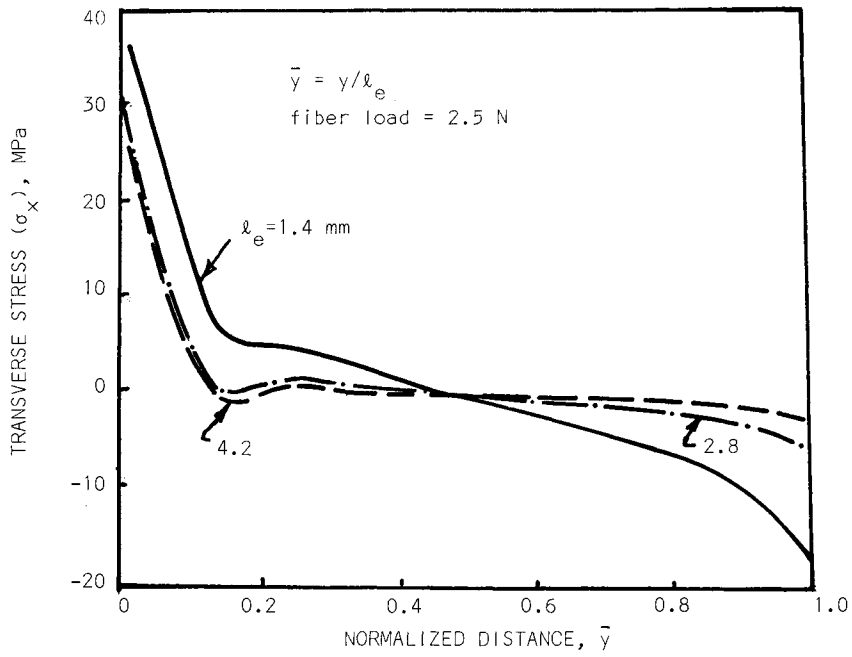
Fig. 8. Transverse normal stress distribution at the interface
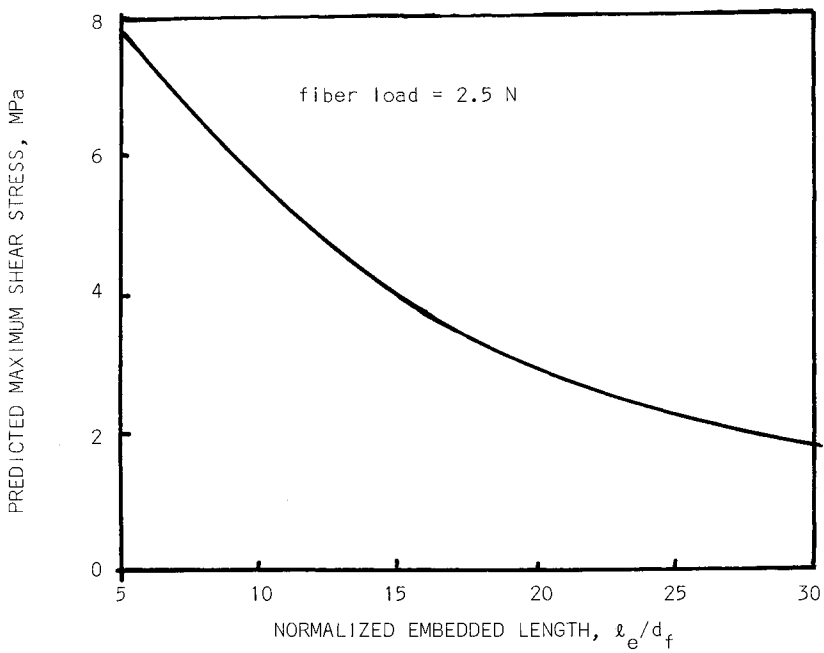
Fig. 9. Predicted (model) maximum shear stress at the interface

Debonding and frictional effects during fibre pull-out in model SiC fibre-reinforced glass composites in relation to fracture resistance

E.P. Butler, H.M. Chan
*Department of Materials Science and Engineering, Whitaker Lab. No. 5,
Lehigh University, Bethlehem, Pennsylvania 18015, U.S.A.*

T.R. Palamides, E.R. Fuller, Jr.
*National Institute of Standards and Technology, Ceramics Division,
Gaithersburg, Maryland 20899, U.S.A.*

ABSTRACT

The influence of a ductile interfacial layer on the toughening effect that a SiC monofilament imparts to a brittle glass matrix was addressed. Micro-mechanical investigation of the fiber/nickel-coating/glass interfaces using the single fiber pull-out test indicated that the fiber/nickel interface was weaker than the glass/nickel interface and that the sliding friction was also lower. The fracture resistance of the nickel coated fiber composite was generally less than that of the composite reinforced with fibers in the as-received condition. The fracture resistance initially decreased with increasing nickel thickness but gradually increased again up to the as received fiber composite level at a nickel thickness of 22 μm. However all thicknesses of nickel fiber coating enhanced the fracture resistance of the composite compared to the unreinforced glass matrix.

KEYWORDS

Ceramic composite, debond strength, frictional shear resistance, fiber pull-out, toughening

INTRODUCTION

The toughening effect that fibers and whiskers engender to brittle ceramics arises from several phenomena; including crack deflection, reinforcement/matrix debonding, crack bridging and frictional pullout. These characteristics are dependent upon the fiber/whisker radius and length, the physical properties of the reinforcement and the matrix, the interfacial chemistry, and the stress state at the interface. In current activities we have concentrated on the interface between the reinforcement and the matrix. Residual stresses at this interface arise primarily from the thermal expansion mismatch between the reinforcement and the matrix, but are influenced by the chemistry of the interfacial bond and the rheological properties of the matrix during processing. This second factor is particularly important for glass matrices. Both factors are processing sensitive so that the residual stresses at the interface at room temperature are thermal history dependent.

In the present study we examine the influence of a ductile interfacial layer on the toughening effect that a single SiC fiber imparts to a brittle glass matrix. The interface mechanics of the system are addressed both as a fiber debond/pullout problem and as a crack/fiber interaction problem.

BACKGROUND

Previous work by Fuller in this area, using the model composite system of SiC monofilaments[1,3] as a reinforcement in a borosilicate glass matrix[2,3] has shown that enhanced crack resistance can be built into the glass. The toughening increment has been shown to be as much as 22% for reinforcement by a single fiber. The work presented here builds upon this experience and examines the influence of metallic layers on this toughening increment.

EXPERIMENTAL PROCEDURE

Sample Fabrication.

Test specimens were fabricated by diffusion bonding of the fibers between borosilicate glass plates under a dead weight load of 1.2 MPa. Specimens were prepared with the fiber surface in the as-received condition as well as with thin metallic nickel coating. The nickel was electrodeposited on the fiber surface to various thicknesses between 1 μm and 22 μm.
The processing conditions for each specimen is detailed in Table 1. Nominally each specimen was fabricated under similar conditions. The processing atmosphere used was helium and the maximum processing temperature for each specimen was 706°C, after which the specimen was cooled to room temperature at nominally the same rate. Accordingly, the rheological response of the glass matrix should be the same for these studies, and the only variable affecting the interfacial properties should be the presence of the metallic interfacial layer and its thickness.

Table 1   Fabrication Conditions for Mechanical Test Samples.

FIBER COATING	TIME AT 660°C	TIME AT 706°C
no Nickel	3hrs:25min	2hrs:20min
1 μm Nickel	3:40	1:45
9 μm Nickel	3:35	1:55
22 μm Nickel	4:00	1:55

---

[1] AVCO SCS-6 SiC Monofilaments.

[2] Pyrex Glass, #7740

[3] Certain trade names and company products are mentioned in the text in order to adequately specify the experimental procedure. In no case does such identification imply recommendation or endorsement by NIST, nor does it imply that the products are the best available for the purpose.

Debond Strength and Frictional Shear Resistance of the Interfaces.

Assessment of the influence of the metallic interfacial layer on the micromechanics of the matrix/nickel/fiber interfaces was achieved using the single fiber pullout test. The test geometry and equipment used are described schematically in fig. 1. The fiber and glass matrix were attached to the testing fixtures using epoxy.
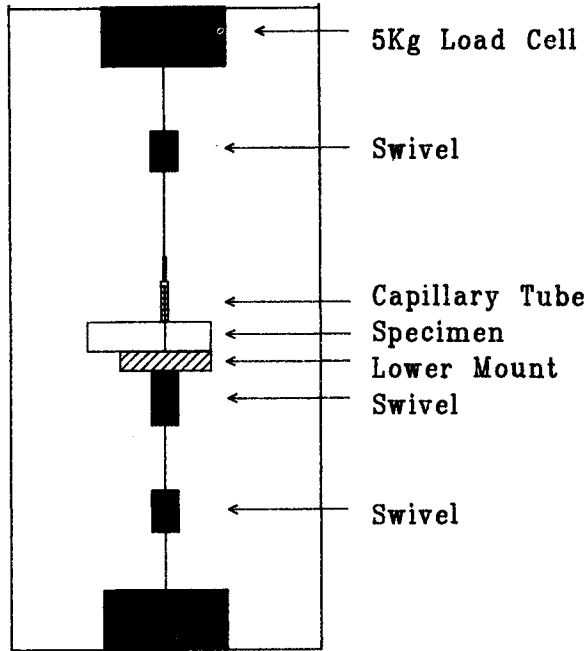
Fig. 1 Arrangement used for single fiber pull-out test.

Fracture Resistance of the Composite.

The crack resistance behavior of the monofilament reinforced glass was established using a fracture mechanics specimen described by Janssen. The geometry of this type of specimen is shown in fig. 2 along with the specimen dimensions used. The double-cleavage drilled-compression (DCDC) specimen is particularly applicable to this situation as the stress intensity factor, K_I, along the crack front is uniform and the crack plane is stable along the specimen mid-plane. Being a decreasing K_I specimen, after initial 'pop-in', an increasing load must be continually applied to cause further crack extension. Thus the crack can be driven at a constant velocity by maintaining a constant stressing rate[4]. The extent of this constant velocity region of crack growth was determined using the

---

[4] Due to the high stiffness of the specimen compared to typical universal testing machines a constant displacement rate test invariably results in a constant stressing rate.

technique of stress wave fractography, discussed by Richter and used by Coyle, on unreinforced glass DCDC specimens. In this technique acoustic waves are introduced into the specimen during crack extension by a piezoceramic transducer coupled to the specimen. This technique causes slight mode II perturbations on the growing mode I crack so that fracture surfaces are rippled. These ripples are most easily observed under reflected light using Nomarsky contrast. For a constant frequency higher velocity cracks produce widely spaced bands, slower crack velocities produce closely spaced bands. The region of the specimen in which there is a constant crack growth velocity is shown in fig. 3. To ensure correct and reproducible interpretation of the toughening effect the fibers were placed in the center of this region.

The DCDC specimen was observed in situ under cross-polarized illumination. Such illumination high lights the crack tip stress contours due to the stress bi-refringent properties of glass. The stress contours associated with the double-cleavage cracks are symmetric about the center hole and the center plane, that is the crack plane of the specimen. The crack tip is easily located by such illumination due to its distinctive pattern. Photographs were taken of the growing crack at various times during loading and from these the crack length was determined as a function of the applied load. From the measured crack length, c, at a given remotely applied compressive stress, σ_{app}, the applied stress intensity factor was determined by Janssen to be;

$$K_{app} = \sigma_{app} \cdot r^{\frac{1}{2}} \; / \; [(c/r)f(c/r)] \tag{1}$$

where r is the radius of the center hole and f(c/r) is a dimensionless constant which can be determined by testing samples of known K_{IC}, in this case the unreinforced glass was used.
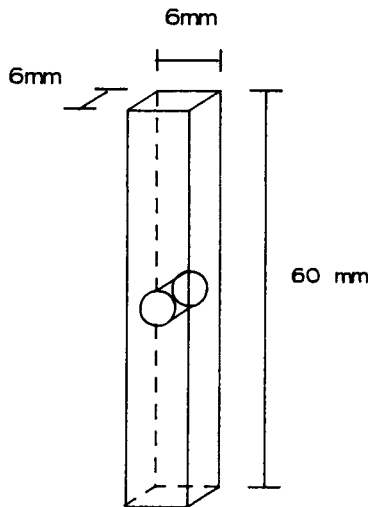
Fig. 2   The DCDC Mechanical Test Specimen.
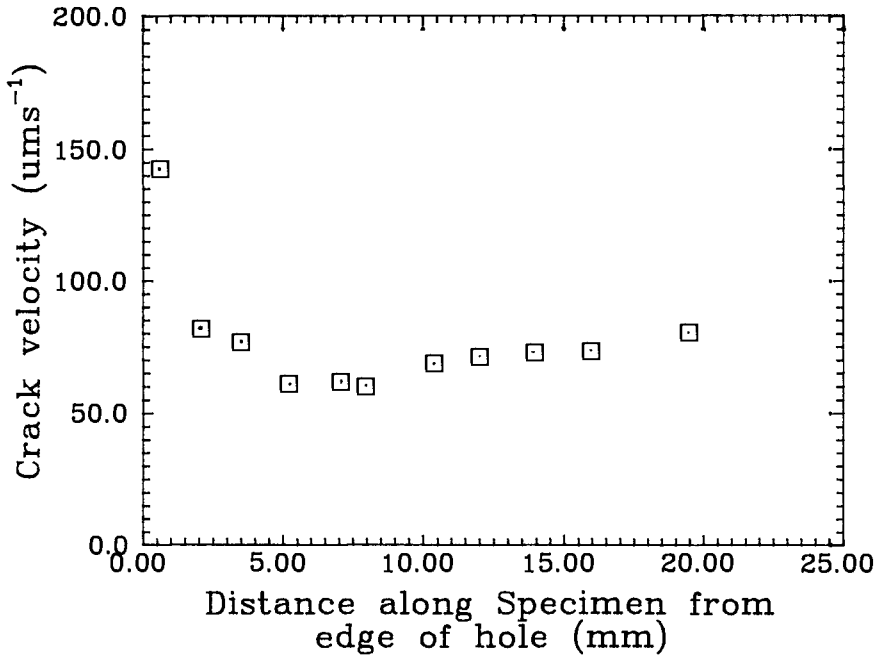
Fig. 3 Crack velocity as a function of crack extension for the DCDC
geometry driven under conditions of constant stressing (or displacement) rate.

RESULTS AND DISCUSSION

Micro-Mechanics of the Interface

Figure 4 shows a typical example of the raw data from a single fiber pullout test.
The debond shear strength, S_d, of the interface is given by:

$$S_d = P_d/2rl \qquad\qquad (2)$$

where P_d is the debond load, r is the fiber radius, and l is the embedded length
of fiber in the matrix. The average frictional shear resistance, τ, is given by:

$$\tau = P_f/2rl \qquad\qquad (3)$$

where P_f is the load as the fiber begins to slide. Eqs. (2) and (3) are an
approximation to the actual behavior, but are sufficient for the present analysis.
     As seen in fig. 5, the debond shear strength and the frictional shear
resistance are sensitive to the thickness of the nickel coating. The as received
fiber has the highest debond strength and frictional resistance. As the thickness
of the nickel coating is increased these two stresses continue to decrease with
the 22 μm coated fiber having the lowest values.
Examination of the specimen after the pullout test revealed that the fibers pulled

away from the nickel coating leaving it still bonded to the glass matrix. Thus, it appears that the SiC fiber/nickel interface is weaker than the nickel/glass interface. Comparison to specimens with as received fibers indicate that the SiC/nickel interface is also weaker than the SiC/glass and has a lower sliding friction.
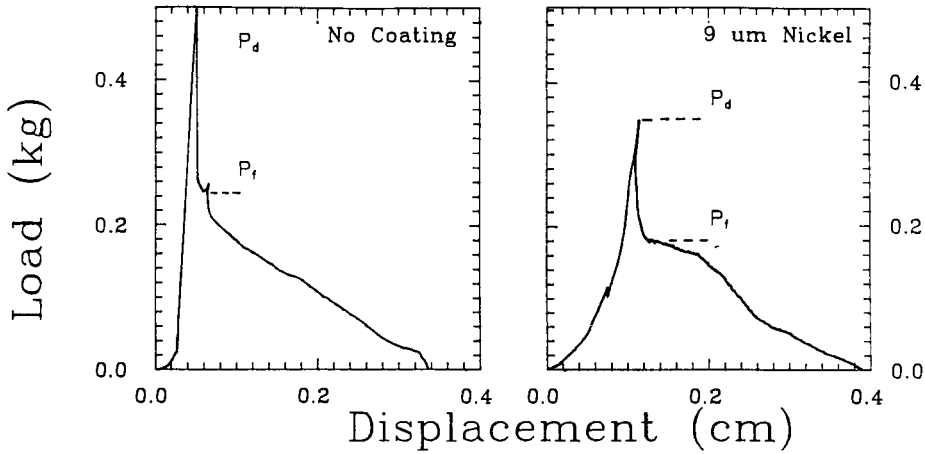
Fig. 4. Load-displacement curves for single fiber pull-out tests: (a) As-received SiC fiber, (b) Nickel-coated SiC fiber, in glass matrix.
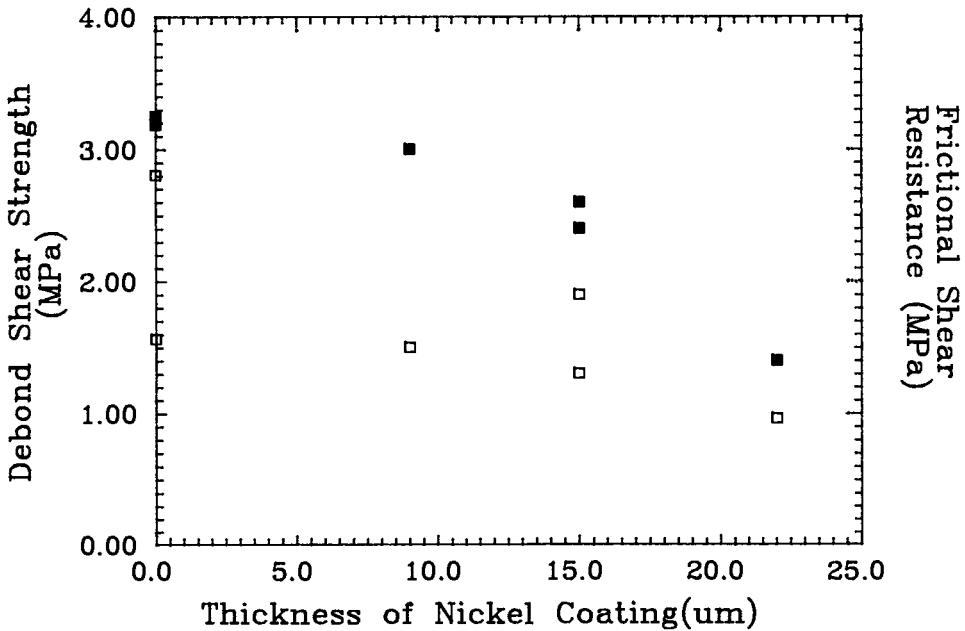
Fig. 5. Debond shear stress (filled squares) and frictional pull-out stress (open squares) as a function of fiber coating thickness.

Fracture Resistance of the Glass/Nickel coated Fiber Composite.

The change in applied stress intensity factor, K_I, as a crack propagated perpendicular to the reinforcing fiber was monitored as a function of crack extension for both nickel coated and as received fiber composites. Two tests were conducted for each composite. The results are shown in fig. 6.
All fibers, regardless of surface preparation, gave an enhanced toughness to the glass composite compared to that of the unreinforced glass. No fibers broke in the path of the advancing crack, but were all debonded and frictionally pulled out. Scatter in the results makes it difficult to assess the effectiveness of the nickel coating from the applied stress versus crack length curves. The toughening effect of the fiber can be quantified as an incremental toughening parameter, K_I^{max}/K_{IC}, where K_I^{max} is the maximum applied stress intensity factor and K_{IC} is the fracture toughness of the unreinforced glass (0.77 MPa·$\sqrt{m}$ in this case). This factor is plotted in fig. 7 as a function of the nickel coating thickness.
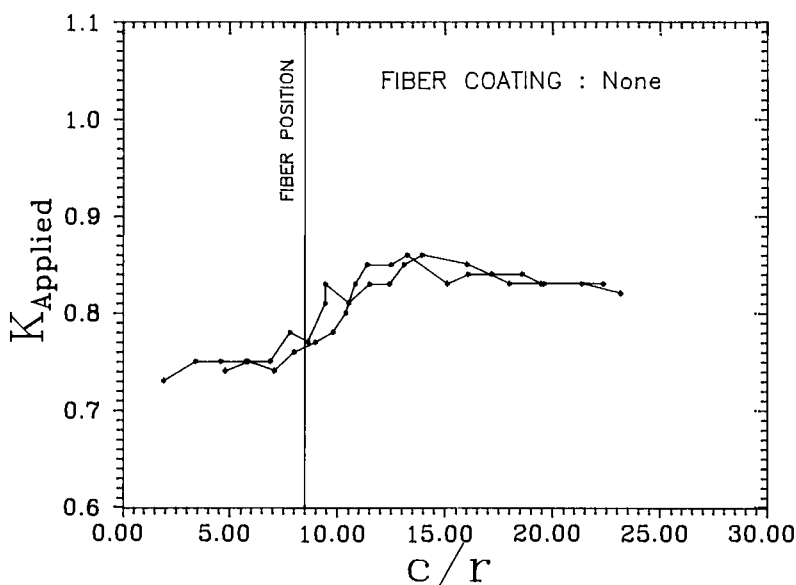
Fig. 6a. Applied stress intensity factor as a function of crack size for the DCDC-fracture mechanics specimen.
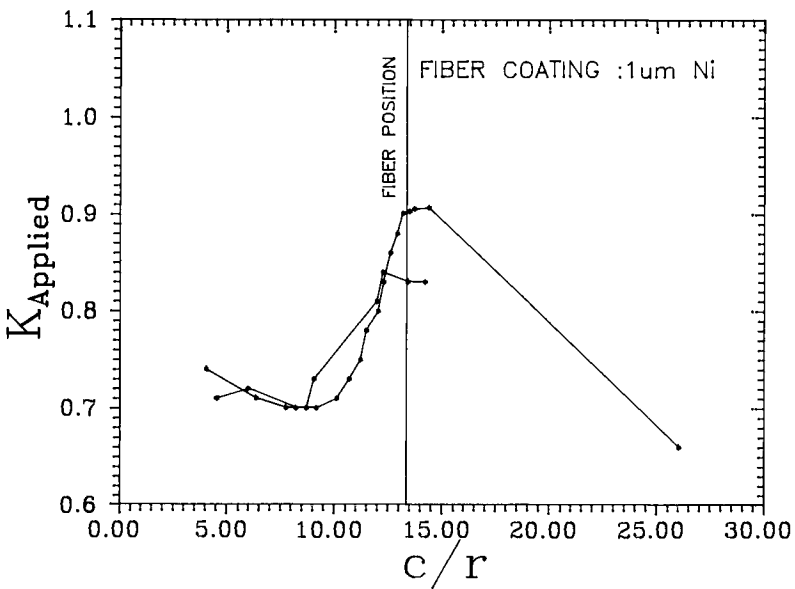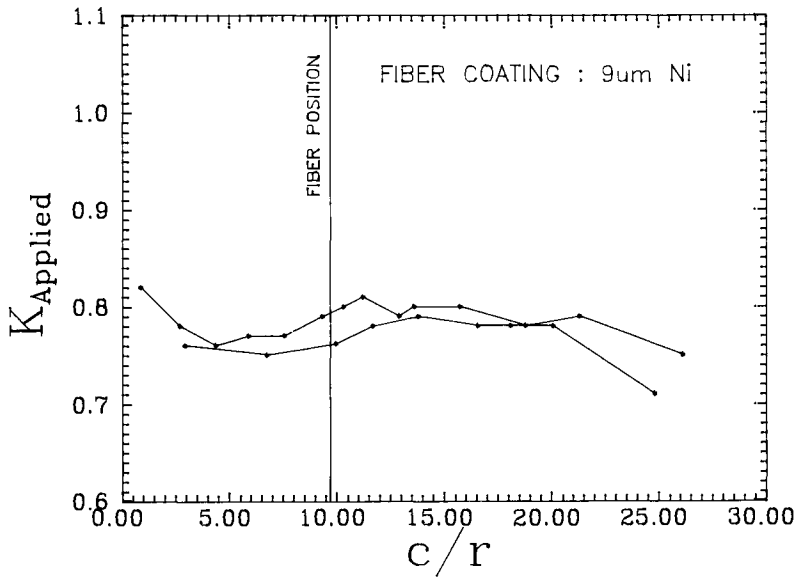
Fig. 6b & 6c. Applied stress intensity factor as a function of crack size for the DCDC-fracture mechanics specimen.
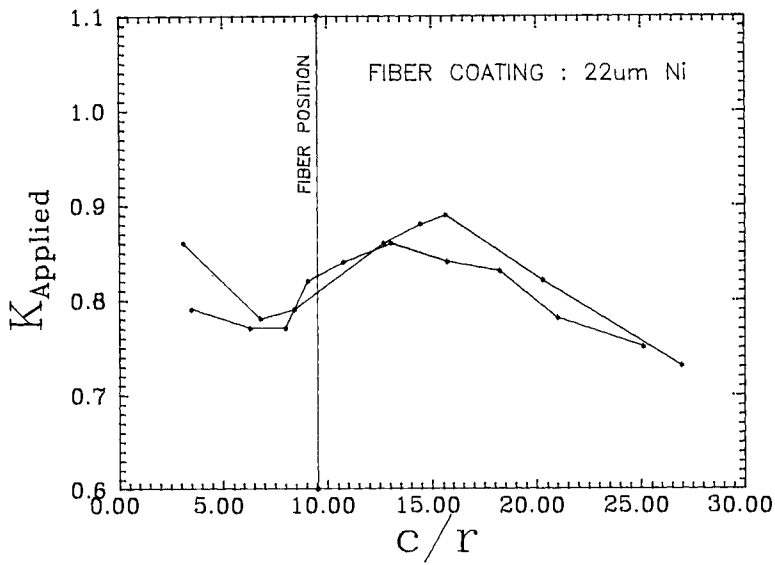
Fig. 6d. Applied stress intensity factor as a function of
crack size for the DCDC-fracture mechanics specimen.
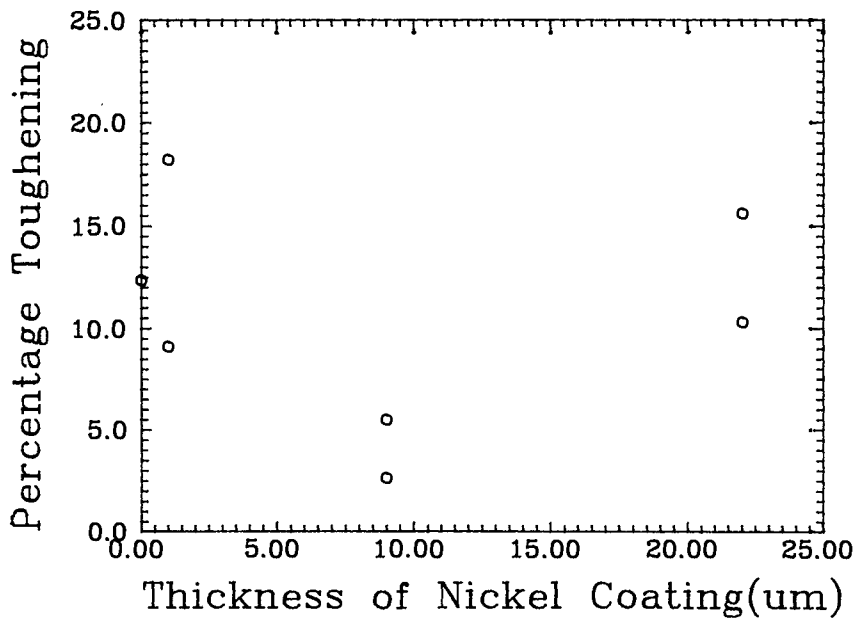
Fig. 7. Toughening increment as a function of fiber coating.

We might expect the same trend in toughening behavior with coating thickness as the debond strength and frictional shear resistance, that is a decreasing toughness increment with increasing coating thickness. This has not unequivocally been observed. The majority of the specimens with coated fibers did indeed have a lower toughness, but two specimens (one at 1 μm and one at 22 μm) had greater toughness than the as received fiber reinforced specimens. It is well to keep in mind that the pullout tests primarily measured the fiber/nickel interface, which was weaker than the fiber/glass interface. However, when a crack interacts with the reinforcement it first encounters the glass/nickel interface. If debonding occurs on this interface, the fiber with its nickel coating intact will frictionally pullout and the crack can only later interact with the nickel/SiC interface. Thus, low interfacial strength of the nickel/SiC interface does not necessarily produce a low toughening increment.

CONCLUSIONS

In summary, metallic coating on reinforcing fibers offer interesting possibilities for enhanced toughening of ceramic composites. However, evidence to date is not conclusive. Further work will concentrate on the improving the processing conditions so that a variety of glass/metal and metal/fiber interface conditions can be examined.

ACKNOWLEDGEMENTS

REFERENCES

E. R. Fuller, Jr., R. F. Krause, Jr., M. D. Vaudin, and T. R. Palamides.   (1989) Toughening Mechanisms in Ceramic Composites. NISTIR 88-4018, National Institute of Standards and Technology, Gaithersburg,MD, also in ORNL/FMP-88/2, Fossil Energy Materials Program,   R. Judkins, Manager, Oak Ridge National Laboratory, Oak Ridge,TN, 1988.

C. Janssen. (1974). Specimen for Fracture Mechanics Studies on Glass. Proceedings of the Xth International Congress on Glass, Kyoto Japan. pp23-30, July 8-13, 1974. The Ceramic Society of Japan, Koyoto,Japan

H.Richter. (1985). Crack propagation in glass under liquids in an intermediate range of crack velocites," pp219-29 in Strength of Inorganic Glass, Ed by C.R. Kurkjian, Plenum Publishing Corp.

T. W. Coyle, E. R. Fuller, Jr., P. Swanson, and T. R. Palamides. (1987). Fracture Mechanics Characterization of Crack/Fiber Interactions in Ceramic Matrix Composites. Ceram. Eng. Sci. Proc., 8 [7-8], pp 630-635

Chemical changes that affect the properties of SiC fibres and whiskers

S. Karunanithy
Atlantic Research Laboratory, National Research Council Canada, Halifax, Nova Scotia, Canada, B3H 3Z1

Abstract

The silica layer present on the surface of SiC fibers and whiskers plays an important role in the fabrication and application of fiber- and whisker- reinforced ceramics. Degradation of the SiC fibers in the composites takes place in the presintering stage during which the surface silica is removed as SiO (g) and the fibers are exposed to further oxidation. Rapid heat-treatment in the presintering stage is therefore essential to minimize fiber damage. SiC whiskers, however, contain only a small amount of silica on the surface and are susceptible to further oxidation during the sintering of the composites. In addition, SiC whiskers undergo degradation in air at temperatures above 1000 $^\circ$C by losing material from the core.

Introduction

Silicon carbide fibers and whiskers are important reinforcement materials for the fabrication of ceramic matrix composites. Reinforcement with these materials leads to tougher ceramics with controlled fracture [1,2]. The successful reinforcement of a sintered matrix by the fibers or whiskers, however, depends on the retention of the high strength of these materials during the fabrication of the composites. The main mechanism of toughening in fiber-reinforced composites involves the pulling- out of the fibers during fracture to dissipate the energy of fracture. The extent of energy dissipation during this process is determined by the fiber/matrix interface which should be weak enough to allow the pull-out of the fibers. Therefore, the chemistry of the fiber surface and the fiber/matrix interface play important roles in all of these aspects [3,4].

The surface of SiC fibers and whiskers contain a coating of silica (SiO_2) formed by the oxidation of these materials during the manufacturing process and subsequent handling. This surface layer provides protection from further oxidation of the fibers, however, the stability of the silica layer itself depends strongly on processing conditions such as the heat-treatment cycle and the environment [5]. Any change in the amount or morphology of this surface layer will affect the properties of the composite materials.

One of the key issues in our continuing research in advanced composite materials is the development of techniques for systematic investigation of the chemical changes in SiC fibers, whiskers and the fiber/matrix interface during the fabrication and in the service environments of the ceramic matrix composites in order to develop improved processing conditions. This paper summarizes some of the initial results obtained in these studies.

Experimental Procedure

A general program used for the fabrication and characterization of SiC fiber- or whisker -reinforced ceramics is shown in Fig. 1.

Samples of composite materials were fabricated by slipcasting slurries of alumina[1] containing SiC fibers [2] or whiskers [3]. These fibers and whiskers were washed with acetone and HCl respectively to remove impurities and were added to an alumina slip. For casting samples the slurry was mixed using a planetary mixer and the pH was adjusted to 4-5 in order to obtain a well-flowing slip.

Slipcasting was carried out using plaster moulds. The green samples were dried in air and sintered in a graphite susceptor vacuum furnace[4] at 1600°C for 2 hours. Infrared spectra were obtained using an FT-IR spectrometer[5]. Samples of SiC fibers, whiskers and composites were analyzed in the form of KBr pellets or Nujol mulls.

[1] Reynolds RC-HP-DBM., [2] Nicalon fibers, diameter 10 μm and length 1 mm, supplied by DOW Chemicals, U.S.A. , [3] Tateho SCW 1-S-1, diameter 0.5-1.5 μm and length 5-20 μm, supplied by the I.C.D. group, New York, [4] Balzers type VSG 02 [5]BOMEM Model DA 3.0.
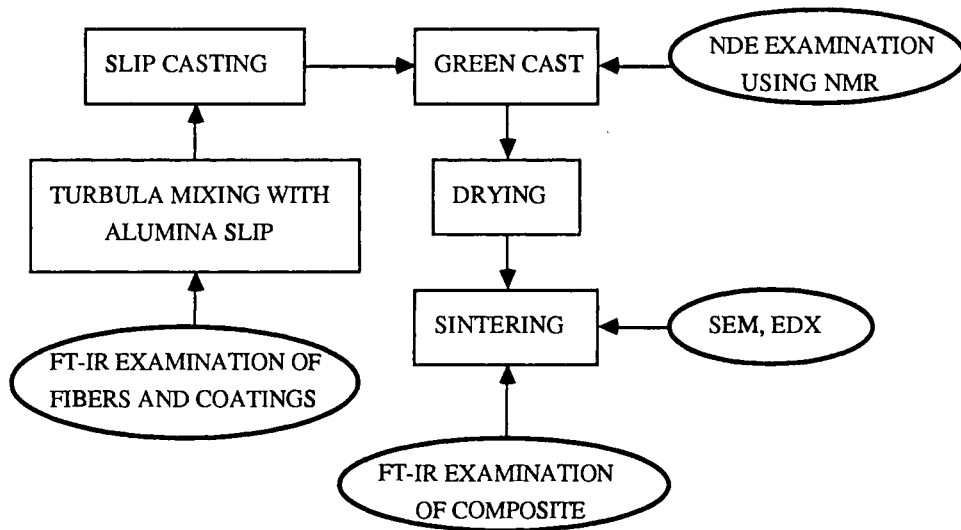
Fig. 1.   Fabrication and Characterization of Ceramic Matrix Composites

Results and Discussion

Infrared spectroscopy provides a simple and useful method of measuring the extent of oxidation of SiC fibers or whiskers. The absorption bands of SiO_2 and SiC -are sufficiently far apart that each band can be measured in the presence of the other. A quantitative method to determine the extent of oxidation from the areas of these bands has been reported [6].

The SiC fibers exhibit high strength and high modulus, however, they contain significant quantities of oxygen in the form of silica (SiO_2) since they are made from polymer precursors which contain oxygen in additon to silicon and carbon. Chemical analysis and FT-IR examination showed that the fibers used in this study contained 21% SiO_2 and 11.7% free carbon. The silica content of these fibers, however, changes during heat-treatment. The fibers heat-treated to 1000 °C for 2 hours in vacuum lost most of the SiO_2 coating exposing the SiC to oxidation. However, rapid heat-treatment of the alumina-SiC fiber composite in the initial stages of the sintering process results in the retention of the SiO_2 coating of the fibers (Fig. 2). Since most of the fiber damage takes place before the sintering of the matrix rapid heat-treatment at this stage minimizes this effect. In addition the loss of surface silica and further damage of the fibers are eliminated once the matrix starts sintering around them.
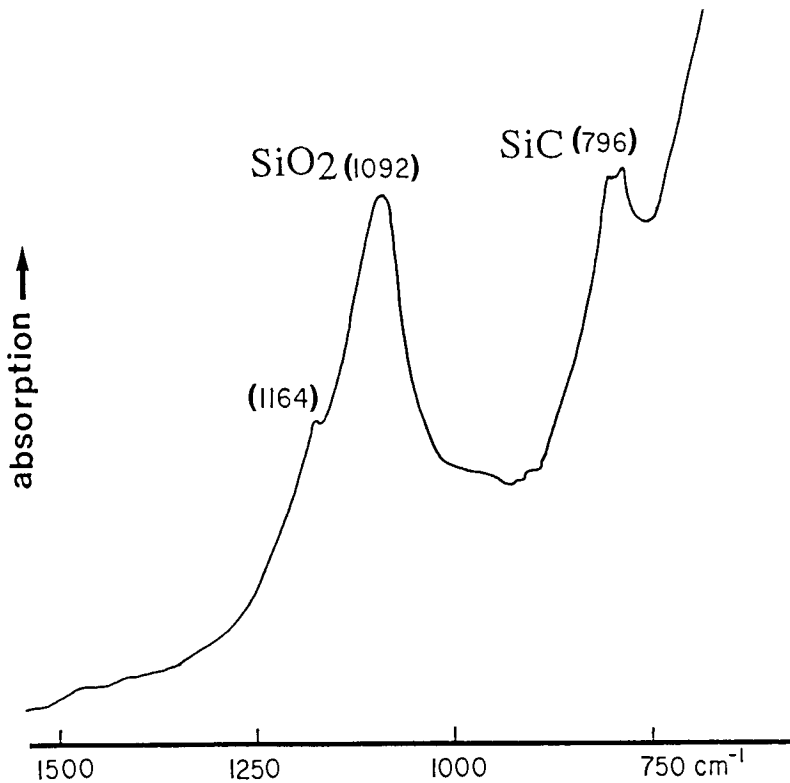
Fig.2.   FT-IR Spectrum of SiC Fiber-Reinforced Alumina

SiC whiskers are derived from rice husks and contain very low amounts of silica compared to the SiC fibers. FT-IR examination of the whiskers used in this study showed that they contained <1% of SiO_2. However, the silica content of these whiskers increased during the sintering process to about 40 %. As described earlier, the green bodies of these composites were slip cast from slurries containing total solids of 60%w and therefore were significantly porous. The large surface area of the whiskers and the lack of protection from the small amount of silica coating present on them make the whiskers susceptible to oxidation by the air remaining in the green body in the presintering stages.   In addition, some areas of the composites showed the presence of cages of whiskers formed due to agglomeration of whiskers during the slip casting process (Fig. 3). In addition to being strength reducing flaws in the sintered composite these agglomerates would increase the amount of air trapped in the green body. Therefore, to reduce oxidation of the whiskers during sintering process the green bodies should be fabricated with higher density. The use of dense slurries to obtain higher green density and the use of dispersants to prevent whisker agglomeration are presently being investigated for this purpose.

The thermal stability of the SiC whiskers is an important aspect for the practical application of the whisker-reinforced ceramics. However, an examination of SiC whisker-reinforced alumina after heat-treating in air at 1000 °C showed that the core of the whiskers became hollow during the heat-treatment (Fig. 4). High-resolution electron microscopic studies [7] on the morphology of the SiC whiskers have shown that the core of the whiskers contained cavities of 1-20 nm in diameter filled with silicon oxycarbides such as Si_2C_2O which decompose according to :

$$Si_2C_2O \;=\; 2\,SiO_{(g)} \;+2\,C$$

The cavities in the core of the whiskers join during the thermal degradation to form the hollow core. The formation of holes in the core of the whiskers would inevitably reduce their strength and reduce the life of the components made from these composites.
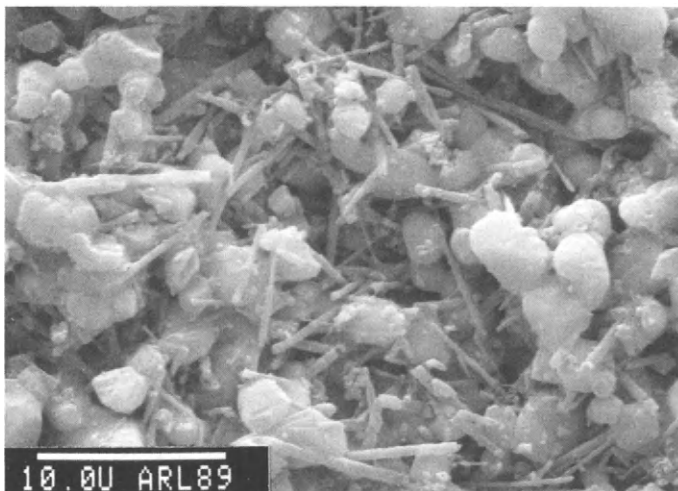
Fig. 3. Whisker-Cage Formed in the Composite
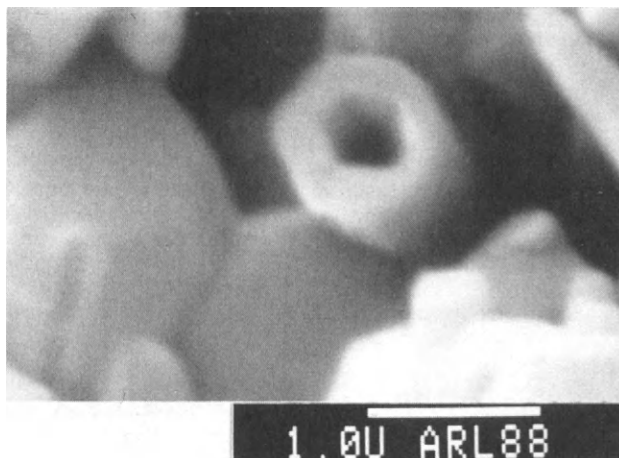
Fig. 4. Cross-Section of a SiC Whisker after the Heat-Treatment of the Composite

Conclusion

The chemical processes described in this paper indicate the necessity of careful processing of the ceramic matrix composites. In addition, evaluation of the materials with respect to their chemical degradation during fabrication and in service will play an important role in the life-prediction of industrial ceramics.

Acknowledgments

The author is grateful to Dr. M. Falk for the use of FT-IR spectrometer , Mr. C. Reithmeier for taking the electron micrographs and Dr. S.G. Whiteway for reviewing this manuscript.

References

1. J.J. Mecholsky, " Engineering Needs of Advanced Ceramics and Ceramic-Matrix Composites" Amer. Ceram. Bull. **68**, 367-375 (1989).
2. W.B. Hillig, "Strength and Toughness of Ceramic Matrix Composites" Ann. Rev. Mater. Sci., **17** , 341-83 (1987).
3. D.C. Cranmer, "Fiber Coating and Characterization", Amer. Ceram. Bull. **68**, 415 -419 (1989).
4. R.J. Kerans, R.S. Hay, N.J. Pagano and T.A. Parthasarathy, "The Role of the Fiber -Matrix Interface in Ceramic Matrix Composites", Amer. Ceram. Bull. **6**, 429-442 (1989).
5. S. Karunanithy, "Chemical Processes that Degrade Composites of Alumina with SiC Whiskers", Mater. Sci. Eng. **A109** (1989) in press.
6. M. Falk and S. Karunanithy, "Determination of SiO_2 in SiC Whiskers by Infrared Absorption Spectroscopy", Mater. Sci. Eng. **A109** (1989) in press.
7. S.R. Nutt, "Microstructure and Growth Model for Rice Hull-Derived SiC Whiskers", J. Am. Ceram. Soc. **71**, 149-156 (1988).

Fabrication of Ni_3Al/Al_2O_3 and Ni/Al_2O_3 composites by pressure casting

S. Nourbakhsh, F.L. Liang and H. Margolin

Department of Metallurgy and Materials Science, Polytechnic University, 333 Jay Street, Brooklyn, New York 11201, U.S.A.

ABSTRACT

Pressure casting has been used to fabricate composites of commercial Ni_3Al (IC50) and Ni reinforced with continuous Zirconia Toughened Alumina fibers, DuPont's 20 μm diameter PRD-166 fibers. To assist infiltration of the fibers by the molten metals small amounts of Y was added to the metals. The microstructure of the as cast composites has been characterized by means of optical and analytical TEM. Addition of 1 at% Y to commercial Ni_3Al resulted in an extensive fiber/matrix reaction during initial stages of infiltration and also in the formation of secondary phases, in the matrix, at or close to the fiber/matrix interface. No secondary phases were observed, in either Ni_3Al or Ni, when the amount of Y addition was reduced to 0.7 at%. The fiber/matrix interface of Ni_3Al-0.7Y composites was delineated with a very thin layer of Zr rich phase, probably ZrO_2. No such layer was observed when Ni was used as the matrix.

KEYWORDS

Composite processing; Pressure casting; High temperature composites; Intermetallic composites; Zirconia Toughened Alumina fiber; Wetting; Ni_3Al; Interface strength; Fiber/matrix reaction.

INTRODUCTION

The key to the development of more efficient, durable, light weight heat engines lies, mainly, in the use of high temperature, high strength and low density materials. Continuous ceramic fiber reinforced intermetallic matrix composite materials are being considered as potential replacements for the currently employed nickel based superalloys. Several techniques are now being used to fabricate intermetallic composites. These include powder metallurgy (Bose and co-workers , 1988; Bose and German, 1988; Povirk and co-workers, 1988; Viswanadham, Mannan and Sprissler, 1987), diffusion bonding (Brindley, 1987; Baumann, Brindley and Smith, 1989), plasma spraying (Spriggs and co-workers,1989) and pressure casting (Nourbakhsh, Liang and Margolin, 1988a). Pressure casting has several distinct advantages over the other techniques. It is relatively simple and economical. There are no limitations on the shape and size of the parts. It allows incorporation of various arrangements of fibers into the matrix; unidirectional; bidirectional; woven; matted and random arrangements of fibers. There is no limitation on the diameter of the fibers.

Pressure casting involves penetration of molten metal into the cavities between preheated fibers in the fiber preform. Exposure to high temperatures and to the molten metal may severely alter the microstructure of the fiber and degrade its mechanical properties or result in an extensive chemical reaction between the fiber and molten metal. These disadvantages have limited the use of pressure casting as an effective method for

producing fiber reinforced metal-matrix composites to low melting temperature matrices such as Al and Mg alloys (Mortensen, Cornie and Flemings, 1988).

Fiber/matrix reaction and fiber degradation can be minimized or totally eliminated by reducing the processing time and temperature. Recently a pressure casting apparatus has been designed and successfully used to fabricate high temperature metal-matrix composites (Nourbakhsh, Liang and Margolin, 1988a). The aim of this paper is to report on the microstructure of pressure cast Ni and Ni_3Al reinforced with continuous Zirconia Toughened Alumina (ZTA) fiber.

FIBER

The fiber employed in the investigations was DuPont's, 20 μm diameter, PRD-166 fiber. PRD-166 fiber contains about 20 wt% partially stabilized ZrO_2 and 80 wt% α-Al_2O_3. The grain sizes of ZrO_2 and Al_2O_3, using TEM, were determined to be 0.15 and 0.3 μm, respectively (Nourbakhsh, Liang and Margolin, 1989a). As can be seen in Fig. 1, the ZrO_2 grains, the dark grains, are uniformly dispersed among α-Al_2O_3 grains. The incorporation and dispersion of partially stabilized ZrO_2 in Al_2O_3 has not only improved the tensile strength of the fiber as compared with the plain α-Al_2O_3 fiber, Fiber FP (Romine, 1987), but has also vastly enhanced the temperature resistance of the fiber as manifested by the lack of Al_2O_3 grain growth upon short exposures to high temperatures during processing (Nourbakhsh, Liang and Margolin, 1989a).
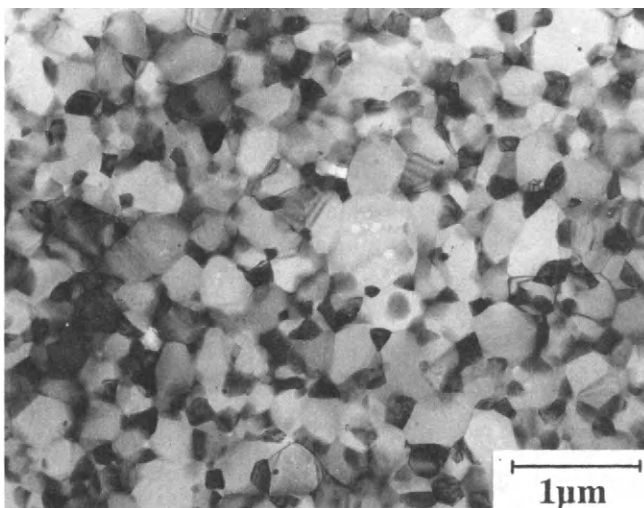
Fig. 1. TEM showing the microstructure of PRD-166 fiber

MATRICES

Initially, pure Ni and commercial Ni_3Al, known as IC50, were used. In both cases, although a gas pressure of about 400 psi was used, the fiber preform could not be infiltrated. The lack of infiltration has been attributed to a high contact angle, θ, between the molten Ni or

Ni₃Al and the fiber. The required minimum pressure for infiltration of a fiber array by molten metal has recently been calculated (Nourbakhsh, Liang and Margolin, 1989b). The analyses indicted a linear relationship between the required pressure for infiltration and the cosine of the contact angle, θ. The contact angle between Ni and Al₂O₃ has been reported to lie in the range 108-111° in vacuum or oxygen free atmosphere (Levitt and Wolf, 1970; Ritter and Burton, 1967). With a contact angle lying in this range, a large drop in the required pressure is expected with a small reduction in the contact angle. One way of reducing the contact angle is to add a suitable alloying element to the metal. Coating of fibers with a suitable material is another alternative, although it may not be as simple and, therefore, cost effective as the alloying addition route.

Several alloying additions, all strong oxide formers, were tried (Nourbakhsh, Liang and Margolin, 1988b). The effectiveness of the alloying addition is judged by the extent of the molten metal infiltration. A Ti addition of 1.2 at% has been observed to be the most effective addition. Although addition of Ti to both Ni and Ni₃Al allowed infiltration of the fiber preform by the molten alloy, it did not produce a strong bond between Ni₃Al and the fibers (Nourbakhsh, Margolin and Liang, 1989). The bond strength between Ni and the fibers, in comparison, was judged to be high. It should be noted that the measurement of interface bond strength is only qualitative and is judged by observing the extent of fiber/matrix interface cracking that occurred during thin foil preparation for transmission electron microscopy observations. Due to severe interface decohesion, during thin foil preparation, no suitable TEM samples from Ni₃Al (IC50) composites could be prepared. Consequently, the fiber/matrix bond strength in Ni₃Al (IC50) composites was judged to be weak. Conversely, no interface cracking has been observed in TEM samples of the Ni composite.

In order to improve the interface bond strength in the Ni₃Al composites attention has been diverted to another alloying addition, Yttrium.

PROCESS

The schematic of the technique employed to fabricate the high temperature ceramic fiber reinforced Ni and Ni₃Al composites is shown in Fig. 2. The metal to be cast is placed inside a bottom pour crucible positioned on top of a ceramic mold containing the fiber preform. The metal and the fiber preform are heated simultaneously but independently, under vacuum inside a chamber, to temperatures above the melting temperature of the matrix. Once the preselected temperatures are reached, the molten metal is poured over the fibers. Application of high pressure inert gas, Ar, forces the molten metal to infiltrate the gaps between the fibers (Nourbakhsh, Liang and Margolin, 1988a).

EXPERIMENTAL PROCEDURE

A series of Ni and Ni₃Al (IC50) composites reinforced with continuous PRD-166 fibers were prepared by the pressure casting technique previously described. The composition of the matrices employed are shown in Table 1. The intermetallic compound, Ni₃Al (IC50), used in this research was obtained from Armco. The wetting agent,Y, was prealloyed with Ni, using vacuum arc melting, to form a master alloy containing 50 wt%Y. The master alloy, in appropriate amounts, was subsequently placed between Ni or Ni₃Al blocks in the melt crucible prior to melting. The prealloying of Y with Ni was an attempt to minimize Y loss due to oxidation during composite processing. The composition of the master alloy was selected such that both the Ni or Ni₃Al and the master alloy have similar melting temperatures.

Table 1   Composition of the Alloys (at%)

Materials	Al	Y	Zr	B	Ni
Ni_3Al-1Y	23.6	1	0.07	1	Bal.
Ni_3Al-0.7Y	23.8	0.7	0.07	1	Bal.
Ni-0.7Y	-	0.7	-	-	Bal.

PRESSURE

MELT

COMPOSITE

PREFORM
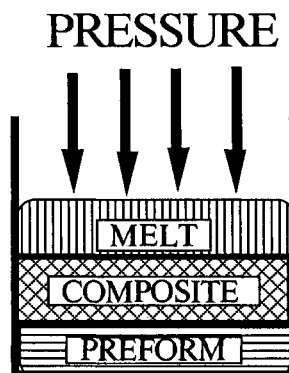
Fig.2. Schematic of the technique

Fig. 3 is a plot of fiber and metal temperatures as a function of processing time for the Ni_3Al-0.7Y composites. Also shown is the applied pressure as a function of time. The arrow, in Fig. 3 marks the time at which the molten metal is poured onto the fibers. The melt crucible and the mold, which were made of high purity Al_2O_3 had been coated, prior to use, with a thin layer of Y_2O_3 to minimize metal/container reaction. The composites fabricated were in the form of disks 54 mm in diameter and 15 mm thick with fibers lying parallel to the face of the disks.

For optical microscopy, samples were cut from the composite disks along a plane normal to the fiber axis. The samples were prepared for examination by grinding through 600 grit paper and were then polished with 1/4 µm diamond paste finished by polishing with 0.05 µm alumina. For transmission electron microscopy, 0.5 mm thick slices, taken normal to the fibers, were cut into 3 mm disks by using an ultrasonic cutter. The disks were then dimpled on both sides and subsequently ion milled under 6 KV to obtain perforation.

RESULTS AND DISCUSSION

The microstructure of Ni_3Al-1Y/PRD-166 composite is shown in Fig. 4. The micrograph is taken from an area from which the molten metal first entered the fiber preform. The molten metal on entering the fiber preform finds an easy path and pushes the fibers aside from its path, thus creating fiber free channels. Channeling is the characteristic of fiber/molten metal systems in which the wetting angle, θ, is larger than 90°, non-wetting systems. In wetting systems, the fibers are pulled into the molten metal by the unbalanced surface tensions and channeling, therefore, does not occur. The molten Ni_3Al-1Y alloy in creating the channels in the preform and passing through them reacts extensively with the fibers on each side of the

channel. Since the temperature of the fiber preform was kept below that of the molten metal, on infiltrating the preform the molten metal temperature and therefore its reactivity decreases. This explains the absence of a noticeable reaction between the molten metal and the fibers in regions away from the channels.
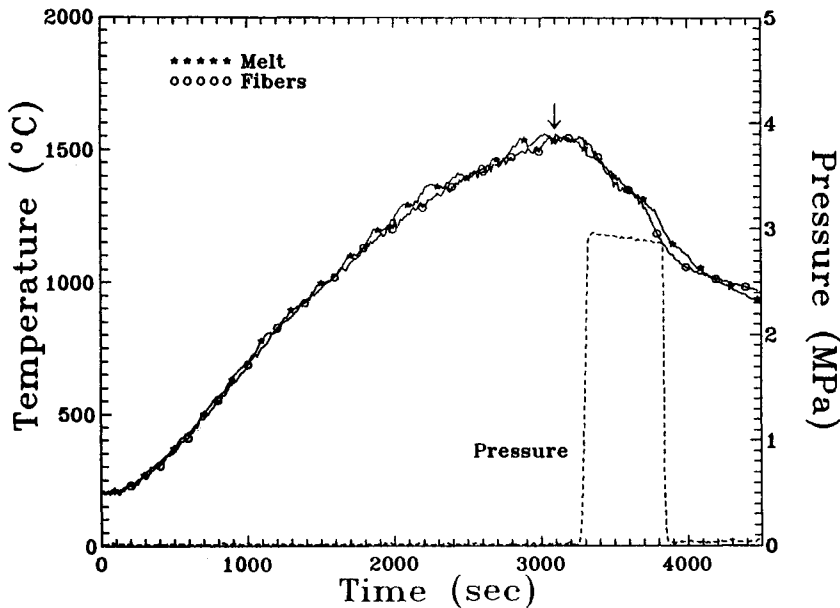
Fig. 3. A plot of fiber and melt temperatures and applied pressure versus processing time.

Also evident in Fig. 4 are second phases, marked by arrows, at the fiber/matrix interface or close to the interface in regions of the matrix away from the channels. The occurrence of second phases and their formation at the fiber/matrix interface is hypothesized to be due to a limited solubility of Y in solid Ni_3Al and the way the solidification takes place in the composite. The maximum solid solubility of Y in Ni_3Al is not known but in Ni, according to the equilibrium phase diagram, is about 0.1 at%. Although as much as 1 at% Y was used, it is expected that most of it was oxidized or reacted with fibers during infiltration. The amount which was remained in the molten metal was not fully soluble in the solid, as the solubility of Y in Ni_3Al is expected to be limited.

Since the thermal conductivity of the ceramic oxide fiber, PRD-166, is smaller than that of the molten Ni_3Al, solidification is expected, on cooling, to start in the center of the interfiber spaces. Due to a low solubility of Y in the solid, Y is rejected into the liquid as the solidification front moves toward the fibers. The Y concentration in the liquid increases progressively as solidification continues and eventually reaches that of the eutectic composition. Finally solidification takes place by the formation of eutectic in some regions of the fiber/matrix interface, the regions which solidifies last. It should be noted that no information regarding the ternary Ni-Al-Y phase diagram is available at present time and therefore the explanation put forward is speculative at this stage. Formation of eutectics at the fiber/matrix interface is highly undesirable as they limit both the efficiency of load transfer across the interface at low temperatures due to their brittleness and reduce the high

temperature capability of the composite due to their lower melting temperatures as compared with the matrix. As a consequence of these observations i.e. extensive fiber/matrix reaction in certain regions of the composite and formation of secondary phases, eutectic, at the interface, the amount of Y addition was reduced to 0.7 at% in subsequent experiments.
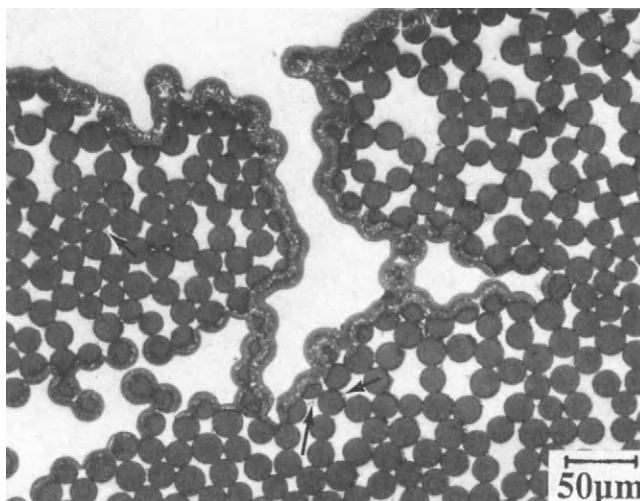
Fig. 4. Optical micrograph showing fiber/matix reaction along the fiber free channels in a Ni$_3$Al-1Y matrix composite. The arrows mark the secondary phases.

Figure 5 is an optical micrograph from a Ni$_3$Al-0.7Y/PRD-166 composite. As can be seen all the interfiber spaces are infiltrated. There is no evidence indicating fiber/matrix reaction or formation of secondary phases at the fiber/matrix interface. Preparation of thin foils for electron microscopy has been successful indicating that the fiber/matrix bond strength was sufficiently strong. No such foils could be prepared when Ti was used as the wetting agent. The microstructure of the composite as revealed by transmission electron microscopy is depicted in Fig. 6. The electron micrograph was taken from a strip of matrix between two fibers.

The matrix contains some dislocations which are most probably formed during cooling from high temperatures as a result of a thermal expansion mismatch between the fiber and Ni$_3$Al matrix. The crystal structure of the Ni$_3$Al matrix, using electron diffraction, was confirmed to be L1$_2$, Fig. 7. No antiphase boundaries or secondary phases, β-NiAl or disordered α, have been observed. Chemical microanalysis of the matrix indicated the absence of Y in the matrix, Fig. 8. The absence of Y bearing compounds and absence of Y in detectable amounts in the matrix suggests that most of the Y addition has been oxidized during melting. The amount which remained was sufficient to wet the fibers adequately.

Figure 6 also reveals the interface between the matrix and two fibers. Although the interface is well defined, there is a thin diffuse dark band, marked by arrows, delineating the interface. An EDX line scan across the interface indicated that the layer is a Zr rich layer containing no detectable amounts of Y. The layer is most likely a ZrO$_2$ layer.
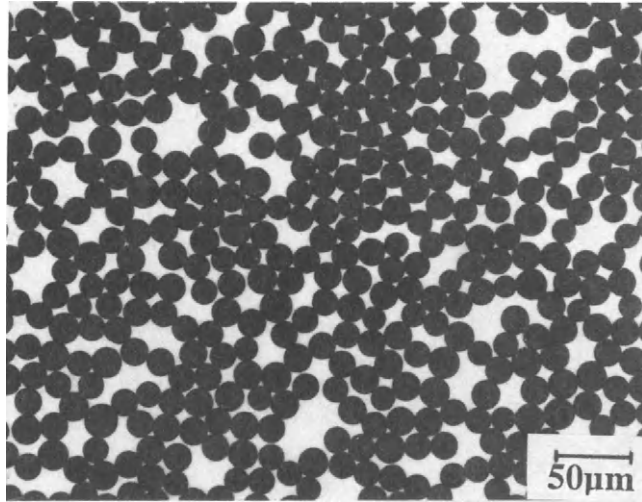
Fig. 5. Optical micrograph indicating the absence of fiber/matrix reaction in a Ni_3Al-0.7Y composite. No secondary phases are present.
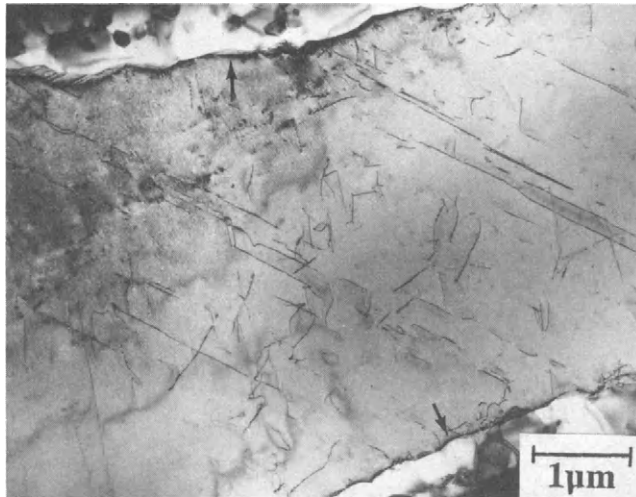
Fig. 6. Transmission electron micrograph showing the Ni_3Al-0.7Y/PRD-166 interface. The arrows mark the Zr rich dark layer delineating the interface.

Two plausible hypotheses concerning the formation of ZrO_2 at the fiber/matrix interface are proposed. The ZrO_2 particles which are close to the fiber surface are swept to the fiber surface by the migration of Al_2O_3 grain boundaries near the fiber surface during processing. Some of the ZrO_2 particles which fail to keep up with the pace of the migrating

boundaries are left behind in the form of spherical particles within the Al_2O_3 grains. As can be seen in Fig. 9 the size of Al_2O_3 grains at the interface is larger than those within the fiber. The micrograph also reveals the spherical ZrO_2 particles within the Al_2O_3 grains at the interface. The ZrO_2 particles reaching the fiber surface might wet the surface and spread on it. Spreading of ZrO_2 on the fiber surface can take place when;

$$\gamma_{ZA} + \gamma_{ZM} < \gamma_{AM} \tag{1}$$

where γ_{ZA}, γ_{ZM} and γ_{AM} are the surface energies of ZrO_2/Al_2O_3, $ZrO_2/matrix$ and $Al_2O_3/matrix$, respectively. The second mechanism involves reduction of Al_2O_3 by Zr, present in small amounts in the Ni_3Al (IC50) alloy, during processing, according to the following reaction;

$$3\, Zr + 2/3\, Al_2O_3 \rightarrow ZrO_2 + 4/3\, Al \tag{2}$$

This reduction reaction is feasible at temperatures below 1000 °C (Kubaschewski and Alcock, 1979), when the free energy of ZrO_2 formation becomes higher than that of Al_2O_3 formation.
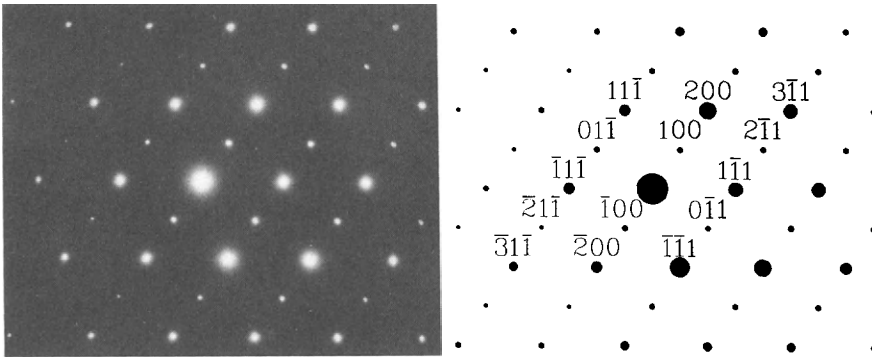
Fig. 7. SAD pattern from the Ni_3Al matrix. The superlattice spots, the weak spots, indicate that the matrix is ordered. Z.A. = [011]

In order to determine which mechanism was responsible for the formation of the ZrO_2 layer at the fiber/matrix interface, a series of casting experiments were carried out in which Ni-0.7Y was used. No interface reaction or secondary phases, eutectics, have been observed in the Ni-0.7Y/PRD-166 composites. The fiber/Ni matrix interface as revealed by TEM is shown in Fig. 10. The dotted background in the matrix is due to dislocation loops resulted from ion milling. EDX microanalysis indicated that no detectable amounts of Y was present in the matrix or Al_2O_3 grains at the fiber surface or at the fiber/matrix interface, similar to the observations made in the Ni3Al-0.7Y composites.

Apart from the ZrO_2 particles which were occasionally observed at the interface, no evidence concerning the existance of a thin layer of ZrO_2 or Zr bearing compounds could be obtained. This observation tends to support the latter mechanism. The ZrO_2 particles at the fiber/matrix interface, as mentioned earlier, are likely brought to the surface by the migration of near surface Al_2O_3 grain boundaries. The interface bond strength in Ni-0.7Y composites as judged by the lack of interface cracking in the TEM samples to be qualitatively higher than that in Ni_3Al-0.7Y composites. The formation of a thin layer of ZrO_2

in the Ni_3Al-0.7Y composites may be responsible for the higher fiber/matrix bond strength as compared with Ni_3Al-1.2Ti composites. The Ti that existed in the matrix might have dissolved away the ZrO_2 layer, once formed, and prevented a strong bond to form. In a previous research in which TiAl was used as the matrix, a substantial dissolution of ZrO_2 from the fiber in the molten TiAl has been observed (Nourbakhsh, Liang and Margolin, 1989c).
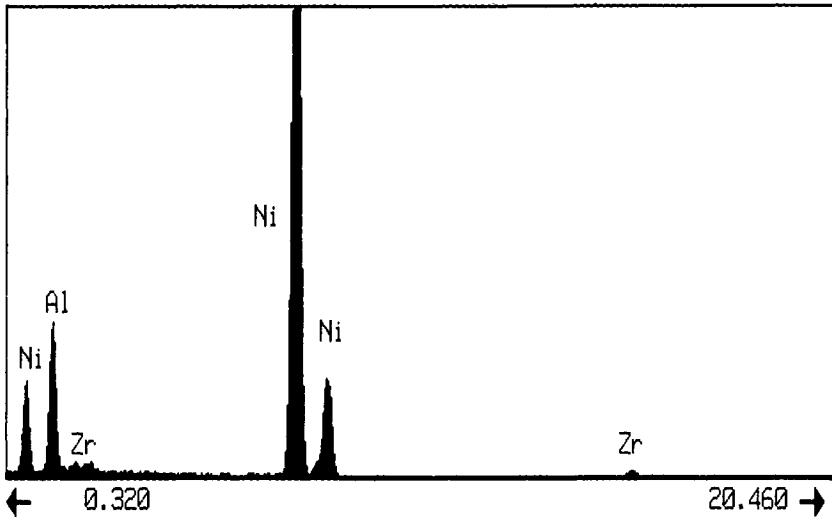
Fig. 8. Energy dispersive X-ray spectra from the Ni_3Al matrix.
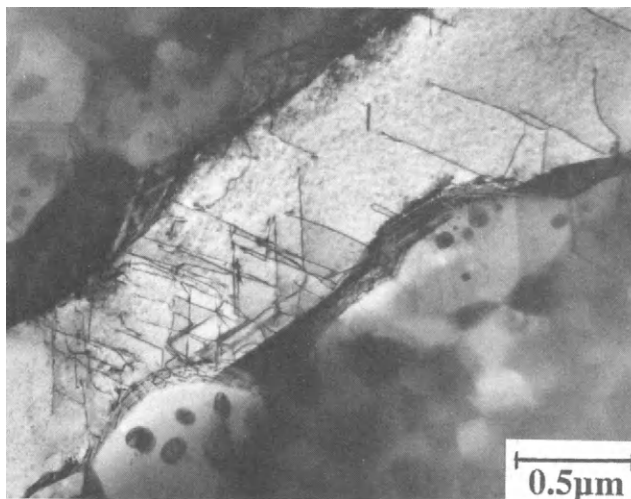
Fig. 9. TEM from a Ni_3Al-0.7Y/PRD-166 composite revealing the spheroidized ZrO_2 particles within the large Al_2O_3 grains at the interface.
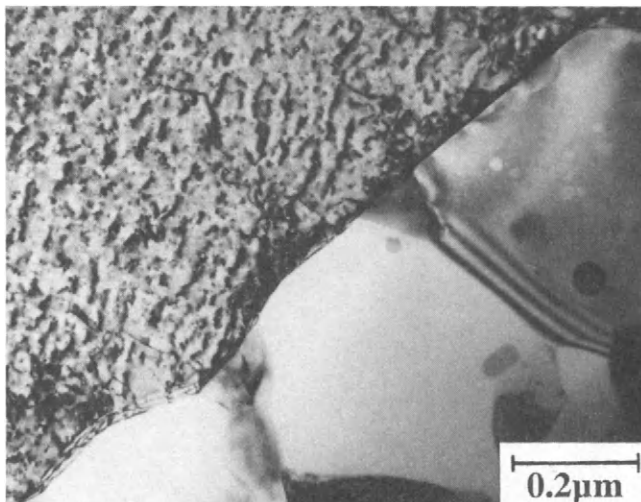
Fig. 10. Transmission electron micrograph showing the Ni-0.7Y/PRD-166 interface.

SUMMARY

A series of Zirconia Toughened Alumina (ZTA) fiber, DuPont's PRD-166, reinforced Ni and Ni$_3$Al composite materials have been successfully fabricated by pressure casting using Y as the wetting agent. Addition of 1 at% Y to the alloys, prior to melting, resulted in extensive fiber/matrix reaction in regions where molten metal first entered the fiber preform and also in the formation of secondary phases, most likely eutectics, at some regions of the fiber/matrix interface. No secondary phases were observed when the amount of Y was reduced to 0.7 at%. The fiber/matrix interface in Ni$_3$Al composites was delineated with a thin layer of Zr rich compound, probably ZrO$_2$. Such a layer was absent in Ni composites. In both composites, Ni-0.7Y and Ni$_3$Al-0.7Y, no evidence for diffusion of Y into the fibers or formation of Y bearing compound at the fiber/matrix interface has been obtained.

REFERENCES

Baumann, S.F., P.K. Brindley, and S.D. Smith (1989). Met. Trans. A, In Press.
Bose, A., R.M. German (1988). Advanced Materials and Manufac. Processes, 3(1), 37.
Bose, A., B. Moore, R.M. German, and N.S. Stoloff (1988). J. Metals, 40(4), 14.
Brindley, P.K. (1987). In C.C. Koch, C.T. Liu and N.S. Stoloff (Eds.), High Temp. Ordered Intermetallic Alloys II, MRS Symp. Proc., 81, 419.

Kubaschewski, O., and C.B. Alcock (1979). Metallurgical Thermochemistry, 5th Edition, Pergamon Press.

Levitt, A.P., and S.M. Wolf (1970). In A.P. Levitt (Ed.),Whisker Technology, Wiley-Interscience, 245.

Mortensen, A., J.A. Cornie, and M.C. Flemings (1988). J. Metals, 40(2), 12.

Nourbakhsh, S.N., F.L. Liang and H. Margolin (1988a). J. Phys. E: Sci. Instrum., 21, 898.

Nourbakhsh, S.N., F.L. Liang, and H. Margolin (1988b). Advanced Materials and Manufac. Processes, 3(1), 57.

Nourbakhsh, S.N., F.L. Liang, and H. Margolin (1989a). J. Mater. Sci. Lett., In Press.

Nourbakhsh, S.N., F.L. Liang, and H. Margolin (1989b). Met. Trans. A., In Press.

Nourbakhsh, S.N., F.L. Liang, and H. Margolin (1989c). Met. Trans. A., Submitted.

Nourbakhsh, S.N., H. Margolin, and F.L. Liang (1989). Met. Trans. A., In Press.

Povirk, G.L., J.A. Horton, C.G. McKamey, T.N. Tiegs, and S.R. Nutt (1988). J. Mater. Sci., 23, 3945.

Ritter, R.E., and M.S. Burton (1967). Trans. Met. Soc. AIME, 239, 21.

Romine, J.C. (1987). Ceramic Engineering and Science Proceedings, 8 , 755.

Spriggs, D., P. Siemers, A. Ritter, L. Davis, and S. Rutkowski (1989). High Temperature Intermetallic Symp., San Fernando Valley ASMI.

Viswanadham, R.K., S.K. Mannan, and B Sprissler (1987). Martin Marietta Corporation, MML TR 87-66C.

The effect of heat treatments on the resistance of aluminum metal matrix composites produced by squeeze-casting

S. Turenne and J. Masounave

Industrial Materials Research Institute, National Research Council Canada, 75 de Mortagne Blvd., Boucherville, Québec, Canada, J4B 6Y4

ABSTRACT

The aim of this study is to improve the understanding of the effect of reaction products at the interface between the fiber and the matrix on mechanical properties. The samples were made by squeeze-casting, using Al_2O_3-SiO_2 preforms as a reinforcement for two aluminum alloys. Following the sample preparation, some samples were heat treated in order to produce a reaction at the alloy-fiber interface. There were different reaction zone thicknesses corresponding to the different heat treatments. Fractographic examinations were done to observe the fracture behavior of the matrix and fiber phases after mechanical testing. These observations suggest the importance of good bonding at the interface between the fiber and the matrix with or without reaction products.

KEYWORDS

Metal Matrix Composites, Squeeze-Casting, Preform, Fractography, Interface.

INTRODUCTION

The enhancement of mechanical properties brought about by fibers in metal matrix composites is mainly due to load transfer from the matrix to the rigid reinforcement. This load transfer is efficient only if the shear strength of the interface region is equal or larger than that of the matrix. To control the quality of the interface, a lot of fabrication conditions related to squeeze-casting have to be taken into account.

The most important parameter is the choice of the alloy. It was already demonstrated that the use of low concentration of magnesium or lithium in aluminum alloys improves the wetting of fiber by the alloy and, consequently, the bonding of the interface (Clegg and co-workers, 1988; Johnston and Greenfield, 1988; Kobayashi and co-workers, 1988). Different techniques to avoid air entrapment are sometimes necessary for good bonding. Again the use of magnesium helps to improve the wetting, even if gas is entrapped. Taftø and co-workers (1988) used a technique based on selfgeneration of vacuum caused by a reaction between magnesium and entrapped oxygen. The effect of pressure during squeeze-casting is known to result in a better adhesion between the matrix and the fibers (Kobayashi and co-workers, 1988). Finally, the time of solidification is also important because it controls the time the fibers are exposed to liquid metal and thus the amount of reaction products at the interface (Das, Clegg and Zantout, 1988).

Following the fabrication procedure, it is possible to modify the nature of the interface by means of heat treatments. The goal of this study is to evaluate qualitatively the effect of heat treatment on mechanical properties.

MATERIALS

The tensile samples were made of two types of aluminum alloy. The aluminum alloy 5083 contains about 4 to 5% of magnesium which is known to improve the wettability of ceramic fibers.

The other alloy employed is the A380 which contains mainly about 8% of silicium and 3,5% of copper. The chemical compositions of these two alloys are given in Table 1. The melting ranges for the alloy 5083 and A380 are 574-638°C and 545-600°C respectively.

TABLE 1 Principal Element Contents for the Aluminum Alloys Used

Alloy	Mg	Si	Cu	Fe	Mn
5083	4,0-4,9	0,40	0,10	0,40	0,4-1,0
A380	0,10	7,5-9,5	3,0-4,0	1,3	0,50

note: the single values represent maximum limits.

Metal matrix composites based on these two alloys were made by infiltrating preforms of Kaowool fibers (53% Al_2O_3, 47% SiO_2) containing 15% fibers by volume unless otherwise mentioned. The fibers are randomly oriented in a planar arrangement and are bond together by means of an inorganic binder.

EXPERIMENTAL PROCEDURE

Squeeze-casting

Samples were fabricated by squeeze-casting of the alloys in a mold which had the shape of tensile specimens. To obtain aluminum matrix composites, the pre-heated preforms were placed in the mold prior to the pouring of liquid metal and application of the load. The detailed procedure is described elsewhere (Turenne and co-workers, 1988). The experimental conditions for the aluminum alloys and for composites are given in Table 2. Some disc-shaped samples were made in order to observe the effect of different heat treatments on the microstructure of composites made of 5083 alloy. For these specimens, the larger dimensions of the disc mold (38,1 mm diameter) as compared to tensile specimen have the advantage that preforms can be used without pre-heating due to the lower surface to volume ratio corresponding to a lower cooling rate. Also, because the cooling rate is a function of the difference between the temperature of the alloy and that of the mold, it was necessary to use a higher temperature of the mold for the squeeze-casting of 5083 alloy because of its higher liquidus temperature. The temperature of the alloy given in Table 2 is measured in the crucible before transportation in a cup from the crucible to the mold. Thus the temperature of the alloy when being poured in the mold is not know exactly.

TABLE 2 Experimental Conditions for the Squeeze-Casting of specimens

Specimen	Pressure (MPa)	Application of the load (s)	Temp. of the mold (°C)	Temp. of the alloy (°C)	Pre-heating of preforms (°C)
5083 and 5083 composites	100	0,3	400	800-810	500
A380 and A380 composites	20,40	0,3	300	775-810	500
disc-shaped 5083	100	0,5	300	800-820	no

*For all the squeeze-cast specimens, the load was maintained during 10 s.

Preliminary tests with our experimental set-up showed that a pressure of nearly 20 MPa is large enough to obtain sound specimens with no shrinkage of samples causing porosity.

After the sample preparation, some of them were heat-treated at different temperatures depending on the aluminum alloys. The heat treatments were done in a tubular furnace under argon atmosphere. After this, the samples were water-quenched at room temperature. For the 5083 disc-shaped samples, the following heat treatments were performed:

      1) 5 hours at 200°C
      2) 3 hours at 450°C
      3) 2,5 hours at 550°C

The aluminum 5083 and 5083-composites tensile specimens were heat-treated following the third treatment. Because 550°C is within the melting rage of the A380 alloy, a heat treatment at 520°C during 2 hours was chosen for this alloy.

Tensile Tests

Prior to the tensile tests, the specimens were polished with 600 grit SiC abrasive paper. The rectangular section of tensile specimens had a width of 10 mm and a thickness varying from 4,5 to 7,1 mm. The gauge length was 50 mm. The tensile tests were done with the help of a servohydraulic MTS machine. The tests were stroke controlled with a displacement rate of 1 mm/min. The samples which showed macroscopic foundry defect on fracture surface were not considered in this study. The amount of tensile tests made allow for qualitative considerations only when comparing different materials.

RESULTS

Effect of Heat Treatments on Microstructures

The microstructures of the alloys and related composites were observed under the optical microscope following final sample polishing with 1 μm diamond paste and etching in some cases. The microstructures of the alloy A380 prior to and after the heat treatment at 520°C are shown in Figs. 1a and 1b. The modification of the Si-rich phase from acicular to spheroid did not happened for the Cu-rich phase. The transformation for the composites made of A380 alloy is similar to transformation of the alloy. The effect of heat treatment on A380 composites is shown in Figs. 2a and 2b. The Si-rich phase underwent transformation to spheroids in the same way as for the unreinforced alloy. This second phase did not tend to surround ceramic fibers. The effect of heat treatment at 550°C on alloy 5083 containing Mg is totally different. Figs. 3a and 3b illustrate the fact that the Mg-rich phase is concentrated around the fibers. The tendency to "wet" the fibers is greater than in the case of A380 alloy where the Si-rich second phase has large "wetting" angles (Fig. 2b).

To observe the evolution of the interface of composites made from alloy 5083, heat treatments at different temperatures were done on disc-shaped samples. Strong etching with Flick reagent was necessary to reveal the reaction product at the interface. The interface layer is visible in Figs. 4b and 4c. The heat treatment at 200°C did not permit the formation of a thick observable layer at the interface (Fig. 4a). The thickness of the layer is more important for the heat treatment at a higher temperature. For the 5083 alloy, the presence of fibers modifies the evolution of the structure of the matrix.
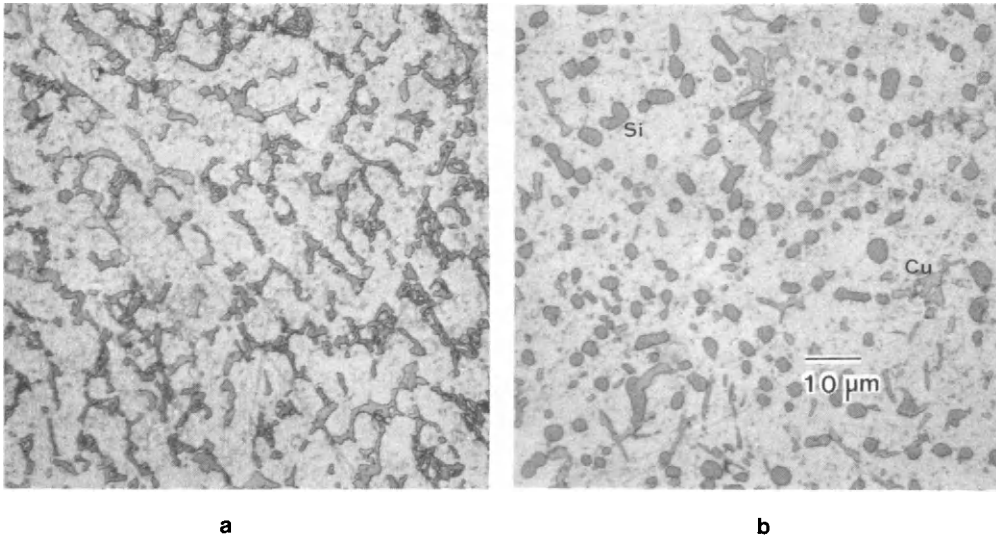
Fig. 1. Microstructures of A380 alloy a) before and b) after heat treatment at 520°C during 2 hours. The Si-rich phase is spheroidized during heat treatment.
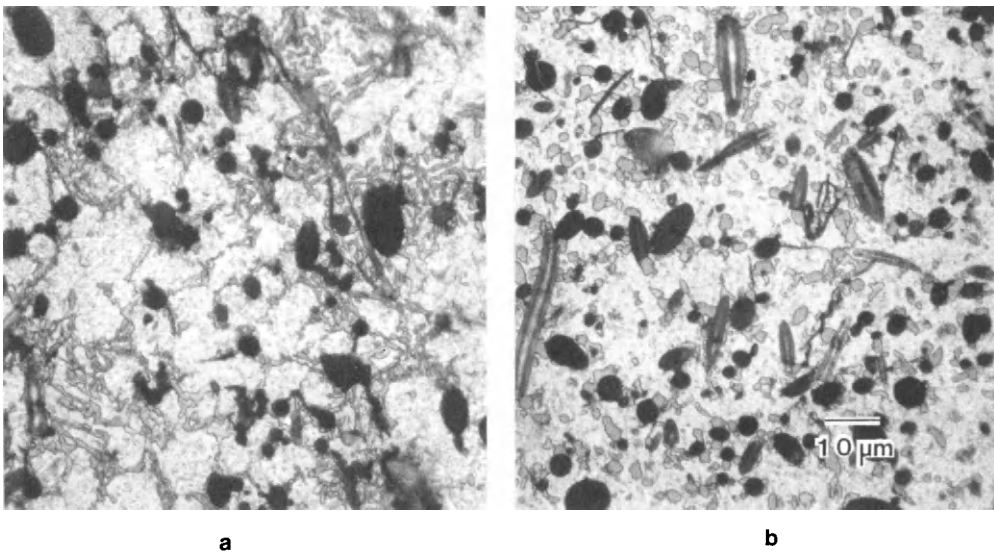
Fig. 2. Microstructures of 15 vol% Al_2O_3-SiO_2/A380 alloy composites a) before and b) after heat treatment at 520°C during 2 hours. The matrix microstructure modification is about the same as the unreinforced alloy.

a   b
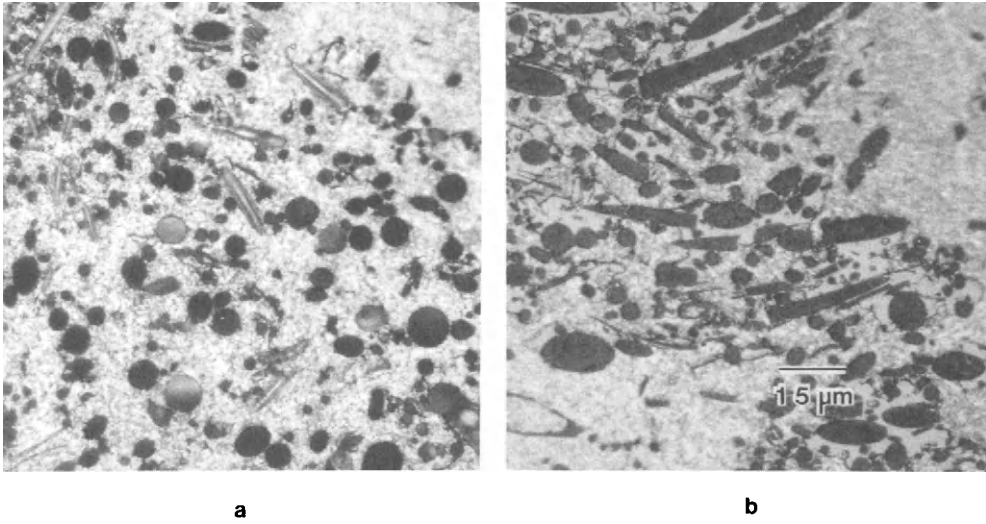
Fig. 3.   Microstructures of 15 vol% Al_2O_3-SiO_2/5083 alloy composites a) before and b) after heat treatment at 550°C during 2 1/2 hours. After heat treatment, the Mg-rich phase surrounds Kaowool fibers.

a   b   c
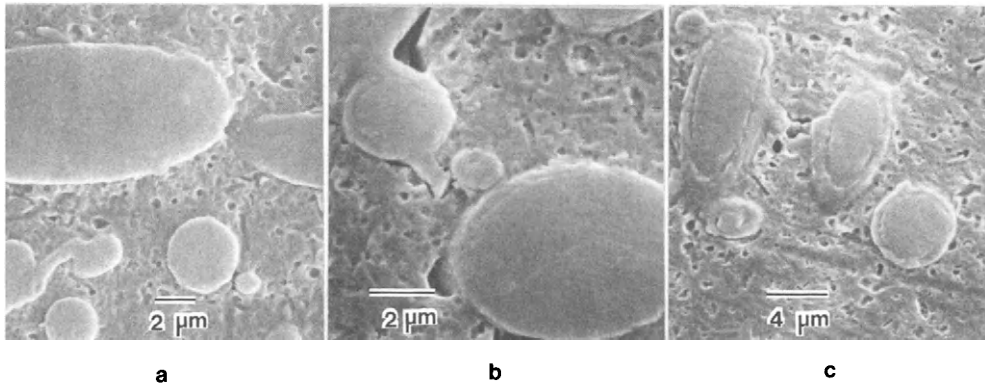
Fig. 4.   Microstructures of 10 vol% Al_2O_3-SiO_2/5083 alloy composites after different heat treatments: a) 5 hours at 200°C b) 3 hours at 450°C and c) 2 1/2 hours at 550°C. The surfaces have been etched with Flick reagent to reveal the reaction product at the interface.

Tensile Test Results

The mechanical properties of squeeze-cast specimens are given in Table 3. The large range given for ultimate tensile strength is due to the small amount of tests; thus these values should not be used to characterize the composite materials made with the alloys considered in this study. Nevertheless, one can observe that the presence of reinforcement do not improve substantially the tensile strength. Also, the heat treatment did not change the mechanical properties of the 5083 alloy, but this is not the case for A380 alloy where yield strength and ultimate tensile strength are increased. For 5083 alloy, the presence of fiber decreased the elongation at rupture; for A380 alloy elongation at rupture remains low with or without reinforcement. The elastic modulus for all these materials is about 71 GPa.

TABLE 3 Mechanical Properties of Squeeze-Cast Al Alloys and Composites

Materials	Yield strength (MPa)	U.T.S. (MPa)	Elongation (%)
5083 alloy	127	200-221	3,7-4,2
Heat treated 5083	127	206-245	3,2-6,2
5083 composite	95	189-196	1,1-1,2
Heat treated 5083 composite	122	136-180	0,4-0,6
A380 alloy	130	205	1,1-1,3
Heat treated A380	206	255	0,9
A380 composite	152	163	0,3
Heat treated A380 composite	165	187-243	0,3-1,1

Fracture Surfaces

To obtain qualitative information on the effect of heat treatments on mechanical properties, the fracture surfaces were observed with the scanning electron microscope. Confirming the results of the mechanical tensile tests, there was no difference in the fracture surface of the 5083 alloy before and after heat treatment. However, for the A380 alloy, there are some characteristics of quasi-cleavage for as-cast fracture surface which are absent after heat treatment. Figure 5a illustrates quasi-cleavage regions and limited dimple formation. The amount of dimple is higher after heat treatment but these ones are smaller; the elongation after rupture is also lower for heat treated A380 alloy.

a   b
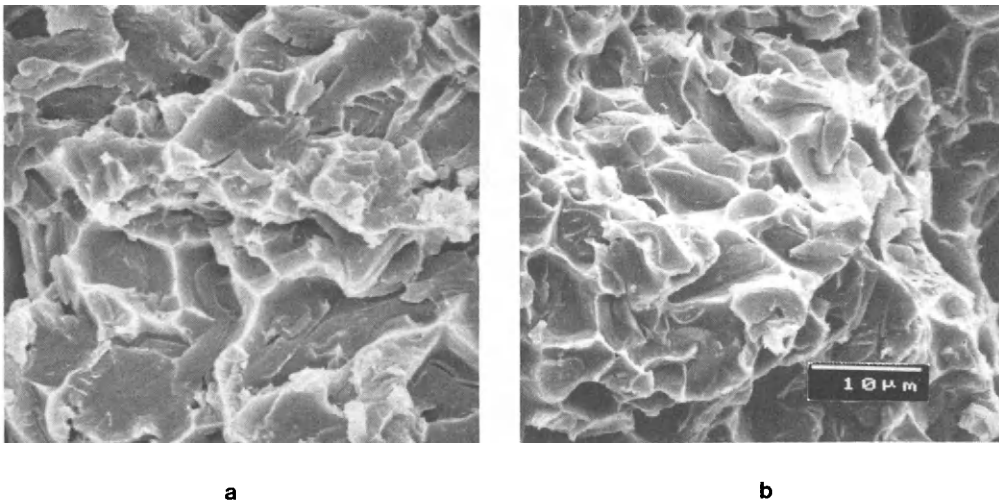
Fig. 5.   Fracture surfaces of A380 alloy a) before and b) after heat treatment at 520°C during 2 hours.

The comparison of fracture surfaces before and after heat treatments brought out a lot of interesting features. For the A380 composites, the fracture surface prior to heat treatment is characterized by fiber pull-out and decohesion at the fiber-matrix interface for fibers parallel to the fracture plane (Fig. 6a). After heat treatment at 520°C, there is no fiber pull out and the fibers parallel to the plane of fracture are broken along their length (Fig. 6b). One should also notice the difference in the behavior of the matrix surrounding the fibers in Figs. 6a and 6b. The fracture surfaces of 5083 composites show, before and after heat treatment, no fiber pull out and fracture of fibers parallel to the plane of fracture (Figs. 7a and 7b). Nevertheless, it is possible to observe in Fig. 7b that heat treatment causes local "attack" of fibers (pointed out by arrows). For 5083 composites, the behavior of the matrix around the fibers seems to be the same, independent of heat treatment.

DISCUSSION

There are a lot of unique effects when adding magnesium to aluminum alloy for composite fabrication. When the alloy solidifies between the fibers of the preform, the magnesium is rejected in the last liquid to solidify. This results in Mg-rich regions around ceramic fibers (Cook, Yun and Hunt, 1988; Quigley and co-workers, 1982). Because magnesium is known to reduce the wetting angle, chemical reactions are possible with the fibers containing SiO_2 and Al_2O_3. Some studies reported reaction products such as $MgAl_2O_4$ and Mg_2SiO_4 spinels, MgO oxide and Mg_2Si intermetallic (Le Petitcorps and co-workers, 1988; Cook, Yun and Hunt, 1988; Johnston and Greenfield, 1988). The time of contact between the liquid metal and the fibers should be long enough to permit chemical reaction. In the squeeze-casting technique, the solidification is very rapid and the contact time is too short for chemical reactions to occur (Cappleman, Watts and Clyne, 1985). Nevertheless the use of magnesium in aluminum alloy leads to good bonding between the fiber and the matrix as can be deduced from the lack of pull out at the fracture surface (Fig. 7a). The heat treatment following specimen fabrication activates the diffusion of magnesium around the fibers and the chemical reaction resulting in a layer of reaction products of about 0,75 µm thick at the interface (Fig. 8). X-ray mapping of the region shown in Fig. 8 confirms the high concentration in magnesium in this layer. The presence of such a layer on the ceramic fibers can explain the loss of strength of the 5083 composite after heat treatment. In the case of aluminum alloy containing magnesium, the presence of fibers modifies the behavior of the alloy during ageing heat treatment. Because the fibers react strongly with magnesium, there is less magnesium to precipitate in the matrix (Friend and Luxton, 1988). This consideration has to be taken into account when matrix heat treatment is envisaged.

For the A380 composites, the squeeze-cast fracture surfaces show fiber pull out and decohesion at the fiber-matrix interface (Fig. 6a). This means that even if the contact between the alloy and the fibers is good after squeeze-casting (absence of porosity) the bonding is very weak. The shear strength of the interface is lower than that of the matrix resulting in poor ultimate tensile strength. The heat treatment did not lead to an observable reaction product at the interface as was the case for Al-Mg alloy. Nevertheless bonding is improved by heat treatment resulting in the absence of pull out and decohesion of fibers parallel to the plane of fracture (Fig. 6b). In some cases, the fracture surface of heat treated A380 composites shows rough fiber surfaces (Fig. 9) indicating that chemical reaction occurs at the interface. The higher strength of this composite after heat treatment can also be partly attributed to an higher strength of the matrix. For the A380 alloy, from a microstructure point of view, the presence of fibers did not change the structure modification of the matrix caused by heat treatment.

This study revealed another interesting characteristic of metal matrix composite using preforms. Because of the nature of preform itself, points of contact between fiber necessarily exist. It was observed in this study that these points of contact act as initiation site for crack propagation in brittle fibers. This aspect is illustrated in Figs. 10a and 10b. It can be seen that in these two cases for 5083 composites (before and after heat treatment), the fiber perpendicular to the plane of fracture initiated crack propagation in the fiber almost perpendicular to it. After the first fiber is broken, there is a stress concentration at the point of contact and the second fiber is subsequently broken. The heat treatment did not modify this mechanism even if a layer of reaction product is formed around the fiber (Fig. 10b). Mirchandani (1987) defined a contiguity ratio which is a measure of the quantity of contact points between particles. This author reported that an increase in contiguity ratio invariably causes a reduction in strength and ductility. From these considerations, it is not surprising to understand that a limited gain in strength is obtained when using preforms as reinforcement. The detrimental effect of contact points can be large enough to mask the gain in strength brought about by fiber addition.

a   b
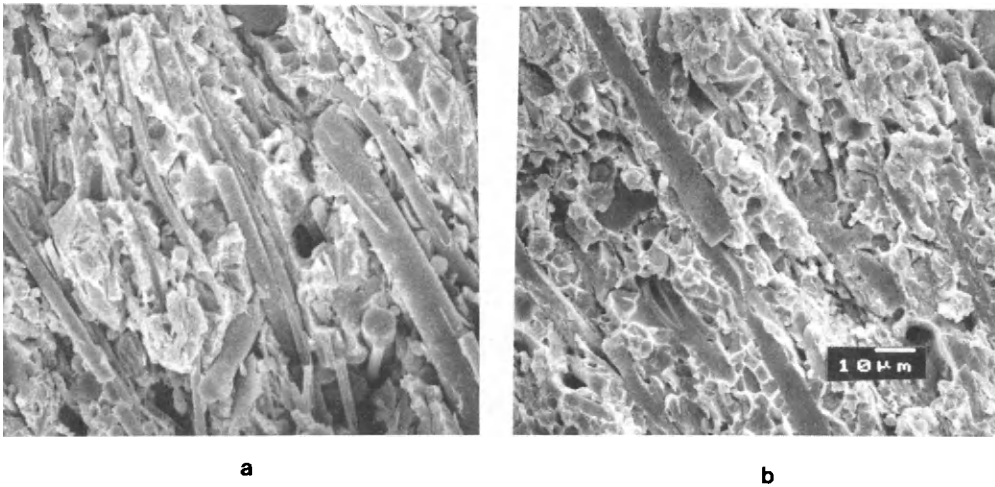
Fig. 6.   Fracture surfaces of 15 vol% Al_2O_3-SiO_2/A380 alloy composites a) before and b) after heat treatment at 520°C during 2 hours. The occurrence of pull out is a characteristic of fracture surface prior to heat treatment.

a   b
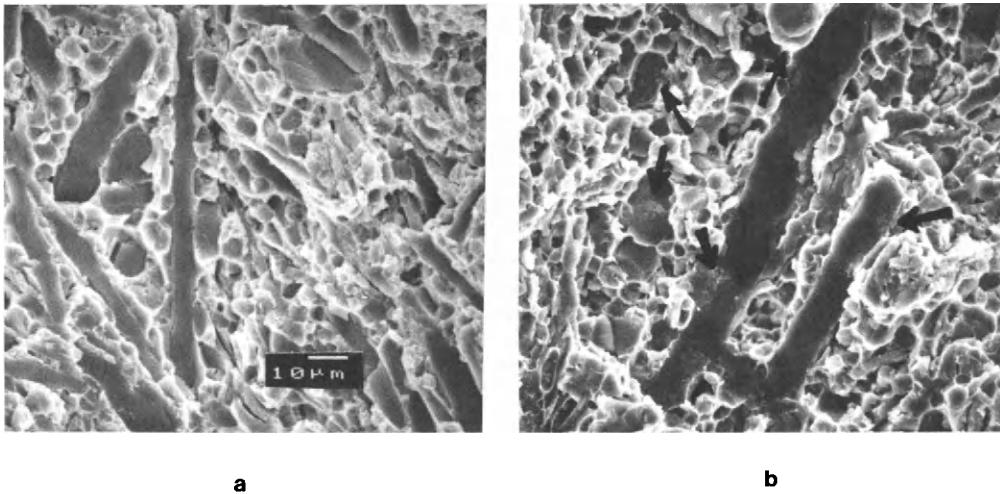
Fig. 7.   Fracture surfaces of 15 vol% Al_2O_3-SiO_2/5083 alloy composites a) before and b) after heat treatment at 550°C. Arrows indicate local fiber attack due to heat treatment.
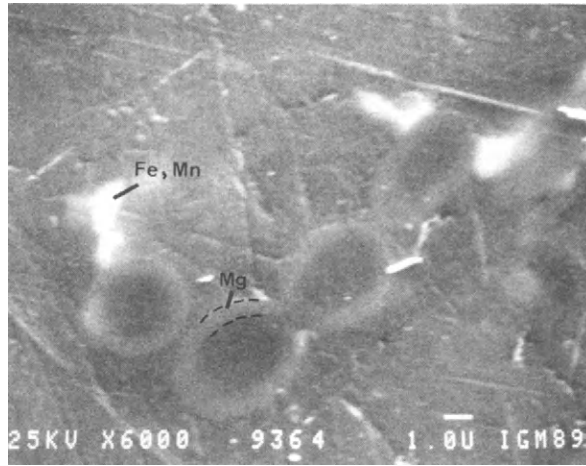
Fig. 8.   X-ray mapping of heat treated 10 vol% Al_2O_3-SiO_2/5083 composites confirms the Mg-rich layer around fibers. The Fe and Mn elements contained in the alloy are also found in the last liquid to solidify.
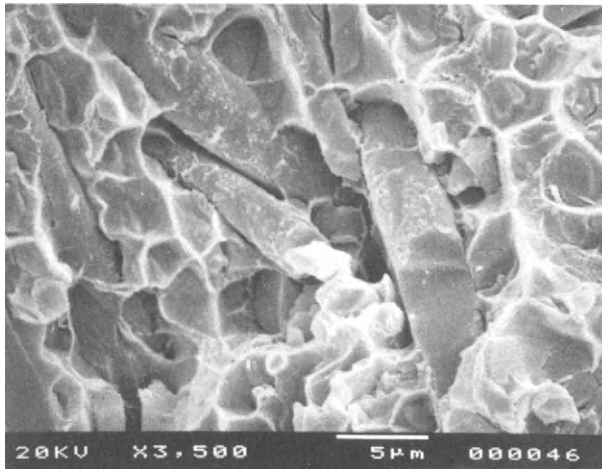
Fig. 9.   The rough surface of fibers in heat treated Al_2O_3-SiO_2/A380 composite suggests chemical reaction at the interface.

a   b
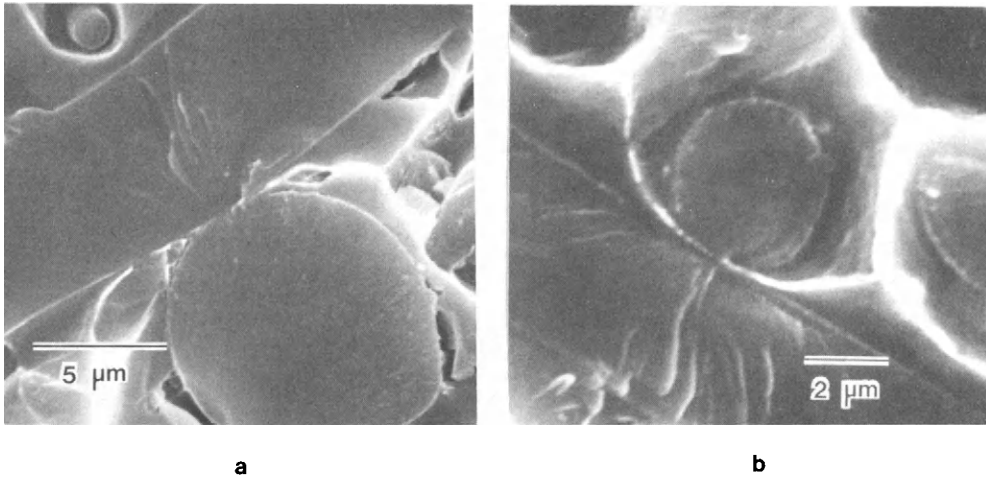
Fig. 10. The detrimental effect of contact points is shown a) before and b) after heat treatment of Al_2O_3-SiO_2/5083 composites. The point of contact acts as a stress concentrator and initiation site for fiber fracture.

CONCLUSION

From the experimental observations made in this study, some features of the effect of heat treatment on structural characteristics can be pointed out:

-   The addition of magnesium to aluminum alloy improves the adhesion between the matrix and the fibers. The heat treatment at 550°C does not improve the bonding which is very good in the as-squeeze-cast specimens. The heat treatment causes chemical reactions to take place at the interface, which can be detrimental for the mechanical properties.

-   For the composites made of Al-Si-Cu alloy (A380), the heat treatment at 520°C improves considerably the bonding between the matrix and the fibers. This results in higher tensile strength of the composite.

-   The effect of contact points between fibers is detrimental for the mechanical properties because they act as initiation sites for crack propagation in fibers.

ACKNOWLEDGEMENT

REFERENCES

Cappleman, G.R., J.F. Watts and T.W. Clyne (1985), The interface region in squeeze-infiltrated composites containing δ-alumina fiber in an aluminium matrix, J. of Mat.Sci., 20, 2159-2168.

Clegg, W.J., I. Horsfall, J.F. Mason and L. Edwards (1988), The tensile deformation and fracture of Al-Saffil metal-matrix composites, Acta Metall, 36, 2151-2159.

Cook, C.R., D.I. Yun and W.H. Hunt Jr. (1988), System optimization for squeeze-cast composites, In Cast Reinforced Metal Composites, S.G. Fishman and A.K. Dhingra (eds.), Proc. of the International Symposium on Advances in Cast Reinforced Metal Composites, 24-30 Sept.; Chicago, Illinois, 195-204.

Das, A.A., A.J. Clegg and B. Zantout;(1988), Enhancement in the properties of a squeeze-cast aluminum magnesium alloy containing delta-alumina fibre, In Cast Reinforced Metal Composites, S.G. Fishman and A.K. Dhingra (eds.), Proc. of the International Symposium on Advances in Cast Reinforced Metal Composites, 24-30 Sept.; Chicago, Illinois, 217-224.

Friend, C.M. and S.D. Luxton, The effect of δ-alumina fibre arrays on the age-hardening characteristic of an Al-Mg-Si alloy, J. of Mat. Sci., 23, 3173-3180.

Johnston, W.D. and I.G. Greenfield (1988), Effect of magnesium concentration on the shear strength of unidirectional alpha-alumina/aluminum composites, In Cast Reinforced Metal Composites, S.G. Fishman and A.K. Dhingra (eds.), Proc. of the International Symposium on Advances in Cast Reinforced Metal Composites, 24-30 Sept.; Chicago, Illinois, 335-340.

Kobayashi, T., M. Yosino, H. Iwanari, M. Niinomi and K. Yamamoto (1988), Mechanical properties of SiC whisker reinforced aluminum alloys fabricated by pressure casting method, In Cast Reinforced Metal Composites, S.G. Fishman and A.K. Dhingra (eds.), Proc. of the International Symposium on Advances in Cast Reinforced Metal Composites, 24-30 Sept.; Chicago, Illinois, 205-210.

Le Petitcorps, Y., T. Stephenson, F. Girot and R. Naslain (1988), Chemical analysis and bonding at the fiber-matrix interface in model aluminum matrix composites, In Cast Reinforced Metal Composites, S.G. Fishman and A.K. Dhingra (eds.), Proc. of the International Symposium on Advances in Cast Reinforced Metal Composites, 24-30 Sept.; Chicago, Illinois, 67-70.

Mirchandani, P.K. (1987), Structure-mechanical properties relations in aluminum-ceramic composites, Ph.D. thesis, Michigan Technological University.

Quigley, B.F., G.J. Abbaschian, R. Wunderlin and R. Mehrabian (1982), A method for fabrication of Al-Al2O3 composites, Met. Trans. A, 13A, 93-100.

Tafto, J., K. Kristiansen, H. Westengen, A. Nygard, J.B. Borradaile and D.O. Karlsen (1988), Studies of interfaces in light metal matrix composites by transmission electron microscopy, In Cast Reinforced Metal Composites, S.G. Fishman and A.K. Dhingra (eds.), Proc. of the International Symposium on Advances in Cast Reinforced Metal Composites, 24-30 Sept.; Chicago, Illinois, 71-95.

Powder processing of intermetallic matrix composites

D. Alman, A. Dibble, A. Bose, R.M German, N.S. Stollof
Rensselaer Polytechnic Institute, Troy, New York 12180-3590, U.S.A.

B. Moore
General Electric Company, MAO, P.O. Box 1021, Schenectady, New York 12301, U.S.A.

ABSTRACT

Composites based upon the intermetallic compounds NiAl, Ni_3Al and Al_3Ta have
been consolidated by several novel techniques incorporating, at least in
part, reactive sintering or hot isostatic pressing of elemental powders.
This paper discusses the resulting microstructures and mechanical properties,
including hardness and tensile or compressive strengths as a function of
test temperature. The properties of the composites are compared to those
of the respective matrix materials, also prepared from powders by identical
techniques. The limitations as well as advantages of such processing techniques
are discussed.

KEYWORDS

Composite, fibers, grain size, hot isostatic pressing, intermetallic compound,
nickel aluminides, reactive sintering, tantalum aluminide.

INTRODUCTION

Intermetallic compounds, especially those containing large quantities of
aluminum, display a number of favorable properties for high temperature structural
use, including low density, high strength at elevated temperatures and excellent
oxidation resistance. However, most of the aluminides are brittle, which
leads to problems in consolidation and during service. One potential means
of improving ductility and/or toughness while increasing strength is to utilize
a fibrous second phase reinforcement. Particulates also can be used for
strength improvements, but usually at the expense of ductility. Powder metallurgical
processes are particularly useful in preparing such composites, as has already
been reported in the Ti_3Al/SiC (Brindley, 1987) and Al_3Ta/Al_2O_3 (Anton, 1988)
systems. This paper reviews efforts to produce both fibrous and particle
strengthened composites of Al_3Ta, Ni_3Al and NiAl by one or more methods based
upon either hot isostatic pressing (HIPing) or reactive sintering. The latter
refers to a process in which an exothermic reaction between two or more elemental
constituents of a powder compact provides enough heat to produce a liquid
phase which markedly reduces sintering time. If the process is carried out
without pressure, it is called reactive sintering. Processes which rely
upon application of uniaxial or isostatic pressure during reactive sintering
are labelled reactive hot pressing and reactive hot isostatic pressing, respectively.

An extensive discussion of the various processing techniques has appeared in previous publications (Moore et al, 1988; Bose et al, 1988, German and Bose, 1989).

ALLOY SYSTEMS STUDIED

The three alloy systems studied in this investigation are Ni_3Al, $NiAl$ and Al_3Ta. Melting points, densities and crystal structure of these compounds are summarized in Table 1. $NiAl$ and Al_3Ta are brittle at room temperature,

TABLE 1   INTERMETALLIC MATRIX ALLOYS

Alloy	Crystal Structure	Melting Pt °C	Density g/cc
$TaAl_3$	DO_{22}	1550	6.9
$NiAl$	B_2	1540	5.9
IC-218*	Ll_2	1390	7.5

* Ni_3Al,Cr,Zr+B

but $NiAl$ undergoes a brittle to ductile (BD) transition at temperatures near 600°C. (No data are available concerning a BD transition in Al_3Ta.) The Ni_3Al alloy chosen for study, IC-218, is a two phase alloy that is ductile at all temperatures between 25°C and 800°C. The nominal composition of this alloy, which was developed at Oak Ridge National Laboratory, is Ni-8.2w%Al, 7.8%Cr, 0.8%Zr and 0.2%B.

Powders of the pure metals Ni, Al and Ta were obtained from various sources, as listed in Table 2. Previous research on Ni_3Al alloys prepared by reactive

TABLE 2   POWDER CHARACTERISTICS

	Size	Shape	Process	Vendor
Ta	4μm	angular	mechanically milled	Cabot
	10μm	angular	hydride/ dehydride	NRC
	-325	angular mesh	hydride/ dehydride	Fansteel
Al	3μm	spherical	gas atomized	Valimet, H-3
	10μm	spherical	gas atomized	Valimet, H-10
	30μm	spherical	gas atomized	Valimer, H-30
Ni	3-7μm	spiky surface	carbonyl	INCO-123

sintering had shown that maximum density of compacts is obtained with fine powders, in the range 10-15 μm (Bose et al, 1988). Therefore, starting powders were obtained in the finest sizes commercially available.

Al_2O_3 was chosen as the fibrous reinforcement for Al_3Ta and IC-218. For both IC-218 and $NiAl$ varying volume fractions of TiB_2 particles were incorporated during consolidation of the alloy.

SINTERING TECHNIQUES

Obtaining dense monolithic samples of each alloy was the first objective
of this investigation. After extensive research it was found that reactive
sintering of elemental powders was not a suitable technique to prepare any
of the matrix alloys.

NiAl

In the case of NiAl, the exothermic reaction was uncontrollable, such that
the heat of reaction was sufficient to destroy crucibles or result in complete
melting of portions of the compact, as shown, for example, in Fig. 1. It
was found by trial and error that the reaction could be diluted by mixing
10 to 25% prealloyed NiAl powder with the elemental powders.

Near fully dense and near net shape Ni-49a%Al samples (0.5 grams wt cylindrical
pellets approximately 6mm in diameter, cold pressed to 70% of theoretical
density) could be produced from a mixture of elemental and prealloyed powders
by reactive sintering at 700°C in vacuum (10^{-6} torr) for 15 minutes. The
optimum amount of prealloyed NiAl powder needed to control the exotherm associated
with reactive sintering of Ni+Al was determined to be dependent on the particle
size distribution of the prealloyed powder. NiAl prealloyed powder was obtained
from two sources. One source was prereacted NiAl produced and milled at
RPI; the other source was prealloyed NiAl powder purchased from Cerac, Inc.
The Cerac NiAl powder possessed a more uniform particle size distribution,
and therefore blending was achieved with less Cerac NiAl powder than with
the RPI powder. The first two sets of bars in Fig. 2 show properties for

	NiAl	NiAl	NiAl	NiAl	NiAl	NiAl
Prealloyed Content	25%*	15%**	15%**	15%**	15%**	15%**
TiB$_2$ Vol%	0	0	5	10	15	20

* NiAl powder produced at RPI
** NiAl powder purchased from Cerac, Inc.
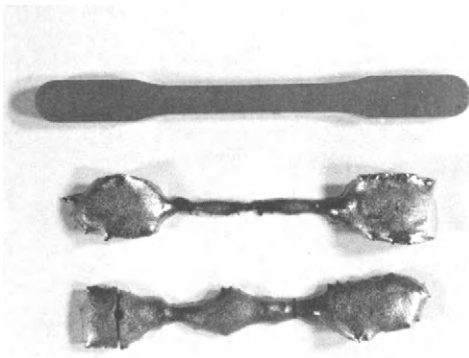
Fig. 1 Excessive reaction of elemental
        Ni+Al powders.
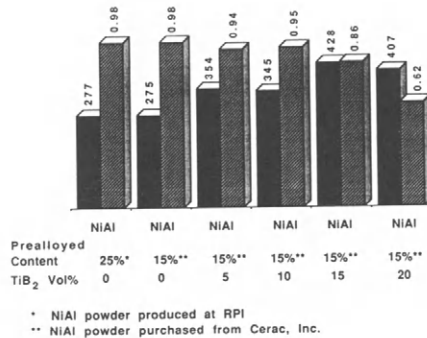
Fig. 2 Effects of % prealloyed NiAl
        and volume fraction of TiB$_2$
        powders on sintered density of
        NiAl.

reactive sintered NiAl with RPI and Cerac powder respectively. Even though
different optimum amounts of prealloyed powders were used, the sintered properties
are essentially equivalent with the two different powders. It was found
that TiB$_2$ powders added to the mixture hindered densification; the maximum
density obtained in a NiAl-TiB$_2$ alloy was 95% with 10v% TiB$_2$ and 15% prealloyed

powder (see Fig. 2). The influence of small amounts of alloying elements on reactively sintered $NiAl/TiB_2$ composites was also studied (see Fig. 3). No significant improvements in hardness or sintered density were noted with 1%Ta, 1%Nb or 5%Cr.

It became evident after obtaining many samples with large residual pores that to produce dense composites, hot isostatic pressing had to be employed. Fully dense microstructures of NiAl and $NiAl/TiB_2$ composites were produced by cold isostatic pressing followed by hot isostatic pressing in a 304 stainless steel can at 1200°C for 60 min at a pressure of 172MPa, using the process outlined in Fig. 4. Typical microstructures are shown in Figs. 5a)-d).

■ Hardness (VHN)
▨ Fractional Sintered Density

REACTIVE HOT ISOSTATIC PRESSING (RHIPing)

1   Ni+Al were mixed to stoichiometric proportions.

2   Compacts were CIPed to a green density of approximately 70% theoretical.

3   Vacuum encapsulated in 304 stainless steel.

4   RHIPed
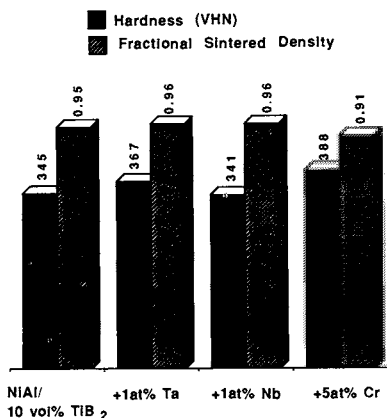
Fig. 3   Effects of alloying elements on sintered density and hardness of NiAl.
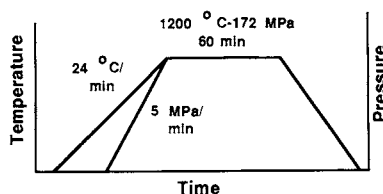
Fig. 4   Schematic of HIP process for NiAl.

Note the more equaixed grain structure produced from a mixture of prealloyed and elemental powders as opposed to the pure elemental powders. Also notice a more refined grain size with the addition of TiB_2 powders (5µm vs 30µm for monolithic NiAl.

Al_3Ta

Reactive hot isostatic pressing (RHIP) was utilized to fabricate samples of Al_3Ta. Control of the process conditions and particle sizes of the elemental powders affected the homogenization and densification of the intermetallic compound.

Since the exact composition of stoichiometric Al_3Ta was not clear from the literature, elemental powders of tantalum and aluminum were mixed in three ratios: 23, 24 and 25 at% Ta. Reactive sintering experiments showed that the optimum powder size was 10µm for both the aluminum and the tantalum powders. The powder mixtures were cold isostaticaly pressed at 200MPa into rods approximately 14 mm in diameter and 80 mm in height. The rods were inserted into stainless steel tubes lined with tantalum foil and coated with an Al_2O_3 slurry to prevent contamination from the can. The samples were evacuated and outgassed at 500°C for approximately 20 hours and then sealed under vacuum. Samples were produced by RHIPing at a pressure of 172MPa and temperatures of 700°C, 900°C
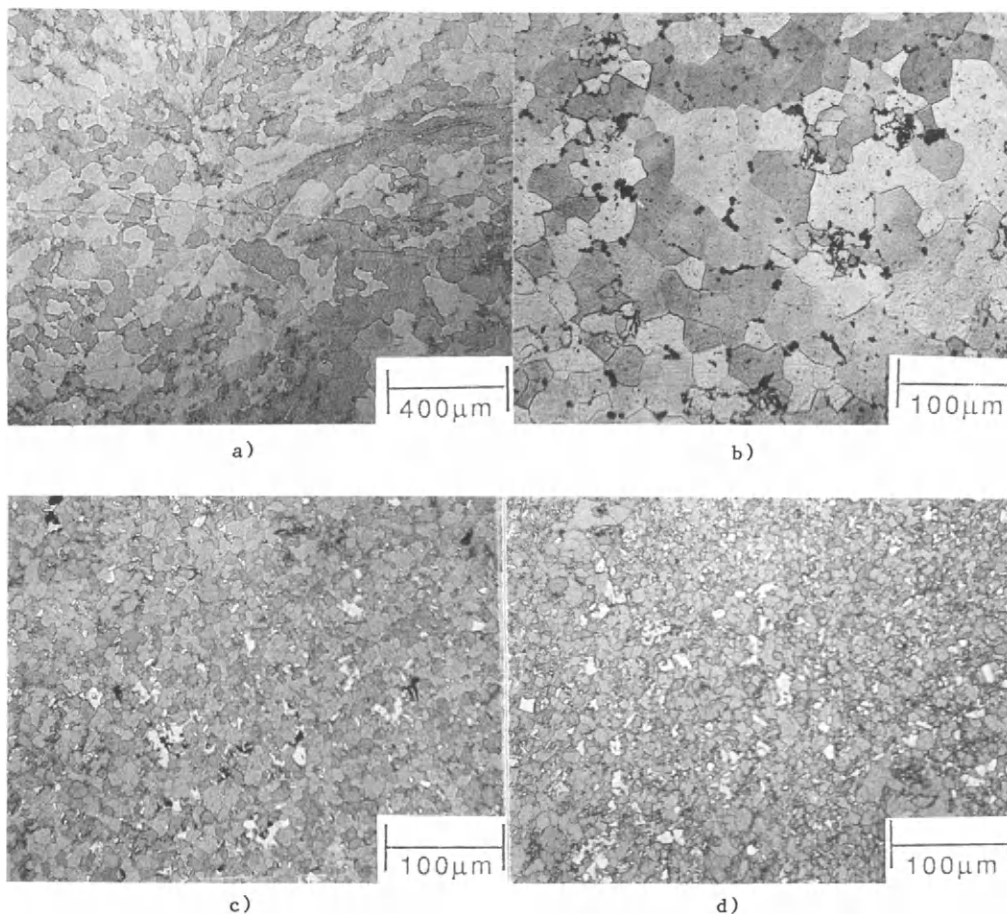
Fig. 5 Microstructures of NiAl+TiB$_2$. a) 0%TiB$_2$, g.s.30μm
        b) 10% prealloyed, 0%TiB, g.s.30μm, c) 10% prealloyed,
        15v%TiB$_2$, g.s.5μm, d) 10% prealloyed, 20v%TiB$_2$,
        g.s.5μm.

or 1200°C, for one hour. Dense, homogenous samples were formed at 23 at%
Ta and 1200°C, as shown in Fig. 6. Microprobe analysis confirmed that the
composition of Al$_3$Ta was approximately 23.3 at% Ta in agreement with a recently
revised phase diagram (Miracle, 1988). Lower temperatures and higher percentages
of tantalum results in incomplete reaction of the starting materials. Heat
treatment at 1100°C for ten hours or at 1200°C for four hours yielded a two
phase microstructure which consisted of Al$_3$Ta and a phase identified as Al$_2$Ta
(Miracle, 1988).

Compacts containing 8at%Fe substituted for Al also were produced by similar
techniques. No change in crystal structure of the alloy was detected. Samples
containing 8at% Fe substituted for Al were produced by RHIPing at a pressure
of 172MPa and a temperature of 1100°C and then heat treated at 1200°C for
4 hours. The resulting microstructure consisted of two phases - a solid
solution Al$_3$Ta phase containing 0.5at% Fe and a ternary phase with a composition
of 32at%Ta, 56at%Al, and 12at%Fe.
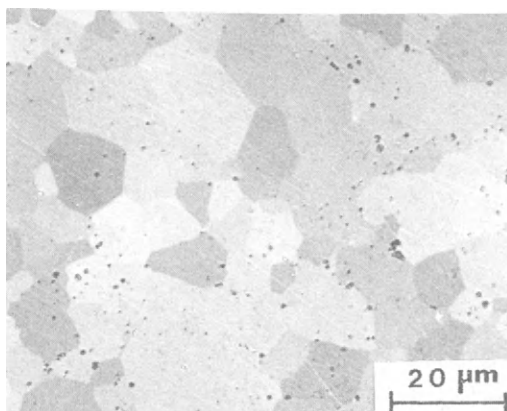
Fig. 6   Microstructure of Al$_3$Ta reactively
HIPed at 1200°C.

Composites with an Al$_3$Ta matrix also were fabricated by RHIPing. Compatibility
tests indicated that Al$_3$Ta did not react with Al$_2$O$_3$ during processing; therefore,
two Al$_2$O$_3$ fibers, FP and Saffil, were selected for further study. Table 3
summarizes the properties of the FP and Saffil fibers. Using the optimum

TABLE 3   CHARACTERISTICS OF Al$_2$O$_3$ FIBERS

	FP	Saffil
length	5-30mm	70-200µm
diameter	20µm	3µm
density	3.9 g/cc	3.3 g/cc
tensile strength	1380MPa	2000MPa
Young's modulus	380GPa	300GPa
max powder diameter for 20 vol % fiber	23µm	4µm
source	DuPont	ICI

consolidation procedure described above, composites were fabricated with
10 vol% of randomly oriented fibers of each type. During processing, the
fibers fractured due to the high pressures. As the volume percent of fibers
was increased, the porosity and amount of second phase present also increased.
This was true for both the FP and the Saffil fibers, but was less severe
in the case of the smaller diameter Saffil. Most of the second phase which
appeared in the Saffil composites occurred around prior particle boundaries.
Representative microstructures are shown in Figs. 7a) and b).

In addition, work is in progress to align these fibers by injection molding.
This process requires the addition of about 40 vol% binder to the powder
mixture. The powder-binder mixture is injected through a die to obtain fiber
alignment and then heated to 450°C for 5 hours in hydrogen to remove the
binder. The samples are then RHIPed as described above. To date, a paraffin-
based liquid appears to be the best binder since it does not contaminate
the reaction in which Al$_3$Ta is formed.

a)   b)
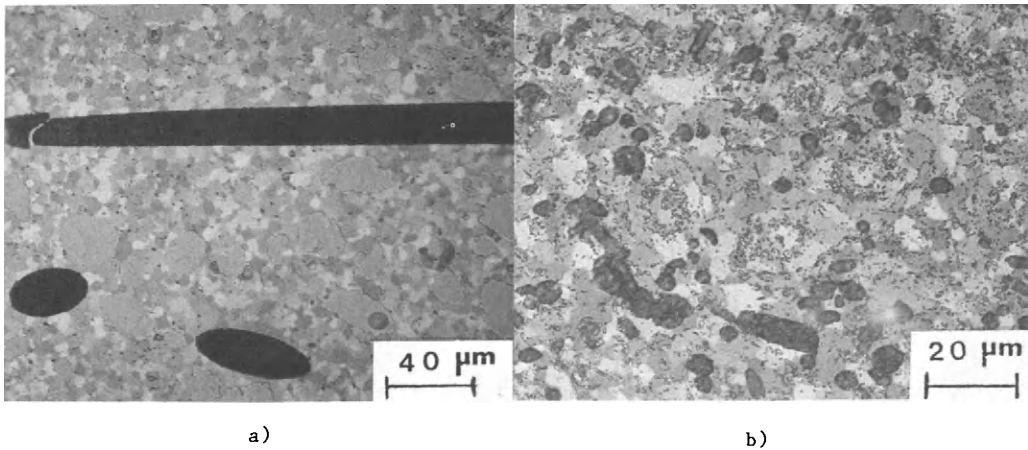
Fig. 7   Microstructures of Al_3Ta composites with 10v%
Al_2O_3 fibers   a) FP Al_2O_3 b) Saffil.

$Ni_3Al,Cr,Zr+B$ (IC-218)

Prealloyed powder of the compound IC-218 was obtained from Homogeneous Metals,
Inc. Analysis of the -100 mesh powder revealed composition of 7.67w%Cr,
8.18%Al, 0.8%Zr, 0.2%B, with 7 ppm of N_2 and 73 ppm of O_2. TiB_2 powder used
in preparing some composites was obtained from Aerospace Corp. FP- Al_2O_3
fibers were obtained from Dupont Corp.

IC-218 and two types of composites with an IC-218 matrix were consolidated
by HIPing. The HIP cycle for the unreinforced matrix was 1100°C, 1 hr, at
a pressure of 172 MPa. The microstructure of IC-218 is shown in Fig. 8a).
Note that the microstructure consists of a γ' matrix with some disordered
second phase. IC-218 with 5v% of short Al_2O_3 fibers also was HIPed at 1150°C
and 172MPa pressure. A typical microstructure is shown in Fig. 8b). IC-218

a)   b)
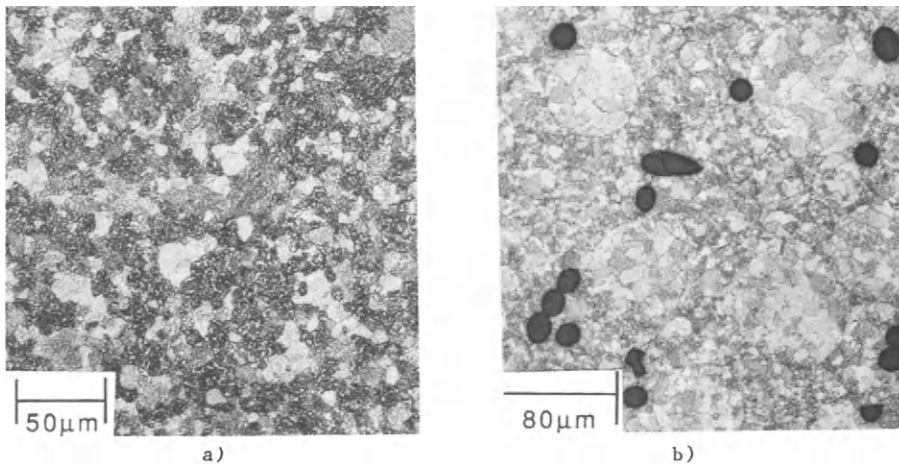
Fig. 8   HIPed microstructure of IC-218 a) matrix alloy
(HIPed at 1100°C) b) 5v%Al_2O_3 fibers (HIPed at 1150°C).

with varying volume fractions of 30µm TiB$_2$ particles was HIPed at 1150°C
for 30 min at a pressure of 172 MPa. The microstructure of a sample containing
10v%TiB$_2$ is shown in Fig. 9. Note that the TiB$_2$ forms a nearly continuous
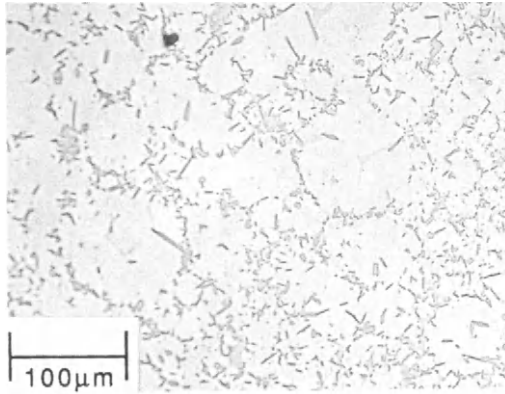
Fig. 9 Microstructure of IC-218 with 10v%TiB$_2$
        particles, HIPed at 1150°C, 172MPa, 30 min.

phase at the grain boundaries. In general the TiB$_2$ had a needle-like or
plate-like appearance.

STRENGTH MEASUREMENTS

The influence of microstructure and particle or fiber content on strength
was carried out by a variety of mechanical tests.

NiAl

Compressive stress strain curves for Ni-49a% Al and several TiB$_2$-reinforced
NiAl alloys were carried out as a function of test temperature. The results
are shown in Fig. 10. Note the rapid rise in yield stress with increasing
TiB$_2$ content. A portion of this strengthening is due to the very fine grain
size (5 µm) of the alloys containing 15 and 20% TiB$_2$ compared to the 30 µm
grain size of NiAl. The remainder of the strengthening is due to the effects
of the TiB$_2$ particles. The strengthening due to TiB$_2$ persists to about 700°C;
there is virtually no effect of TiB$_2$ on strength at 800 and 950°C.

IC-218

The tensile properties of IC-218 and IC-218 with 5v% Al$_2$O$_3$ fibers as a function
of temperature are compared in Fig. 11. It can be seen that the fibers did
not raise the yield stress and, by reducing ductility to near zero at all
but room temperature, had a deleterious effect on ultimate tensile strength.

Tensile properties of IC-218/TiB$_2$ composites are shown in Fig. 12. Only
the alloy containing 10%TiB$_2$ showed a higher yield strength than IC-218 at
25°C; however, at 600°C an increase in strength with 5% and 10% TiB$_2$ was
noted. Note also in Fig. 12 the rise in yield stress with temperature that
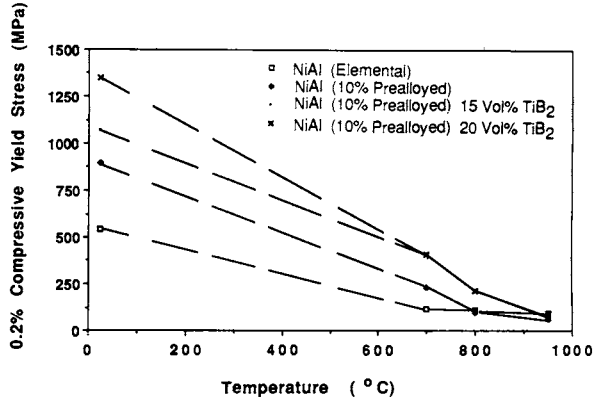
Fig. 10   Compressive yield stress vs temperature
          for NiAl alloys.
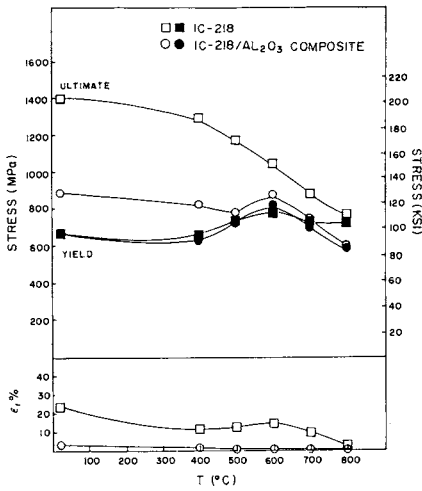
Fig. 11   Effect of temperature on
          tensile properties of IC-218
          and IC-218-5v%Al$_2$O$_3$ fibrous
          composites.
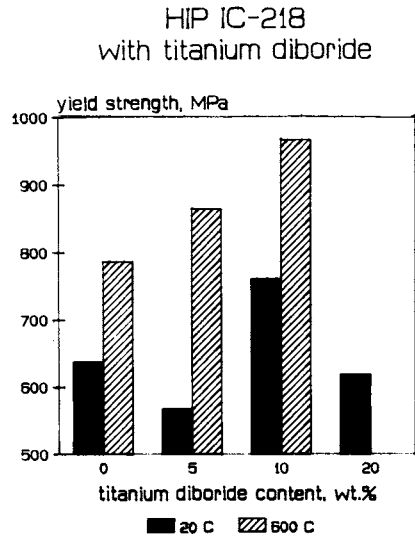
Fig. 12   Effect of temperature and
          TiB$_2$ content on tensile
          yield strength of IC-218.

is characteristic of this alloy. The ductility decreased substantially with
all contents of TiB$_2$, the effect being greater with increasing %TiB$_2$.

Al$_3$Ta

The strength of monolithic Al$_3$Ta has been measured in compression as a function

of temperature, see Table 4. Note the rapid weakening at elevated temperatures.
The addition of 8%Fe replacing Al leads to a significant improvement in high
temperature strength. Also, hardness tests have been carried out on several
compositions. The Vicker's hardness of Al_3Ta was 369 DPH. This value varied
little for the Al_3Ta which formed at various compositions or HIPing temperatures.
The addition of fibers also had little effect upon the hardness. The hardness
of the Al_2Ta phase which formed in some samples was approximately 450 DPH.
The Vicker's hardness of the solid solution strengthened Al_3Ta + Fe was
391 DPH. This hardness of the ternary phase with 12% Fe was 571 DPH.

TABLE 4   COMPRESSIVE PROPERTIES OF Al_3Ta ALLOYS

Alloy	Temp (C)	Yield Stress (MPa)
Al_3Ta	25	531
Al_3Ta-8a%Fe	25	372
Al_3Ta-8a%Fe	750	765
Al_3Ta	950	41
Al_3Ta-8a%Fe	950	198

DISCUSSION

Densification of intermetallic matrix composites can be accomplished by HIPing
either elemental or prealloyed matrix material with compatible reinforcements.
The consolidation conditions (temperature, pressure, time) do not substantially
differ from those utilized for the matrix alone. However, the ability to
achieve full density is inhibited somewhat by the presence of the reinforcements.
Reasons for similar processing cycles are the low volume frations of ceramic
phases and the grain size refinement often observed after HIP of the composite.
For many of the intermetallic compounds the primary densification mechanism
involves grain boundary diffusion. Although the ceramic second phase inhibits
densification, it has a beneficial grain size refinment effect. This latter
change ensures more and shorter diffusion paths for densification. Because
of the long range ordered structure of these compounds, the lattice diffusivity
is low. Consequently, grain boundaries and grain boundary diffusion is necessary
for rapid densification. Two of the three alloy systems studied, $Ni_3Al,Cr,Zr+B/TiB_2$
and $NiAl/TiB_2$ show considerable strengthening relative to the matrix alone.
In the case of NiAl some of the strengthening arises from grain refinement,
with the grain size being reduced from 30μm to 5μm by the TiB_2 particles.
However, a Hall-Petch analysis of the contribution from grain size refinement
to strengthening can account for only a portion of the observed strengthening,
see Table 5. The balance is provided either by direct strengthening by the
particles (unlikely due to their large size) or by impurity contamination,
predominantly oxides on prior particle boundaries. Post-consolidation analyses
of the NiAl compacts revealed an oxygen content of about 500 ppm. It is
well known that the mechanical properties of intermetallic compounds are
extremely sensitive to compositional variations, either Al content or impurity
levels (Stoloff, 1985).

Contamination is only one of the problems affecting the properties of these
composites. In the case of the fibrous composites IC-218/Al_2O_3, lack of
wetting between fiber and matrix leads to premature nucleation of cracks
at the fiber/matrix interfaces and severe loss of ductility. Two remedies
are required: a dopant for better wetting and fiber alignment to allow the
work of pull out to contribute to overall fracture resistance. Injection

TABLE 5   CONTRIBUTION OF GRAIN REFINEMENT TO STRENGTHENING
BY TiB$_2$ at 25°C.

	Grain Size (μm)	Yield Stress (MPa)
NiAl (10% prealloyed)	30	890
NiAl (10% prealloyed) calculated from Hall Petch*	5	1000
NiAl (10% prealloyed) 15 vol % TiB$_2$	5	1060
NiAl (10% prealloyed) 20 vol % TiB$_2$	5	1350

* Hall Petch data from Schulson (1985)

molding offers some hope of overcoming the alignment problem, but contamination from a polymeric-base binder must be avoided in the final product. Initial efforts to develop injection molded composites have established that the average powder particle diameter must be less than the fiber diameter to accomplish alignment. Unfortunately, powders of the size required, of the order of 10 μm or less, are either very expensive or unavailable. Reactive processing using elemental powders remains an attractive route for densification from injection molded small particles.

ACKNOWLEDGMENT

REFERENCES

Anton, D.L. (1988). In High Temperature/High Performance Composites, MRS Symposia, V. 120, MRS, Pittsburgh, PA, 1988, 57-64.
Bose, A., B. Moore, N.S. Stoloff and R.M. German (1988). In PM Aerospace Materials 1987, MPR Publ. Serv. Ltd, Shrewsbury, England, 4.1-4.13.
Brindley, P. (1987). In N.S. Stoloff and others (Eds.) High Temperature Ordered Intermetallic Alloys II, MRS Symposia V. 81, MRS Pittsburgh, PA, 419-424.
German, R.M. and A. Bose (1989). Mat. Sci. and Eng., A107, 107-116.
Miracle, D. (1988). Wright Aeronautical Labs, Wright Patterson AFB, Ohio, unpublished research.
Moore, B., A. Bose, R.M. German and N.S. Stoloff (1988). In F. Lemkey and others (Eds.) High Temperature/High Performance Composites, MRS Symposia V. 120, MRS, Pittsburgh, PA, pp. 51-56.
Schulson, E.R. (1985). In High Temperature Intermetallic Alloys, MRS Symposia 39, MRS, Pittsburgh, PA, pp. 193-204.
Stoloff, N.S. (1985). In C.C. Koch and others (Eds) High Temperature Ordered Intermetallic Alloys, MRS Symposia 39, MRS, Pittsburgh, PA, pp. 3-27.

Particle incorporation studies in support of the Dural process

A.D. McLeod, C. Gabryel, D.J. Lloyd and P. Morris

Alcan International Ltd., Kingston Research and Development Centre, P.O. Box 8400, Kingston, Ontario, Canada, K7L 5L9

ABSTRACT

The Dural process manufactures metal matrix composites by mechanically mixing a particulate reinforcement into an aluminium alloy matrix. A technique that uses the measurement of contact impedance has been developed to study the wetting rate of particulates. One matrix/particulate reaction that not only affects wetting rate, but can also affect subsequent composite properties is the formation of spinel, $MgAl_2O_4$, on Al_2O_3 in Mg-containing alloys.

KEYWORDS

Metal matrix composites; particulate incorporation; interfacial phenomena; wetting rate; spinel formation kinetics.

INTRODUCTION

The incorporation of a particulate material into molten aluminium alloys involves a number of physical and chemical processes. The particle may react with vaporized alloy components above the melt. Heat is exchanged between the particle and the melt. The particle comes into contact, and possibly reacts with the film or skin on the alloy. The particle must penetrate this film, and be wet by the alloy. Other chemical reactions may take place during the spreading stage and continue after complete incorporation.

The role of wetting in particle incorporation has been reviewed elsewhere (Banerji, Rohatgi and Reif, 1984; Russell, Cornie and Oh, 1986). Delannay, Froyen and Deruyttere (1987) demonstrate that a need exists for more studies of a fundamental nature concerning wetting under dynamic conditions. Traditional wetting studies for molten aluminium using the sessile drop technique have been carried out (John and Hausner, 1986; Laurent, Chatain and Eustathopoulos, 1987 – for example). These studies are always complicated by the presence of an intact alumina film on the surface of the molten metal drop at temperatures below about 850°C. Unfortunately, the temperature range of interest for MMC fabrication is usually lower.

Contact angles and surface tension data can, however, be used to calculate the force balance on a particle at the liquid/gas interface. Force balance models have been developed by Neumann and co-workers (Rapacchietta and Neumann, 1977; Smith, Absolom, Spelt and Neumann, 1986). They have created force balance models for spheres and cylinders at liquid/gas interfaces. Ilegbusi and Szekely (1988) have added a dynamic element to their work through the consideration of an additional drag force. These models do not consider either the effects of the skin on the melt surface or the effects of particle shape.

So, a need exists for experimental techniques that will supply relevant data on the wetting of particulate under conditions similar to those encountered during composite fabrication. Most room temperature techniques (Kaya and Koishi, 1988) are difficult to apply at high temperature. Cornie and co-workers (Oh, 1987) have used a pressure infiltration apparatus to measure the relative infiltration distances for various temperatures and alloy compositions on carbides. This method, however, has limited applicability to MMC fabrication techniques wherein relative motion between the particle and metal is critical.

Oki and Choh and co-workers (Choh, Kammel and Oki, 1987; Choh and Oki, 1987; Choh and Hibino, 1985a, 1985b) have measured the wettability of carbon and SiC disks submerged in aluminium alloy melts. The sintered disks are held, without agitation, at 900 to 1100°C under a salt flux - covered melt in air or under vacuum without the flux. Photographs are taken of the disk after it has been removed from the melt at various times. The amount of wetting is measured by using image analysis and elemental distributions are measured for completely wetted disks.

This paper describes a technique of wetting rate measurement that is based upon the concept developed by Oki and Choh. Through the use of electrical impedance analysis, the technique should supply a dynamic measurement of wetting while the liquid metal is flowing past the submerged disk. This new technique is still being developed and only preliminary results will be presented here.

Another series of experiments that are underway concern the kinetics of the formation of spinel, $MgAl_2O_4$, in MMC's reinforced with alumina particulate and having Mg-containing matrices. Spinel has not been found on pressure infiltrated alumina fibres as a result of the short contact times of this fabrication technique (Cappleman, Watts and Clyne, 1985; Clegg, Horsfall and Briscoe, 1987). It is noted that both of these investigations found an enrichment of Mg in the fibre surface. The increased contact time encountered when molten metal mixing techniques are used for MMC fabrication has been found to leave spinel on alumina fibres. Mehrabain and co-workers (Levi, Abbaschian and Mehrabian, 1978, 1979; Munitz, Metzger and Mehrabian, 1979) in particular, have used various analytical techniques to identify and characterize the spinel formed. Hikosaka, Miki and Kawamoto (1987) have also noted the formation of spinel, as well as $CaAl_2O_4$ on vortex-stirred alumina particulate in aluminium alloys containing Mg and Ca.

Spinel formation is important in that not only does the reaction consume an important alloying element, but the reaction must also be an integral part of the incorporation of alumina reinforcements into Mg-containing alloys. It is generally accepted that Mg acts as an aid for alumina incorporation. This is an interesting observation since some measurements show that while Mg reduces the contact angle of Al on Al_2O_3 (Wolf, Levitt and Brown, 1966), the contact angle of Al-Mg alloys on $MgAl_2O_4$ is actually higher than on Al_2O_3 (Weirauch, 1988). Taftø and co-workers (1988), from their work in incorporating alumina into Mg-based alloys, have speculated that Mg acts to remove nitrogen and oxygen from the particle surface, thus aiding wetting.

This paper describes the technique used to make measurements of the rate of spinel formation in liquid Al-Mg alloys. A better understanding of the mechanism and kinetics of spinel formation will be linked with the results of wetting rate measurements to provide information on the role of Mg in incorporating alumina reinforcements.

EXPERIMENTAL

Wetting Rate Measurement

A diagram of the apparatus is shown in fig. 1.
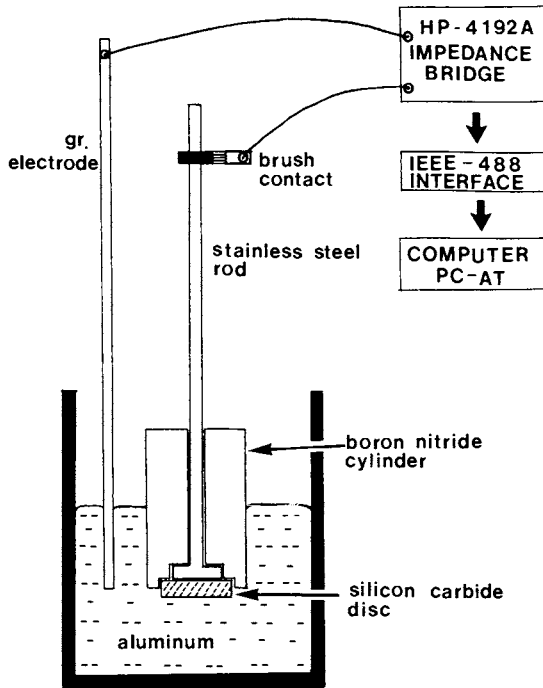
Fig. 1   Wetting Rate Apparatus

The SiC disks, 2.5 mm thick by 19 mm dia., are prepared by sintering a lightly pressed green body at $1050°C$ for 2 hrs.   This produces a friable disk of about 50% porosity. The paint is also used to glue the disk to the stainless support and contact. Zirconia cement is used to insulate the sides of the disk from the melt.   The BN cylinder is used to insulate the stainless rod from the melt. To date, measurements have been made upon graphite and graphite coated with alumina particulate.   An HP4192A impedance analyzer, controlled by a personal computer (PC-AT) through an IEEE-488 interface measures the impedance spectrum of the system.

When a disk is first placed into the melt, it will be covered with gas which is, in turn, covered by the alumina skin.   Before the particles on the surface of the disk touch metal, the gas must be removed and the skin penetrated.   The impedance between the particles and the metal will decrease as the particles come into contact with the metal.   However, the impedance of the entire system, electrodes, leads, graphite paste, etc., is composed of a number of elements, relating to the construction of the apparatus.   Taking impedance measurements as a function of frequency should allow the separation of the contributions of these elements from the whole

spectrum. This separation is aided by the consideration that only the contact impedance between the disk surface and the melt should change.

The impedance analyzer measures both the amplitude and phase shift of the current through the test system as a function of frequency and applied voltage. The instrument supplies the following components of the complex impedance, Z:

$$Re(Z) = |Z| \cos(\theta) \qquad and \qquad Im(Z) = |Z| \sin(\theta),$$

where θ is the angle of the phase shift. Re(Z) is related to the ideal resistive components of the system, and Im(Z) is produced by the inductive and capacitive components. Figure 2 shows a series of impedance spectra, that is plots of Im(Z) versus Re(Z), taken for an alumina powder glued to the surface of a graphite disk with carbon paint. These spectra were taken in the frequency range of 400 Hz to 1 MHz.
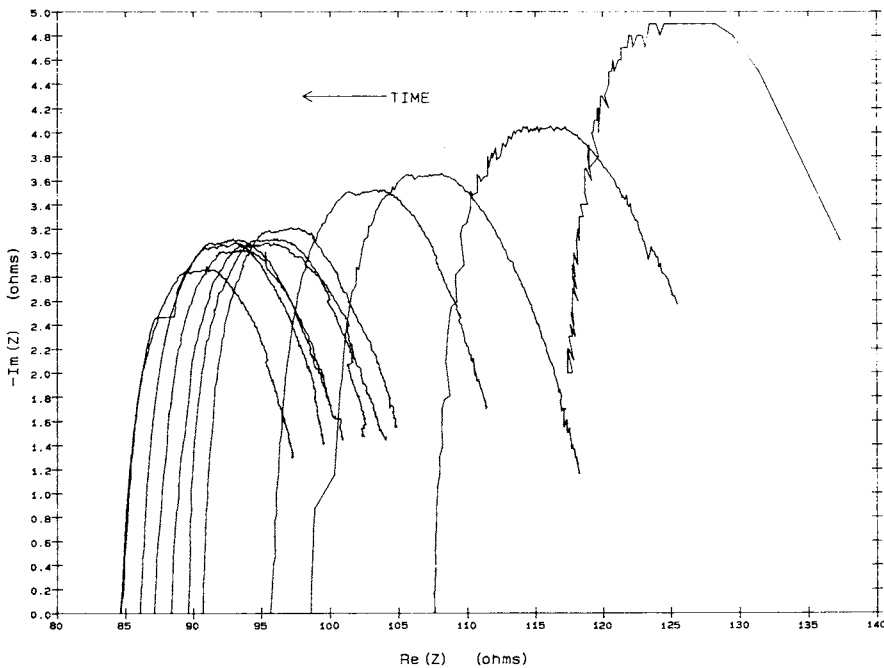
Fig. 2   Impedance Spectra as Taken at Various Times for Alumina on Graphite

These measurements were made for a super purity aluminium melt at 700°C. In contrast to these values, the impedance of the graphite disk alone is less than 0.5 Ω at all times.

Each impedance curve is the sum of two semicircular arcs. The resolution of these arcs through the application of non-linear regression techniques (Tsai and Whitmore, 1982) will yield the values of the individual impedances. As a first approximation, the intercept of the curves with the x or "real" axis can be plotted against time as shown in fig. 3.
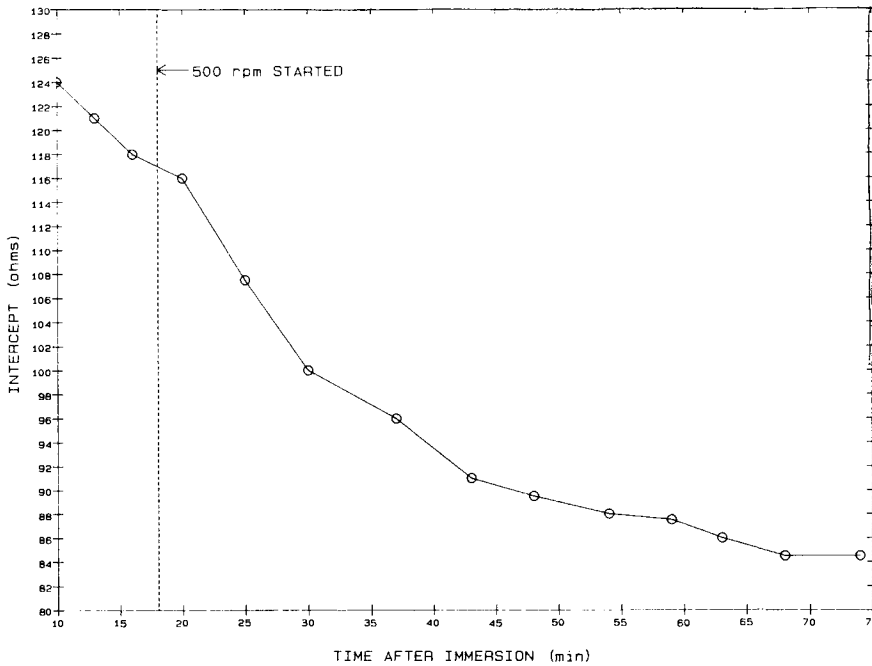
Fig. 3   Intercept Position as a Function of Time

It can be seen that the gradient of the curve increases after stirring has begun.   These results encourage further work with sintered alumina and SiC disks.

Spinel Formation

Spinel, $MgAl_2O_4$, forms according to the reaction:

$$3\underline{Mg} + 4Al_2O_3 == 2Al + 3MgAl_2O_4$$
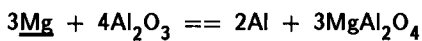
Thermodynamic calculation shows that the equilibrium concentration of Mg for the reaction is 0.02 wt% at 700°C.   While the spinel, as a reaction product, has been identified in mixed composites, little work has been presented on the rate at which the compound forms.

In this work, a ground fused type of alumina particulate, having a mean size of 10 μm, was mixed to a 15 vol% level into super purity aluminium using a mixing apparatus.   Mg was added to a level of 1 wt% to the melt at 700°C.   The molten composite was stirred at 100 rpm.   Samples were taken at various times.   Results are presented here as wt% Mg vs. time in fig. 4.
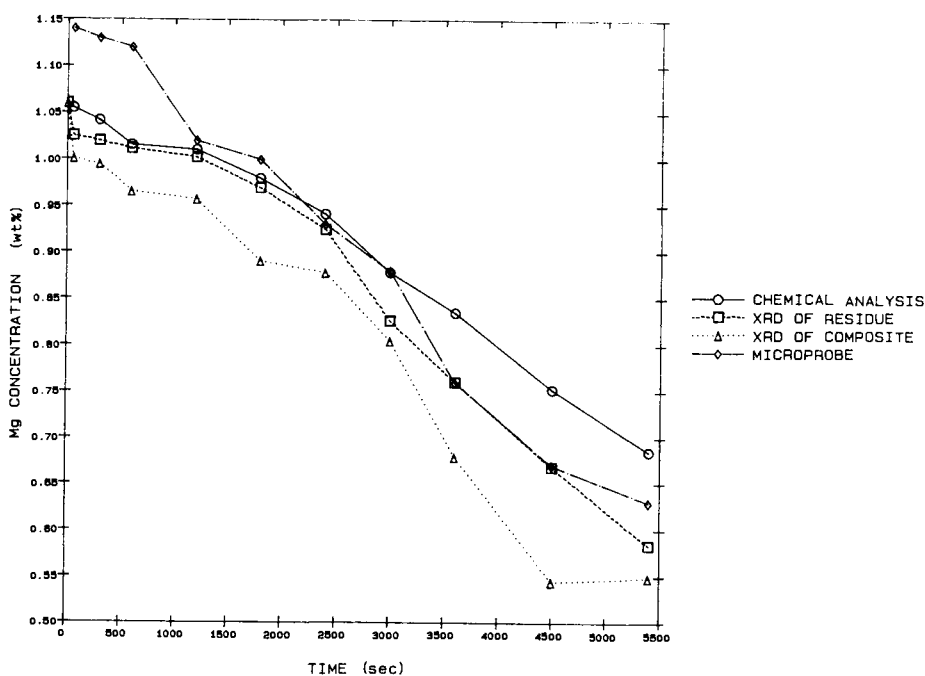
Fig. 4   Consumption of Mg by Spinel formation at 700°C

After various techniques that could be used to measure the progress of the reaction were evaluated, one which is based upon chemical analysis of the dissolved matrix, has been selected as the most accurate technique. The matrix of the reacted composite is leached away with a mixture of hydrochloric and nitric acids. The residue, the alumina and spinel, is filtered, washed and dried. The resulting solution is analyzed using standard ICP techniques. The residue has been examined under an SEM. An example of reacted particulate is shown in fig. 5. The $MgAl_2O_4$ forms as discrete crystallites at certain sites on the alumina particles.

X-ray diffraction can be applied to either the residue or a section of the composite itself. The weight ratio, $MgAl_2O_4$:Al_2O_3 is 1.20 ± 0.03 times the ratio of the net peak intensities. The conversion factor was arrived at by calibration with standards containing 3 to 30 wt% spinel in alumina. The XRD analysis of the residue can be used to calculate an expected wt% Mg value via a mass balance, if an initial (time=0) wt% Mg is assumed. Thus, the XRD results can be used to confirm the results of the chemical analysis. XRD analysis of a composite section is the least accurate method because of the reduced intensity of the spinel peak resulting from dilution by the matrix.

Microprobe analyses can also be used to confirm the chemical analysis results. For this technique, an area free of any particulate is selected for analysis. Ten separate probe analyses are made within the area, providing a mean wt% Mg as well as a standard deviation.
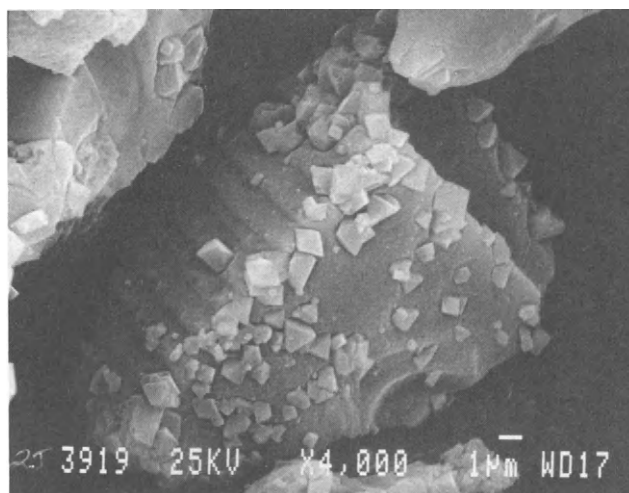
Fig. 5   Scanning Electron Micrograph of Alumina Particles after 90 min.

The chemical analysis technique has been applied to the results of experiments carried out on various other alumina materials. Further work will have to be carried out at other temperatures and Mg concentrations before a model of the spinel growth kinetics can be formulated.

ACKNOWLEDGEMENTS

REFERENCES

Banerji, A, Rohatgi, PK, Reif, W. (1984). Role of Wettability in the Preparation of Metal-Matrix Composites Metall (Berlin), 38, 656-661.

Cappleman, GR, Watts, JF, Clyne, TW. (1985). The Interface Region in Squeeze-Infiltrated Composites Containing (delta)-Alumina Fibre in an Aluminium Matrix. J. Mat. Sci. 20, 2159-2168.

Choh, T, Kammel, R, Oki, T. (1987). Wettability of Graphite to Liquid Aluminum and the Effect of Alloying Elements on it. Z. Metallkd. 78, 286-90.

Choh, T, Oki, T. (1987). Wettability of SiC to Aluminum and Aluminum Alloys Mater. Sci. Technol., 3, 378-385.

Clegg, WJ, Horsfall, I, Briscoe, NA. (1987). A Microstructural Study of Aluminum-(delta)-Alumina Composites Microbeam Anal. 22nd, 233-236.

Delannay, F, Froyen, L, Deruyttere, A. (1987). The Wetting of Solids by Molten Metals and its Relation to the Preparation of Metal-Matrix Composites, J. Mat. Sci., 22, 1-16.

Hikosaka, T, Miki, K, Kawamoto, N. (1987). Fabrication of Aluminum-Ceramic Particle Composites by Vortex Method. Aichi-ken Kogyo Gijutsu Senta Hokoku, 23, 41-48.

Ilegbusi, OJ, Szekely, J. (1988). The Engulfment of Particles by an Electromagnetically Stirred Melt, J. Colloid Interface Sci., 125 567-574.

John, H, Hausner, H. (1986). Influence of Oxygen Partial Pressure on the Wetting Behavior in the System Al/Al$_2$O$_3$. J. Mat. Sci. Lett. 5 549-551.

Kaya, N, Koishi, M. (1988). The Wetting Properties of Powders and Devices for Measuring Them. Kona (Hirakata, Jpn.) [Powder Science and Technology in Japan]. 6, 86-97.

Laurent, V, Chatain, D, Eustathopoulos, N. (1987). Wettability of SiC by Aluminum and Al-Si Alloys. J. Mater. Sci., 22 244-250.

Levi, CG, Abbaschian, GJ, Mehrabian, R. (1979). Interactions Between Alumina Fiber and Aluminum Alloys Under Vigorous Convection. Failure Modes Compos. 4, 370-391.

Levi, CG, Abbaschian, GJ, Mehrabian, R. (1978). Interface Interactions During Fabrication of Aluminum Alloy-Alumina Fiber Composites, Met. Trans. 9A, 697-711.

Munitz, A, Metzger, M, Mehrabian, R. (1979). The Interface Phase in Al-Mg/Al2O3 Composites. Met.Trans. 10A, 1491-1497.

Oh, SY. (1987). Wetting of Ceramic Particulates with Liquid Aluminum Alloys. [PhD. Dissertation for MIT]

Oki, T, Choh, T, Hibino, A. (1985a). Effects of Va Group and Vla Group Elements on the Wettability Between SiC and Molten Aluminum Keikinzoku, 35, 663-669.

Oki, T, Choh, T, Hibino, A. (1985b). Effects of IVa Group Elements on the Wettability Between SiC and Molten Aluminum. Keikinzoku, 35, 670-677.

Rapacchietta, AV, Neumann, AW. (1977). Force and Free-Energy Analyses of Small Particles at Fluid Interfaces II. Spheres J. Colloid Interface Sci. 59, 555-567.

Russell, KC, Cornie, JA, Oh, SY. (1986). Particulate Wetting and Particle: Solid Interface Phenomena in Casting Metal Matrix Composites - Interfaces in Metal-Matrix Composites, Ed: Dhingra, AK, Fishman, SG., pp. 61-91.

Smith, RP, Absolom, DR, Spelt, JK, Neumann, AW. (1986). Approaches to Determine the Surface Tension of Small Particles: Equation-of-State Considerations. J. Colloid Interface Sci., 110, 521-532.

Taftø, J, Kristiansen, K, Borradaile, JB, Westengen, H, Nygard, A, Karlsen, DO. (1988). Studies of Interfaces in Light Metal Matrix Composites by Transmission Electron Microscopy, in Cast Reinforced Metal Composites, Ed: Fishman, SG and Dhingra, AK., pp. 71-75

Tsai, YT, Whitmore, DH. (1982). Nonlinear Least-Squares Analyses of Complex Impedance and Admittance Data for Solid Electrolytes Solid State Ionics. 7, 129-139.

Weirauch, DA. (1988). Interfacial Phenomena Involving Liquid Metals and Solid Oxides in the Magnesium-Aluminum-Oxygen System. J. Mater. Res. 3, 729-739.

Wolf, SM, Levitt, AP, Brown, J. (1966). Wetting and Bonding Between Aluminum Alloys and Sapphire. [Technical Report #AMRA TR 66-19, Available from CFSTI as #AD 638523].

Processing of Al-Li-SiC$_p$ materials using co-deposition of multi-phased materials

M. Gupta, F.A. Mohamed and E.J. Lavernia

Materials Section, Department of Mechanical Engineering, University of California, Irvine, California 92717, U.S.A.

ABSTRACT

In the present study, the effect of matrix solidification on the resulting size and distribution of SiC$_p$ during spray atomization and co-deposition was investigated. The microstructure of the spray deposited materials was characterized as a function of cross-sectional thickness for a single experiment, as well as for different processing variables for distinct experiments. In order to assess the effect of SiC$_p$ particulates on the microstructural evolution during processing, the unreinforced Al-Li material was also studied. The microstructural studies were accomplished using scanning and optical microscopy. Finally, the observed microstructural features and the computed thermal and solidification conditions of the atomized matrix were discussed concurrently.

KEYWORDS

Spray Atomization and Deposition; Metal Matrix Composites; Aluminum-Lithium; Silicon Carbide Particulates; Variable Co-Deposition of Multi-phased Materials (VCMM).

INTRODUCTION

The attractive mechanical and physical properties that can be obtained with metal matrix composites (MMCs) such as high specific modulus of elasticity and strength have been documented extensively (Fishman, 1986; Flom and Arsenault, 1986; Howes, 1986; Mortensen and co-workers, 1986; Nardone and Prewo, 1986). Discontinuous silicon carbide/aluminum (SiC/Al) composites, for example, offer a 50 to 100 percent increase over the modulus of unreinforced aluminum and offer a modulus equivalent to that of titanium but at a third less density (McDanel, 1985). Because their properties can be tailored to specific structural applications, MMCs have become increasingly popular over the past two decades. It has been estimated that by the late 1990's the worldwide market for composite materials will reach $23 billion (Forney, 1986).

The behavior of MMCs is dependent upon, and in many cases can be predicted from the individual properties of the two phases. The reinforcement phase can be in the form of short or long whiskers, fibers, particulates, or a combination of these. Many of the MMCs produced today, however, do not exhibit the ideal properties that would be expected based on rule of mixture calculations. In general, this behavior has been attributed to reinforcing particulate degradation and poor matrix-to-particulate bonding resulting from matrix-particulate interfacial reactions during processing (Brown and Marcus, 1984). The particulate/matrix interfaces play the most important role in the behavior of metal matrix composites because the mechanical properties are largely limited by the efficiency of the particulate/matrix bond. The interface is the link between the matrix and the reinforcement that is necessary to accomplish the appropriate load transfer (Flom and Arsenault, 1986a, 1986b).

The interface can be defined as the region separating the reinforcement from the matrix. It can be less than one atomic layer thick for a coherent interface, or it can consist of several hundred microns which include a reaction layer and therefore contain one or more new phases. It can consist of mechanical locking or a chemical bond between the phases. The interface region can also consist of more than one interface, as in the case of a composite containing coated reinforcing phases (Salkind, 1979). In any case, the interfaces at the reinforcement/coating, coating/reaction zones, and reaction zones/matrix areas may have characteristics distinct from either reinforcement or matrix.

Unfortunately, and despite its twenty year history, the technology for fabricating MMCs remains in a relatively immature stage. While fabricating techniques for organic matrix composites are well defined, progress in processing of MMCs has been hindered by high chemical reactivity and poor wettability commonly found between the reinforcements and the matrix.

Metal matrix composites have been produced by numerous techniques, including pressure infiltration, blending of hard particulates with fine powders, and castings (Divecha, Fishman and Kumar, 1981; Erich, 1987). Although these approaches have been carried out to various degrees of success, there is ample experimental evidence suggesting that there are some important drawbacks. With blended elemental powder metallurgy (PM) techniques, one is limited by the oxide content associated with large surface areas, particularly when used with readily oxidizable alloy systems, such as Mg, Al, Li, Cr, Si, Ti, Hf, etc (Papazian, 1988). In pressure infiltration, for example, the resultant grain size is relatively coarse, segregation takes place, and porosity is usually present (Mortensen and co-workers, 1988); all of these factors have been shown to have an adverse effect on mechanical behavior. Castings also suffer from the drawbacks associated with pressure infiltration techniques; furthermore, the relatively long exposures of the strengthening particulates with the molten matrix can cause undesirable interfacial reactions (Ochiai and Osamura, 1987).

One of the most important factors that determines the stability of MMCs is the chemical and physical nature of the interface. Chemical reactions at the interfaces of MMCs are a result of thermodynamic instabilities that are due to the difference in chemical potentials of the matrix and the reinforcement species. The high temperatures commonly encountered during casting of MMCs, for example, provide the driving force for interfacial diffusion that result in complex chemical reactions. The matrix-reinforcement interface also acts as an enhanced diffusion path for interactions between the environment, the matrix and the reinforcement. It is widely accepted that although limited interfacial reactions may be beneficial, extensive interfacial reactions are generally detrimental to a composite's mechanical behavior.

In the graphite/Al system, for example, the reactions between the aluminum matrix and graphite reinforcing fibers are well known (Brown and Marcus, 1984). Without an effective reaction barrier, aluminum carbide (Al_4C_3) grows at a fast rate above 550 °C resulting in a degradation of the graphite fibers. In the case of Ti/Al_2O_3 composites one would expect from free energy considerations that the alumina is stable with respect to elemental titanium; experimental data, however, indicates that alumina can be unstable with respect to oxygen dissolution in titanium at 1000 °C (Brown and Marcus, 1984). Similar behavior has been reported in the Ni/Al_2O_3 system (Brown and Marcus, 1984). It was reported that the formation of the $NiAl_2O_3$ spinel at the interface was suppressed by a 20 wt% chromium (Cr) addition to the matrix. Cr has a greater affinity for oxygen than nickel, and hence it maintains a lower than critical partial pressure of oxygen in the Ni-Cr solid solution. In superalloy composites, it has been reported that maintaining a ceiling level on the cumulative Fe, Co, and Cr concentrations decreases reaction zone growth kinetics (Fishman, 1986).

Although reaction zone kinetics in MMCs can be altered to a certain degree by chemical control of the matrix, care must be exercised to minimize the secondary effects that might result from reaction products at the interface. Hall and co-workers (1983) reported that the metal reaction zone formed on the metal side of a SiC/Ni based superalloy consists of a complex mixture of four phases: γ-Ni$_3$Al, β-NiAl, α-Cr and a ternary Ni-Si-Al phase. Silicon, however, was shown to alter the chemistry, morphology, and size of the δ' phase in the δ-δ' microstructure.

From the above discussion, it is apparent that in order to promote wetting and minimize undesirable interfacial reactions during metal matrix composite fabrication, it is necessary to control the thermodynamic conditions at the interface. One approach currently being utilized to achieve interfacial thermodynamic control is to simultaneously atomize the matrix material, inject the reinforcing phases into the atomized spray, and deposit the multi-phased mixture onto a substrate or shaped container. This process, termed Variable Co-Deposition of Multi-phased Materials (VCMM), is currently being studied, not only for processing of MMCs but also for the manufacture of gradient materials with prescribed variations in reinforcement type and volume fraction (Lavernia, 1989). Recent results suggest that the costs associated with VCMM processing are substantially lower than those of comparable PM processes (Jacob, Schoenung and Lavernia, 1989). The VCMM process was developed in view of the attractive combinations of structure and properties reported for spray atomized and deposited materials (Annavarapu and co-workers, 1988; Bricknell, 1986; Fiedler and co-workers, 1987; and Lavernia and Grant, 1988). In analogous studies, other investigators have reported successful incorporation of SiC particulates into an aluminum matrix using the Osprey process (Singer, 1983; Willis, 1988) and a modified gas metal arc welding torch (Burhmaster, Clark and Smart, 1988).

The objective of the present study is to provide preliminary results on the effect of matrix solidification on the microstructural evolution during VCMM processing of Al-Li-SiC$_p$ materials. The selection of an Al-Li binary alloy (solid solution) as a matrix material was prompted by the results of Delannay, Froyen and Deruyttere, (1987), and Wolf, Levitt and Brown, (1966). Their work indicates that lithium effectively enhances the wettability of ceramics by molten metals by segregating to the interfacial region and weakening any oxide layers present. These results are supported by the work of Webster, (1982). In addition, lithium effectively reduces the density and increases the modulus of the MMC.

The objective of the present study was accomplished through qualitative and quantitative characterization of the size, volume fraction and distribution of SiC$_p$ particulates using VCMM. In order to assess the effect of SiC$_p$ particulates on the microstructural evolution during processing, the unreinforced Al-Li material was also studied. In addition, the effect of the thermal and solidification conditions of the atomized matrix on the resulting distribution of SiC$_p$ were discussed using existing numerical models.

EXPERIMENTAL

Reynolds Metals Company provided the aluminum lithium master alloy as cast ingots, 100mm x 200mm x 600mm. The ingots were inspected for major defects, and chemically analyzed in preparation for atomization. The chemical analysis of the remelt alloy was Al-2.1 Li (in wt %).

The SiC particulates were obtained from the Superior Graphite Company. The size distribution of the SiC particulates (β phase) was the following: $d_{90} = 5$ μm, $d_{50} = 3$ μm, and $d_{10} = 1$ μm; 99% of the distribution was less than 15 μm. The bulk and particle density was 0.78 and 3.1, respectively; the surface area was 8.3 m^2/g. In order to ensure moisture desorption from the surface of the particulates, the particulates were vacuum degassed at 800 ^{o}C for 30 minutes prior to the experiments.

VCMM Processing

During VCMM, the matrix material is disintegrated into a fine dispersion of droplets using high velocity inert gas jets (see Fig. 1). Simultaneously, one or more jets of strengthening phases are injected into the atomized spray at a prescribed spatial location (see Fig. 2). Interfacial control is achieved by injection of the reinforcing particulates at a spatial location where the atomized matrix spray contains a limited amount of volume fraction liquid. Hence, contact time and thermal exposure of the particulates with the partially solidified matrix are minimized, and interfacial reactions can be controlled. In addition, tight control of the environment during processing insures minimal oxidation. For cases where the reactivity between the matrix material and the reinforcements is negligible, the reinforcing phases can be introduced in the liquid alloy matrix prior to spray deposition (Ast and Zielinski, 1982).

Thermocouple
Stopper Rod
Zirconia Crucible
Induction Coils
Alloy Melt
Atomizer
Vertical Pneumatic Control
Atomization Cone
Environmental Chamber
Spray-Formed Material
Substrate
Horizontal Pneumatic Control
Pressurized Water

20°
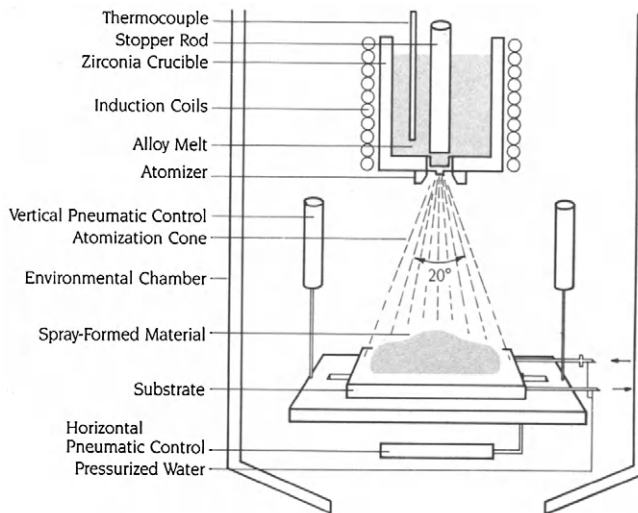
Figure 1. Schematic diagram of experimental apparatus
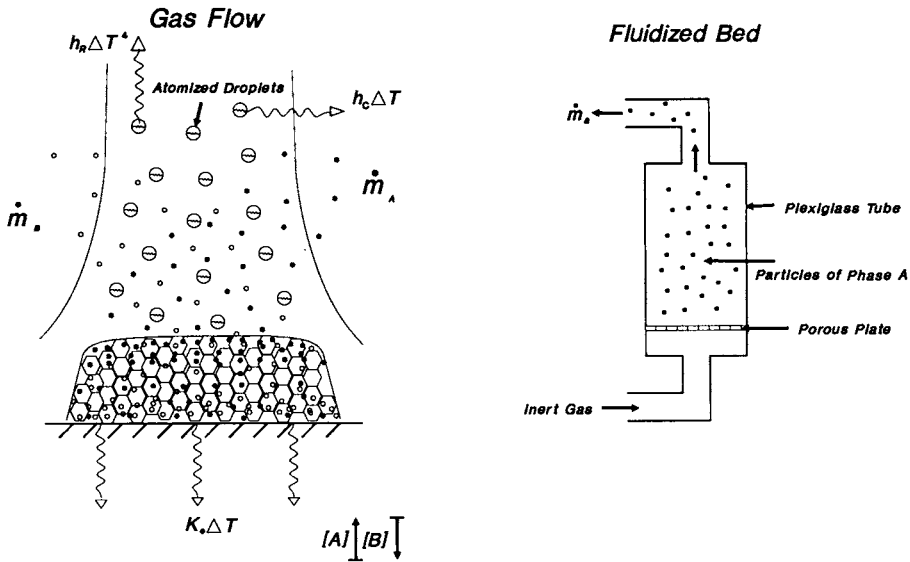
Figure 2. Schematic diagram showing, a) VCMM processing, and b) fluidized bed.

In the present study, the injection of the strengthening phases was accomplished utilizing a suitably designed fluidized bed (see Figure 2). As the gas flow through the static bed of SiC particulates is increased, the bed begins to expand and reaches a condition known as *minimum fluidization*. Further increase in the gas pressure leads to an increase in the value of the void fraction. The void fraction asymptotically approaches unity with continued fluidization. In the present study, we utilized the following equations for calculating void fraction, conditions for minimum fluidization, terminal velocity, and mass flow rate of the gas and particulates (Geiger and Poirier, 1973):

$$w = 1 - (\text{bulk density} / \text{particle density}) \qquad \text{Eqn. 1}$$

$$Re_{Dmf}' = \{(33.7)2 + 0.0408\ Ga\}^{1/2} - 33.7 \qquad \text{Eqn. 2}$$

$$Ga = D_p^3\ (\rho_s - \rho)\ \rho\ g\ /\ \eta^2 \qquad \text{Eqn. 3}$$

$$V_t = D_p^2\ (\rho_s - \rho)\ g\ /\ 18\ \eta \qquad \text{Eqn. 4}$$

$$1/(f)^{1/2} = 4.0\ \log (Re_{Dmf}'\ (f)^{1/2}) - 0.40 \qquad \text{Eqn. 5}$$

$$W = \pi\ D^2\ \rho\ v\ /\ 4 \qquad \text{Eqn. 6}$$

where Re_{Dmf}' is the Reynold's number for minimum fluidization; Ga is Galileo's number; D_p is the size of the SiC particulates; ρ and ρ_s are the densities of the carrier fluid and the solid particulates, respectively; g is the acceleration due to gravity; η is the viscosity of the carrier fluid; V_t is the terminal velocity of the particulates; f and D are the friction

factor and diameter of the fluidization chamber, respectively; W is the mass flow rate; and v is the average operating gas velocity. The experimental parameters used in the present investigation are listed in Table 1.

Table 1. Input Parameters for Fluidized bed

Parameter	Value
Bulk Density	780 kg/m^3
Particulate Density	3.1 X 10^3 kg/m^3
Length of Fluidizing Chamber	0.241 m
Diameter of Fluidizing Chamber	0.05 m
Particulate Size	5 X 10^{-6} m
Density of Argon	1.68 kg/m^3
Viscosity of Argon	2.2 X 10^{-5} kg/m s
Height of Fluidizing Bed	0.19 m
Injection Time for SiC_p	30 s
Mass Flow Ratio of SiC_p/gas	0.18[1]

[1]Determined experimentally

Three VCMM experiments were conducted for this study; the primary experimental variables used during each experiment are listed in Table 2. In addition, a fourth experiment was conducted for the binary Al-Li matrix material, using experimental conditions identical to those listed for Experiment 3, except for the atomization pressure which was increased to 1.38 MPa.

Table 2. Experimental Variables used in Study.

Variable	Experiment Number		
	1	2	3
Matrix Alloy	Al-Li	Al-Li	Al-Li
Reinforcement	SiC_p	SiC_p	SiC_p
Atomization Pressure	1.2 MPa	1.2 MPa	1.2 MPa
Atomization Gas	Argon	Argon	Argon
Fluidized Bed Gas	Argon	Argon	Argon
Injection Angle[1]	30o	20o	90o[2]
Fluidization Pressure	0.69 MPa	0.69 MPa	0.69 MPa
Flight Distance	0.41 m	0.41 m	0.41 m
Pouring Temperature	840 oC	840 oC	850 oC
Metal Delivery Tube Diameter	3.30 mm	3.27 mm	3.33 mm
Atomization Nozzle Pressure condition[3]	~0	6.9 KPa	~0

[1]The injection angle refers to the relative angle between the spray of SiCp and the concentric vertical axis of the atomized matrix.
[2]The 90o injection was conducted at a matrix flight distance of 0.15 m.
[3]Positive and zero values represent pressurization and metal free-fall, respectively.

Optical Microscopy

Optical microscopy was conducted on polished and etched as - deposited samples using conventional and Differential Interference Contrast (DIC) techniques. The size, volume fraction, and distribution of the SiC particulates was quantitatively characterized using a Buehler Omnimet II Image Analyzer.

Scanning Electron Microscopy (SEM)

SEM studies were conducted using a HITACHI S-500 microscope. The samples were cut to a thickness of 0.5 cm and mirror polished using conventional techniques. The polished samples were then examined in secondary electron mode for microstructural details; point analysis was carried out at selected regions of the sample surface to detect the presence of silicon.

RESULTS

Fluidized Bed

The operating conditions for the fluidized bed used in this study were calculated from Eqns. 1 - 6, in combination with the input parameters shown in Table 1. The results are shown in Table 3.

Table 3. Operating Conditions of Fluidized Bed

$$w = 0.74$$
$$\Delta P = 1.9 \times 10^{-3} \text{ MPa}$$
$$Re_{Dmf'} = 7.95 \times 10^{-6}$$
$$Ga = 0.013$$
$$V_t = 0.0019 \text{ m/sec.}$$
$$f = 3.08$$
$$v = 6.24 \text{ m/sec.}$$
$$W_{gas} = 0.0204 \text{ kg/sec.}$$
$$W_{SiC} = 0.00368 \text{ kg/sec.}$$

Structural Characterization

Optical Microscopy. Optical microscopy was conducted on coupons of the VCMM Al-Li-SiC$_p$ material; one example taken from Experiment 2 is shown in Figure 3. This figure reveals the presence of an equiaxed grain morphology, with an average grain size of 68 μm. This grain morphology has also been reported by other investigators (Lavernia and Grant, 1986; Ruhr et al, 1989; Bricknell, 1986). The average grain size for Experiments 1-3 were determined as 71 μm, 68 μm and 66 μm, respectively. Optical microscopy was also performed on the spray deposited binary Al-Li matrix material (see Figure 4). The microstructure of the binary alloy consists of equiaxed grains, 207 μm in diameter (compares with ingot metallurgy grain size of 1270 μm). Optical micrographs were taken from experiments 1 - 3, using Differential Interference Contrast (DIC); the results are shown in Figures 5 - 7, respectively. The use of DIC photography was used in this study to facilitate identification of the SiC particulates in the matrix.
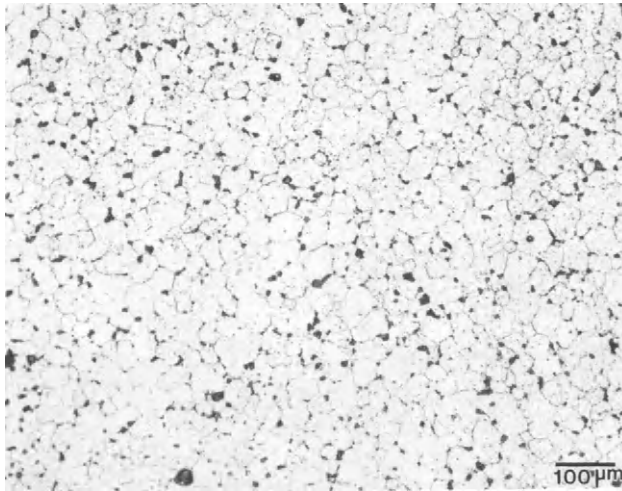
Figure 3. Optical micrograph showing equiaxed microstructure of Al-Li-SiC$_p$ material.
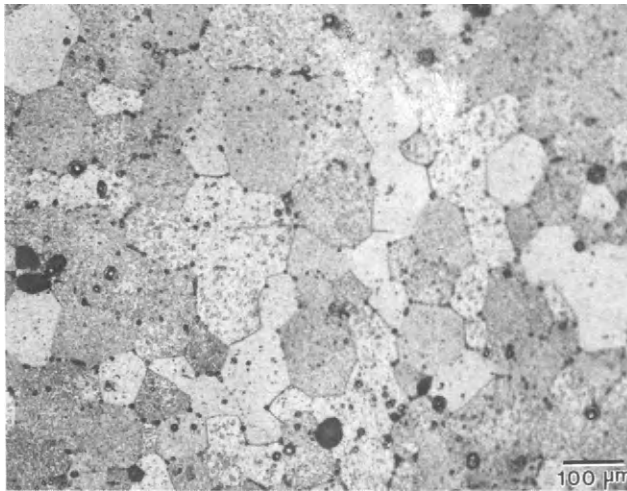
Figure 4. Optical micrograph showing equiaxed microstructure of Al-Li material.
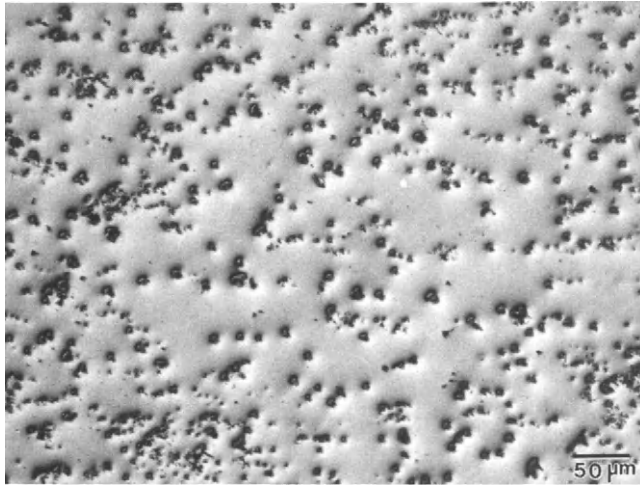
Figure 5. Optical DIC micrograph from Experiment 1 showing distribution of SIC$_p$.
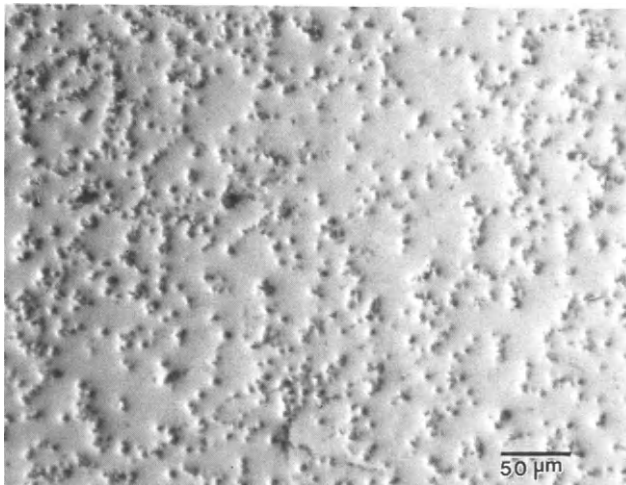
Figure 6. Optical DIC micrograph from Experiment 2 showing distribution of SIC$_p$.
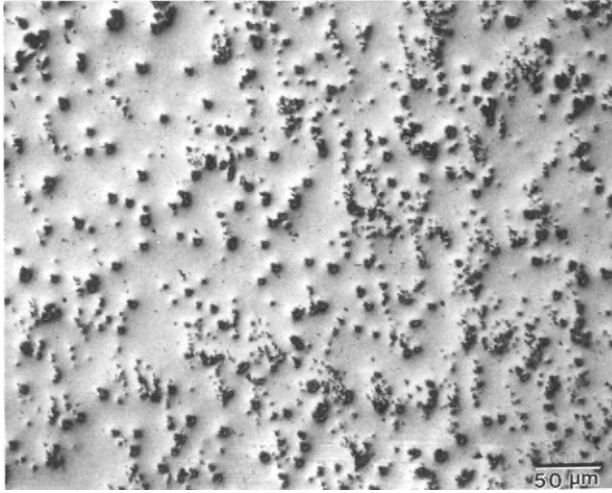
Figure 7. Optical DIC micrograph from Experiment 3 showing distribution of SIC$_p$.

Image Analysis. Image analysis was conducted on a number of samples taken from Experiments 1 - 3 in order to characterize the size, distribution, and location of SiC$_p$ in the matrix. The size and distribution of the SiC particulates obtained from image analysis were then used to compute the SiC$_p$ interparticle spacing according to the formula discussed by Nardone and Prewo (1986):

$$\lambda = (l\,t\,/\,f)^{1/2} \qquad \text{Eqn. 7}$$

where λ is the interparticle spacing; and t, l and f are the thickness, length, and volume fraction of the SiC$_p$, respectively. The results of the image analysis and the computed interparticle spacings, λ, are shown in Table 4. The frequency histograms corresponding to the size distribution of the SiC particulates from Experiment 1 are shown in Figure 8.

Table 4. Image Analysis Results

Sample #[1]	Equivalent Diameter (μm)[2]				Vol. Fraction (%)				Interparticle Spacing (λ, μm)
	Min.	Max.	Mean	σ	Min.	Max.	Mean	σ	
1A	0.57	9.00	**2.70**	2.01	1.92	8.33	**3.49**	1.82	14.48
1B	0.57	10.00	**2.71**	2.10	2.89	6.15	**4.56**	1.13	12.69
1C	0.57	12.00	**2.10**	1.76	4.40	13.44	**7.89**	1.91	7.48
2A	-------not determined-------						**9.6**[3]		8.71[4]
2B	-------not determined--------------								
2C	-------not determined-------						**11.65**[3]		7.91[4]
3A	0.57	11.00	**2.76**	2.13	4.69	7.19	**6.12**	0.85	11.14
3B	0.57	10.00	**2.86**	2.12	4.38	6.10	**5.13**	0.50	12.62
3C	0.57	9.00	**3.34**	2.16	1.34	3.16	**2.49**	0.54	21.16

[1]A, B, C designations refer to top, center and bottom regions, respectively, of the spray deposited Al-Li-SiCp.
[2]The equivalent diameter is a measure of the size of the SiC particulates.
[3]These values of the volume fraction were determined using quantitative metallography.
[4]These values were computed from Eqn. 7 for a SiCp size of 2.7 μm.
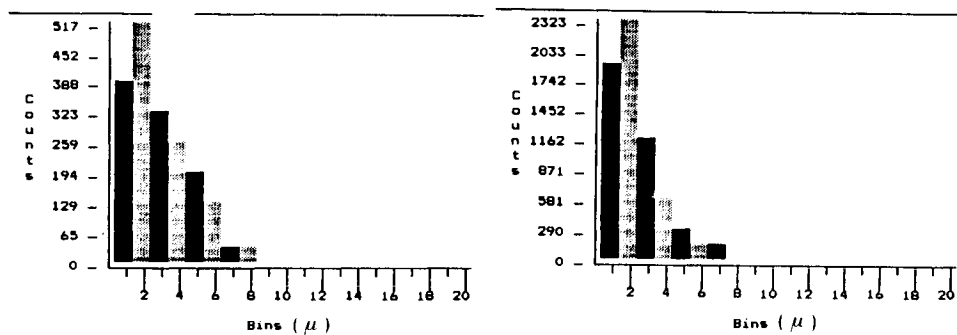
Figure 8.   Frequency histogram showing SiCp size distribution for a) top and
            b) bottom regions of Experiment 1.

SEM/EDAX Analysis. Scanning electron microscopy of samples removed from the central portion of the spray deposited material revealed a fairly uniform distribution of SiCp throughout the matrix (see Figure 9). In addition, SEM analysis also shows the presence of a finite amount of non-interconnected porosity (see Figure 10). The micron sized pores were preferentially located at the grain boundaries, and exhibited an irregular, facetted morphology. The distribution of pores in the microstructure was found to be bimodal, with a large proportion of pores in the 1-2 μm and 10 μm size ranges; the volume fraction of porosity was estimated to be approximately 4-5%.

EDAX analysis was conducted on VCMM samples in order to assess the presence of the SiC_p, and to distinguish the particulates from other metallurgical features (see Figure 11).
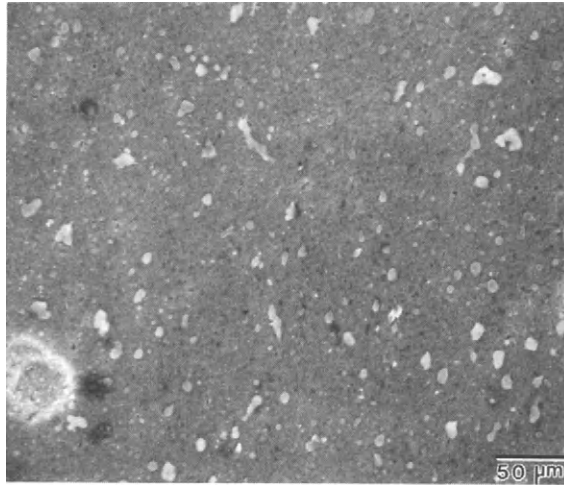
Figure 9. SEM photograph showing SiC_p size distribution.
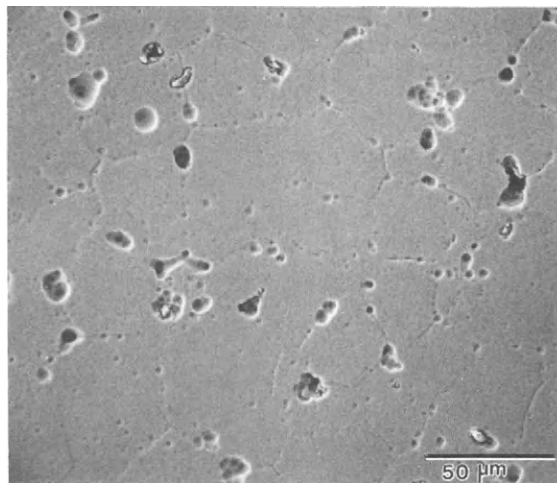
Figure 10. SEM photograph showing location and morphology of porosity.
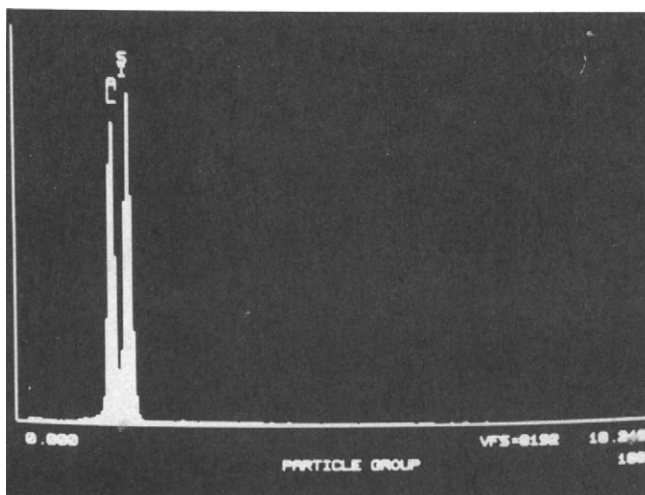
Figure 11. EDAX spectrum of SiC_p in Al-Li matrix.

Numerical Model

Recently, various investigators have modeled the various solidification and heat transfer phenomena during atomization (Levi and Mehrabian, 1982; Mathur, Apelian and Lawley, 1988; Lavernia and co-workers, 1988; Gutierrez and co-workers, 1989). In these studies, the thermal histories of droplets in flight are calculated using a lumped parameter approximation. In the present paper, we applied the model developed by Lavernia and co-workers (1988) to the experimental conditions used in the present study; the specific input parameters are shown in Table 5. The results are shown in Figure 12.

Table 5. Input Parameters used in numerical model.

Variable	Description	Value
C_{pg}	Specific heat of argon	518.8 J/kgK
C_{pm}	Specific heat of Al	0.86 KJ/kgK
H_f	Heat of fusion of Al	398 KJ/kg
k_m	Al thermal conductivity	209 W/mK
T_L	Liquidus temperature	640 °C
T_S	Solidus temperature	600 °C
ρ_m	Al density	2.7 g/cm^3
γ	Ratio of Cp/Cv for gas	1.65
T_N	Nucleation temperature	610 °C
σ_m	Melt surface tension	0.840 kg/s^2
ρ_g	Gas density	1.654 kg/m^3
μ_g	Gas viscosity	1.7X10^{-5} kg/ms
μ_m	Melt viscosity	0.001 kg/ms
P_g	Atomization gas pressure	1.20 MPa[1]

[1]The gas atomization pressure used for the Al Li binary materials was 1.38 MPa.
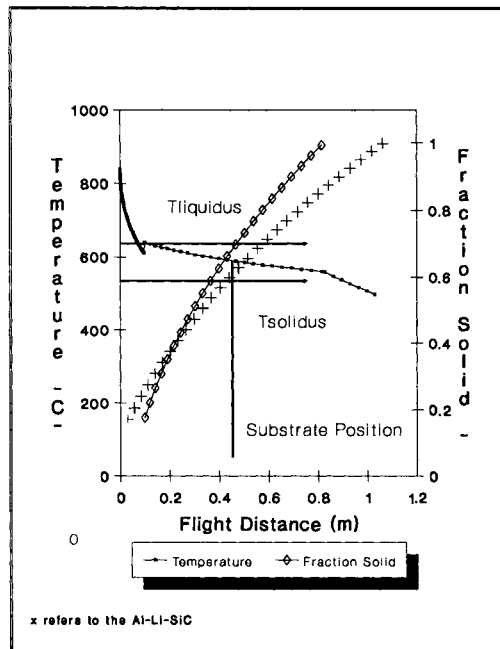
Figure 12. Computed temperature and fraction solid for Al-Li-SiC$_p$, and Al-Li materials.

The numerical model predicts, as shown in Figure 12, that at the moment of impact the droplet distribution of the binary alloy is comprised of solid powders (d_{16} = 23 μm, f_s = 1), droplets with some proportion of liquid phase (d_{84} = 275 μm, f_l> 90%), and a substantial fraction of powders in the mushy state (d_{50} = 84 μm, f_l = 30%). For the Al-Li-SiC$_p$, the droplet distribution consists of solid powders (d_{16} = 30 μm, f_s = 1), droplets with some proportion of liquid phase (d_{84} = 290 μm, f_l> 90%), and a substantial fraction of powders in the mushy state (d_{50} = 92 μm, f_l = 42%). In the following sections, the salient microstructural features observed in the VCMM Al-2.1Li-SiC$_p$ and Al-Li materials, and the numerical results are discussed concurrently.

DISCUSSION

Grain Structure

The grain morphology of the VCMM material was equiaxed; this observation is in agreement with previous findings (Lavernia and Grant, 1986; Ruhr and co-workers, 1989; Gutierrez and co-workers, 1989). Lavernia (1989) proposed that the formation of an equiaxed grain morphology during spray deposition is a result of three simultaneous processes: (1) dendrite arm fragmentation, (2) nucleation/grain multiplication, and (3) constrained growth.

Regarding the grain size, the predictions of the numerical model are reasonable in view of the relatively coarse grains observed experimentally for the SiC$_p$ containing material (68μm). This grain size is approximately 75% coarser than those reported by other investigators for spray deposited aluminum alloys (Lavernia and Grant, 1988a; 1988b). The coarse grain size found in the present investigation is thought to have developed

first, as a result of an excessive amount of liquid phase contained in the droplet distribution at the moment of impact with the deposition surface, and second, due to the lack of secondary precipitates to prevent grain boundary migration during solid state cooling. Gutierrez and co-workers (1989), for example, reported grain sizes ranging from 12-25 μm for a spray deposited high strength aluminum alloy. Their results show, however, that the average droplet size contained only 10-15 volume fraction liquid at the moment of impact with the substrate; this is substantially lower than that achieved in the present investigation (Al-Li-SiC$_p$, V_{fl} = 41%; Al-Li, V_{fl} = 30%).

Comparison of the grain size of the Al-Li binary alloy to that of the Al-Li-SiC$_p$ material indicates that the presence of the SiC particulates effectively reduces the grain size by approximately 67%. This is notwithstanding the fact that the droplet distribution of the AL-Li-SiC$_p$ contained a substantially higher amount of liquid phase at impact (V_{fl} = 41%) as compared to the conditions present for the Al-Li material (V_{fl} = 30%, see Figure 12). The finer grain morphology of the Al-Li-SiC$_p$ is thought to result from a combined effect of three distinct mechanisms: enhanced heat transfer, increased solidification prior to impact, and grain boundary pinning effects. During flight, the SiC$_p$ spray from the fluidized bed effectively enhances the convective heat transfer from the matrix droplets as a result of its lower temperature and high relative velocity. Regarding solidification, it is known that during flight, solidification of the matrix is catalyzed heterogeneously as a result of one or a combination of the following: bulk heterogeneous nucleation within the droplet, surface oxidation processes, or collisions between the droplets. In the present study, however, collisions between the droplets and SiC particulates must also be considered. Finally, after impact with the substrate, the SiC particulates will effectively slow down grain boundary migration during solid state cooling.

Porosity

Microstructural analysis revealed the presence of a bimodal distribution of non-interconnected pores, with a large proportion of pores in the 1-2 μm and 10 μm size ranges; this is consistent with previous findings (Lavernia and Grant, 1986; Ruhr and co-workers, 1989; Bricknell, 1986). The origin of porosity in spray deposited materials can be traced to three possible sources: gas entrapment, solidification shrinkage, and interstitial porosity (Lavernia, 1989). The available experimental evidence suggests that porosity develops from interstices formed as the droplets impact on one another, leaving micron sized, irregular cavities as they overlap. This mechanism is consistent with the results of Lavernia and Grant (1988), and Ogata and co-workers (1986) who reported a correlation between deposition conditions such as spray density, powder size, and fraction solidified, and the amount of porosity present throughout the deposit. In addition, this mechanism is consistent with the irregular morphology of the pores observed in this study.

The presence of fine grain boundary pores observed in the present study is in agreement with the findings of other investigators (Lavernia and Grant, 1986; Ogata and co-workers, 1986; Gupta Mohamed and Lavernia, 1989). Although the origin of this phenomenon is not completely understood, it has been suggested by Lavernia, (1989) and Gutierrez and co-workers, (1989), that during impact and solidification these fine pores effectively pin grain boundaries, preventing their migration.

SiC Particulate Size and Distribution

In order to verify the computed mass flow rate of the SiC$_p$ shown in Table 3, several fluidized bed experiments were conducted independently. The results of these experiments indicate a SiC$_p$ mass flow rate of approximately 1.6 g/sec. Although this is substantially lower than the computed value of 3.68 g/sec. (see Table 3), it is not

unreasonable in view of the large number of assumptions incorporated into Eqns. 1 - 6. If the calculated and measured values of the SiC_p mass flow rates, and the mass flow rate of the Al-Li matrix are taken into consideration, it is possible to estimate an upper bound of the volume fraction of the SiC_p that can be anticipated. Such calculations yield a volume fraction of SiC_p in the 4.2% - 8.5 % range. This compares favorably with the observed SiC_p volume fraction, as averaged over all three experiments (6.8%, see Table 4).

The results shown in Table 4 indicate variations in volume fraction of SiC_p with thickness. In Experiment 1, the SiC_p spray was aimed at the deposition surface, but inclined at an angle of 20° from the matrix spray (see Table 3). Whereas in Experiment 3 injection of the particulates was accomplished by aiming the SiC_p spray at 90° from the matrix spray. These results indicate that it is possible to taylor the resulting variations in volume fraction of SiC_p through changes in the injection angle. The higher volume fraction of SiC_p observed for Experiment 2 was a result of the pressurization condition at the metal delivery tube (see Table 2). This behavior, which is caused by the relative position of the metal delivery tube to the gas jets, has been studied extensively (Baram and co-workers, 1988). In the present study, the pressurization effect reduced the metal flow rate of the matrix, effectively decreasing the Al-Li/SiC_p mass flow ratio, hence resulting in higher SiCp concentration.

Regarding the size distribution of the SiC_p, the results from Table 4 (d_{50} = 2.7 μm) are consistent with the initial SiC_p size (d_{50} = 3.0 μm). The slight reduction in particulate size can be attributed to the difficulties associated with fluidizing the coarse SiC particulates. These results also suggest that the processing methodology does not favor clustering of the SiC particulates. This is consistent with the lower number of counts for particulate sizes greater than 8 μm (see Figure 8).

In terms of the location of the SiC_p in the Al-Li matrix, the computed interparticle spacings from Table 4 indicate that the particulates were randomly distributed throughout the matrix (i.e., not preferentially located at the grain boundaries). This was also confirmed through SEM analysis (see Figure 9). After impact with the substrate, retention of a suitable particulate dispersion throughout the matrix is facilitated by the presence of primary dendrite debris resulting from droplet impact. In related studies on rheocast metal matrix composites, Mehrabian, Riek and Flemings, (1973) showed that the presence of primary solid phases during solidification promotes mechanical entrapment and prevents agglomeration of the strengthening particulates. In addition, it is plausible that the intermediate solidification velocities present during impact and solidification (1-2 mm/sec., Ruhr and co-workers, 1989) promote entrapment of the SiC_p according to the mechanisms discussed by Stefanescu and co-workers, 1987.

Regarding the nature of the interface between the SiC_p and the Al-Li matrix, work is in progress in order to asses the effect of processsing on the interface..

CONCLUSIONS

i.   The preliminary results presented in this paper suggest that VCMM processing can be successfully utilized to manufacture MMCs with prescribed variations in SiC_p concentration.

ii.   The SiC particulates were found to promote substantial grain refinement, relative to the unreinforced material. The finer grain morphology of the Al-Li-SiC_p was discussed in terms of three distinct mechanisms: enhanced heat transfer, increased solidification prior to impact, and grain boundary pinning effects.

iii.   Quantitative analysis of the size and distribution of the SiC_p in the Al-Li microstructure indicated minimal agglomeration. Retention of a suitable particulate dispersion throughout the matrix was facilitated by the presence of primary dendrite debris resulting from droplet impact.

ACKNOWLEDGEMENTS

REFERENCES

Annavarapu, D. Apelian, and A. Lawley (1988). Met. Trans., 19A, 3077-3085.

Ast, D. G., and P. G. Zielinski (1982). "Preparation of Metallic Glasses with Second Phase Particles", Rapid Solidification Processing Principles and Technologies, III, Proceedings of the Third Conference on Rapid Solidification Processing, held at the National Bureau of Standards, Dec. 6-8, Gaithersburg, MD., 384-389.

Baram, J.C., M.K. Veistinen, E.J. Lavernia, M. Abinante and N.J. Grant (1988). Journal of Materials Science, 23, 2457-2463.

Bricknell, R. H. (1986). Met Trans., 17A, 583-590.

Brown, L. D., and H. L. Marcus (1984). "Interfacial Reactions in Metal Matrix Composites", Metal and Ceramic Composite Processing Conference Proceedings Volume II, 13-15 November, Battelle's Columbus Laboratories, Columbus, Ohio.

Buhrmaster, C. L., D. E. Clark, and H.B. Smart (1988). Journal of Metals, 40, No. 11, 44-45.

Delannay, F., L. Froyen, and A. Deruyttere (1987). Journal of Materials Science, 22, 1-16.

Divecha, A. P., S. G. Fishman, and S. D. Kumar (1981). Journal of Metals, 3, No. 9, 12-17.

Erich, D.L. (1987). International Journal of Powder Metallurgy, 23, No. 1, 45-54.

Fiedler, H. C., T. F. Sawyer, R. W. Koop, and A. G. Leatham (1987). Journal of Metals, August, 39, No. 8, 28-35.

Fishman, S. G. (1986). Journal of Metals, 38, No. 3, 26-28.

Flom, Y., and R.J. Arsenault (1986). Journal of Metals, 38, No. 7, 31-34.

Flom, Y., and R.J. Arsenault (1986). Materials Science and Engineering, 77, 191-197.

Forney, R. C. (1986). Journal of Metals, 38, No. 3, 18-20.

Geiger, G.H., and D. Poirier (1973) Transport Phenomena in Metallurgy, Addison-Wesley publishing Co.

Gutierrez, E., E. J. Lavernia, G. Trapaga, J. Szekely, and N. J. Grant (1989). Met. Trans., 20A, 71-85.

Gupta, M., F. Mohamed, and E. Lavernia (1989). Conference Proceedings of the Al-Li-V International Conference, Williamsburg, VA, March 27-31.

Hall, .E. L., Y. M. Kouth, M. R. Jackson, and R. L. Mehan (1983). Met. Trans., 14A, 781.

Howes, Maurice A. H. (1986). Journal of Metals, 38, No. 3,.28-29.

Jacob, J., J.M. Schoenung, and E.J. Lavernia (1989). Proceedings of the University -Industry Advanced Materials Conference, sponsored by the Materials Research Society (MRS), Denver Colorado, March 6-9.

Juarez-Islas, J. A., H. Jones, and W. Kurz (1988). Mat. Sci. and Eng., 98, 201-205.

Katgerman, L., and B. Vande Brandt (1985). Conference Proceedings, Aluminum Powder Metallurgy, held during the TMS-AIME fall meeting, Toronto, Canada, 65-78.

Lavernia, E. J. and, N. J. Grant 1986, International Journal of Rapid Solidification, 2, No. 2, 93-106.

Lavernia, E. J., and N. J. Grant (1988). Materials Science and Engineering, 98, 381-394.

Lavernia, E. J., E. Gutierrez, J., Szekely, and N. J. Grant (1988). International Journal of Rapid Solidification, 4, No. 1/2, 89-124.

Lavernia, E. J. (1989). University of California at Irvine, current research.

Levi, C. G., and R. Mehrabian (1982). Met. Trans., 13A, 221-234.

Mathur, P., D., Apelian, and A. Lawley (1988). Acta Metallurgica, in press.

McDanels, D. L. (1985). Met. Trans., 16A, 1105.

Mehrabian, R., R. G. Riek, and M. C. Flemings (1974). Met. Trans., 5A, 1899- 1905.

Mortensen, A., M. N. Gungor, J. A. Cornie, and M. C. Flemings (1986). Journal of Metals, 38, No. 3, 30-35.

Mortensen, A., J. A. Cornie, and M. C. Flemings (1988). Journal of Metals, 40, No. 2, 12 -19.

Nardone, V.C., and K. W. Prewo (1986), Scripta Metallurgica, 20, 43-48.

Ochiai, S., and K. Osamura (1987). Met. Trans., 18A, 673-679.

Ogata, K., E. J. Lavernia, G. Rai, and N. J. Grant (1986). International Journal of Rapid Solidification, 2, No. 1, 21-35.

Papazian, J. (1988). Met. Trans., 19A, 2945-2953.

Rioja, R. J., and E. A. Ludwiczak (1986). Al-Li-III, Conference Proceedings, The Institute of Metals, London, 471-482.

Ruhr, M., I. Ucok, E. J. Lavernia, and J. Baram (I989). Metastable Phases and Microstructure of a Rapidly Solidified AL-Li-Mn-Zr Alloy, Conference Proceedings Symposium on Light-Weight Alloys for Aerospace Applications during the 1989 Annual TMS meeting, February 28-March 3, Las Vegas, Nevada.

Salkind, M. L. (1979). "The Role of Interfaces in Fiber Composites", in Surfaces and Interfaces II, Physical and Mechanical Properties, J. J. Burke, N. L. Reed, and V. Weiss editors, Syracuse University Press, 417-445.

Singer, A. R. E. (1983). Annals of the CIRP, 32, 145-149.

Stefanescu, D.M., B.K. Dhindaw, S.A. Kacar and A. Moitra (1987). Met. Trans., 19A, 2847-2855.

Webster, D. (1982). Met. Trans., 13A, 1511-1519.

Willis, T. C. (1988). Metals and Materials, 4, No. 8, 485-488.

Wolf, S. M., A. P. Levitt, and J. Brown (1966). Chemical Engineering Progress, 62, No. 3, 74-78.

Interfacial phenomena between molten metals and alloys and alumina substrates

A.C.D. Chaklader

Department of Metals and Materials Engineering, The University of British Columbia, Vancouver, British Columbia, Canada, V6T 1W5

Abstract

The interfacial phenomena between alumina and molten metals (alloys) have been investigated in this program. The bonding between these two dissimilar phases was studied with respect to the wetting and non-wetting behaviour, as determined by the sessile drop technique. It has been shown that the addition of alloying metallic elements having higher oxidation potential than those of bulk metal enhances wetting and results in higher work of adhesion. Similarly addition of surface active agents such as oxygen will definitely improve the wetting and bonding characteristics of metals to alumina. In spite of this success in achieving bonding between metals (or alloys) and alumina, the problem of expansion coefficient mismatch, which results in very large stresses, remains. Simple calculations show that the stresses on cooling from the molten metals to ambient temperature is in the order of 0.5 to 1 GPA for Cu-,Fe-,Ni-Al_2O_3 systems. It is desirable to alloy Fe, Ni and/or Cu with other metals to lower the expansion coefficient of the alloys, bringing closer to α-Al_2O_3. It may thus be possible to produce an Al_2O_3-alloy composite, without imposing severe stress in the system.

Keywords: Alumina, Wetting, Metals (alloys), Interface, Stresses

1.0 Introduction

Nearly forty years have elapsed, since attempts were made to develop new high temperature creep resistant structural materials based on a combination of ceramic and metal phases. It was just after the Second World War, that the development in Germany of high-speed cutting tools, using tungsten carbide and an alloy steel was brought to the attention of the Western world. Since then numerous attempts have been made both in the industrial laboratories and at the universities to develop cermets, but it is known to everyone that the number and types of cermets successfully developed for commerical use, have been very few indeed.

The early expectations of being able to develop strong and tough materials by combining ceramic and metallic phases has not been generally realized, although some of the cermets commercially available have more creep-resistance and have better stress-rupture properties at elevated temperatures than do the superalloys. Earlier research activities in this field were product oriented and most of the work was ad hoc in nature. Recent studies have shed considerable light on the problems and difficulties of making cermets of any desired characteristics.

The development of ceramic-metal composites is based on the premise that the mechanical properties of metals, especially the ability to undergo plastic flow, can be combined with the high temperature properties of brittle ceramics in a product that would be suitable for structural applications at elevated temperatures.

Depending on the nature of their use, cermets can be divided into different groups: (a) high temperature structural cermets – e.g. refractory oxides and carbides combined with high strength refractory metals and alloys: (b) ordinary or low temperature structural cermets – glass or SiC whiskers and particulates with low melting metals and alloys such as Al, Cu etc. and (c) non-structural cermets – such as cutting tools.

In ceramic-metal composites or cermets, the most important criteria for obtaining desirable properties are:

a. bonding across the interface (wettability), and
b. expansion coefficients compatibility

1.1 Bonding (General Considerations)

In this section bonding by mechanical interlocking at the interface will not be be considered.

In most cermets, where strength is an important requirement, the first thing that should be considered is the fundamental factors affecting the bonding of heterogeneous systems.   This is particularly important for optimum stress transfer across the phase interface so that the whole system is uniformly stressed.   In the case of polyphase ceramics or metallics such as mixed oxides or alloys, bonding does not give rise to any special problem.   This is primarily due to the fact that the nature of bonding across the phase interface is similar in each case, i.e. ionic or covalent (or mixed) in the case of non-metallic systems, and metallic or semi-metallic bonding in the case of metals and alloys.   When two phases of dissimilar bonding character are mixed, poor bonding across the interface results.   For example, metal-oxide systems generally show poor bonding across the interface.   To improve the bonding characteristics between metals and oxides several approaches have been made.   One approach to the problem is to add a third phase to obtain a satisfactory bond in metal-oxide systems.   The best known example is the addition of TiN in Ni-MgO cermets[1].   It has been postulated that TiN partially reacts with MgO in an inert atmosphere, resulting in bonding; at the same time TiN, which is a metalloid, forms a bond with the metal phase. Thus, a metal-metalloid-oxide transition type of bond can be realized.

Bonding which is effected by an interfacial chemical reaction only, such as to form a solid solution as a third phase, e.g. bonding in nickel-chromium-alumina cermets, is commonly referred to as chemical bonding.   In the case of the chromium-alumina system, the chromium is superficially oxidized to form Cr_2O_3 which is structurally isomorphous with Al_2O_3 and thus readily forms a solid – solution at the interface[2].

Cermets in which some chemical reaction and a limited amount of penetration along grain boundaries occur are considered to be in the mixed group.   This type of cermet is illustrated by certain metal oxide systems in which the basic metal phase does not readily wet the ceramic.   A second metal with greater affinity for oxide ceramics is added in small proportions to enhance wetting and hence better bonding between the phases occurs (e.g. $Ni-Ti-Al_2O_3$[2]).   Thus bonding between alumina and the metal phase has been achieved in a number of systems by the formation of complex oxide-layer at the interface[3].   For example, formation of SnO_2 at the Sn-Al_2O_3 interface and complex oxides in Fe-FeO with Al_2O_3[4], Cu-Al-Al_2O_3[5,6], Cu-Ti-Al_2O_3[7], Cu-Sn(or Ti)-Al_2O_3[8] have been postulated and in some cases verified in the development of interfacial bond.

1.2 Wetting

It has been known for a long time that wetting of a solid by a liquid is intimately related to the bonding across their interface. Wetting between two phases is a direct reflection of the compatibility of mutual bond types. In addition, wetting also controls the distribution of a liquid phase in a solid matrix, when a composite is sintered at high temperatures. The microstructure of a sintered compact and thus its properties, are influenced by the wettability between the metal and ceramic phases (exception: hot-pressing of powder mixtures). A non-wetting liquid metal will tend to be isolated in localized pockets in a ceramic matrix during sintering. In this case, a continuity of the ductile phase cannot be maintained. The formation of a strong bond which results from wetting between dissimilar phases is a prime consideration for structural stability of cermets at elevated temperatures. Poorly bonded cermets are often characterized by the "sweating" or "oozing" out of the metal from the compact during elevated temperature use. For these reasons more efforts have been directed towards the understanding of wetting between two dissimilar phases and the factors affecting it, than any other aspects of research involving composites.

1.2.1 Energy Consideration

1.2.1.1 Solid-Liquid-Vapor Equilibrium

The relationship between the surface and interfacial energies determines to a large extent the wetting of a solid surface by a liquid. The equilibrium shape of a liquid drop on a solid surface conforms to the minimum total surface and interfacial energy for all the phase boundaries present, as shown in Figure 1. An energy balance on a sessile drop, neglecting the gravitational force is given by the Young-Dupré equation[9]:

$$\gamma_{sl} = \gamma_{sv} - \gamma_{lv} \cos\theta \qquad\qquad 1(a)$$
$$\text{(in the presence of a vapor)}$$

or

$$\gamma_{sl} = \gamma_{sg} - \gamma_{lg} \cos\theta \qquad\qquad 1(b)$$
$$\text{(in the presence of a gaseous phase)}$$

where γ_{sl} = Interfacial tension
γ_{sv} or γ_{sg} = Surface tension of the solid
γ_{lv} or γ_{lg} = Surface tension of the liquid
and θ = Contact angle between the liquid drop and solid.

Subscripts S and G stand for the vapour or gaseous species in the system.

If the solid-liquid interfacial energy (γ_{sl}) is greater than the surface energy (γ_{sv}) of the solid (assuming contribution from the component of γ_{lv} is small) then the liquid tends to form a ball having a small interface area. On the other hand, if the solid vapour interface energy (γ_{sv}) is high, the liquid tends to spread out to eliminate this interface (Figure 1). It is generally accepted that $\theta > 90°$, indicates a non-wetting behaviour, conversely $\theta < 90°$ implies that the liquid wets the surface of a solid.

1.2.2 Solid-Liquid Equilibrium[10]

Whether the distribution of the liquid phase is along the grain boundaries or in an isolated pocket at triple grain corners will depend upon the relative magnitude of the grain boundary energy (γ_{ss}) and the interfacial energy (γ_{sl}).

To impart substantial ductility into the cermet composite at a temperature when the ceramic phase is brittle, the ratio of the grain boundary energy (γ_{ss}) to phase boundary energy (γ_{sl}) should be greater than 1.7. This corresponds to a dihedral angle (ϕ) of less than 60°. A knowledge of the surface energy (or surface tension) values is important in determining the compatibility of ceramic and metal phases with respect to the distribution of the second phase both during fabrication (i.e. sintering) and during subsequent use at elevated temperatures.

1.3 Compatibility

Compatibililty in expansion coefficients is a major problem in cermets, as in almost all cases the metallic phase has a higher expansion coefficient than that
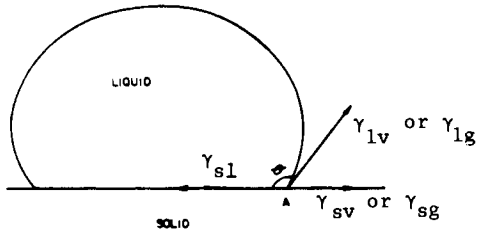
Fig. 1: Surface tension forces   Fig.2: Ni–Cu–Al$_2$O$_3$ composite (hot-pressed,
acting on a sessile drop.   electroless plated alumina particles
                                              first by Cu and then by Ni, porosity
                                              ~2%) dark areas alumina particles.

of the non-metallic phase. The mismatch at the interface can create large stresses resulting in cracking or interface separation. This problem can be partially overcome in an idealized cermet, having a continuous metal matrix with dispersed hard ceramic particles. Ceramic being the lower expansion coefficient phase, will be always under compression and consequently the metal matrix in tension. This is a desirable state as ceramics are usually very strong under compression. A microstructure of this type shown in Figure 2. This cermet was produced by electroless plating of alumina particle first with Cu and then with Ni, and then subsequently hot-pressing the composite[11].

2.0 Alumina-Metal (Alloy) Systems

Norton and Kingery[12] determined the interfacial tensions (γ_{sl}) of Al$_2$O$_3$–Ni, –Fe, –Pb and –Ag and also the effect of solute components in decreasing the γ_{sl} values. Subsequently, the effect of additions of In, Sn, Cr and Ti on the interfacial tension between liquid Ni and solid Al$_2$O$_3$ was studied by Kurkjian and Kingery[13]. The addition of Cr and Ti drastically reduced the interfacial tension between Ni and Al$_2$O$_3$ but In and Sn, although very surface active in liquid nickel, did not at all affect the interfacial tension. Norton and Kingery[14] considered that the decrease in interfacial tension is due to transfer of solute atoms from the bulk of the liquid to the interface with the formation of solute metal-oxygen bonds, the oxygen being part of the Al$_2$O$_3$ lattice. This process is equivalent to the chemisorption process and is directly related to the standard free energy of the oxide. This transfer may be represented by

$$xM + yO = M_xO_y \quad - \Delta F_{MO}$$
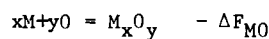
where
$$-\Delta F_{MO} = RT \ln k; \quad k = \frac{M_xO_y}{(M)^x(O)^y} \tag{2}$$

The free energy change for this reaction is directly related to the standard free energies of the formation of the oxide of solutes.

Using the same approach, McDonald and Eberhart showed that the work of adhesion (W_{AD}), which is equal to $\gamma_{sv} + \gamma_{lv} - \gamma_{sl}$ (according to Dupré's equation), can be related with the free energy of formation of oxides (ΔF_f) as follows:

$$W_{AD} = -a\,\Delta F_f^° + b \tag{3}$$

where a and b are constants and both positive.

These workers have shown that the calculated theoretical values of the work of adhesion and that of the experimental data generated by Armstrong et al[2] agrees quite well with the above equation. This is shown in Figure 3.

2.1 Effect of Oxygen on Metal-Alumina Systems

An alternative approach to enhance wetting is to introduce oxygen in metal-oxide ceramic systems[16]. Although Holden and Kingery[17] and Monma and Suto[18] observed a sharp drop of the liquid tension of Fe and Cu, respectively, when a small amount of oxygen or sulphur was introduced with the system, these workers did not extend their studies into the wetting behaviour of these systems on oxides. Similarly, Eremenko and Naidich[19] investigated the lowering of surface tension of Cu, Ag and Ni by introducing oxygen into the system. All these workers used the sessile drop technique to carry out their investigations. In addition to Eremenko and co-workers investigations, Chaklader and co-workers[16] also studied the wetting of sapphire by copper with oxygen. The change of contact angle θ with oxygen is shown in Figure 4.
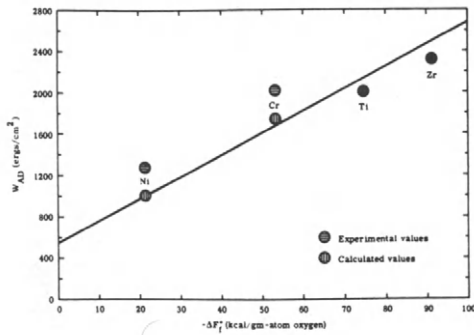
Fig. 3: Experimental and theoretical work of adhesion on sapphire for various liquid metals under vacuum[15].
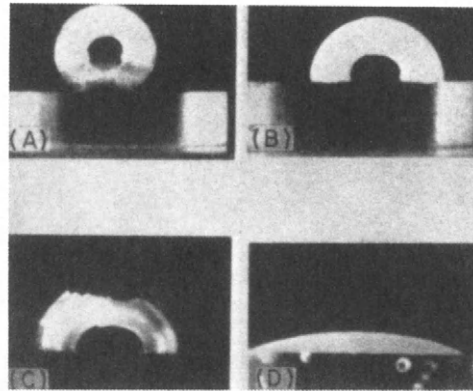
Fig. 4: Sessile drop photographs: (A) pure Cu, (B) Cu with 0.15 wt% O_2, (C) Cu with 0.75 wt% O_2, drop was not completed melted, and (D) Cu with 10.0 wt% O_2 (X5)[16]

Subsequent investigations at the University of British Columbia were aimed at developing a thermodynamic model which could be used to predict the wetting behaviour between a metal and an alumina substrate in the presence of oxygen[20].

In developing this model a dearth of accurate sessile drop data with known oxygen partial pressures and with very pure metal (5N or better) was accutely felt. This lack of data prevented us from developing and verifying a better model than that we have produced so far. We have produced accurate sessile drop data using 5N Cu and Ag with known PO_2, measured by an oxygen probe, but no similar data for Ni-, Fe- and Co-Al_2O_3 systems (with 5N metals) are available.

2.1.1 γ_{1g} vs PO_2

The effect of impurities in Cu (3N+ versus 5N) on the γ_{1g} values is shown in Figure 5. There are three distinct stages in the variation of γ_{1g} with PO_2. At very low PO_2 (say $<10^{-12}$ atms) γ_{1g} is only slightly affected. According to Turkdogen[21] during this stage the surface of the molten metal is only partially covered by the solute atoms (oxygen in this case). At the second stage γ_{1g} is drastically reduced with increasing PO_2, reaching a constant value of γ_{1g} asymptotically.
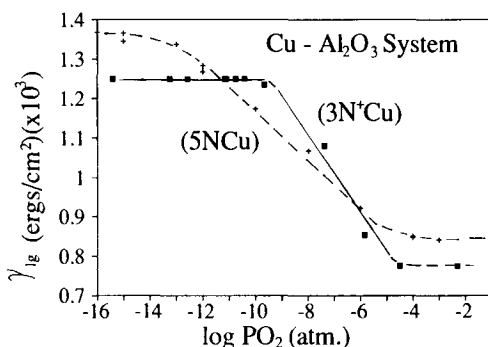
Fig. 5: Liquid surface tension of copper vs log PO_2.

Gibb's absorption equation has been used by several workers[22] to describe the constant slope of the second stage which is due to saturation of the surface of the molten metal by oxygen, resulting in the formation of a monolayer, which is given by

$$\Gamma_o^\circ = -\frac{2}{2.303\ RT}\ (\frac{\partial \gamma_{1g}}{\partial\ \log\ PO_2}) = -\frac{\partial \gamma_{1g}}{RT\ \partial\ \ln\ a_o} \qquad (4)$$

where a_o is the activity of oxygen in bulk metal and R is the gas constant. From the straight line portion of the curve in Figure 5, the surface concentration (Γ_o°) value can be easily calculated. The surface concentration Γ_o° (in mol. cm^{-2}) in turn, can be converted to an area of surface associated with each oxygen atom, called the surface coverage, S, which is given by

$$S_o = \frac{1}{\Gamma_o^\circ N} \qquad (5)$$

where N is Avogadro's number. Thus, from the knowledge of the surface coverage (S_o), Γ_o° can be calculated.

If the oxygen partial pressure at which the monolayer formation is complete ($\Gamma^\circ = \Gamma^\circ_o$) is identified at $[PO^c_2]$ and the corresponding liquid metal interfacial energy by γ^c_{lg}, the integration of Equation 4 results in

$$\gamma^c_{lg} - \gamma_{lg} = -\frac{2.303RT}{2} \Gamma^\circ_o \left[\log PO^c_2 - \log PO_2\right]$$

or rearranging

$$\gamma_{lg} = \gamma^c_{lg} - \frac{2.303RT}{2} \Gamma^\circ_o \left[\log PO_2 - \log PO^c_2\right] \qquad (6)$$

2.1.2 Estimation of γ^c_{lg} and PO^c_2

There is no direct method to estimate γ^c_{lg}. However, all plots of γ_{lg} vs log PO_2 for systems of Cu[22], Ag[23], Ni[19b], Fe[17] suggest the interfacial energy value, at which the surface is almost saturated with solute, is ~ 95 to 96% of the interfacial energy of the pure liquid (γ^p_{lg}) i.e. $\gamma^c_{lg} = 0.96 \gamma^p_{lg}$.

Both Belton[24] and Turkdogen[21] have shown that the absorption of surface active solutes on metal surface can be described by the Langmuir isotherm. Combining the Langmuir isotherm and Gibb's absorption equation, Belton derived an equation for the reduction of the surface tension of a liquid metal by a surface active solute as follows:

$$\gamma^p_{lg} - \gamma^c_{lg} = RT \Gamma^\circ_o \ln (1 + k\, a_i) \qquad (7)$$

where k is an equilibrium constant and can be estimated using Belton's approach of fractional surface coverage and a_i is the activity of the solute (i) in the bulk metal.

Replacing γ^c_{lg} by γ^p_{lg}, Equation 7 can be rewritten

$$0.04\, \gamma^p_{lg} = RT \Gamma^\circ_o \ln (1 + k\, a^c_o) \qquad (8)$$

where a^c_o is the activity at which $\gamma_{lg} = \gamma^c_{lg}$. Once Γ°_o is estimated it is possible to obtain the a^c_o using the above equation, which then can be converted to PO^c_2 using Sievert's law.

Introducing Equation 6 into Equation 1 and replacing γ^c_{lg} with γ^p_{lg} lead to

$$\gamma_{sl} = \gamma_{sg} - \cos \theta \left\{0.96\, \gamma^p_{lg} - \frac{2.303\, RT\, \Gamma^\circ_o}{2} \left[\log PO_2 - PO^c_2\right]\right\} \qquad (9)$$

This equation still contains an unknown experimental parameter θ, the values of which are needed to calculate γ_{sl} as a function PO_2. This is the ultimate objective.

2.1.3 Evaluation of θ

It should be possible to estimate θ using some thermodynamic measurements. From this consideration, several workers[25] attempted to correlate cs θ with γ_{lg} and a linear relationship was found to exist between these parameters for many liquid metal/ceramic systems. It has not been possible to incorporate such a relationship into Equation 9 to eliminate θ. An attempt to correlate θ with PO_2 was made previously[20], which was partly successful. Recognizing the fact that both γ_{sl} and θ changes with PO_2, for almost all systems studied so far, it can be argued that the change of θ with PO_2 is a direct reflection of the change of the solid-liquid interfacial energy γ_{sl}. A plot of θ vs γ_{sl} is shown in Figure 6.
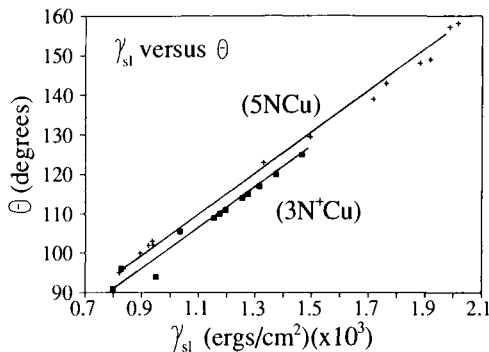
Fig. 6:   Variation of the contact angle θ with the change of solid-liquid
          interfacial energy (γ_{sl}) for Cu-Al$_2$O$_3$ system (between 1100 and 1200°C).

The relationship between θ and γ_{sl} can be expressed as

$$\theta = m \, \gamma_{sl} + c \tag{10}$$

where m is the slope and c is the intercept. This can be converted to

$$(\theta - 90 \text{ deg}) = m \, (\gamma_{sl} - \gamma_{sg}) \tag{11}$$

as when $\theta = 90°$, $\gamma_{sl} = \gamma_{sg}$. Equation 11 contains only one unknown (m), which may
be correlated with thermodynamic parameters such as free energy of formation of
the compound at the solid-liquid interface. Many investigators[26] in the past
tried to correlate the interfacial behaviour with the free energy of formation of
the metal compound at the interface. Mehrotra and Chaklader[23] considered that
for an oxide surface, such as sapphire, attraction to oxygen for chemisorption
may not be favourable, instead, formation of the compound at the liquid-solid
interface may provide the driving force for solute migration at the solid-liquid
interface. For systems with Al$_2$O$_3$ - Cu, -Ni and -Fe, assuming that the formation
of the spinel phase is the driving force, these workers obtained a linear
relationship for $\partial\theta/\partial\gamma_{sl}$ vs $\Delta F°/T$ with a slope of ~ -1.0, which gives

$$(\theta - 90 \text{ deg}) = (\frac{\Delta F^{\circ}}{T} + .056) \, (\gamma_{sl} - \gamma_{sg}) \tag{12}$$

where ΔF° is the free energy of formation of the spinel phase at the metal-
alumina interface and T is the temperature of experiment in degree Kelvin.   If
some other compound is formed, the value of the numerical constant may have to be
changed.

2.1.4   Final Equations and Verifications

Using Equations 9 and 12, it is possible to calculate the value of γ_{sl} as a
function of PO$_2$ with the known value of γ_{lg}^{p} and γ_{sg}, when log PO$_2$>log PO$_2^{c}$. When
log PO$_2$< log PO$_2^{c}$, it has been shown that[23]

$$\gamma_{sl} = \gamma_{sg} + \cos \theta \, [\, (\frac{\gamma_{lg}^{p} - \gamma_{lg}^{c}}{\log PO_2^{p} + \log PO_2^{c}}) \, (\log PO_2 + \log PO_2^{p}) + \gamma_{lg}^{p}] \tag{13}$$

The theoretical lines and experimental data are shown in Figure 7.   Theoretical
plots for Fe-, Ni- and Co- Al$_2$O$_3$ systems are shown in Figure 8.
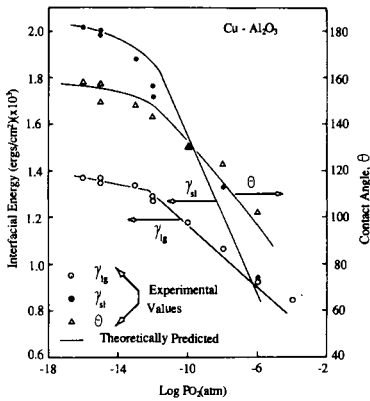
Fig. 7: Plots of theoretically
         predicted γ_{1g}, γ_{s1} and θ
         vs log PO_2 for Cu-Al$_2$O$_3$
         system at 1423K. Experimental
         values are also shown[23].
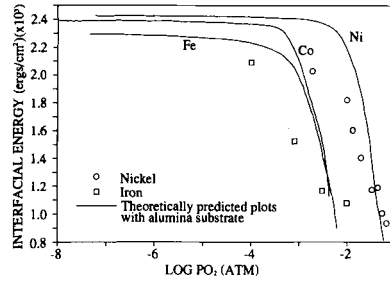
Fig. 8: Plots of theoretically
         predicted γ_{s1} vs log PO_2 for
         Fe-, Ni- and Co-Al$_2$O$_3$ systems.
         Experimental data of iron[17]
         and nickel[19(b)] are also
         included.

3.0 Interfacial Stresses in Composites

As mentioned previously, one of the compatibility requirements to develop stable cermet systems is the matching of the expansion coefficients of the alumina substrate and the metal phase. The stress on the metallic phase between alumina particles (as shown in Figure 2) cooled to the ambient temperature can be calculated using a simple equation[27]

$$\sigma_i = K \ (\alpha_r - \alpha_i)\Delta T \qquad (14)$$

where K is the bulk modulus, and is equal to $-P/(\Delta V/V)$. This is also equal to $E_i/3(1-2\ \mu_i)$. P is the hydrostatic pressure, E is the elastic modulus, α_r the resultant (or bulk) expansion coefficient and α_i is the expansion coefficient of the ith phase. In the absence of any knowledge of α_r, an average value of (α_{av}) of the expansion coefficients $[(\alpha_i + \alpha_j)/2]$ can be used as an approximation. However, the maximum stress would be if α_r is taken as α_j (ie. the concentration of the α_i phase is very small). Equation (13) can be rewritten as

$$\sigma_m = \frac{E_m\Delta T \ (\alpha_{av} - \alpha_m)}{3 \ (1-2\mu_m)} \qquad (15a)$$

$$\text{or} \qquad \sigma_m = \frac{E_m\Delta T \ (\alpha_{Al_2O_3} - \alpha_m)}{3 \ (1-2\mu_m)} \qquad (15b)$$

In addition, Oel and Frechette[28] have derived an expression to calculate the stresses that would be set-up when two dissimilar phases (having E_1 and E_2 the elastic modulus, μ_1 and μ_2 the Poisson's ratio and the difference in expansion coefficient $\Delta\alpha$) were sandwiched at T_1 and changed to another temperature T_2. The stress in the outer layer of the sandwich (metal phase) is given by ($\sigma_z = 0$)

$$\sigma_x = \sigma_y = \frac{E_1 E_2 \Delta\alpha\Delta T}{(1-\mu_1)(1-\mu_2)} \ / \ [\frac{2E_1}{1-\mu_1} + \frac{E_2}{1-\mu_2}] \qquad (16)$$

using equations (15a), (15b) and (16) the values of the stress on a large number of metals (also commercial alloys) with alumina have been calculated and are shown in Table 1. For the calculations, the elastic modulus, Poisson's ratio and the expansion coefficient for alumina were taken as 245 GPa, 0.3 and 8.6 x $10^{-6}/°C$, respectively. Similar values for all the metallic phases used for calculations were taken from the Metals Handbook[29]. Also for the calculations, the ΔT values were taken as the $(T_m - T_{r.t})$ i.e. from the melting temperature of the metallic phase to the ambient temperature.

It is apparent from the Table and equations (15a) and (15b), the stress as calculated by eq. (15a) is half that of the values obtained by eq. (15b). It should be pointed out that stress values obtained by eq. (15b) would be the upper limit of the stress in the metal phase. Conversely eq. (15a) will give the lower limit. It may not be proper to calculate the stress on the metallic phase in a composite using eq. (16) which was developed to calculate stress in a sandwich combination. But it is included here to indicate the nature of stress when two dissimilar phases are combined.

It is quite evident that the maximum stress level in Cu-, Ni- and Fe-Al_2O_3 systems can be quite large in the order of 0.5 to 1.0 GPa. However, alloying these elements to produce lower expansion coefficient materials may help in reducing the stress in these phases.

TABLE 1

Stresses in the Metallic Phases in Al_2O_3 - Metal Composites

Metal	Equation (15a) Stress MPa	Equation (15b) Stress MPa	Equation 16 Stress MPa
Zr	216.7	433.4	442.9
Ti	7.81	15.63	13.9
Cr	0.49	0.99	1.7
Sn	- 49.7	- 99.48	-110.8
Al	-269.5	-538.90	-613.4
Fe	-340.5	-680.97	-515.2
Brass	-408.0	-823.97	-767.3
1020	-444.3	-888.55	-566.3
Au	-473.2	-946.40	-442.9
Ag	-480.4	-960.95	-674.5
Cu	-514.8	-1029.58	-795.0
Ni	-571.2	-1142.49	-695.4
304 SS	-998.4	-1996.73	-1329.0

(-) indicates tension

Conclusions

It has been shown by a large number of workers that the reduction of solid-liquid interfacial energy (γ_{sl}) can be achieved both by alloying with other solutes of higher oxidation potential e.g. Zr, Ti etc. and adding oxygen into the system. The resulting wetting at the interface should enhance bonding at the interface. However, the stress generated in the system because of the expansion coefficient mismatch can be very large in the order of 0.5 to 1.0 GPa, which may result in the disruption of bonding at the interface. Again alloying a metallic phase with other elements to bring the expansion coefficient nearer to the ceramic phase will definitely improve the overall bonding at the interfaces.

REFERENCES

1.   Hower Jr., L.D., J.W. Londeree Jr., and H.F.G. Ueltz (1951). J. Am.
        Ceram. Soc., 34, 309-313.
2.   Armstrong, W.M., A.C.D. Chaklader, and J.F. Clarke (1962). J. Am.
        Ceram. Soc., 45, 115-118.
3.   Rivollet, I., D. Chatain, and N. Eustathopoulus (1987). Acta Metall.,
        35, 835-844.
4.   Sakata, K., T. Ohkoshi, and K. Nii (1986). J. Jpn. Inst. Met., 50,
        654-658.
5.   Naka, M., Y. Hirono, and I. Okamoto (1986). J. High Temp. Soc. Jpn., 12,
        250-255.
6.   Naka, M., Y. Hirono, and I. Okamoto (1984). Trans. Jpn. Welding Res.
        Inst., 13, 201-206.
7.   Nicholas, M.G., M.J. Waite, and T.M. Valentine (1980). J. Mater. Sci.
        15, 2197-2206.
8.   Standing, R., and M.G. Nicholas (1978). J. Mater. Sci., 13, 1509-1514.
9. (a) Young, T. (1805) Phil. Trans., p. 74; T. Young, Misc. Works, Vol. 1;
        p. 432, Ed. Peacock, J. Murray, London, 1855.
   (b) Dupré, A., Théorie Méchanique de la Chaleur (1869) Gauthier-Villars,
        Paris, p. 369.
10.   Kingery, W.D. (1960).   Introduction to Ceramics, John Wiley and
        Sons, N.Y.
11.   Chaklader, A.C.D., and K.R. Linger (1976). Composites, 10, 239-244.
12.   Norton, F.H., and W.D. Kingery (1952). U.S. Atomic Energy Comm. Publ.
        NYO-3141 NYO-6294 to 6296.
13.   Kurkjian, C.R., and W.D. Kingery (1956). J. Phys. Chem., 60, 961-963.
14.   Norton, F.H. and W.D. Kingery (1955). U.S. Atomic Energy Comm. Publ.
        NYO-4631.
15.   McDonald, J.E., and J.E. Eberhart (1965). Trans. Met. Soc., AIME, 233,
        512-517.
16.   Chaklader, A.C.D., A.M. Armstrong and S.K. Misra (1968). J. Am. Ceram.
        Soc. 51, 630-633.
17.   Halden, F.A., and W.D. Kingery (1955). J. Phys. Chem. 59, 557-559.
18.   Monma, K., and H. Suto (1960). J. Jpn. Inst. Mets. 24, 374-377.
19.(a) Eremenko, V.N., Yu. V. Naidich and A.A. Nosonovich (1960). Zh. Fiz.
        Khim., 34, 1018-20.
   (b) Eremenko, V.N., Yu. V. Naidich (1960). Izv. Akad. Nauk. SSSR, Otd. Tekh.
        Nauk, Met. Topl., 2, 53-55.
   (c) Eremenko, V.N., Yu. V. Naidich (1957). Ukr. Khim. Zh. 23, 573-578.

20.   Chaklader, A.C.D., W.W. Gill and S.P. Mehrotra (1981).   Surfaces and
        Interfaces in Ceramic and Ceramic-Metal Systems, Eds. J. Pask and
        A. Evans, Mat. Sci. Res. Vol. 14, Plenum Publ, N.Y.
21.(a) Darken, L.S., and E.T. Turkdogen (1970).   Heterogeneous Kinetics at
        Elevated Temperatures, Eds. G.R. Belton and W.L. Worrall, Plenum Press,
        New York.
   (b) Turkdogen, E.T. (1970).   Physical Chemistry of Oxygen Steelmaking,
        Thermochemistry and Thermodynamics, U.S. Steel Publ.

22.(a) O'Brien, T.E. and A.C.D. Chaklader (1974). J. Am. Ceram. Soc., 57, 329–
        332.
   (b) This paper.
23.   Mehrotra, S.P. and A.C.D. Chaklader (1985). Met. Trans., 16B, 567–575.
24.   Belton, G.R. (1976). Met. Trans. 7B, 35–42.
25.(a) Rhee, S.K. (1970). J. Am. Ceram. Soc., 53, 386–389, 426, 639–641.
   (b) Rhee, S.K. (1971). J. Am. Ceram. Soc., 54, 332–334.
   (c) Eberhart, J.G. (1967). J. Phys. Chem., 71, 4125–4126.
   (d) Shafrin, E.G., and W.A. Zisman (1972). J. Phys. Chem., 76, 3259–3267.
26.(a) Benzamin, P. and C. Weaver (1960). Proc. Roy. Soc. (London) 254, Series A
        177–183.
   (b) Humenick, M. and W.D. Kingery (1954). J. Am. Ceram. Soc., 37, 18–23.
27.   Timoshenko, S. and J.N. Goodin (1970). Theory of Elasticity, McGraw–Hill,
        New York.
28.   Oel, H.J. and V.D. Frechette (1967). J. Am. Ceram. Soc., 50, 542–549.
29.   Metals Handbook, Desk Addition (1985). Am. Soc. for Metals, Ohio, U.S.A.

Microdesigning of B₄C-Al cermets

Aleksander J. Pyzik
Advanced Ceramics Laboratory, Central Research, The Dow Chemical Company,
Midland, Michigan 48674, U.S.A.

Ilhan A. Aksay
Department of Materials Science and Engineering, and Washington Technology Center,
University of Washington, Seattle, Washington 98195, U.S.A.

ABSTRACT

The B4C/Al cermet combines a ceramic's high hardness, stiffness, and low density with a metal's ability to dissipate tensile stress. Early attempts to fabricate fully dense boron carbide/aluminum composites were mostly unsuccessful for two key reasons: (i) chemical reactions during processing proceed faster than densification, thereby resulting in porous materials, and (ii) B4C is not readly wet by Al unless process conditions are accurately controled. In this paper, application of the infiltration technique leading to fully dense B4C/Al cermets with tailorable microstructures is discussed. Control of the mixing, densification and post-heat treatment processes results in multi-ceramic composites with a reacted metal or in composites with the metal retained in desired amount. The primary advantage of the infiltration approach is that the distribution, the geometry, and the chemistry of both the ceramic and metal phases can be altered separately.

KEYWORDS

Composites, boron carbide, aluminum, cermets, infiltration, wetting, microstructure evolution.

INTRODUCTION

Although the idea of developing boron carbide-metal composites is not new, past attempts to develop these cermets in most cases have not been successful (Wilkins, Cline and Honodel, 1969; Manning and Gurganus, 1969; Lindley and Gazza, 1973). Difficulties encountered with either the lack of wetting of boron carbide by the liquid metal or fast kinetics of the chemical reactions yielded porous materials.

During liquid phase sintering, the liquid tends to achieve a state of local equilibrium and rearrange to denser packed regions. The liquid phase moves into the agglomerates due to capillary suction, and thus, the volume originally occupied by the metal powder remains as a void. The dense B4C/Al agglomerate regions support the formation of binary and ternary compounds as solid bridges between B4C grains, so the densification process stops due to the formation of a solid skeleton (Pyzik, Aksay and Sarikaya, 1987). The resultant microstructures are characterized by the existence of large voids surrounded by fairly dense areas. Even the application of the hot isostatic pressing (in order to increase kinetics of solid rearrangement), results in

materials with closed porosity due to the formation of reaction products (Halverson and others, 1989). Smaller metal particles and better distribution result in the faster chemical reactions and undesirable ceramic bridging.

In this paper, we illustrate a solution to the processing problems in B4C/Al system via infiltration. In this approach liquid rearrangement, not solid, is required to achieve fully dense materials.

EXPERIMENTAL PROCEDURE

Boron carbide (ESK 1500) used in this study was characterized by an average particle size of 3.5 micrometers with a surface area of 7.85 m^2/g contained, as major impurities, 1500 ppm of Si, 800 ppm of Zr, 250 ppm of Ti, and 200 ppm of Fe. A sedimentation process was used to remove all particles larger then 3 micrometers. The aluminum powder (Alcoa 1400) had a surface area of 0.625 m^2/g, an average particle size of 6.5 micrometers, and major impurities of 150 ppm Fe and 100 ppm Si.

In order to prepare boron carbide compacts, powders were dispersed in water. The suspensions were ultrasonically agitated, the pH was adjusted using 0.01 M HCl or 0.1M NaOH, and the suspensions were aged for 12 hours before casting on a plaster of Paris mold. B4C compacts were dried for 24 hours at 105°C and then sintered in a graphite element furnace (Astro Model 2570) in flowing argon. The heating rate was 25°C/minute and the cooling rate was about 10°C/minute. Samples were sintered in two different setups. In the first setup, B4C compacts were placed into a graphite crucible on dense B4C bars to prevent contact of the sample with the crucible walls. In the second, B4C compacts were placed into a high purity carbon powder bed. The infiltration was carried out in a graphite element Astro furnace under 50 to 100 millitorr vacuum, at temperatures ranging from 1150°C to 1200°C. The infiltration setup is shown in Fig. 1.
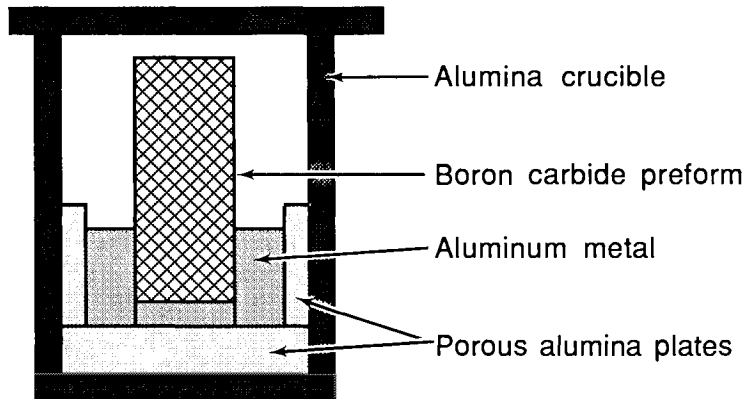
Fig. 1. The experimental setup used for infiltration.

Theoretical densities were measured by the water immersion technique. Porous B_4C preforms were characterized by SEM. Dense samples were polished down to 0.05 micrometer using diamond paste and an alpha alumina suspension on velvet cloth. The x-ray diffractometer was used to identify chemical reaction products. The quantity of phases formed, their continuity and grain size were determined by the line counting technique (Exner, 1970) from optical micrographs.

Zeta potential measurements were completed with Rank Brother Particle Micro-Electrophoresis Apparatus Mark II. Measurements were made in cylindrical cell on the upper stationary plane using dilute suspensions (0.01 wt.% of solid). At least ten readings were completed for each sample.

The wettability was measured under 10^{-5} torr vacuum in a Brew (Model 466) tantalum refractory metal furnace. The temperature was measured using a calibrated optical pyrometer and a W-Re 5-26 thermocouple. The wetting angle was observed in situ directly through a side port using a telescope through which photographs were taken to document the wetting angle. The hot pressed B_4C substrates (from Ceradyne Co.) used for the wetting experiments were polished down to 0.25 micrometer, using diamond paste.

RESULTS AND DISCUSSION

In the process of infiltration, the liquid moves through channels of a ceramic preform, filling empty spaces. The ability of the liquid aluminum to penetrate into the structure of porous boron carbide depends mainly on the wetting characteristics and on the hydraulic resistance of the ceramic powder.   The rearrangement of solid particles, so difficult to obtain in chemically reactive systems, becomes a less important condition in achieving fully dense materials. Therefore, as long as the thickness of the porous substrate is optimized, and sufficient quantity of liquid is available, densification proceeds very rapidly.
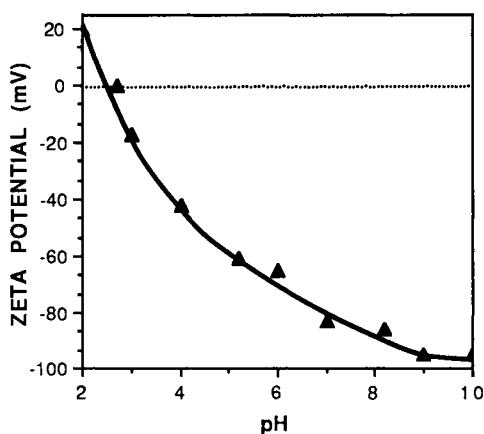
Fig. 2. Zeta potential of B_4C
as a function of pH.
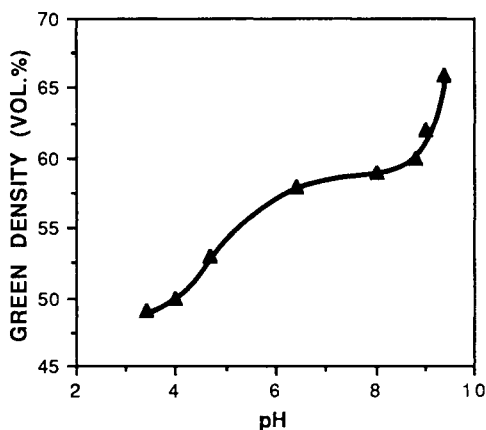
Fig. 3. Correlation between pH of B_4C
slurry and density of slip cast samples.

In liquid phase sintering, hot pressing, or hot isostatic pressing, the development of microstructures mainly depends upon processing temperature and time. On the other hand, in the infiltration technique, microstructures can be altered in the following processing stages: (i) dispersion and consolidation, (ii) sintering, (iii) infiltration, and (iv) post-heat treatment. The primary advantage of the infiltration approach is that the distribution, the geometry, and the chemistry of both the ceramic and metal phases can be controlled separately.

Dispersion and Consolidation

The density and microstructure of the green boron carbide body can be controlled by colloidal dispersion and consolidation techniques. Depending upon the chemistry of the boron carbide surface and the level of powder impurities, the electrostatic potential may vary significantly from powder batch to batch. In general, however, boron carbide powders are negatively charged and have, in water, an isoelectric point between pH 2.3 and 2.7. The boron carbide powder used in this study showed behavior similar to colloidal silica, forming stable aqueous suspensions in a wide range of pH (Fig. 2).

A maximum ceramic loading of 48 volume % was obtained at pH 9.4, which corresponds to the state of highest electrostatic charge. With reduction of pH, the viscosity increases and ceramic loading decreases to achieve 41 volume % at pH 8 and 27 volume % at pH 4. As can be seen in Fig. 3, pH conditions of boron carbide slurry directly affect density of the slip cast samples, ranging from 49 to 66 volume % of theoretical. As reported elsewhere (Aksay, 1984), highly dispersed suspensions result in microstructures characterized by large domains of particles and small voids. Conversely, the small domains and large second and third generation voids are formed from the flocculated suspensions. Therefore, by controlling forces acting among boron carbide particles in the aqueous suspension, one can change not only overall porosity but also pore size distribution in the consolidated green boron carbide body.
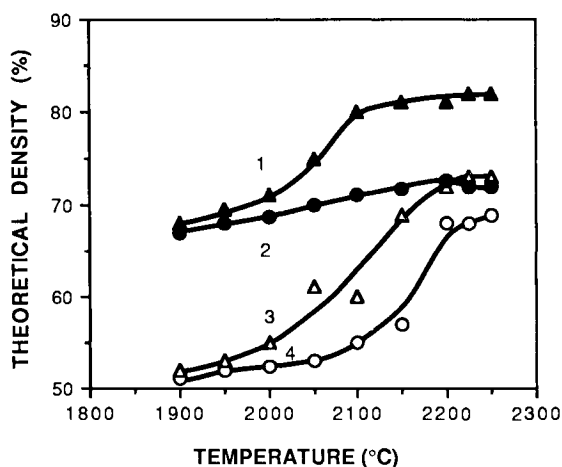
Fig. 4. Density of B4C, sintered with no extra carbon (2 & 4), and sintered in a carbon bed (1 & 3).

Sintering

The density and microstructure of the green boron carbide preform can be further changed in the sintering process. The objective here is to form ceramic skeletons with controllable density, channel size, ceramic grain size, and grain continuity. At high temperature, microstructure evolution of boron carbide is very rapid. The magnitude of this process mainly depends upon the initial microstructure of the boron carbide greenware, presence of the free carbon in the system (Schwetz and Grellner, 1982), sintering temperature and time (Kuzenkova and others, 1979), and rate of heating to maximum sintering temperature (Dole, 1985).
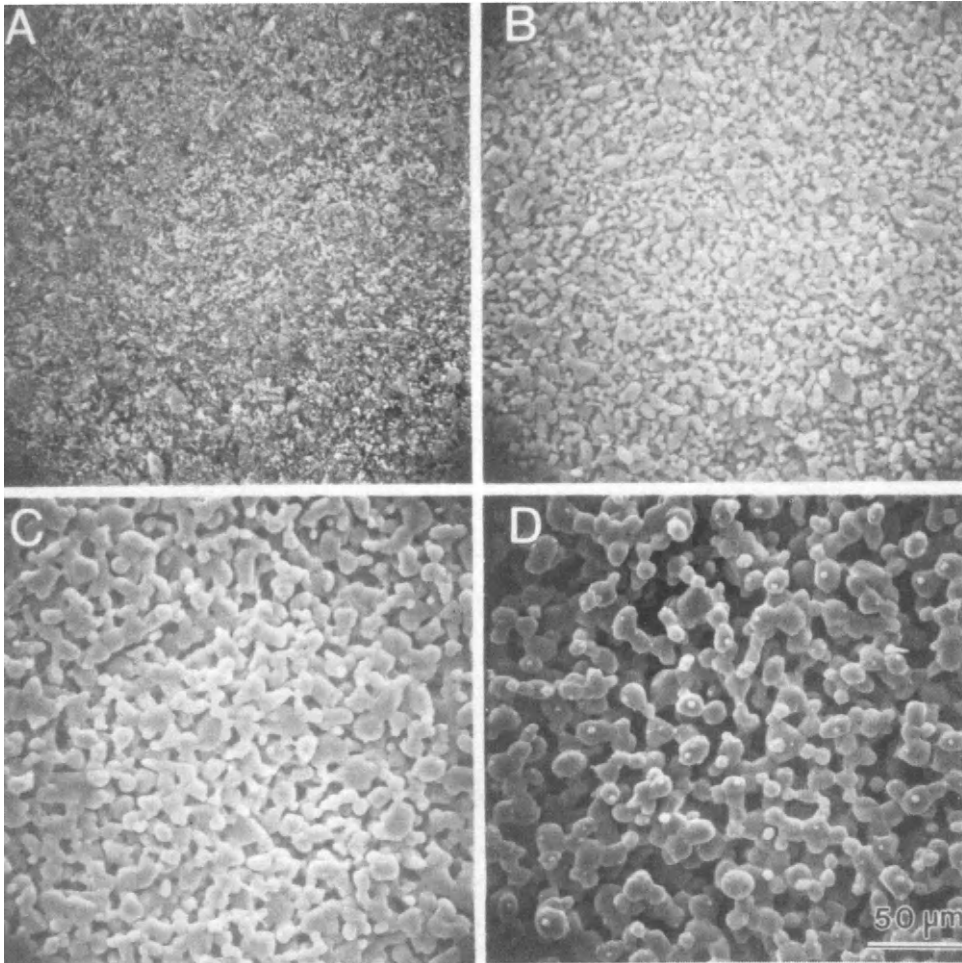
Fig.5. Boron carbide sintered for 30 minutes at (A) 1900°C, (B) 2050°C, (C) 2150°C, and (D) 2225°C.

In our experiments, the rate of heating and the sintering time were kept constant. The sintering was conducted using two types of boron carbide compacts, each with different microstructures. The first, 66% dense, was obtained from a well dispersed suspension. The second, 50% dense, was prepared from a partially flocculated suspension at pH 4. The microstructure of the second material was characterized by the existence of large voids between small domains of boron carbide particles. Both materials were sintered between 1900°C and 2225°C for 30 minutes in both the presence and absence of carbon (see experimental procedure). The densification curves, shown as a function of temperature and carbon presence, are presented in Fig. 4. The final densities of B4C samples not being in direct contact with graphite approach only 69 and 74 volume % of theoretical (curves 2 & 4). The same samples sintered in a carbon bed have densities of 77 and 82 volume % of theoretical (curves 1 & 3). The increase of the sintering temperature above 2225°C does not result in any evidence of further densification. During sintering above 1900°C, a slow densification takes place along with coarsening of the pore-grain structures. The rate of microstructure coarsening increases rapidly above 2100°C, and spontaneous grain (and pore) growth occurs about 2225°C. The differences in B4C microstructures obtained by sintering at various temperatures are presented in Fig. 5.

The presence of carbon in the B4C system not only changes sintering behavior, but also slows coarsening of pore-grain structure. Figure 6 shows the fracture surface of two boron carbide samples (66 vol.% dense) sintered at 2200°C for 30 minutes. The sample sintered in a carbon bed has finer microstructure and smaller interconnected channels than the same greenware sintered in a carbon free environment. The control of the greenware formation and sintering processes permits achievement of porous B4C preforms with densities ranging from 50 to 82 volume %, controllable grain and channel size, and a well or weakly developed network of necks between the B4C grains.
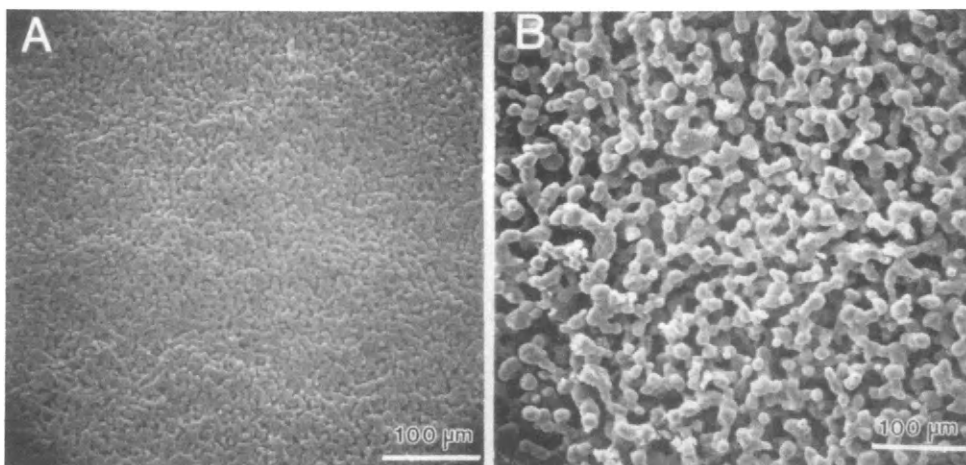
Fig.6. Boron carbide sintered at 2200°C for 30 minutes in (A) a carbon bed, and (B) with no extra carbon.

Infiltration

The ability of liquid aluminum to penetrate porous boron carbide depends upon wetting thermodynamics and the size of channels in the ceramic body.   As reported elsewhere (Halverson, Pyzik and Aksay, 1985), wetting in B_4C/Al system changes as a function of the processing temperature. In this paper we illustrate that even at the same temperature, wetting kinetics vary, depending upon the pre-infiltration process.

Figure 7 shows the values of contact angles, measured at 1180°C on three differently prepared B_4C substrates. The first substrate, characterized by a freshly polished surface, was used for the wetting experiment directly after polishing was finished. The second substrate was left in desiccator for 4 weeks in hopes of mimicking the surface conditions in the green B_4C preform. The third substrate was heat-treated at 2200°C for 0.5 hour to match the sintering conditions. Results indicate significant differences in contact angles as well as in the kinetics of wetting between boron carbides   prepared in the above described   manners.   Data show that a higher infiltration temperature is required to fill sintered samples than is needed to fill green boron carbide preforms. Furthermore, the infiltration temperature can be reduced by removing a layer of B_2O_3. The reduced kinetics of wetting in sintered boron carbide is a consequence of the slow rate of mass transport across the B_4C-Al interface.   As a result, very fast chemical reactions, characteristic for this system, are reduced, and a cermet with sintered B_4C becomes more chemically stable than a green B_4C-Al system.
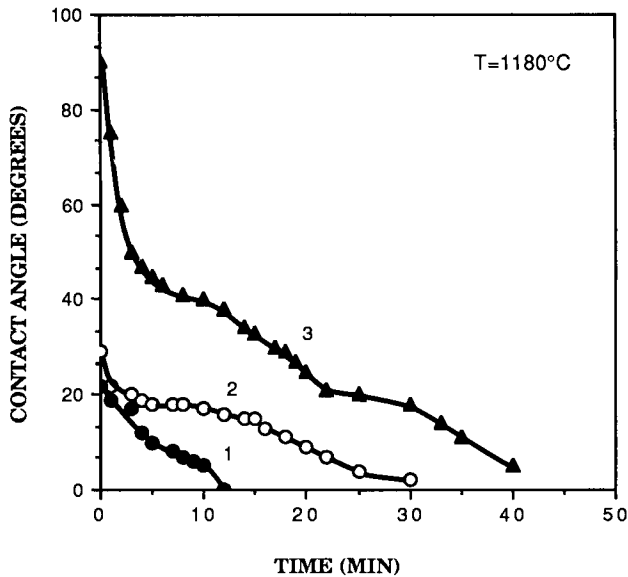
Fig. 7. Contact angle of molten Al on B_4C at 1180°C, as a function of time and surface of boron carbide. 1- freshly polished surface, 2- surface oxidized at room temperature, and 3- surface heat-treated at 2200° for 30 minutes.

The sintering temperature of boron carbide has a profound effect on its chemical reactions with liquid aluminum. Figure 8 shows the phase formation in the B_4C-Al system as a function of boron carbide sintering temperature. Even though the total content of phases formed was calculated using a simple line counting technique, the existing trend seems to be very obvious. The higher the sintering temperature of B_4C above 2000°C, the more chemically stable is the B_4C/Al system. The evolution of the infiltrated microstructures as a function of boron carbide sintering temperature is presented in Fig. 9. Microstructure 9a corresponds to the green B_4C infiltrated with aluminum at 1150°C. The material is fully dense, even though the depletion of the metal phase is significant. Microstructures 9b, 9c, and 9d show sintered and then infiltrated B_4C. Again, the higher the sintering temperature, the fewer the chemical reaction products. Therefore, sintering of B_4C greenware changes not only the final density, grain size, and grain connectivity, but it also can be used to control the chemistry of B_4C/Al composites.
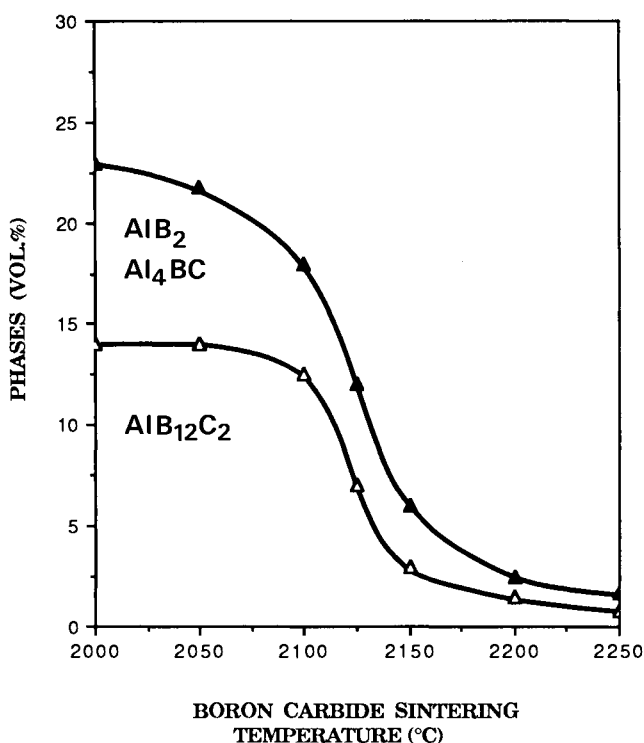
Fig. 8. Phase formation in the B_4C/Al system as a function of boron carbide sintering temperature.
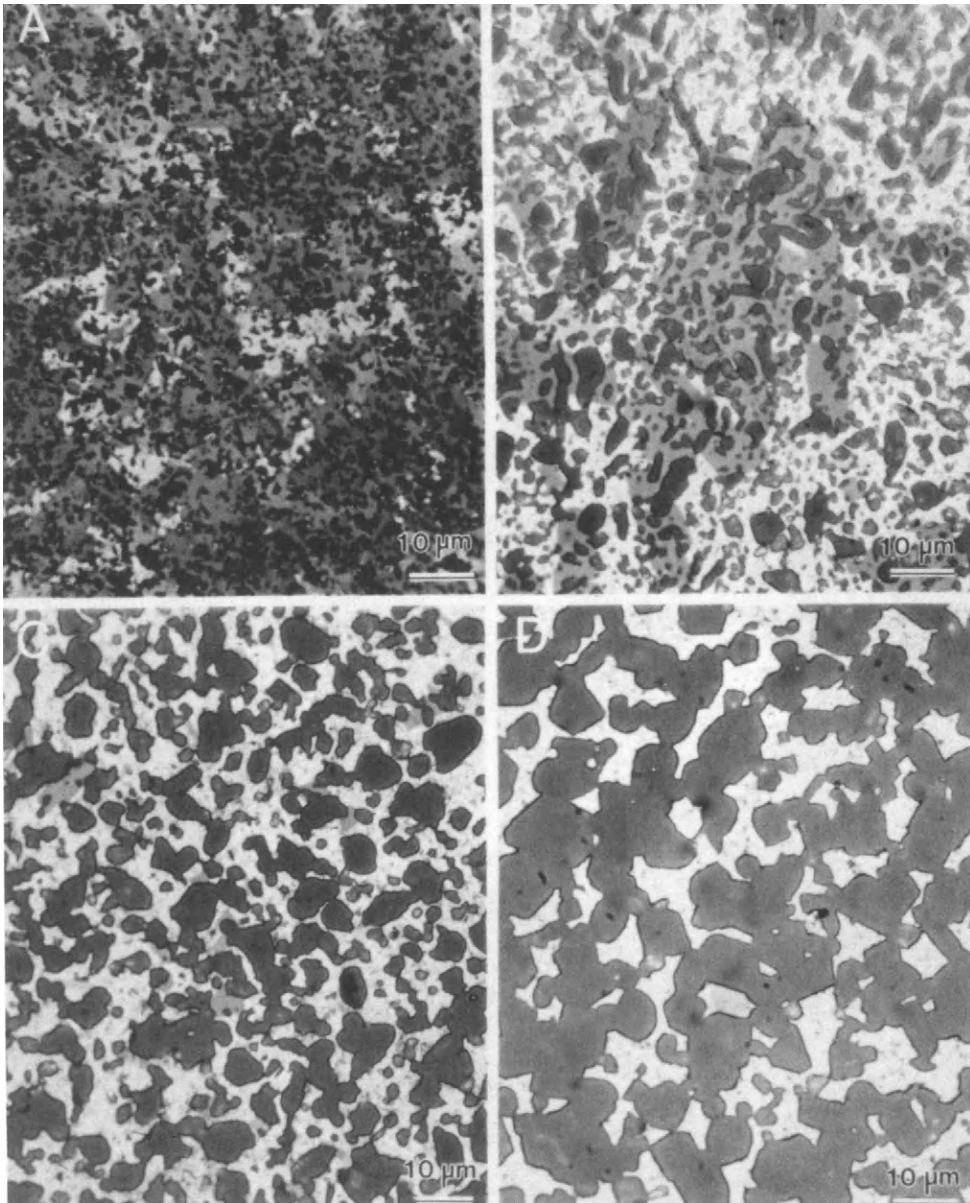
Fig. 9. Microstructures of B₄C/Al cermets, infiltrated at 1180°C for 30 minutes, as a function of boron carbide sintering temperature. (A) green B₄C, (B) B₄C sintered at 2050°C, (C) B₄C sintered at 2150°C, and (D) B₄C sintered at 2225°C.

Post Heat-treatment

By using the infiltration approach, two major types of microstructures can be formed. The first occurs when green or below 2000°C sintered boron carbide has been infiltrated. In this type of cermets, most of the metal reacts to form binary and ternary B-C-Al phases. Typically, from about 35 volume % of aluminum introduced to the system, only 5 to 16 volume % remains unreacted in the final product, after infiltration is finished. The final quantity of metal depends upon time at infiltration temperature, which in turn is affected by sample size. By applying prolongated infiltration time or post-heat treatment at low temperature, the metal becomes mostly depleted, forming various ceramic phases (Halverson and others, 1989). Theoretical densities of this type of B_4C/Al cermet range from 2.6 to 2.7 g/cc. The microstructure of a fully dense cermet is characterized by the presence of small boron carbide particles surrounded by large grains of other ceramic phases, such as AlB_2, Al_4BC and $AlB_{12}C_2$. The controlled depletion of Al in the already dense cermet leads to the formation of a new category of multi-ceramic, hard, light, boron carbide based composites.

A second type of B_4C/Al microstructure can be formed from B_4C sintered above 2000°C and is characterized by the interpenetration of ceramic and metal networks. The degree of this interpenetration can be tailored from the metal matrix type (see Figure 9a), where most of the ceramic grains are separated, through growth of some grains and necks (Figure 9b), to a skeleton type (Figure 9c), where both ceramic and aluminum form continuous skeletons. The chemical reactions between boron carbide and aluminum still occur; however, they are very slow. By applying post heat-treatment below infiltration temperature, changes in composition and microstructure occur. The microstructure consists mainly of a two-phase network $(B_4C-AlB_{12}C_2)$ interpenetrating with aluminum which has been depleted partially by formation of AlB_2 and Al_4BC. Theoretical density of these composites ranges from 2.56 to 2.6 g/cc.
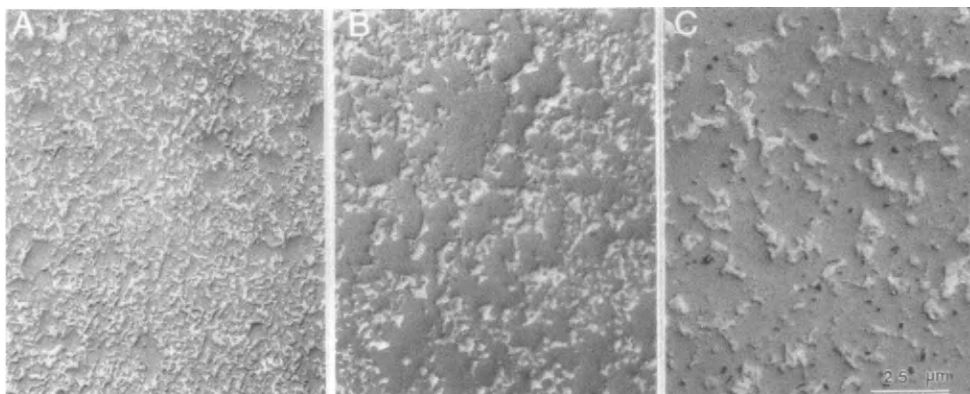
Fig.10. Evolution of the B_4C/Al microstructure as a function of the post-heat treatment process.

CONCLUSIONS

Long lasting attempts to fabricate dense boron carbide-aluminum composites have been successfully completed. Understanding of the densification mechanisms and reaction thermodynamics in the chemically incompatible B_4C/Al system led to application of the infiltration approach. In the infiltration process, liquid phase rearrangement, rather then solid particles rearrangement, is required to form fully dense materials. The utilization of the infiltration technique permits tailoring of the cermet's microstructure and fabrication of materials designed to the specific application.

The distribution, the geometry and the chemistry of both the ceramic and metal phases are altered separately during processing. Microstructures can be changed in the following processing stages: (i) dispersion and consolidation, (ii) sintering, (iii) infiltration, and (iv) post-heat treatment. Control of the processing conditions results in the multi-ceramic composites with a reacted metal and a variety of B-C-Al phases, or composites where the metal is retained in the desired amount, and the only major phases are B_4C and Al.

ACKNOWLEDGEMENT

REFERENCES

Aksay, I.A. (1984). In J.A. Mangels and G.L. Messing (Ed.), *Advances in Ceramics*, Vol. 9. The American Ceramic Soc., Colombus, OH, pp. 94-104.

Dole, S.L. (1985). Sintering of boron carbide. *Ph.D. Thesis*, Rensselear Polytechnic Inst., Troy, N.Y. pp.14 - 43.

Exner, H.E. (1970). Methods and significance of particle and grain size control on cemented carbide technology. *Powder Metallurgy* , 13, 26, pp. 429 - 448.

Halverson, D.C., A.J. Pyzik, I.A. Aksay, and W.E. Snowden (1989). Processing of boron carbide - aluminum composites. *J. Amer. Ceram. Soc.*, in press.

Halverson, D.C, A.J. Pyzik, and I.A. Aksay (1985).Processing and microstructural characterization of B_4C/Al cermets. *Ceram. Eng. and Science Proc.*, 6, 7-8, The American Ceram. Soc., pp. 736 -744.

Kuzenkova, M.A., P.S. Kislyi, B.L. Grabchuk, and N.I. Bodnaruk (1979). The structure and properties of sintered boron carbide. *J. Less - Common Metals,* 67, 217-223.

Lindley, M.W., and G.E. Gazza (1973). Some new potential ceramic-metal armor materials fabricated by liquid metal infiltration. *Report AD-769742*, Army Materials and Mechanics Research Center, Watertown, MA.

Manning, C.R., and T.B. Gurganus (1969). Wetting of binary aluminum alloys in contact with Be, B_4C and Graphite. *J. Amer. Ceram. Soc.*, 52, 3, 115-118.

Pyzik, A.J., I.A. Aksay, and M. Sarikaya (1987). In J.A. Pask and A.G. Evans (Ed.), *Ceramic Microstructures' 86. Role of Interfaces*, Vol. 21, pp.45-54.

Schwetz, K.A., and W. Grellner (1982). The influence of carbon on the microstructure and mechanical properties of sintered boron carbide. *J. Less - Common Metals* , 67, 217-223.

Wilkins, M.L., C.F. Cline, and C.A. Honodel (1969). Light armor. *Report UCRL-7-1817*, Lawrence Livermore National Laboratory, Livermore, CA.

Modelling of ceramic to metal brazed joints—a fracture mechanics finite elements approach

F. Taheri and J.G. Murphy

Advanced Materials Engineering Centre, P.O. Box 1618, Station M, Halifax, Nova Scotia, Canada, B3J 2Y3

ABSTRACT

Increasingly, in many aerospace and combustion engine applications, alloys are being coated by protective layers of ceramic, which are usually subjected to large thermal stresses.

In spite of the progress in coating and brazing technology, many problems remain to be resolved. One of the tools recently employed to analyze such problems is the finite element method (FEM). Researchers have applied this method to verify the effects of irregularities, which are the major cause of crack initiation and debonding in the brazed components.

On the other hand, this problem, which is analogous to the cracked media problem, has been examined by linear elastic fracture mechanics (LEFM). Unfortunately, the analytical solution to this problem is quite complex in nature, and is solvable only for simple geometrical cases.

In this study the braze problem is analyzed by a special purpose fracture mechanics finite element program. The applicability of this program is shown, and the results are verified against the analytical complex solution. This results are also compared to the results obtained by ordinary an finite element program. The advantages in using special purpose fracture element for this type analysis is also discussed.

KEYWORDS

Finite element, enricehed element, fracture mechanics, braze joint, ceramic, crack, residual stress.

INTRODUCTION

Many of the alloys used today in aerospace and automotive applications are being coated by ceramics or other materials, because they are increasingly been used at elevated temperatures. These components, either at the time of ceramic to metal joining, or during their operational life span, experience large thermal fluctuations and gradients. The residual stresses resulting from such temperature variations and the inherent mismatch in the thermomechanical properties of the materials, often cause

debonding of the coating, or if the coating material is strong enough, fracture of the coating material.

One of the configuration for bonding ceramic to metal that is being increasingly used is the brazing process. In this operation, a sandwich consisting of a ceramic layer, metal braze alloy interlayer(s) and a metal substrate is fused by application of heat and/or pressure.

Some mathematical and numerical solutions have been formulated to investigate the state of residual stresses in such domains. One of the most versatile numerical techniques is the finite element method (FEM), which have recently gained popularity among engineers. In this method a component is subdivided into a number of smaller elements. Then the behaviour of the overall structure to applied load is detected based on the assemblage of the individual characteristics of the subelements.

On the other hand, fracture mechanics analysis, which is based on the a priori existence of flaws in the component has been also used to characterise related residual stress problems (Erdogan, 1965; England, 1963; Sih and Rice, 1963; Charreyron et al. 1986, 1987). However, these fracture mechanics solutions are mostly based on the use of a complex stress function and involve the use of specialized, complex mathematics and even so, are usually only formulated for idealized, simple cases.

In a recent paper by Charreyron et al. (1987), brazed ceramic to metal joints were modeled by finite element. To idealized and characterize the stress pattern in such brazing problems, a fine mesh consisting of 8000 elements, was used. Then, a closed formed solution was proposed which was based on the fracture mechanics approach.

An objective of this paper is to briefly introduce the applicability of the finite element method to the readers that are unfamiliar with the subject. Then, a special purpose fracture mechanics finite element program, FAST will be introduced, by which the braze problem will be analyzed using both the finite element method and fracture mechanics, in a unified system. The stress intensity factors and stress distribution based on this approach will be compared with the closed form solution, to determine its validity. Lastly, the subject of the economics behind performing a proper finite element analysis as well as the essence of using special purpose fracture mechanics finite element program will be discussed.

FINITE ELEMENT APPROACH

Prior to the advent of computers, most structural problems were analyzed by the classical methods. That is, through the application of mathematics and materials science, solutions for the strength of idealized and simplified shapes were determined. Historically, designers approximated the real and complex structures which they wished to analyze by using simplified cases that conformed with one of the available classical solutions. Because this process is so uncertain, designers normally use factors of safety and other arbitrary overdesigns to ensure safe structures.

Later, numerical solutions such as the finite difference method became popular in assisting engineers to obtain more exact solutions for a variety of engineering problems by solving the appropriate partial differential equations. However, this

approach, though very powerful, is only suitable for uniform geometries, and is limited by the extensive computational requirements.

Although the classical origin of the finite element method is often attributed to a paper written by Turner et al. (1956), its real popularity began in the late 1960s and early 1970s, which coincides with the commercial availability of mainframe computers.

Since then FEM, a mathematical tool, has become widely used by engineers to analyze most continuous systems. In this method the domains are broken down into discrete elements for which descriptive equations are written. These equations then are assembled globally and solved for the unknowns. The development of the FEM made possible the analysis of many engineering problems that were previously too complex to study by classical or other numerical methods. The method has become an industry-wide standard analytical technique.

FRACTURE MECHANICS

This method assumes the presence of crack, a priori, for which the stresses are assumed to be singular at the crack tip. In the case of ceramic/metal brazing, the cooling of the brazed part combined with the mismatch of the materials properties results in the development of residual stresses that often cause in debonding of the ceramic from the metal substrate. If the coating material is brittle and strong, fracture of the joint on the ceramic becomes likely. Since the integrity of such engineering problems can no longer be characterised by using the working stress or limit state, fracture mechanics is often chosen as a suitable approach to deal with such problems. By this approach the integrity of a component is measured based on LEFM limiting quantities, such as critical stress intensity factor K_{ic}. The fundamental requirement for use of this factor is an accurate knowledge of the stress field around the crack tip for the relevant structural geometry, loading and boundary conditions. Unfortunately the analytical solutions present today are only valid for simple domains and physical parameters, though mathematically the solutions are quite complex.

In reality, physical assemblies of interest in fracture problems are often subjected to complex loading and boundary conditions, and often are geometrically irregular. It is for this reason that engineers have attempted to seek solutions for fracture problem by means of numerical techniques. One of the most widely and reliable numerical techniques is FEM. The traditional FEM, however, fails to accurately determine the stress field around the crack. However, researcher Charreyron et al. (1987) have used ordinary finite element programs to qualitatively determine the state of stress and the possible location of crack initiation. Another approach that also used is to adapt extremely fine meshes (often in the order of 1/1000 of the crack length), in the vicinity of the cracks to come up with reasonable result for displacements. Then through mathematical interpolation techniques, reasonable stress intensity factors for the crack tips are extrapolated.

Unfortunately, the above techniques are tedious, extremely time consuming and require large amount of computer storage, resulting in very costly solutions. Furthermore, the stress field, hence the Ks are very sensitive to such adaptive mesh.

Due to nature of shape functions used in conventional FEM formulation, no matter how fine a mesh one adopts, crack tip singularity will not be achieved; therefore this practicality and feasibility of this method is lost.

FRACTURE MECHANICS FINITE ELEMENT PROGRAM

As discussed earlier, the numerical modellings of the stress field around the crack, and calculation of the crack tip stress intensity factors creates new difficulties. This problem was first resolved by collocation and the conformal mapping (Bowie, 1956; Bowie and Neal, 1970). Both methods gave satisfactory results as long as the loading and geometry of the cracked plate were kept simple. Byskov (1970) developed a special triangular crack tip element in which the crack tip stress intensity factors could be calculated regardless of the geometry of the cracked plate. Barsoum (1976) formulated an eight node quadrilateral isoparametric crack tip element. He showed that when the mid side nodes of the eight node element are moved to the quarter point nearest the crack tip, a $r^{-1/2}$ singularity is achieved in the strain field around the crack tip. Following his work, Pu and Hussain (1978) obtained the same result when the intermediate nodes of a 12 node quadrilateral isoparametric element were moved to 1/9 and 4/9 positions nearest the crack tip.
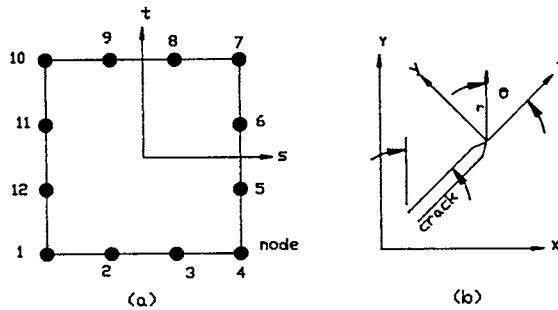
Fig. 1. (a) 12 node isoparametric element
(b) crack tip local axis

Gifford and Hinton (1978) achieved similar singularities near the crack tip by formulating a special 'enriched' element.

Concept of Enriching an Element

This concept was originated by Benzley, and was later refined by Gifford and Hinton (1978). Essentially, there are two extra terms (degrees of freedom) added to the usual displacement function of a 12-node quadrilateral isoparametric element (figure 1). It takes the form of:

$$u(s,t) = \Sigma N_i u_i + K_I [f_1 (s,t) - N_i f_{1i}] + K_{II} [g_1 (s,t) - N_i g_{1i}]$$

$$v(s,t) = \Sigma N_i v_i + K_I [f_2 (s,t) - N_i f_{2i}] + K_{II} [g_2 (s,t) - N_i g_{2i}]$$

[1]

Where:

(s,t) =   Local coordinates associated with the isoparametric element.

N_i =   Usual isoparametric shape function.

K_I, K_{II} =First and second mode stress intensity factors.

$f_{1,2}(s,t)$ =

$\qquad\qquad$ } Functions depending on the geometry of the crack.

$g_{1,2}(s,t)$ =

Functions $f_{1,2}$ and $g_{1,2}$ are complex trigonometric functions, having numerous terms which are employed to define the orientation of the crack.

By this method the singularity on the crack tip is achieved by the use of two extra degrees of freedom, namely K_I and K_{II} (the stress intensity factors). For a detailed mathematical formulation of such an element, the reader should consult the papers by Gifford and Hinton (1978) and Gifford (Gifford 1979).

Finite Element Program FAST

APES (Axisymmetric Planar Elastic Structures) is a special purpose finite element program designed to solve two dimensional plane/axisymmetric fracture problems (Gifford, 1979). This program has gone under a series of modification (Mufti and Taheri, 1987), and the new improved version is called FAST (acronym for Fracture Analysis of STructures).

FAST comprises of two modules, FAST-I and FAST-II; FAST-I, the FEM module, and FAST-II, the fatigue calculation module.

FAST utilizes a twelve node quadrilateral isoparametric element and 'enriched' twelve node isoparametric element to simulate crack tip singularities. One of the most outstanding features of FAST-I is its automatic mesh regeneration capability. An initial FEM grid representing the cracked geometry is prescribed by the user. The mesh in the vicinity of the crack is then readjusted automatically to extend the crack by a user specified increment Δa. In addition to such information as nodal displacement, stresses (σ_x, σ_y, σ_z, σ_{xy}), and the principal stresses. In addition, FAST-I provides values of stress intensity factor(s) at the crack tip and also tabulates crack length and corresponding stress intensity factors.
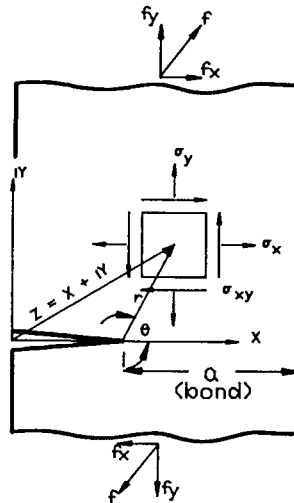
Fig. 2. The crack and its notations

These values then will be used by FAST-II in the fatigue cycle calculation.

MODELLING THE BRAZED PROBLEM

Fracture Mechanics Solution

Treatment of the subject of residual stress by fracture mechanics is not a new development. England (1956), Erdogan (1956), and Sih and Rice (1956) all provide analytical solutions for the case of crack bounded by dissimilar materials. Recently Charreyron et. al. (1986, 1987), in a series of papers, have provided a closed form solution for the braze problem with a crack. All the earlier solutions as well as the most recent one are based on the complex stress function formulated by Muskhelishvili (1953). Muskhelishvili gave the displacement and stress field in terms of the complex stress function:

$$\sigma_{x,k} + \sigma_{y,k} = 2[\phi_K(z) + \overline{\phi_k(z)}]$$

$$\sigma_{y,k} - \sigma_{xy,k} = 2 \ (\bar{z}-z) \ \phi_k^{'}(z) - \phi_k(z) - \overline{\phi_k(z)} \quad\quad [2]$$

$$2E_k \ / \ (1+\nu_k) \ [(\partial u_{x,k}/\partial y) + (\partial u_{y,k}/\partial x)] = (3 - \nu_k) \ \phi_k(z) + \phi_k(\bar{z}) + (\bar{z}-z) \ \overline{\phi_k^{'}(z)} + \alpha_k\Delta t$$

where:

k = 1, z is in the substrate and z is in the coating material.
σ_x, σ_y and σ_{xy} are the stresses in x, y and shear stress respectively.
E = Young's modulus.
v = Poisson's ratio.
  u_x and u_y = the displacement in x and y directions (see figure 2).

By proper imposition of boundary conditions along the bond and at infinity the complex potential ϕ can be calculated (Charreyron et al. 1987) as:

$$\phi(z) = -(E^*\epsilon)/2 \ * \ [1 - (z/ \ (z^2 - a^2)^{1/2})] \quad\quad [3]$$
for differential thermal contraction loading

and

$$\phi(z) = (f_x+if_y)/2 \ * \ [1/ \ (z^2 - a^2)^{1/2})] \quad\quad [4]$$
for the case where an external load f is present.

In equation 3, $E^* = 0.5 \ * \ [1/E_1 + 1/E_2]^{-1}$ \quad\quad [5]

and ϵ is the differential strain due to the thermal expansion mismatch $\Delta\alpha$, and f is the external force. The detail derivation of the above equations is given in the paper by England (1965).

One should bear in mind that the adherents elastic moduli mismatch parameter ζ has been omitted in the above relations. This is equivalent to treating the braze as a

rigid interface.   This is due to the fact that parameter ζ is very small for ceramic/metal joints of commercial interest (see Charreyron et al., 1987).   However, readers interested in the effect of such parameters are referred to the aforementioned reference.

(a) Brazed section's dimension

	Metal	Ceramic
E (MPa)	168,000	200,000
ϑ	0.31	0.23
α (°/°C)	13.6e-6	10.20e-6

FEM mesh of half section symmetry
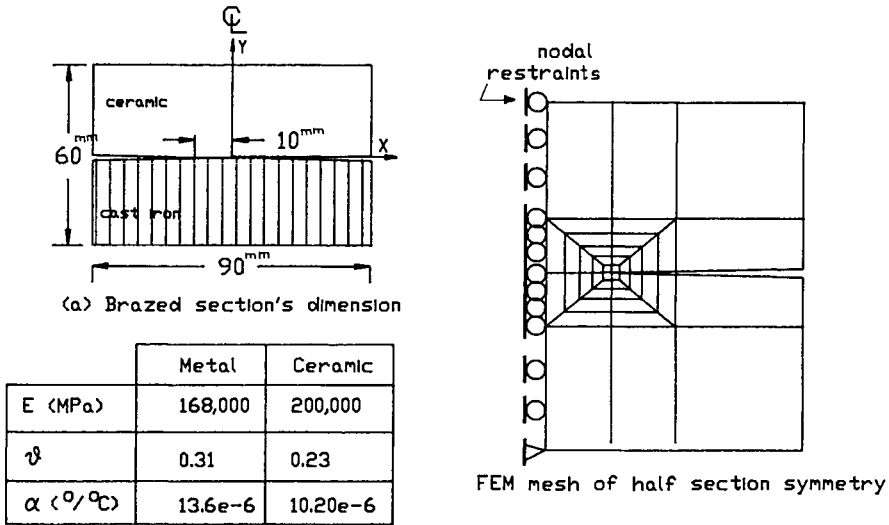
Fig. 3. Brazed section idealized by fracture mechanics

The expression for displacement and stress field can now be expressed in more familiar form as:

$$\sigma_y + i\, \sigma_{xy} = K/\, (2\pi)^{1/2} r \tag{6}$$

$$\Delta u_y + i\, \Delta u_x = 2K/E^* \quad (r/2\pi)^{1/2} \tag{7}$$

where K the stress intensity factor is given by

$$K = K_I + i\, K_{II} = i\, E^* \epsilon (a\pi)^{1/2} \tag{8}$$

where:

K_I and K_{II} are mode I and II stress intensity factors, and a is the half bond length (see figure 1).

Finite Element Modelling of the Brazed Joint

As discussed earlier, the objective of this study is to demonstrate a reliable and

economical technique for the determination of the stress field around the cracks that are results of thermal residual strains in the brazing process.

For this purpose a plate with dimensions and material properties as shown in figure 3 was modeled by FAST. Because of the cubic nature of the polynomials used in the formulation of the shape functions (N_i, see equation 1), one only needs a low number of elements to model the domain. Furthermore, K_I and K_{II}, the mode I and II stress intensity factors, are calculated directly as two extra degrees of freedom in the displacement function of the 'enriched' element; therefore, as long as the elements surrounding the crack tip are sized in the order of 1/20 to 1/30 of the crack length, the values of K_I and K_{II} are calculated quite accurately. FAST also uses 4x4 gaussian integration scheme as well as cubic shape functions to interpolate the stress field.

Table 1 tabulates the results of mode II stress intensity factor for the braze problem as calculated based on the analytical solution (equation 8), and as calculated by FAST.

TABLE 1   Comparison of Analytical and FEM Results of K_{II}

ε	E_1	E_2	E^*	K_{II} (Analytical)	K_{II} (FEM)
($\times 10^{-3}$)	(MPa)	(MPa)	(MPa)	$MPa(mm)^{1/2}$	$Mpa(mm)^{1/2}$
2.16	168,000	200,000	45,652	552.7	511.3

The three stress components obtained by FEM are plotted in figure 4. Similar plots based on the analytical solution are shown in figure 5. It can be seen that with the use of a coarse mesh (only 38 elements, see figure 3), the results correlate favourably. In these plots, the tensile and compressive stresses are represented in by positive and negative signs respectively. The normalized plot of tangential stress in figure 4 and 5 illustrate the singularity in the stress field due to mode II stress intensity. In addition the plot of Normal stress (σ_y), indicates the absence of stress along the joint (indicating mode I stress intensity is almost zero). Finally, the shear stress contours are concentrated along the bound interface.

For the sake of comparison the same plate was modeled by ordinary finite element methods using 160 elements. The results of the three stress components are plotted in figure 6. It can bee seen that in spite of the fine mesh used to model the problem, the near crack tip stress field differs noticeably from those plotted by the analytical results and none of the patterns indicates the presence of the stress singularity at the crack tip.

Figure 7 compares the normalized σ_y from FAST and ordinary FEM analysis. Although the overall patterns of the stress field are very similar, the ordinary FEM

Brazed section idealized with fracture

Shear Stress $\frac{2\sigma_{xy}}{E^* t}$

Tangential Stress $\frac{2\sigma_{xx}}{E^* t}$

Normal Stress $\frac{2\sigma_{yy}}{E^* t}$
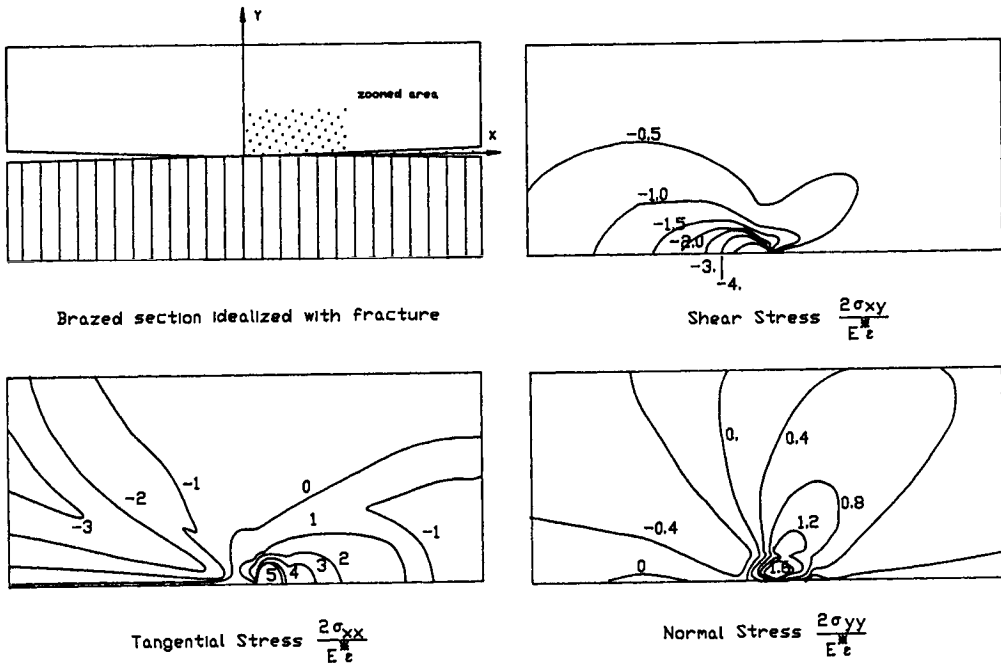
Fig. 4. Normalized stress contours based on FAST's results

fails to successfully determine the stress singularity near the crack tip.

Charreyron et al. (1987) have done extensive research on the same topic. They have used a FEM mesh with 8000 elements to model the same problem. This type of analysis has two drawbacks: i) the amount of time to prepare the data for the computer is extremely large, and ii) the computer CPU time required to solve a mesh of that magnitude becomes extremely costly. Furthermore, due to the nature of the displacement field in the ordinary FEM (as discussed earlier), the prediction of the stress singularity still remains a difficult task with this approach.

As it can be noticed, the authors' fracture mechanics model ignore the presence of the thin braze layer (the reason was explained earlier). Ordinary FEM analysis can only be utilized to model all three layers to get quantitative answers as to whether the braze has yielded. Charreyron et al. (1987) have used this approach as well as elastic-plastic FEM to study the stress variation when the yield strength of the brazing layers varies. Figure 8 shows the distribution of Von-mises stress along the ceramic/metal interface. These results are based on the assumption that the braze behaves purely elastic. The high stress concentration close to the free edge as well as the nearby stress fluctuations indicates the presence of a stress singularity close to the edge. By using elastic-plastic FEM, and proper modelling of the braze, the

Brazed section idealized with fracture

Shear Stress $\dfrac{2\,\sigma_{xy}}{E^{*}\varepsilon}$

Tangential Stress $\dfrac{2\,\sigma_{xy}}{E^{*}\varepsilon}$

Normal Stress $\dfrac{2\,\sigma_{xy}}{E^{*}\varepsilon}$
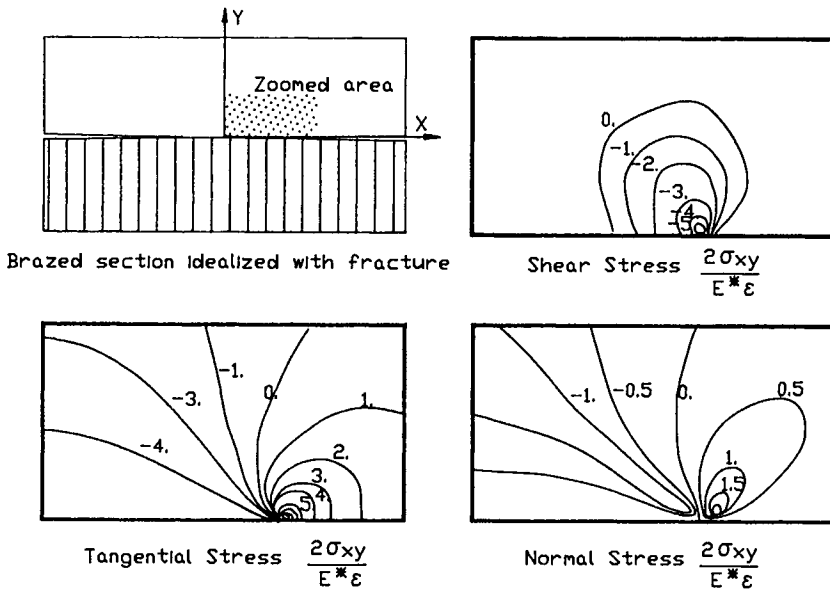
Fig. 5.   Normalized stress contours based on the analytical solution

Brazed section idealized with fracture

Shear Stress $\dfrac{2\,\sigma_{xy}}{E^{*}\varepsilon}$

Tangential Stress $\dfrac{2\,\sigma_{xy}}{E^{*}\varepsilon}$

Normal Stress $\dfrac{2\,\sigma_{xy}}{E^{*}\varepsilon}$
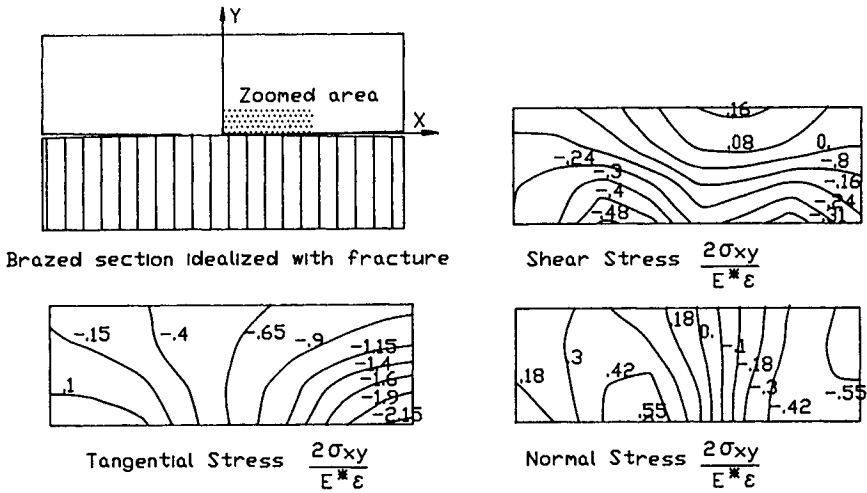
Fig. 6. Nolmalized stress contours by ordinary FEM

(a) Analytical   (b) FAST
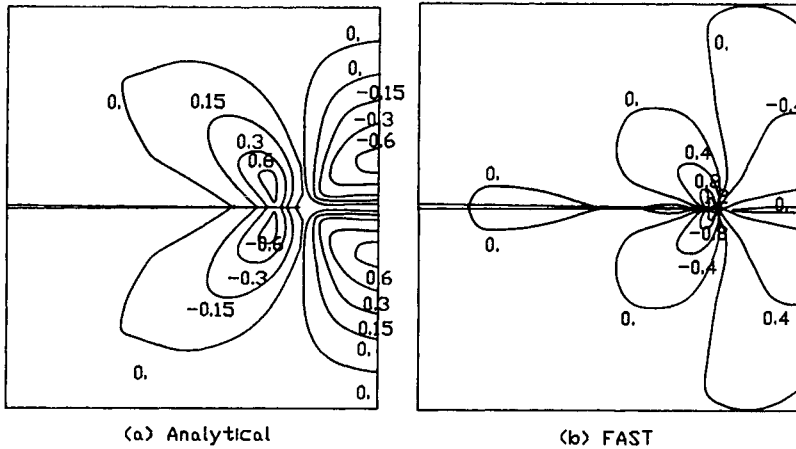
Fig. 7. Comparison of Y-stresses

magnitude of the stresses will decline, conforming with the true behaviour of the domain and the fracture mechanics results.

CONCLUSION

FAST, a special purpose fracture mechanics finite element program was introduced. The ceramic/metal braze problem was analyzed by fracture mechanics. The analytical results based on Mushkelishevili complex stress function were plotted and compared to the results obtained by FAST. The comparison indicates that near crack stress field can be successfully predicted by FEM. The importance of the use of the proper FEM approach was also discussed. The comparison of ordinary FEM as compared with special purpose FEM showed that ordinary FEM approach fails to accurately predict the crack tip singularity, as well as being an

Fig. 8. Maximum principal stress on the ceramic-braze interface

extremely time consuming and costly approach. If one needs to model the problem in a more accurate manner, an elastic-plastic fracture mechanics FEM should be used,

so that the proper material behaviour of the braze layer could also be modeled. Future work will examine these parameters in conjunction with a proper fracture mechanics model.

REFERENCES

Barsoum, R.S. (1976). On the use of isoparametric finite element in linear fracture mechanics. International Journal for Numerical Methods in Engineering, 10, pp. 25-37.

Bowie O.L., (1956). Analysis of infinite plate containing radial cracks originating at the boundary of an internal circular hole. Journal of Mathematics and Physics, 25, pp. 60-71.

Bowie, O.L. and Neal D.M. (1970). Modified mapping-collocation technique for accurate calculation of stress intensity factors. International Journal of Fracture Mechanics, 6, pp. 199-206.

Byskov, E. (1970). The calculation of stress intensity using the finite element method with cracked elements. International Journal of Fracture Mechanics, 6 (2), June, 1970, pp. 159-167.

Charreyron. P.O., Patten, D.O., and Miller, B.J. (1987). Modelling of ceramic to metal brazed joints. International Forum on Joining Structural Ceramics, American Ceramic Society, Pitsburg, PA.

Charreyron. P.O., and Miller, B.J. (1986). Fracture Mechanics Modelling of Ceramic-metal attachement. Presented at the 2nd International Symposium of Ceramic Materials and Components in Engines. Lubeck-Travenmunde, Germany, April 14-16.

England, A.H. (1965). A crack between dissimilar Media. Journal Applied Mechanics, 32, pp. 400-403.

Erdogan, F. (1965). Stress distribution in bonded dissimilar Materials with cracks. Journal Appllied Mechancis., 32, pp. 403-410.

Gifford, L.N. (1979). APES - finite element fracture mechanics analysis. Revised Documentation , David W. Taylor, Naval Ship Research and Development Centre.

Gifford, N., Hinton, P.D. (1978). Stress intensity factors by enriched finite elements. Engineering Fracture Mechanics, 10, pp. 485-496.

Muskhelishvili, N.I. (1953) Some Basic Problrms of the Mathematical Theory of Elsticity. P. Noodhoff Ltd.

Mufti, A.A. and Taheri, F. (1986). FAST: A computer aided design program for fracture mechanics.Technical Report CADCAM TR 86-09, Technical University of Nova Scotia, Halifax, Nova Scotia.

Pu, S.L. and Hussain, M.A. (1978). The collapsed isoparametric element as a singular element for crack problems. International Journal for Numerical Methods in Engineering, 12 (11), pp. 1727-1742.

Sih, G.C., and Rice, J.R. (1965) Plane problems of cracks in dissimilar Media. Journal Applied Mechanics, 32, pp. 418-423.

Turner, M.J., Clough, R.W., Martin, H.C. and Topp, L.J. (1956). Stifness and deflection analysis of complex structures. Journal of Aeronutical Science. 23, pp.805-825.

The joining of niobium to reaction bonded silicon carbide

J.R. McDermid, M.D. Pugh and R.A.L. Drew
Department of Mining and Metallurgical Engineering, McGill University,
Montreal, Québec, Canada, H3A 2T5

ABSTRACT

The objective of this study was to join reaction-bonded silicon carbide (RBSC) to niobium (Nb) for use in high temperature applications. The filler material employed was a Si-15Nb-5Ti alloy manufactured in-house. It was found that Nb-RBSC joints could be formed. However, due to insufficient reactivity of the filler material with respect to the ceramic, inadequate adherence of the brazing material to the ceramic was observed. It was also found that excessive porosity and cracking (due to cooling stresses) existed within the filler material of the joints; this must be eliminated in order to form joints with consistent properties. By using chemical and microstructural information obtained from experimental joints to estimate material properties, it was found that the finite element method (FEM) could be used to predict the location of high stresses and high stress gradients within the experimental joints resulting from coefficient of thermal expansion (CTE) stresses generated during cooling from the bonding temperature. Using the FEM, it was also found that the majority of the CTE stresses were generated during the first 500°C of cooling.

KEYWORDS

metal-ceramic joining; brazing; reaction-bonded silicon carbide; niobium; finite element method.

INTRODUCTION

One of the challenges presently facing the materials engineer in the design of advanced heat engines is in the successful joining of structural ceramics with the existing metallic support structure. In order to exploit the high temperature properties of structural ceramics in these applications, metal-ceramic joints must have both mechanical and chemical stability at temperatures approaching 1000°C.

There are several problems which must be addressed in metal-ceramic joining, the most important of which are coefficient of thermal expansion (CTE) mismatch, chemical incompatability between the various materials in the joint and (for brazing), the non-wetting of the ceramic by the liquid filler material.

High temperature brazing is one of the joining methods currently receiving attention for commercial applications. In order for brazing to be successful, however, the liquid filler material must wet the ceramic. If insufficient wetting of the ceramic is obtained using only the desired brazing material on the ceramic

surface, sufficient wetting can usually be obtained by altering the ceramic surface by some of the standard metallizing techniques or by making the brazing material "active" (Nicholas, 1985; van Houten, 1959). Brazing materials can be made active by additions of Ti to them; the Ti usually promotes wetting by reacting with the surface oxide on the ceramic to form TiO_2.

Chemical incompatability between the joint materials can result in the formation of deletorious phases within the base materials arising from the joining reactions. It was shown by the present authors that the joining of reaction-bonded silicon carbide (RBSC) to Inconel 600 using a nickel-based brazing alloy (McDermid, 1989a) or an iron-based brazing alloy (McDermid, 1989b) resulted in the decomposition of the RBSC to form low-melting point (~900°C) silicide phases and carbide phases. It was also found by Mehan and co-workers (1976, 1979, 1981) that RBSC reacted extensively with nickel-based superalloys. When the two are brought into intimate contact at temperatures in excess of 900°C, silicide and carbide phases tend to form. The conclusions of both sets of workers was that the high temperature properties of the ceramic had been seriously degraded. It was also found by the above workers (McDermid, 1989a, 1989b; Mehan, 1976, 1979, 1981) that the large CTE mismatch between the two materials (i.e. $\Delta \alpha = 10 \times 10^{-6}°C^{-1}$) resulted in cracking and failure of the joint at the metal-ceramic interface; a result of the high stresses generated during cooling of the joints from the bonding temperature.

Several methods have been proposed to alleviate the problems of high CTE mismatch stresses in metal-ceramic joining and extensive chemical reactions with nickel-based superalloys. One of these methods involves placing refractory metal interlayers (usually Mo, Nb or W) between the ceramic and the metal to provide a layer of intermediate CTE between the two materials, thereby reducing the CTE mismatch stresses (Suganuma, 1984; McDermid, 1989c), and providing a chemical barrier beween the ceramic and the superalloy (McDermid, 1989c). However, finite element method (FEM) calculations performed by the authors (McDermid, 1989c) to estimate the effects of various refractory metal interlayers (Mo, Nb and W) on the residual CTE stresses in Inconel 600-RBSC joints concluded that a more favourable stress distribution could be obtained by forming a simple butt joint between the refractory metal and the RBSC. This assembly could then be mechanically joined to the superalloy, thus providing the advantages of a simpler joint geometry and avoiding a multi-step bonding process. However, refractory metals do not have good oxidation resistance and are strong carbide formers. The former difficulty is especially true of Mo and W.

Niobium and niobium-based alloys have potential high-temperature applications to 1350°C in both the coated and uncoated states. In particular, disilicide coated niobium alloys can be used in high-temperature oxidizing environments in static applications such as rocket nozzel parts and protective skins (Inouye,1984). Because of the greater potential to protect Nb in oxidizing environments compared to the other two refractory metals, it was decided to pursue the joining of Nb to RBSC by brazing and to assess the joining mechanisms and properties of this joining system.

EXPERIMENTAL

Starting materials consisted of reaction-bonded silicon carbide and industrially pure (>99.98%) cold-rolled Nb rod. High purity Si, Nb and Ti powders were used to manufacture the brazing material (Si-15Nb-5Ti) in-house. This particular alloy composition was chosen to make it compatible with both of the starting materials and because Si-15Nb is the lowest melting point eutectic compostion (~1375°C, Argent,1984) in the Si-Nb system. The Ti was added to make the filler material "active". X-ray diffraction showed that the RBSC consisted of α-SiC and cubic Si; image analysis of typical microstructures determined that the continuous Si phase comprised approximately 10 wt. pct. of the RBSC. A typical microstructure of the as-received RBSC is shown in Fig. 1. The strength of the RBSC was determined using 4-point modulus of rupture (MOR) bars cut from larger plates and surface ground prior to testing. It was found that $\sigma_{0.632}$ was

315MPa and that the Weibull modulus was 7.4; the apparently low value of the Weibull modulus stems from the cutting and grinding of test bars from the larger plates.
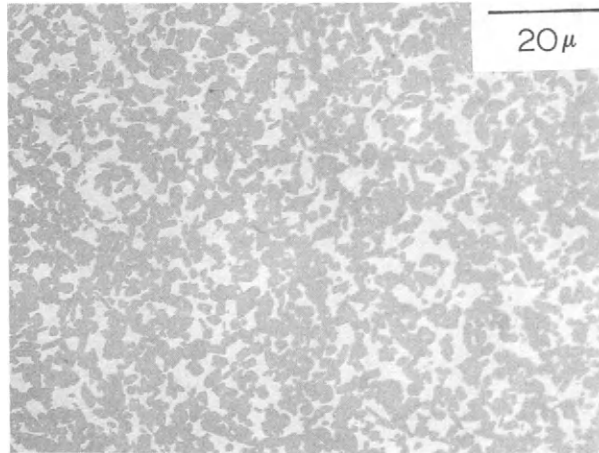
Fig. 1: Optical micrograph of as-received RBSC.

Joining experiments were performed in a vertical tube furnace under a Ti gettered flowing Ar atmosphere. Joints consisted of 9mm x 9mm x 6mm Nb and RBSC blocks which had been previously surface treated to promote wetting by the brazing material. The brazing material was applied in the form of a paste in quantities sufficient to form a layer 0.5mm thick upon solidification, as suggested by Nicholas and Mortimer (1985) for metal-ceramic brazements. All joining materials were contained within a boron nitride (BN) jig to ensure proper alignment of the joint of throughout the brazing cycle. Joints were heated to the brazing temperature of 1500°C at 100°Cmin-1, held at temperature for between 5-60 min. and cooled to room temperature at 3°Cmin-1.

After removal from the BN brazing jig, specimens were cross-sectioned, polished and examined by optical and scanning electron microscopy (SEM). Chemical analysis of the joint constituents was performed using an energy dispersive spectroscopy (EDS) unit attached to the SEM.

Finite element method (FEM) calculations were performed and correlated with observed phenomenon in the experimental joints. The finite element mesh used in these calculations is shown in Fig. 2. This FEM mesh models a cylindrical butt joint 9mm in diameter with the materials being of the same thicknesses as found in the experimental joints. Due to joint symmetry, only half of the joint is modelled in this mesh. Reasons for the selection of the various materials shown in Fig. 2 will be outlined in subsequent sections. The mechanical properties used for Si and RBSC are given in Table 1; these properties vary only slightly between room temperature and 1300°C for these materials. The variation of the tensile modulus (E) and CTE (α) as a function of temperature for Nb are shown in Fig. 3.

Table 1:Mechanical Properties used in FEM Calculations

Material	E (GPa)	G (GPa)	v	α ($\times 10^6 °C^{-1}$)
RBSC	380	156	0.22	5.04
Si	110	44	0.25	2.90
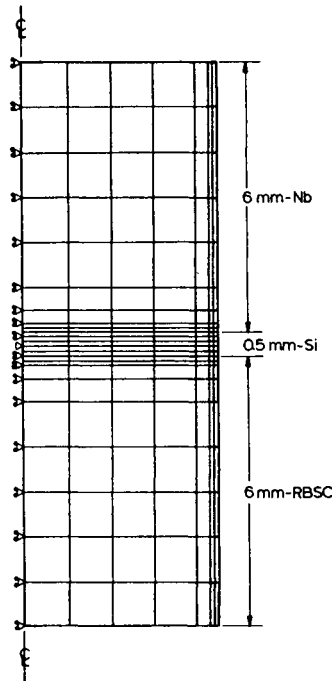
Fig. 2: Mesh used in FEM calculations.

RESULTS AND DISCUSSION

A. Joining Experiments

Fig. 4 shows a backscattered electron image (BEI) of a Nb-RBSC joint held at 1500°C for 20 minutes. From the Figure, it can be seen that the cross-section can be divided into three distinct zones, labelled A, B, and C on Fig. 4.

Zone A is essentially pure Nb and was virtually unaffected by the joining process; the composition of this zone, as determined by EDS, was Nb-5 atom pct. Si at the interface
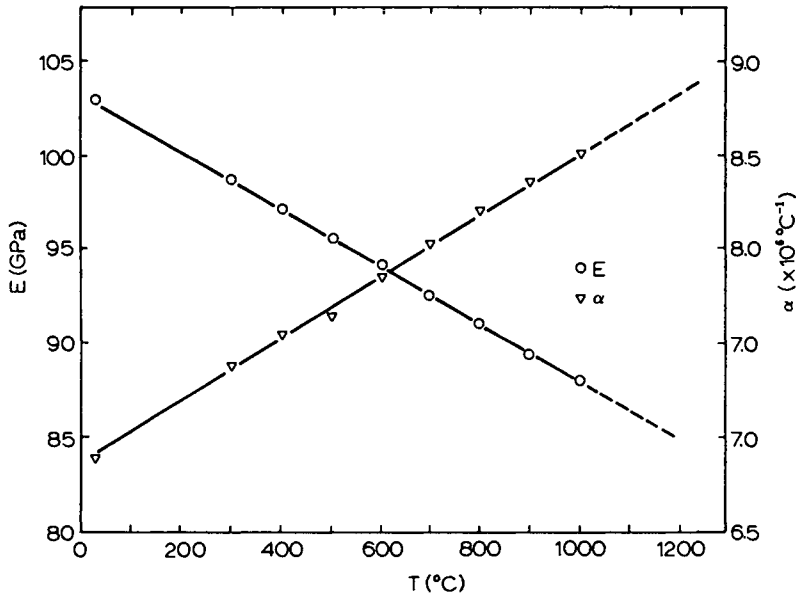
Fig. 3: Variation of CTE (α) and tensile modulus of Nb with temperature.
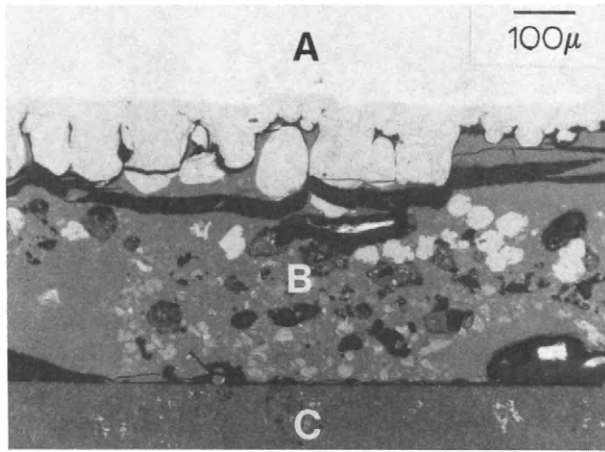
Fig. 4: BEI image of a Nb-RBSC joint cross-section.

and quickly became pure Nb within 0.2mm of the interface. Zone B is the original filler material; the features within this zone will be discussed below.

Zone C is the RBSC; it can be seen that there has been some reaction of the filler material with the Si phase of the RBSC (light areas in zone C in Fig.5). By EDS, it was determined that these light areas within the RBSC were $NbSi_2$. However, it was expected that, due to

the "activation" function of the Ti in the filler material, some Ti would be present within the RBSC and that a more extensive joining reaction would be observed between the brazing material and the ceramic. Also, little joining reaction was observed for longer brazing times and no decomposition of the α-SiC was observed. Sessile drop experiments performed using the brazing alloy found that the contact angle with the RBSC was 35°, which is slightly above the maximum contact angle of 30° suggested by Moorhead and Keating (1986) for good adherence of the alloy to the substrate. The above observations point to poor adherence of the brazing material to the ceramic.

A higher magnification BEI image of zone B is presented in Fig. 5. From this micrograph, it can be seen that there are three distinct phases within zone B, marked M, α and β on the micrograph. The compositions of these phases, as determined by EDS, are given in Table 2.
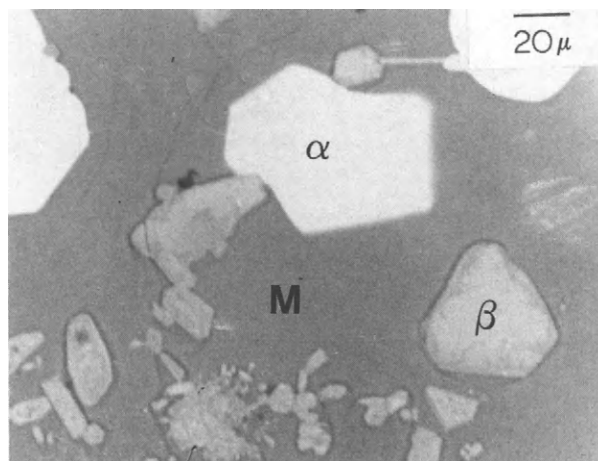
Fig. 5: BEI image of zone B phases.

Table 2: Compositions of Zone B Phases

Phase	Composition
M	Si-2a/oNb (s.s.)
α	$NbSi_2$
β	Ti-22a/oNb-5a/oSi (oxide or s.s.)

The continuous, or matrix, phase (M) is a Si-2 atom pct. solid solution and has, therefore, largely the mechanical properties of Si; this observation was later used in performing the FEM modelling of the joints as discussed below. The phase marked α in Fig. 5 was found, by EDS, to be $NbSi_2$. The presence of both M and α phases is consistent with the predictions of the Nb-Si phase diagram for an Si-15Nb alloy (Argent,1984; Hansen, 1958).

The β-phase was found to consist of Ti-22a/oNb-5a/oSi. However, due to its highly facetted morphology and from the available phase diagram data (Argent, 1984; Hansen, 1958; Levin, 1964; Levin, 1975), it is thought that this phase is a TiO_2-Nb_2O_5 spinel with small amounts of Si or SiO_2 solid solution. This finding is not certain since no oxygen

analysis has been performed on this phase to date. However, its existence would be consistent with the supposed function of Ti within the joining system: that of reacting with the surface oxide of the ceramic to promote wetting of the ceramic by the filler material. As can be seen in Fig. 4, a large proportion of β-phase is concentrated at the zone B-zone C interface. If, in fact, this phase is an oxide, the existence of this amount of β would indicate that there was a large amount of oxygen present within the braze layer-RBSC system.

B. Finite Element Modelling

An examination of Fig. 4 will show that there was extensive cracking within the filler material, next to the Nb, which was probably due to CTE mismatch stresses. Based on the EDS analysis, it was decided to perform FEM analyses on the joint system, using the material properties of Si. This was used to determine if the FEM could be used to show how the CTE stresses developed and were distributed within the joint as it was cooled from the stress-free temperature of 1300°C (the solidification temperature of the filler material).

Fig. 6 shows an isostress contour plot of a full Nb-Si-RBSC joint cooled through 1300°C; the stresses shown (in MPa) represent the principle stresses at the element centroid. It can be seen that the highest stresses and stress gradients occur just inside the filler material layer next to the Nb; this coincides with the location of the observed cracking within the experimental joints (see Fig. 4). Also, the existence of high porosity within the filler material (see Fig. 4) would tend to intensify the effect of the high stress gradients.

ΔT= -1300°C
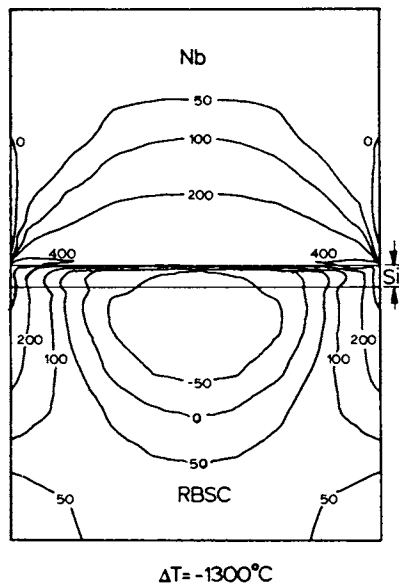
Fig. 6:   Isostress contour plot of Nb-RBSC joints from FEM calculations.

In order to understand the manner in which the CTE stresses developed as the joint was cooled from the stress-free temperature (1300°C), a series of calculations were performed

in which the joint was cooled through various temperatures from 1300°C and the maximum stress vs. the temperature change (-ΔT) was determined, the results of which are shown in Fig. 7. In this Fig., -ΔT = 500°C corresponds to a final joint temperature of 800°C; ΔT = 600°C corressponds to a final joint temperature of 700°C etc. From this plot, it can be seen that the majority of the residual stresses develop within the first 500°C of cooling (i.e. from 1300°C to 800°C). This is the temperature range for the stress relief of Nb and its alloys, and so shows promise for reducing the CTE mismatch stresses within the joints by in situ heat treatment during the brazing cycle.
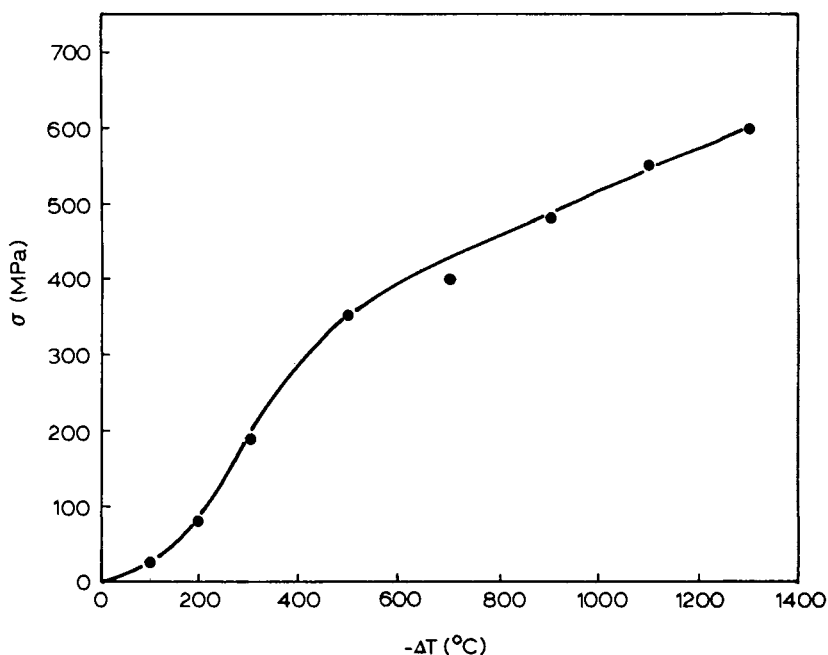
Fig. 7: Peak stress (σ) vs. -ΔT for Nb-Si-RBSC joints.

CONCLUSIONS

1. Nb-RBSC joints can be formed using a Si-15Nb-5Ti alloy as a filler material. However, in order to increase the adherence of the alloy to the ceramic, a way must be found to increase the reactivity of the filler material with respect to the ceramic.

2. Excessive porosity exists within the filler material in the final joints. This must be eliminated in order to form strong joints with consistent properties.

3. Finite element analyses can be used to predict the locations of high stress regions and high stress gradients within the metal-ceramic joints. These analyses can be made more accurate when correlated with chemical analysis and microstructural observations in actual joints to predict the material characteristics of the various regions within the model.

4. Finite element analyses of Nb-RBSC joints show that the majority of the CTE mismatch stresses are generated during the first 500°C of cooling from the joining temperature. Further work on reducing the magnitude of the residual stresses will concentrate on this temperature range.

REFERENCES

Argent, B.B. (1984). In H. Stuart (Ed.), *Proceedings of the International Symposium, Niobium '81.* The Metallurgical Society of the AIME, Warrendale. pp. 325-415.

Hanson, M. (1958). *Constitution of Binary Alloys, 2nd. Ed.* McGraw-Hill Co. New York.

Inouye, H. (1984). In H. Stuart (Ed.), *Proceedings of the International Symposium, Niobium '81.* The Metallurgical Society of the AIME, Warrendale. pp. 615-636.

Levin, E.M., C.R. Robbins and H.F. McCurdie (1964). In M.K. Reser (Ed.), *Phase Diagrams for Ceramists.* The American Ceramic Society, Columbus. pp. 69, 142.

Levin, E.M. and H.F. McCurdie (1975). In M.K. Reser (Ed.), *Phase Diagrams for Ceramists, 1975 Supplement.* The American Ceramic Society, Columbus. pp. 167-170.

McDermid, J.R., M.D. Pugh and R.A.L. Drew (1989a). The interaction of reaction-bonded silicon carbide and Inconel 600 with a nickel-based brazing alloy. *Met Trans. A.,* accepted for publication.

McDermid, J.R., M.D. Pugh and R.A.L. Drew (1989b). The interaction of reaction-bonded silicon carbide and Inconel 600 with an iron-based brazing alloy. *Can. Met. Quart.,* in preparation.

McDermid, J.R., M.D. Pugh and R.A.L. Drew (1989c). In D.S. Wilkinson (Ed.), *Proceedings of the International Conference on Advanced Industrial Materials.* Pergamon Press, New York. pp. 169-177.

Mehan, R.L. and D.W. McKee (1976). Interaction of metals and alloys with silicon-based ceramics. *J. Mat. Sci.,* 11, 1009-1018.

Mehan, R.L. and R.B. Bolon (1979). Interaction between silicon carbide and a nickel-based superalloy at elevated temperatures. *J. Mat. Sci.,* 14, 2471-2481.

Mehan, R.L. and M.R. Jackson (1981). In J.A. Pask and A. Evans (Eds.), *Materials Science Research, vol. 14.* Plenum Press, New York. pp. 513-523.

Moorhead, A.J. and H. Keating (1986). Report No. ORNL-6262. Oak Ridge National Laboratory.

Nicholas, M.G., and D.A. Mortimer (1985). Metal-ceramic joining: a critical evaluation. *Mat. Sci. Tech.,* 1, 657-665.

Suganuma, K. and others (1984). Effect of interlayers in ceramic-metal joints with thermal expansion mismatches. *J. Amer. Ceram. Soc.,* 67(12), C256-C257.

van Houten, G.R. (1959). A review of metal-ceramic bonding. *Ceram. Bull.,* 38(6), 301-307.

Effects of Si and Mg dopants on the kinetics of aluminum alloys nitridation

H. LeHuy and S. Dallaire
*Industrial Materials Research Institute, National Research Council Canada,
75 de Mortagne Blvd., Boucherville, Québec, Canada, J4B 6Y4*

ABSTRACT

Combustion reactions of molten aluminum alloys with nitrogen atmosphere have been carried out to determine to what extend dense Al/AlN composites could be obtained. The present paper describes the effects of dopants such as Si and Mg on the kinetics of aluminum nitridation. A micro-thermal balance with a heating temperature up to 1500°C was used to measure the sample weight gain as aluminum was converted to aluminum nitride. Microstructural analyses of reaction products revealed that a columnar aluminum/aluminum nitride structure has grown outward from the metal surface. The reaction kinetics are complex, particularly in the temperature range of 900-1300°C. The overall weight gain involves not only the nitridation reaction but also the movement of molten metal to the reaction surface. It was found that dopants sustained the reaction by altering the surface area of the growth front. In optimal conditions, the complete conversion of Al into AlN could be achieved in an hour.

KEYWORD

Ceramic-Metal Matrix Composite; Liquid Aluminum Nitridation; Magnesium-Silicon Dopants; Thermal balance; X-Ray diffraction.

INTRODUCTION

Recent progress concerning new developments in the fabrication of ceramic-metal matrix composites by directed reaction of molten aluminum alloys with gaseous oxidants have been reported. The novelty point of this emerging technique is the use of dopants to accelerate and to sustain the transformation (Newkirk and co-workers, 1986). The resultant product is a three-dimensional interconnected ceramic network containing residual metals. Under adequate conditions, the reaction rate is constant over time. Previous reports on the formation of Al/AlN are promising; reaction rates in the Al/AlN system are of the order of minutes rather than hours (Creber and co-workers, 1988). Moreover, as opposed to conventional ceramic processing, the directed nitridation does not require high temperatures.

This study is aimed at determining how the technology related to the directed reaction of molten alloys with gas can be applied to form nitride ceramics. This paper gives results obtained on the kinetics of nitridation of Mg, Si-doped aluminum alloys and describes the resulting microstructures.

EXPERIMENTAL DETAILS

A micro-thermal balance having a readability of 1 µg and a weighing resolution of ±10 µg was used to measure the sample weight gain as the aluminum was converted to aluminum nitride. Specimens weighing approximately 130 mg were placed in alumina crucibles having inner section of 30 mm^2 in order to introduce them into the environmental chamber. The chamber was then purged and the temperature was increased and maintained at 650°C for 15 minutes in order to remove any entrapped gas. This temperature was sufficient to melt the aluminum alloys but was too low to initiate the alloy nitridation. Constant heating rate of 4°C/min from 650 to 1450°C in flowing purified nitrogen atmosphere (at a constant flowrate of 13.5 cm^3/min) was then applied. Specimen temperatures and weight changes were recorded with a computer at a rate of 30 readings per minute. The sample was then cooled down to room temperature at a rate of 15°C/min. Specimens were weighed before and after nitridation test to compare them with the micro-thermal balance data.

Five aluminum alloys with different Mg and Si content have been selected for this investigation. These alloys were prepared in 2 kg batches from commercial purity metals. Base aluminum was first melted in an electric furnace and the alloying elements were thereafter added. Then, the molten alloys were cast on steel plates. The composition of these alloys, determined by optical spectrometer, is given in Table 1.

RESULTS

Nitridation Reaction

Sample weight changes with temperature of 3 different Al alloys containing 10 wt% Si and 0, 5 and 10 wt% Mg are plotted in Fig. 1. Because, in directed nitridation, the reaction is controlled through the interface between the molten metal and the reactive gas (in this case the crucible section), it is more convenient to express the reactions by weight changes per surface unit. Furthermore, the quantity of molten metal used for each test covered approximately 1.5 mm thick the crucible bottom. These curves show the dramatic variations in weight gain that can be achieved by using doping elements.

Table 1 - CHEMICAL COMPOSITION OF ALUMINUM ALLOYS

No.	NOMINAL COMPOSITION	ELEMENT (weight percent)					
		Si	Mg	Fe	Zn	Cu	Al
1	Pure Aluminium	- --	-	-	-	--	99.999
2⁺	10Si	9.3	0.1	0.9	2.3	3.1	bal
3	10Si-5Mg	9.5	5.5	0.8	2.5	3.2	bal.
4	10Si-10Mg	8.8	10.8	0.7	2.4	2.8	bal.
5	5Mg	0.4	4.8	0.6	0.2	1.0	bal.
6	5Si-3Mg	4.8	2.9	0.5	1.2	1.5	bal.
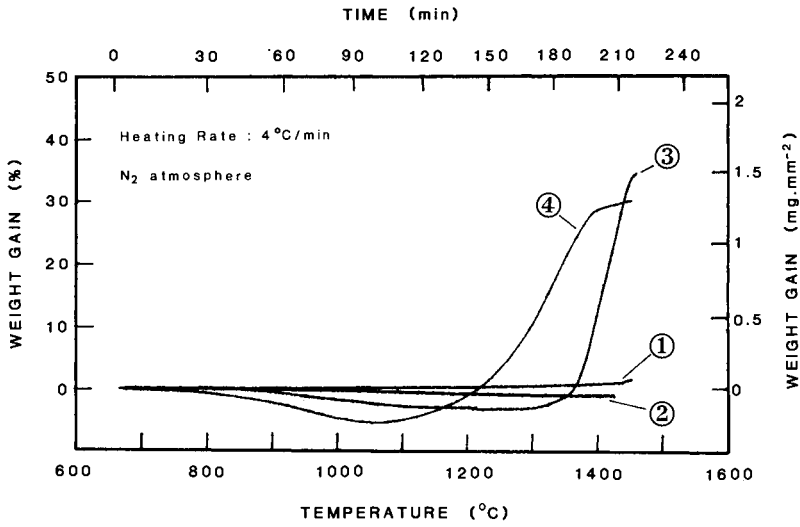
Fig. 1. Effect of Mg on base Al-Si alloys showing weight gains
during heating in nitrogen atmosphere.
Curve 1: pure Al (99.999%)
Curves 2 to 4:   Al alloys containing 10 wt% Si plus
0, 5 and 10 wt% Mg respectively.
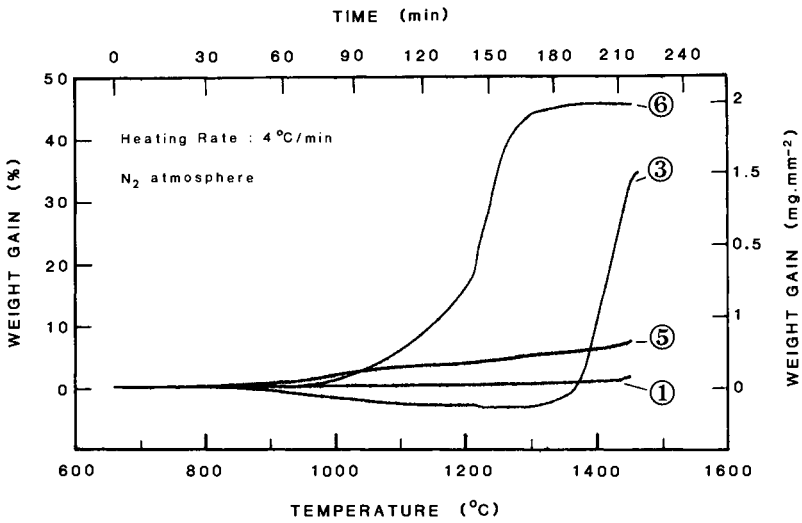
Fig. 2. Effect of Si on base Al-Mg alloys showing
the combined effect of Si and Mg dopants.
Curve 5: Al-5Mg
Curve 6: Al-3Mg-5Si.

For comparison, the nitridation behavior of 99.999% pure aluminum is also shown (curve 1). In this case, a protective nitride film was formed on the surface and limited further reaction; thus the sample weight remained practically unchanged during the 4 hour heating test. The curve 2 shows the behavior of an Al alloy containing only Si. A small loss in weight was observed for the temperatures studied. The combined effect of Mg and Si on the nitridation reaction is shown in curves 3 and 4. With the Al -10Si -5Mg alloy (curve 3), a material loss was observed when heating up to 1350°C, thereafter the nitridation reaction started as indicated by the rapid increase in sample weight. By increasing the Mg content to 10% in Al -10Si -10 Mg (curve 4), the starting reaction temperature was lowered to 1100°C, but the material loss in the earlier stage of heating was larger.

The combined effect of Si and Mg is well illustrated in curves shown in Fig. 2. With only Mg (curve 5), a negligible weight gain of 10% in the initial value was observed at the end of the heating period. By lowering the Si and Mg contents to Al -5Si -3Mg (curve 6), the starting reaction temperature is lowered to 1000°C. At 1200°C, the weight gain is so accelerated that the nitridation was completed after 30 min. The total weight gain was about 45% of the initial weight at the end of the heating period. These results and those shown in Fig. 1 point out that, in the Al-Si-Mg alloy system, both Si and Mg are required for accelerating the nitridation growth.

Reaction Kinetics

Because weight gain during heat treatments resulted from thermally activated phenomena, it was considered that an Arrhenius-type law can be used to describe the process:

$$v = v_0 \, \exp \left\{ -\frac{Q}{RT} \right\}$$

(1)
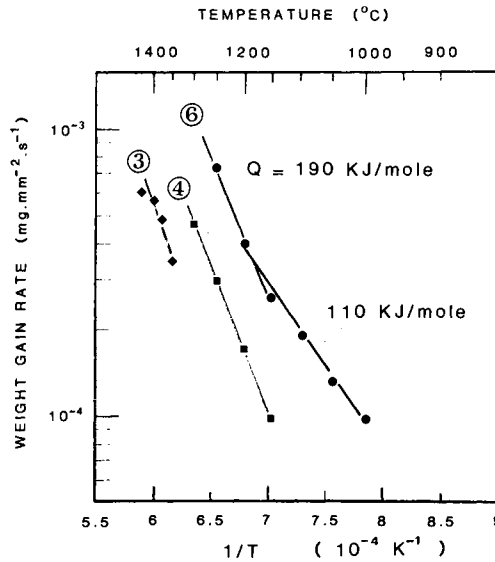
Fig. 3. Arrhenius plots of weight gain rates versus 1/T.
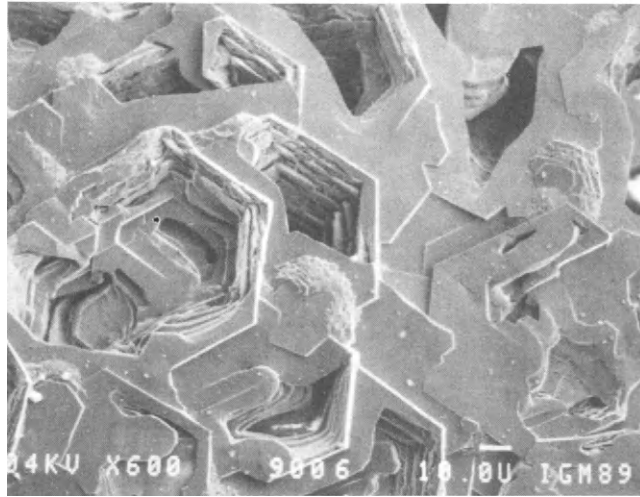
Fig. 4. Microscopic structure of the exposed surface formed on
         Mg, Si-doped aluminum alloy at 1000°C, showing
         hexagonal cells by which molten metals seep out.

where v (mg/mm^2.s)   is the weight gain rate at a determined temperature;

   Q (kJ/mole),   the apparent activation energy of the nitridation process;

   R,   the Boltzmann constant;

   T(K),   the heat treating temperature;

and v_0,   a constant.

Figure 3 shows three Arrhenius-type curves of Mg and Si-doped aluminum alloys. The activation energy Q described in equation (1) is then derived from the slope of the fitting curve. For the nitridation of Al - 5Si -3Mg alloy (curve 6), the calculated value of the activation energy is equal to 110 kJ/mole in the range of 1000-1200°C, in agreement with reported data (Creber and co-workers, 1988). At temperatures above 1200°C, the activation energy for the nitridation of the 3 alloys is found higher (190 kJ/mole).

Microstructural Studies

Figure 4 shows the microstructural aspect of the surface of products grown from a Mg, Si-doped aluminum alloy at relatively low temperature (1000°C) for 24 hours. It consists in a hexagonal cellular structure. X-Ray diffraction pattern of the exposed surface (Fig. 5a) showed mainly basal plane {0001} peaks. This indicates that the hcp AlN (a=3.1$\underline{1}$, c=4.9$\underline{8}$) grows perpendicularly to the surface in the direction of [001]. Unreacted Al metal was also detected on the surface. In a recent study of the directed oxidation of aluminum, Newkirk and co-workers (1988) have described the general features concerning the growth process. For a nitridation reaction, the transformation products are initially formed on the molten metal surface and with proper conditions they grow
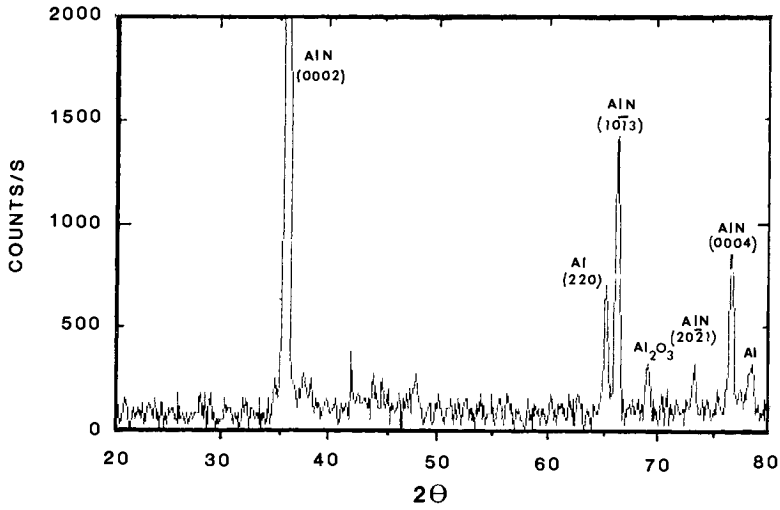
Fig. 5a. X-Ray diffraction pattern of the nitrided surface of an
Al-3Mg-5Si alloy treated in nitrogen atmosphere at
1000°C during 24 hours, showing the directional
AlN growth in the [001] direction.
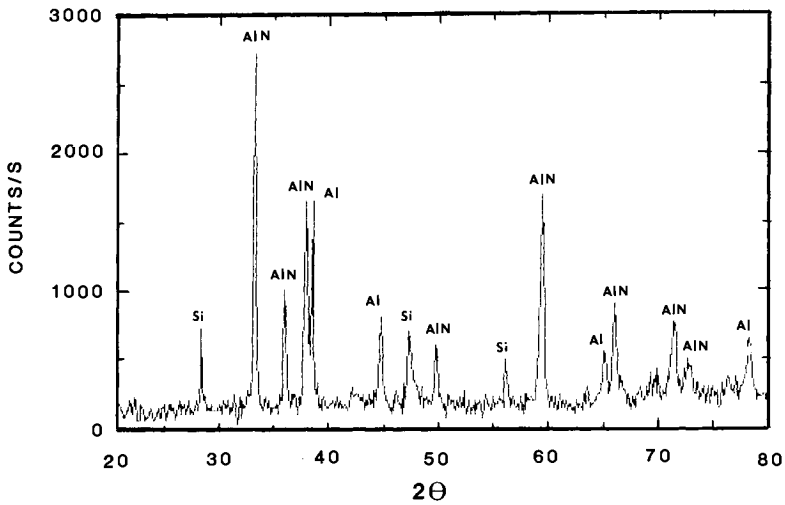
Fig. 5b X-Ray diffraction pattern of ground powder
obtained from the same material as in a) showing
residual Si and Al metals.
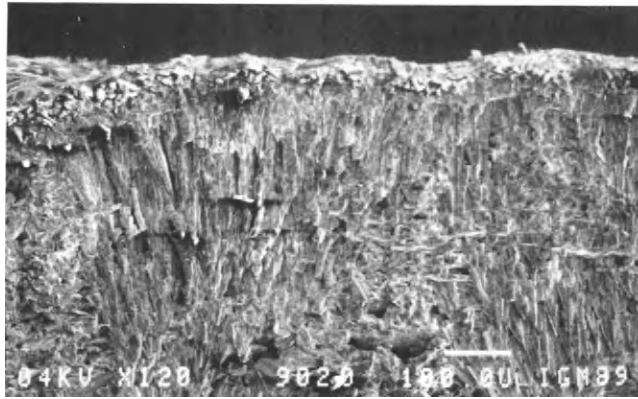
Fig. 6. Transverse fracture surface of reacted product
showing the directed nature of growth process.

outward with a continuous supply of metal at the reaction front. The hexagonal cells shown in Fig. 4 are traces of the molten alloy wicking along channels within the nitrided product. The orientation of the growth process is clearly confirmed by the fibrous character shown in a transverse fracture (Fig 6). However, the powder obtained by grinding the reacted material was identified as a mix of AlN and unreacted Si (A4, a=5.4$\underline{4}$) and Al (fcc, a=4.0$\underline{6}$) metals. A typical diffraction pattern of this kind of powder is shown in Fig. 5b.
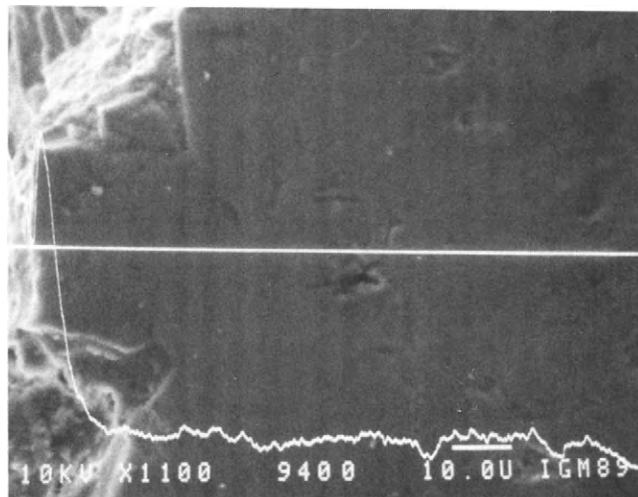
Fig. 7. Electron microscope analysis showing
Mg variation through a reacted layer.

DISCUSSION

Observation of the Nitrides

By contrast with the oxidation of molten Al and Al-Mg-Si alloys which have been studied quite extensively (Drouzy and Fontaine, 1970; Haginoya and Fukusako, 1983), the accelerated growth of AlN on these alloys has not been reported. The role of these alloying elements in the nitridation cannot be directly derived from previous observation. Indeed, it has been recognized that magnesium nitride (Mg_3N_2) is sublimed at 700°C and remains unstable above 800°C whereas the oxides of the same metal on the form of MgO and $MgAl_2O_4$ are very stable (Weast, 1988). Moreover, by scanning Mg within the nitrided product, it was found that this element is more concentrated on the surface of the reacted layer (Fig. 7). Thus, the effect of Mg in contact with nitrogen is inferred as it follows. Magnesium in the vicinity of the surface is selectively nitrided and sublimed, inducing sample weight loss in the earlier stage of heating as indicated by the weight changes in Figs. 1 and 2. Pores are formed on the surface, promoting formation of hcp AlN cells. The decrease of Mg content on the surface is compensated by the diffusion of this element toward the molten alloy. The mechanism of directed growth, proposed by Newkirk and co-workers (1986) with continuous wicking of molten Al through unstable grain boundary, is there enhanced by the diffusion of Mg. However, the magnesium alone could not sustain the directed nitridation, the presence of Si as a dopant is required although its role is different.

Figure 8 shows the location of Si within the reacted product. Contrary to Mg, Si is distributed throughout the transverse section forming a columnar structure (the white phases in the microstructure). X-Ray diffraction pattern, shown in Fig. 5b, indicates that Si remains metallic even when reacted at 1000°C. On reviewing silicon nitridation, Riley (1983) has pointed out that, although the reaction between silicon and nitrogen is a thermodynamically spontaneous process, the reaction is low within the interval of temperatures studied. However, when studying the oxidation of Si in terms of Wagner's theory, Atkinson (1988) has pointed out that the growth of SiO_2 is an example of a process controlled by inward oxygen transport. Thus, if nitrogen is transported as molecules along short circuit pathways in the same manner than oxygen in SiO_2, this transport process is not important in circumstances in which Si is not in direct contact with gaseous reactant, when separated by an AlN
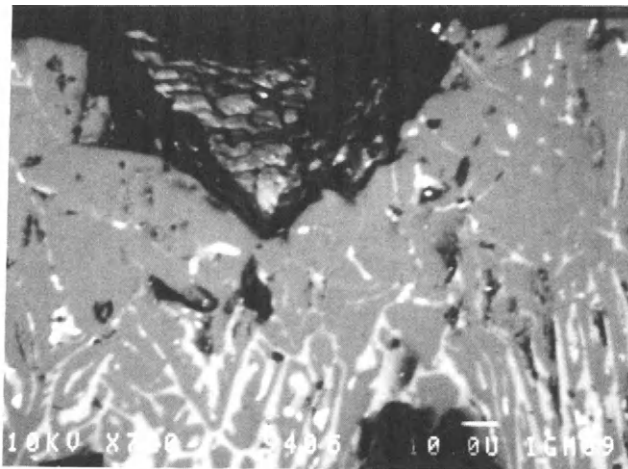
Fig. 8. Backscattering electron image of reacted layer
showing the location of Si (white phases).

Table 2 - SPECIFIC WEIGHT GAINS OF NITRIDED ALUMINUM ALLOYS

NO	ALUMINUM ALLOYS	WEIGHT CHANGES			UNREACTED ALUMINUM (%)
		Measured	corrected* (mg)	calculated**	
1	Pure	10.9	10.9	60.6	82
2	10Si	5.2	5.2	55.5	91
3	10Si-5Mg	43.5	50.4	50.7	0.6
4	10Si-10Mg	38.0	52.3	51.3	-
5	5Mg	17.4	23.7	63.7	63
6	5Si-3Mg	57.7	61.5	60.1	-

* Corrected for the Mg loss.
** Assuming that Al is entirely transformed into AlN.

layer. Work is currently in progress to understand the influence of high temperature and high gas pressure on accelerated growth. Studies of other alloying elements of the Group IVB also help to shed more light on this phenomenon.

Effect of Mg and Si on the nitridation rate

Table 2 summarizes the results obtained after heating Mg, Si-doped aluminum alloys. The measured weight changes (column 3) are the differences in weight before and after nitridation. These overall results take into account the fact that, during the cooling period, samples are exposed to the nitrogen atmosphere and could be quantitatively higher than those deduced from micro-thermal balance data. Because magnesium was sublimed, the corrected weight changes (column 4) are compensated for metal loss. On the contrary, for the calculated weight changes (column 5) it is supposed that all Al was transformed into AlN and Si remained in metallic form. Therefore, the unreacted portion (column 6) is the difference of the two last values. Results suggest that the nitridation reaction was practically completed for the 3 Al-Mg-Si alloys studied. The main difference between these alloys is the temperature at which the transformation was initiated.

CONCLUSIONS

It was attempted to explain the combined effect of Mg and Si on accelerated nitridation growth as it follows:

1) The transformation product on the surface is non-protective in contrast to the behavior of pure Al or single doped alloys. Columnar AlN growth is sustained by seeping molten metal.

2) Magnesium diffuses towards the surface of the nitrided product and it is sublimed. Very little amount of Mg remains in the reacted product.

3) Although Si was found essential for sustaining the reaction, its effect on the transport process is very different from that of magnesium. Si metal remained distributed throughout the transformation product.

REFERENCES

Atkinson A., (1988). Metals Science and Technology, 4, (12), 1046.
Creber D.K., Poste S.D., Aghajanian M.K..and Claar T.D. (1988). Ceram. Eng. Sci. Proc., 9, (7-'9), 975.
Drouzy M. and Fontaine D. (1970). Revue de Métallurgie, 67, 775.
Haginoya I. and Fukusako T. (1983), Trans. Japan Ins. of Metals, 24, (9), 613.
Newkirk M.S., Urquhart A.W. Zwicker H.R. and Breval E. (1986). J. Mater. Res., 1 (1), 81.
Riley F.L. (1983). Progress in Nitrogen Ceramics, ed. F.L. Riley, NATO ASI Applied Science Series E No 65, Martinus Nijhoff Publishers, 121.
Weast R.C. (1988). Handbook of Chemistry and Physics, Physical Constants of Inorganic Compounds, CRC Press, ed. R.C. Weast.

Refractory carbide coatings on carbon fibres for metal matrix composites

D.D. Himbeault, R.A. Varin and K. Piekarski
Faculty of Engineering, University of Waterloo, Waterloo, Ontario, Canada, N2L 3G1

ABSTRACT

Carbide coatings of tungsten carbide, chromium carbide and titanium carbide were applied to PAN type carbon fibres by a liquid metal transfer agent (LMTA) technique using copper and tin as transfer agents. It was found that smooth and uniform coatings of chromium carbide and titanium carbide could be applied by the LMTA technique when using tin as a transfer agent. The effect of the coating on the strength of the fibres was evaluated by performing single fibre tensile tests and the strength was found to decrease with increasing coating thickness. Aluminum alloy composites reinforced with titanium carbide coated fibres were successfully produced by a liquid infiltration technique. Substantial improvement over the matrix strength was observed as the tensile properties of the composite were found to approximate the rule of mixtures values.

KEYWORDS

Composite materials; Carbon fibres; Carbide coatings; Carbon fibre strength; Composite tensile properties

INTRODUCTION

The major problems encountered in the development of carbon fibre-metal matrix composites are the reactivity of carbon with many metals and the poor wetting characteristics of carbon fibres by liquid metals. To overcome these problems, carbon fibres may be coated with refractory carbides which will make the fibres wettable and inhibit any reaction between the matrix and the fibres. To date, the usual method of applying such a protective coating to carbon fibres has been by the chemical vapor deposition (CVD) process. However, the use of CVD in the production of metal matrix composites has not met with any significant commercial applications due mainly to the relatively high cost of the process. The present study examines alternative methods of coating fibres with refractory carbides in the hope these methods will be more economical.

Two methods of coating carbon fibres with refractory carbides were examined: an electroplating-heat treating method (Himbeault, 1988) and a liquid metal transfer agent (LMTA) method (Himbeault, 1989; Ovcharenko, 1981; Rashid, 1972). Both these methods are similar in that they consist of diffusing a refractory element to the surface of the fibres through a metal transfer agent inert with carbon. On reaching the fibre surface the refractory element reacts with carbon from the fibre to form a carbide coating on the fibre. A number of refractory carbides are available for use as coating materials, however this study limits itself only to coating fibres with tungsten carbide, chromium carbide and titanium carbide. As well, only the metals of copper and tin are used as diffusion mediums for the refractory elements.

The strength of a fibre is known to decrease if it is coated with a brittle material (Honjo, 1986; Phillips, 1971), therefore, single fibre tensile tests were performed on the coated fibres. In addition, aluminum alloy matrix composites reinforced with coated fibres were prepared by using a liquid metal infiltration technique and the tensile properties of the composite were evaluated.

EXPERIMENTAL

Fibres used in this study are polyacrylonitrile (PAN) based fibres sold under the trade name of Fortafil 6T from the Great Lakes Corporation. The fibres have a reported strength of 3.4 GPa and an elastic modulus of 400 GPa. Prior to use, fibre surfaces were cleaned of any organic substances by passing them through a furnace at $800°$ C containing an argon atmosphere.

In the electroplating-heat treatment method, a Cu-1%W alloy was electroplated on carbon fibres using an electrolyte and current density as described by Clark (1952). After electroplating, the fibres were heat treated at $1020°$ C under high vacuum. TEM samples of the copper alloy coatings were prepared by ion beam thinning for the as-plated material and by electrochemical jet thinning using a 30% nitric acid in methanol solution.

The LMTA technique consisted of submerging a carbon fibres bundle in a melt of copper (or tin) in which is dissolved a refractory element. The immersion was done under an argon atmosphere for specific time durations as given in Table 1. The composition and the temperature of the melts are also given in Table 1.

Table 1. Experimental Conditions for LMTA Carbide Coating

Bath Composition	Temperature °C	Immersion Time, min.
Cu-5%W	1115 C	120 - 960
Sn-5%W	1200 C	5 - 30
Cu-3%Cr	1150 C	0.5 - 30
Sn-2%Cr	700 - 1150 C	0.25 - 10
Cu-10%Ti	1050 C	0.5 - 10
Sn-1%Ti	900 - 1055 C	0.25 - 10

Following the coating procedure, the fibres are surrounded by the metal transfer medium. To obtain single fibres separate from the metal for observation and testing, the metal was removed by dissolving it in either 20% HCl to dissolve the copper alloy material or 20 % HCl -10% HNO_3 to dissolve the tin alloy material.

The strength of carbide coated single fibres was evaluated according to ASTM standard D3379. This consists of mounting the fibres on cardboard tabs which aid in gripping and aligning the fibre in the testing machine. The tensile testing was carried out using an Instron tensile testing machine. The gage length of the specimens was about 1 cm and the crosshead speed was 0.005 cm/min. The cross sectional area of each specimen was measured by mounting the gage section in epoxy and magnifying the cross section to a total magnification of 6700X on an optical microscope.

Two aluminum alloy matrices based on casting alloys were examined, namely Al-12%Si and Al-10%Mg. To produce the composite specimens, approximately 500-1200 fibres were attached to a carbon frame to hold the fibres while they are immersed in a tin-titanium melt. Following this procedure, the fibres are coated with approximately a 0.1 μm layer of titanium carbide and are also surrounded by a tin alloy matrix. The fibres are then immersed for 1 minute in a melt of an aluminum alloy at a temperature $60°$ C above the liquidus temperature. During this operation, the former tin matrix dissolves in the aluminum alloy melt, resulting in the fibres being surrounded by the aluminum alloy. When the fibres are removed from the Al alloy melt, they are passed through a slit in a die to squeeze out excess aluminum from the bundle. The result is a composite in the form of a wire with an approximate diameter of 0.6 mm and 70 mm in length.

The composite wires were tensile tested by first mounting the composite on cardboard tabs with epoxy to assist in gripping and aligning the specimen in an Instron tensile testing machine. The gage

length of the specimens was approximately 2 cm and the crosshead speed of the tests was 0.01 cm/min. The extension was measured with an extensometer mounted on the gage section and the cross sectional area of each specimen was determined after the specimen was tested by measuring the area from a photomicrograph of a crossection of the gage section. The fibre volume fraction V_f was determined by counting the fibres observed on a composite cross section and using the relation

$$V_f = (N \times A_f) / A_t \tag{1}$$

where N is the number of fibres, A_f is the average cross sectional area of a single fibre and A_t is the total cross sectional area. The matrix properties were evaluated from specimens cast from the same aluminum alloy melts in which the coated fibres has been immersed for the composite fabrication.

RESULTS AND DISCUSSION

Carbide Coatings

Tungsten Carbide. Figure 1 shows the electrodeposited copper-tungsten coating before and after heat treatment for 1 hour at $1020°$ C. In the as-plated condition, the grain structure of the deposit is too small to be resolved in the optical micrograph, however after the heat treatment, a grain size of approximately 1 μm can be seen in the coating. Given the small grain size of the copper-tungsten deposit after the heat treatment received would indicate that grain growth in the deposit is restricted. In fact, in specimens annealed for 24 hours at $1020°$ C, no further significant grain growth occurred in the material.
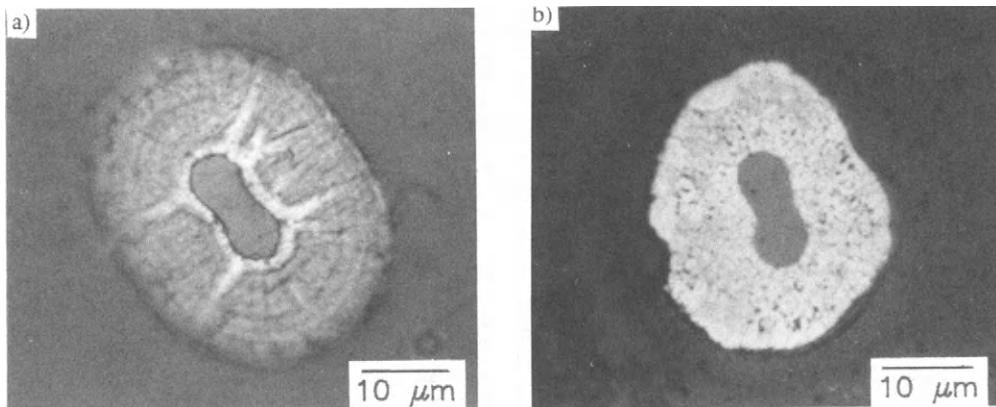
Fig.1. Cross section of the electrodeposited Cu-W coating on a carbon fibre: a) As-plated, b) after heat treatment at $1020°$ C for 1 hr.

The surface of a fibre heat treated for 1 hour at $1020°$ C, followed by removal of the electrodeposited coating, is shown in Fig. 2. Only a few particles appear on the fibre surface, which in an EDXS analysis are found to be rich in tungsten. X-ray diffraction analysis verified these particles to be mainly W_2C with a small amount of WC. This coating would not provide sufficient protection to the carbon fibre since no significant layer is formed. Hence, this method does not appear promising as a method to coat carbon fibres with tungsten carbide.
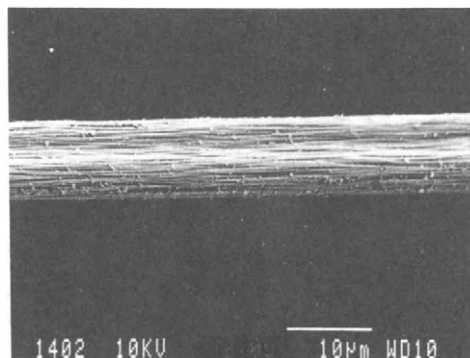
Fig. 2. Tungsten carbide particles on a carbon fibre after heat treatment
and removal of the Cu-W coating.

TEM observation of the electrodeposited material both before and after heat treatment, shown in Fig. 3, was performed to understand why tungsten was not diffusing to the fibre surface to form a carbide layer. In the as-plated material, the fine grain structure, consisting of aligned columnar grains, can be seen. Electron diffraction patterns (see inset) did not detect any tungsten phase in spite of the 1% tungsten present. This indicates tungsten is in atomic dispersion in the copper, which is interesting since under equilibrium, tungsten is reported to be insoluble in liquid and solid copper (Hansen, 1958). After heat treatment, small precipitates are seen throughout the material, some of which are strongly believed to consist of tungsten because of the occurrence of tungsten diffraction in the electron diffraction pattern of the material (see inset). The tungsten, although in atomic dispersion in the material after electroplating, is in a non equilibrium condition in this state and upon heat treatment precipitates as fine particles. Hence tungsten, for the large part, remains as particles in the electrodeposited material and does not diffuse to form a carbide layer on the fibre. Also, the tungsten precipitates could certainly be responsible for the inhibited grain growth observed in the material as they would hinder grain boundary motion.

Carbon fibres coated with tungsten carbide by the LMTA technique using copper and tin as transfer mediums are shown in Fig. 4. It can be seen in both cases that the carbide does not form a smooth continuous layer on the fibre, but rather grows as discrete particles on the fibre to give a corn cob appearance. In the case of the fibre coated using a copper transfer medium, the fibre can seen to be eroded by the reaction and it shrinks away from the coating. These coatings are therefore not seen as being protective to the carbon fibres.

Chromium Carbide. Figure 5 shows the surface morphology of chromium carbide coatings formed by the LMTA technique using copper and tin as transfer agents. A definite improvement in the uniformity of the chromium carbide coatings over those of the tungsten carbide can be seen. It can also be seen that the chromium carbide coatings formed using the tin transfer agent are much smoother than those using the copper transfer medium. X-ray diffraction analysis identified the coating formed using the copper melt to be Cr_3C_2 and the coating formed using the tin bath to be Cr_7C_3 and Cr_3C_2.

Assuming the growth of the carbide layer is controlled by a diffusional parabolic growth mechanism, the thickness of the carbide layer on the fibres can be described by the equation

$$x^2 = At \qquad\qquad\qquad\qquad (2)$$

where x is the carbide thickness, A is the growth constant, and t is the immersion time in the melt.
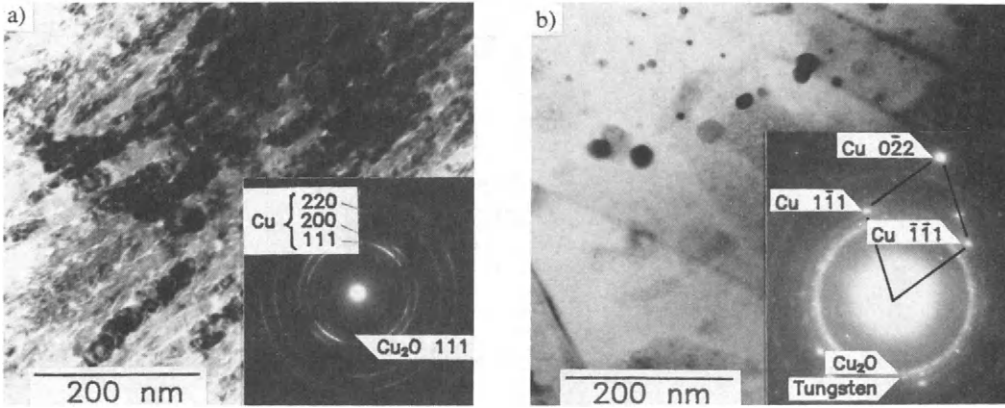
Fig. 3. TEM micrograph of the Cu-W material: a) as plated, b) after heat treatment.
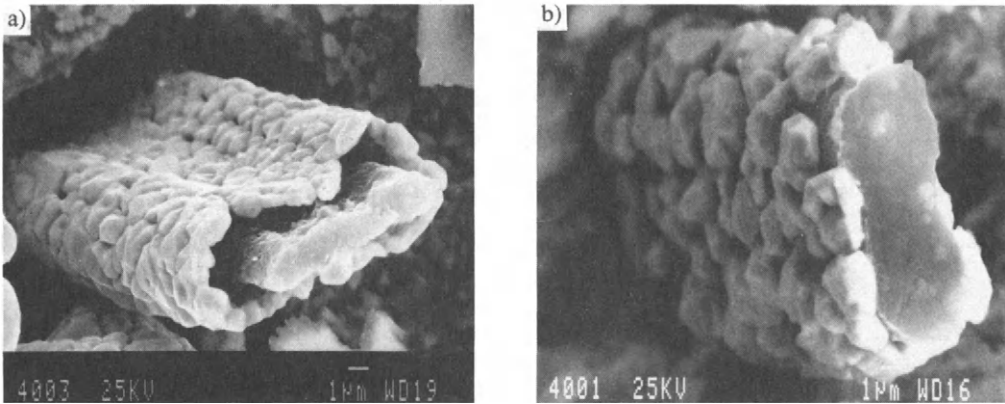
Fig. 4. Tungsten carbide coatings formed on a carbon fibre by the LMTA technique: a) copper transfer medium, b) tin transfer medium.

The carbide thickness formed on the fibres as a function of the square root of the immersion time in the copper and tin alloy melts is shown in Fig. 6. A positive thickness intercept at $t = 0$ for the data suggests an equation of the form

$$(x - x_o)^2 = At \tag{3}$$

should be used, where x_o is the carbide layer which spontaneously forms on wetting of the alloy with the carbon fibres. This spontaneous carbide formation is similar to that observed by Mortimer (1974) where the wetting of a carbon substrate by a Cu-Cr alloy is associated with the formation of a carbide layer of significant thickness. This spontaneous layer is important because it is an indication of the thinnest carbide layer which can be applied to the carbon fibres by this method, and, as shall be seen later, obtaining thin coatings will be very desirable.
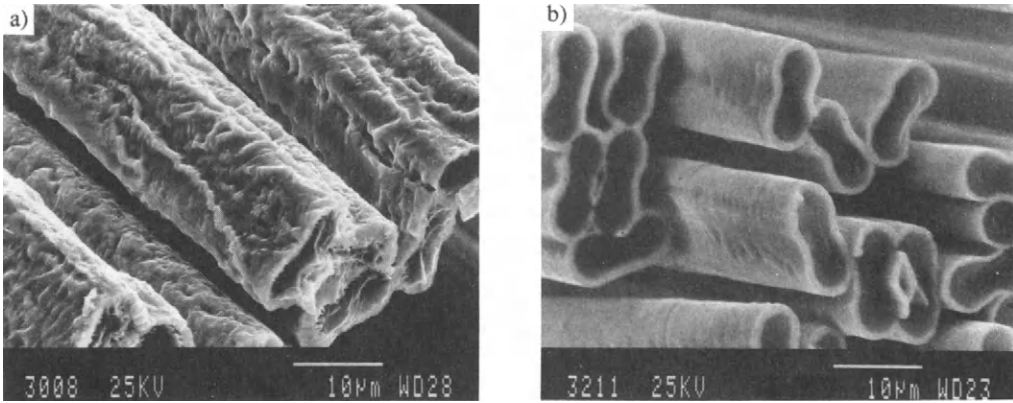
Fig. 5. Morphology of the chromium carbide coating formed on carbon fibres by the LMTA technique: a) using a copper transfer agent, b) using a tin transfer agent.
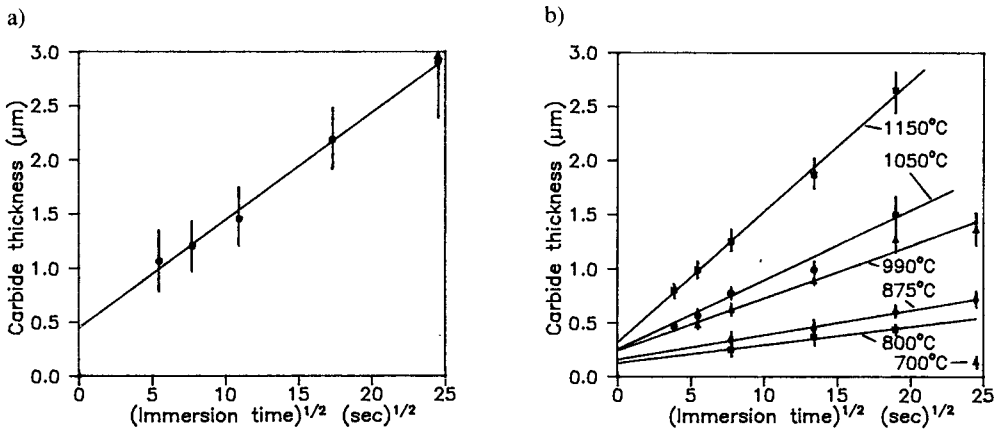
Fig. 6. Growth of the carbide coating formed by the LMTA technique as a function of time and temperature: a) copper transfer agent, b) tin transfer agent.

Titanium Carbide. Figure 7 shows the morphology of the titanium carbide coatings obtained by the LMTA technique using copper and tin as transfer agents. The carbide layer grown using a copper transfer medium is seen to have a very irregular and rough appearance. This type of irregular carbide growth is similar to the fragmented carbide growth observed by Mortimer (1974) on carbon substrates in contact with Cu-10%Ti at 1150° C. This type of growth was said by Mortimer to resemble that observed when an oxide film undergoes 'breakaway ' due to interfacial decohesion. On the other hand, the carbide layer grown using a tin transfer medium is very smooth and uniform on the fibres.

The growth rate of the carbide as a function of the square root of the immersion time in the tin alloy
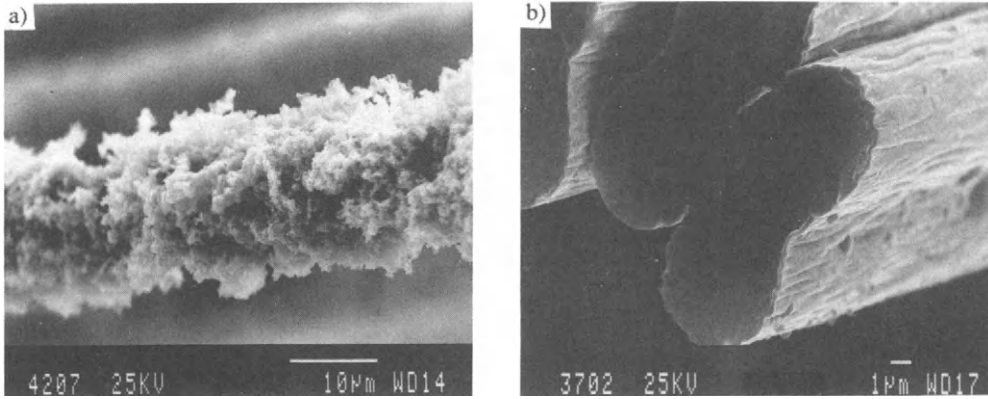
Fig. 7. Morphology of the titanium carbide coating formed by the LMTA technique: a) using a liquid copper transfer agent, b) using a liquid tin transfer agent.

melt is shown in Fig. 8 a. As with the chromium carbide formation, the titanium carbide growth also shows a spontaneous carbide formation at time t = 0. However, comparing the values of x_o of chromium carbide and titanium carbide, titanium carbide has a smaller spontaneous carbide formation for the same given temperature, as seen in Fig. 8 b. Given this fact, thinner carbide coatings can be obtained with titanium carbide than with chromium carbide.
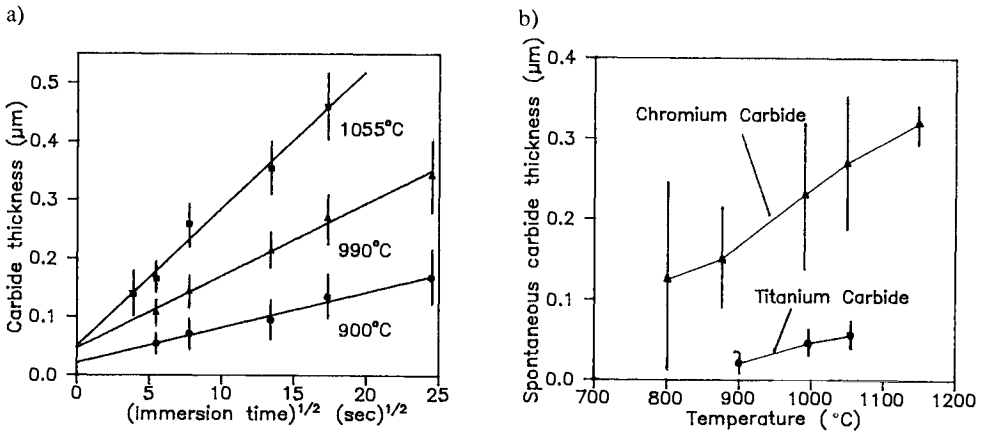
Fig. 8. a) Growth of the titanium carbide layer as a function of immersion and temperature, and b) the value of the spontaneous carbide layer formed on wetting for titanium carbide and chromium carbide.

Fibre Strength

The fracture mechanism of a fibre with a brittle coating were theoretically analysed by Ochiai (1981a, 1981b, 1979). On elongation, cracks are expected to form in the brittle coating because the coating has a lower strain to failure than the fibre. The crack results in a notch effect on the fibre, the size of the notch being equal to the thickness of the coating. The fibre is able to maintain the applied load after the formation of the cracks in the coating until the stress level is favorable for the crack to extend into the fibre. With this behavior, the strength of a coated fibre is given by

$$\sigma = (1/1.12)\sqrt{EG/\pi c} \tag{4}$$

where E is the modulus of elasticity of the fibre, c is the coating thickness and G is the strain energy release rate of the fibre.

The variation of the average strength of the coated fibres with coating thickness is shown in Fig. 9 a. The strength of the chromium carbide and titanium carbide coated fibres is essentially the same. A plot of equation (4) for the fracture strength of the coated fibres is shown in fig. 9 b. The fracture strength of the chromium carbide coated fibres appear to follow equation (4), with the extrapolation of the data passing through the origin as predicted. The strain energy release rate of the fibres, G, was calculated by linear regression analysis to be 3.98 J/m^2. The surface energy of the carbon fibres, γ, may be inferred from G to a first approximation by the relation (Ochiai, 1981a)

$$\gamma = G/2 \tag{5}$$

Thus, $\gamma = 1.99\ J/m^2$, which is in good agreement with the value of 2.33 J/m^2 obtained by Baker (1978).

a)   b)
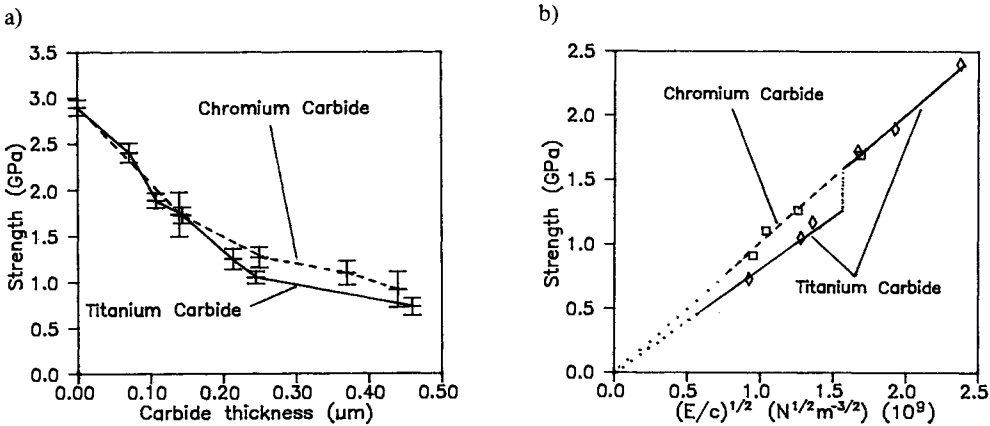
Figure 9. a) Variation of the strength of carbide coated fibres as a function of coating thickness, and b) as a function of $\sqrt{E/c}$

From fig. 9b), the fracture strength of titanium carbide coated fibres appear to have two separate regions of fracture behavior. In the first region where the coatings are thinner than 0.15 μm, the fracture behavior is similar to that of chromium carbide coated fibres. In the second region where the coatings are thicker, the slope of the line is decreased, giving a value of $G = 2.52\ J/m^2$, hence, $\gamma = 1.26 J/m^2$. This change in slope may be attributed to the 'onion skin' structure of carbon fibres. There is general agreement that the outer surface of high modulus fibres consists of a sheath of highly

ordered crystallites with the basal planes oriented parallel to the fibre surface, beneath which are more random oriented crystallites which make up the core. For a thinly coated fibre, the crack must propagate perpendicular to the basal planes of the graphite with makes up the sheath. For a thicker coated fibre, the sheath may be entirely consumed to form the carbide layer, thus the crack propagates through the more randomly oriented fibre core which may contain basal planes arranged more or less parallel to the crack surface. Since the basal planes have a lower surface energy than those perpendicular to it, the·observed value of γ will be lower for the thicker coated fibres in which the sheath is consumed, than in the thinly coated fibres in which the fibre sheath still remains.

The fracture strength of chromium carbide coated fibres probably does not show two regions like that of titanium carbide because less carbon is consumed to produce a given layer of chromium carbide than of titanium carbide. Thus, the sheath of the carbon fibre may not be entirely consumed in the chromium carbide coated fibres.

The present single fibre tests show that it is desirable to have the thinnest coatings possible so as not to seriously affect the strength of the fibres. As has been shown earlier, the thinnest carbide coatings produced were with titanium carbide. For this reason, titanium carbide coatings applied by the LMTA technique using tin as a transfer agent appear very promising in the development of metal matix composites. Therefore, the composites produced in this study are made using titanium carbide coated fibres.

Composite Tensile Properties

Figure 10 shows the microstructure of the aluminum alloy matrix composites reinforced with titanium carbide coated fibres. Successful infiltration of the aluminum alloy in the fibre bundle was achieved without any observable interaction between the matrix and the fibres. The Al-10%Mg alloy matrix composite was found to contain a second phase of Mg_2Sn, which undoubtedly formed from a reaction between the magnesium in the matrix alloy and the tin from the previous coating process. In the Al-12%Si matrix composite, the matrix consisted largely of the Al-Si eutectic with some residual tin phase remaining in the matrix. As a result of the varying number of fibres in each composite and the varying cross sectional area of each composite, the volume fraction of the composites produced was found to range from 2% to 26%.
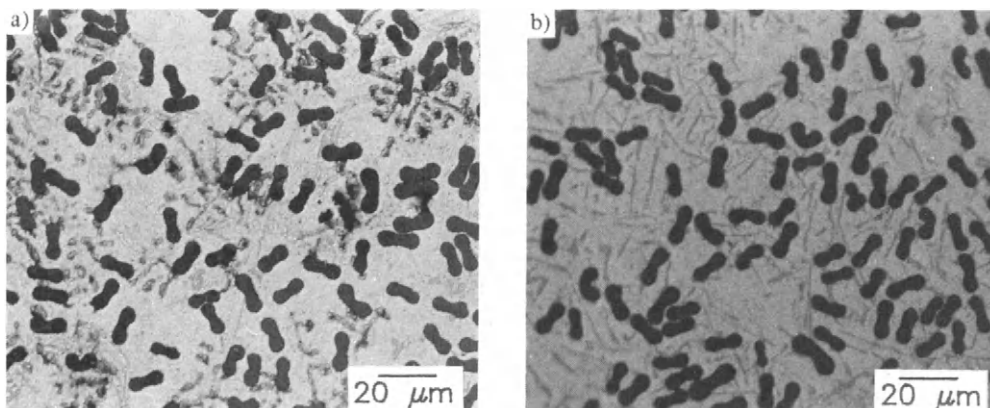
Fig. 10. Optical micrograph of the cross section of the aluminum alloy matrix composites: a) Al-10%Mg matrix, b) Al-12%Si matrix.

The results of the tensile tests for the aluminum matrix composites are shown in Fig. 11. In both cases substantial strengthening over that of the matrix strength has been achieved. Rule of mixtures predictions based on results from the single fibre tests are also shown in Fig. 11. The elastic modulus results for the composites, though having some degree of scatter, are consistent with the rule of mixtures. The strength results display scatter as well, however all the strengths are below the rule of mixtures prediction. These lower strengths may be due to several factors: fibre spacing in the composite not being uniform, the presence of the tin intermetallic in the matrix, or the slight curvature observed in several composite wires occurring due to uneven cooling or solidification of the composite.

a)

b)
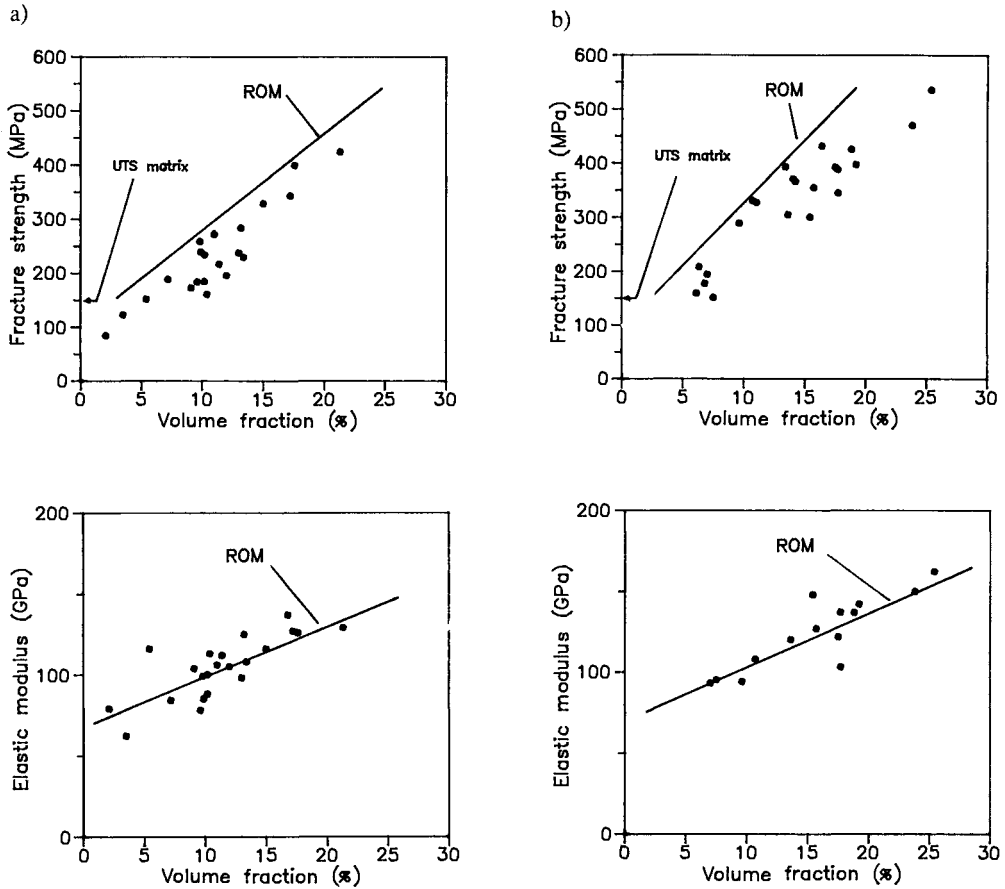
Fig. 11. Fracture strength and elastic modulus results for the aluminum matrix composite: a) Al-10%Mg matrix composite, b) Al-12%Si matrix composite.

The fracture surface of an Al-Mg matrix composite is shown in Fig. 12 which is representative of all the composites tested. Very little fibre pull out was observed, as the length of most pull outs was only in the order of a few fibre diameters. This indicates that good bonding was acheived between the fibre and the matrix. As well, evidence of ductile behaviour in the matrix seen in the form of necking in the inter-fibre regions indicates the matrix contributes some toughness to the composite.
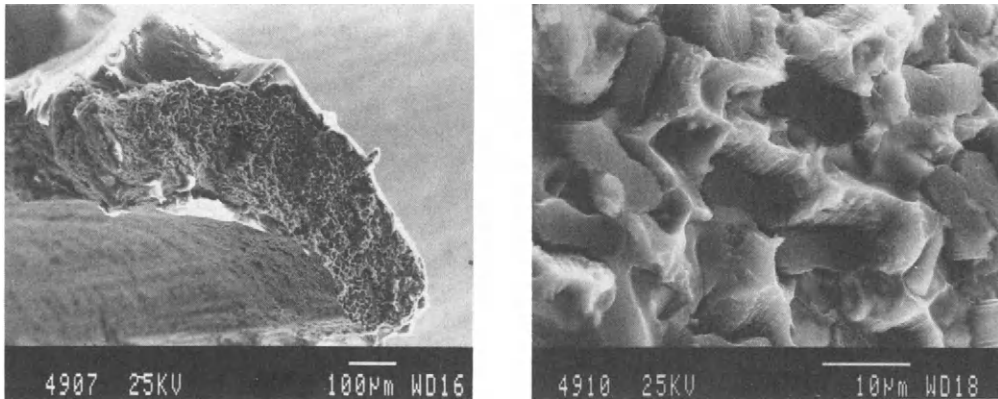
Fig. 12. Scanning electron micrograph of the fracture surface of an Al-Mg matrix composite.

CONCLUSIONS

Carbide coatings of tungsten carbide, chromium carbide and titanium carbide were applied to carbon fibres by a liquid metal transfer agent (LMTA) technique using both copper and tin as transfer agents. The smoothest and most uniform coatings obtained were of chromium carbide and titanium carbide applied by using a tin transfer agent, however, the thinnest coatings obtained were with titanium carbide.

The strength of the carbide coated fibres was found to decrease with carbide thickness. A coating of 1.0 μm results in a 30% decrease in strength of the fibres.

Aluminum alloy-titanium carbide coated fibre composites have been successfully produced by a liquid infiltration method. The tensile fracture strength of the composites was found to be slightly below the rule of mixtures predictions and the elastic modulus was found to be consistent with the rule of mixtures.

ACKNOWLEDGMENTS

REFERENCES

Baker, S.J. and W. Bonfield (1978). Fracture of aluminum coated carbon fibres. J. Mater. Sci., 13, 1329-34
Clark, W.E. and M.H. Lietzke (1952). The mechanism of the tungsten alloy plating process. J. Electrochem. Soc., 99, 245-9
Hansen, M. and K. Anderko (1958). Constitution of Binary Phases. McGraw-Hill, New York, p. 649
Himbeault, D.D., R.A. Varin and K. Piekarski (1988). Coating of graphite fibres with tungsten carbide using solid and liquid copper as a transfer medium. Metall. Trans., 19A, 2109-13
Himbeault, D.D., R.A. Varin and K. Piekarski (1989). Carbon fibres coated with chromium carbide using the liquid metal transfer agent technique. Metall. Trans., 20A, 165-70

Honjo, K. and A. Shindo (1986). Influence of carbide formation on the strength carbon fibres on which silicon and titanium have been deposited. J. Mat. Sci., 21, 2043-8

Mortimer, A., M.G. Nicholas and R.M. Crispin (1974). The compatibility of carbon with copper alloys containing chromium, titanium or vanadium. Intern. Conf. on Carbon Fibres, Their Place in Modern Technology, The Plastics Inst., London, 101-04

Ochiai, S. and Y. Murakami (1979). Tensile strength of composites with brittle reaction zones at interfaces. J. Mater. Sci., 14, 831-40

Ochiai, S. and Y. Murakami (1981a). Theoretical predictions of the tensile strength of fibres as a function of thickness of brittle zones on the fibre surfaces. Metall. Trans., 12A, 1155-61

Ochiai, S. and Y. Murakami (1981b). Theoretical predictions of the tensile strength of fibres with brittle layers on their surfaces. Z. fur Metallkunde, 72, 827-31

Ovcharenko, V.E., O.A. Kashin, E.F. Dudarev, A.A. Zabolotskii and S.E. Salibekov (1981). Effect of surface structure of carbon fibres on the strength in the application of carbide coating in a metal melt. Sov. Powder Met. and Met. Ceramics, 20, 564-7

Phillips, K., A.J. Perry, G.E. Hollox, E. DeLamotte and H.E. Hintermann (1971). The mechanical properties of carbon fibres coated with titanium carbide. J. Mater. Sci. Letters, 6, 270-3

Rashid, M.S. and C.D. Wirkus (1972). Development fo carbide coatings for graphite filaments. Ceramics Bull., 51, 836-39

Characterization of the interface reactions in Al-SiC composites and of their effect on the composition of the Al-Mg matrix

Jean-Gabriel Legoux, Gilles L'Espérance
Centre for Characterization and Microscopy of Materials, (CM)²,
Département de génie métallurgique, Montréal, Québec, Canada, H3C 3A7

Harvé Ribes, M. Suéry
Génie physique et mécanique des matériaux, URA CNRS 793,
Institut national polytechnique de Grenoble, Saint-Martin d'Hères, France

ABSTRACT

This paper is concerned with Al-5%Mg alloys reinforced by as received and oxidized SiC particles using the compocasting technique. Particular attention is given to the characterization of the reactions that occur at the particle-matrix interface by extensive analytical electron microscopy involving TEM, EDS, EELS, SEM and Auger. The observations show that the nature and the extent of the interfacial reactions strongly depend on the holding time of the composite above the liquidus either during elaboration or during further remelting. In the case of as-received particles, Al_4C_3 formation occurs only during remelting whereas for oxidized particles, Mg-rich phases form during elaboration. These phases act as a diffusion barrier thus reducing degradation of SiC by aluminium.

KEYWORDS

Metal-matrix composites, aluminium alloys, silicon carbide, interfaces, electron microscopy, chemical reaction.

INTRODUCTION

Metal matrix composites are the focus of intensive work since about ten years and of these materials, the discontinuous ceramic reinforced aluminium composites appear to have the greatest industrial potential. These composites can be fabricated by many techniques among them the liquid or semi-solid casting processes. In these processes, the ceramic particles, essentially SiC and Al_2O_3 are introduced into the liquid or semi-solid alloy which is thereafter cast either to final shape or to billet for further processing. This processing can sometimes consist of complete remelting of the billet for special casting purposes, especially when the user is not the producer. Extended contact between the liquid metal and the ceramic reinforcement is then involved so that interaction can occur leading to possible interfacial reaction products. The knowledge of these reactions is of primary importance for the fabrication of the composites and consequently for their mechanical properties.

The aim of this work is the study of the reaction between liquid aluminium and silicon carbide particle reinforcing phase using the binary Al-5%Mg alloy. The SiC particles were used either in the as delivered condition or after artificial oxidation. Special attention is given to the interface region by microanalytical electron microscopy and to the change of matrix composition as a consequence of interfacial reactions.

MATERIALS AND EXPERIMENTAL PROCEDURE

The aluminium alloy used in this work is a Al-5wt%Mg prepared from pure Al and Mg. It was reinforced by black SiC particles of 13 μm average diameter obtained by PRESI (France) using a modified compocasting technique in which, after addition of the particles to the semi-solid alloy, the melt is completely remelted and solidified under a pressure of 100 MPa. The details of the fabrication procedure are given elsewhere (1). Particles were used either in the as delivered condition of after artificial oxidation in air at 1100°C for 2 hours. This oxidation produces an oxide layer of approximately 50 nm thick as determined by Auger spectroscopy (2). This value is much greater than the thickness of the oxide layer found on the as received particles, close to 5 nm.

The remelting experiments were performed with an induction furnace, using a small graphite crucible. Specimens (20 mm diameter and in height) were machined from the as-cast ingots, reheated up to 800°C, maintained for 20 mn at this temperature then quenched. The temperature was controlled by a thermocouple put in the middle of the sample.

Optical scanning and transmission electron microscopy was performed with both as-cast and remelted composite specimens. Thin foils were prepared by ion thinning at 20° and at 4 kV of mechanically polished and dimpled sections. The microstructure was examined using bright field imaging, focussed probe microdiffraction, and electron energy loss and energy dispersive x-ray spectroscopy (EELS and EDS). The microscopes used included a Philips CM-30, a JEOL 2000 FX and a JEOL 200 CX.

RESULTS AND DISCUSSION

1. As cast microstructures

Figure 1 shows the microstructure of the Al-5%Mg/SiC composite elaborated with as received particles. These particles have an oxide layer of about 5 nm thick. The microstructure of the composite elaborated by the compocasting technique is seen to have a fairly uniform distribution of particles; only a few areas appear depleted in SiC. Transmission electron microscopy (fig. 2) reveals a very clean and straight interface, free of any intermetallic phases. This indicates the absence of a reaction between the molten aluminium alloy and SiC particles during elaboration. Contrary to many authors (3-7), no Al_4C_3 has been observed as a result of the following reaction:

$$4 \text{ Al} + 3 \text{ SiC} = Al_4C_3 + 3 \text{ Si}. \tag{1}$$
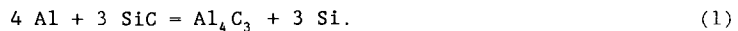
Such reaction, however, should not occur for temperatures lower than 650°C (6). The same authors have studied the kinetics of formation of Al_4C_3 for 0,6 Al - 0.4 SiC mixes and showed that 0.03 molar fraction of SiC was consumed by reaction 1 at 668°C and 0.05 at 700°C after 100 hours. In the present case, our materials are elaborated at 630°C in the semi-solid state and the melt is reheated to 700°C for only $\approx$ 5 min before casting. Thus it is admissible that the material is not maintained over 650°C for a sufficiently long time to form Al_4C_3. The prevention of reaction (1) during the elaboration of composites by the compocasting technique has also been observed for A-356 and 6061 alloys (1,8).

Figure 3 shows a typical micrograph of the composite made with artificially oxi-
dised particles. As for the other material studied, SiC particles are uniformly
distributed. In addition, however, another phase identified as Mg_2Si by (EDS)
in the scanning electron microscope (SEM) was observed in the matrix and occa-
sionnally surrounding SiC particles. As explained below, Si in the original
binary Al-5%Mg alloy originates from the liberation of Si from the SiO_2 layer of
the artificially oxidised particles as a result of a reaction at the molten
Al-5%Mg/SiO_2-SiC interface. The solubility of Si in the resultant ternary
Al-5%Mg-Si alloy is very small which causes precipitation of Mg_2Si (9).

A number of interfacial reactions between the oxidised particles and the molten
alloy are possible including:

$$3\ SiO_2 + 4\ Al \quad = \quad 2\ Al_2O_3 + 3\ Si \tag{2}$$

$$SiO_2 + 2\ Mg \quad = \quad 2\ MgO + Si \tag{3}$$

$$2\ SiO_2 + 2\ Al + Mg = MgAl_2O_4 + 2\ Si. \tag{4}$$
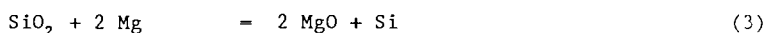
The TEM micrograph in figure 4a shows the presence of a microcristalline layer
around the particle. This layer has very straight edges and is about 200 nm
thick which is of the same order of magnitude as that of the oxide layer around
the particles. This is an indication that this layer originates from the reac-
tion of SiO_2 with the molten Al-5%Mg alloy. Attack of SiC is not observed.
Such attack was not observed in the case of the composite elaborated with as
received particles so it is not surprising that it does not occur in the case of
particles surrounded and therefore protected to some extent by a 200 nm thick
oxide (SiO_2) layer.

EDS analyses (fig. 4b) show this layer to be rich in Mg and Al, which can be the
result of reaction 3 or 4 resulting in the formation of MgO or $MgAl_2O_4$. EDS
analyses yielding the Mg/Al ratio can be used to investigate the phases formed
in this polycristalline layer. The Mg/Al ratio varies considerably in this
layer, from 0,2 to 1.0 indicating the presence of more than one phase. A ratio
of 0,5 is expected for $MgAl_2O_4$ (since the calculated Cliff-Lorimer K_{Mg-Al} factor
used to quantify EDS analyses is close to 1 (10) so that a larger ratio indi-
cates the presence of MgO. A ratio smaller than 0.5 could arise from the
entrapment of Al in this layer during its formation.

Electron diffraction can also be helpful to distinguish these phases. MgO is
cubic with $a_o = 8,12$ Å and $MgAl_2O_4$ has a spinelle structure with $a_o = 8,08$ Å.
These structures and therefore their diffraction patterns are very similar (11).
The only difference is the (111) reflection of the spinelle which is not pos-
sible for MgO. The diffraction pattern in figure 4c shows the presence of that
(111) $MgAl_2O_4$ ring. Spinel formation has been reported by other authors for
alloys with low Mg contents: A 356 (0,3% Mg) (8), 6061 (1% Mg) (2) and binary
Al-Mg alloys with 2-4% Mg (12). The formation of MgO has also been reported in
the 2124 alloy (1.5%Mg) (13) and for higher Mg contents in binary Al-Mg alloys
(8% Mg) (12). In our case (5% Mg) it seems reasonable that a mixture of MgO and
$MgAl_2O_4$ is formed.

2. Remelting experiments

In order to evaluate the behavior of these materials when held at high tempera-
ture one sample of each type of material was remelted at 800°C for 20 min. Fig-
ure 5 shows a typical microstructure of a remelted sample. Both materials ela-
borated with as received and oxidised SiC particles exhibit a similar micro-
structure with large Mg_2Si eutectic lamella. The presence of this large amount
of Mg_2Si indicates the rejection of a fairly large quantity of Si in the molten
binary Al-5%Mg matrix. As it will be demonstrated later, the reactions leading
to this rejection are different in the two materials.

The significantly damaged and irregular contour of an as received SiC particles
after remelting is seen in Figure 6. Very large columnar grains identified as
Al_4C_3 known to be detrimental to the properties of the composite (3-7,15) can be
seen all around the SiC particle. The formation of Al_4C_3 according to reaction
1 leads to the rejection of Si in the melt which eventually results in the for-
mation of Mg_2Si.

The interface of artificially oxidised SiC particles after remelting has a rela-
tively regular contour but appears to be constituted of two zones as shown in
figure 7a. This interface, however, is chemically more complex than that after
remelting of the composites elaborated with as received particles. The EDS x-ray
line scan across the interface shown in figure 7b also reveals these two
regions: region I is rich in Mg and Al and region II is rich in Al and Si.

Region I is very similar to the oxide layer initially formed during the elabora-
tion (figure 4): it is polycristalline, rich in Mg and Al with large variations
of the Mg to Al ratio similar to the as elaborated initial oxide layer (0.2 to
1). The thickness of this layer is also similar to that of the initial oxide
and EELS analyses show the systematic presence of oxygen (figure 8). It there-
fore appears that the original $MgAl_2O_4$-MgO oxide layer formed during elaboration
of the composite is unchanged during remelting.

Zone II is formed between this oxide layer and SiC. This zone is rich in Al and
Si with a ratio of Al to Si of about 4 to 1 and quite stable in all areas of
this zone as measured with EDS. In addition, EELS analyses of sufficiently thin
areas rich in aluminium between the oxide layer and SiC show the presence of
carbon. There is a number of possible phases which contain Al, Si and C includ-
ing $Al_4Si_2C_5$ (15), Al_8SiC_7 (16) and Al_4SiC_4 (17). However, the presence of Si
in a ratio of 1 to 4 to aluminium and carbon suggests that this region is
Al_4SiC_4 and not Al_4C_3 as in the case of as received particles.

The following reaction is considered to be responsible for the formation of
Al_4SiC_4:

$$4 \text{ SiC} + 4 \text{ Al} = Al_4SiC_4 + 3 \text{ Si} \tag{5}$$
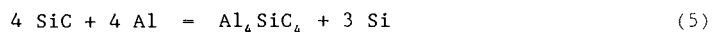
This reaction (as for reaction (1)) requires diffusion of Al towards the silicon
carbide and therefore across zone I ($MgAl_2O_4$-MgO) in the case of oxidised par-
ticles. On the other hand, the decomposition of SiC in both reactions liberates
Si which has to diffuse towards the melt.

In the case of oxidised particles, the diffusion coefficient of Al and Si in the
MgO-$MgAl_2O_4$ oxide layer should be considerably lower than in the liquid. Pala-
dino & Kingery (18) who studied the diffusion of Al in Al_2O_3 reported values 10^5
- 10^6 lower than that in liquid aluminium. This lower diffusion rate of Al
through the oxide layer reduces the degradation of SiC compared with that for as

received particles (figures 6 and 7a). On the other hand, the reduced diffusion rate of silicon towards the melt causes a certain entrapment of Si between the $MgO\text{-}MgAl_2O_4$ oxide layer and the non-attacked SiC. This will favour the formation of Al_4SiC_4 compared with Al_4C_3 which tends to form when Si is free to diffuse to the melt as in the case of particles for which there is no initial diffusion barrier (oxide) formed during elaboration.

CONCLUSIONS

A detailed characterization of the interface reactions in Al-5%Mg/SiC composites elaborated with a compocasting technique was carried out. As received and oxidised particles were incorporated in the semi-solid melt. The main conclusions of the investigation are:

For as-received particles:

1. For as cast composites no reaction between the SiC particles and molten aluminium was observed. This is because of the relatively short periods of time and low temperatures involved during elaboration with the compocasting technique which limit the degradation of the SiC particles and thus prevent the formation of Al_4C_3.

2. Holding at 800°C for 20 minutes of the as-cast composites resulted in the extensive formation of Al_4C_3. This reaction leads to the rejection of a considerable amount of Si into the melt giving rise to the formation of a large quantity of coarse Mg_2Si in the originally binary Al-Mg matrix.

For oxidized particles

3. The SiO_2 layer surrounding the SiC particles reacts with the molten Al-Mg alloy to produce a complex oxide containing MgO and $MgAl_2O_4$. The reaction of SiO_2 to form these oxides also liberates Si in the melt which again results in the formation of Mg_2Si. The latter, however, is finer and is formed in a smaller quantity than in the case of the remelting of the composite elaborated with as received particles. This is considered to be the result of the fact that the reaction is limited to the thickness of the SiO_2 layer. The latter therefore indirectly protects the SiC particles as a result of the eventual formation of the $MgO - MgAl_2O_4$ oxide (see also conclusion 4).

4. During remelting of the composite at 800°C, the $MgO\text{-}MgAl_2O_4$ oxide layer formed during casting acts as a diffusion barrier for Al and Si. This reduces the degradation of the SiC particles and causes the formation of Al_4SiC_4 instead of Al_4C_3.

ACKNOWLEDGEMENT

REFERENCES

1) MILLIÈRE C. and SUÉRY M., Mater. Sci. Technol, 1988, 4, pp.   41-51.

2) RIBES H., SUÉRY M., L'ESPÉRANCE G., LEGOUX J.G., submitted to mettrans A..

3) ISEKI T., KAMEDA T., AND MARUYANA T., J. of Mater. Sc. 19 (1984), pp. 1692-1698.

4) KANNIKESWAREN K., LIN R.Y., J. of Metals, sept. 87, pp. 17-19.

5) LLOYD D.J., CHAMBERLAND B., "Cast reinforced metal composites" A.S.M. Conference Proceedings, Chicago 1988, pp. 263-271.

6) VIALA J.C., FORTIER P., BERNARD C. and BOUIX J. "Developments in the Science and Technology of Composite Materials", Proc. of the First European Conf. on Comp. Mat., ECCM-1, Bordeaux, France, sept. 1985, A.R. Bunsell, P. Lamicq and A. Massiah, eds., pp. 583-588.

7) KOHYAMA A., IGATA N., Conference Proceedings of the Firth International Conference on Composite Materials ICCM 5, Edited by W.C. Harrigan, J. Strife, A.K. Dhingra, A.S.M. publication, San Diego 29-30 July 1985, pp. 609-621.

8) RIBES, H., SUÉRY, M., Scripta. Met., in Press.

9) Metallurgical Handbook, vol. 8, 8th edition, ASM, p. 396,397.

10) WOOD J.E., WILLIAMS D.B., GOLDSTEIN J.I., J. Microsc. 133 (pt. 3): 255-274, 1984.

11) MUNITZ A., METZER M., MELTRABIAN V.R., met trans A., vol 10A, oct. 1979, pp. 1491-1497.

12) KARLSEN D.O., BORRADAILLE J.B., GJONNES J., TAFTO J., "Mechanical and Physical behavior of metallic and ceramic composites", International Symposium on metallurgy and materials science 5-9 sept. 1988, Editors S.I. Andersen, M. Lilmolt, O.B. Pederson, pp. 421-426.

13) NUTT S.R., CARPENTER R.W., Mater. Sc. and Eng. 75, (1985), pp. 169-177.

14) Handbook of chemistry and physics, 67th edition, 1986-1987, CRC Press, p. B-68

15) INOVE, J. of Mat., 15, 575 (1980)

16) KIDWELL, J. Appl. Cry, 17, 481 (1976).

17) BURZACK, J. Am. Ceram. Soc., 44, 299 (1961)

18) PALADINO A.E., KINGERY, W.D., J. Chemiphys, 37, 957 (1962).
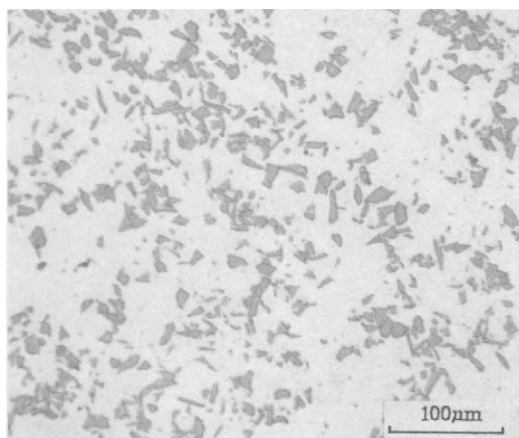
FIGURE 1: Optical micrograph of the Al-5%Mg alloy with 10% as received SiC
particles showing a fairly uniform distribution of particles.
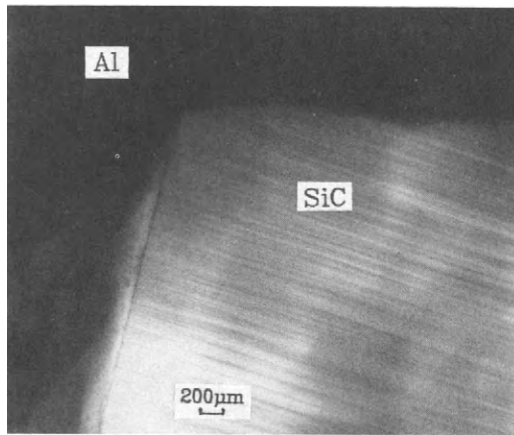
FIGURE 2:   TEM micrograph of the interface between Al-5%Mg and SiC. No
            interfacial reaction product is observed.
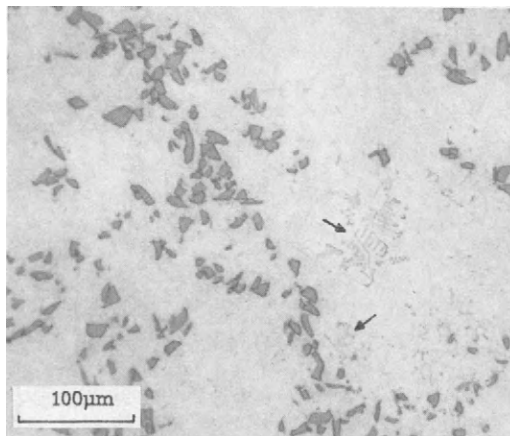
FIGURE 3:   Optical micrograph of Al-5%Mg with 10% of artifically oxidized
            particles. Mg_2Si precipitates are formed in the matrix
            (arrows).

a)

b)

c)
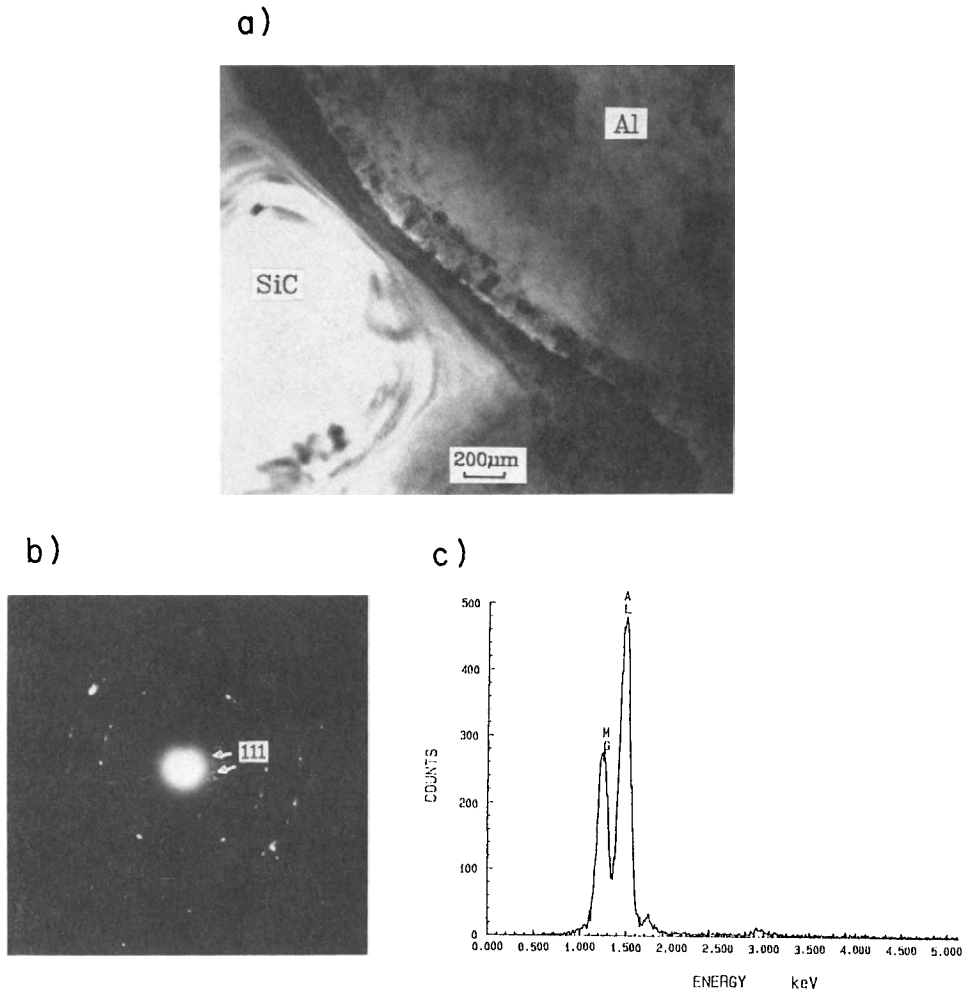
FIGURE 4 a): TEM micrograph of the interface between Al-5%Mg and oxidized
            SiC particles.   The arrow points to a polycristalline complex
            oxide layer.

        b): EDS spectrum from the polycristalline layer shown in 4 a.

        c): Electron diffraction pattern of the polycristalline layer
            (fig. 4 a).
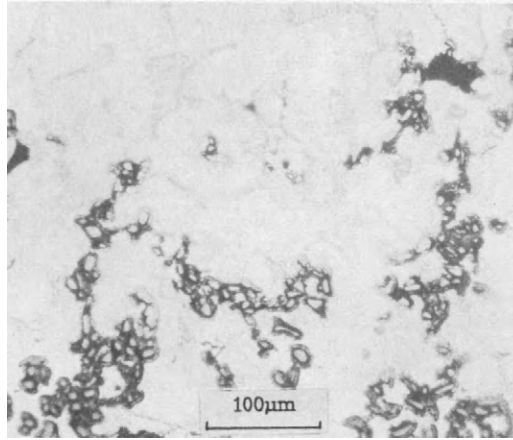
FIGURE 5:   Optical micrograph of a remelted sample of Al-5% Mg with 10% as received SiC particles.

a)

b)
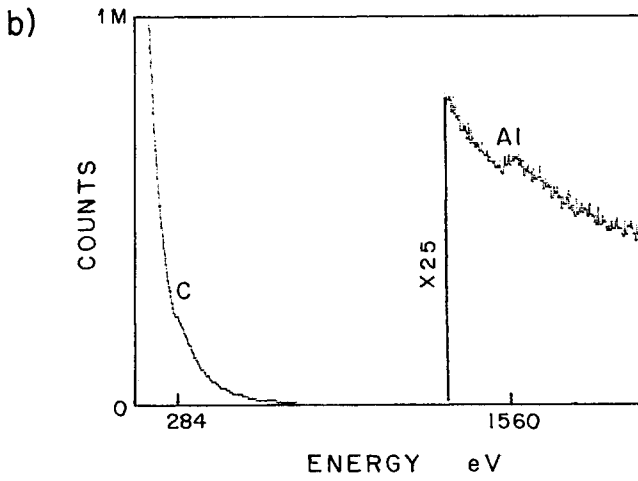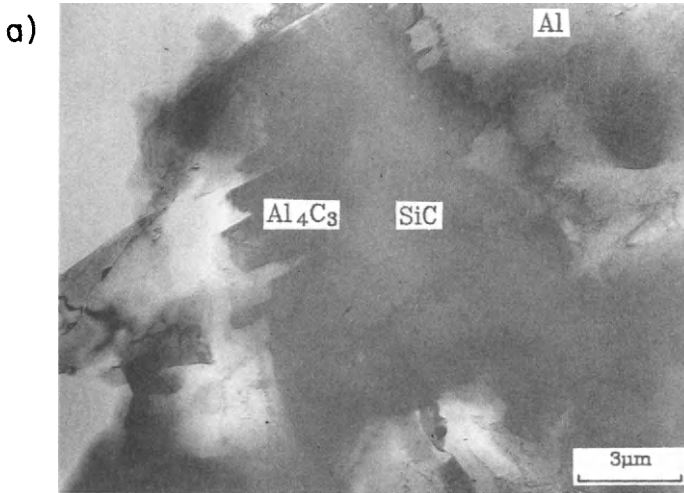
FIGURE 6 a): TEM micrograph of the matrix/SiC interface of the remelted
              composite with 10% as received SiC. The large crystals
              growing perpendicularly to the SiC particles are Al_4C_3 (see
              fig. 6 b).

         b): EELS spectrum of Al_4C_3.
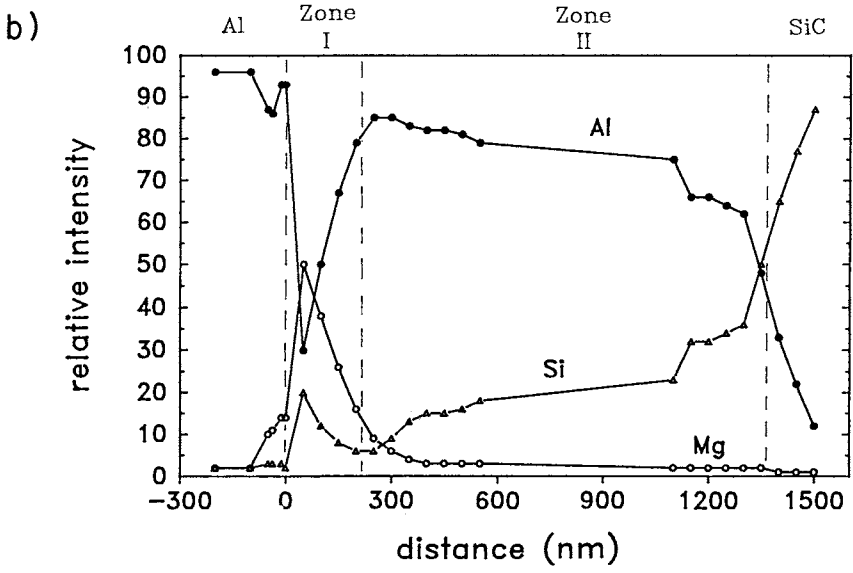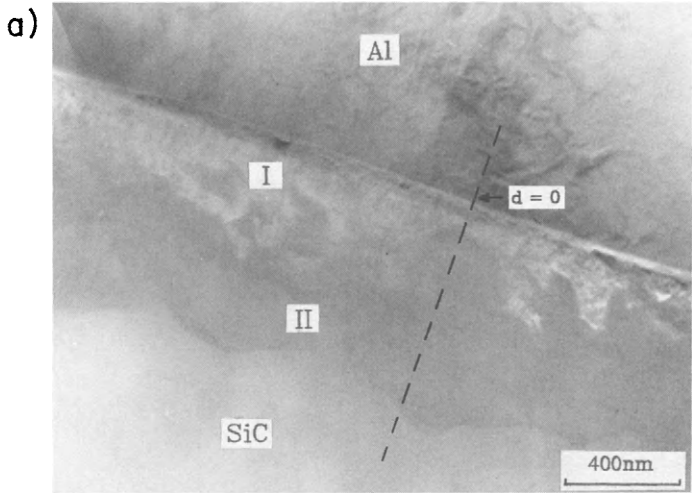
FIGURE 7 a): TEM micrograph of the interface between the Al-5%Mg matrix and
            oxidized SiC particles after remelting.

      b): EDS line scan across the zones I and II in fig. 7 a.
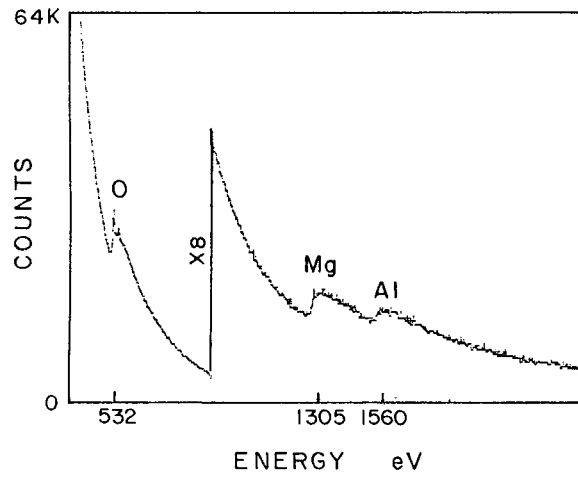
FIGURE 8:   EELS spectrum obtained from zone I (see fig. 7 a).

Aqueous corrosion behaviour of plasma sprayed coatings

B. Arsenault, B. Champagne, P. Lambert and S. Dallaire

Industrial Materials Research Institute, National Research Council Canada, 75 de Mortagne Blvd., Boucherville, Québec, Canada, J4B 6Y4

ABSTRACT

The aqueous corrosion degradation of ceramic and metallic coatings plasma-sprayed onto steel substrate were assessed by measuring their bond strengths as a function of salt spray exposure time. The bond strength-corrosion time dependence of Cr_2O_3, $AlO_3.TiO_2$, $ZrO_2.MgO$, NiCr and Cr_2O_3/NiCr coatings were measured. The severity of the aqueous corrosion attack depends more upon the difference in the electrochemical potentials between the coating and the substrate than in the amount of the open porosity. For large differences in the electrochemical potentials, as in the case of Cr_2O_3 and Cr_2O_3/NiCr, a severe drop in bond strength is observed. For small differences in the electrochemical potential, the corrosion is less severe and a reduction in bond strength with corrosion time is only observed after longer period of corrosion or this reduction is more gradual.

KEYWORDS

Thermal Spray Coatings, Plasma, Ceramic, Aqueous Corrosion, Bond Strength.

INTRODUCTION

The very high temperatures generated in plasma spraying make possible to apply coatings of most materials such as refractory alloys, superalloys, cermets and ceramics. The use of coatings provides production equipment with specific surface properties for severe environments which eliminate expensive materials. However, engineering applications based on thermal sprayed coating, require high interfacial mechanical bond strength between the substrate and the coating. Even though, the bond strength of as-sprayed coatings may be adequate for various applications, these coatings may suffer from degradation for applications where aqueous environment is involved (Knotek, 1987; Raman, 1985; Arata, 1983-1984). Indeed, in such environment, plasma-sprayed coatings tend to lose their initial adhesive strength and may eventually spall catastrophically with the growth of corrosion products at the coating-substrate interface. This paper is aimed at studying the bond strength behaviour of plasma-sprayed coating in aqueous environment and proposes an experimental approach to evaluate the corrosion attack in such environment.

MATERIALS AND EXPERIMENTAL PROCEDURE

Three commercial oxide powders (Cr_2O_3, $AlO_3.TiO_2$, $ZrO_2.MgO$) and a commercial NiCr powder were plasma-sprayed onto low carbon steel (SAE 1010) substrate (Fig. 1). The chemical compositions of the powders are given in Table 1. A Plasmadyne unit was used for plasma spraying. Prior to spraying, substrates were grit-blasted with 0.8-1.2 mm corundum particles.

The shape of the specimens used as substrates consists in 2.54 cm diameter cylinder in accordance with the ASTM C-633-79 procedure for bond strength measurement. Plasma-sprayed coatings were deposited on one end of cylinders and afterwards, urethane (rubber) was applied on the external surfaces of the cylinders. The cylinders were then exposed to a severe corrosion environment in a salt spray cabinet according to the ASTM B-117-85 method various periods of time. The maximum exposure time used in this work was 1000 h.

Metallographic examination of cross-sections:

A special technique is used for this purpose and consists in making a small flat surface on the edge of two studs (one stud without coating and the other with a coating and having been subjected to corrosion) glued together in accordance with the ASTM C-633-79 procedure. This flat surface was prepared for metallographic examination to characterize the extent of corrosion at the coating-substrate interface as well as the rupture mode.

Corrosion potential measurements were carried out with a Keithley (Model 616) high impedance electrometer on pieces of coatings extracted from substrates. Specimens were immersed in 3.5 wt% NaCl aqueous solution and readings were taken with a saturated calomel reference electrode.

The open porosity of plasma-sprayed coatings was determined by an hydrostatic method which consists in weighting specimens (dried and infiltrated with water) in air and in water (Rogozhin, 1985). The open porosity (P_0) was calculated according to the following formula:

$$P_o = \frac{(m_2 - m_2)\, r_s}{((m_3 - m_2)\, r_w) - m_s \cdot r_s}$$

where r_s is the density of the metal substrate, r_w the density of distilled water, m_s the weight of the substrate in air, m_1 is the substrate and coating in air, m_2 is the weight of substrate and coating infiltrated with water in air and m_3 is the weight of substrate and coating infiltrated with water in water.

TABLE I – CHEMICAL COMPOSITIONS OF POWDERS

POWDERS	CHEMICAL COMPOSITIONS (wt%)							
	Al_2O_3	Cr	Cr_2O_3	Fe_2O_3	MgONi	SiO_2	TiO_2	ZrO_2
Cr_2O_3	–	.08	98.4	.02	–	.03	.03	–
$Al_2O_3.TiO_2$	87.2	–	–	–	–	.02	12.83	–
$ZrO_2.MgO$	–	–	–	–	24	–	–	76
NiCr	–	20	–	–	80	–	–	–
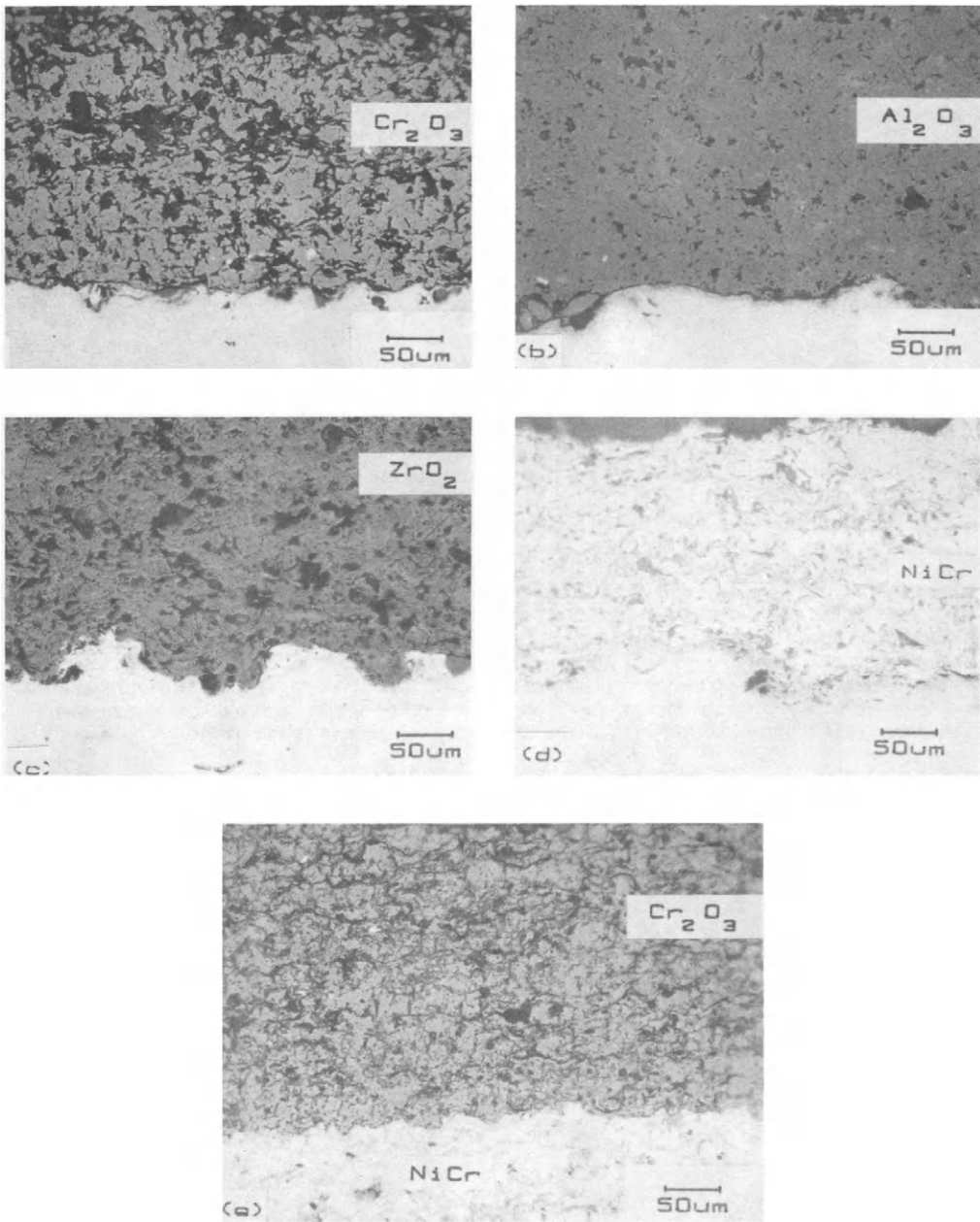
Fig. 1 - As sprayed Coating before corrosion exposure to salt spray test
a) Cr_2O_3; b) $AlO_3.TiO_2$; c) $ZrO_2.MgO$; d) NiCr; e) $Cr_2O_3/NiCr$
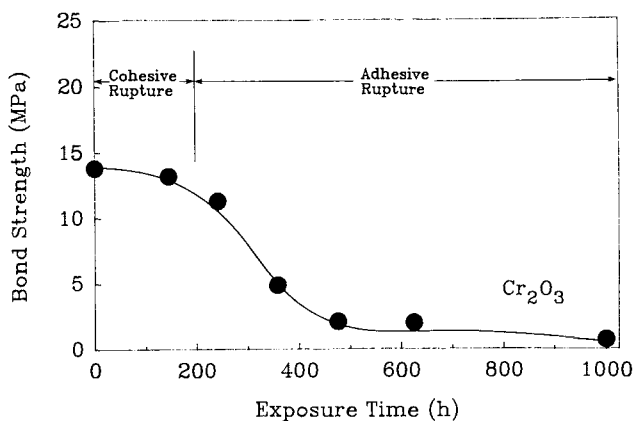
Fig. 2 - Bond strength of Cr_2O_3 coating
as a function of corrosion time

RESULTS AND DISCUSSION

The damaging effects of aqueous corrosion on plasma-sprayed coatings can be assessed by measuring their bond strength as a function of the corrosion time. By measuring the variation of the coating bond strenght the effect of the corrosion attack occuring at the coating-substrate interface is assessed. Therefore, the behaviour of the bond strength is a good indication of the coating susceptibility to the corrosion attack. Two types of bond strength-corrosion time dependence can be generally observed. For the ideal case of non-corroding situations, the bond strength of coatings should remain stable with exposure time. For substrate-coating combinations susceptible to corrosion, a different behaviour is observed: a sharp transition from high to low bond strength is seen in severe corrosion conditions.

Figures 2 to 6 illustrate the variation in bond strength of Cr_2O_3, $AlO_3.TiO_2$, $ZrO_2.MgO$, NiCr and Cr_2O_3/NiCr coatings. It is worthy to note that the bond strength of these 5 coatings changes in a different way with corrosion exposure time. If the three ceramic coatings are first considered, it is seen that the initial adherence of Cr_2O_3 and $AlO_3.TiO_2$, (Figs. 2-3) is maintained only over a very
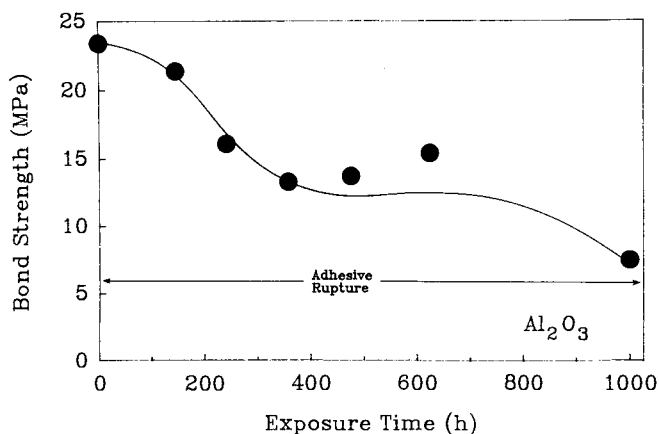
Fig. 3 - Bond strength of $Al_2O_3.TiO_2$ coating
as a function of corrosion time
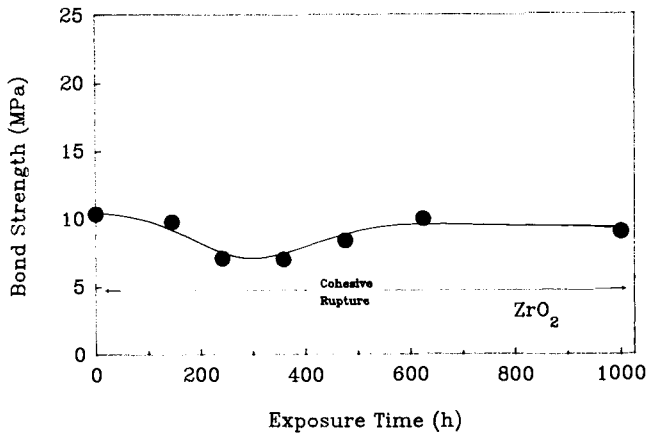
Fig. 4 - Bond strength of $ZrO_2.MgO$ coating
as a function of corrosion time

short period of exposure (200 h), and followed by a rapid decrease of the bond strength. The onset of the transition of the bond strength is much more rapid for Cr_2O_3 that finally exhibits negligible bond strength equivalent to spalling conditions after similar exposure time than $AlO_3.TiO_2$ or $ZrO_2.MgO$ (Fig. 4). In comparison with Cr_2O_3, the bond strength of the $AlO_3.TiO_2$ coatings is less lowered by the corrosion exposure even though a threefold reduction of its initial adherence occurred. The $ZrO_2.MgO$ plasma sprayed coating however, (Fig. 4) behaved differently. A slight reduction of the bond strength after 200 h of exposition is observed and it does not seem to be caused by a serious degradation of the coating but more likely by the modification of internal stresses distribution within the coating by some corrosion products. Indeed the initial bond strength is restored after 600 h of corrosion exposure.
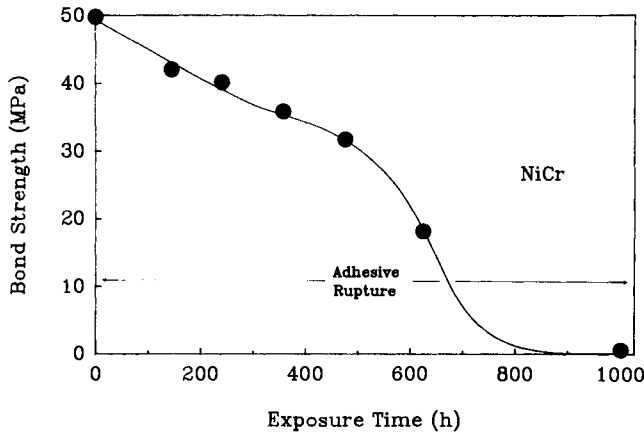
Fig. 5 - Bond strength of NiCr coating
as a function of corrosion time

In the early stage of the corrosion exposure (150 h), and before any reduction of the coating bond strength, the formation of a large amount of corrosion products (red rust $Fe_2O_3.nH_2O$) is seen on the top of the Cr_2O_3, Cr_2O_3/NiCr, and NiCr coatings. Cr_2O_3 coatings presented the earliest appearance of corrosion products on the top surfaces. For the $AlO_3.TiO_2$, a significant amount of corrosion products was observed and in the case of the $ZrO_2.MgO$, just a few brown spots have emerged on the surface without any progress. Cr_2O_3 coatings are rarely used in industrial applications without an underlayer or bond coat. Consequently, the bond strength corrosion time dependence of NiCr and Cr_2O_3/NiCr coatings were studied (Figs.5-6) in order to better understand the effect of a NiCr underlayer on the corrosion mechanisms of a plasma sprayed ceramic coating. NiCr coating is a relatively inert material with a very good bond strength. During the corrosion exposure however, corrosion products rapidly emerged at the surface of the coating and this was followed by a rapid and a severe decrease of the bond strength from 50 MPa to a negligible value equivalent to spalling condition after 1000 h exposure (Fig. 5). In the case of the Cr_2O_3/NiCr duplex coating (Fig.6), the initial adherence is not changed with respect to Cr_2O_3 coating (Fig. 2). The amount of corrosion products that emerged on the surface is lower than for Cr_2O_3 and the onset of the transition from high to low bond strength is delayed. Noteworthy Cr_2O_3/NiCr finally exhibited negligible bond strength, which is equivalent to spalling conditions, after similar exposure time. In order to evaluate the importance of the corrosion products at the interface, cross-sections of specimens after different exposure times were examined. Figures 7 to 11 illustrate typical metallographic cross-sections of coatings after 1000 h of salt spray exposure.
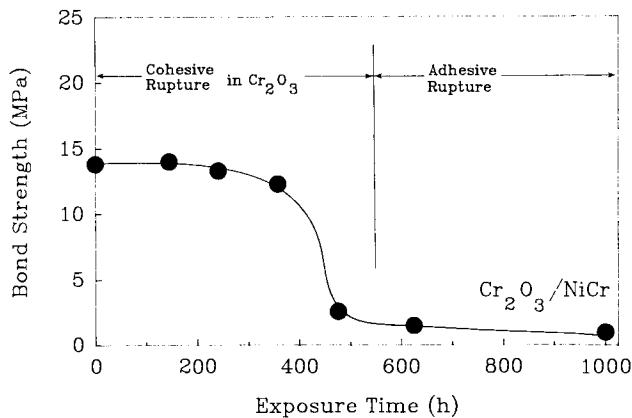
Fig. 6 - Bond strength of Cr_2O_3/NiCr coating as a function of corrosion time

For Cr_2O_3, $AlO_3.TiO_2$, NiCr and Cr_2O_3/NiCr coatings, the presence of a layer of corrosion products very well defined at the substrate-coating interface is seen. In the case of $ZrO_2.MgO$, some corrosion products were present but it was not in the form of a continuous layer of corrosion products. The most important layer of corrosion products ($\approx$ 80 μm) was developped for Cr_2O_3 coatings.

The corrosion products found at the interface are red rust (ferrite Fe_2O_3) and some black oxide (likely magnetite, Fe_3O_4). The formation of Fe_2O_3 and Fe_3O_4 is in accordance with the Pourbaix diagram [Pourbaix, 1974]. It is interesting to note that the presence of these corrosion products was detected before a significant decrease of the bond strength occurred. Ferrite (Fe_2O_3) was found at the surface of the Cr_2O_3 coating only within the first 100 h during which period the bond strength was almost constant.
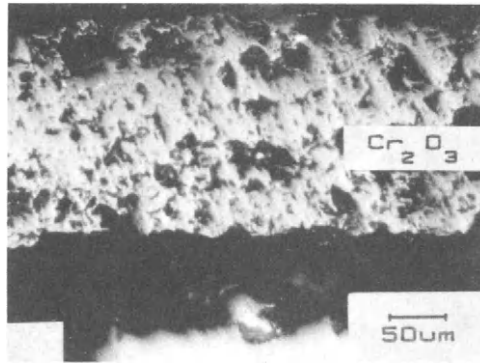
Fig. 7 - Metallographic cross-section of Cr_2O_3
Coating after 1000 of salt spray exposure

Formation of the corrosion product layer

At the beginning of the corrosion test, many corrosion sites are initiated in the contact zones i.e.: between the electrolyte and the substrate through the open porosity of the coating. These corrosion sites are uniformly dispersed, contiguous to the surface of the coating. A very important fact is that these sites are very active because they provide a path to chemically active ions to reach the substrate, and they also create differential aeration cells. These oxygen concentration cells are based on the fact that the O_2 density is high at the tip of the pores, where a cathodic reaction (reduction of water into hydroxide ions) occurs. For regions where the coating adheres to the steel, the O_2 density is lower and we observed an anodic reation (dissolution and oxidation of the iron) takes place.
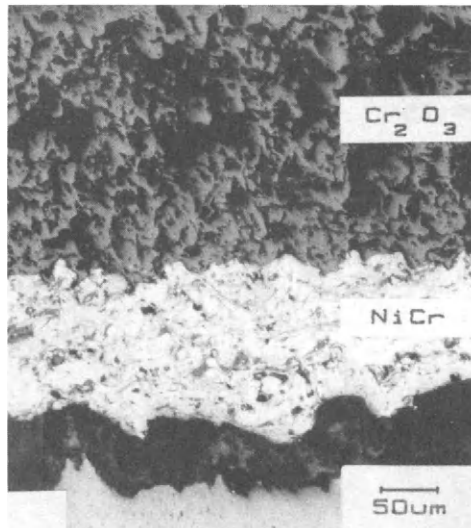
Fig. 8 - Metallographic cross-section of Cr_2O_3/Ni Cr coating
after 1000 h of salt spray exposure
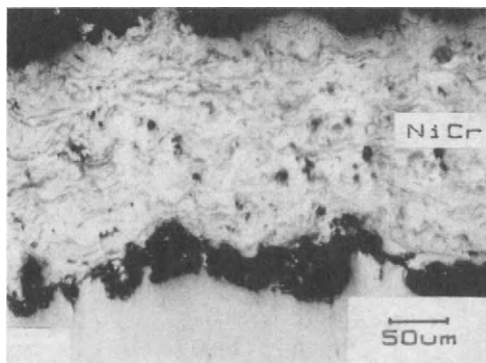
**Fig. 9 - Metalloghraphic cross-section of NiCr coating
after 1000 h of salt spray exposure**

Because the density of the corrosion products is much less than the density of steel, a large volume expansion occurs. Therefore, the formation of corrosion products at these sites leads to protrusion of Fe_2O_3 through the coatings. As mentioned earlier, during this initiation period, the bond strength is not yet affected. As the corrosion progresses, the corrosion sites grow to form a continuous layer of corrosion products between the coating and the substrate (Figs. 7-8-9-10). Therefore, the onset of the transition of the bond strength corrosion exposure time dependence is related to the formation of a layer of corrosion products at the coating-substrate interface. It has been also noted that the corrosion product layer can be responsible of a change in the rupture mode of some coatings. For coatings where the rupture mode is initially cohesive, the presence of a corrosion product layer will change the rupture mode to adhesive. This can be noted in Figs. 7-8 for Cr_2O_3 and Cr_2O_3/NiCr.
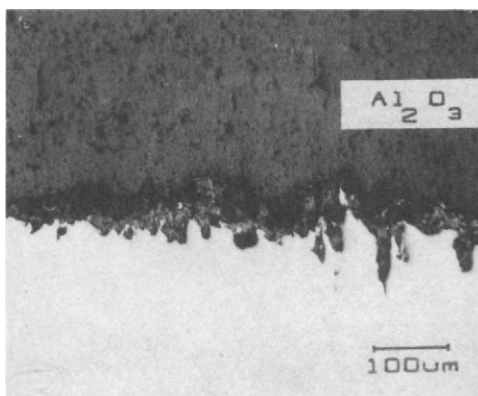
**Fig. 10 - Metallographic cross-section of $Al_2O_3.TiO_2$ coating
after 1000 h of salt spray exposure**

TABLE II

Coating	Open porosity %	Coating Thickness (μm)	Initial Bond Strength MPa	Electrochem. Potential mV/SCE
Cr_2O_3	8.2%	215	15	+350
$Al_2O_3.TiO_2$	3.5%	375	24	-250
$ZrO_2.MgO$	8.3%	224	11	-700
NiCr	-	200	50	-300
Cr_2O_3/NiCr	-	215/200	15	+350
Sand blasted carbon steel	-	-	-	-700 -500*

* At immersion.

Table 2 shows the amount of open porosity measured on different coatings. The open porosity is the same for Cr_2O_3 and $ZrO_2.MgO$, i.e.: 8%. Since the amount of corrosion sites is function of the amount of open porosity, Cr_2O_3 and $ZrO_2.MgO$ should have similar number of corrosion sites. Therefore, the number of corrosion sites cannot solely explain the difference in bond strength-corrosion time dependence and the corrosion rate (Fig. 11) between these two coatings. Consequently, for the same open porosity, different kinetics take place, and have to be explained in terms of electrochemistry. Electrochemical measurements (Table 2) revealed that $ZrO_2.MgO$ coating has an electrochemical potential in the neighbourhoud of -700 mV/ECS after 2 hours of stabilization in comparison with + 350 mV/ECS for Cr_2O_3coatings. The grit-blasted steel substrate has a potential of -500 mV/ECS at immersion and in the neighbourhood of -700 after stabilization.
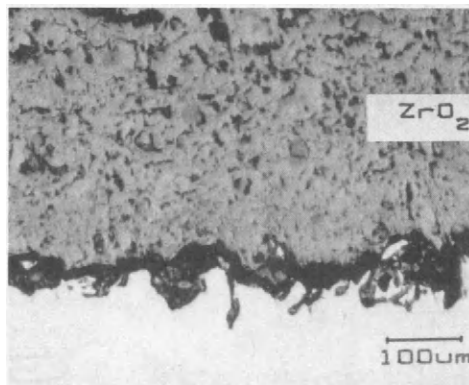
Fig. 11 - Metallographic cross-section of $ZrO_2.MgO$ coating
after 1000 h of salt spray exposure

Among all the coatings only the $ZrO_2.MgO$ had a potential close to the steel substrate. All the other coatings have an electrochemical potential more positive than the steel substrate (Table 2), thus making a large potential difference that acts as a galvanic cell, which generates a corrosion current and leads to a severe corrosion rate of the steel substrate. The potential difference varies from one coating to another such as 1050 mV for Cr_2O_3 and Cr_2O_3/Ni, 400 mV for NiCr, 450 mV for $Al_2O_3.TiO_2$ and a negligible difference for $ZrO_2.MgO$.

As reported in Table 2, the $Cr_2O_3/NiCr$ coatings had the same electrochemical potential than Cr_2O_3. In spite of a lower access for corrosion site (lower porosity and larger thickness), the large potential difference of 1050 mV enhanced the corrosion mechanisms and a similar corrosion rate is observed. Therefore, the use of a NiCr underlayer is not an adequate aqueous corrosion barrier and a suitable bond coat for Cr_2O_3 coating. Considering the NiCr coating alone, the onset of the bond strength decrease and the formation of a corrosion product layer interface are again explained by the galvanic cell generated by the electrochemical potential difference of 400 mV.

$AlO_3.TiO_2$ coating has a potential difference of 450 mV with a porosity of 3%. It should be considered that this coating is much more thicker (375 μm) instead of 200 μm for NiCr which likely explains that the corrosion rate is moderate.

The absence of a noticeable galvanic cell between $ZrO_2.MgO$ and the steel substrate and the presence of 8% of open porosity explains the presence of some brown spots on the top of these coatings without the formation of a layer of corrosion products at the interface (Fig. 11). Therefore, this coating maintains an adequate bond strength after having been exposed to salt spray for 1000 h and has the lower corrosion rate among all these coatings.

CONCLUSIONS

1. A corrosion degradation occured for all the ceramic coatings studied in this study. The rate of corrosion largely differed depending upon the electrochemical potential between the ceramic and the substrate and upon the open porosity.

2. Corrosion is not suppressed with 80 Ni - 20 Cr undercoating for Cr_2O_3.

3. $ZrO_2.MgO$ is the only coating in this study that maintained its bond strength after a salt spray exposure of 1000 h.

4. Cr_2O_3, $AlO_3.TiO_2$, NiCr and $Cr_2O_3/NiCr$ coatings deposited on carbon steel are susceptible to corrosion attack. They displayed a sharp transition from their initial bond strengths to lower bond strengths with corrosion exposure time.

5. The experimental approach presented in this study can assess the performance of a plasma-sprayed coating in humid environment by means of bond strengths.

REFERENCES

Knotek, O., R. Elsing, and H.R. Heintz (1987). Surface Coating and Technology, 30, 107.
Raman, A., G. Nnaike, A. Choudhury, and C.R. Das (1985). Corrosion Science, 25, (2), 107-115.
Arata, Y., A. Ohmori, J. Morimoto, J. Kudoh, M. Kishida, Osaha, and Kinki (1983). 10th International Thermal Spraying Conference, 80.
Arata, Y., A. Ohmori, G. Zhou, and J. Xue (1984). Transactions of Japanese Welding Research Institute of Osaka University, Japan. Report 1, 13, 27.
Arata, Y., A. Ohmori, G. Zhou, J. Xue, and G. Li (1984). Transactions of Japanese Welding Research Institute of Osaka University, Japan. Report 2, 13, 107.
Rogozhin, V.M., L.V. Akimova and E.E. Kutakova (1985). Soviet Powder Metallurgy and Metal Ceramic.
Pourbaix, M. (1974). Nace, Houston, Texas, USA, 2nd Edn., 312.

Assurance of structural reliability in ceramics

David J. Green
Department of Materials Science and Engineering, The Pennsylvania State University, University Park, Pennsylvania 16802, U.S.A.

ABSTRACT

In order to utilize ceramics in structural applications, it is important to understand the parameters that control their strength. To assure the reliability of ceramics in such applications several approaches are available; improving the toughness of ceramics, developing processing techniques to eliminate critical flaws, proof testing, non-destructive evaluation and the introduction of residual surface compression. The aim of this paper is to review these various approaches within the framework of linear elastic fracture mechanics, especially in terms of the micromechanics of the brittle failure process.

INTRODUCTION

During the last 20 years, there have been dramatic improvements in the strength and fracture toughness of ceramic materials. This has opened up many possible new applications for ceramics, especially those in which one can take advantage of the hardness, stiffness and high temperature stability associated with covalently-bonded ceramics. Unfortunately, ceramics are prone to brittle failure and often have a large scatter in their strengths. This brittle fracture generally persists to high temperatures, is often catastrophic and occurs with little warning. This lack of toughness and the difficulty in controlling crack propagation in ceramics are invariably key questions in applications that involve structural stresses. The wide strength distributions associated with ceramics can also create design problems as failure probability may be unacceptably high, even at relatively low stresses. Thus, a key strategy in the structural use of ceramics is to be able to identify means for increasing their reliability (Marshall and Ritter, 1987). The aim of this paper is to discuss various approaches that can be used to improve the strength of ceramics.

FRACTURE MECHANICS AND STRENGTHENING

For many ceramic materials, linear elastic fracture mechanics can be used in a relatively straightforward way to understand the relationship between fracture toughness and strength. Assuming that ceramics contain 'crack-like' defects as a result of their processing, the stress intensity factor, K, indicates the amplitude of the stresses near the crack tips. For tensile opening of the crack (mode I), K_I is also related to the applied stress by

$$K_I = \sigma Y \sqrt{c} \tag{1}$$

where σ is the applied stress, c is the surface crack size (for an internal crack, the crack length is 2c) and Y is a geometric constant that depends on the loading and the crack shape (Lawn and Wilshaw, 1975). For crack propagation to occur K_I reaches a critical value, K_{IC}. In the current ceramic literature, this latter parameter is generally called the *fracture toughness* of the material. For the critical condition we can write Eq. 1 as

$$\sigma_f = K_{IC}/[Y\sqrt{c}] \tag{2}$$

where σ_f is the fracture stress. One can use Eq. 2 as a guide to the general features that one would utilize to increase the strength of a ceramic material. Clearly one approach would be to increase the fracture toughness value without changing the crack size. It has been found that **toughening mechanisms** are available in ceramics and these usually involve manipulating and tailoring the microstructure.

A second approach to increase strength would be to determine the source of the defects that lead to the formation of critical cracks and then to find ways to eliminate or reduce the size of these flaws. It is important to recognize here that ceramics contain various populations of defects that compete as failure origins and within these populations, the defects lead to critical cracks of various sizes. Thus, the strength of ceramics is best represented as a statistical distribution that reflects these variations in defect type and size. A popular approach has been to use the empirical, two parameter Weibull distribution to describe the strength of ceramics (DeSalvo,1970), i.e.,

$$\ln(1/[1-F]) = LV(\sigma/\sigma_0)^m \tag{3}$$

where F is the failure probability, L is a loading factor that describes the stress state in the body, V is the stressed volume and σ_0 and m are the parameters that describe the location and width of the strength distribution respectively. The parameter m is often called the Weibull modulus. For materials that fail from surface flaws, V in Eq. 3 is replaced by the stressed area of the body.

In order to obtain **the critical flaw size reduction**, there are two basic approaches, i.e., one can improve the techniques by which the material was made *(improved processing)* or one can find techniques to eliminate materials that will have the largest critical cracks. This latter approach generally involves the use of *non-destructive evaluation* to find the most important defects or *proof testing* (stressing all

components prior to use) and eliminating those that fail or those that give a signal (e.g., acoustic emission) that the failure process is underway. Another approach to non-destructive evaluation is to measure a property that is somehow linked to the failure process. For example, sound velocity or acoustic attenuation may be linked to the 'damage' within a material.

The final approach to increasing reliability is related to the applied stresses. Clearly, if the design is changed such that the applied stress is reduced, the component is less likely to fail. An alternative, related approach is to introduce **macroscopic residual stresses** in a material such that the applied stresses in the vicinity of the fracture origin are reduced. In ceramics, surface flaws are often a major flaw population and thus techniques that place the surface in compression can be used to reduce the effective tensile stress acting on these flaws. In many applications, the maximum applied stress often occurs at the surface, (e.g., contact damage, thermal stresses) and one expects that surface cracks will control the failure processes. For these cases, residual surface compression will be useful in increasing reliability. In terms of the failure criterion, residual surface stresses will modify Eqs. 1 and 2. If one includes the stress intensity factor associated with the macroscopic residual stresses, one obtains

$$K_I = \sigma Y \sqrt{c} + \sigma_R Y' \sqrt{c} \qquad (4)$$

where σ_R is the surface residual stress and Y' is the geometric constant associated with the crack and residual loading geometry. For the failure condition, $K_I = K_{IC}$ and we obtain

$$\sigma_f = (K_{IC} - \sigma_R Y' \sqrt{c}) / [Y \sqrt{c}] \qquad (5)$$

For residual compression σ_R is negative and hence we expect to increase the strength of the material.

In the above discussion it was assumed that the condition for crack propagation is when $K_I = K_{IC}$. In some situations, however, cracks can grow below K_{IC}. This sub-critical crack growth is often associated with stress corrosion or with creep processes occurring at or near the crack tip. These processes lead to a time-dependence of strength that must be taken into account for design purposes. For Eq. 1, this implies that c increases in a stable fashion with time under stress. Provided one can assess the crack growth rate under stress, it is reasonably straightforward to modify the above analysis to take into account sub-critical crack growth (Ritter, 1978, Davidge, 1979). Stable crack growth is also associated with localized residual stress fields in ceramics. For example, contact events (Lawn, 1983) and second phase inclusions (Green 1983a) can give rise to such stresses. The general form of Eqs. 2 and 5 are not changed by sub-critical crack growth or by stable growth in residual fields. It must, however, be understood that c may not represent the initial sizes of cracks in these equations but rather their (final) critical size.

There are some effects that can substantially change the philosophy outlined in Eqs. 2 and 5. The first is that the fracture resistance can be characterized by a single parameter, K_{IC}. It has been realized recently that some ceramics can exhibit *R curve behavior*. The

CRACK LENGTH
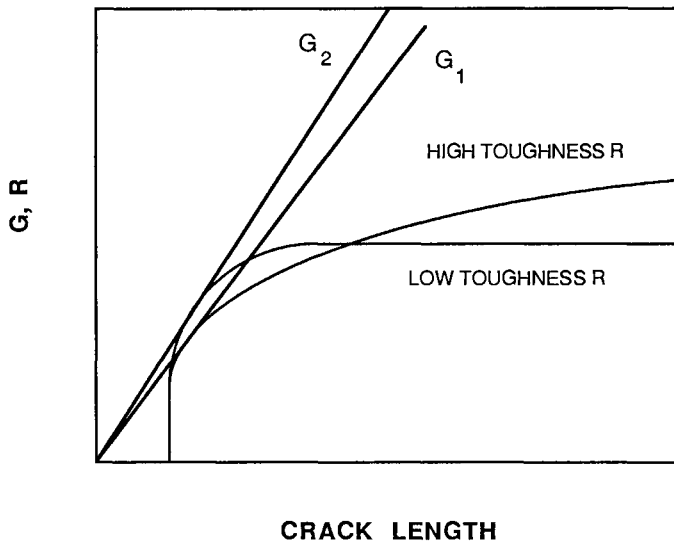
Figure 1. R curves for materials with different plateau level toughness
         values showing the material with the lower toughness can have
         a higher strength.

implication is that the crack resistance force R, changes as the crack
propagates. For several ceramics it has been shown that R increases as
the crack length increases. This has several important influences on the
strength of ceramics. For example, Fig. 1 compares the R curves for two
different materials. In this approach we consider the crack extension
force G (related to K), recognizing that crack extension occurs when G =
R. The increasing value of R allows the cracks to grow stably until we
reach the point when the G curves are tangent to the R curves, G_1 and G_2
in Fig. 1. For all crack lengths beyond this, the crack extension force
is larger than the crack resistance force and unstable fracture occurs.
As illustrated in Fig. 1, the material with the lower (plateau) crack
resistance force fails at a higher G than the the material with the
higher plateau R value (Marshall, 1986). For a given crack length, G is
a function of the applied stress, so that as $G_2 > G_1$ one obtains a lower
strength for the higher toughness material. It should also be mentioned
that some of the high toughness ceramics can show substantial non-linear
elastic behavior. For these materials, increasing toughness tends to
increase the non-linearity and failure is more akin to the yielding
phenomenon found in metals. Thus increasing toughness can lead to a
decrease in strength. This effect has been observed and discussed for
transformation-toughened ceramics (Swain and Rose, 1986, Evans and
Cannon, 1986).

A second important feature of (increasing) R curve behavior is that it
increases the tolerance of a material to large flaws; they are more
difficult to extend than small flaws. This implies that R curve behavior
will tend to narrow the strength distribution (Kendall et al, 1986, Cook
and Clarke, 1988). As pointed out earlier this effect can be important
in the structural design of ceramic components.

For this paper, the effects associated with R curve behavior will be
neglected and we will consider the structural reliability of ceramics
simply in terms of Eqs. 2 and 5.

TOUGHENING MECHANISMS

As pointed out in the last section, improving the fracture toughness of
a ceramic can increase its strength provided there is no change in the
critical crack size (Eq. 2). It is also important to note that improving
the toughness of ceramics also has an important role in improved
resistance to contact damage. That is, cracks are more difficult to
nucleate and their influence on strength degradation is less, the higher
the fracture toughness of the material.

The mechanisms that can lead to toughening can be categorized into three
types, and these are shown schematically in Fig. 2. *Crack tip
interactions* occur when a crack tip interacts directly with an obstacle
in the microstructure. For *crack tip shielding*, events are triggered by
the high stresses in the crack tip region in a way that reduces these
stresses. In the third category, ligaments of some type are left behind
the advancing crack tip. This *crack bridging* makes it more difficult
for the crack faces to open and hence hinders crack propagation. Crack
bridging is often accomplished using frictional forces between the
bridge and the surrounding materials, e.g., poorly bonded fibers and
large grains (weak bridging). In other cases, the bridge may strongly
pin the crack faces together and the bridge must be deformed or broken
during the fracture process. These toughening mechanisms have been
reviewed recently (Clarke and Faber, 1987, Green, 1988, Green, Hannink
and Swain, 1988) and a summary will be given below.

A. Crack Tip Interactions.

The primary aim of this type of mechanism is to place obstacles in the
crack path to impede crack motion. These obstacles could be second phase
particles, whiskers, fibers or possibly, regions that are simply
difficult to cleave. There are two different types of consequences that
can occur if the crack motion is impeded by an obstacle. In one case,
although the crack is pinned by the obstacle, it can by-pass the
obstacle by *bowing* around either side of it, remaining on virtually the
same plane. In the other case, the crack could attempt to completely
avoid the obstacle by *deflecting* out of the crack plane. The deflection
of the crack front can be accomplished by tilting of the crack path or
twisting of the crack front. In a real situation, a combination of
bowing and deflection is expected to occur. It is important to note that
crack bowing must be a precursor to the crack bridging mechanism.

1. Crack Bowing. This mechanism has been analyzed theoretically and it
has been shown by two different types of calculations, to lead to an
increase in fracture toughness (Lange, 1970; Evans, 1972). These
analyses do have the shortcoming that they assume the obstacles to be
impenetrable. Later work showed that, it is possible to adjust the
calculated toughening to account for obstacle strength (Green, 1983b).

2. Crack Deflection. If a crack is deflected out of the plane that is
normal to the applied tensile stress, the reorientation of the crack
plane leads to a reduction of the crack extension force on the deflected

1. Crack Tip Interactions

??

obstacle

2. Crack Tip Shielding

process
zone

3. Crack Bridging

* Weak
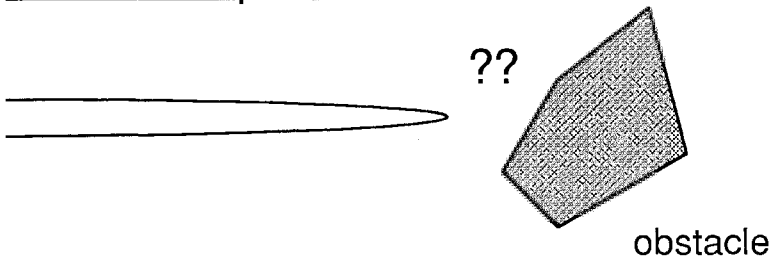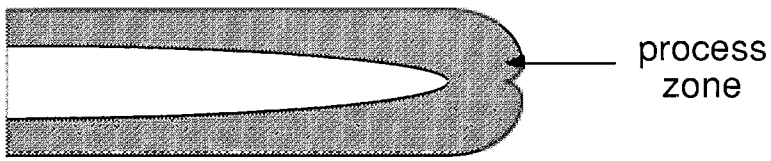
* Strong
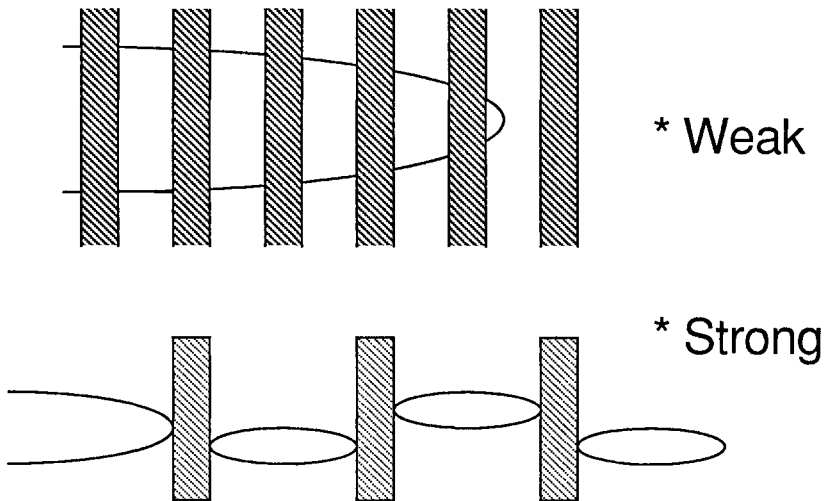
Figure 2. Schematic illustrations of general toughening
mechanisms in ceramics.

portion. For a random array of obstacles, it has been shown that the toughening increment depends on the volume fraction and shape of the particles (Faber and Evans, 1983a). For a given volume fraction of obstacles, shaped as rods, discs or spheres, it has been shown that rods are the most effective in increasing toughness. Measurement of fracture toughness values and crack deflection angles in SiC, Si_3N_4 and a glass-ceramic have been shown to be consistent with the predictions of this mechanism (Faber and Evans, 1983b; Faber and Evans, 1983c).

B. Crack Tip Shielding.

There are two mechanisms that have been identified as leading to crack tip shielding, viz., transformation toughening and stress-induced microcracking.

1.Transformation Toughening. An elegant approach to the toughening of ceramics is the use of a stress-induced phase transformation (Evans and Cannon, 1986; Green, Hannink and Swain, 1988). The most success has been in the use of zirconia-based materials. Zirconia has a high temperature tetragonal phase that usually undergoes a martensitic phase transformation to monoclinic during cooling (~ 1000ºC). In this direction, the transformation involves a 3 to 5% volume increase and a simple shear of ~16%. These large transformation strains invoke large transformation stresses in a material. Thus, when one considers the thermodynamics of the transformation, the strain energy due to the transformation needs to be taken into account. This has the effect that the tetragonal phase, if constrained, can be retained to lower temperatures. In addition, undercooling will also be possible if the monoclinic phase is difficult to nucleate. Indeed, it is possible to retain the tetragonal phase to below room temperature provided the zirconia particle size is below a critical value. For these materials, it has been shown experimentally that the phase transformation can be induced in the vicinity of a crack and that such materials possess high fracture toughness. Fracture mechanics calculations have shown that a mechanism in which the phase transformation is induced by the high stresses near a crack tip would explain the increase in fracture toughness (McMeeking and Evans, 1982; Marshall, Drory and Evans, 1983; Budiansky, Hutchison and Lambroupolos, 1983). These various studies used different theoretical approaches but came to identical conclusions and thus, give a compelling argument about the way the toughness develops and the parameters that control the process. It was shown theoretically that these materials should give R curve behavior as the transformed zone extends behind the stably growing crack. For long cracks, the toughening reaches an asymptotic limit and the toughening (ΔK_{IC}) associated with the limit is given by

$$\Delta K_{IC} = 0.21 E V_t e^T \sqrt{h} / [1 - \upsilon] \qquad (6)$$

where E and υ are the Young's modulus and Poisson's ratio of the material, e^T is the volumetric transformation strain, V_t is the volume fraction of material transformed by stress and h is the height of the transformation zone. There are a variety of assumptions in Eq. 6 and other analyses have considered a wide variety of other possibilities but these other approaches only make changes to the numerical constant in Eq. 6. Thus, the parameters that control fracture toughness in these materials are relatively well understood. The major exception is that one cannot predict in a quantitative fashion the zone height.

2. Microcrack Toughening. Ceramics that contain localized residual stresses are known to be capable of microcracking (Green, 1983a). These residual stresses arise in ceramics as a result of thermal expansion anisotropy in single phase materials, phase transformations and thermal expansion or elastic mismatch in multiphase materials. It is also expected that regions of low toughness, such as grain boundaries, would be attractive sites for such cracks. It has been known for some time, that these microcracks can form spontaneously during the fabrication process, provided the grain or particle size, is above a critical value (Green, 1983a). An attractive proposition, in terms of fracture toughness, is to fabricate materials in which the particle size is below that for spontaneous microcracking but in which microcracks could be stress-induced. In terms of fracture, one would expect that the microcracks would form in a zone around large cracks, much in the same way as a stress-induced phase transformation zone forms. The creation of a microcrack zone around a propagating crack is expected to reduce the stresses near the crack tip, giving rise to shielding. It has been shown by various theoretical analyses that stress-induced microcracking should lead to improved fracture toughness (Evans and Faber, 1984; Hutchison, 1987). Indeed, the mechanics involved is very similar to that associated with transformation toughening and should similarly give rise to R curve behavior.

C. Crack Bridging.

This mechanism has been shown to be important in frictionally bonded fiber composites, in large-grained Al_2O_3 and possibly whisker- and metal-reinforced ceramics. In order to determine the effect of crack bridging on fracture toughness, it is necessary to know the force-displacement relationships for the ligaments.

The addition of continuous carbon or SiC fibers to glasses or ceramics has been studied since about 1970 and it has been found, in some cases, that unidirectional fiber composites do not undergo catastrophic failure in tensile loading. This 'ductile' type of behavior for a material composed of two brittle components is particularly attractive for structural applications. In the optimum materials, the tensile loading behavior is initially elastic until at a particular stress, a crack passes through the matrix. This crack, however, by-passes the fibers and leaves them available for load carrying and they completely bridge the crack. Further loading causes the formation of regularly-spaced, bridged, matrix cracks until at the peak load, the fibers fail. The ensuing failure, however, is not catastrophic as the fibers continue to pull out of the matrix; the fibers act as frictional bridges. In these materials the final failure is not the result of the propagation of a single crack and thus, a fracture toughness value cannot be defined. It is, however, possible to use fracture mechanics to describe the conditions at which the first crack passes through the matrix (Marshall, Cox and Evans, 1985). Under some circumstances, the matrix cracking stress is determined to be independent of the pre-existing flaw size (flaw-tolerant material). For other situations, a crack may not be fully bridged as described above. That is, a bridging zone of limited extent, is formed behind the crack and moves with the crack. The behavior of such a material is brittle but a toughness increase is associated with the partial bridging. Such partial bridging has been associated with the high fracture toughness values obtained in whisker-reinforced ceramics.

TABLE 1. Fracture Toughness Values for Selected Ceramics and Glasses

Material	K_{IC} (MPa.$\sqrt{m}$)
Soda Lime Silica Glass	0.74
Aluminosilicate Glass	0.91
Aluminum Oxide	2.9 – 4.6
Silicon Nitride	2.0 – 4.0
Silicon Carbide	4.0
Whisker Reinforced Aluminum Oxide	4.0 – 9
Zirconia Toughened Ceramics	2.0 – 17
Tungsten Carbide (Cobalt bonded)	12

Anstis et al, 1981: Swain and Rose, 1986
Becher et al, 1986

Some typical K_{IC} values are given in Table 1, which shows that various ceramics are now available with values > 5 MPa.$\sqrt{m}$. In particular, one can see the effectiveness of zirconia, whisker and metal phase toughening. As pointed out above, one cannot ascribe a K_{IC} value to fiber composites with fully-bridged cracks.

CRITICAL CRACK SIZE REDUCTION

As pointed out earlier, reduction of the critical crack size in a ceramic will lead to an improvement in strength (Eq. 2). Three ways are often used to accomplish this; improved processing, non-destructive evaluation and proof testing and these will be discussed below. It is important to note that these approaches usually do not account for flaws produced during service. For example, contact damage, fatigue effects or environmentally-induced flaws are possibilities that would need to be understood in the structural design and hence factored into a materials test program.

A. Improved Processing.

The low toughness of ceramics combined with the inability to relax high stresses leads to relatively easy crack nucleation and formation. Thus microstructural defects, when combined with high stresses, are prime candidates for precursors to crack formation. Stress concentrations will occur when there are regions in the microstructure that have different elastic constants than the surrounding material. For example, voids or impurity inclusions could be the cause of such stress concentrations. The presence of voids is particularly common and may be the result of incomplete sintering, inhomogeneous densification or the burn-out of organic impurities (Lange, 1986). The other common source of high stresses are those that arise when one part of the microstructure has a volume or shape mismatch with the surrounding material. These residual stresses are usually associated with phase transformations, chemical reactions, thermal expansion anisotropy or mismatch in thermal expansion coefficients.

The use of fractography is often a key element in identifying the
defects that lead to crack formation. Failure origins can often be
traced to steps in the processing. For example, Fig. 3 shows two failure
origins in Al_2O_3/ZrO_2 composites; a porous alumina agglomerate and a
large alumina grain. Both defects are probably a result of poor mixing
or inadequate particle size control in the fabrication process. The low
toughness and stress concentration associated with the porous
agglomerate and the easy cleavage associated with a large single crystal
appear to have led to failure. This type of information, in which the
fracture origin is clearly identified with a processing step, can be a
key in indicating routes for improving the processing, and hence
obtaining substantial strength increases (Lange, 1986). Figure 4 shows
that one can often improve strengths dramatically using this type of
philosophy. It is important to realize that these various types of
processing defects will give rise to a distribution of critical crack
sizes and hence to a strength distribution. Moreover, as illustrated in
Fig. 5, there will be a competition between various types of flaw
populations. Thus removal of one flaw will then reveal the next most
severe type of flaw or one may have mixed flaw types. For example,
agglomerates are shown in Fig. 5 as the worst flaw population, i.e.,
they have the highest failure probability at a given stress. Removal of
these defects is shown to lead to a mixed group of competing failure
origins, i.e, voids and large grains. In some cases, it may be more
important to find ways to reduce the width of the strength distribution
rather than to eliminate a particular flaw type. That is, it may be
preferable to change the fracture stress at some low failure probability
rather than attempting to increase the average strength.

B. Non-destructive Evaluation.

A direct but difficult approach to reducing the critical flaw size is to
identify a means to non-destructively determine the size of cracks
within the microstructure. If this can be accomplished then one could
simply not use those components that contain cracks larger than a given
size. In terms of Eq. 2, this will allow one to identify the minimum
strength of a component. The removal of specimens with strengths less
than a particular value will also change Eq. 3 to a three-parameter
Weibull equation, i.e.,

$$\ln(1/[1-F]) = LV([\sigma - \sigma_t]/\sigma_0)^m \qquad (7)$$

where σ_t is the minimum strength of a component. This truncation of the
strength distribution by a minimum strength is shown schematically in
Fig. 6. Clearly, sub-critical crack growth would allow this minimum
strength to change with time under stress but this can be accounted for
in the design, if the crack growth rate behavior is known. For many
ceramics, the non-destructive identification of flaws can be difficult
as their size is small, usually < 100 μm. Substantial effort has gone
into acoustic wave scattering in order to identify surface flaws,
inclusions and voids (Evans, 1979, Marshall et al, 1983). These
approaches seem to have met with mixed success and may be costly. It may
be that high toughness ceramics are more amenable to non-destructive
evaluation, especially if the failure process involves some type of
damage accumulation, e.g., as in some fiber composites. Moreover, larger
cracks can be tolerated in high toughness ceramics and may therefore be
easier to detect.
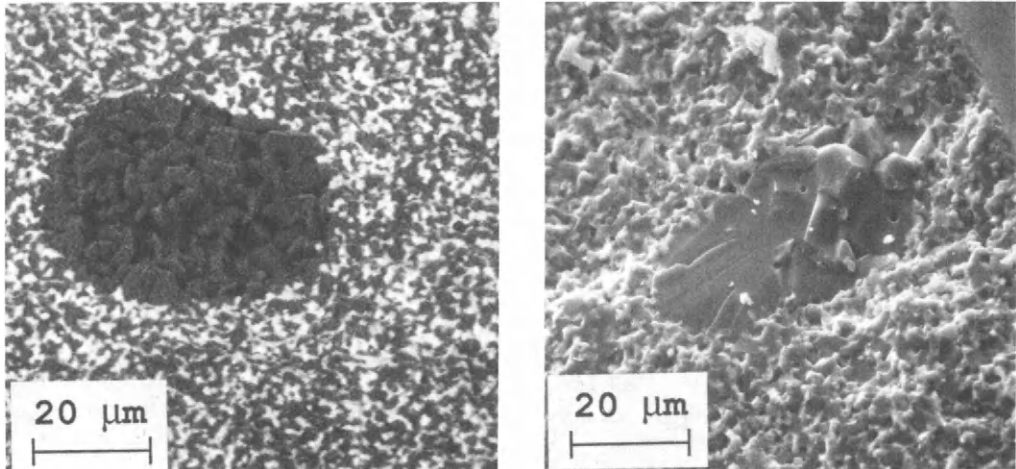
Figure 3. Failure origins associated with poor mixing in
        alumina/zirconia composites; left, porous alumina
        agglomerate, right, large alumina grain.

PROCESSING APPROACH
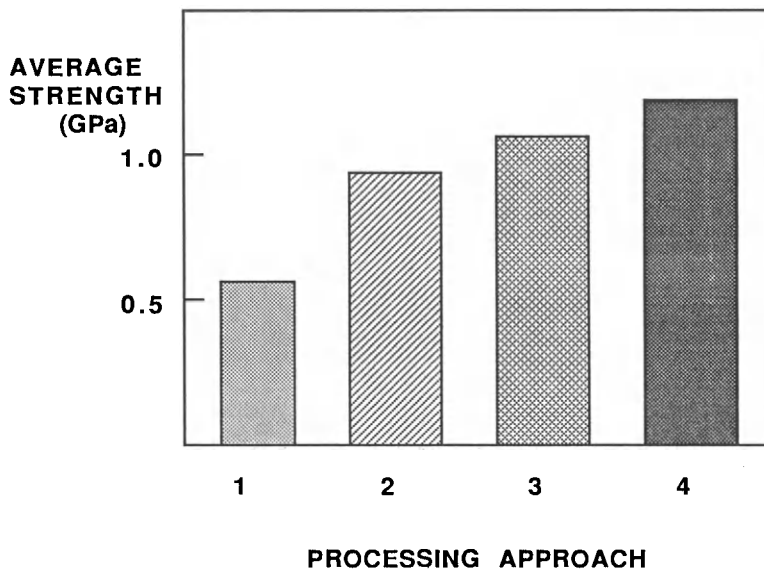
Figure 4. Improvement in average fracture stress produced by
        identifying failure origins in alumina/zirconia composites
        and adjusting the processing procedure to eliminate these
        defects (after Lange, 1986)

LN APPLIED STRESS
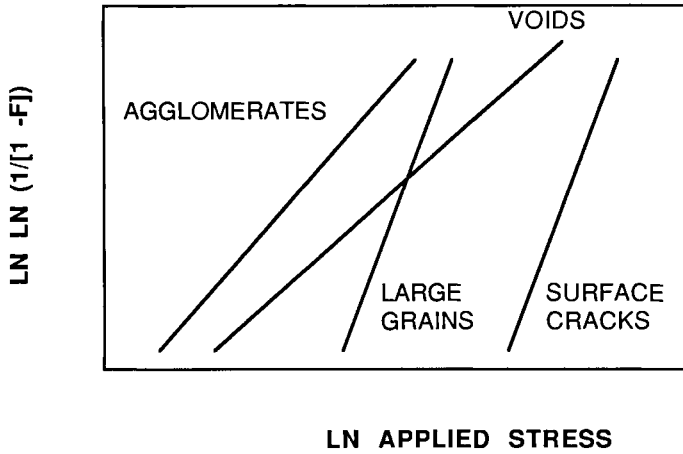
Figure. 5.   Schematic illustration of competing failure
              populations. Removal of one population reveals other
              types.

LN APPLIED STRESS
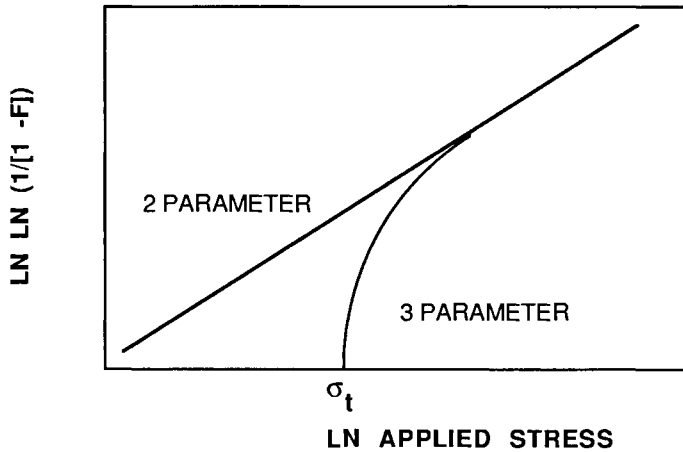
Figure 6.   Removal of materials with strengths below a
             given value truncates the strength distribution.
             For the case of a two-parameter Weibull distibution,
             a three-parameter Weibull distibution would result.

Even if one does identify a defect non-destructively, one must still be able determine its severity, i.e., determine the critical size of the crack into which it will evolve. Progress has been made in understanding the failure process associated with inclusions or voids. For example, voids have been modelled as a spherical void with a surrounding 'saturn' crack, (Green, 1980). For inclusions, models have been constructed based on the differences in elastic moduli, coefficients of thermal expansion and toughness values between the inclusion and the matrix (Evans, 1979). In particular, for silicon nitride these models have been used to predict fracture stress from the size of a variety of flaw types (Evans, 1979).

An alternative approach to using non-destructive evaluation for predicting strength from defect size is the measurement of some property that can be linked to strength. For example, in work on the space shuttle tiles, it was found that tensile strength was correlated with sound velocity (Zimmerman, 1980). Thus a simple measurement was available to detect tiles of low strength. Figure 7 shows a typical set of data for this strength-velocity correlation. Clearly, the correlation was relatively poor but it was statistically possible to remove some of the lowest strength tiles. It was later shown that a relationship between fracture toughness (strength) and sound velocity would be expected for these types of highly porous materials (Green, 1983c) These types of non-destructive measurements may also be useful in assessing damage to a component. Figure 8 shows the relationship determined from measuring the acoustic spectrum of a highly porous, open cell ceramic that had been subjected to thermal shock. It was possible in this work to relate the shift of resonance peaks to the decrease in tensile and compressive strength of the material (Orenstein and Green, 1989). In Fig. 8, the shift of one of the resonance peaks has been used to calculate the Young's modulus of the ceramic.

C. Proof Testing.

Another way of identifying components that contain large flaws is to stress the materials prior to their use. Components that survive the proof test would then be used in service. In some cases, acoustic emission is also used to detect any damage that occurs during the proof test. If possible, these tests need to be performed in an atmosphere free of any environmental effects on crack growth and with rapid unloading. Moreover, the proof stress distribution should be similar to the service stress to assure that one is stressing an equivalent set of flaws. For these situations, the strength distribution will be truncated at the proof stress, i.e., the proof stress will be equivalent to the minimum strength. As discussed in the last section, a two-parameter Weibull distribution would be changed to a three-parameter distribution by such a proof test (Eq.7, proof stress = σ_t). In some cases, it may not be possible to perform a proof test in an inert environment. For these cases, one must then take account of the sub-critical crack growth. Approaches based on fracture mechanics are available to accomplish this (Ritter, 1983). Figure 9 shows the comparison of the predicted change in a strength distribution of the space shuttle tile material during a proof test with experimental strength data on materials that survived, (Green, Ritter and Lange, 1981). In this case, the fracture mechanics approach gave excellent agreement with the measured data and showed that the established proof test procedure was adequately truncating the distribution.
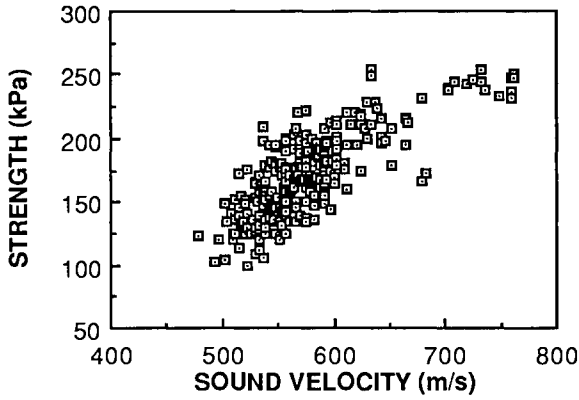
Figure 7. Relationship between tensile strength and sonic velocity for the LI 900 space shuttle tile materials.
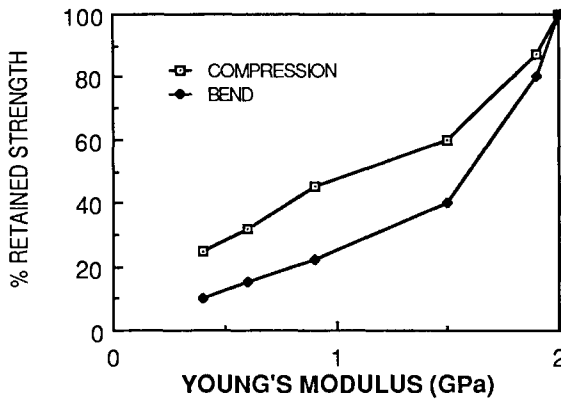
Figure 8. Relationship between the non-destructively determined Young's modulus and the retained strength (bending and compressive) for a thermally-shocked open cell ceramic.
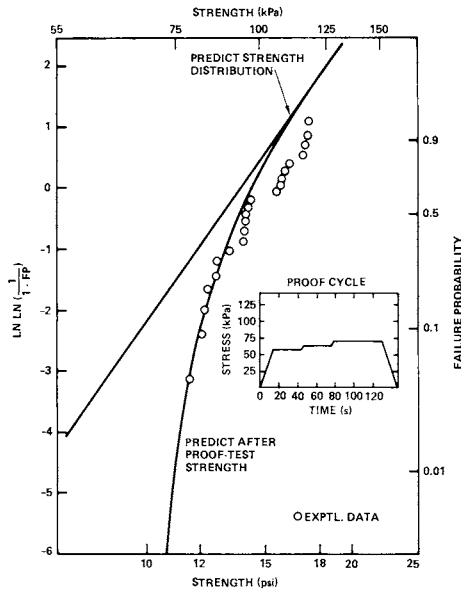
Figure 9. Effect of a proof test on the space shuttle tile system. The
straight line represents a fit of tensile strength data to
the two-parameter Weibull equation. The curved line shows the
predicted strength change after a 70 kPa proof test. The open
circles show the experimental data for the tensile strengths
of specimens that survived the proof test. The proof test was
found to adequately truncate the distribution.

TABLE 2. Average and Standard Deviation of Fracture Stress Data
for an Ion-Exchanged Glass.

EXCHANGE TIME (h)	AVERAGE FRACTURE STRESS (MPa)	STANDARD DEVIATION (MPa)	CV
0	166.7	36.1	0.217
4	452.9	182.3	0.403
9	700.5	153.8	0.220
16	638.6	131.8	0.206
24	483.3	87.1	0.180
64	381.9	58.8	0.154

CV Coefficient of Variation (Standard Deviation/Mean)

RESIDUAL SURFACE COMPRESSION.

As shown in Eq. 5 the introduction of residual surface compression is expected to increase the strength of brittle materials **that fail from surface cracks**. This idea has been exploited in glass technology for some time and is usually known as tempering (LaCourse, 1972). In physical tempering, the glass is rapidly cooled from some pre-determined temperature. A variety of chemical tempering techniques are available and these include ion exchange, surface crystallization, cladding and surface de-alkalinization. Similar ideas have been attempted on polycrystalline ceramics and substantial strengthening has been obtained (Kirchner, 1979). More recently, it has been recognized that transformation-toughened zirconia ceramics could be strengthened by the introduction of surface compression. For these materials, the aim is generally to induce the phase transformation on the external surface of a component. The volume increase associated with the transformation places the surface in compression. The techniques that have been used to introduce these stresses have been reviewed recently (Green, Hannink and Swain, 1988).

The primary aim of introducing residual surface compression is to increase the strength of a material. Table 1 shows some typical data for an ion-exchanged, soda lime silica glass (Beck, 1989). For these materials, the surface compression is a result of exchanging larger potassium ions for the smaller sodium ions. There are several important effects to be noted in Table 2. Firstly, although the glass can be substantially strengthened, one may also increase the width of the strength distribution. It has been shown theoretically that such an effect can be expected, as the strengthening depends on the depth of the compressive layer relative to the surface crack size (Tojek and Green, 1989). As specimens contain a range of crack sizes, one expects the (initially) stronger specimens (smaller cracks) to be strengthened more than the weaker. It is thus important to choose processing conditions such that all the surface cracks will lie within the zone of maximum compression. As shown in Table 2, long exchange times tend to reduce the strengthening. This is a result of the structural relaxation that can occur at the exchange temperature. The change in the coefficient of variation produced by the ion exchange (Table 2) is in reasonable agreement with the theoretical analysis (Tojek and Green, 1989). For ion-exchanged soda lime silica glass, it has been found that surface compression can also give substantial benefits in terms of contact damage resistance. For example, it was found that indentation loads ~200g were sufficient to nucleate cracks on a stress-free surface but on ion-exchanged surfaces, loads in the range 1 to 2 kg were necessary (Tandon and Green, 1989).

REFERENCES

Anstis, G. R., P. Chantikul, B. R. Lawn and D. B. Marshall. (1981). A critical evaluation of indentation techniques for measuring fracture toughness, J. Am. Ceram. Soc., 64, pp. 533-43.
Becher, P. F., T. N. Tiegs, J. C. Ogle and W. H. Warwick. (1986). Toughening of ceramics by whisker reinforcement. In, R. C. Bradt, A. G. Evans, F. F. Lange and D. P. H. Hasselman (Eds.), Fracture Mechanics of Ceramics, Vol. 7, Plenum Press, New York, pp. 61-73.
Beck, R. J. (1989) Strength statistics of ion-exchanged glass, BS

Thesis, The Pennsylvania State University.

Budiansky, B., Hutchison, J., and Lambroupolos, J. C. (1983). Continuum theory of dilatant transformation toughening in ceramics, _Int. J. Solids Struct._, _19_, pp. 337-55.

Clarke, D. R., and K. T. Faber. (1987). Fracture of ceramics and glasses, _J. Phys. Chem. Solids_, _48_, pp. 1115-57.

Cook, R. F., and Clarke, D. R. (1988). Fracture stability, R-curves and strength variability, _Acta Metall._, _36_, pp. 555-62.

DaSalvo, G. J. (1970). Theory and structural design applications of Weibull statistics. Report WANL-TME-2688, Westinghouse Electric Corporation, Pittsburgh.

Davidge, R. W. (1979). _Mechanical Behavior of Ceramics_, Cambridge University Press, Cambridge, England.

Evans, A. G. (1972). The strength of brittle materials containing second-phase dispersions, _Phil. Mag._, 26, pp. 1327-44.

Evans, A. G. (1979). Structural and microstructural design in brittle materials. Special Fifth Year Report, ARPA/AFML Contract F33615-74-C-5180. Prepared by D. O. Thompson and R. B. Thompson, pp. 200-14.

Evans, A. G., and K. T. Faber (1984). On the crack growth resistance of microcracking brittle materials, _J. Am. Ceram. Soc._, _67_, pp. 255-60.

Evans, A. G., and R. M. Cannon. (1986). Toughening of brittle solids by martensitic transformations, _Acta Metall._, _34_, pp. 761-800.

Faber, K. T., and A. G. Evans (1983a). Crack deflection processes - I. Theory, _Acta Metall._, _31_, pp. 565-76.

Faber, K. T., and A. G. Evans (1983b). Crack deflection processes - II. Experiment, _Acta Metall._, _31_, pp. 577-84.

Faber, K. T., and A. G. Evans (1983c). Intergranular crack deflection processes in silicon carbide, _J. Am. Ceram. Soc._, _66_, pp. C94-96.

Green, D. J., J. E. Ritter, Jr, and F. F. Lange. (1982). Fracture behavior of low density fibrous silica, _J. Am. Ceram. Soc._, _65_, pp. 141-46.

Green, D. J. (1983a). Microcracking mechanisms in ceramics. In, R. C. Bradt, A. G. Evans, F. F. Lange and D. P. H. Hasselman (Eds.), _Fracture Mechanics of Ceramics_, Vol. 5, Plenum Press, New York, pp. 457-78.

Green, D. J. (1983b). Fracture toughness predictions for crack bowing in brittle particulate composites, _J. Am. Ceram. Soc._, _66_, pp. C4-5.

Green, D. J. (1983c). Non-destructive evaluation of low density fibrous ceramics. In, D. O. Thompson and D. E. Chimenti (Eds.), _Review of Progress in Quantitative Nondestructive Evaluation_, Vol 2A, Plenum Press, New York, pp. 651-61.

Green, D. J. (1988). Micromechanisms of brittle failure in ceramics. In, W. R. Tyson and B. Mukherjee (Eds.), _Proceedings of the International Symposium on Fracture Mechanics_, Pergamon Press, New York, pp. 19-47.

Green, D. J., R. H. J. Hannink, and M. V. Swain (1988). _Transformation Toughening of Ceramics_, CRC Press, Boca Raton, Florida.

Hutchinson, J. W. (1987). Crack tip shielding by microcracking in brittle solids, _Acta Metall._, _35_, pp. 1605-19.

Kendall, K., N. McN. Alford, S. R. Tan and J. D. Birchall, (1986). Influence of toughness on Weibull modulus of ceramic bending strength, _J. Mater. Res._, _1_, pp. 120-23.

Kirchner, H. P. (1979). _Strengthening of Ceramics; Treatments, Tests and Design Applications_, Marcel Dekker, New York.

LaCourse, W. C. (1972). The strength of glass. In, L. D. Pye, H. J. Stevens and W. C. LaCourse, (Eds.), _Introduction to Glass Science_, Plenum Press, New York, pp. 451-512.

Lange, F. F. (1970). Interaction of a crack front with a second phase dispersion, *Phil. Mag.,* *22,* pp. 983-92.

Lange, F. F. (1986).Processing-related fracture origins: IV, elimination of voids produced by organic inclusions, *J. Am. Ceram. Soc.,* *69,* pp. 66-69.

Lawn, B. R. and T. R. Wilshaw. (1975). *Fracture of Brittle Solids,* Cambridge University Press, Cambridge, England.

Lawn, B. R. (1983).The indentation crack as a model surface flaw. In, R. C. Bradt, A. G. Evans, F. F. Lange and D. P. H. Hasselman (Eds.), *Fracture Mechanics of Ceramics,* Vol. 5, Plenum Press, New York, pp. 1-26.

Marshall, D. B., A. G. Evans, B. T. Khuri-Yakub, J. W. Tien and G. S. Kino. (1983). The nature of machining damage in ceramics, *Proc. R. Soc. London,* *A 385,* pp. 461-75.

Marshall, D. B., M. D. Drory, and A. G. Evans. (1983). Transformation toughening in ceramics. In, R. C. Bradt, A. G. Evans, F. F. Lange and D. P. H. Hasselman (Eds.), *Fracture Mechanics of Ceramics,* Vol. 6, Plenum Press, New York, pp. 289-307.

Marshall, D. B., B. N. Cox and A. G. Evans (1985) The mechanics of matrix cracking in brittle-matrix fiber composites, *Acta Metall.,* *33,* pp. 2013-21.

Marshall, D. B. (1986). Strength characteristics of transformation-toughened zirconia, *J. Am. Ceram. Soc.,* *69,* pp. 173-80.

Marshall, D. B. and J. E. Ritter, Jr. (1986). Reliability of advanced structural ceramics and ceramic matrix composites - A review, *Am. Ceram. Soc. Bull,* *66,* pp. 309-17.

McMeeking, R. M., and A. G. Evans. (1982). Mechanics of transformation toughening in brittle materials, *J. Am. Ceram. Soc.,* *65,* pp. 242-46.

Orenstein, R. M., and Green, D. J. (1989). The use of dynamic resonance as a means of reliability analysis for structural ceramics. 91st Annual Meeting of The American Ceramic Society, Indianapolis.

Ritter, Jr., J. E. (1978). Engineering design and fatigue failure of brittle materials. In, R. C. Bradt, A. G. Evans, F. F. Lange and D. P. H. Hasselman (Eds.), *Fracture Mechanics of Ceramics,* Vol. 4, Plenum Press, New York, pp. 667-86.

Ritter, Jr., J. E. (1983). Assessment of reliability of ceramic materials. In, R. C. Bradt, A. G. Evans, F. F. Lange and D. P. H. Hasselman (Eds.), *Fracture Mechanics of Ceramics,* Vol. 5, Plenum Press, New York, pp. 227-51.

Swain, M. V., and L. R. F. Rose. (1986). Strength limitations of transformation-toughened zirconia alloys, *J. Am. Ceram. Soc.,* *69,* 511.

Tojek, M. M., and D. J. Green. (1989). Effect of residual surface stress on the strength distribution of brittle materials, *J. Am. Ceram. Soc.,* to be published.

Tandon, R., and D. J. Green. (1989). Unpublished Data.

Mechanical properties of silicon nitride particulate composites

T.B. Troczynski, D. Ghosh and S. Das Gupta

The Electrofuel Mfg. Co. Ltd., Toronto, Ontario, Canada, M6K 1W8

ABSTRACT

Ceramic/ceramic particulate composite based on Si_3N_4 and a carbo-nitride dispersed phase is developed and tested for bend strength, hardness, fracture toughness and elevated temperature deformation characteristics. The dispersed pariculate phase allows for better control of microstructure development.

KEYWORDS

Silicon nitride, ceramic/ceramic composites, strength, fracture, reliability, stress relaxation.

INTRODUCTION

Silicon nitride is a leading candidate for applications of high-technology ceramics under extreme conditions of high tempera-ture, stress, wear and thermal shock. Due to the nature of its cova-lent bonding, however, it can not be fully densified by solid-state sintering of pure material, even at elevated pressures (e.g. HIP-ping). In fact all dense Si_3N_4-based ceramics are multiphase materials, containing residual impurities and sintering additives. These can form continuous grain-boundary phases determining high-temperature properties of the material (Jack,1976). Si_3N_4 for high-temperature applications is usually sintered with the assistance of yttrium (or La, Ce, Nd etc.) compounds and alumina. As all silicon nitride powders contain a surface layer of silica, the grain-boundary phase in sintered materials is a complex glass containing all involved ions.

Two major approaches to improve high-temperature properties of Si_3N_4-based ceramics involve A:crystallisation of the inter-granular glass into refractory compounds of yttria, silica and alumina (for example, yttria-alumina garnet $5Al_2O_3 \cdot 3Y_2O_3$ or yttria-silicates $Y_2O_3 \cdot nSiO_2$, n=1, 1.5, 2) and B: formation of solid solutions by substitution of Si by Al and N by O, resulting in SIALON. In fact, the processes A and B can proceed simultaneously and spontaneously, leading sometimes to undesired final phase compo-sition . Both approaches are only partially successful. It is dif-ficult to achieve complete crystallisation of the grain boundary phases, especially if it requires substantial compositional changes (e.g. the garnet formation). New developments in this area involve discovery of glasses crystallising with little compositional change in the system containing Nd_2O_3 (Lewis, 1988). Solid solubility of the intergranular phase is possible only for aluminum and oxygen in β'-Si_3N_4. Metallic ions of the sintering additive (Y) are partially soluble only in α'-Si_3N_4, the phase of generally lower toughness and higher hardness.

Mechanical properties of dense (sintered or hot pressed) Si_3N_4-based ceramics are sensitive to original powder morphology, chemistry and processing as well as thermal treatment history. The reported room-temperature values of mechanical properties vary in wide range (bend strength 400-1000 MPa, fracture toughness 3-10 MPa√m, Vickers hardness 13-20 GPa). Part of the scatter results from different techniques of the sample preparation and measurement procedures. The scatter of high-temperature properties is additionally sensitive to amount and crystallinity of intergranular phases.

Fracture toughness of silicon nitride ceramics (and therefore room-temperature strength, through the Griffith relation) is decided by the amount and morphology (i.e. aspect ratio) of elongated grains of β'-Si_3N_4 (Wotting, 1988). Hardness of these materials is more sensitive to density and phase composition than morphology (Babini,1987).

Most structural ceramic applications demand high strength, hardness and toughness. One of the approaches of microstructural engineering aimed at maximization of these properties is exploration of particulate composite systems. Positive effect of SiC dispersion on mechanical properties of silicon nitride has been shown previously (Lange, 1973, Buljan, 1987c, Greil, 1987). The fracture toughness of Si_3N_4 matrix was improved when coarse-grain ($^-30$ μm) SiC particles were utilised.
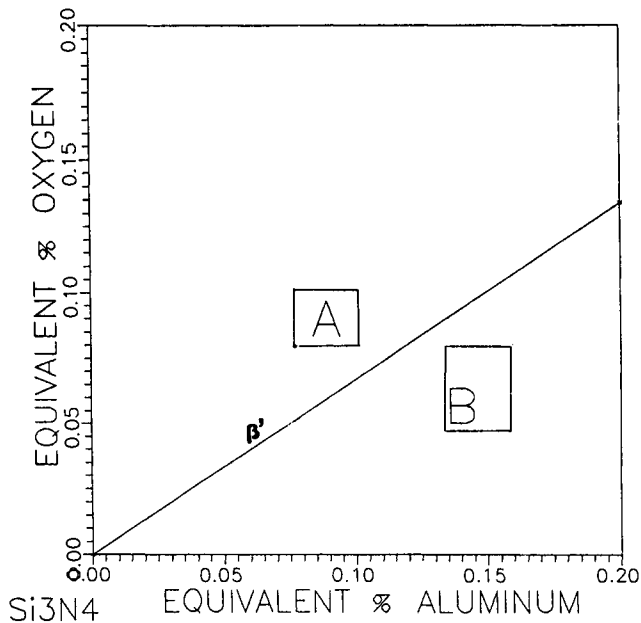
Fig. 1. Compositions of materials type A and B projected on aluminum/oxygen equivalent plane.

In this paper we present results of investigation of Si_3N_4-based particulate composites carried out at Electrofuel under the Industrial Research Assistance Progrm (IRAP/NRC). A number of carbide/nitride phases (called later MCN) and SiC particles were distributed in Si-Al-O-N-Y matrix for microstructural refinement and improvement of tribological properties. The materials (pure and composite) were tested for flexular strength and short-term deformability in a wide range of temperatures. Room-temperature data includes also hardness, fracture toughness and elastic properties.
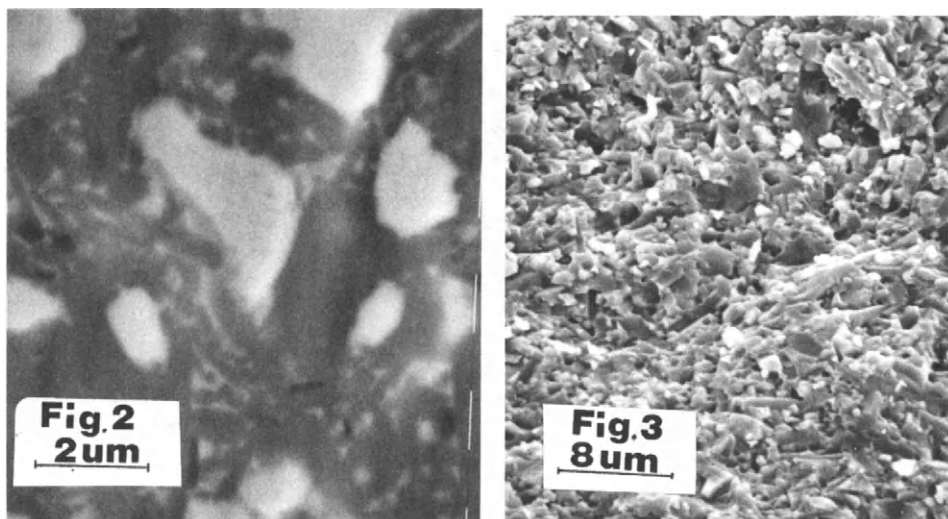
Fig. 2. Hot pressed carbonitride/Si_3N_4 composite - polished section.

Fig. 3. Hot pressed carbonitride/Si_3N_4 composite - fracture surface.

EXPERIMENTAL PROCEDURES

The matrix material compositions fall within region A or B when projected on the equivalent oxygen/equivalent aluminum plane of the Si-Al-O-N-Y system , Fig. 1. The composites contained 15 to 25 vol% of MCN (the dispersed phase) and 4 to 9 wt% Y_2O_3 and Al_2O_3 (the sintering additives). The materials were hot pressed (HP) to 99.5% relative density at 1700 to 1750°C or pressureless sintered to 98.5% relative density at 1800°C. Typical microstructures of the hot pressed composites are shown in Fig. 2 and Fig. 3. The high-magnification micrograph of Fig. 2 (bar=2 μm) presents the polished section of the composite based on an A-type matrix. The carbonitride particles (large light grains) limit growth of the elongated β'-Si_3N_4 grains (grey). The intergranular phase appears brighter than the silicon nitride phase due to segregation of yttria, which is insoluble in β'-Si_3N_4. The lower magnification micrograph (Fig. 3, bar=8 μm) is a fracture surface of the composite based on B-type matrix. Both materials exhibit fine microstructure, with the grain thickness limited to ~2 μm.

The composites and pure matrix materials were tested for four-point-bend strength (span ratio 40/20mm and 25.4/12.7 mm at room temperature and 20/10 mm at elevated temperatures), fracture toughness at room temperature using 98N Vickers indentation (Niihara, 1982) and controlled-flaw fracture in 4-point bending (Chantikul, 1981); Vickers hardness; elastic properties (ultrasonic pulse-echo technique, Bhardway, 1986).

Load relaxation (LR) at 1000-1400°C allowed the determination of short-term deformation properties of the hot pressed and sintered materials. According to analysis of behaviour of viscoelastic solid (Krausz, 1975), relaxation of stress S in time t under constant strain conditions can be described by formula (1) :

$$Ln(S/S_0) = C \cdot Ln (D \cdot t + 1) \qquad (1)$$

where $S=S_0$ at $t=0$ and C and D are constants characteristic for the material and environment. For Si_3N_4 tested at elevated temperatures C $\approx$ 1 and therefore stress relaxation is a linear function of time :

$$S = S_0 - R \cdot t \qquad (2)$$

where R [MPa/min] is characteristic for the material at a given temperature. At high temperatures the testing system deforms along with the specimen material so it is difficult to maintain strictly constant strain conditions. The measured values of the load relaxation were corrected for relaxation of the testing system. The experimental procedure involved the following steps for each temperature (typically 1000,1100,1200 and 1300°C): -loading of the machine and the bending rig, but without the sample, to a pre-calculated load level that would result in 100 MPa stress in subsequently bend sample; -record of the load relaxation at fixed grips, in the machine only (curves 'A' in a schematic Fig. 4) and determination of slope 'm'; -loading and record of fixed-grips load relaxation for the machine with test sample (curves 'B' in Fig. 4) and calculation of slope 'M'; -determination of the load relaxation due to deformation of the sample only :

$$P = P_0 - (M - m) \cdot t \qquad (3)$$

and the bend stress relaxation :

$$S = S_0 - R \cdot t \qquad (4)$$

where $\qquad R = 1.5 \cdot (M - m) \cdot (L1 - L2)/(B \cdot W^2) \qquad (5)$

L1 and L2 are the bending spans, B and W the specimen's depth and width respectively.

Analysis of the R-parameter vs. temperature allowed for determination of thermal loss-of-rigidity points in short-termstressing applications. The information generated by LR studies, in conjunction with bend strength vs. temperature data, defines application limits for Si_3N_4 cutting tools.
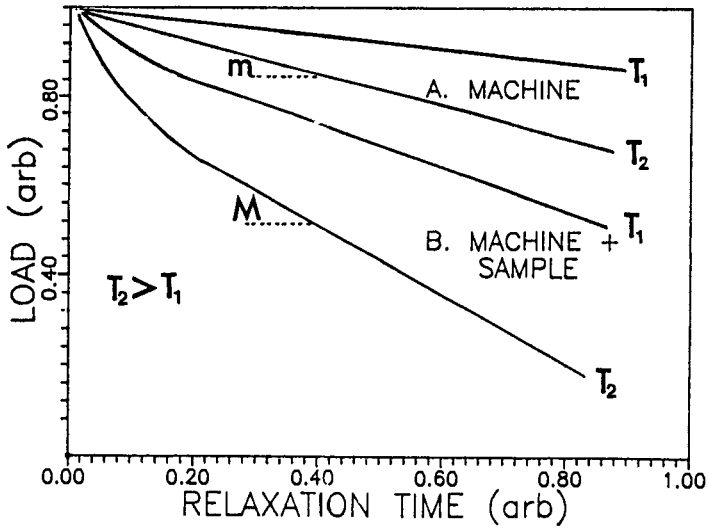
Fig. 4. Schematic representation of the load-relaxation test output.

TABLE 1 Room Temperature Properties of
Si₃N₄ Particulate Composites

PROPERTY	B1-PLS		B2		A
	PURE	COMPOSITE	PURE-PLS	COMP. - HP	COMPOSITE-HP
STRENGTH MPa(STD)	463 (52)	538 (40)	535 (50)	685 (62)	742 (80)
WEIBUL MODULUS	7.8	11.1	9.9	11.1	9.8
FRACTURE TOUGHNESS MPa√m	7	7	8	7	7
CRITICAL FLAW, μm	60	40	60	30	20
HARDNESS,GPa	17	16	17	18	15-16
WEAR RESIST. FACTOR, W	18	17	20	18	17
YOUNGS MODULUS,GPa	300	330	300	350	330
POISSON RATIO	0.27	0.26	0.27	0.26	0.26

RESULTS AND DISCUSSION

Table 1 presents room-temperature   properties   of   MCN/Si$_3$N$_4$
particulate composites and pure matrix materials type A,B1 andB2.
Table 2 presents the effect of additional dispersion of SiC particles
(10 and 20vol%) in A-type composite. Hardness of the multi-
particulate composite ceramic increases at unchanged fracture
toughness and elastic properties. The results of bend strength
testing (25°C) appear as Weibull plots in   Fig.   5A to   5E. The
elevated temperature   strength and relaxation data for HP and PLS
materials appear in Fig. 6 and Fig. 7.
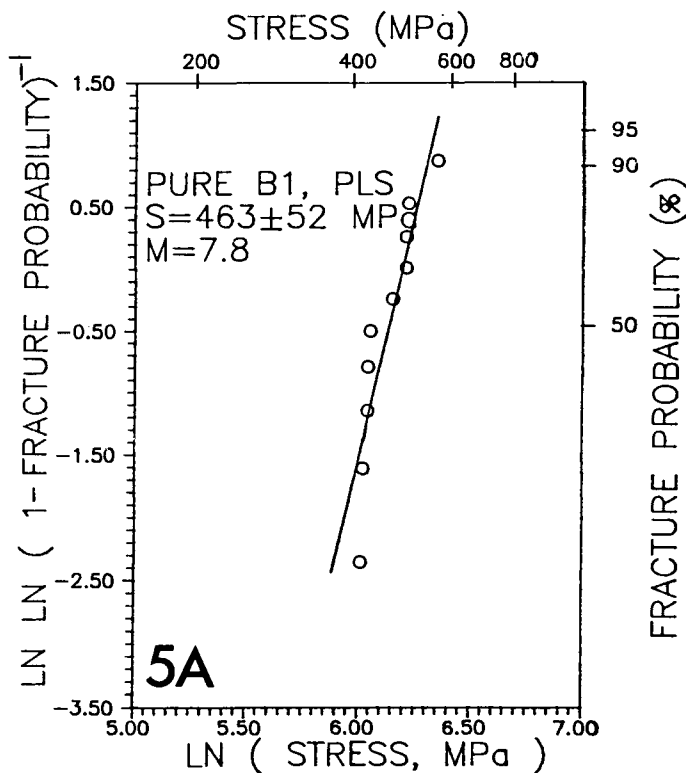
Fig. 5.   Room temperature bend strength for Si$_3$N$_4$-based ceramics:
         (A) Pure B1, PLS.   (B) Composite B1, PLS. (C) Pure B2, PLS.
         (D) Composite B2, HP. (E) Composite A, HP.
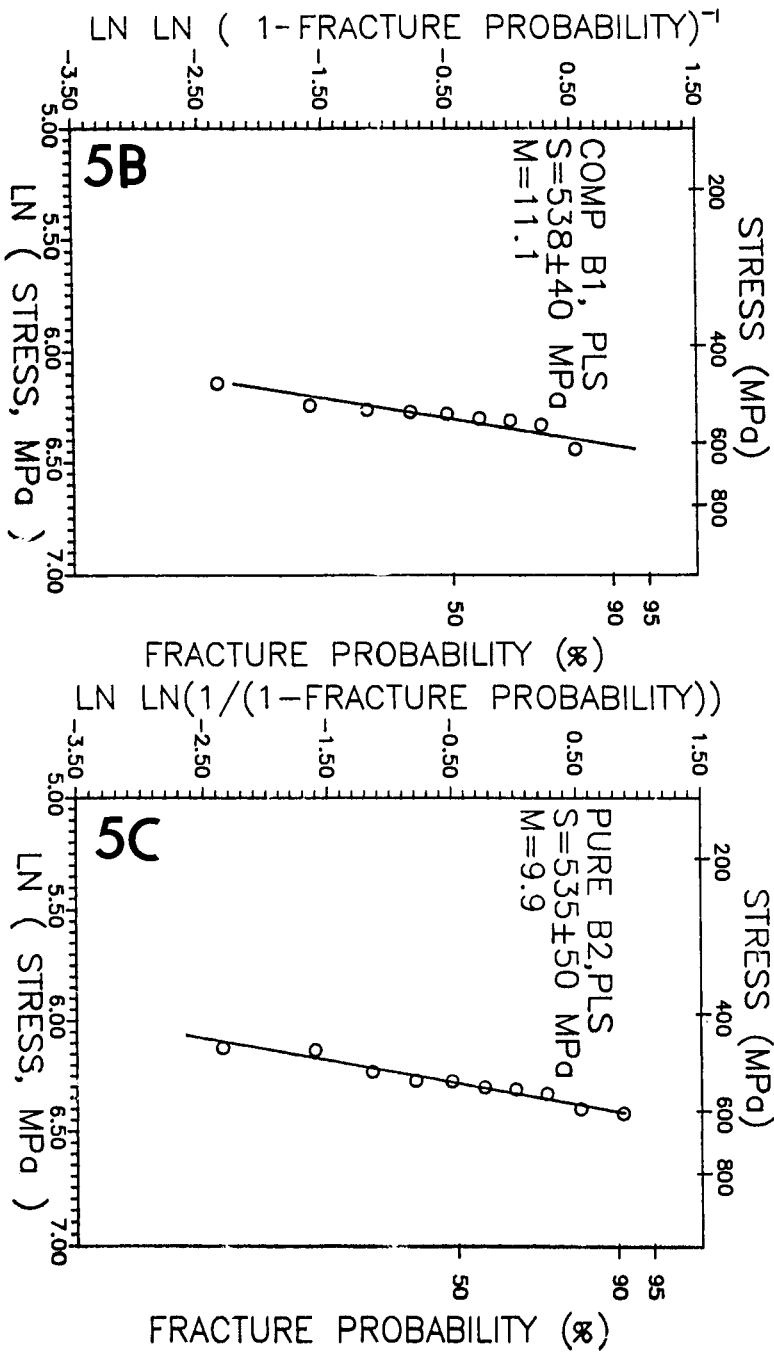
Fig. 5. Continued.
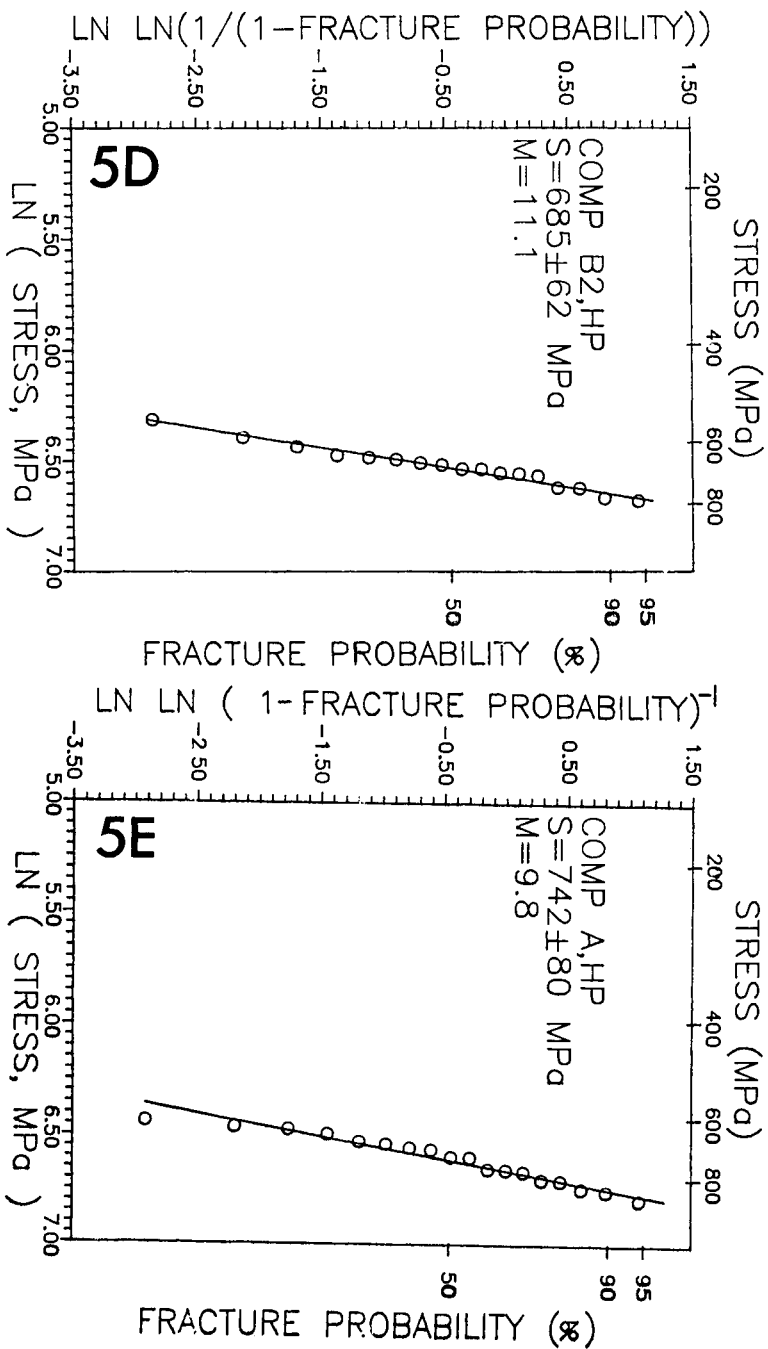
Fig. 5. Continued.

Figure 5A is the stress vs. fracture probability diagramfor PLS-B1 material and Fig. 5B for the same ceramic containing 15 vol% MCN particles. Dispersion of the particulate phase results in an increase of the average strength by ˜20%. Also the Weibull modulus increases by ˜30%. Since the particles dispersion does not appreciably change the material's fracture toughness, Table 1, the effect should be attributed to microstructural refinement (e.g. grain and/or flaw size reduction). Careful examination of the microstructure presented in Fig. 2 provides evidence of the grain-growth limitation by the carbonitride. Indirect proof of this conclusion is average size of the fracture-initiating flaw in both materials (calculated according to the Griffith equation). For the particulate composite, the critical flaw size decreases to 40 μm, compared to 60 μm for similarly processed matrix material B1, as shown in Table 1.

The concurrent effect of MCN dispersion and hot pressing for the materials based on B2 matrix is shown in Figs. 5C and 5D. Hot pressing of the composite material reduces theaverage fracture initiating flaw size by half, to ˜30 μm. The effect is emphasised by higher fracture toughness of the pressureless sintered, pure materials B2 with low additive content, Tab. 1.The hot pressed ceramic based on type A matrix (e.g. low-Z, higher-oxygen sialons), exhibit the highest bend strength,Fig. 5E. The average strength of 742 MPa at moderate fracture toughness of 7 MPa√m reveals the effect of improved microstructure (20 μm flaw size). This is achieved at a sacrifice of the composite hardness (15-16 GPa vs. 17-18 GPa for the HP materials based on type B matrix).

The values of fracture toughness [MPa√m] and hardness [GPa] can be combined into a wear-resistivity-factor $W = K^{0.75} \cdot \sqrt{H}$ (Buljan, 1987b) allowing for anticipation of the material's wear resistivity at room temperatures. For the particulate composites W varies in the range 17 to 18. For the pure pressureless sintered materials, W varies in the range 18 to 20 due to strong effect of the fracture toughness on the wear resistivity factor W.

The advantageous local properties of the ceramic/ceramic composites (i.e. microstructurally controlled fracture toughness, hardness and thus wear resistivity) can only be utilised in conjunction with advantagous global properties (i.e. narrow distribution of flaw sizes). The above results prove that optimization of the two parameters can be approached and achieved in silicon nitride particulate composites.

Table 2   Effect of SiC Particles on A-MCN-Si$_3$N$_4$
             Composite Properties.

vol% SiC	H, GPa	K, MPa√m	E, GPa	Poisson Ratio
0	15-16	7	332	0.27
10	17	6.3	330	0.26
20	17-18	7.3	-	-

Fig. 6 (bend strength) and Fig. 7 (stress relaxation) present results of elevated temperature testing. The only significant difference can be observed between materials obtained by hot pressing and by presureless sintering. The bend strength is constant up to ˜1000°C at ˜700 MPa for HP and ˜500 MPa for PLS materials. Loss of strength in the range 1100-1200°C to the level of 300 MPa is common for both HP and PLS pure and composite materials. Dispersion of the carbonitride has no effect on elevated-temperatures mechanical properties of the composite. Short-term load relaxation data reveal similar trends. The stress relaxation below 1100°C is smaller than 1 MPa/min or 1%/min of the initial stress. PLS materials relax faster than HP materials, pure or composite. The stress relaxation increases significantly between 1100 and 1200°C with narrowing difference between PLS and HP ceramics. No attempt was undertaken to effect values of bend strength or stress relaxation by crystalization of the grain boundary glassy phase. We expect that the crystalization heat treatment will extend short term mechanical stability of Si_3N_4 particulate composites beyond presently determined edge of 1100°C.
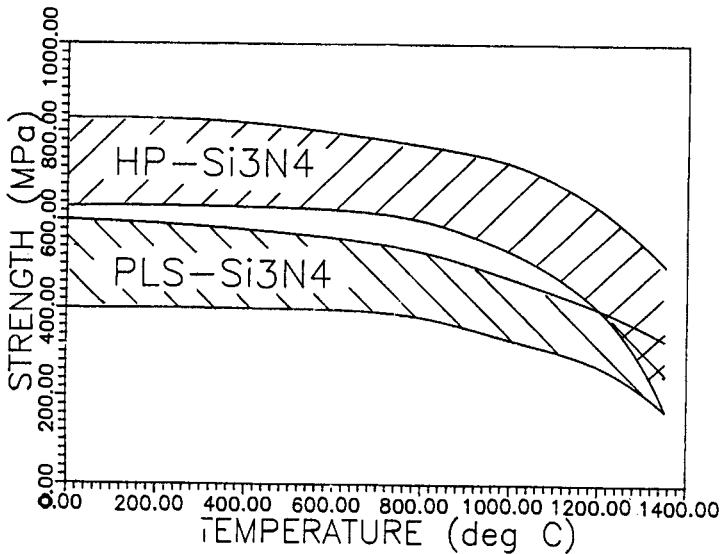
Fig. 6. Compilation of elevated-temperature strength of pure and composite, hot pressed and pressureless sintered Si_3N_4-based ceramics.
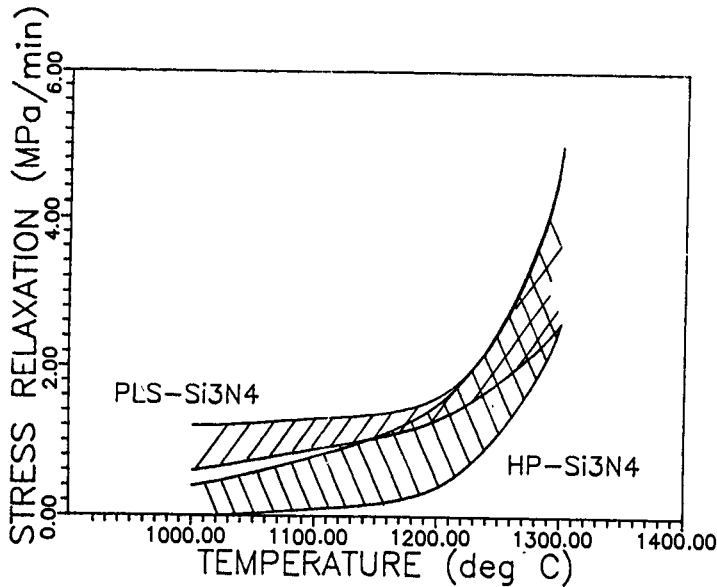
Fig. 7. Compilation of elevated-temperature stress-relaxation parameters R for pure and composite, hot pressed and pressureless sintered Si_3N_4-based ceramics.

CONCLUSIONS

Ceramic/ceramic particulate composites were developed for Si_3N_4 matrix material with dispersion of a number of carbide/nitride particles. The optimized processing routes resulted in high density materials, presureless sintered and hot pressed. The effect of a second carbonitride phase was studied for low alumina/high oxygen (type A) and high alumina/low oxygen (type B) matrices. The principal effect of the second phase is microstructural refinement. The particulate composites reveal better bend strength and reliability whileother mechanical properties (hardness, fracture toughness, temperature dependence of strength and short-term stress relaxation) remain unchanged.

Application of hot pressing (instead of presureless sintering) results in a decrease of the processing defects at a 10-20% sacrifice in the fracture toughness. The loss of toughness is partially offset by generally higher hardness of the hot pressed materials.

Acknowledgement

REFERENCES

Babini, G. N., A.Bellosi and C.Galassi (1987). In P. Vincenzini (Ed.)
   High Tech Ceramics, Elsevier Science Publishers, Amsterdam, pp.
   1371-1380.
Bhardwaj, M. C. (1986). Principles and methods of ultrasonic
   characterisation of materials. Adv. Ceram. Mater. 1, 311-324.
Buljan, S. T., A. E. Pasto and H. J. Kim (1989). Ceramic whisker- and
   particulate composites: properties, reliability and applications.
   Am. Ceram. Soc. Bull. 68, 387-394.
Buljan, S. T., V. K. Sarin (1987a). Silicon nitride based composites.
   Composites 18, 99-106.
Buljan, S. T. and V. K. Sarin (1986). Design and wear resistance of
   Si_3N_4-based composites. In E.A. Almond, C. A. Brookes and R. Warren
   (Ed.), Inst. Phys. Conf. Series No. 75, Adam Holger Ltd, Bristol,
   pp. 873-882.
Buljan, S. T., J. G. Baldoni and M. L. Huckabee (1987c). Si_3N_4-SiC
   composites. Am. Ceram. Soc. Bull. 66, 347-352.
Chantikul, P., G. R. Anstis, B. R. Lawn and D. B. Marshall (1981). A
   critical evaluation of indentation techniques for measuring fracture
   toughness : II, strength method. J. Am. Ceram. Soc. 64, 539-543.
Greil, P., H. Tanaka and G. Petzow (1987). In P. Vincenzini (Ed.)
   High Tech Ceramics, Elsevier Science Publishers, Amsterdam, pp.
   1011-1022.   `
Jack, K.H. (1976). Sialons and related nitrogen ceramics.
   J.Mat.Sci.,11,1135-1158.
Krausz, A. S. and H. Eyring (1975). Deformation Kinetics, Chapt. 3 :
   Fundamental Deformation Processes, John Wiley & Sons, New York.
Lange, F. F. (1973). Effect of microstructure on the strength of
   Si_3N_4-SiC composite system. J. Am. Ceram. Soc. 56, 445-449.
Lewis, M. H., G. Leng-Ward and C. Jasper (1988). In G. L. Messing
   E. R. Fuller, Jr. and H. Hausner (Ed.), Ceramic Powder Science II,
   The Am. Ceram. Soc., Westerville, OH, pp.1019-1033.
Niihara, K., A. Nakahira and T. Hirai(1984). The effect of
   stoichiometry on mechanical properties of boron carbide, J. Am.
   Ceram. Soc. 67, C-13-C-14.
G. Ziegler, J. Heinrich and G. Wotting (1987). Review : Relationship
   between processing, microstructure and properties of dense and
   reaction bonded silicon nitride. J. Mat. Sci. 22, 3041-3086.

Ultrasonic NDE of advanced ceramics

Patrick S. Nicholson
Ceramic Engineering Research Group, McMaster University,
Hamilton, Ontario, Canada, L8S 4L7

ABSTRACT

The development of a database for the ultrasonic NDE of advanced-ceramic components is described. High frequency (≤ 100 MHz), high power transducer development was involved and the probes are used to examine model spherical inclusions (voids (≥ 20 μm), ZrO_2, MgO, V_2O_5 and Pt inclusions (≥ 30 μm)) in model matrices (glass, crystallized glass and partially stabilized zirconia). Actual frequency spectra obtained from these defects as a function of defect size are compared with their calculated spectra based on scattering theory and very good agreement is obtained. Surface breaking cracks associated with Vickers and Knoop indents in glass and Si_3N_4 are also characterized down to ~30 μm size.

INTRODUCTION

The NDE of advanced ceramics is a vital step in their acceptability. It is also one of the most significant hurdles still to be cleared. Ceramic materials present unique challenges and these will be reviewed. Throughout the discussion it is assumed that NDE of advanced ceramic components means the economic evaluation of 100's to 1000's of components per day. This requirement severely limits the use of exotic techniques. Equipment should be robust and simple, cheap and reliable and above all speedy and accurate. Following metallurgical experience, this means fast ultrasonic scanning or multielement female-configuration static transducers. The required defect resolution in advanced ceramics severely limits the use of X-ray analysis. Surface flaw detection with dye penetrants may not be possible for micrometer-sized defects in ceramics. Conventional metal penetrants are recommended but unproven (1).

This paper reviews the specific problems associated with the evaluation of dense ceramic components. This approach is judged the most useful as a literature-review could leave the reader without a clear perception of the problems. The complexity of the mathematically modelling defects in real ceramics led us to develop a systematic experimental pedagogy. This involved examination of model defects (voids, spherical inclusions, indent-cracks) in model ceramic matrices (glass, crystallized glass, partially-stabilized-zirconia (PSZ)). Initial optical definition facilitated interpretation of the ultrasonic signals and a database was thus created. Regular defect shapes allowed wave physics modelling and prediction methodologies to be developed.

In parallel with the detection of smaller and smaller model defects (≤ 20 μm voids; ≤ 30 μm inclusions and cracks) the development of high frequency (≤ 100 MHz) high-power (≥ 130 dB s.n.r) transducers was pursued. This work is also reviewed.

UNIQUE ULTRASONIC NDE PROBLEMS POSED BY CERAMICS

The overall requirement for the satisfactory NDE of advanced ceramics is the definition of flaws ≤ 10 μm, 10 mm deep in terms of their size, shape and chemistry. A 10 μm flaw in high performance Si_3N_4 can reduce the expected strength from $\simeq 1500$ MPa to $\simeq 250$ MPa. Added to these restrictions are the physical properties of covalent/ionic-bonded ceramic materials, i.e. high sound velocity and attenuation characteristics. Sound velocities are double those in metals reducing the depth of penetration of focussed

ultrasound (V(longitudinal) in Al_2O_3 is 12,000 m/sec). This is equivalent to the higher refractive index effect on focussed light. To increase this depth, larger diameter transducers are needed. This requires larger electrode diameters on very thin piezoelectric diaphragms and the accompanying increase of capacitance renders the poling of these crystals difficult. The dielectric constant (d) of the piezoelectric element of the transducer must be reduced. Thickness coupling (k_t) must be maximized and radial coupling (k_p) minimized to increase element poling efficiency.

As sound passes through an elastic medium, its energy is absorbed. This phenomenon (attenuation) increases almost exponentially with the sonic frequency (2). 10 μm flaws require sonic wavelengths $\simeq 60$ μm i.e. a frequency of ≤ 100 MHz. Attenuation is therefore high so transducer power must be increased if the sound is to penetrate 10 mm. These frequencies require very thin piezoelectric crystals ($\simeq 30$ μm) ($= \lambda/2$). This thickness (t) increases as the sonic velocity in the piezoelectric crystal increases and so capacitance problems reduce. The mechanical strength of such thin piezoelectric crystals becomes a factor. Grain sizes should be $\simeq 2$ μm giving ~16 grains/section. Inclusion defects must be totally absent from the piezoelectric crystal and exaggerated grain growth in these anisotropic systems avoided. Both lead to mechanical breakdown via microcracking at poling voltages. To summarize, ceramic piezoelectrics must have low d, high k_t, low k_p, high sonic velocity, fine grain size and zero defects. The physics and methodology of the ultrasonic characterization of ceramics was recently reviewed (2).

The higher velocity in ceramics is somewhat offset by their lower density and the acoustic impedance (velocity x density) of advanced ceramics is similar to that of metals. For economic reasons, water is used as the scanning couplant in the present work. Although it will always be necessary to NDE finished components, recently the NDE of green ceramics has been investigated (3,4). Whilst making excellent economic sense, such NDE leaves some important fired defects undetected. A number of these are shown in Figure 1 (5).

Defects that develop during sintering often lead to premature failure. Agglomerates have marginally different density to their powder host so will be missed by green NDE. Their enhanced local sintering leads to porosity (Figure 1(a)), a severe flaw only detectable following sintering. Organic inclusions (such as the-fibre-that-was of Figure 1(b)) will also only evidence via ghost porosity following firing. Oxide inclusions of similar acoustic impedance to the host matrix (Al_2O_3 in PSZ, Figure 1(c)) will be undetected. In each case these were the fracture-initiating flaws. The inevitable porosity of greenware must limit the frequency of penetrating ultrasound which in turn limits its resolution. Gross defects such as density gradients and large metallic inclusions can probably be detected, making greenware NDE a limited but valuable economic tool.

Many papers report the "detection" of defects (6,7) with indications of the size to 25 μm at depths of 3 mms but the results are qualitative. Use of the reliability methodologies recently developed (8) require accurate knowledge of the flaw size and modern components require their quantitative characterization at 10 mm depth. At the end of the 1970's activity in ultrasonic NDE of ceramics reached a peak. The Stanford group reported the use of high frequency contact transducers to detect bulk defects (9). They also reported the use of wedge transducers to detect surface cracks down to 60 μm size (10). The frequencies used precluded penetration and contact transducers excluded scanning, both requirements for the economic NDE of real components.

The acoustic microscope has been used (11) to detect and characterize surface and subsurface defects in Si3N4 and SiC. 100 μm pores and cracks were detected. A 150 μm diameter flaw 400 μm deep in hot pressed SiC was detailed. Clearly the acoustic microscope is a useful research tool but as an on-line evaluator of up to 1000 components/day its value is limited. A recent development is scanning laser acoustic microscopy (SLAM). This technique has been used to detect 20 to 430 μm voids up to 2 mm deep. A plastic coverslip is placed on the ceramic to give a reflective coating. Voids between 50 and 400 μm diameter in Si3N4 were detected with 90% probability if within 1 μm and 1400 μm of the surface respectively (12). Depth, time and preparation limitations preclude this technique from on-line NDE of advanced ceramic components.

WAVE PHYSICS MODELS FOR DATA-BASE DEVELOPMENT OF DEFECTS IN CERAMICS

The general failure of the "head-on" approaches to defect characterization in real advanced ceramics led to the data-base development pedagogy via model defects in model ceramic matrices described herein. The use of spherical scatterers means sensible wave-physics analysis can lead to realistic predictions.

An important piece of information is contained in the first peak of the reflected signal from a defect in the time-domain. If the reflector is a void, its acoustic impedance (density × velocity of sound) is zero so its reflective factor is negative i.e. the first peak of the time-domain reflection is phase inverted. If the reflector has an acoustic impedance (i.e. solid) the initial peak is positive and no such phase inversion occurs. Qualitative size information for an inclusion is also contained in the time signal. If the scatterer is a large inclusion, its initial reflection and that from the transmitted wave exiting later are differentiable. Their time difference can be used to estimate the defect size.

If the chemistry of the defect is known, quantitative size information is contained in the spectrum of reflected frequencies. Any time-domain signal can be constructed from a series of simple-harmonic-waves of different frequency and appropriate amplitude. This process is known as the Fourier transformation and, by plotting the frequencies and amplitudes, a spectrum for the defect in the frequency domain is obtained. This spectrum will be characterized by its frequency at maximum amplitude (FMA) and its full-width-at-half-maximum amplitude (FWHM).

The scattering of a single frequency plane wave has been treated in detail (13). The scattering amplitudes are calculated for individual waves using the continuity of stresses and strains at the interface between a matrix and a spherical inclusion and are functions of the longitudinal and transverse speeds of sound and density of the matrix (C_{11}, C_{t1}, and ℓ_1) and same parameters for the inhomogeneity (C_{12}, C_{t2}, and ℓ_2). In the reference these scattering amplitudes are used to determine the total scattering cross-section for the wave whereas our interest lies in the scattering of the longitudinal waves which are given by the scattering amplitude A_m. These can then be used to determine the pressure at the transducer as:

$$p_r(k) = P_R \, k \, a \, (1 + i) \exp\{-ikR\} \sum_{m=0}^{\infty} (2m + 1) A_m \tag{1}$$

where the transducer to inclusion distance, R, which is also the focal length of the transducer, is much larger than the sphere radius, a. The quantity i is $\sqrt{-1}$. The pressure, p_r, is a function of the wavenumber of the longitudinal ultrasound in the matrix, k, and P_R is the pressure at the site of the sphere. The pressure amplitude at the focus of the transducer can be determined by expanding the equations of O'Neil (14)

$$p(\omega) = \partial \omega^2 S_f \, \frac{\exp[i(\omega t - k' \Delta z)]}{k'} \tag{2}$$

where

$$k' = (k/2)\{1 + [1 + (D/2A)2]1/2\} \tag{3}$$

Here D is the diameter of the transducer and ω is the angular frequency of the wave such that $\omega = C_{11}k = 2\pi f$ where f is the frequency. Δz is the distance from the center of the sphere which is at the focal point of the transducer. The quantity S_f is the amplitude of particle oscillation at the site of the sphere. This value is not easily determined due to attenuation within the couplant and reflections at the sample surface. Therefore, it is better to express the pressure $p(\omega)$, and hence $p_r(k)$, in terms of relative amplitudes.

Using these equations, it is possible to determine the relative amplitude of a wave of single frequency backscattered from a spherical inclusion at the focal point of a transducer. An incoming pulse of ultrasound consists of a distribution of frequencies with different amplitudes which can be estimated from the reflection off a flat surface (usually chosen as the front reflection) in the focal plane of the transducer (15). Each element of the distribution is then multiplied by the corresponding frequency in the sphere's response spectrum to obtain a spectrum of backscattered frequencies. It is easier to handle a

mathematical distribution with fixed parameters for the frequency (f) distribution of the incoming pulse. The distribution chosen to approximate that of the pulse is Gaussian with the following form;

$$p_i(f) = p_a \exp\left\{-4\ell n(2)\left(\frac{f-f_a}{f_{FWHM}}\right)^2\right\} \qquad (4)$$

where p_i is the pressure of the incoming pulse and p_a is the pressure at the maximum amplitude which will be taken as a unity. f_a is the frequency at the maximum amplitude (FMA) or center frequency of the distribution and f_{FWHM} is the frequency full width at half the maximum amplitude (FWHM) of the distribution.

The total expected pressure at the transducer for a spherical inhomogeneity in the focal zone of the transducer can be written as:

$$P_T(f) = \frac{C_{11}a}{2\pi f} \exp\left(-i\frac{C_{11}R}{2\pi f}\right) \exp\{-4\ln(2)\left(\frac{f-f_a}{f_{FWHM}}\right)^2\} \sum_{m=0}^{\infty}(2m+1)A_m \qquad (5)$$

where $P_T(f)$ is the relative pressure for the backscattered longitudinal wave. The summation over the scattering amplitudes will modify the Gaussian shape of the signal spectrum so the effect of density and sound velocities of both matrix and inclusion and the inclusion dimension can be measured from the change in FMA and FWHM of the magnitude spectra. The differences are attributable to resonances of the sphere with certain frequency components present in the sound pulse which physically represent creeping waves that circumnavigate the sphere (16).

The theoretical and experimental FMA and FWHM values will be compared for model defects in model ceramic matrices.

THE DEVELOPMENT OF HIGH FREQUENCY, HIGH POWER ULTRASONIC TRANSDUCERS

This aspect becomes important as the targetted defect size decreases. Central are high quality piezoelectric ceramics. The parametric goals are low dielectric constant (<200), low dielectric loss ($<.01$), high sound velocity (V >5 km/sec), small grain size (~2 μm), density $\sim100\%$ theoretical, low radial coupling ($k_p<10\%$), high thickness coupling ($k_t>50\%$), low internal damping ($Q_m<200$) and high transmitting (d_{33}) and receiving (g_{33}) coefficients. The most important practical aspect of high frequency transducer construction is the working thickness of the element. This must be 0.5λ so, for 100 MHz, t = 0.005 V. Lead metaniobate (LMN) and sodium potassium niobate (SPN) ceramics were developed by sintering and hot-pressing. Their properties are summarized in Tables 1 and 2.

High frequency planar transducers of 64 and 83 MHz were developed using SPN elements of 56 and 40 μm thickness respectively. The effective diameter of the positive gold sputtered electrodes were 4 mm and 2.5 mm respectively. The capacitance of the 85 MHz element was 0.46 μF and the inductance needed to offset the resulting low capacitance was 7.6 nh. A unique property of these SPN transducers was their excitability at three frequencies via tone burst excitation. Figure 2 shows the output of the 85 MHz SPN transducer at 85, 65 and 30 MHz. Beam profiles for 57 and 70 MHz SPN transducers focussed with a curved crystabond lens are shown in Figures 3 and 4. The -3 dB envelope of these transducers is significant. The focal diameter decreases with increasing frequency (for a 60 MHz SPN transducer excited at 60, 30 and 15 MHz, see Figure 5). The excitation of SPN transducers at 3 frequencies means that once a defect is located at the lower frequency, it can be inspected in detail without moving the transducer.

LMN-BaO elements were lapped to 28 μm and generated 100 MHz frequency (Figure 6). 2 mm diameter gold electrodes were applied. These elements have the advantage that they can be excited by conventional impulse excitation equipment.

Table 1   Piezoelectric, Dielectric and Elastic Properties of LMN Ceramics*

	LMN	(+Rb$_2$O)	(+Cs$_2$O)	(+BaO(1))	(+BaO(2))	(+BaO(3))
Density (gm/cc)	6.33	6.36	6.36	5.50	5.91	5.70
Dielectric constant	330	340	342	180	700	1400
Dissipation Factor (@1 kHz)	0.06	0.06	0.06	0.02	0.01	0.015
Piezoelectric Coefficients						
$k_t\%$	42	44	40	50	50	50
$k_p\%$	~14	~14	~14	>12	>10	>10
$d_{33}(10^{-12}$ C/N)	77	78	70	68	105	170
$g_{33}(10^{-3}$ Vm/N)	26	26	25	41	17	13.5
Qm	<20	<20	<20	500	<15	<20
Sound velocity (km/s)	4.4	4.5	4.4	6.8	4.4	4.8

* Ceramics available from BM Hitech, Collingwood, Ontario, CANADA.

Table 2   Piezoelectric, Dielectric and Elastic Properties of SPN Ceramics

	Sintered	Hot-Pressed (Or SF/FD)
Density (gm/cc)	4.28	4.45
Dielectric constant	260	380
Dissipation Factor (@1 kHz)	0.02	0.016
Piezoelectric Coefficients		
$k_t\%$	42	45
$k_p\%$	34	45
$d_{33}(10^{-12}$ C/N)	90	120
$g_{33}(10^{-3}$ Vm/N)	33	33
Qm	140	210
Sound velocity (km/s)	6.5	6.8

The ever thinner elements for higher frequencies display increasing capacitance which opposes high frequency performance. In a series of experiments, the optimum size of the back electrode was determined (17) for different thicknesses of the two groups of elements. Starting with ~100 µm thick elements, electrodes of 1 mm diameter were deposited and the capacitance and signal strength measured. Larger electrodes were deposited over the previous ones and the measurements repeated; the series was: 1, 1.5, 2, 2.5, 3.2, 4 and 5 mm diameter. The elements were lapped down and the experiment repeated. Each series yielded a curve which showed an optimum diameter for the two materials. Fig.7 compares the optimum electrode sizes for SPN and LMN having relative dielectric constants of 400 and 135 respectively. Low dielectric constant materials allow larger electrodes and hence are more powerful.

A focussed 30 MHz transducer was made with an optimised back electrode and a 13 mm radius lens; in spite of the small electrode size an increase in signal round trip efficiency of over 10 dB compared with commercial 6.3 mm diameter transducers was observed.

The focussing of high frequency transducers creates problems of attenuation losses in lenses, especially near the edges where the lenses are thick. With increasing thickness, alternate zones of signal reinforcement and cancellation (Fresnel rings) are generated which distort the output. A lensless focussed transducer, was developed using four quadrant elements positioned in a low pyramid. Scans over the 2.5 mm diameter flat target at different distances revealed a normal beam profile for a 30 MHz transducer. From contour plots at various distances, a beam profile was generated (Fig. 8) indicating the strength of the field at −3 dB, −10 dB and −20 dB. The most useful portion of this transducer lies between 12 and 22

mm. A strong output was recorded and higher frequency lensless focussed transducers are being developed based on this principle.

These transducers were used to examine the model defects in the model ceramic matrices now to be described.

CHARACTERIZATION OF THE MODEL DEFECTS IN MODEL CERAMIC MATRICES

The following systems were examined; glass and voids (30 µm diameter minimum) (18), glass and ZrO_2, MgO and V_2O_5-inclusions (50 µm diameter minimum) (19) crystallized glass and inclusions (20) and fully dense partially-stabilized-zirconia (PSZ) containing Pt inclusions (50 µm minimum diameter) (21). Surface-breaking cracks associated with Vickers and Knoop indents in glass and Si_3N_4 were also examined. The results in comparison with the model developed in Section III will now be presented.

The calculated and measured FMA and FWHM of the frequency spectra are plotted as a function of defect size for voids in glass (Figure 9), ZrO_2 and MgO inclusions in glass (Figure 10) and ZrO_2 in crystallized glass (Figure 11). A density map for a 50 µm Pt sphere in dense PSZ with a locator loop of platinum (100 µm-diameter wire) is shown in Figure 12. A 2 minute scan detected this defect. The FMA and FWHM for Pt spheres in PSZ vs. defect size are shown in Figures 13 & 14.

The agreement between theory and experiment is good. If the type of defect is known, its size can be determined by combination of the FMA and FWHM of its frequency spectrum. The MgO point which plots off the predicted line was shown to be a decohesed defect on polishing to investigate. The depth of the 50 µm Pt inclusion (Figure 12) was 5 mm. In fact <100 µm Pt defects have been detected through 30 mms of PSZ. To use the model it is necessary to know (or estimate) the density and sound velocity of the defects. In some cases the chemistry of inclusion type defects may be unknown. Elastic modulus information is contained in the Franz surface wave that circumnavigates the defect. This wave is presently being investigated as a possible source of chemical information.

Surface-breaking cracks have been examined in glass and Si_3N_4. A display of a Vickers indent and its corner cracks impressed in glass is shown in Figure 15. This defect was examined with the cracked surface next to the transducer with the latter angled 12° to the surface normal. The pyramid and cracks can clearly be seen. The crack lengths are ~100 µm but their width is <5 µm. A similar pattern in hot-pressed silicon nitride but with the indented surface under the sample i.e. examined through the material, is shown in Figure 16. The indent and cracks scatter the sound so the returning signal amplitude is reduced leading to depressions in the carpet diagram. Assuming the deepest depression corresponds to the indent, four other depressions of less depth but of greater depth than the background are located at angles (Figure 17) corresponding to those seen in the optical micrograph (Figure 18). The indentation cracks are difficult to resolve in this micrograph but the one at 3 o'clock is off-axis, a fact detected by the ultrasound (Figure 17).

Surface-breaking cracks induced by a Knoop indentor are of simpler geometry. Two large indents (400 µm long) were impressed in glass and a smaller indent (70 µm long, 8 µm wide) was impressed between them. An ultrasonic density map and the corresponding micrograph are shown in Figure 19. The intrusion of the couplant (H_2O) into the crack facilitates its detection as the velocity of the sound in water is one twelfth that in the ceramic. The ultrasonic wavelength imaging the crack is therefore much shorter so its size resolution is increased. The same transducers used to characterize bulk defects were used to examine these surface cracks.

SUMMARY

The development of a database for defects in advanced ceramics via model-defects in model-ceramics has been described. This work involved the development of high-frequency, high-power ultrasonic transducers and their synthesis is described starting with improved quality piezoelectric ceramics. SPN and LMN-based transducers with frequencies up to 100 MHz and power ≥130 dB were used to

characterize voids and inclusions in glass, crystallized glass and partially-stabilized-zirconia in a scanning mode with water couplant. The characteristics of the calculated and experimental frequency spectra agreed closely, facilitating size prediction. The smallest defects characterized were 20 µm voids, 30 µm inclusions and 30 µm × 8 µm surface-breaking cracks.

ACKNOWLEDGEMENTS

REFERENCES

Bhardwai,M.C. (1986). Principles and Methods of Ultrasonic Characterization of Materials, Adv. Ceram. Matls. 1 (4)311-324.

Derkacs, T., I.M. Matay and W.D. Brentnall (1978). High Frequency Ultrasonic Evaluation of Ceramics for Gas Turbines. J. of Eng. for Power, 100, 549-552.

Emerson, P. Pratt & Whitney (Canada) Ltd. – private communication.

Evans, A.G., G.S. Kino, B.T. Khuri-Yakub, and B.R. Tittmann (1977). Failure Prediction in Structural Ceramics. Matls. Eval., 35 (4) (1977) 85-96.

Gaunard, G.C., E. Tanglis, H. Uberall, and D. Brill (1983). Interior and Exterior Resonances in Acoustic Scattering: I-Spherical Targets", Il Nouvo Cimento 768 153-175.

Jones, M.P., E.V. Blessing, C.R. Robbins (1986). Dry-Coupled Ultrasonic Elasticity Measurements of Sintered Ceramics and Their Green States. Matls. Eval., 44 (1986) 859-862.

Khuri-Yakub, B.T., G.S. Kino, and A.G. Evans (1980). Acoustic Surface Wave Measurements of Surface Cracks in Ceramics. J. Am. Ceram. Soc., 63 (1-2) 65-71.

Kuppermann, D.S. L. Pahis, D. Yuhas and T.E. McGraw, (1980). Acoustic Microscopy Techniques for Structural Ceramics. Bull. Am. Ceram. Soc., 59 (8) (1980) 814-816, 839-841.

Kupperman, D.S., H.B. Karplus. (1984). Ultrasonic Wave Propagation Characteristics of Green Ceramics. Bull. Am. Ceram. Soc., 63,1505- 1509.

Marshall, D.B. and J.E. Ritter (1987). Reliability of Advanced Structural Ceramics and Ceramic Matrix Composites - A Review. Bull. Am. Ceram. Soc., 66 (2) 309-317.

O'Neil, H.T. (1978). Theory of Focussing Radiators", J. Acoustic Soc. Am. 63 68-74.

Patel, N.D., A. Grzymek, and P.S. Nicholson. A Study on Piezoelectric Properties and Optimum Electrode Sizes for High Frequency Transducers. (submitted for publication)

Roth, D.J. and G.Y. Baaklini (1986). Reliability of Scanning Laser Acoustic Microscopy for Detecting Internal Voids in Structural Ceramics. Ad. Ceram. Matls., 1 (3) 252-258.

Schuldies, J.J. and T. Derkacs (1978). Ultrasonic NDE of Ceramic Components. Ceramic Gas Turbine Demonstration Prog. Rev. p.g 429-448.

Stockman, A.and P.S. Nicholson (1986) Ultrasonic Characterisation of Model Defects in Ceramics, Part I. Voids in Glass - Theory and Practice. Matls. Eval., 44 756-761.

Stockman, A. and P.S. Nicholson (1987). Ultrasonic Characterization of Microspherical Inclusions in Zirconia. ASNDT/Am. Ceram. Soc. Proc. NDT Ceramics Conf., Boston, August 1987.

Stockman, A., P. Mathieu and P.S. Nicholson (1987). Ultrasonic Characterization of Model Defects in Ceramics. Part II - Spherical Oxide Inclusions in Glass - Theory and Practice. Matls. Eval. 45 736-742.

Stockman, A., P. Mathieu and P.S. Nicholson. Ultrasonic Characterization of Model Defects in Ceramics. Part III. Spherical Inclusions in Opaque Crystallized Glass - Theory and Practice. submitted to Matls. Eval. (1987).

Sung, J., P.S Nicholson, submitted to J. Am. Ceram. Soc.

Tittmann, B.R., E.R. Cohen, and J.M. Richardson (1979) Scattering of Longitudinal Waves Incident on a Spherical Cavity in a Solid. J. Acoust. Soc. Am., 63 68-74.

Tuell, A., C. Elbann, and B.B. Chick (1969). Ultrasonic Methods in Solid State Physics, pp. 161-179, Academic Press, N.Y.
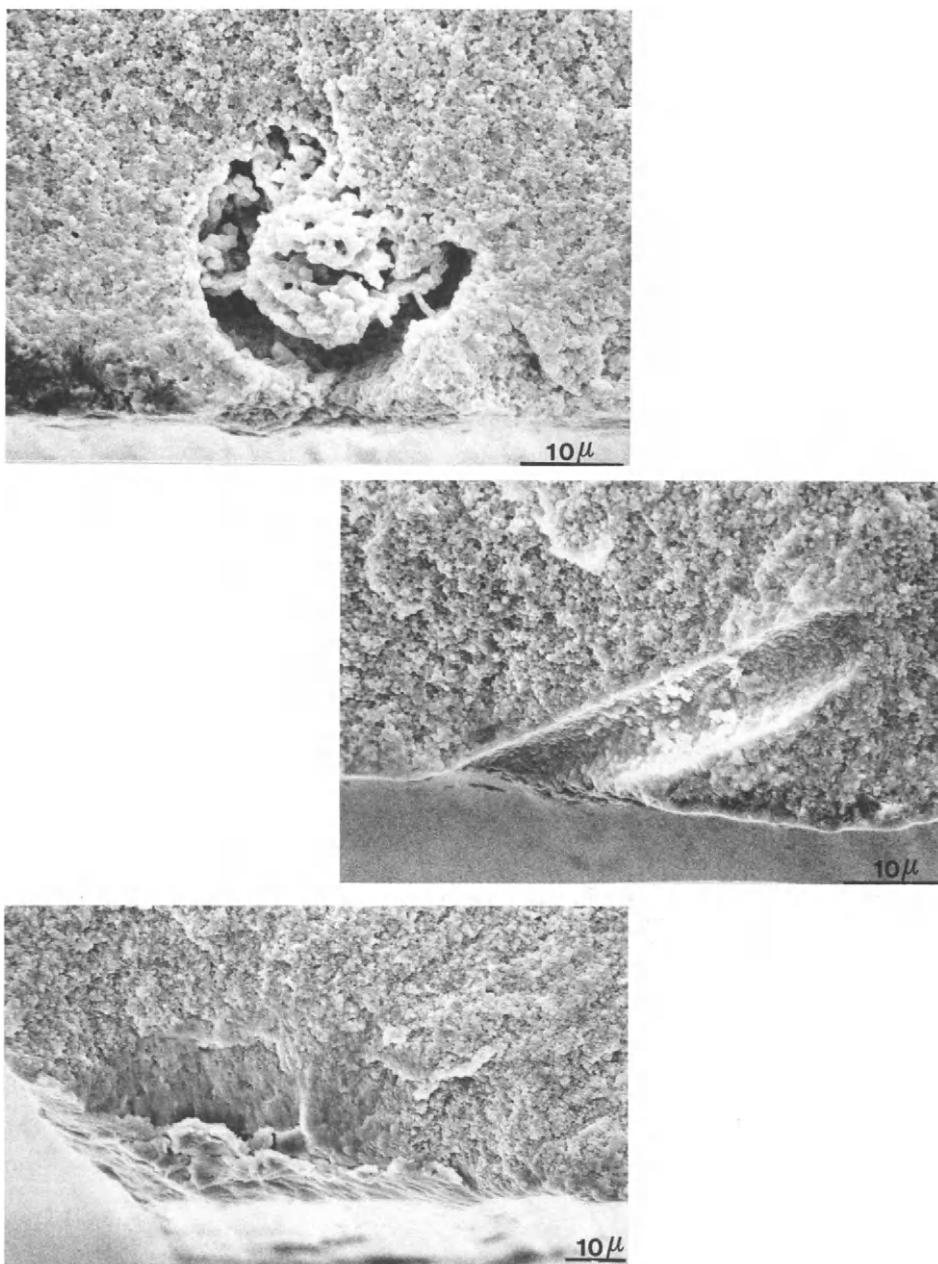
Figure 1   (a)   Agglomerate defect in partially-stabilized zirconia
            (b)   Residual pore following burn-out of an organic fibre from partially-stabilized
                  zirconia
            (c)   Alumina inclusion in partially-stabilized zirconia
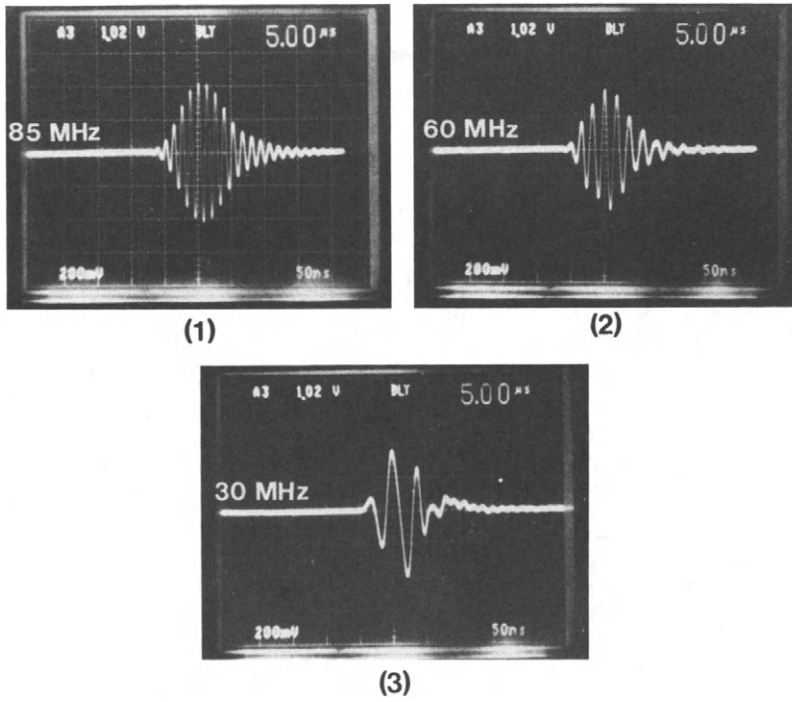
Figure 2   Typical outputs of an SPN transducer tone-burst excited at;
              (1) 30 MHz; (2) 60 MHz; (3) 85 MHz.
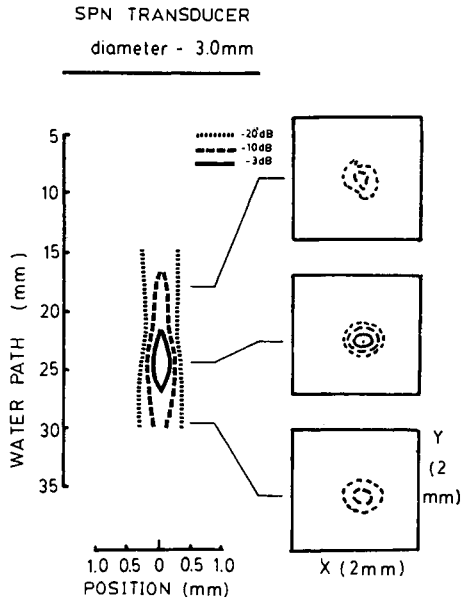
Figure 3   Beam profile of a 57 MHz SPN

              transducer with a crystabond lens.

SPN TRANSDUCER   70 MHz
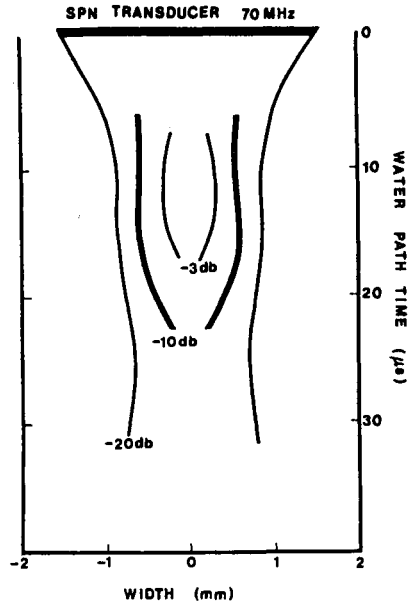
Figure 4   Beam profile of a 70 MHz SPN transducer with a crystabond lens.
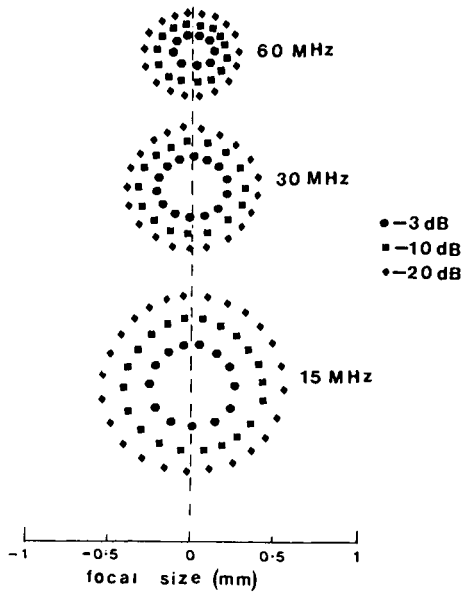
Figure 5   Focal diameter of a 60 MHz focussed SPN transducer excited at 15, 30 and 60 MHz.

LMN (BM 920) TRANSDUCER
100 MHz

output signal

without matching network   with matching network
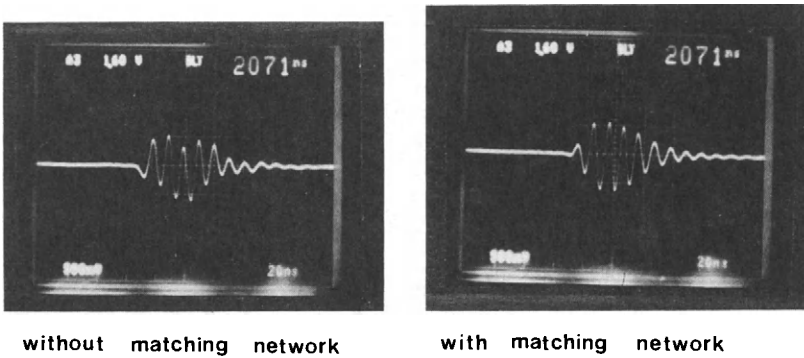
Figure 6   Output signals of a 100 MHz LMN piezoelectric ceramic crystal (a) without; (b) with a matching network.
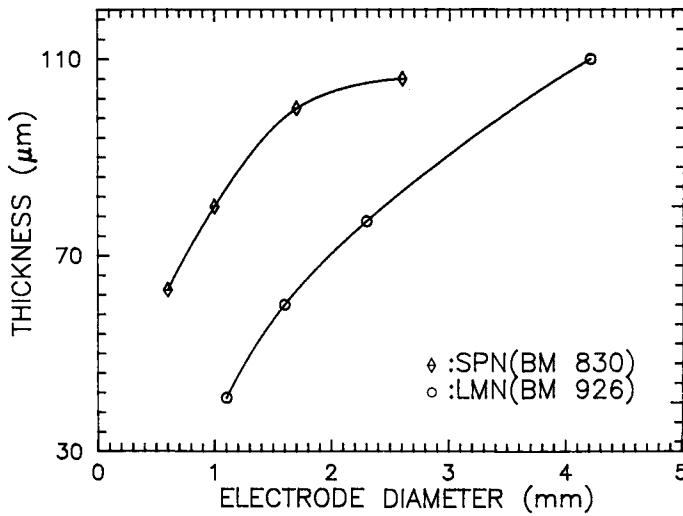
Figure 7   Comparison of optimum electrode size as a function of thickness between SPN and LMN having dielectric constant of 400 & 135 respectively.

Pyramid   transducer   (LMN)
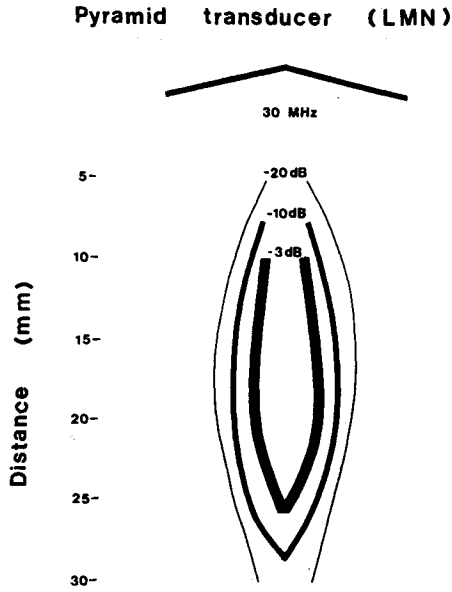
Figure 8   A beam profile of 30 MHz lenseless focussed transducer.
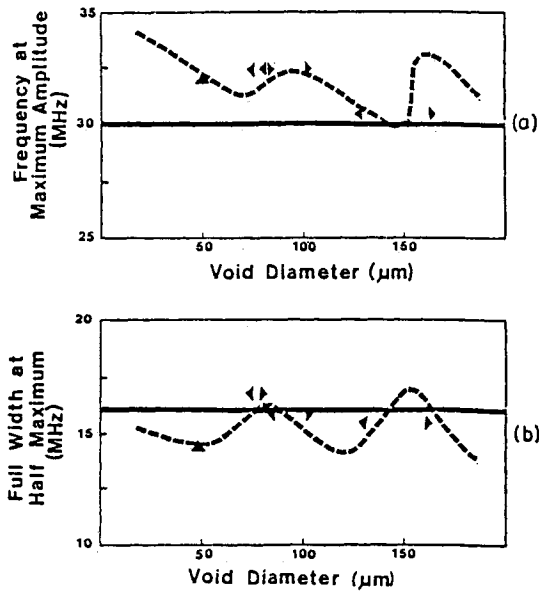
Figure 9   Comparison of measured (triangles) and calculated (dotted lines) data for
                  (a) FMA vs. void diameter.
                  (b) FWHM vs. void diameter.
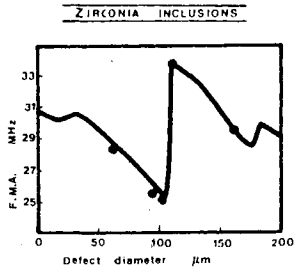
Figure 10A

FWHM calculated (solid line) and experimental (points) for
(a) ZrO_2 inclusions in glass
(b) MgO inclusions in glass.
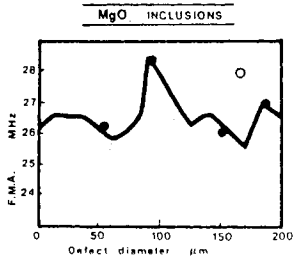
Figure 10B

FMA calculated (solid line) and experimental (points) for
(a) ZrO_2 inclusions in glass
(b) MgO inclusions in glass.
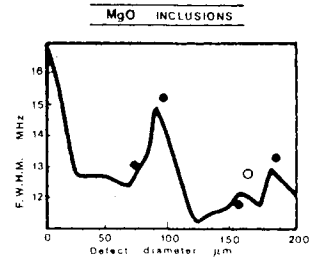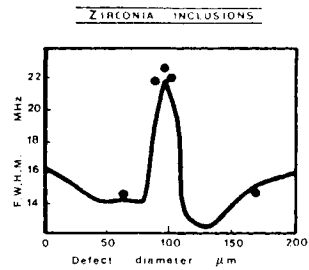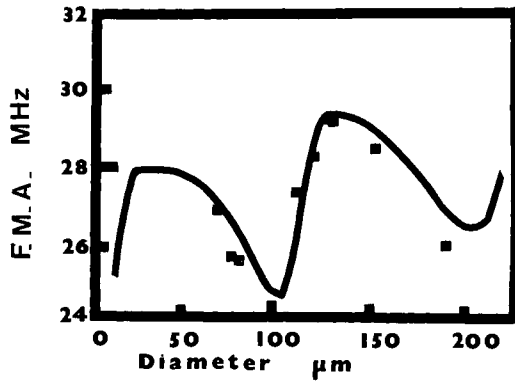
Figure 11   FMA and FWHM for ZrO_2

inclusions in crystallized glass

vs. defect size.
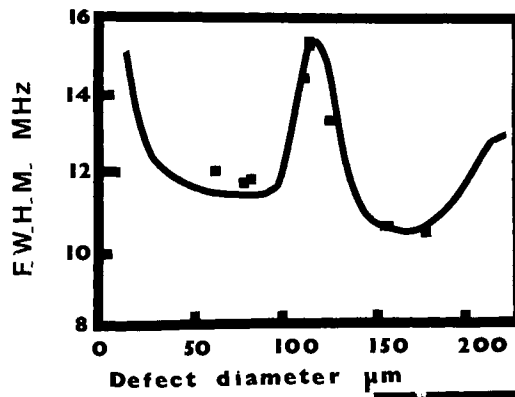
CRYSTALLIZED

DENSITY PLOT
SYMBOL   AND   RANGE

	$<$	$<=$	0.600
0.600	$<$	$<=$	0.720
0.720	$<$	$<=$	0.840
0.840	$<$	$<=$	0.960
0.960	$<$	$<=$	1.080
1.080	$<$	$<=$	1.200
1.200	$<$	$<=$	
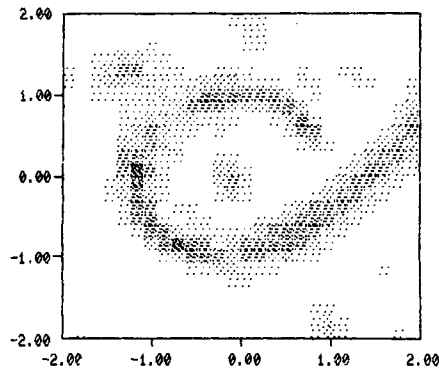
Figure 12

Density map of a 50 µm Pt

inclusion and its Pt-wire locator

loop, 4 mms deep in dense PSZ.
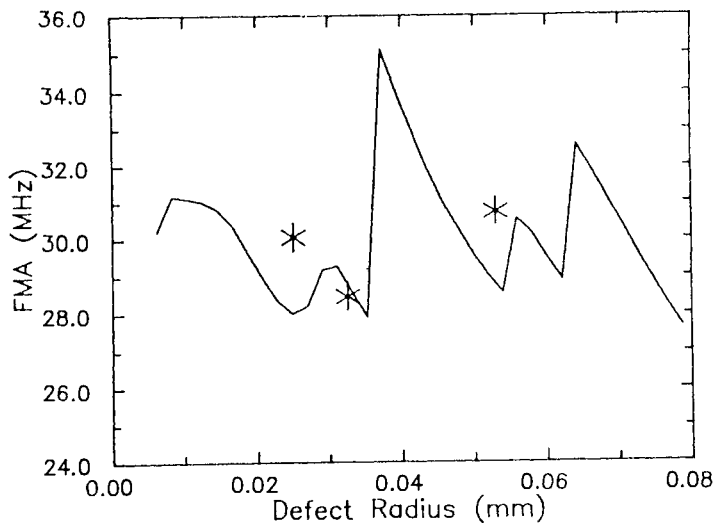
Figure 13   FMA versus defect radius for platinum particles in zirconia. Solid lines are derived from theory and asterisks are data points and error estimates.
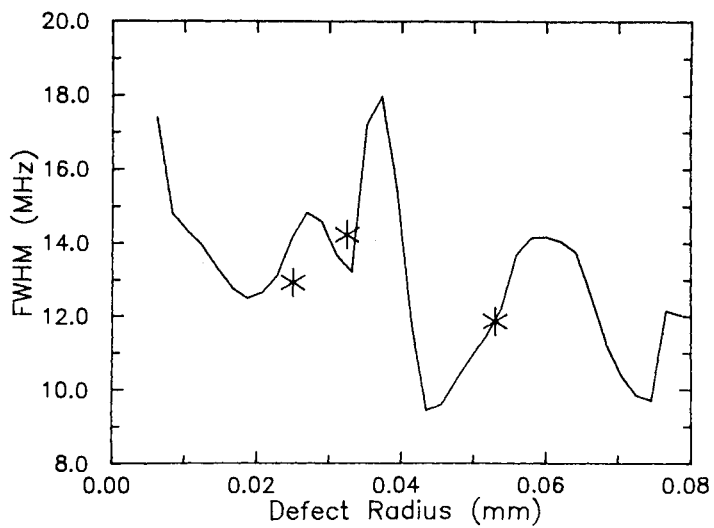
Figure 14   FWHM versus defect radius for platinum particles in zirconia. Solid lines are derived from theory and asterisks are data points and error estimates.
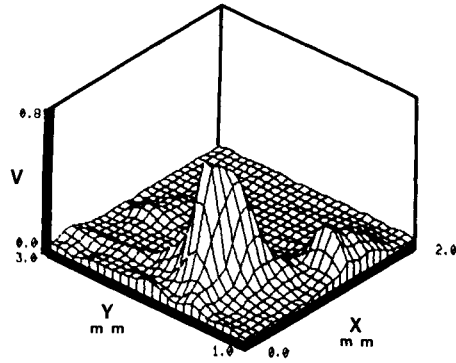
Figure 15   Carpet diagram of a Vickers diamond micro-indent in glass (corner cracks 100 μm long, 1-2 μm wide) (indent on top surface).
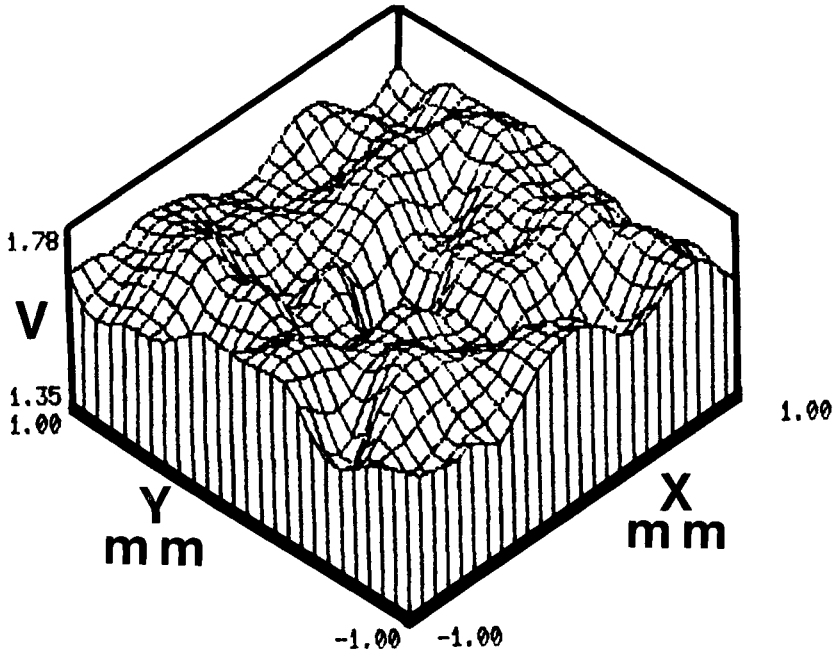
Figure 16   Carpet diagram of a Vickers diamond micro-indent in Si_3N_4 (indent on bottom surface).
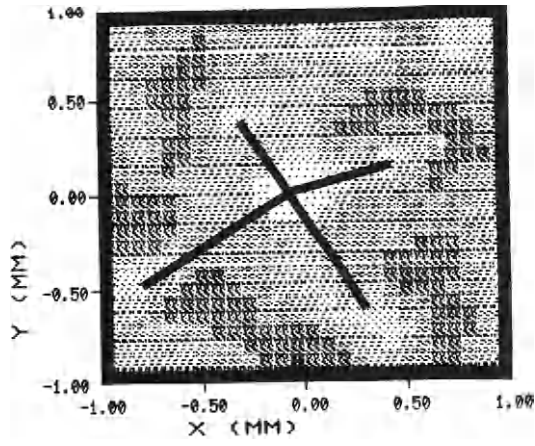
Figure 17   Density map of indent of Figure 16.
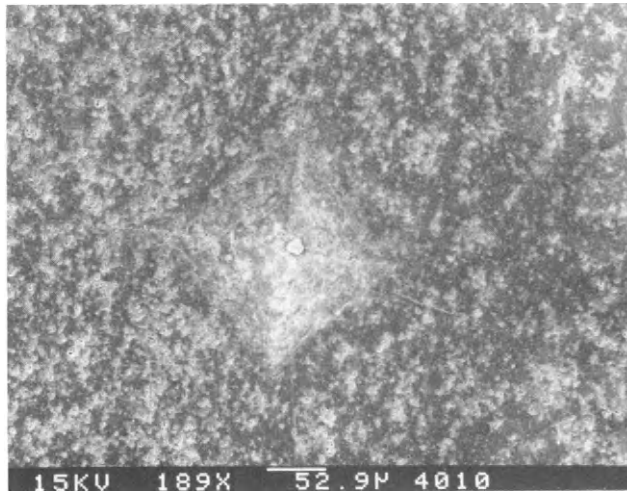
Figure 18   SEM micrograph of indent in Si_3N_4 (of Figures 16 and 17).
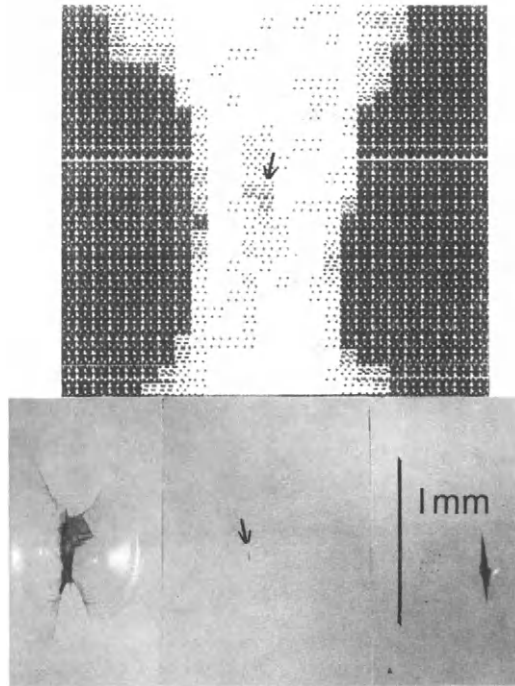
DENSITY PLOT OF A
70 µm INDENT

Figure 19   Density plot of micrograph of a 70 µm Knoop indent in glass (two 400 µm indents used as locators).

Mechanical properties of reaction-bonded silicon nitride-metal composites

N. Claussen and N.A. Travitzky

Technical University of Hamburg-Harburg, Advanced Ceramics Group,
D-1200 Hamburg 90, Federal Republic of Germany

ABSTRACT

Reaction-bonded silicon nitride (RBSN)–metal composites were fabricated by a spe-
cial pressure-infiltration technique. The metals used were aluminum, aluminum
alloys and silicon. The composites, which are readily electro-discharge machined,
exhibit improved fracture toughness, strength and wear resistance. After thermal
treatment in air or nitrogen , the surfaces of the samples can be "sealed" by
the respective oxide or nitride formation which enhances the wear resistance and
prevents the metal phase from sweating-out when used at ambient pressures and tem-
peratures above the respective melting points.

KEYWORDS

RBSN-metal composites; aluminum; silicon; titanium-aluminum alloy; pressure infil-
tration; fracture toughness; strength; hardness; wear resistance; joining.

INTRODUCTION

The fracture toughness of ceramics can be enhanced by incorporation of a ductile
metal phase. The main toughening mechanism in this case results from crack bridg-
ing of plastically deforming metal inclusions (Sigl, 1988). One of the preferred
techniques to fabricate ceramic-metal composites, where the inherent properties
of the ceramic dominate the overal properties, is by pressureless infiltrating
a porous body by the liquid metal which, however, has to wet the ceramic phase.
This is the case for most carbides, i.e., Si-SiC composites can easily be made by
infiltration processing (Kieffer, 1969). Problems usually arise with oxides and
nitrides where either the wettability by the metal must be improved, e.g., by al-
loying, or pressure has to be applied during the infiltration (Jangg, 1971).

RBSN, a potential engineering ceramic meterial, typically exhibits a porosity of
> 15 %, most of it open (RBSN with < 3 % open porosity has been prepared though).
It is hence desirable for some applications to fill the pores with a metal phase
in order to improve the mechanical and surface properties. Leimer (1975) has
tried to infiltrate RBSN with a number of metal alloys. However, in spite of rea-
sonable wettability by some alloys, infiltration could only be observed when re-
actions with the Si_3N_4 matrix took place. These were essentially Si and Mg alloys
with a high Ca content. The mechanical properties of infiltrated and reacted RBSN
composites were not improved when compared to the RBSN matrix alone.

In this work, a gas-pressure technique was successfully applied to infiltrate va-
rious RBSN types with Si, Al and Al-Ti alloys.

INFILTRATION

RBSN bodies with open porosities of a) ~18 % (Anawerk), b) ~ 15 % (Hoechst Ce-
ramTec) and c) ~ 25 % (Iscar) were placed in an Al_2O_3 crucible and covered with
a metal plate (Al and Al alloys) or embedded in metal powder (Si) as shown in

Fig. 1. The system was heated in a gas-pressure furnace in vacuum to above the melting temperature of the metal (Al and Al alloys between 775 and 825°C, Si at 1575°C). The body was held down by an Al_2O_3 pin after melting. Thereafter, Ar gas pressure between 5 and 90 bar was applied for a short period of time (5-30 min). On cooling, the pressure was kept until the metal had solidified.

A pressure of ~ 20 bar was sufficient to fill pores with diameters down to < 1 µm with Al.
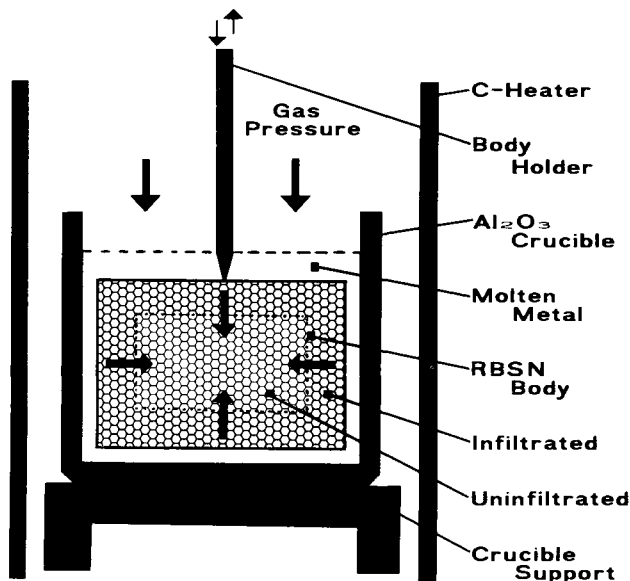
Fig. 1. Schematic diagram of gas-pressure infiltration of RBSN.

MECHANICAL PROPERTIES

Fracture strength and ISB fracture toughness (Chantikul, 1981) were measured in 4-point bending. For comparison, ICL toughness (Anstis, 1981) was also determined. The results are compiled in Table 1. In all cases, the properties of infiltrated RBSN are considerably improved. Al and the Al alloy (2.5 wt. % Mg, 5 wt. % Si and 1 wt. % Zn) especially enhance the fracture toughness of a-RBSN (from 2.7 to 5.6 MPa$\sqrt{m}$), while the hardness is only doubled. As expected of the more brittle Si, toughening is less pronounced (to 3.9 MPa$\sqrt{m}$), hardness, however, is tripled (from 5.1 to 15.3 GPa). The less porous b-RBSN exhibits an even greater hardness increase when infiltrated with the Al alloy. The opposite effect is shown by the high-porosity c-RBSN.

The toughness increase can be related to crack bridging of the ductile phase as demonstrated in Fig. 2. The Al phase has necked down to sharp edges (see arrows in Fig. 2b).

Table 1 Mechanical Properties of Metal-Infiltrated RBSN

	Material	Bending Strength (Mpa)	Fracture Toughness (Mpa$\sqrt{m}$)		Hardness HV10(100N)
			ISB	ICL	
RBSN (Annawerk)	not infiltrated	227±15	2.70±0.15	—	510
	Al-alloy	450±18	4.52±0.11	5.23±0.15	1170
	Al (99.9%)	478±15	5.00±0.20	5.58±0.14	1100
	Si (99.99%)	427±20	3.90±0.20	4.74±0.11	1530
	Ti-39wt.%Al	510±20	n.m.	4.90±0.50	1524
RBSN (Hoechst)	not infiltrated	n.m.	n.m.	—	550
	Al-alloy	n.m.	n.m.	5.00±0.08	1340
RBSN (Iscar)	not infiltrated	n.m.	n.m.	—	216
	Al-alloy	n.m.	n.m	4.15±0.10	900
	Si (99.99%)	n.m.	n.m	3.60±0.20	960

a)

b)

10μm
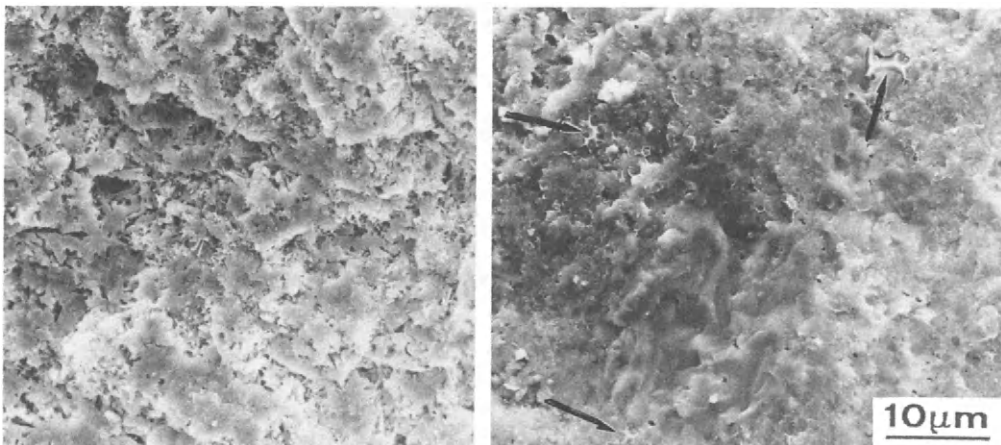
Fig. 2. SEM fracture surface of 18 % porosity RBSN,
a) uninfiltrated, b) infiltrated with 99.9 % pure
aluminum. Al has plastically deformed to sharp
edges (arrows).

Wear properties were determined by a pin-on-disc test on 220 and 1000 mesh SiC paper. If the relative wear of the uninfiltrated a-RBSN is taken to be 100, the improvement by the infiltration of pure Al was 22.5 and 39.8 and that of Si 14.6 and 17.3 for the coarse and fine SiC, respectively, hence an increase in wear resistance by a factor of up to ~ 7 is observed. Further improvement was obtained by an air or N_2 anneal which led to oxide or nitride "sealing" of the surface.

CONCLUSIONS

Pressure infiltration of RBSN results in considerably enhanced mechanical properties. The case of electro-discharge machining and the possibility of surface sealing for enhanced wear and corrosion properties may render the composites an attractive engineering material.

ACKNOWLEDGMENT

REFERENCES

Anstis, G. R., Chantikul, P., Lawn, B. R., Marshall, D. B. (1989). J.Am.Ceram. Soc., 64, 533-38.
Chantikul, P., Anstis, G. R., Lawn, B. R., Marshall, D. B. (1981). J.Am.Ceram. Soc., 64, 539-43.
Jangg, G., Kieffer, R., Gugel, E., Kollwentz, W., Jicinsky, G. (1971). Ber.Dt. Keram.Ges., 48, 262-67.
Kieffer, R., Eipeltauer, E., Gugel, E. (1969). Ber.Dt.Keram.Ges., 46, 486-90.
Leimer, G., Gugel, E. (1975). Z.Metallkde., 66, 570-76.
Sigl, L., Exner, H. E. (1988). Met.Trans.A., in press.

Effect of temperature on the mechanical behaviour of a SiC particulate reinforced Al alloy

S.F. Corbin and D.S. Wilkinson
Department of Materials Science and Engineering, McMaster University,
Hamilton, Ontario, Canada, L8S 4L7

ABSTRACT

The tensile behaviour of a particulate SiC reinforced aluminum alloy has been investigated over a range of temperatures, and for two different heat treatments. The fracture mode depends on testing temperature, with a transition from void nucleation at cracked SiC particles at room temperature to void nucleation by decohesion of the particulate/matrix interface at high temperatures. The strengthening afforded by the particulates also varies with temperature and with matrix temper, and is greatest when the matrix is soft. These effects cannot be explained using standard models such as those based on shear lag analysis. The effect of hold time at high temperature on fracture behaviour has also been studied and correlated with electron microscopy of the SiC/matrix interfacial region.

INTRODUCTION

In the past several years, the reinforcement of various aluminum alloys with SiC particulates has received considerable attention. The addition of particulates increase room temperature mechanical properties such as strength and modulus, as well as secondary properties such as wear resistance. Significant improvements in strength retention with increasing temperature are also observed. Thus, some particulate reinforced aluminum alloy composites may be capable of performing satisfactorily at temperatures up to 200 C higher than those available with unreinforced alloys. In this paper, we describe some results on tensile behaviour as a function of temperature and heat treatment, for a 2014 Al alloy reinforced with 20 wt% SiC particulates.

High temperature mechanical behaviour is usually interpreted by comparison with room temperature properties. Therefore, Table I presents yield strength data for a variety of SiC particulate reinforced aluminum alloys. The strengthening imparted by the SiC particles is measured by the ratio of the composite yield strength (s_{cy}) to that of the matrix (s_{my}). It is clear from the Table that the strengthening ratio varies with matrix alloy and heat treatment. For example 20 vol.% SiC particulates, increase strength by about 1.2 in 6061-T6 and 2014-T6. However, much greater strengthening is observed

Table I: Yield data for unreinforced and SiC particulate reinforced alloys

Material	Ref.	Yield Strength (MPa)	Strengthening Increment (s_{cy}/s_{my})	Reinforcement
PM 6061-T6 matrix	[2]	357	-	N/A
20 Vol% SiCp/ 6061-T6	[2]	414	1.16	particulates t=1 micron L=4 microns a=4
IM 2014-T6	[2]	414	-	N/A
20 Vol% SiCp/ 2014-T6	[2]	489	1.18	particulates t=1 micron L=4 microns a=4
1100 Al annealed	[3]	35.2	-	N/A
20 Vol% SiCs/ 1100 Al annealed	[3]	204	5.80	spherical a=1
IM A356-T6	[4]	200	-	N/A
18 Vol% SiCp/ A356-T6	[4]	331	1.66	particulates t=10.5 microns L=13 microns a=1.23

Definitions
PM-Powder metallurgy produced   IM-Ingot metallurgy produced
L=length of particulate
t=thickness of particulate s_{my}-matrix yield strength
a=aspect ratio of particulate s_{cy}-composite "   "

Note: values are expressed as an average.

in 1100 Al and the A356 foundry alloy. Thus, softer alloys show a much greater strengthening due to particle additions than do higher strength alloys in peak-aged conditions. In addition SiC morphology is likely to play a role.

Many models for particulate and fibre strengthening have been developed. The most prominent are those based on the concept of load transfer from the matrix to the particle during the application of a stress. Recently Nardone and Prewo [1] have proposed a modified shear lag model which predicts a composite yield strength of

$$s_{cy} = s_{my}[V_f(a+4)/4 + V_m] \qquad (1)$$

where V_f and V_m are the volume fraction of the particulates and matrix respectively and a is the aspect ratio of the reinforcement. Calculations of the composite yield strength according to equation (1) are presented in Table II for the materials listed in Table I. Included is the difference between the calculated and experimental measurements. The model describes the strengthening seen in the 6000 and 2000 series alloys fairly well, at least in T6 peak aged condition. However, eq.

Table II: Comparison of measured yield strengths with those calculated using the modified shear lag model for particulate composites.

Material	Ref.	Measured Yield Strength (MPa)	Calculated Yield Strength (MPa)	Percent Difference
20 Vol% SiCp/ 6061-T6	[2]	414	428	+3
20 vol% SiCp/ 2014-T6	[2]	489	498	+2
20 Vol% SiCs/ 1100 Al annealed	[3]	204	39	-80
18 Vol% SiCp/ A356-T6	[4]	331	211	-39

(1) predicts that the strengthening ratio should depend only on volume fraction and aspect ratio, and not on the matrix properties. Consequently, it greatly underestimates the strengthening ratio seen for the materials whose matrix has a lower yield strength (such as 1100 Al and A356). Any theory or model describing the behaviour of discontinuous MMC's should attempt to explain these differences in strengthening ratio seen between matrix type.

PROCEDURE

The material studied was a 2014 alloy reinforced with 20 wt.% of SiC particulates. Small cylindrical tensile samples (12.5 mm. gauge length by 3.5 mm. diameter) were machined from the as received stock. These samples were then heat treated to the T6 condition. Two of the samples were subsequently annealed at 410 C for 3 hours with an O-type condition resulting. Tensile tests were performed at room temperature, 200, 300 and 400 C for the T6 condition. Similar tests were carried out at room temperature and 400 C only, for the O condition. Each specimen was held in the furnace at temperature for half an hour prior to testing*. True fracture strain was measured using cross sectional area measurements before and after fracture. Approximate measurements of the .2% offset yield strengths were also made from the stress-strain curves generated using the stroke of the testing machine as a measure of strain. Hardness values of the matrix material in the composite after exposure to the testing temperature were also determined using a Vickers hardness indentor on polished sections.

Both SEM observation of fracture surfaces and metallographic observation of cross sections taken near the fracture surface were used to determine the mechanism of damage leading to failure at different temperatures.

---

* Literature values for the unreinforced 2014 alloy were also tabulated for furnace holding times of half an hour. Thus direct comparisons could be made between the composite and unreinforced materials.

RESULTS

The microstructure of the composite, following solutionizing at 500 C is shown in Figure 1. The micrograph was taken with polarized light to give grain contrast. The SiC particulates appear as light and dark flecks in the Al matrix. The aluminum grains show up as light and dark grey contrast. The mean particulate size has been determined to be 13 microns, although they range in size from about 5 to 25 microns. The mean aspect ratio has been determined as 1.23. The Al grain size is between 100 and 200 microns.
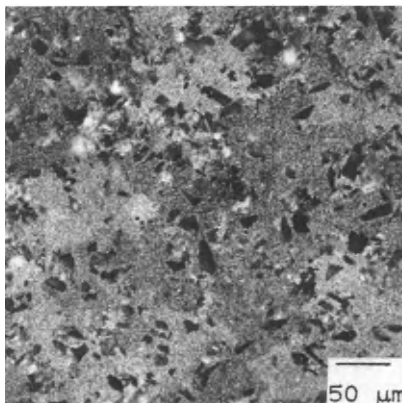
Figure 1: Microstructure of as-recieved material, indicating SiC particulate distribution.

Mechanical Properties

The UTS, yield strength and fracture strain for the T6 composite are shown as a function of temperature in Fig. 2. The greatest reduction in strength occurs between 300 and 400 C, while the fracture strain increases significantly over the same temperature range. Comparing the results with literature values for the unreinforced 2014 indicates that the SiC particles have no significant impact on strength at room temperature. However, as the temperature increases, the composite retains its strength, while that of the base alloy decreases rapidly above 200 C. The maximum composite strengthening ratio occurs at around 300 C.

In order to assess the effects of heat treatment on strength, annealed samples were also tested at both room temperature and 400 C (Fig. 3). Both strength and fracture strain maintain a temperature dependence. Thus not all of the strength loss in the T6 conditioned material can be attributed to coarsening processes. In addition, microhardness was measured at room temperature, following tensile testing. Readings were taken in particle-free regions of the microstructure. Three different regions of the microstructure were measured for each sample. The average room temperature hardness for each sample, as a function of prior test temperature, is plotted in Fig. 4. The hardness readings indicate that very little microstructural change has occurred in going from room temperature to 200 C. However, from 200 C to 400 C a substantial loss in hardness occurs. It is also interesting to note that the T6 sample tested at 400 C has a hardness very close to that of the annealed composites. This indicates that almost complete
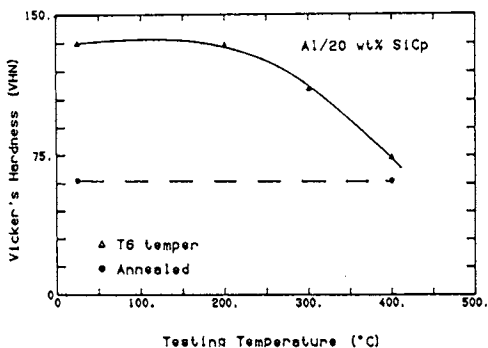
Figure 4: Vicker's Hardness values at room temperature following tensile testing at a range of temperatures.
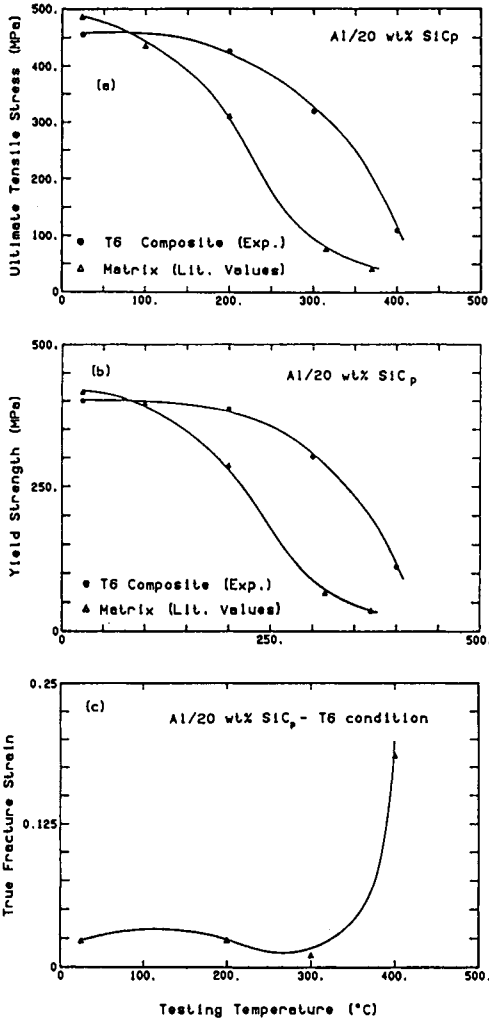
Figure 2: Mechanical behaviour of the composite as a function of temperature, tested following a T6 heat treatment. Data for the unreinforced alloy are shown for comparison.
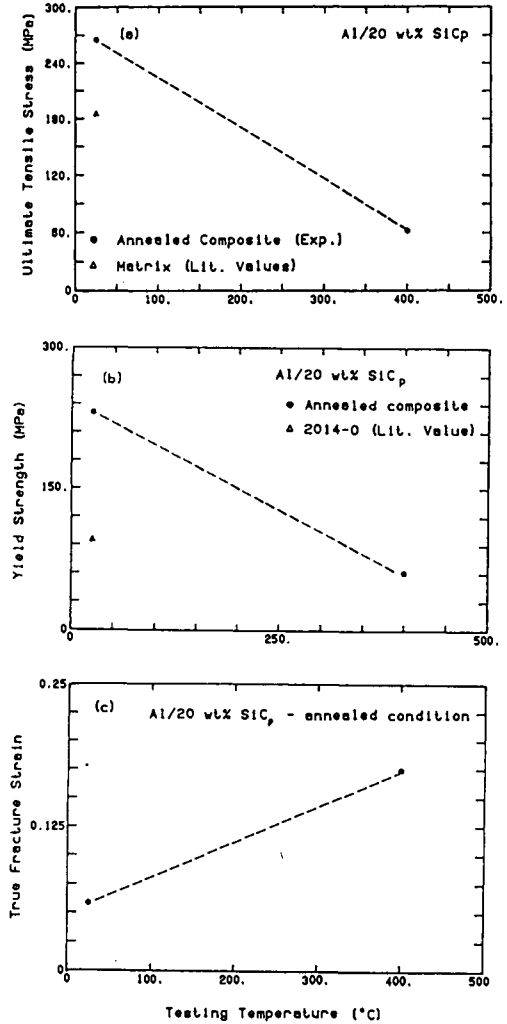
Figure 3: Mechanical properties of the composite tested in O – annealed condition. Testing in this condition was performed at room temperature and 400 C only.

annealing has occurred at this testing temperature. Readings on both annealed samples indicate little microstructural change in going from room temperature to 400 C.

Consistent with the observations made above in reference to data in the literature, the SiC particulates do provide room temperature strengthening when the material is in the annealed state. The strength ratio is 2.4 for yield and 1.4 for the UTS. This is in sharp contrast to ratios of less than one for material in the T6 condition.

The stress-strain curves are shown in Fig. 5. The room temperature T6 composite is the only sample that fractures while it is still work hardening (i.e. there is no evidence of tensile instability). This may account in part for the low strengthening ratio of UTS in this material. All the other samples show at least some degree of necking. The effects of annealing on tensile behaviour at room temperature and 400 C, are clearly illustrated in Fig. 5. The strain to failure at room temperature is increased by annealing, while that at 400 C is decreased.
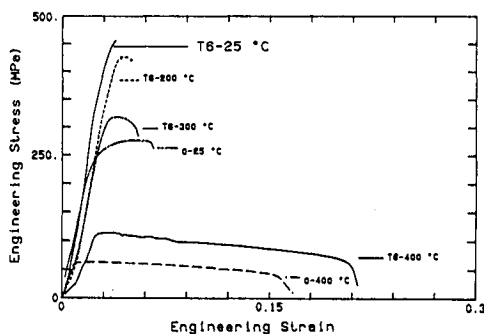
Figure 5: Stress-strain curves in both conditions over a range of temperatures.

Fractographic Observations

Fracture surfaces and metallographic cross sections of the T6 material were examined following testing at room temperature and 400 C. Fig. 6 shows the room temperature specimen. The fracture surface is indicative of ductile fracture in the matrix, accompanied by fracture of the particles. The side of the specimen remains smooth after testing with no evidence of cracking. Fig. 7 shows the composite specimens tested at 400 C. In this case, extensive cracking is found on the side face below the fracture surface. The fracture surface indicates a transition to particle/matrix decohesion with increasing temperature.

Polished cross sections are shown in Figs. 8 and 9. Following room temperature testing (Fig. 8) there is evidence of considerable void formation below the fracture surface. These voids are relatively small and appear to originate at the particle/matrix interface in regions of clustered particles. Close examination of the micrograph reveals several fractured particles. Extensive research by Zok [5] on this material at room temperature confirms that particle fracture is the dominant mode of void nucleation. After testing at 400 C (Fig. 9), many more voids are seen. In addition these voids have grown to a much larger size. Again, they are associated with clustered particle regions and appear to initiate at the particle/matrix interface. Close examination of the micrograph reveals a marked absence of cracked or fractured particles.

The fracture surfaces of samples tested in the annealed condition have not been examined to date. However, polished cross sections have been prepared. Following room temperature testing, very little evidence of particle cracking is found below the fracture surface (Fig. 10). Instead voids develop by decohesion at the interface. These voids are still associated with clustered regions (the voids are difficult to see, but are indicated by out of focus regions near particle clusters). Following testing at 400 C, the annealed sample (with the exception of a few voids near the fracture surface) is free of voids below the fracture surface (Fig. 11). This is in sharp contrast to the T6

a)

a)

b)
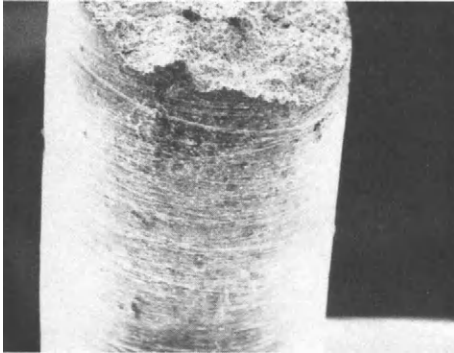
b)
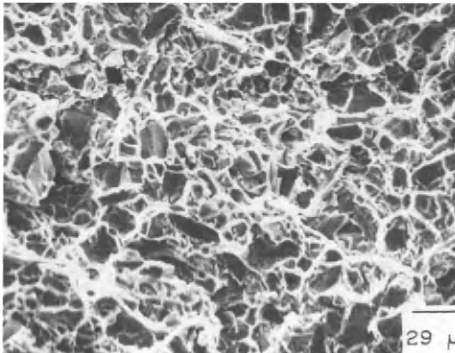
Figure 6: Fracture of the T6 composite at room temperature showing a) an absence of cracking and b) fractured SiC particles on the fracture surface.
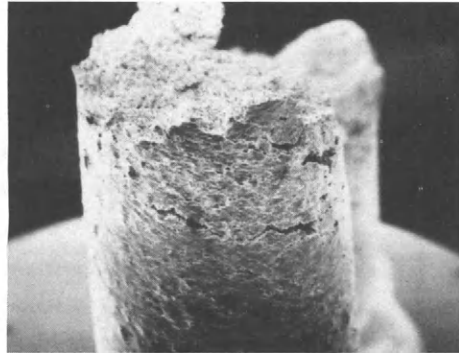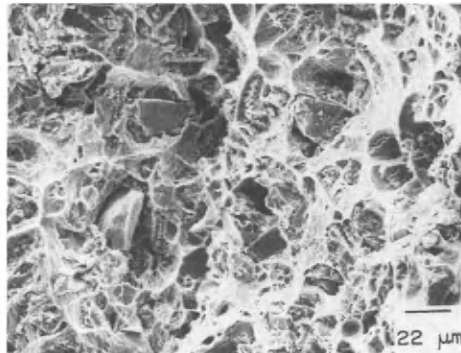
Figure 7: Fracture of the T6 composite at 400 C showing a) extensive cracking along the side of the specimen, and b) the fracture surface.

specimen tested at 400 C (Fig. 9).

DISCUSSION

The dependence of strength on temperature is markedly different in the composite than in the unreinforced alloy. For the T6 aged material the strengthening ratio s_{cy}/s_{my} increases with temperature and reaches a maximum at around 300 C. This is the case for both ultimate and yield strengths. Similar results for other alloy systems reinforced with SiC have been reported in the literature [4,6]. This result cannot be explained by the modified shear lag theory. According to eq. (1), the temperature dependence for composite strength s_{cy} scales as that for the matrix s_{my}. Thus, this theory predicts a constant s_{cy}/s_{my} ratio with changing temperature, in contrast to the experimental results.

The shear lag theory is also unable to explain the increase in strengthening ratio with annealing. Since composite strength is predicted to scale directly as the matrix yield strength, annealing should not change this ratio, unless a change in particulate volume
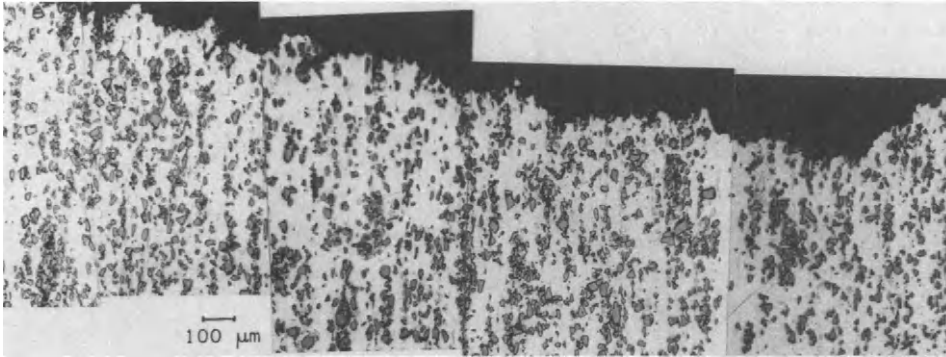
Figure 8: A polished cross-section below the fracture surface for the T6 composite tested at room temperature.
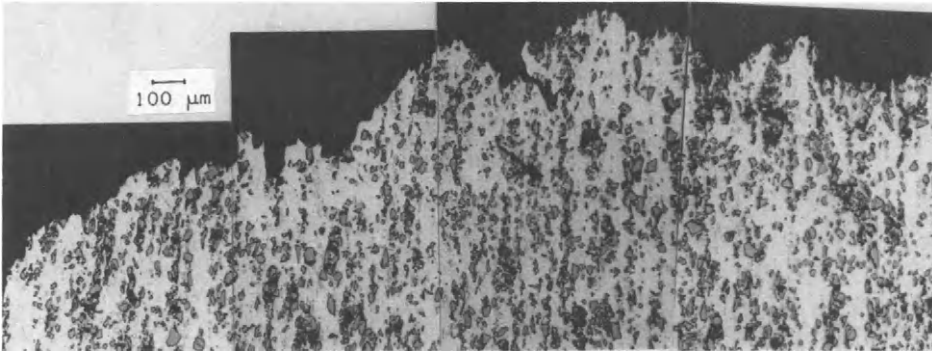
Figure 9: A polished cross-section below the fracture surface for the T6 composite tested at 400 C.
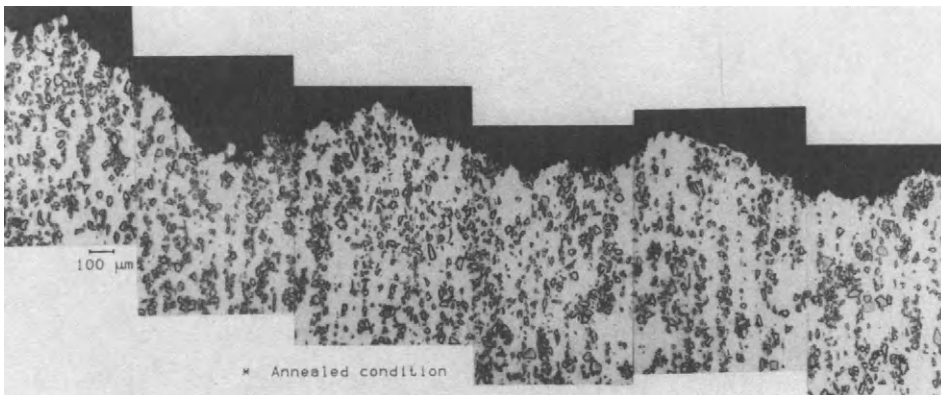
Figure 10: A polished cross-section below the fracture surface for the annealed composite tested at room temperature.

fraction or aspect ratio develops, which is clearly not the case. Experimentally, it is apparent that the strengthening ratio is quite sensitive to matrix strength. Soft alloys are able to gain far greater benefit from the addition of particulates than high strength alloys. Thus, the effect of work hardening capability on composite stengthening needs to be recognized.

The most dramatic drop in strength and increase in failure strain for the T6 composite occurs from 300 C to 400 C. This also corresponds to a change in fracture mode from one of void nucleation at cracked particulates or within the matrix, with relatively little general damage away from the fracture plane, to one involving extensive internal cavitation which is nucleated at the particulate/matrix interface. The reduction in strength at 400 C is due to a combination of creep effects and microstructural changes. It is clear from the annealed material that even with a relatively stable microstructure some loss of strength can be expected due to thermally activated flow processes. It is also clear from the hardness measurements that significant matrix softening occurs very quickly at 400 C. This also accounts for the change in damage mode. Particle fracture requires achieving high local stresses within the SiC particles. This can only be attained when the matrix strength is high. As the strength decreases fracture no longer occurs, thus leading to higher failure strains and eventual failure by particle/matrix decohesion.

The annealed composite also experiences a drop in strength and increase in failure strain at 400 C. The magnitude of the stress drop, as a percentage of its original room temperature strength, is about the same as that for the T6 composite (ie. about a 76% reduction). However, the magnitude of strain increase is substantially lower than that seen for the T6 composite. A number of comments can be made about these observations. First, following annealing the composite exhibits a relatively stable microstructure. The hardness readings support this contention. It is clear however, that some microstructural changes do occur over time at 400 C. This is evident from the difference in fracture behaviour between the T6 composite tested at 400 C (following a hold of 30 minutes), and the 400 C - annealed composite tested at 400 C. In the latter case, the composite had seen over 4 hours at temperature prior to testing. As a result, the amount of internal
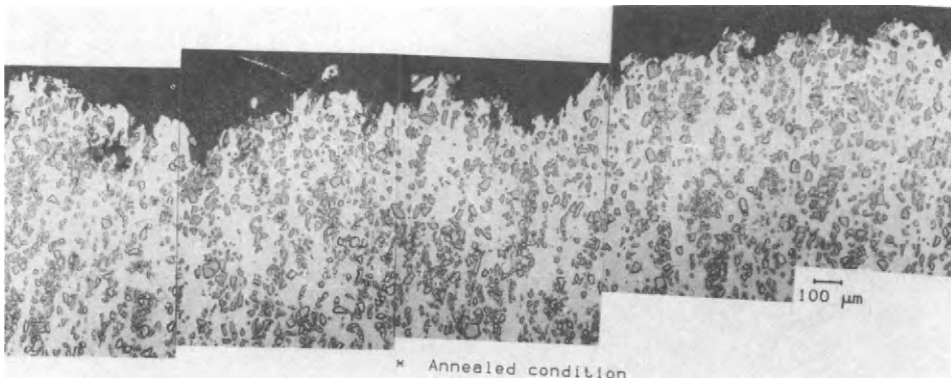
Figure 11: A polished cross-section below the fracture surface for the annealed composite tested at 400 C.

damage at the   particulates is reduced dramatically. In order to investigate this further, electron microscopy was used. Samples were annealed at 410 C for 1/2 hour and 4 hours. The microstructure in the vicinity of the SiC particles has been studied. To date only a small number of particles have been studied. However, a number of features are evident (Fig. 12). First, there are a number of large precipitates on the SiC/matrix interface. These have been identified as predominantly $CuAl_2$. The number and size of these increases with annealing time. Related to these interfacial precipitates is a matrix region surrounding the particulates which is largely free of precipitates. This suggests that as annealing proceeds a soft precipitate-free region develops around the SiC particles which makes it more difficult to build up the stress concentrations necessary to promote interfacial decohesion. Thus the amount of damage observed behind the fracture surface decreases with time at 400 C. There is even a decrease in failure strain with time at 400 C. This is also indicative of a loss of damage tolerance, perhaps due to the coarsening of the $CuAl_2$ precipitates along the SiC/matrix interface.

CONCLUSIONS

It is clear that reinforcing 2014 Al with 20 wt% of SiC particulates substantially improves the material's strength retention with increased temperature, as compared to that of the unreinforced alloy. This result cannot be explained by a model based on the shear lag theory. Differences in strength due to matrix temper and matrix type also are not explained by the shear lag type model. It is clear that the strength of these materials depends much more on the properties and microstructure of the matrix than was previously thought. Therefore, models and experiments that explore matrix microstructural effects are needed to fully understand the behaviour of these materials.

The fracture mode of the composite changes with temperature. At room temperature void nucleation is dominated by cracking of the particulates followed by ductile failure of the matrix. At higher temperatures and in the annealed materials, less particulate cracking
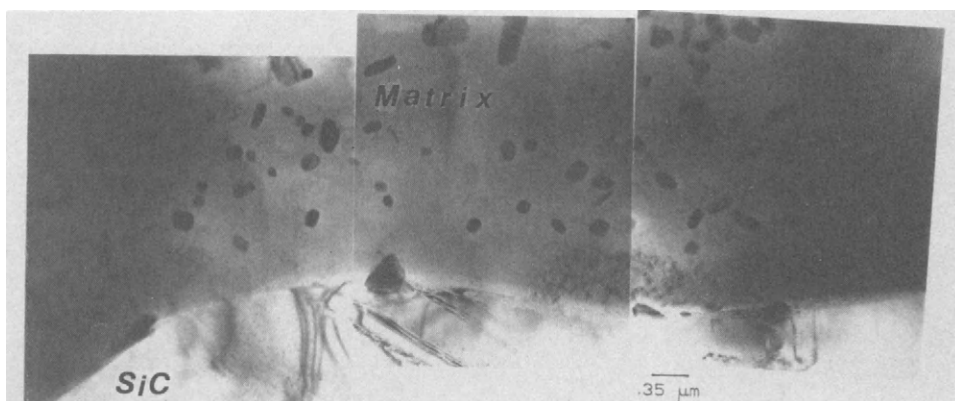
Figure 12: Transmission electron micrographs of the composite annealed for 0.5 hours at 410 C.

occurs and particle/matrix decohesion provides void nucleation for ductile failure of the matrix. With continued annealing at 400 C local microstructural changes in the vicinity of the particulates contribute to a loss of damage tolerance and a decrease in ductility. The consequences of this observation for service conditions consisting of lower temperatures but much longer times needs to be explored.

REFERENCES

1. V.C. Nardone and K.M. Prewo, Scripta Metall., Vol. 20, 1986, pp. 43-48.

2. V.C. Nardone, Scripta Metall., Vol. 21, 1987, pp. 1313-1318.

3. M. Taya and R.J. Arsenault, Scripta Metall., vol. 21, 1987, pp. 349-354.

4. Duralcan April Product Data Package, 1989.

5. F. Zok, Ph.D. Thesis, McMaster University, Hamilton, Ontario, Canada, 1988.

6. A. Sakamoto, H. Hasegawa and Y. Minoda, Proc. ICCM V, (AIME, Philadelphia, 1985), pp. 699-709.

Mechanical properties and fracture behaviour of zinc-aluminum metal matrix composites

J.S.H. Lo, S. Dionne, L. Dignard-Bailey, M. Sahoo
CANMET/MTL, Energy, Mines and Resources, 568 Booth Street,
Ottawa, Ontario, Canada, K1A 0G1

J.C. Farge
Noranda Research Centre, 240 Hymus Blvd., Pointe Claire, Québec, Canada, H9R 1G5

ABSTRACT

The low material and processing costs of zinc-aluminum alloys have increased the employment of the alloys over cast aluminum, bronze, and cast iron in automotive applications. However, the elevated temperature (>100°C) properties of zinc-aluminum alloys were found to be unsatisfactory. This has limited the extent of applications of the alloys.

One viable approach of improving the elevated temperature properties is by reinforcing zinc-aluminum alloys with alumina fibers. In this work, the mechanical properties and fracture behaviour of Al_2O_3/zinc-aluminum composites produced by squeeze casting were evaluated and correlated with their microstructure.

KEYWORDS

Metal matrix composites; zinc-aluminum alloys; alumina fibers; squeeze casting.

INTRODUCTION

Zinc-aluminum (Zn-Al) based alloys have found considerable industrial applications since their first discovery. This is primarily due to their excellent castability, fluidity, and good mechanical properties (Magnus, 1982). Initially, Zn-Al alloys such as ZA-35 were developed for their wear resistance and bearing properties (Mihaichuk, 1981). Later, Zn-Al alloys with various contents of aluminum, such as ZA-12, were developed for casting prototype parts, and subsequently ZA-8 and ZA-27 for general foundry purposes.

In this work, a Zn-Al based alloy with approximately 32 wt % aluminum was studied. This material is known for its high strength/density ratio and can therefore compete satisfactorily with other foundry alloys such as copper, aluminum or cast iron.

Despite the attractive room temperature properties of Zn-Al alloys, the elevated temperature mechanical properties were found to be unsatisfactory. Essentially, degradation of tensile strength and creep resistance occurs at temperatures around 100°C. Considering the low melting temperature of these alloys, a temperature of 100°C corresponds to almost 0.49 T_m of some of the alloys. With this limitation, the extent of applications of the alloys is restricted to those for low service temperature environments.

An attractive possibility of improving the high temperature properties of Zn-Al alloys up to 150°C is by fiber reinforcement to form composite materials. The potential advantages which can be gained include improvement in strength, modulus of elasticity, creep, fatigue and wear resistance. Similar work on Zn-Al alloy (Das, 1986; Guerriero, 1986; Dent, 1986) has demonstrated the benefit of fiber reinforcement.

Noranda Technology Centre was interested in evaluating the microstructure, mechanical properties, creep and wear resistance of zinc-aluminum alloys reinforced with alumina fibers. Hence, a collaborative project was initiatied with MTL/CANMET. In this paper, some of our initial results on mechanical properties and fracture behavior of Al_2O_3/Zn-Al composites are discussed. Results on wear and fatigue characteristics of the test materials, which are presently being compiled, will be reported later.

MATERIALS

All squeeze cast materials evaluated in this work were fabricated by JPL Transportation Products Inc., Engine Products Group., Cleveland, Ohio for Noranda Technology Centre. The chemical composition (wt %) of the squeeze cast Zn-Al alloy is given as follows:

Al	Cu	Fe	Mg	Si	Zn
32.5%	2.06%	0.065%	0.012%	0.012%	balance

Squeeze cast samples were in the form of discs, with dimensions of 130 mm in diameter and 40 mm in thickness. In performing a chemical analysis on an unreinforced squeeze cast disc, a variation in chemical composition with respect to the disc thickness was noted. This is shown in Fig. 1, with the different aluminum contents varying as a function of the disc's thickness. This variation in composition is believed to be the result of the processing conditions, since a similar analysis on a squeeze cast ZA-27 disc, fabricated at CANMET, did not exhibit such phenomenon (Lo, 1989).

	Composition (wt %)			Density (g/cc)
	Al	Cu	Zn	
1	35.1	2.1	62.8	4.62
2	35.3	2.1	62.6	4.66
3	34.3	2.2	63.5	4.76
4	33.2	2.2	64.6	4.79
5	30.2	2.3	67.5	4.87
6	31.2	2.3	66.5	4.81
7	25.5	2.5	72.0	5.11
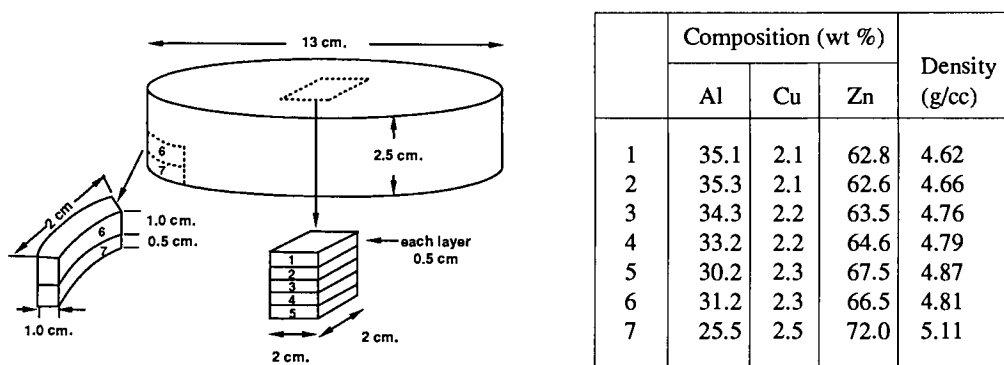
Fig. 1. Variation of aluminum content along the thickness of a squeeze cast Zn-32Al disc.

In addition to the Zn-32Al discs, discs reinforced with alumina fibers were also fabricated by squeeze casting. The reinforced discs were produced using 10 vol % and 20 vol % alumina fiber preforms made by ICI. The Saffil alumina fibers in the preforms, were reported to consist of 96-97% delta alumina and 3-4% silica (ICI product literature) which was confirmed by microprobe analysis. Closer examination of fiber surfaces revealed the presence of patches and films of SiO_2 (Fig. 2), which are the binder material for bonding fibers together. The other function of the SiO_2 binder is to form the body of a preform, consisting of a three dimensional network of inter-connecting fibers.

The volume fractions of fiber in the squeeze cast discs were determined at CANMET by quantitative metallography using a Quantimet 920 image analyzer. Basically, in an area of 160 mm^2, 200 fields (0.8 mm^2 each) were analyzed to quantify the fiber volume fractions. Though initially preforms with 10 vol % and 20 vol % of Al_2O_3 fibers were used, the analysis on the squeeze cast composite discs indicated the volume fractions to be 12 vol % and 24 vol % respectively. It is possible that the volume of the preforms could have been reduced during the squeeze casting operation, thereby increasing the volume fractions of fiber in the matrix.
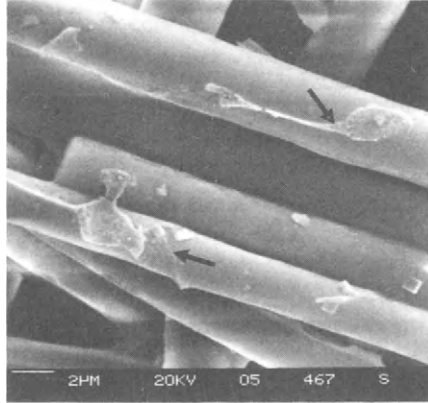
Fig. 2. SiO_2 patches and films on Al_2O_3 fibres in the perform (arrows).

RESULTS

Metallography

The microstructures of permanent mould cast and sand mould cast Zn-Al alloys have been described in detail (Sahoo, 1986; Barnhurst, 1983), and Zn-Al alloys are known to have relatively complex multi-phase microstructures. The binary phase diagram of these alloys is given in Fig. 3. In the case of a Zn-Al alloy containing 32% aluminum (Zn-32Al), solidification of the melt begins with the formation of Al rich dendrites (α phase) and proceeds with the formation of proeutectic β phase around the primary dendrites. The residual liquid solidifies according to the eutectic transformation. Following the eutectoid transformation, the resulting Zn-32Al consists mainly of lamellae of $\alpha + \eta$ and of η phases. A copper-rich ϵ phase ($CuZn_4$), is formed in the Zn enriched η phase in copper-containing alloys. Iron is present in the form of faceted $FeAl_3$ particles in Zn-Al alloys.

The presence of the above phases is shown in a polished section of a sample, which was observed with back scattered electron mode of a scanning electron microscope to provide an atomic contrast image
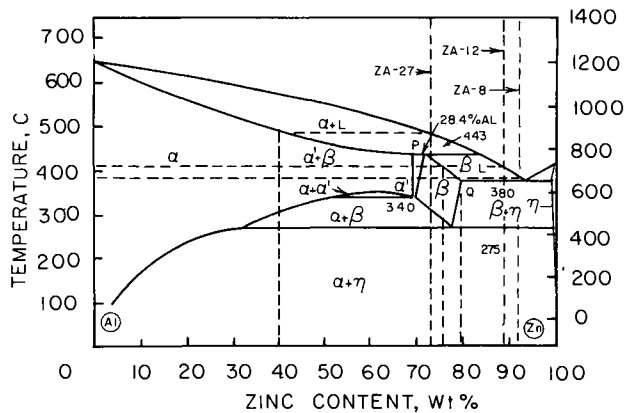
Fig. 3. Al-Zn equilibrium phase diagram.

(Fig. 4). In this figure, the dark regions represent the primary cores of Al rich $\alpha + \eta$ eutectoid which are surrounded by light regions of Zn rich $\alpha + \eta$ eutectoid. The light regions display a continuous rim of fine precipitate resulting from eutectoid transformation. The white interdendritic regions are Zn rich η phase with islands of $\alpha + \eta$ phase resulting from the transformation of the eutectic β phase. Etching the sample with 2% Nital reagent revealed the presence of ε phase precipitates contiguous to the Zn enriched η regions (Fig. 5).

The incorporation of fibers in the Zn-32Al alloy had a significant effect on the size of dendrites in the matrix alloy. As shown in Fig. 6a-c, the size of dendrites is reduced as the volume fraction of fibers is increased. A closer view of the microstructure of fiber reinforced Zn-32Al shows that the dendrites
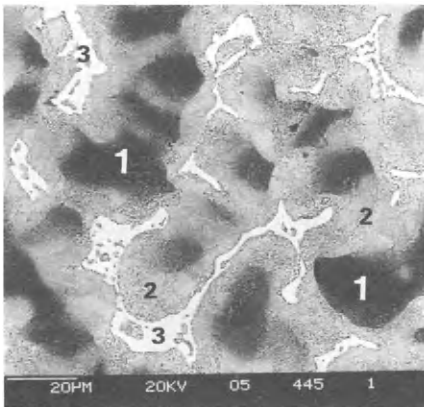
Fig. 4. Atomic contrast micrograph (BSE) of as-polished, unreinforced squeeze cast Zn-32Al showing Al-rich primary cores of $\alpha + \eta$ eutectoid (1), Zn-rich outer dendrite layers of $\alpha + \eta$ eutectoid (2) and interdendritic $\eta + \varepsilon$ phases (3).
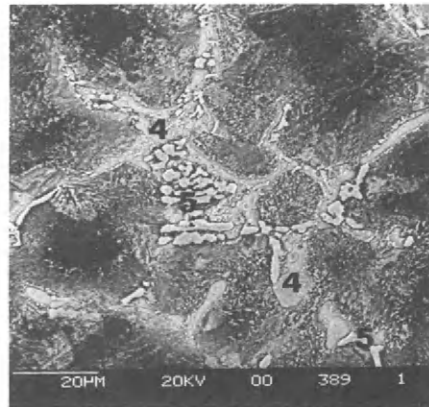
Fig. 5. SE micrograph of Nital etched, unreinforced squeeze-cast Zn-32Al showing (4) η and (5) ε phases.

have grown predominantly into the spaces between fibers, so that the latter are surrounded by zinc rich phases (Fig. 7a and 7c). This observation rules out the possibility of fibers acting as nucleation sites for Al rich primary in the matrix alloy. In comparing the reinforced and unreinforced materials, it was found that the volume fraction of η phase decreases with an increase of volume fraction of fiber. When the volume fraction of fiber is 12 vol %, most of the fibers are surrounded by η phase (Fig. 7b). However, when the volume fraction of fiber is 24% (Fig. 7d), the percentage of η rich phase is much less, more of the fibers are surrounded by Zn rich $\alpha + \eta$ eutectic and the ε phase is found adjacent to fibers.

The fibers in the preform are mostly aligned randomly in the transverse plane, and this fiber arrangement was retained after squeeze casting as shown in Fig. 8a. The SiO_2 binder in the preform also plays a role in the reinforced composites. In examining polished sections of the composites, dark silicon rich regions between fibers and at fiber/matrix interfaces were revealed (Fig. 8b). These were identified using energy dispersive X-ray analysis on specimens examined in the scanning electron microscope.

Mechanical Properties

In this work, only the results of tensile and instrumented impact tests of squeeze cast Zn-32Al, and its composites with 12 vol % and 24 vol % alumina fibers are reported. Standard tensile (6.35 mm gage
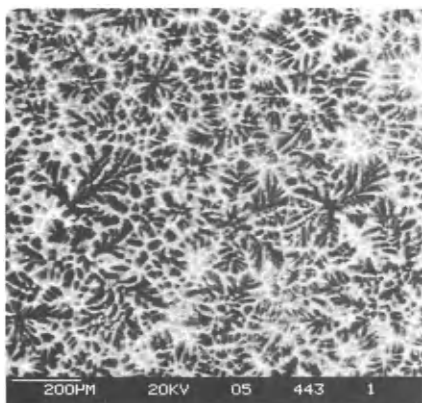
Fig. 6(a). Unreinforced, squeeze-cast Zn-32 Al.
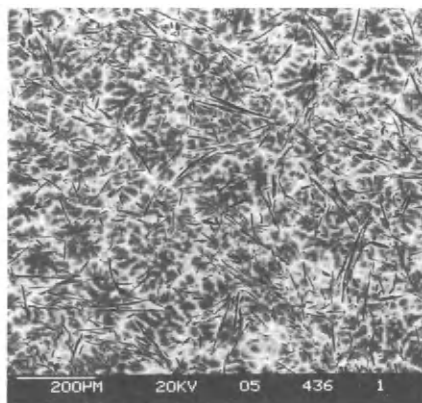
Fig. 6(b). 12 vol % Al_2O_3 reinforced Zn-32Al (planar view).
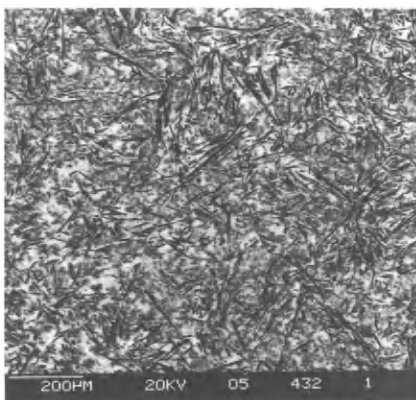
Fig. 6(c). 24 vol % Al_2O_3 reinforced Zn-32Al (planar view).

diameter and 25.4 mm gage length) and full size, unnotched Charpy impact test specimens were machined from the transverse section of the squeeze cast discs. All tests were performed in compliance with recommended ASTM standards.

Table 1 lists the tensile test results of both Zn-32Al alloy and its composites. It is clear that at room temperature, the unreinforced alloy exhibited significantly higher tensile properties than its reinforced counterparts. However, at elevated temperatures, the benefit of fiber reinforcement begins to show by providing improved tensile strength. This phenomenon is most apparent when the UTS of the unreinforced and reinforced materials are compared (Fig. 9).

The measured values of Charpy impact energy of the reinforced and unreinforced Zn-32Al are listed in Table 2. In the case of unreinforced Zn-32Al, the Charpy impact energy values were found to increase with increasing test temperatures. Despite the fact that there was a decrease in the initiation energy
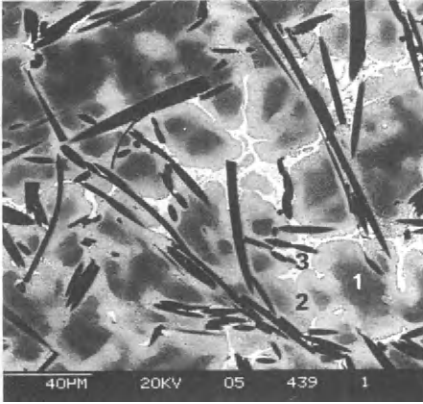
Fig. 7(a). Atomic contrast image (BSE) of as-polished 12 vol % Al$_2$O$_3$ reinforced Zn-32Al composite (planar view) showing (1) Al-rich $\alpha + \eta$, (2) Zn-rich $\alpha + \eta$, and (3) $\eta + \epsilon$ interdendritic phases.
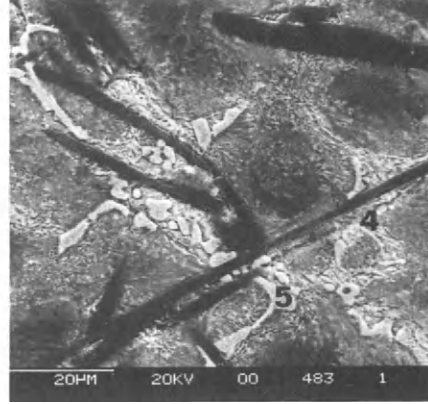
Fig. 7(b). SE micrograph of Nital etched, 12 vol % Al$_2$O$_3$ reinforced Zn-32Al composite (planar view) showing (4) η and (5) ϵ phases.
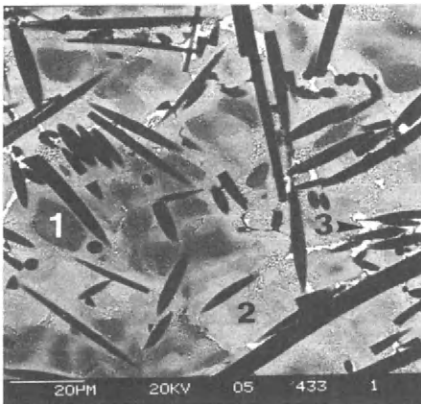
Fig. 7(c). Atomic contrast image (BSE) of as-polished 24 vol % Al$_2$O$_3$ reinforced Zn-32Al composite (planar view).
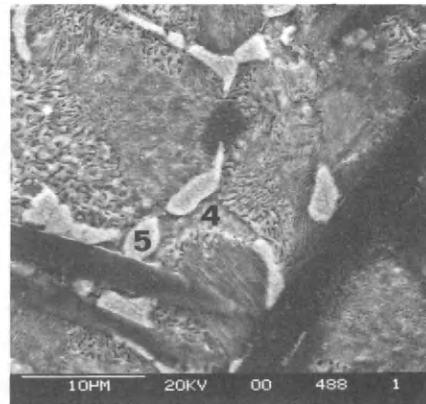
Fig. 7(d). SE micrograph of Nital etched, 24 vol % Al$_2$O$_3$ reinforced Zn-32Al composite (planar view).

with an increase in temperature, the corresponding increase in propagation energy at higher temperatures resulted in an overall increase in impact energy. The decrease in maximum sustained load during impact testing at higher test temperatures is conceivable, since the material becomes ductile and starts losing its load bearing capacity at elevated temperatures.

For the reinforced composites, the effect of test temperature on Charpy energy values was rather insignificant. For both the 12 vol % and 24 vol % alumina fiber reinforced Zn-32Al, the decrease in initiation energy with an increase in test temperature was not as pronounced as in the case of the unreinforced alloy. In addition, the propagation energy was so low that no increase in overall Charpy energy
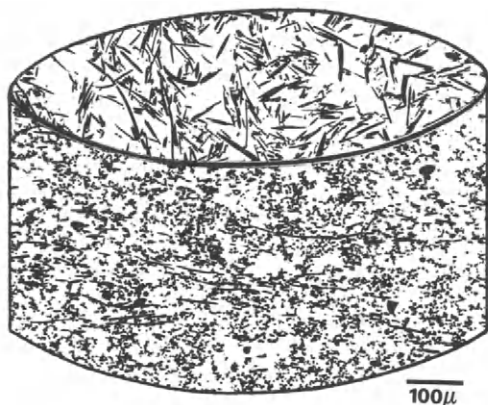
Fig. 8(a). Optical micrograph of as-polished, 24 vol % Al_2O_3 reinforced Zn-32Al showing fiber arrangement in radial and planar directions.
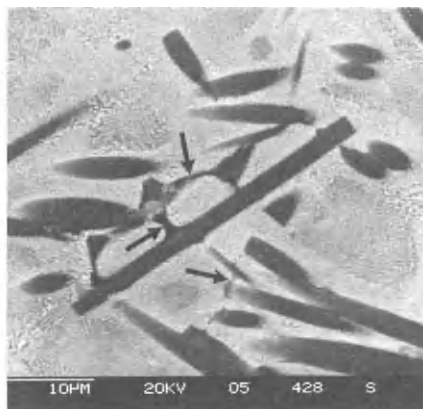
Fig. 8(b). SE micrograph of as-polished, 24 vol % Al_2O_3 reinforced Zn-32Al showing SiO_2 films between fibers (arrows).

value has resulted. This insensitivity to test temperature is indicated in the minimal decrease in maximum sustained load at higher test temperatures. It is probable that the Charpy energy values measured in the Zn-32Al composites are so low, that the effect of temperature is not measurable by this test.

Fractography

Figure 10a shows the fracture surface of a squeeze cast Zn-32Al tensile specimen which was tested at 25°C. The surface is composed of quasi cleavage interspersed with fine dimples. In some areas, fracture of iron rich particles ($FeAl_3$) is evident. When the same material was tested at 150°C, failure was

TABLE 1 Uniaxial Tensile Test Results for Squeeze Cast Zn-32Al, and Al_2O_3 Reinforced Zn-32Al Composites

Test temperature	YS (MPa)	UTS (MPa)	El (%)
Unreinforced Zn-32 Al			
25°C	332.5 ± 19.4	404 ± 12.5	7-13
100°C	199 ± 12.1	268 ± 7	16-18
150°C	100.6 ± 5.8	156 ± 3	7-13
12 vol % Al_2O_3 reinforced Zn-32 Al			
25°C	—	288 ± 11.2	0.03-0.25
100°C	194.2 ± 16.6	281.8 ± 23.4	0.60-1.23
150°C	124.4 ± 15.1	142,1 ± 19.1	2.24-2.66
24 vol % Al_2O_3 reinforced Zn-32 Al			
25°C	—	293 ± 23	0.05-0.11
100°C	251.3 ± 9.7	260.3 ± 17.4	0.18-0.44
150°C	169.9 ± 13.8	183.1 ± 13.8	0.32-0.52
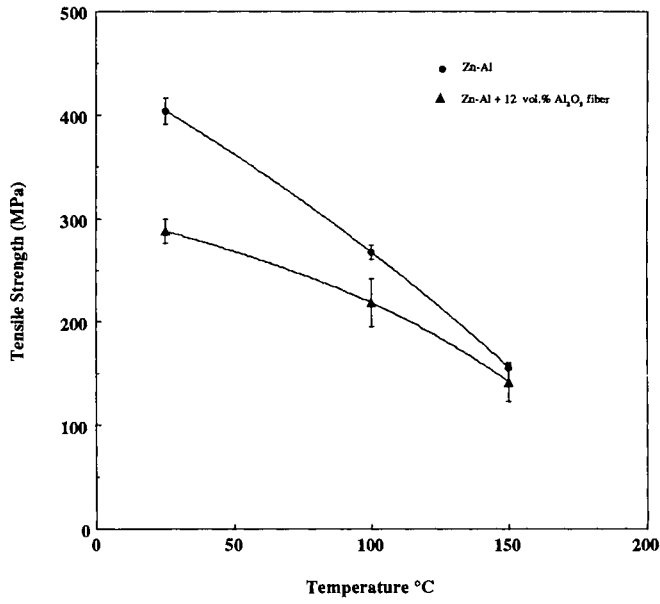
Fig. 9(a).   Ultimate tensile strength as a function of test temperature for squeeze cast unreinforced and
12 vol % Al_2O_3 reinforced Zn-32Al.
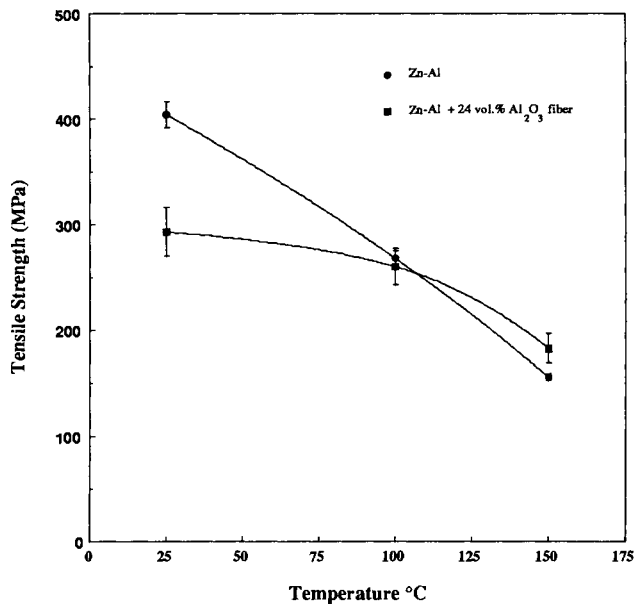
Fig. 9(b).   Ultimate tensile strength as a function of test temperature for squeeze cast unreinforced and
24 vol % Al_2O_3 reinforced Zn-32Al.

TABLE 2 Charpy Impact Test Results (Unnotched Specimens) of Squeeze-Cast Zn-32Al Alloy and Composites

Material	Test temperature (°C)	Maximum load (kN)	Initiation energy* (J)	Propagation energy** (J)	Total energy (J)
Unreinforced Zn-32Al	25	16.3 ± 0.3	56.3 ± 5.1	29.2 ± 6.2	85.5 ± 5.5
	100	14.7 ± 0.3	43.8 ± 0.7	51.1 ± 17.5	94.9 ± 17.5
	150	12.5 ± 0.3	37.1 ± 2.6	93.4 ± 7.3	130.5 ± 6.4
12 vol % Al_2O_3 Zn-32Al	25	10.24 ± 1.0	2.29 ± 0.3	0.14 ± 0.04	2.43 ± 0.33
	100	9.01 ± 1.6	2.03 ± 0.9	0.22 ± 0.11	2.25 ± 0.88
	150	8.49 ± 1.6	2.10 ± 1.0	0.17 ± 0.09	2.27 ± 1.13
24 vol % Al_2O_3 Zn-32Al	25	11.89 ± 0.8	2.64 ± 0.4	0.17 ± 0.03	2.82 ± 0.46
	100	10.85 ± 0.3	2.40 ± 0.1	0.13 ± 0.01	2.53 ± 0.14
	150	10.75 ± 0.4	2.85 ± 0.3	0.13 ± 0.02	2.98 ± 0.30

* Energy at maximum load
** Total energy - Energy at maximum load
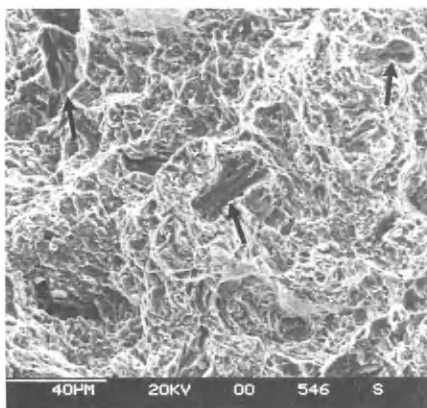
Fig. 10(a). SEM fractograph of a squeeze cast, unreinforced Zn-32Al tensile specimen tested at 25°C (arrows indicate $FeAl_3$).
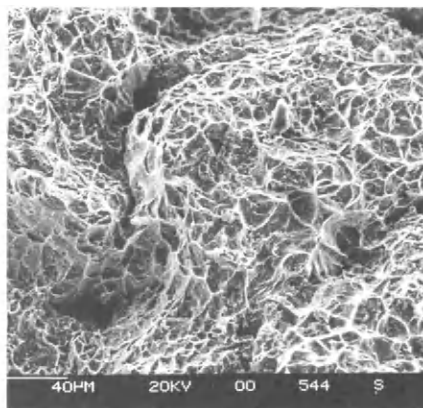
Fig. 10(b). SEM fractograph of a squeeze cast, unreinforced Zn-32Al tensile specimen tested at 150°C.

more ductile, with larger dimples and no quasicleavage being present on the fracture surface (Fig. 10b). This finding correlates well with the tensile values measured at 25°C and 150°C (Table 1).

Metallographic examinations were performed on Zn-32Al tensile specimens which were sectioned at a plane perpendicular to the fracture surface and polished. It was noted that for specimens tested at room temperature, the fracture mode was primarily by transgranular failure. Occasionally, cracks propagated through the η phase and along the η/zinc rich eutectoid interface, but transgranular failure appeared to be the dominant mode of failure. When the alloy was tested at 150°C, the fracture paths were found to proceed preferentially along the η/zinc rich eutectoid interfaces resulting in a fully interdendritic failure (Fig. 11).
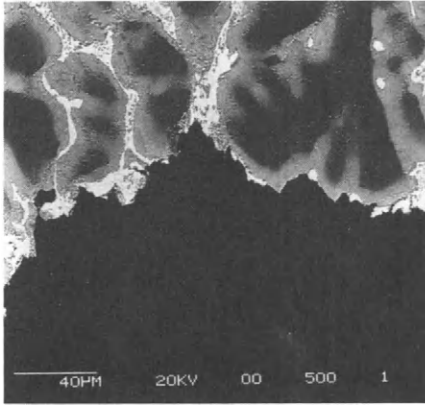
Fig. 11. Atomic contrast image (BSE) of sectioned and polished tensile specimen of squeeze cast, unreinforced Zn-32Al (test temperature 150°C) showing the $\eta + \varepsilon$ interdendritic phases at the fracture surface.
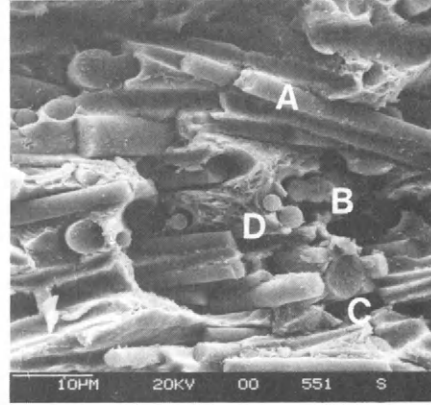
Fig. 12. SEM fractograph of a 24 vol % Al_2O_3 reinforced Zn-32Al tensile specimen tested at 25°C (A: interfacial debonding, B: fiber pullout, C: fractured fibers, D: dimples in matrix).

In the case of reinforced Zn-32Al, the fracture behaviour of specimens reinforced with 12 vol % and 24 vol % Al_2O_3 fibers was rather similar. In essence, cracking proceeded preferentially along the fiber/matrix interfaces, and occasionally along the η/eutectoid interfaces. This seems to suggest that the interfacial strength between the fiber/matrix is weaker than the interfacial strength between η/eutectoid. In addition to the fiber/matrix interfacial debonding, the fracture of fibers as well as fiber pullout were also observed on the fracture surfaces (Fig. 12 & 13). Fine dimples were found in the matrix
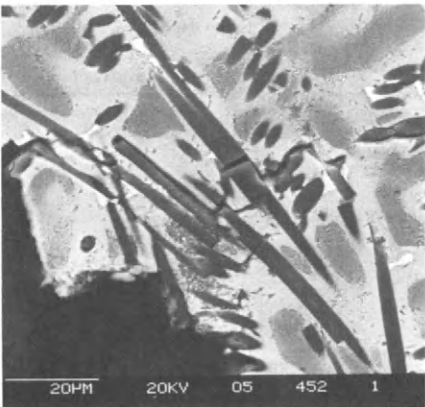
Fig. 13. Atomic contrast image (BSE) of sectioned and polished tensile specimen of 24 vol % Al_2O_3 reinforced Zn-32Al (test temperature 25°C) showing fiber/matrix debonding and fiber cracking.
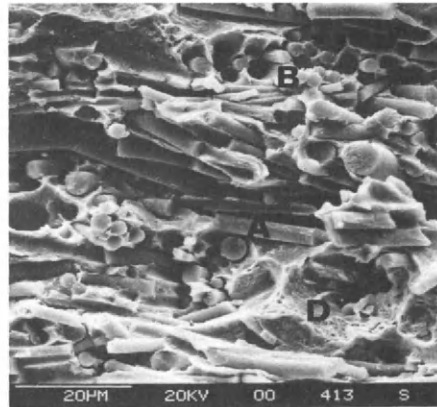
Fig. 14. SEM fractograph of a 24 vol % Al_2O_3 reinforced Zn-32Al composite tensile specimen tested at 150°C.

between the decohered and fractured fibers. The fracture surfaces of reinforced samples tested at elevated temperatures were similar to those tested at room temperature. Despite the higher test temperatures, the fracture surfaces exhibited little ductility (Fig. 14) and the same mechanisms of fracture operative at room temperature were observed.

It has been mentioned above that the SiO_2 film, which was present on the fiber surface of the preform, was retained on the fiber surfaces even after the squeeze casting operation. Considering that the Al_2O_3 fibers are almost completely covered by SiO_2 film, the fiber/matrix interfaces actually consist of Al_2O_3/ SiO_2/Zn-32Al layers. It is possible that fracture could propagate either along the SiO_2/Zn-32Al or Al_2O_3/SiO_2 interfaces, or through the SiO_2 layer. Further investigation with Auger electron spectroscopy would be required to confirm the mode of fracture.

DISCUSSION

The present study shows that the presence of alumina fibers in the Zn-32Al alloy affects both the micro-structure and the mechanical properties of the unreinforced alloys. During solidification of Al_2O_3/Zn-32Al, the dendrite size is significantly reduced with the presence of fibers. Essentially, following the squeeze casting operation, the SiO_2 binder which is used to hold the fibers together in the preform, remains as an interconnecting network between the fibers. The molten Zn-32Al has to infiltrate and solidify in the spaces between fibers, resulting in finer dendrite sizes.

From the limited test data, it is shown that the impact energy values were drastically reduced when Zn-32Al was reinforced with Al_2O_3. This is the case even when tests were performed at elevated temperatures (around 150°C). With dynamic loading, as in the case of impact tests, the results of fractographic examination indicated no change in failure mode in both reinforced and unreinforced Zn-32Al tested at temperatures between 25°C to 150°C.

In the case of static loading, such as tensile testing, the room temperature tensile strength of Zn-32Al was also found to be higher than that of Al_2O_3/Zn-32Al. However, at elevated temperatures, Al_2O_3/Zn-32Al composites exhibited a comparable or even higher tensile strength than Zn-32Al. This phenomenon can probably be explained by the observed fractographic features. When a tensile Zn-32Al sample was fractured at room temperature, cracking tended to proceed in a transgranular manner. However, at elevated temperatures, a transition of transgranular to intergranular mode of failure was found. This transition is likely due to the weakening of the η phase and η/eutectoid interfaces at elevated temperatures. In the case of Al_2O_3/Zn-32Al, with the smaller volume fraction of η phase, the same failure mode of fiber/matrix interfacial debonding is operative at both room and elevated temperatures. Considering the degradation in strength of the η phase at elevated temperatures, it is conceivable that the fiber/matrix interfacial strength becomes higher than that of η/eutectoid, providing a higher tensile strength in the Al_2O_3/Zn-32Al than in unreinforced Zn-32Al at elevated temperatures.

CONCLUSIONS

1. Alumina fibers in squeeze cast discs of Al_2O_3 reinforced Zn-32Al were found to be aligned randomly in the transverse plane. The fiber arrangement of the preforms was retained after the squeeze casting operation.

2. Microstructures of the Zn-32Al and Al_2O_3/Zn-32Al squeeze cast materials were composed of Al rich $\alpha + \eta$ eutectoid and interdendritic phases composed of η and ϵ ($CuZn_x$). The dendrite size and volume fraction of η were found to decrease as the volume fraction of Al_2O_3 fibers was increased.

3. Charpy impact properties of the Al_2O_3/Zn-32Al composites were significantly lower than that of the unreinforced Zn-32Al. No improvements in the Charpy energy values of the Al_2O_3/Zn-32Al composites were measured when the tests were conducted at elevated temperatures.

4. Although the unreinforced Zn-32Al had higher tensile strength than its reinforced counterparts at room temperature, reinforcement with alumina fibers did provide improved elevated temperature (100 and 150°C) tensile properties.

REFERENCES

Barnhurst, R.J., E. Gervais and F.D. Bayles (1983). AFS Transactions, 91, 569.

Das, A.A., B. Zantout, M.M. Yakoub, and A.J. Clegg, (1986). Int. Symp. on Zinc-Aluminum (ZA) Casting Alloys, ed. G.P. Lewis, R.J. Barnhurst and C.A. Loong, Seris 25-5/1, No. 1, 213.

Dent, P.N. and S. Murphy (1986). Int. Symp. on Zinc-Aluminum (ZA) Casting Alloys, ed. G.P. Lewis, R.J. Barnhurst and C.A. Loong, Seris 25-5/1, No. 1, 127.

Guerriero, R., J.B. Parse, and I. Tangerini, (1986). Int. Symp. on Zinc-Aluminum (ZA) Casting Alloys, ed. G.P. Lewis, R.J. Barnhurst and C.A. Loong, Seris 25-5/1, No. 1, 229.

Kubel, E.J. Jr. (1987). Advanced Materials and Processes inc. Metal Progress, 7, 51.

Lo, J., (1989). Unpublished work.

Magnus, B., M. Melus and G. Croeg (1982). La Fonderie Belge, 4, 1927.

Sahoo, M., L.V. Whiting, V. Chartrand and G. Weatherall (1986). Trans. of American Foundrymen's Society, 94, 225.

Erosion resistance of aluminum matrix composites

S. Caron, P. Thibault, S. Turenne, F.G. Hamel and J. Masounave
Industrial Materials Research Institute, National Research Council Canada,
75 de Mortagne Blvd., Boucherville, Québec, Canada, J4B 6Y4

ABSTRACT

The addition of ceramic reinforcement to a metal matrix usually improves the wear resistance of metals. The purpose of this investigation is to evaluate the slurry erosion resistance of different types of aluminum matrix composites. The erosion tests were done using an apparatus developed in-house.

Two volumetric concentrations of alumina particles were tested. The increase in concentration of particles from 20% to 45% by vol. did not improve the erosion resistance. Also, the effect of particle size was negligible in the range studied. The independence of the erosion wear with respect to these structural parameters can be explained by a protection effect brought about by the particles of the composites.

INTRODUCTION

Over the past five years, the production of metal matrix composites (MMCs) has exceeded the laboratory level. However, users are usually reluctant to use new materials before having general knowledge of their behavior. The use of these materials will be limited as long as extensive information on their properties (corrosion resistance, fatigue and toughness, to name a few) is not available.

The price of these high-tech materials is also a limitation on their use. Depending on the fabrication process, the price for a MMC ingot is generally higher than $20 per pound. If it is remembered that the price for a pound of aluminum alloy is generally lower than $2 per pound, it is understandable that the properties have to be really good to justify the use of MMC. Today only those processes which incorporate particles in liquid alloys are affordable. Particles are inexpensive materials for reinforcement, and a foundry process is not expensive. The only large-scale existing industrial process uses particle-incorporation in liquid alloy.

In spite of inescapable problems, MMCs offer interesting advantages. Some of them are: high strength to weight ratio, the capacity to retain their strength at high temperature, high resistance to abrasion and erosion. Actually, there is insufficient information on the last point. In order to characterize the erosion resistance of these newly developed materials, some studies were conducted with sand blasting apparatus. However, such results cannot be related to phenomena that arise when the erosion is caused by flowing abrasive slurries. In this paper we will study the wear mechanisms occurring when a slurry impinges on an alumina-particulate/aluminum composite. The effects of impingement angle, volumetric fraction and size of particulates in the composites were studied. The influence of the microstructure of the matrix on the wear resistance of MMCs is of great interest.

EXPERIMENTAL PROCEDURE

Fabrication of MMCs

In order to achieve a complete and homogeneous incorporation of the reinforcement-particulates, a foundry proprietary process developed at IMRI was used to make a cast composite alloy. In this process, most of the detrimental effects associated with the vortex or compocasting methods (Ghosh and co-workers 1984; Millière and Suéry, 1988) have been overcome. Excessive amounts of porosity, partial or complete rejection of particulates, incorporation into the matrix of the oxide surface layer and slow rate of particulate addition, are some of the related problems discussed in the literature (Ghosh and co-workers, 1984; Millière and Suéry, 1988; Prabhakar and Rohatgi, 1977; Mehrabian and co-workers, 1974).

Samples containing 45% and 20% by vol. of 150 mesh (100 μm) and 80 mesh (180 μm) commercial grade alumina, in a 5083 aluminum matrix, were cast in open molds. This aluminum alloy was chosen for its high magnesium content (4%) which is well known to promote the wetting of the particles by the alloy. The samples containing 20% by vol. of both sizes of alumina particles were solidified in copper molds in order to avoid the risk of particle rejection (McCoy and Wawner, 1988) caused by growing dendrites, and to ensure that settling will not occur. The solidification rate of these samples was about 50°C/sec as estimated from the temperature measurement by a thermocouple situated 5 mm above the chilled surface.

Samples with alumina content of about 45% by vol. were also produced using the settling behaviour of these particles in liquid aluminum alloys. According to the Stokes' law of settling (Rohatgi and co-workers, 1988; Geiger and Doirier, 1973), one can compute the time during which the alloy would have to remain liquid before solidification, to ensure that all the particles become deposited on the bottom of the mold. Assuming a particle average diameter of 100 μm, the predicted settling velocity is:

$$V_p = \frac{2R_p(\rho_p - \rho_m)g}{9\mu} = 4.5mm/sec$$

where:

V_p = settling velocity

R_p = partice radius

ρ_p = particle density = 3740 kg/m³ (alumina)

ρ_m = matrix density = 2650 kg/m³ (5083)

μ = viscosity of molten metal = $1.3 \times 10^{-3} N\cdot s/m^2$

However, because the effective viscosity of an alloy containing nearly 50% by vol. of solid phases is increased, the real settling velocity would be much lower. Therefore, preheated refractory molds have been used to achieve the slow cooling rate necessary for complete settling. The cooling rate for samples containing 45% by vol. of particles was determined to be around 0.5°C/sec. However, even with such a large difference in solidification conditions, samples containing no particles solidified under both conditions demonstrate indistinct hardness of about 69 HRB.

In order to verify the effect of solidification rate on microstructure and on erosion resistance, some unreinforced specimens were made by squeeze-casting technology using an experimental set-up described elsewhere (Turenne and co-workers, 1988). The die and ram were heated to a temperature of 300°C. The melted 5083 alloy was heated to 810°C in order to avoid fast solidification of a large volume of alloy prior to load application. The ram was inserted in the die to obtain the maximum pressure of 80 MPa within 0.5 second. The load was maintained during 10 seconds to permit complete solidification of the disc-shaped specimen (38.1 mm dia.). The high pressure during solidification leads to sound specimens. As the hardness of the ductile matrix material has no prime effect on the erosion resistance of MMCs (Finnie and co-workers, 1967), it is reasonable to assume that the different molding procedures used to produce the samples have no effect on the results.

Erosion Testing

Erosion tests were performed using an apparatus based on an air-powered double-diaphragm slurry pump. The slurry was pumped from a tank containing about 7 l of water with a silica sand concentration of 10% by wt. The sand particles lay between 200 and 300 μm in size. The pumped slurry was projected against the surface of the specimen, then recirculated. The velocity of the erodent particles has been assumed equal to the velocity of the slurry jet (having a diameter of 4.7 mm) because the sand concentration was high enough to jusify this approximation. The velocity of the slurry was measured by an electromagnetic flowmeter. Tests were made with slurry velocities of 18 m/s. The sample holder permitted the attack angle of the jet to be set at 15 to 90°. The slurry erosion tests were continued for a period of 15 minutes in order to obtain significant mass losses of the specimens. Before and after erosion tests the specimens were cleaned in an ultrasonic bath, dried and weighed.

The wear of specimens is expressed by volume loss. This quantity is evaluated from the mass losses of specimens and the densities of the alloy and the alumina particles. The volumetric fraction of alumina particles in the different composites was evaluated from determination of surface area of particles and matrix by image analysis.

RESULTS

Volume Loss as a Function of Attack Angle

The wear values were reported as volume losses in order to compare the erosion resistance of the different materials tested. From visual examination of eroded surfaces, some specimens were eliminated due to macroscopic defects such as agglomeration of particles or macroporosities. These macroscopic defects are mainly due to defective blades of the stirring system. The macroscopic defects were observed mostly in the case of cast specimens with a high volume fraction of 45% and particle size of 100μm. The effect of macroscopic defects is illustrated in Fig. 1 at large attack angle of the slurry jet. Fig. 1 shows a maximum of erosion for an attack angle of the slurry jet of about 30°. In Fig. 2, the volumetric fraction of alumina particles is 20% compared to the results of Fig. 1 obtained for composites with the same particle size (100 μm) but with particle concentration of 45% by vol. The level of erosion is similar for the two composites with different volumetric fraction.

For the composites made of alumina particles of 180 μm, the erosion values are reported as a function of slurry jet attack angle in Fig. 3. The results for the particle volumetric fraction of 20% and 45% are again comparable within the experimental scatter range. The effect of attack angle of the slurry jet can be summarized by an increase in erosion at glancing angles up to 30° followed by an

erosion plateau independent of attack angle. One should note that the wear in
Fig. 3 for composites made of 180 μm particles is similar to that obtained for
composites containing particles of 100 μm size (Fig. 2).

For comparison, the erosion wear of unreinforced 5083 alloy is illustrated in
Fig. 4. This curve shows that the erosion wear of this alloy is independent of
the fabrication technique (casting, squeeze-casting or cold-rolling) of the
specimens. The maximum of erosion at 30° is much more pronounced than that of
the composites. For an atack angle of 90°, the erosion of the aluminum alloy is
about 50% higher than that of the composites.

SEM Observations

The eroded surfaces of some specimens were observed using a scanning electron
microscope. The observations were made at the maximum erosion depth of the
erosion profiles. Fig. 5 shows that at the glancing attack angle, the aluminum
alloy covers partially the alumina particles indicating that considerable plastic
deformation of the alloy occurs. The particle breakage is more important for the
90° incidence angle as shown in Fig. 6. The distance between particles that is
"seen" by abrasive particles is estimated to lay between 200 and 500 μm. This
estimate came from observations of eroded surfaces as shown in Fig. 7.

DISCUSSION

As it can be seen in Fig. 4, the different fabrication processes have virtually
no effects on the erosion resistance. The results from the squeeze-cast
specimen, slowly solidified cast specimens and the rolled specimens are very
close to each other. All these specimens are almost completely free of porosity,
which leads to small dispersion in the results. The erosion resistances of cast
specimens are also in the same order of magnitude. Such results also mean that
the solidification rate of this aluminum alloy has no effect on its erosion
resistance. Therefore, the microstructure of this alloy has no influence on its
erosion resistance due to the small amount of Mg-rich second phase. It has to be
pointed out that the absence of effect of the microstructure is specific to the
erosion test used in this study. It is possible that this test can be too severe
to discriminate the three different microstructures tested.

A very important observation is that the erosion resistance, within the data
scatter range, is about the same for all the composite specimens, independently
of the size of the reinforcement or its volumetric concentration (Fig. 8). Only
slight differences can be observed. From Mirza and co-workers (1989), it is
known that in cases where the interparticulate distance in MMCs is approximately
equal to the size of the abrasive erodent, one should observe an independence of
the erosion rate versus the particle size and the interparticulate distance.
This rule is valid as long as all the dimensions, including the size of the
reinforcement particulate, stays in the same order of magnitude. In the actual
case the diameter of erodent particles lies between 200 μm and 300 μm, which is
in the same range than the interparticulate distances.

In regard to Fig. 8, it may be pointed out that there must be a threshold value
on the particle volumetric fraction below which an increase in erosion occurs.
This value could represent an interesting compromise between the fabrication
difficulties and performance, since more particles do not yield better results.
The same argument can be applied to the size of the reinforcement particles.
Problems for wetting small particles in aluminum alloys are increasing rapidly
when decreasing the size of particles. For a good erosion resistance
application, the use of large particles is preferred from the fabrication point
of view.

CONCLUSION

The following conclusions are based on the erosion test results and on the different observations made on the worn specimens.

- The cooling rate and the fabrication process have negligible effects on the erosion resistance of 5083 aluminum.

- There is no advantage to incorporate more than 20% by vol. and smaller than 180 µm alumina particles in 5083 aluminum alloy if maximum erosion performance measured accordingly to the present study is required.

- The erosion resistance of alumina particles-aluminum alloy composite is two times higher than that of the unreinforced aluminum alloy.

ACKNOWLEDGEMENT

REFERENCES

Finnie, I., J. Wolak and Y. H. Kabil (1967). J. of Mater., 2, 682-700.
Geiger, G. H. and D. R. Doirier (1973). In Transport Phenomena in Metallurgy, Addison-Wesley Pub. Co.
Ghosh, P. K., S. Ray and R. K. Rohatgi (1984). Trans. of the Japan Inst. of Met., 25, 440-444.
McCoy, J W. and F. E. Wawner (1988). In Cast Reinforced Metal Composites. S. G. Fishman and A. K. Dhingra (eds), Proc. of the International Symposium on Advances in Cast Reinforced Metal Composites, 24-30 Sept., Chicago, Illinois, 237-242.
Mehrabian, R., R. G. Riek and M. C. Flemings (1974). Met. Trans., 5, 1899-1905.
Millière, C. and M. Suéry (1988). Mater. Sci. Technol., 4, 41-51
Mirza, J., S. Turenne and J. Masounave (1989). To be published in Can. J. of Civil Eng.
Prabhakar, K. V. and R. K. Rohatgi (1977). In Quality Control of Engineering Alloys and the Role of Metals Science. Proc. of International Conference, Delft (Delft University of Technology), 215-224.
Rohatgi, P. K., F. M. Yarandi and Y. Liu (1988). In Cast Reinforced Metal Composites. S. G. Fishman and A. K. Dhingra (eds), Proc. of the International Symposium on Advances in Cast Reinforced Metal Composites, 24-30 Sept., Chicago, Illinois, 249-255
Turenne S., C. Le Déoré and J. Masounave (1988). In Wear Resistance of Metals and Alloys, G. R. Kingsbury (ed), World Materials Congress, 24-30 Sept., Chicago, Illinois, 39-45.
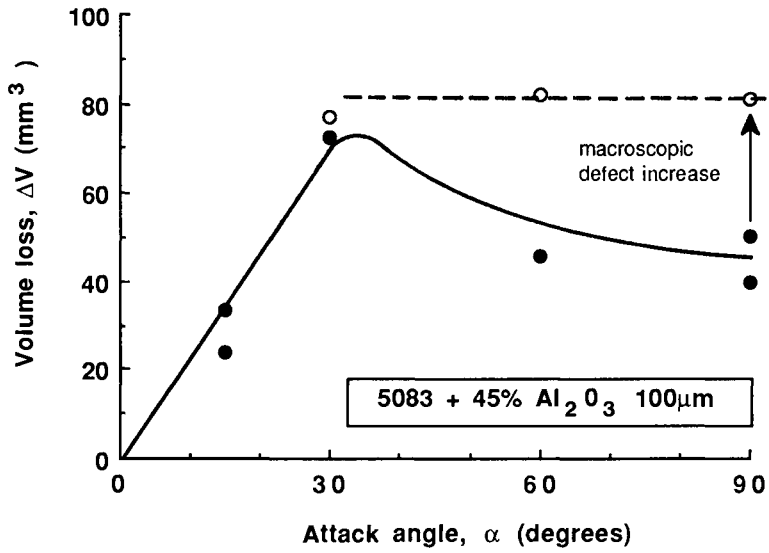
Fig. 1. Volume loss as a function of attack angle for composites made of 100 μm alumina particles in a concentration of 45% by vol.
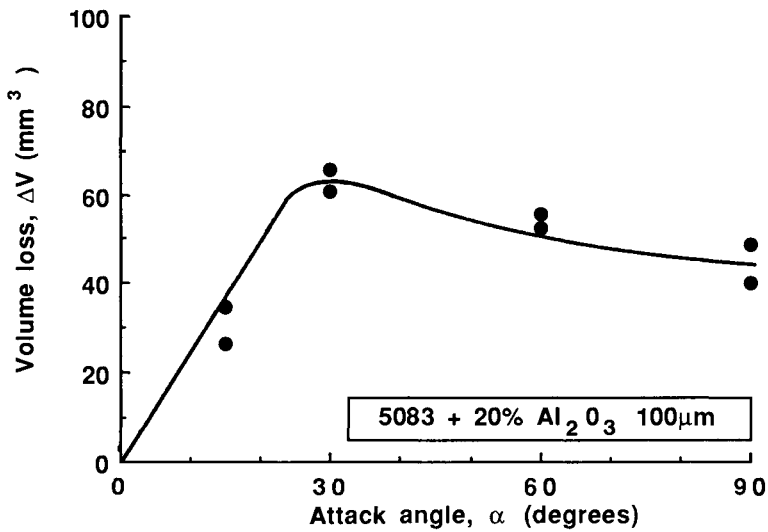
Fig. 2. Volume loss as a function of attack angle.for composites made of 100 μm alumina particles in a concentration of 20% by vol.
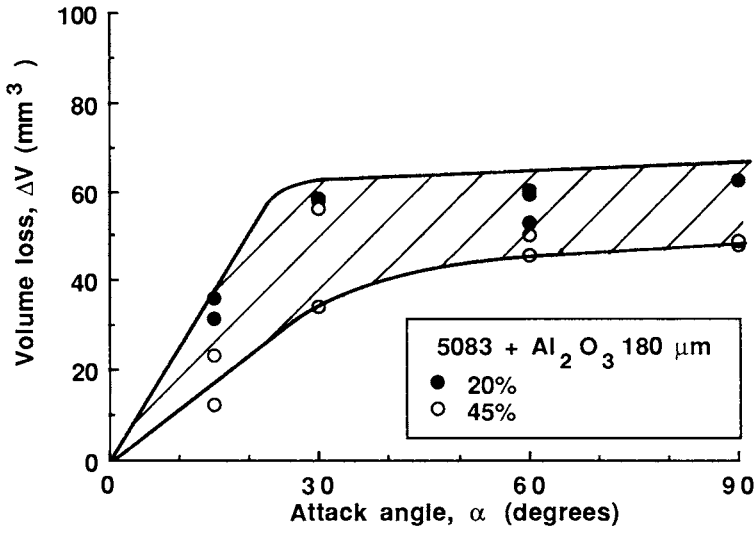
Fig. 3. Volume loss as a function of attack angle for composite made of 180 µm alumina particles.
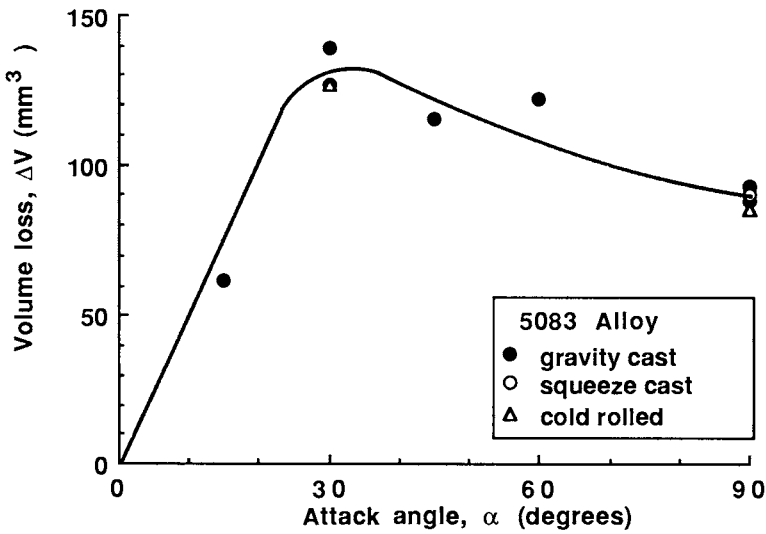
Fig. 4. Volume loss of 5083 alloy for different fabrication technique as a function of attack angle.
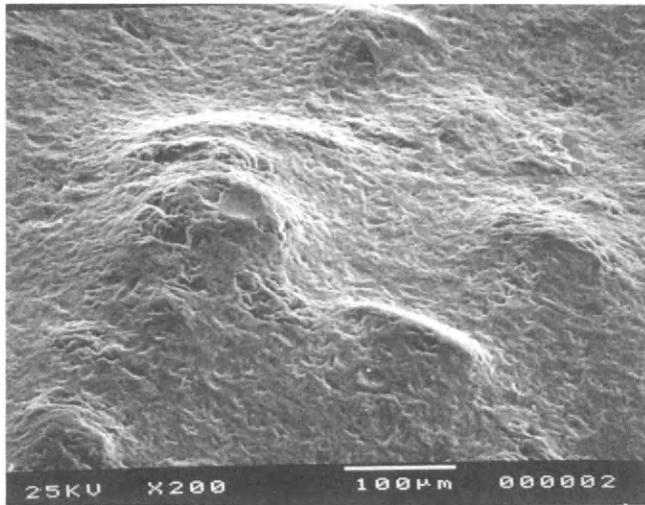
Fig. 5. Partial covering of alumina particle by aluminum alloy, 20% by vol.
with 100 μm alumina particles.
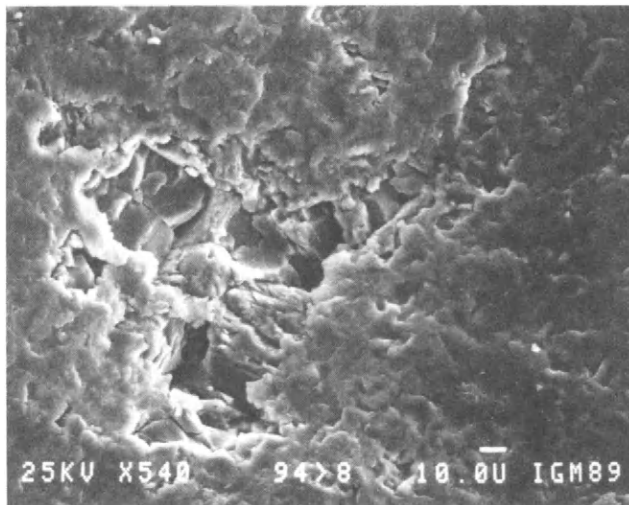
Fig. 6. Breakage of alumina particles for normal incidence erosion, 45% by vol.
with 100 μm alumina particles.
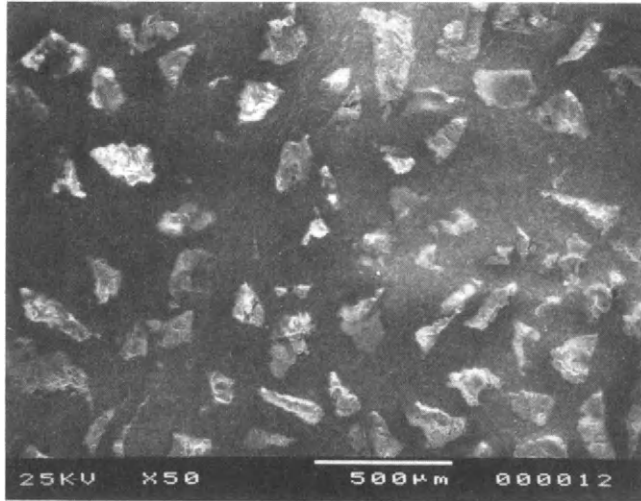
Fig. 7. Eroded surface showing alumina particles. 45% by vol. with 180 μm alumina particles.
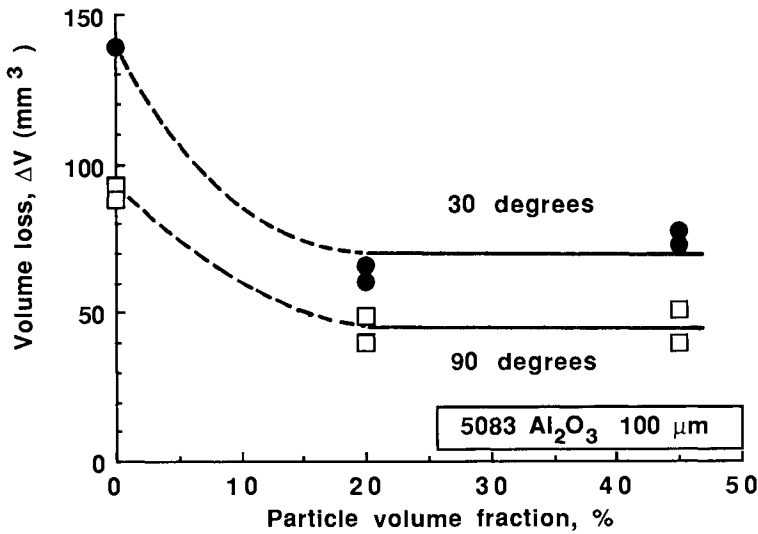
Fig. 8. Volume loss as a function of particle volume fraction in the composite.

Crack stability and crack velocity considerations in fracture of metal-ceramic composites

Adam J. Gesing and Gene Burger

Alcan International Limited, Kingston Research and Development Centre, P.O. Box 8400, Kingston, Ontario, Canada, K7L 5L9

ABSTRACT

Both static and cyclic fatigue can take place in metal–ceramic composites. They occur as strength degradation and delayed failure in service which may involve both exposure to cyclic loads and a reactive environment. Discussed in this paper are the development of a design methodology for components made of particulate–filled ceramic/metal–matrix composites (PFCMMCs) which can account for both crack size (R–curve) and crack velocity effects in delayed failure under cyclic and static loading. The interaction of the crack velocity and crack extension effects in determining the crack resistance curve is discussed and a combined crack resistance–velocity–extension R–V–Δa diagram is proposed as a basis for structural component design in PFCMMCs. The design logic is based on allowing a small extension of microflaws while assuming that the crack extension forces remain below the fatigue threshold of the macrocracks.

INTRODUCTION

Under demanding applications, bulk metals often have insufficient temperature capability, hardness, wear or erosion resistance. Ceramics can provide these properties but at the cost of increased brittleness. Composites provide a means of combining some of the desirable properties of the component phases into a useful engineering material. There has been an interest in recent years in the fields of both ceramic and metal–matrix composites. We will concentrate on discontinuous composites containing a particulate filler phase and will review the state of knowledge about factors governing their mechanical properties and design methodologies for composite components.

TOUGHENING AND FATIGUE MECHANISMS IN PARTICULATE-FILLED CERAMIC/METAL-MATRIX COMPOSITES

Toughness refers to the amount of energy dissipated in the extension of a major crack by a unit area. The energy can go into generating a new surface or be converted to heat or sound by plastic or viscous flow or by friction between sliding non–planar crack surfaces. Toughness is evaluated from the load–displacement record measured remotely from the crack. Thus the measured quantity depends on:
- the energy dissipated in the specimen including the propagation of multiple cracks,
- crack branching, crack deflection, plastic and viscous flow in the crack tip process zone,
- microcracking and microcrack linking ahead of the crack tip,
- plastic flow and friction due to bridging and interference between crack faces in both the crack wake region of the main crack and the secondary crack branches or microcracks.

In the case of particulate–filled ceramic/metal–matrix composites (PFCMMCs) in which the matrix contains ceramic and metal phases continuously interconnected, one observes brittle fracture with no significant plastic deformation or microcracking off the main crack plane. The apparent fracture toughness of such a composite, however, is significantly increased over that of a monolithic ceramic. In this case it is expected that the dominant toughening effects will occur in the crack wake region and be due to crack bridging by filler grains and plastically deforming metal filaments (Evans, 1988).

The industry is increasingly aware that for composites, toughness is an engineering concept and not a material property; it depends on crack extension, crack geometry, stress distribution, sample size, load/displacement boundary conditions, as well as on crack velocity and stability considerations. In an effort to account for the effect of crack extension and crack stability considerations, toughness is plotted as a function of crack extension, thus forming the crack resistance curves (R–curves).

A typical R–curve for an alumina ceramic is shown in Fig. 1 (Steinbrech, 1988). For a one–dimensional through–thickness edge crack in a compact tension specimen, crack resistance increases as the bridging zone in the crack wake increases and levels out at large crack extensions as a constant length of the bridging zone is achieved. The R–curve for a two–dimensional half–penny shaped microcrack extending on a tensile surface of a bend bar begins at a much lower level, but increases at a higher rate than the through–thickness macrocrack of the same length. This can be attributed to the difference in the way the microcrack and macrocrack sample the microstructure.
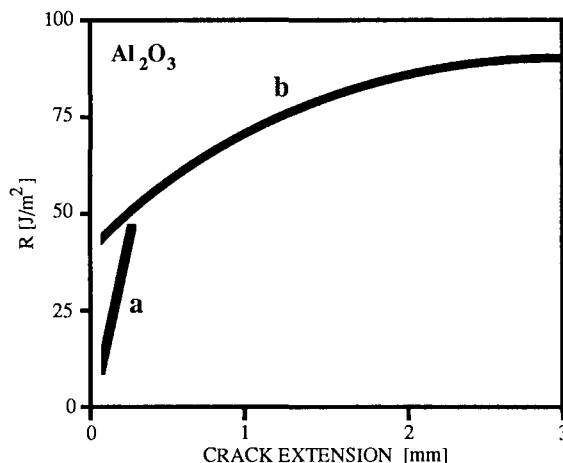
Fig. 1 R–curves for alumina: a) penny–shaped surface cracks and b) through macrocracks, after Steinbrech (1988).

A macrocrack is confined to a macroscopically plane surface and thus is easily pinned by toughening micro–structural features, whereas the microcrack is much more free to initially seek the path of least resistance. Since the microcrack extension is two dimensional, the geometrical constraint builds up quickly causing the R values to catch up with the macrocrack curve. Crack stability is evaluated by comparing the R–curve with the crack extension force, G^1. The crack extends when G=R. Propagation, however, becomes unstable when dG/da > dR/da. The point of instability is typically taken as the indication of the material toughness. In a material exhibiting a pronounced R–curve, the toughness is non unique since it depends on the initial flaw size and the loading boundary conditions. Further, in a material with a rapidly rising initial portion of the R–curve, multiple small cracks can be initiated as the ones that grow are arrested due to the steep R–curve. This type of behaviour is desirable as it removes the sensitivity of the material strength to the surface finish and makes it more tolerant of the in–service surface damage.

---

[1] The choice of a suitable measure of the crack extension force depends on the nature of the material and the component geometry. When linear elastic fracture mechanics are applicable (no macroscopic plasticity), stress intensity, K, or strain energy release rate, G, can be used interchangeably: $G = K^{2}*(1-v^2)/E$. In the case when plasticity becomes important, the J–integral or equivalent energy–momentum integral formulations of the crack extension force need to be considered. In the case of PFCMMCs, the continuous brittle ceramic matrix is expected to limit the plasticity in the metal phase to local, microscopic dimensions. Hence, we will use the linear elastic strain energy release rate, G, as the appropriate measure of the crack extension force.

In ceramic/metal-matrix composites, one expects an even more pronounced R-curve behaviour. In alumina, bridging in the crack wake extends until the crack opening displacement reaches approximately one quarter of the grain size (Steinbrech, 1988). The larger filler particle sizes and plastic deformation of the metal filaments should significantly increase the length of the bridging zone and hence the range of crack extension over which the rising portion of the R-curve develops.

Increases in toughness for a given flaw size convert directly to increases in load-carrying capacity through linear elastic fracture mechanics relationships. Fatigue effects degrade this capacity as a function of time. Under constant load or displacement, slow crack growth may take place. Under high loads and inert environments, thermally activated bond breakage can become the rate-controlling process. In chemically active environments and/or at lower crack extension forces, chemical reaction may couple to the crack extension. The rate-controlling steps then can be either the stress-independent transport of reactants/products to/from the crack tip, or stress-dependent reaction kinetics at the crack tip. The threshold stress below which a particular reaction is no longer thermodynamically favoured to occur at the crack tip is also predicted. In PFCMMCs, increased crack tip shielding may shift the apparent thresholds to higher crack extension force levels. A larger number of phases in the microstructure, however, increases the number of possible fatigue reactions which may become rate controlling, and the number of chemical reactions which may cause degradation in reactive environments.

Stable slow crack growth is also possible under cyclic loading. Under cyclic load or displacement boundary conditions, a new set of potential time-dependent damage mechanisms becomes possible. Both extrinsic and intrinsic mechanisms, reviewed by Dauskardt (1989), are possible. Two mechanisms are potentially directly applicable to PFCMMCs. One is the fretting wear of bridging particles, which leads to a gradual decrease in the contribution of these particles to toughening. In this case, the rate of the fretting fatigue could become the rate-controlling factor. The second mechanism, which may control the rate of the macrocrack advance, is the intrinsic mechanical fatigue, controlled by dislocations, of the metallic ligament bridges. Cyclic loads in chemically-active environments can be particularly damaging. Synergistic effects can take place where access of the corrosive species is facilitated by the cyclic pumping action of the crack faces and by the cyclic mechanical damage at the crack tip which exposes new sites for crack tip reactions. As discussed above, the complex chemistry of the PFCMMCs may make these considerations particularly important.

The type of the load cycle is also very important. In ceramics it has been shown that the fully reversed compression-tension cycle is much more damaging than the tension-tension cycle for the same ΔG (Nikkila, 1989). This differs from the behaviour of ductile metals where the effective ΔG is measured only above the crack closure load (Dauskardt, 1989). PFCMMCs would be expected to behave like ceramics due to the continuous ceramic phase in the microstructure.

THE DEPENDENCE OF SLOW CRACK GROWTH ON CRACK SIZE

Crack size is a relative concept. The crack can be small in comparison with: 1. the microstructural features, 2. sample dimension constraints, 3. chemical reaction transport process lengths, and 4. mechanical crack stability considerations (Dauskardt, 1989). It has been repeatedly demonstrated that the behaviour of small natural flaws may differ from that of artificial indentation flaws, and certainly differs from the behaviour of large cracks in fracture mechanics specimens. Slow crack growth behaviour is either observed directly in fracture-mechanics type specimens for large cracks, or is inferred from times to failure at a constant load or fracture stress dependence on loading rate.

A comparison of the data obtained for alumina by Gesing (1982) for microcracks and large macrocracks indicates a lower threshold crack extension force and higher susceptibility to slow crack growth for the microflaws, Fig. 2. Corroborating data derived from time-to-failure measurements has recently been published by Fett (1988). His data also include the behaviour of short through-thickness cracks in alumina growing from notches in single edge notched beam (SENB) specimens, Fig. 3. These cracks initially decelerate with an increasing crack extension force and then later accelerate. This behaviour is analogous to the behaviour of short cyclic fatigue cracks in metals. In both cases, it is an artifact of the increase in crack resistance with crack extension. There is no data in the literature separating slow crack growth effects from the effects of a rising R-curve. In PFCMMCs, similar effects are expected and may be even more pronounced because the relatively large filler size gives the microstructure a coarse scale, and cracks smaller than the filler size behave as microstructurally small cracks.
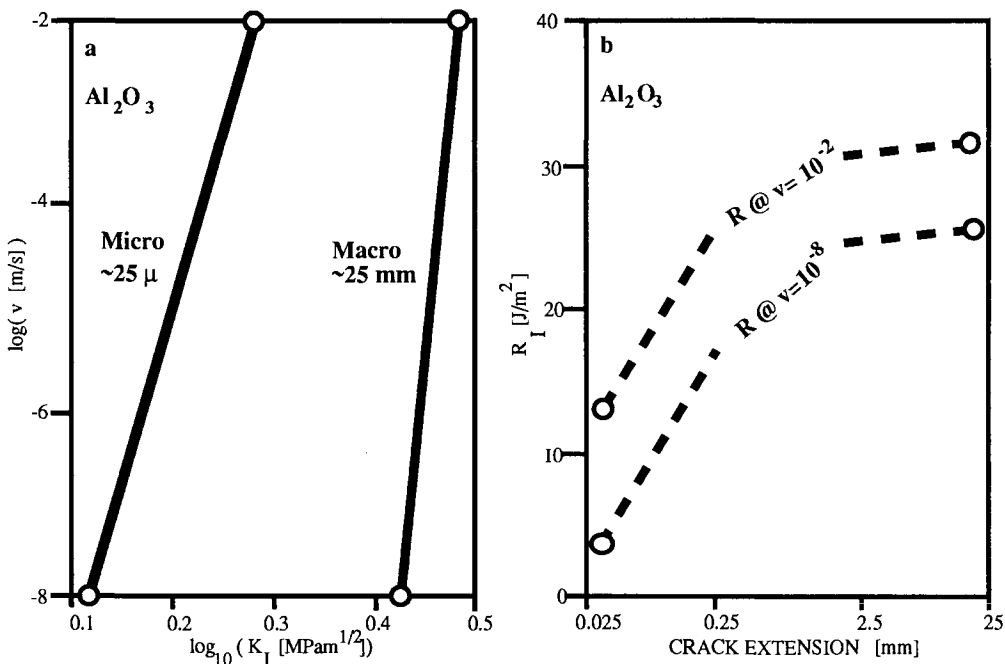
Fig. 2. a) Comparison of crack velocity behaviour of microflaws and macrocracks in alumina (Gesing, 1982) and b) points on the R-v-Δa diagram derived from this data.
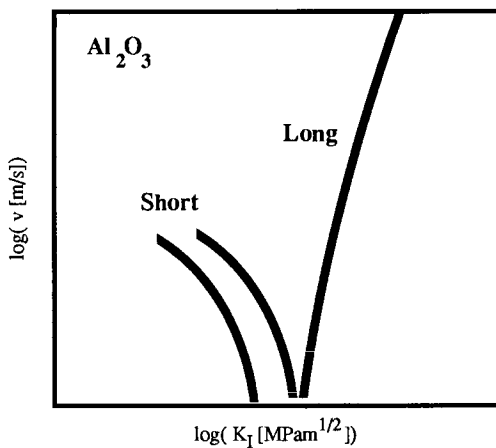
Fig. 3. Non-unique deceleration of short cracks in alumina with increasing crack extension force due to sharply rising crack resistance in the short crack region (Fett, 1988).

THE DEPENDENCE OF CRACK RESISTANCE CURVES ON CRACK VELOCITY

Crack resistance curves are typically measured on double cantilever beam (DCB) or compact tension (CT) fracture mechanics specimens at a slow, constant crosshead speed giving a stable fracture throughout, but with

a variation in the crack velocity. In an inert environment under static load, only a thermally–activated bond breakage mechanism can lead to a small reduction in the measured crack resistance. In chemically active environments or under cyclic loading, however, the threshold value of the crack extension force at crack arrest or at initiation of slow stable extension can be significantly different from the toughness value measured at the onset of instability. The designs based on the toughness values are apt to be non–conservative, and R–curves measured by stable crack extension depend on the instantaneous values of crack velocity. The size of the crack tip shielding process zone depends on the crack velocity. This has been clearly demonstrated in cyclic fatigue of metals and partially stabilized zirconia (PSZ). Step changes in the applied ΔG lead to transient velocity excursions: abnormally high values after load increase, and abnormally low values after load decrease. These effects are attributed to the new crack extension taking place in the shielding process zone characteristic of the old crack velocity (Dauskardt, 1989). For a long crack, the velocity effects are superposed onto the horizontal portion of the R–curve, so that unique v–G or da/dN–ΔG diagrams are obtained regardless of the actual crack length. For either microstructurally or mechanically small cracks, however, the velocity effect is superposed on the sharply–rising portion of the R–curve and non–unique velocities are measured as a function of applied stress intensity. One must account for the actual crack size to sort out this effect in the small crack region.

CRACK RESISTANCE-VELOCITY-EXTENSION DIAGRAMS

The present objective is to produce a design diagram accounting for both the crack extension and crack velocity effects on the measured crack resistance. In theory, such a diagram should allow the calculation of the lifetime of a sample by the integration of crack velocity along a path in the crack extension–crack resistance plane. As shown in Fig. 4, for a particular crack, sample geometry as well as loading boundary conditions crack extension force contours can be plotted on the same diagram. Under the same restrictions the crack velocity is assumed to be a unique function of the crack extension force and crack extension. The path followed on the diagram depends on the rate of change of the crack extension force dG/dt which depends on both the loading rate and crack velocity. Once the crack extension force exceeds the threshold resistance to slow crack growth, the crack may extend and does so at a velocity prescribed by the appropriate crack growth law which describes velocity as a function of crack extension force and amount of crack extension, or equivalently the crack propagation
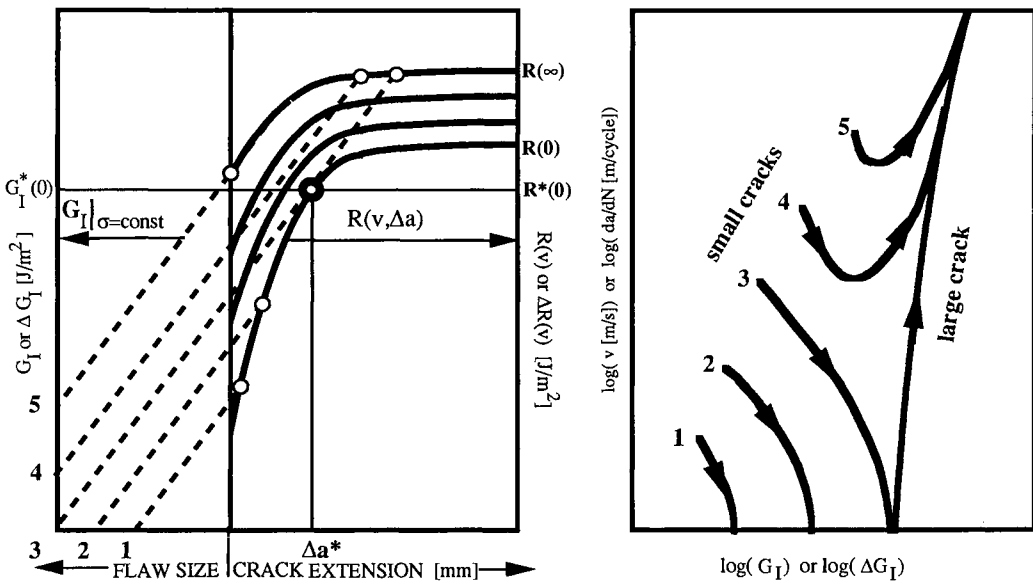
Fig. 4. a) Schematic of the R–v–Δa diagram. Crack extension forces are plotted on the same diagram for constant load conditions. b) Crack velocity diagram derived from the R–v–Δa diagram predicting non–unique crack deceleration in the short crack region.

resistance as a function of crack velocity and extension. The crack stability condition dG/da >,=,< dR(v,Δa)/da determines if the crack accelerates, continues at constant speed or decelerates and arrests as G approaches the R(v=0) threshold resistance contour. In an accelerating crack, the crack propagation resistance increases as the crack velocity increases, which can result in a return to stable crack propagation. For an arbitrary form of the crack resistance function, the time to failure can be estimated by a numerical integration of the crack velocity with respect to time along the path in the G–Δa plane. Closed solutions may be possible for particular empirical forms of crack velocity and R–curve laws, but this goes beyond the scope of the present discussion.

There is no data in the literature properly separating the crack size and velocity behaviour to allow the plotting of a complete crack resistance–velocity–extension diagram. The closest to what is needed is the data on zirconia composites by Torczynski (1987). He simultaneously measured crack resistance curves in chevron notched bend specimens while continuously monitoring crack velocity by the potential drop method. His results are shown in Fig. 5. There is a close correlation between crack resistance and crack velocity. Both increase at the beginning of the test, and both decrease as the crack approaches the back face of the specimen under a constant crosshead displacement rate. Torczynski's data, however, trace only a single path through the crack resistance–velocity–extension diagram. Further, the chevron notch specimen geometry used by Torczynski does not lend itself to easy interpretation in terms of crack extension.

In principle, in order to define a complete crack resistance–velocity–extension diagram, one needs to observe the crack size as a function of time while monitoring the applied load and load point displacement. Ideally for large cracks, multiple specimens would be used. Each specimen would be broken under displacement control, such that a constant crack velocity would be maintained and a series of constant velocity crack resistance curves be obtained. Alternatively, a series of load relaxation curves could be obtained on a single specimen. From the knowledge of the compliance characteristics of the specimen, both crack size and crack velocity data can be obtained from the load relaxation traces. In this way, crack velocity can be associated with each crack resistance–crack extension point and constant velocity contours can be drawn in on the diagram, Fig. 6.

Obtaining data in the small crack region is more difficult. Assuming an empirical form of the crack velocity and R–curve laws, one may be able to calculate the appropriate parameters from the strength distribution degradation data under service conditions. Fett (1988) published microcrack velocity data calculated from the distribution of times to failure assuming a constant crack resistance. There are no similar data accounting for the increasing R–curve. A more direct method is to observe the growth of the microflaws in-situ under static or cyclic tensile stress in a microscope. One needs to know the average net section stress, crack length and crack opening displacement as a function of time for a distribution of flaw sizes. R. Steinbrech (1988) has measured R–curves by in-situ microscopic observation of arrested cracks in alumina, but has not extended his measurements to evaluate the effect of crack velocity on his measurements.
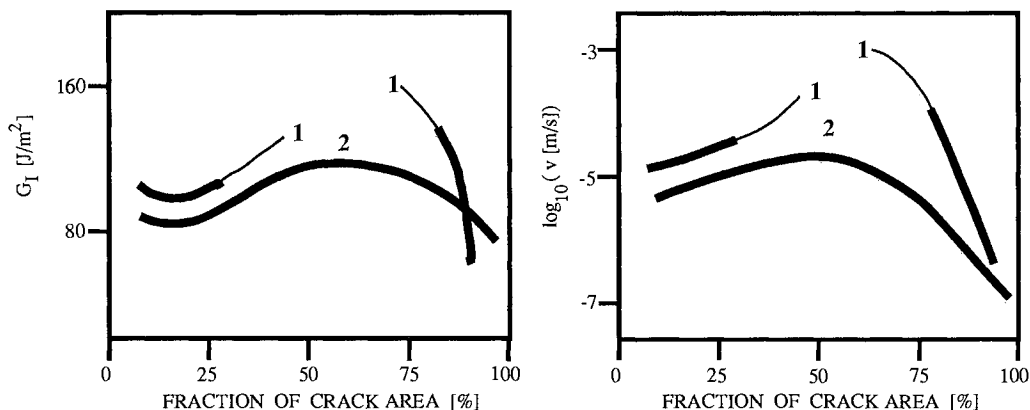
Fig. 5. Crack resistance and crack velocity data for zirconia–hafnia solid solutions (Torczynski, 1987)

CRACK EXTENSION [mm]
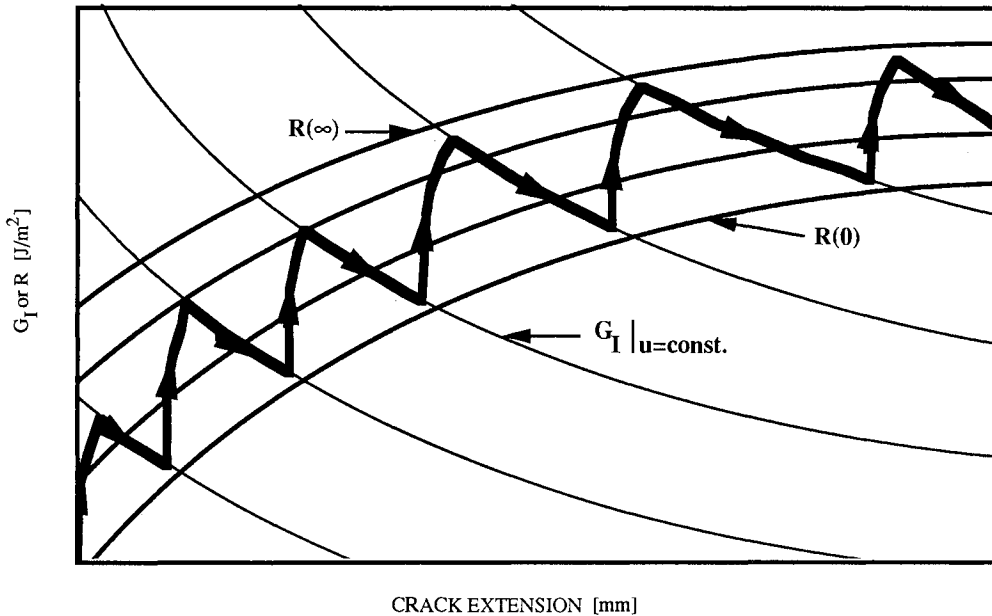
Fig. 6. Load relaxation procedure for the determination of R-v-Δa diagrams.

R-curves are in general non unique. Their values depend on crack velocity, stress state and the amount of constraint exercised by the type of specimen used. One could question design procedures based on a quantity which, strictly, is not a material property. However, for highly brittle materials such as ceramics and PFCMMCs, the crack opening mode I stress state has been shown to be most damaging. Further, structural component design for extended lifetimes is concerned with the extension of pre-existing surface or processing flaws to a critical size which is substantially smaller than the component size. Under these conditions unique R-v-Δa diagrams are expected and these diagrams should become useful design tools. At this time it is not clear how significant the effect of the complex triaxial stress states will be on the short crack portion of the R-v-Δa diagrams. This subject is beyond the scope of this paper and will be addressed in detail in the future.

COMPONENT DESIGN AND LIFETIME PREDICTIONS

For component design, one must be able to calculate and guarantee the probability of survival of the large majority of components in a service environment under loading conditions. Typically, in structural applications one is concerned with the initiation and propagation of multiple microcracks from the pre-existing natural or machining flaws and the development of one dominant crack which then propagates to failure. Because the mechanical energy supplied by the loading system is split between all the extending microcracks care must be exercised in applying fracture mechanics concepts to the microcrack initiation and microcrack damage accumulation portions of the lifetime. Until the dominant crack is formed, it does not make sense to lump the energy dissipated by the individual microcracks under a "shielding effect" of the microcracked process-zone.
The near threshold behaviour is particularly important because the majority of the lifetime is spent at very low crack velocities and failure is imminent when large crack sizes and high velocities are attained. This underlines the importance of separating the crack size and crack velocity for small cracks; otherwise non-unique behaviour is observed. It is typically assumed that in ceramics, sharp microcracks pre-exist in the material and there is no microcrack initiation period necessary, with a similar behaviour expected in PFCMMCs. The initiation, however, may become important under cyclic loading in conditions where the crack growth rate is controlled by the intrinsic cyclic fatigue of the metal bridging filaments.

For design purposes, one needs a statistical characterization of the pre-existing flaw size distribution and a

modification of that distribution by the simultaneous extension of multiple microcracks under the service conditions. In the presence of a sharply rising crack propagation resistance, stable multiple microcrack extension is observed because small flaws decelerate and arrest under constant applied stress. The situation becomes unstable when the R—curve flattens out allowing the larger flaws to accelerate and eventually lead to a single dominant crack causing failure. The key to the design for long lifetimes in structural applications will not be the behaviour of the one dominant flaw, but the time required for the microflaws to extend to the critical unstable size defined by the knee in the R—curve.

For material ranking and development, R—curve and crack velocity measurements are very useful. For practical designs, however, simpler conservative criteria are needed. For PFCMMC materials, which are apt to exhibit both fatigue crack extension and a pronounced crack resistance curve, a safe criterion would be that for a largest stable microflaw, the crack extension force would not exceed the static fatigue threshold or threshold __R for cyclic loading. The largest stable microcrack size is defined by the knee of the R—curve. This type of design criterion would allow a subcritical extension of the microflaws but would ensure that there would not be sufficient crack extension force for the subcritical propagation of a macrocrack.

The design procedure would start with the stress analysis of a component. Then, assuming the maximum stable microcrack size, one can calculate the crack extension force distribution. The design would be modified until the crack extension force at any point is below the fatigue threshold values. The components with the flaws exceeding the largest stable microcrack size would be eliminated by a suitable non—destructive testing procedure or a proof test.

Laboratory measurements of cyclic fatigue effects are typically performed under constant cycle conditions. However it was amply documented in metals and more recently also in PSZ that load cycle transients can significantly affect crack propagation rates. Consequently one will need to know the service loading spectrum and the specific restraint conditions to be able to perform the lifetime simulations for the actual components. The safe criterion would again be that the peak stresses must not develop stress intensities above the fatigue thresholds for largest stable microcracks.

This type of a design procedure would be overly conservative for ductile metals which have very low fatigue thresholds and also very low stress intensity exponents in the Paris crack velocity equation. For ceramics and PFCMMCs, however, one observes very high stress intensity exponents and fatigue threshold values which are a substantial fraction of the toughness. Hence, in this case, it is not recommended that the service load exceed the fatigue threshold at any time. Designs based on fast fracture criteria are likely to be non conservative unless the safety factors used bring the applied stress intensities fortuitously below the fatigue threshold values.

CONCLUSIONS

We have discussed the toughening and fatigue crack propagation mechanisms which are likely to be active in the particulate—filled ceramic/metal—matrix materials. It was shown that both R—curve and subcritical crack propagation are likely in these materials. The interaction between these two effects was shown to be responsible for non—unique crack growth behaviour of small cracks under both static and cyclic loading conditions. Methods for gathering the combined R—curve and crack velocity data to separate these effects were proposed. This new data should allow an improvement in the definition of the fatigue threshold resistances and the maximum stable microcrack size. Safe, simple design procedures based on these concepts were proposed.

REFERENCES

Dauskardt, R., Marshall, D., Ritchie, R.O. (1989). Submitted to J. Am. Ceram. Soc.
Evans, A.G. (1988). Mat. Sci. and Eng., A105/106, 65–75.
Fett, T., and Munz, D. (1988). CFI, Ceram. Forum Int., 61(9–10), 446–453.
Gesing, A.J. (1982). Ph.D. Thesis, The Pennsylvania State University, State College, Pennsylvania, USA.
Nikkila, A.-P., and Mantyla, T.A. (1989). Proc. of the 13th Annual Conf. on Composites and Advanced Ceramics, Cocoa Beach, Florida (to be published).
Steilnbrech, R.W., and Schmenkel, O. (1988). J. Am. Ceram. Soc., 71(5), C271–C273.
Torczynski, T.B. (1987). Ph.D. Thesis, McMaster University, Hamilton, Ontario, Canada.

Friction at ceramic and metal contacts over a range of temperatures

T. Dickerson, H. Fessler and J.J. Webster
Department of Mechanical Engineering, University of Nottingham, Nottingham, NG7 2RD, England

ABSTRACT

Square bars were compressed between the edges of two discs to give Hertzian line contacts, less than 1 mm wide. The first 3 mm of ceramic on ceramic and ceramic on metal sliding was observed.
Over the test range static coefficients of friction are independent of disc radius and sliding speed, decrease with decreasing surface roughness and increasing contact force.
Friction generally increased with temperature. Above 300°C stick-slip was found to occur between metal and ceramic components.

KEYWORDS

Cast Iron, Ceramic, Contact, Friction, Nimonic, Reaction-Bonded Silicon Nitride, Slip, Stick, Zirconia

INTRODUCTION

Ceramic components are becoming more widely used. Because ceramics are generally brittle, they are susceptible to high localised stresses; they cannot yield locally like metallic components. High localised stresses occur in regions of contact between components. The contact stress distribution usually depends on the value of the coefficient of friction. In order to model such contacts, friction data are required. The work presented here is part of a project to study contact problems associated with ceramics.

Friction is usually quantified by the coefficient of friction, defined as the ratio of the tangential to normal force at the limit of, and during relative motion. Generally two friction coefficients are quoted; μ_s, the force ratio that is just large enough to cause gross sliding and μ_d, the dynamic ratio during sliding.

Much previous data (Czichos, Becker, Lexow, 1987; Sutor, 1984; Yust, Carigana, 1984) has been produced while wear testing materials, with frictional coefficients determined after many hundreds or thousands of metres of sliding, after a steady state dynamic coefficient has been reached. Fessler and Fricker (1984) studied the initial 1mm of sliding of hardened steel rollers over reaction-bonded and hot-pressed silicon nitride, at room temperature, primarily with lubricants. Stanley, Sivill and Fessler's (1976)·study of as-fired reaction-bonded silicon nitride, sliding between hardened steel knife edges, also at room temperature, was less exhaustive.

This paper reports results for frictional behaviour in the initial 3mm of sliding, although static friction is the main subject of this investigation. Unlubricated, Hertzian-type contacts between cylindrical discs and flat bars of several materials and surface finishes were tested under different normal loads, at different speeds over a range of temperatures.

NOMENCLATURE

AF	as fired,
Al	aluminium,
CI	cast iron,
EM	end milled,
Gr	ground,
MS	mild steel, unhardened,
N	normal force intensity
Ni	Nimonic 70 nickle alloy,
Po	polished,
SN	reaction-bonded silicon nitride,
T	tangential force intensity
Tu	turned,
μ_d	dynamic coefficient of friction,
μ_{MAX}	the maximum dynamic coefficient of friction,
μ_s	static coefficient of friction after 0.04mm of sliding, $\mu_{0.04}$ (Mode B) or the first peak, μ_p (Modes A and C).

CONTACT GEOMETRY AND LOADING

The test configuration is shown in Fig. 1. The normal loads which clamp the bar between the two discs were produced by the forces F generated by dead weights (not shown) and kept constant throughout each test. The application of the normal load created two Hertzian line contacts on opposite faces of the bar, typically between 0.02 mm and 0.80

Fig. 1 Testing arrangement

mm wide. The discs were held in wedges which prevented their rotation. A universal testing machine was used to produce displacement-controlled sliding and monitor the frictional load. The machines chart recorder produced records of the cross head movement and frictional load. The bars were 4.0 and 4.6mm square, 50mm long; the discs were the same thickness as the mating bar and 25mm in diameter. Contact zones of various radii were ground onto some discs. Most bars were pulled between the discs, but some ceramic bars were pushed to prevent fracture. Temperatures up to 1000°C were produced by radient spot heaters. The experimental techniques have been described more fully by Dickerson (1988).

MATERIALS AND SURFACE SPECIFICATION

The materials, surface finishing processes and roughnesses used are listed in Table 1. Ten to twenty measurements were taken in the direction of sliding. The choice of materials was dictated, in the main, by likely ceramic-metal combinations, with other metal-metal and ceramic-ceramic tests to complement these.

TABLE 1 Material and Surface Specifiation

Matl	E	Hardness	Surface Finish ± Standard Deviation μm CLA				
	—	—					
	GPa	VPN/50	AF	EM	Gr	Po	Tu
Al	71	128	--	0.41±.03	--	--	0.13±.01
CI	110	224	--	--	0.30±.06	--	0.39±.30
MS	210	185	--	--	--	--	no test
Ni	110	203	--	--	0.70±.34	--	--
SN	200	596	2.50±.40	--	0.19±.04	0.06±.01	--
Zi	100	723	0.24±.05	--	--	--	--

The reaction-bonded silicon nitride components were buffed with a clean buffing wheel to remove the loose alpha-phase wiskers. Ground components had the direction of lay in the sliding direction. After grinding, polished surfaces were finished with diamond paste. All components were cleaned in Inhibosol before use and left to dry in air. The humidity during the tests was not controlled.

RANGE OF INVESTIGATION

In addition to studying temperature effects, effects due to sliding speed, contact radius, normal force and surface finish were studied. Table 2 lists the range of tests carried out. For each material and surface finish combination indicated only the parameter stated was varied for that set of tests. Unless otherwise stated tests are at room temperature with sliding speed of 1 mm/min and a contact radius of 12.5mm with the bars in tension.

TABLE 2 Variables studied with
Materials and Surfaces

Disc Material (process)	Bars Material (process)			
	Al(EM)	CI(Gr)	Ni(Gr)	SN(AF)
Al(Tu)	Load			Load
MS(Tu)				Load Speed Repeat
SN(AF)	Load Speed	Temp Repeat Radius Temp Temp	Temp	Temp Load*
SN(Gr)				
SN(Po)				
Zi(AF)				

* Bar in tension

THEORETICAL CONSIDERATIONS

Cattaneo (1938) and Mindlin (1949) showed that when a tangential force is applied to a frictional Hertzian contact, a zone of micro-slip occurs at the contact edge, with adhesion in the centre. As the tangential force increases, the micro-slip zone enlarges until $T/N = \mu_s$. In this idealised topographically smooth contact it would be expected that the transition from static to dynamic friction would be smooth. In real contacts surface irregularities may lead to discontinuities in the friction force due to necessary flow or fracture of surface

asperities. It would also be expected that under controlled sliding, the tangential force may fluctuate as different parts of the nominal contact surfaces come into acual contact. Johnson (1985) deals with this subject in more detail.

RESULTS

Response to Loading

Three modes of behaviour were identified from the load-displacement records; typical records are shown in Fig. 2. The smooth, steep initial sections of the curves are assumed to show the elastic deformation of the machine and the contacting bodies. Fig. 2a (curves i, ii and iii) contains examples of Mode A behaviour. The tangential force increases to a peak value after which it decreases. The peak
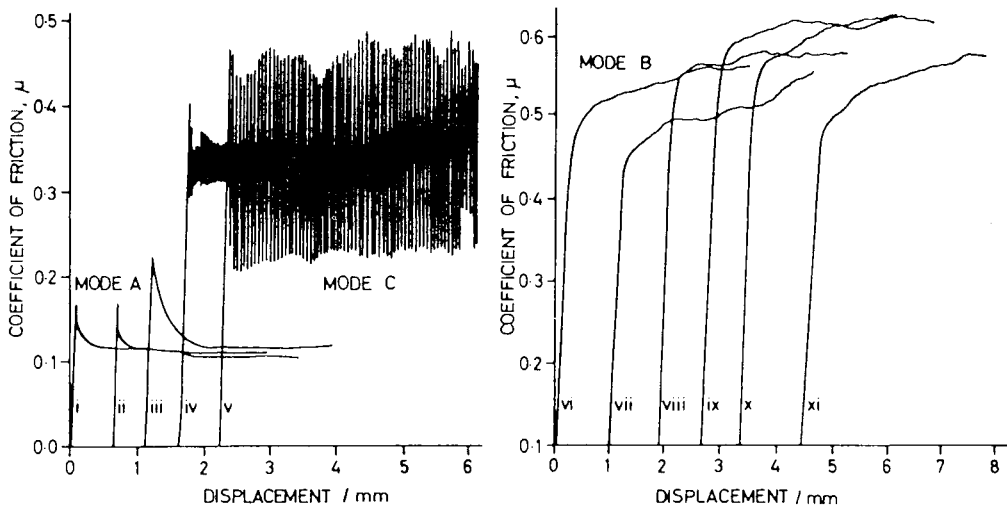
Fig. 2. Tangential force - displacement curves

(a)Polished silicon nitride bars, ground cast iron discs, N=62 N/mm
Ref.   i   ii   iii   iv   v
Temp/°C   27   140   285   410   560

(b)As fired silicon nitride bars bars, turned mild steel discs, N=72 N/mm, 24°C.

gives μ_s; after that, gross sliding is assumed to occur. Fig. 2b illustrates Mode B behaviour with gradual transition from static to sliding. In order to quantify the static coefficient in Mode B type tests, a criterion for μ_s was defined as the value after 0.04 mm of sliding, $\mu_{0.04}$. μ_p generally occurred after 0.04 mm of sliding, making $\mu_{0.04} \approx \mu_p$. Mode C behaved like mode A except that stick-slip oscillations occurred during sliding (curves iv and v in Fig. 2a).

Once sliding had started, frictional resistance varied.   Minor pertabations of μ_d in modes A and B are caused by surface irregularities.   Stick-slip in mode C is thought to be caused by adhesion in oxide layers as the effect only occurred at high temperatures and was highly temperature-dependent, as shown in Fig. 2a and by Dickerson (1988).   Sliding friction can also be desribed by smooth curves drawn through these irregularities.   During sliding μ_d increased (e.g. curve vii in Fig. 2b), became fairly constant (eg curve iii) or decreased.   Evidence showed that these overall changes were caused by surface modification due to wear and material transfer.

Repeatability.

A qualitative indication of repeatability is given by Fig. 2b, which shows the behaviour in six nominally identical tests.   Because large variations in the measured values of the coefficient of friction have been reported (Sutor;1984) for nominally identical tests, an estimate of the likely scatter of results was required.   Two sets of nominally identical tests were carried out with the bar made of the softer material and one set with the discs being softer.   The results are shown in Table 3; the mean and the coefficient of variation are quoted.

TABLE 3   Repeatability of coefficient of friction

Material(process)		No. of tests	Normal force N/mm	Coef. of friction	
Bar	Disc			μ_s	μ_{max}
CI(Gr)	SN(AF)	5	115	0.32±7%	*
CI(Gr)	SN(AF)	6	112	0.31±7%	*
SN(AF)	MS(Tu)	6	72	0.42±12%	0.49±6%

* Maximum and static values identical

Czichos, Becker and Lexow (1987) reported on a large number of nominally identical tests, carried out under stringent conditions in many different laboratories throughout the world.   Coefficients after 1000m of sliding were found to have coefficients of variation of ±9% to ±13% within any one laboratory and ±18% to ±20% when results from different laboratories were combined.   Table 3 shows a range of errors of ±7% to ±12%, which is less than the above.   Figure 3 contains data obtained in four different sets of tests, carried out on three different testing machines on three seperate days; this indicates a scatter of about ±20%.   The spread of results is taken as typical of all the other tests carried out and is used as a criterion of signifiant trends.

Sliding speed.

Table 4 shows results for two sets of tests in which the sliding speed was the only variable.

No trends could be identified in the data.   Because the variations are less than would be expected by from nominally identical tests, sliding speed, over the range tested, has no significant effect coefficient of friction.   A constant rate of 1mm/min was used for all other tests.

TABLE 4 Sliding Speed

Material(Process)		No. of tests	Normal force N/mm	Speed Range mm/min	Coef of friction	
Bar	Disc				μ_s	μ_{max}
Al(EM)	SN(AF)	4	63	0.5-20.0	0.47±2%	*
SN(AF)	MS(Tu)	5	72	0.02-50.0	0.46±10%	0.51±4%

* Maximum and static values identical

Contact radius

Some tests were carried out with contact radii of 12.5, 62.5, 125 mm and nominally flat contacts 5mm long. A summary of the results is shown in Table 5.

TABLE 5 Radius Change

Material(Process)		No. of tests	Normal force N/mm	Temperature °C	Coef. of friction	
Bar	Disc				μ_s	μ_{max}
CI(Gr)	SN(Gr)	5	56	100	0.17±5%	0.17±6%
CI(Gr)	SN(Gr)	4	56	400	0.26±6%	0.34±12%

Again the variation is less than expected for nominally idential tests. The μ_{max} values at 400°C were recorded while the system was undergoing mode C oscillations and this accounts for the larger spread of values. This adds further weight to the traditional notion that friction is independent of the nominal contact area. All other tests were carried with 12.5 mm radii.

Normal force.

A number of tests over a relatively limited range of normal forces at first indicated that there was no identifiable effect on the friction coefficients due to a change in this parameter. A summary of these results are in Table 6. Figures 4-7 also demonstrate this over a range of temperature which is dealt with subsequently.

TABLE 6 Some Normal Force Effects

Material(Process)		No. of Tests	Temperature °C	Normal force N/mm	Coef. of friction	
Bar	Disc				μ_s	μ_{max}
Al(EM)	Al(Tu)	4	24	23-112	0.17±3%	0.29±10%
Al(EM)	SN(AF)	8	24	23-88	0.46±10%	*
CI(Gr)	SN(AF)	4	27	19-123	0.28±12%	*
CI(Gr)	SN(AF)	3	280	19-123	0.50±6%	*
SN(AF)	Al(Tu)	5	24	23-88	0.48±8%	0.58±3%
SN(AF)	MS(Tu)	6	24	23-88	0.45±7%	**

*   Maximum and static values identical.
** Coefficients still increasing at the end of some tests.

Two sets of tests over a much larger range (2-500 N/mm) were carried

out with as-fired silicon nitride discs and bars; a significant trend
was observed and is illustrated in Fig. 3. Both the static and the
maximum coefficient of friction show lower values with increasing
normal load.

It was thought that this normal force effect could be due to weakening
of ceramic surface asperities under large normal forces; the asperities
would then break off more easily when a tangential force was applied,
reducing friction. However a normal pre-load of 490 N/mm had no
apparent effect on the friction coefficients. Stanley, Sivill and
Fessler (1976) found a similar trend but over a smaller range of normal
forces for hardened steel knife edge contacts on silicon nitride.
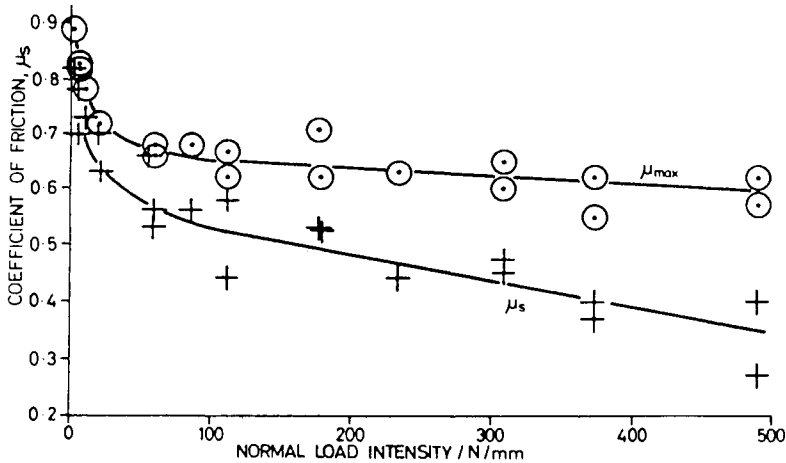
Fig.3 Normal force effects at room temperature for as-fired silicon
nitride bars and discs.

Surface finish.

Figure 5 shows some of the effects of surface finish for cast iron bars
sliding between silicon nitride discs. Below the transition
temperature from mode A to C, a fine surface finish reduces friction,
as would be expected. Above the transition temperature there is no
significant difference and increased scatter probably because surface
bonding controls frictional resistance. Figure 6 however shows the
results for Nimonic bars between as-fired and ground silicon nitride
discs. Execpt for one result at room temperature, there is no
significant difference due to surface finish.

Temperature

All combinations tested showed increases of coefficient of friction
with increasing temperature.

Mode A, below 300°C, and mode C at higher temperatures was observed
for cast iron bars between silicon nitride (Figs. 4 and 5) and
Zirconica discs (Fig. 7). For these material combinations the

tangential force-displacement characteristics for low temperatures were as illustrated in Fig. 2a by curves i to iii and for high temperatures by iv, v and Dickerson (1988). At the transition temperature there appears to be a discontinuity of coefficient of friction for as-fired silicon nitride only (see Fig. 5). Mode B behaviour occurs for silicon nitride (Fig. 7) and Nimonic (Fig. 6) bars between silicon nitride discs, but at very high temperatures, above 800°C, some stick-slip was evident with the latter.
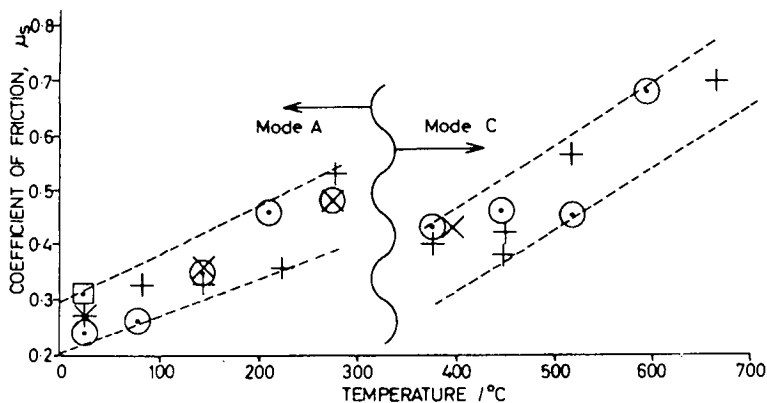
Fig. 4 Normal force effects for ground cast iron bars between as-fired silicon nitride discs. N /(N/mm)   19   62   115   123
Symbol   o   +   x
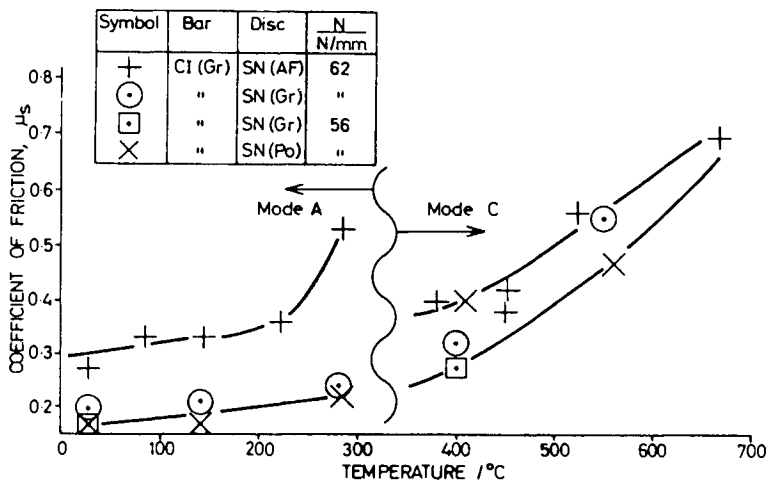
Fig. 5 Surface finish effects for ground cast iron bars.

Symbol	Bar	Disc	$\frac{N}{N/mm}$
⊙	Ni (Gr)	SN (AF)	55
+	"	"	19
✕	"	SN (Gr)	"

Mode B

COEFFICENT OF FRICTION, μ_s

TEMPERATURE /°C
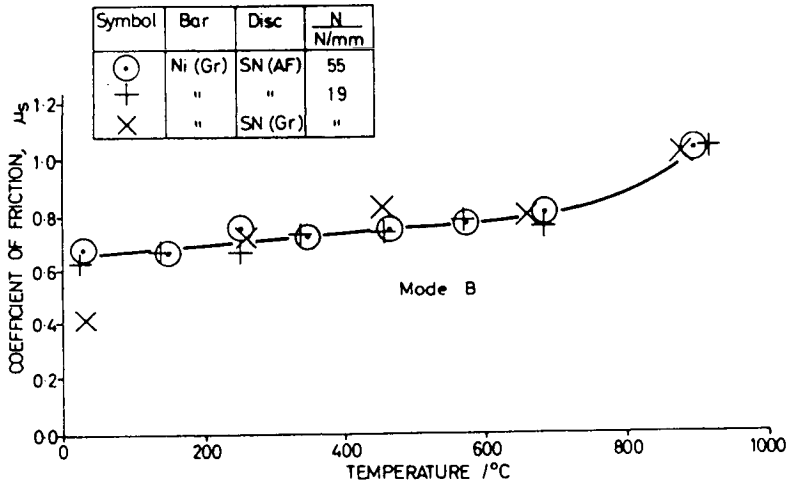
Fig. 6 Surface finish and normal force effects for ground Nimonic bars.

Symbol	Bar	Disc	$\frac{N}{N/mm}$
⊙	SN(AF)	SN (AF)	19
+	"	"	55
✕	CI (Gr)	Zi (Gr)	"

Mode B

Mode "A"

Mode C

COEFFICENT OF FRICTION, μ_s

TEMPERATURE /°C
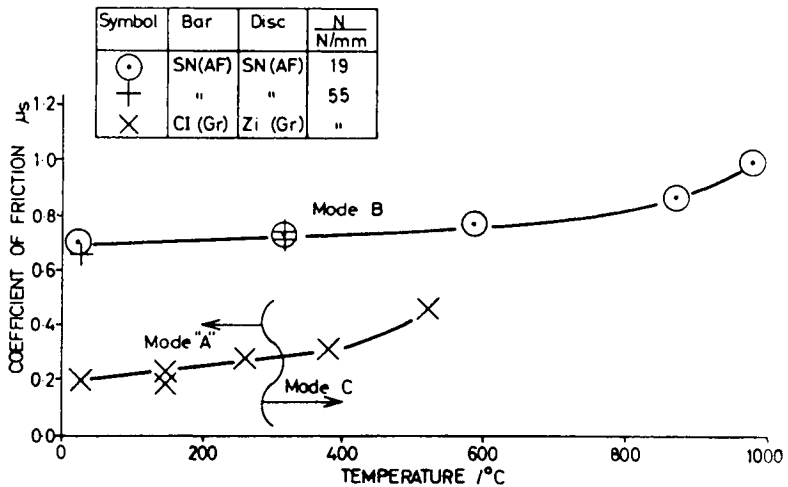
Fig. 7 Normal force effects for silicon nitride and cast iron bars between Zirconia discs.

DISCUSSION

It is generally assumed that there are two main mechanisms that cause frictional tractions (Bowden and Tabor; 1964), surface bonding and material displacement; the total frictional traction is due to a combination of these. Bowden and Tabor (1964) observed that when

materials come into atomically close contact, bonding can take place.
They proposed that when real surfaces come into contact, only few
points touch, causing high localised stresses and subsequent plastic
deformation which leads to intimate contact at those points.
On examination of the mating surfaces evidence of material displacement
was rife. In all cases material was transferred from the softer to the
harder material. Microscopic examination after the tests showed that
the material transfer tended to cause islands projecting above the base
material. With a harder disc, material continually builds up in the
contact; in extreme cases contacts of similar materials will result.
If the disc is softer, the impregnated surface is pulled out of the
contact. Reaction-bonded silicon nitride and aluminium gave similar
values of μ_s but significantly different μ_d. With aluminium bars μ_d was
still falling at the end of the 3 mm tests, but with silicon nitride
bars a reasonably constant value was obtained after about 1 mm of
sliding. Thus, as sliding progressed, μ_d was controlled by surface
modification.

A general increase of friction was observed with temperature; the
increase was most marked with metal-ceramic contacts. A possible
explanation of this is that, as the materials get hotter, plastic flow
is more pronounced, increasing the actual contact/bonding area. The
loss of strength of materials as temperature increases may be
compensated by larger areas to be sheared. More material was
transferred as temperature increased.

Mode A (see Fig. 2a) response was found in all cast iron bar tests and
with aluminium bars between silicon nitride discs. Mode B (see Fig.
2b) occurred for silicon nitride bars between aluminium discs and
Nimonic between silicon nitride discs. In other combinations the
response was not so distinct. In mode B μ_s was difficult to determine
because of the uncertainty of the outset sliding.

The substantial drops after the peaks in Fig. 2a were attributed to
the lubricating properties of cast iron. No other reasons were found
why mode A or B should be present for particular material and surface
combinations.

It is generally assumed (Halling; 1975) that μ_s greater than μ_d; it has
been shown here that this is not necessarily the case, particularly
with virgin contacts and material transfer.

CONCLUSIONS

Three different responses were identified. Mode A, with μ_s greater
than μ_d, occurred for cast iron and aluminium bars sliding between
ceramic discs. Mode B, with μ_s less than μ_d occurred for Nimonic bars
and silicon nitride bars sliding between aluminium discs. Other
combinations (see Table 2) showed less distinct behaviour than the
above. Mode C describes a stick-slip movement which only occurred at
high temperatures.

Surface modification controlled the dynamic frictional behaviour.

Variation of contact radius and speed of sliding had no significant
effect on the friction coefficients.

Normal force generally does not affect the coefficients, but for as-

fired reaction-bonded silicon nitride sliding on itself, the value decreases with increasing normal force.

A finer surface finish can reduce friction.

In general, friction increases with contact temperature. At temperatures above 300°C stick-slip may occur with metal bars.

ACKNOWLEDGMENTS

REFERENCES

Bowden, F. P., D. Tabor (1964). *The friction and lubrication of solids, Part II*. Oxford University Press. Chap IV.

Cattaneo, C. (1938). Rendiconti dell accademia naeionale dei llineci. *Sul Contatto di due Corpi Elastici, 27,*.

Czichos, H., S. Becker, and J. Lexlow (1987). Multilaboratory tribotesting: results from the Versailles advanced materials and standards programme on wear test methods. *Wear*, 114, 109-130.

Dickerson, T. (1988). Friction measurement between ceramics and metals. *Int.J.High Technology Ceramics*, 4, 333-340.

Fessler, H., D. C. Fricker (1984). Friction at broard and narrow contacts between silicon nitride and hardened steel. *Brit. Ceram. Proc.*, 5, 129-143.

Halling, J. (1975). *Principles of tribology*. MacMillan, London. p72.

Johnson, K. L. (1985). *Contact Mechanics*. Cambridge University Press, London. Chap. 7.

Mindlin, R. D. (1949). Compliance of elastic bodies in contact. *Trans. Am. Soc. mech. Engrs.*, 16, 259-268.

Stanley P., A. D. Sivill, H. Fessler (1976). Unit strengths consept in the interpretion of beam test results for brittle materials. *Proc. Instn. Mech. Engrs.*, 190, 585-595.

Sutor, P. (1984). Tribology of silicon nitride and silicon nitride-steel sliding pairs. *Ceram. Eng. & Sci. Proc.*, 5, 460-469.

Yust, C. S., and F. J. Carignan (1984). Observations on the sliding wear of ceramics. *Proc. Am. Soc. of Lub. Engrs.*, 1-8.

Tribological aspects of ceramic composites in conforming contacts

H.M. Hawthorne

Tribology and Mechanical Laboratory, National Research Council Canada, Vancouver, British Columbia, Canada, V6S 2L2

ABSTRACT

When sliding against themselves in continuously conforming contacts, SiC whisker reinforced Al_2O_3 and a modified Si_3N_4/SiC whisker composite exhibit stable, high friction characteristics in both air and high vacuum. Friction coefficients remain between 0.5 - 0.8 in either environment with wear rates about 10^{-4} mm^3/Nm in vacuum and an order of magnitude lower in air. In contrast, SiC/TiB_2 and Si_3N_4/SiC whisker composites can develop variable, or low, sliding friction in vacuum, similar to polymer composites. The structure and properties of interfacial wear debris controls the friction and wear behaviour of both the ceramic and polymer tribosystems, but the frictionally stable ceramic composites should be more suitable for long term use in vacuum brake applications.

KEYWORDS

Ceramics; composites; wear; friction; vacuum; brakes; interfacial wear debris; space mechanism materials.

INTRODUCTION

It is now well established that third body interfacial layers, or transfered, or friction films, are readily formed from wear debris generated at the dry sliding surfaces of metals, polymers, ceramics and composites (Godet, 1984). Indeed, in many cases it is the formation and properties of such debris films which determines the friction and wear behaviour of the materials in the sliding system. (Ajayi & Ludema, 1989; Briscoe & Tabor,1980; Godet, 1984; Heilmann & co-workers, 1983). This is particularly so in areal contacts because of easy debris trapping, a fact exploited in the development of both high and low friction tribosystem components, such as brakes (Anderson, 1980) and self-lubricating bushings (Lancaster, 1973), respectively.

An asbestos/phenolic resin composite was previously found to exhibit unstable sliding friction characteristics in continuously conforming, clutch-type, contacts in high vacuum (Trenouth & MacKenzie, 1986; Hawthorne, 1987). This was shown to be related to the inevitable generation and behaviour of dry wear debris layers on specimen surfaces in this environment, rendering this material unsuitable for extended use in future space mechanisms (Hawthorne, 1986, 1987). Alternative materials with stable friction and wear properties in vacuum are now being researched. The results from studies of four ceramic composites are presented here and discussed in relation to the nature of third body debris layers formed at the sliding surfaces of conforming contact specimens in-vacuo.

EXPERIMENTAL

Materials

Four types of ceramic composite materials were obtained from a commercial
source.[1] These were alumina reinforced with 25% silicon carbide whiskers,
silicon carbide with 20% titanium diboride particles, silicon nitride with 30%
silicon carbide whiskers, and silicon nitride with both 20% silicon carbide
whiskers and 20% of an additional component. Minor amounts of sintering aids
were also present in all these specimens. A polymer composite studied for
comparison was polyetheretherketone (PEEK) containing 30% glass fibres[2]. All
compositions are nominal weight per cent. Typical physical properties of the
ceramic materials are listed in Table 1.

TABLE 1 Ceramic Composite Specimen Physical Properties *

Specimen Type	Grade	Porosity (%)	Hardness (GPa)	Fracture Toughness (MPa m$^{1/2}$)
Al_2O_3/SiC	SWA-8925	$\lesssim$ 1	21	6.8
Si_3N_4/SiC	S5G5-8730	0	17.5	6.9
$Si_3N_4/SiC/(X)$	S5G7T-8720	$\lesssim$ 1	17.7	6.6
SiC/TiB_2	TSC-7615	$\approx$ 3	28.8	4.5

* Data courtesy of manufacturer.

Parallel faced, flat annular ring specimens (approx. 40 mm o.d., 30 mm i.d. and
1.6 mm thick) were made from the hot-pressed ceramic blanks by diamond cutting
and grinding. These were bonded to aluminium holders and their test surfaces
finished by 30 and 6 μm diamond lapping, to give initial surface roughnesses
(R_a) of 0.05 ± 0.02 μm. Machined polymer specimens were similarly prepared and
both these and the steel countersurfaces were finished with 1000 grit SiC paper
to a roughness of ≈ 0.2 μm. Three radial slots, 120° apart, were cut into the
bearing surfaces of some specimens.

Friction and Wear Experiments

The friction and wear behaviour of specimen pairs, sliding unidirectionally, was
studied using a conforming contact tribometer, the essentials of which are
represented schematically in Fig. 1. This provided relatively smooth sliding of
high friction materials at moderate speeds in an axially stiff system which
minimized friction-induced resonant vibrations while allowing a modicum of self-
alignment between the continuously contacting specimen surfaces. Experiments
were performed in air and under clean (hydrocarbon-free) high vacuum conditions,
below 1.3 x 10^{-4} Pa (10^{-6} Torr). Specimens could be heated in-situ and degassing
species determined by a MS residual gas analyser. Friction torque was recorded
during all tests and wear was determined by specimen weight loss measurements.
Test sliding speed was 0.18 m/s and several normal loads between 10 and 60 N
(approx. 0.02-0.12 MPa bearing pressure) were used.

---

[1] The Electrofuel Manufacturing Co., Toronto
[2] Victrex PEEK 450GL30, LNP Engineering Plastics
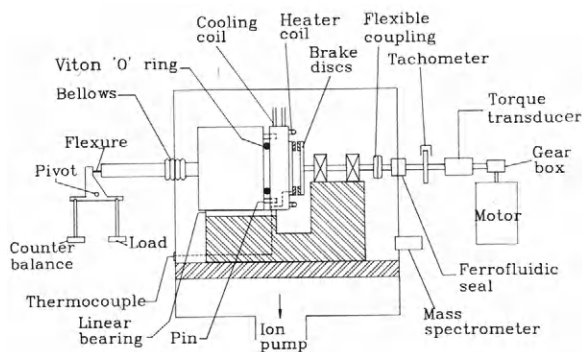
Fig. 1. Schematic illustration of high vacuum tribometer.

Sliding was carried out nominally at room temperature but, depending on the material, frictional heating could raise specimen disc bulk temperatures by up to 50 Centigrade degrees.

Experiments involved sliding of like-on-like material pairs. Both unslotted specimen pairs and slotted/unslotted combinations were used. Friction behaviour was studied and wear was measured both with new specimens and those which had previously been "run-in" to an equilibrium frictional condition. Specimen geometry and sliding conditions were similar to those of an intended friction brake application except that testing was continuous over long periods to accelerate the accumulation of sliding distance.

RESULTS AND DISCUSSION

The ceramic composites all had a very fine scale microstructure, with evenly dispersed reinforcement phases, as shown in Fig.2. The polymer based composite also had a similar heterogeneous microstructure, but on a coarser scale.

Friction

The friction behaviour of the ceramic and polymer composites sliding against themselves in air and in vacuum is shown in Fig. 3. In most cases the trends are similar for slotted and unslotted specimen tests but friction is usually higher in the former. In air all composites exhibit high friction over long sliding distances. All results tend towards friction levels around 0.55 and 0.7 in these experiments, as if the contact geometry had more influence than the type of friction material. In vacuum, two extremes of friction characteristics are evident. These are a continuing high friction level, such as for the data of the Al_2O_3/SiC and modified Si_3N_4/SiC composites, and a large decrease to low friction levels, as for the PEEK/GF and some Si_3N_4/SiC specimen results. This latter behaviour is similar to that observed previously for asbestos/phenolic composites (Hawthorne, 1986, 1987). The remaining ceramic composite (SiC/TiB_2) has variable sliding friction characteristics, exhibiting both high and low values, sometimes in a periodic fashion, as in Fig.3c. In a repeat unslotted disc test, the Si_3N_4/SiC material showed a more gradual decrease to low friction levels (to 0.2 at 4 Km), followed by periodic high and low values like the SiC/TiB_2 system.

(a)

(b)

(c)

(d)

(e)
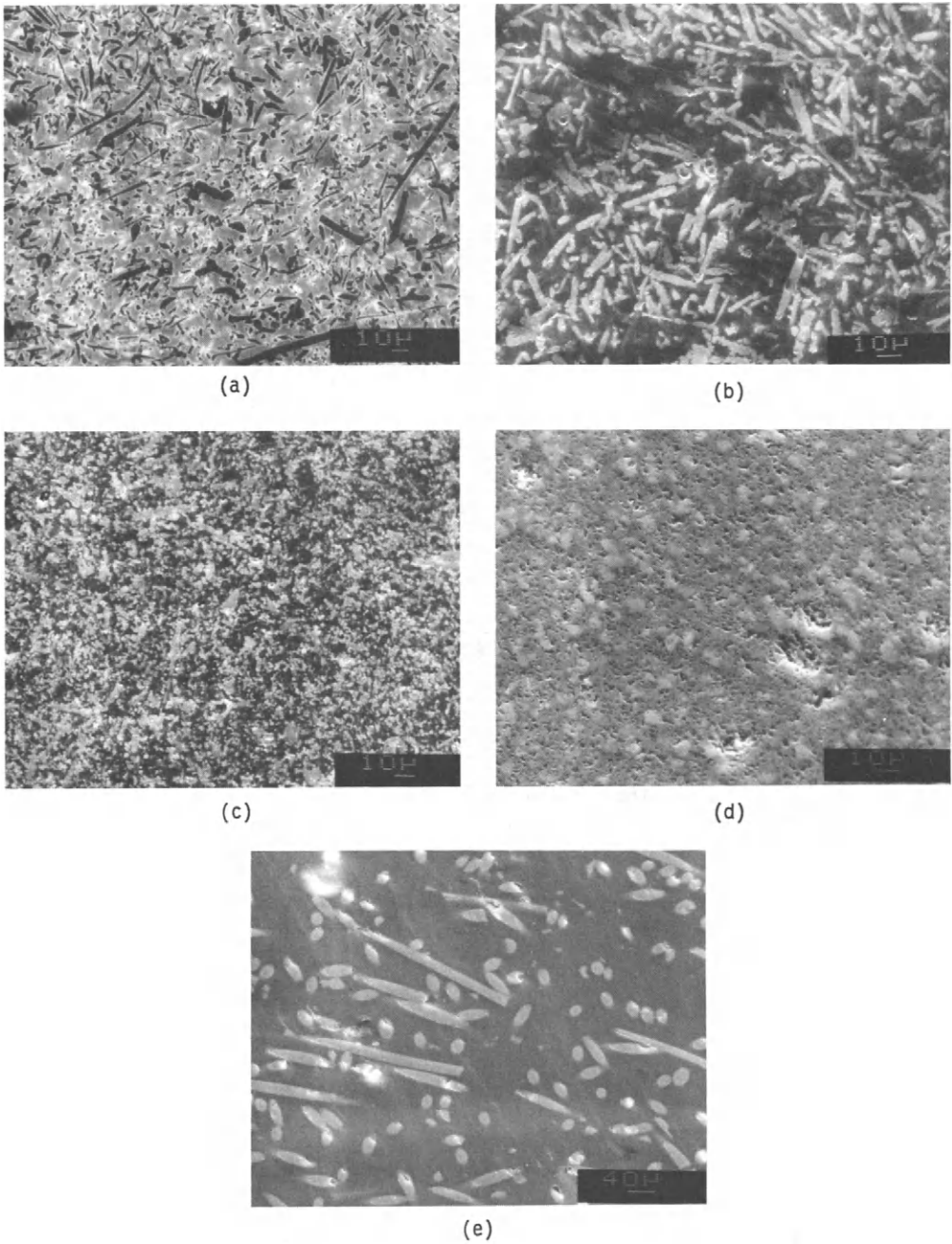
Fig. 2. SEM micrographs of polished surfaces of composite specimens.
a) Al_2O_3/SiC, b) Si_3N_4/SiC, c) $Si_3N_4/SiC/X$, d) SiC/TiB_2, e) PEEK/GF.
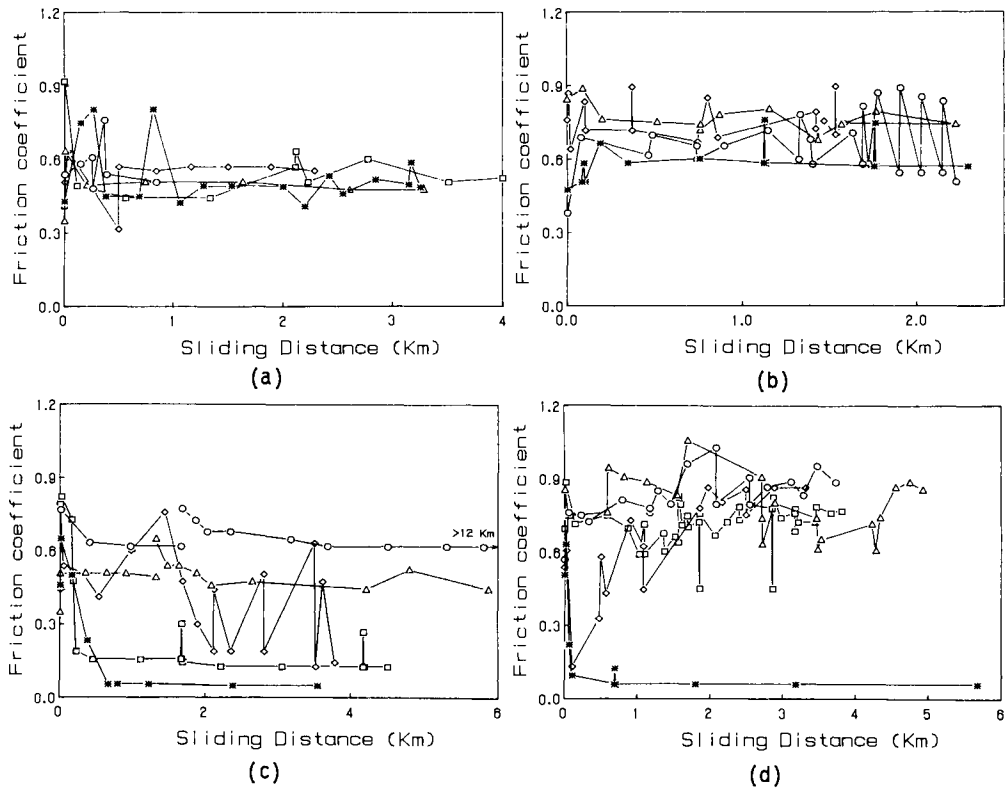
Fig. 3. Friction trends for specimens sliding (a),(b) in air, and (c),(d) in vacuum, . Figs. (a) and (c) are for unslotted disc pair; (b) and (d) are for slotted/unslotted disc pair.
O Al_2O_3/SiC, □ Si_3N_4/SiC, △ Si_3N_4/SiC/X, ◇ SiC/TiB_2, ✳ PEEK/GF.

After sliding in the present highly conforming contact experiments, all specimen surfaces were covered to various extents by wear debris. Of the specimens tested in vacuum, the two ceramic composites with consistent high friction showed a matt texture spread over most of both disc surfaces like those in Figs. 4a and 4b. Those with low or erratic friction appeared streaky, like Fig. 4c. The PEEK composite either had a few streaks on both discs or several isolated debris patches on one disc surface and a matching smear on the other, as seen in Fig. 4d. Closer examination of the worn surfaces more clearly distinguished between those ceramic specimens which had been sliding with high or low friction in vacuum, as shown in Fig. 5. The streaks are lightly smeared bands (Fig. 5e) or a mix of island arcs raised above the unworn surface and scores, presumably from abrasion by debris on the mating surface. The matt textured surfaces consist of a dense, evenly dispersed, bed of debris. (Note that Figs. 5 c,d & e show specimens from different experiments). The patches of wear debris on the PEEK/GF specimens, Fig. 6, are clusters of relatively large raised islands, while the streaks appear similar to the raised arcs on the worn ceramic specimens. The different microstructure of the finely textured and isolated island wear debris on the ceramics is seen in Fig. 7. The features in Fig. 7a are similar to those observed previously in polymeric composites and referred to as smeared debris tongues (Hawthorne, 1986, 1987).
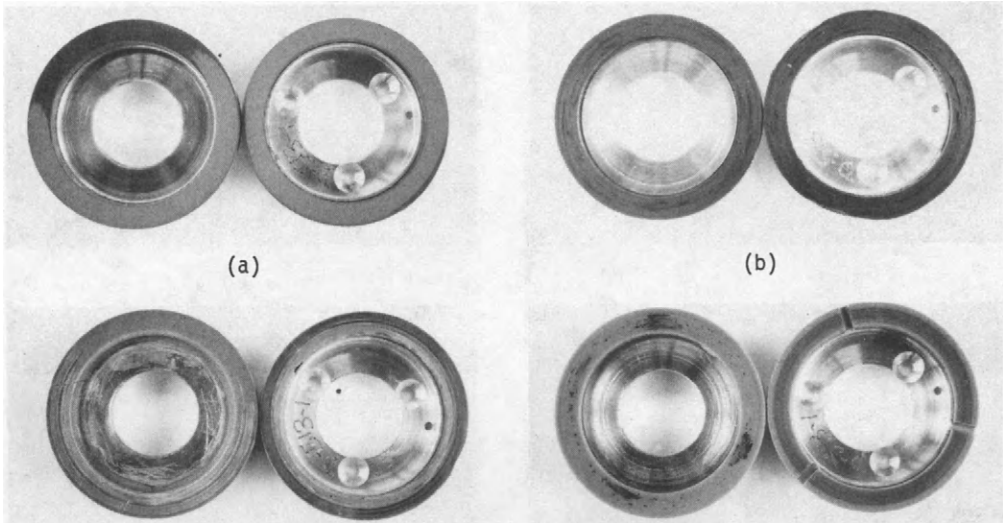
Fig. 4. Typical worn specimen surfaces after extensive sliding in vacuum.
a) Al_2O_3/SiC, b) Si_3N_4/SiC/X, c) Si_3N_4/SiC, d) PEEK/GF

The correlation of friction level with worn surface appearance prompts a ration-lization of the in-vacuo friction behaviour of the various composites in the conforming disc tribosystem based on the fraction of the nominal bearing area actually in contact. In theory, sliding friction is proportional to real contact area, A_r, since friction force, F_f, is given by

$$F_f = A_r \tau$$

where τ is the shear strength of the interface. The raised patches or streaks of the low friction specimens cover around 5% of the total disc area, whereas the small, densely dispersed islands of worn, high friction specimens cover up to about 25%, as shown in Fig. 7a. This is roughly the ratio of the low to high friction coefficients (forces) for the ceramics in the sliding experiments. Yust and co-workers (1988) reported variable friction related to the level of debris at the interface of a ceramic composite sliding in air. This analysis implies a similar shear strength at the sliding surfaces of the different materials, emphasizing mechanical over chemical or micro-structural aspects, in accord with Godet's (1984) views of tribological third-body mechanics. The question remains as to what governs the form of the interfacial debris in the conforming contact.

Figure 8 indicates that the debris islands or smeared tongues on worn surfaces of both ceramic and polymeric composites consist of aggregates, or compacts, of fine debris particles. The fragmentation and mechanical mixing of wear debris within the interface in sliding tribosystems reportedly produces particles on the order of 0.1 and 0.01 µm in ceramic composites (Yust and co-workers, 1988) and polymeric brake compositions (Rowson, 1978), respectively. Consistent with this is the fact that separate particles of the reinforcement phases cannot be detected in present debris, or that from other worn brake material composites (Hawthorne, 1987; Rowson, 1978).
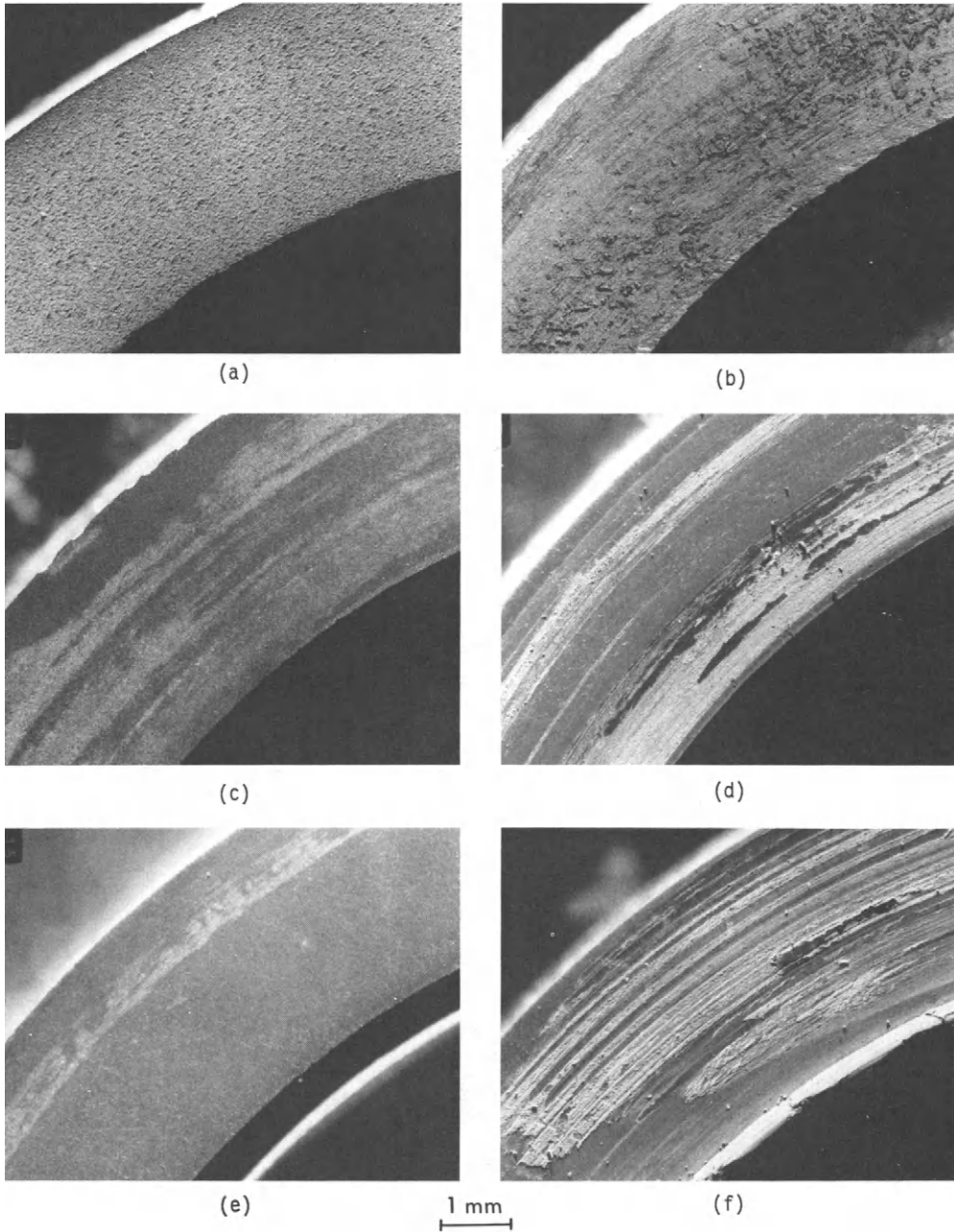
Fig. 5. Wear debris patterns on worn ceramic composite disc surfaces after
    sliding in vacuum at different friction levels. a) Al_2O_3/SiC ($\mu \approx 0.9$),
    b) Si_3N_4/SiC/X ($\mu \approx 0.65$), c) SiC/TiB_2 ($\mu \approx 0.85$), d) SiC/TiB_2 ($\mu \approx 0.35$),
    e) SiC/TiB_2 ($\mu \approx 0.2$), Si_3N_4/SiC ($\mu \approx 0.15$).

(a)   1 mm   (b)
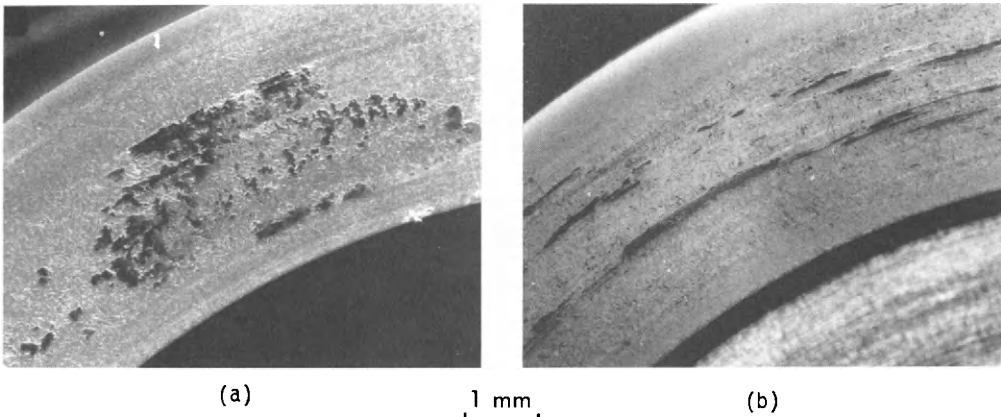
Fig. 6. Two different wear debris patterns observed on worn PEEK/GF disc
surfaces after sliding at low friction in vacuum.

(a)   0.05 mm   (b)
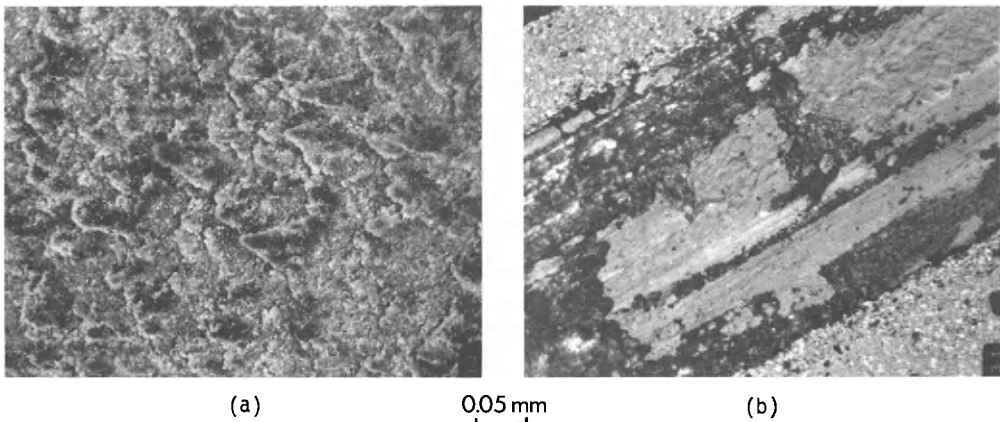
Fig. 7. Optical micrographs of typical wear debris features on ceramic specimen
surfaces with (a) matt and (b) streaky appearance as in Fig. 5.
a) Al_2O_3/SiC b) SiC/TiB_2

The detailed mechanisms of debris formation, comminution, migration and
consolidation into compacts of differing structure and properties in sliding
contacts are largely unknown. However, factors involved in determining the
extent of agglomeration and cohesion of minute wear debris particles into the
tongues or larger islands of the present tribosystems likely include the
chemical composition of their precursors and particle surface energy. Ajayi and
Ludema (1989) found adhesion differences between wear debris films on covalent
and ionic ceramic surfaces sliding in air and they proposed that Van der Waals
and electrostatic forces determine debris film characteristics. Ambient
environment is also an important parameter, as shown by the present, and other
studies on ceramics (e.g. Shimura & Tsuya, 1977; Semenov & Katsura, 1979; Ajayi
& Ludema, 1989). As the in-vacuo sliding friction of asbestos/phenolic
composites was found sensitive to traces of moisture within conforming contacts,

both hydrogen bonding and electrostatic forces were considered possible factors controlling the interfacial wear debris behaviour of organic based composites (Hawthorne, 1986; 1987). Hydrogen bonding would be less likely in ceramics, but it should be possible to search for direct evidence of this and electrostatic effects in appropriate interfaces.

Finally, the periodic changes in friction level shown by some ceramic specimens, such as the SiC/TiB$_2$ composite, are due to delamination of debris islands, producing large flakes, as seen in Fig. 9 . These are similar in size to the large debris features in Fig. 7b. Don and Rigney (1985) developed a model for such flake formation in metals based on alternate sliding, with different friction coefficients, at the debris layer-substrate and interlayer interfaces.

(a)   (b)
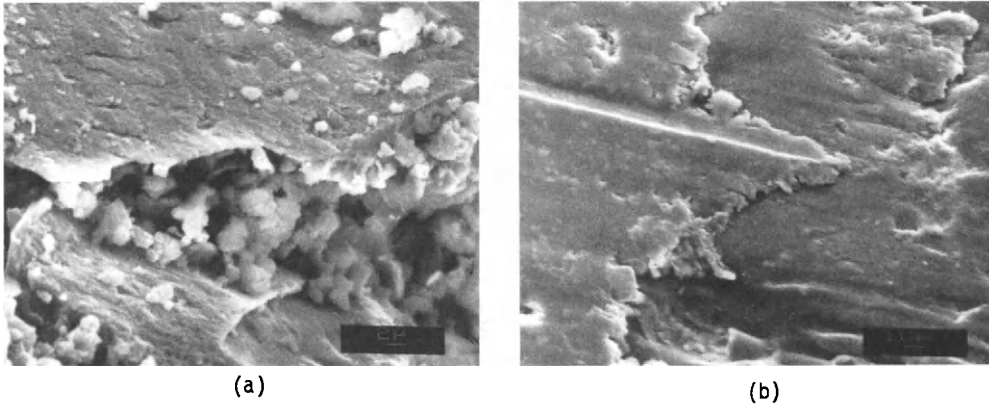
Fig. 8. Typical layers of aggregated wear debris on surfaces of ceramic and polymer composites after sliding in vacuum. a) Al$_2$O$_3$/SiC b) PEEK/GF.
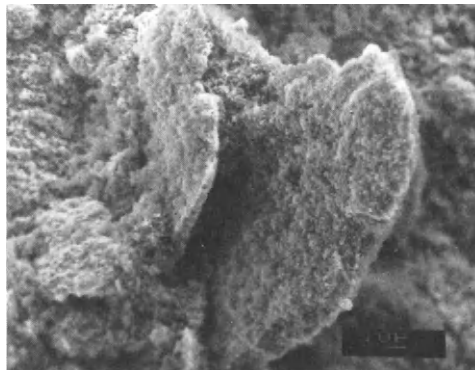
Fig. 9. Large flakes of wear debris recovered from material shed from surfaces of SiC/TiB$_2$ specimens when sliding, with variable friction, in vacuum.

Wear

The wear results obtained so far from like-on-like material disc sliding experiments are summarized in Table 2. It is emphasized that these values reflect only the wear debris lost from the sliding interface, plus any loose material readily dislodged from the worn surfaces by air blowing before weighing. Strongly adherent debris was not taken into account since it is a durable element of the sliding tribosystem. It might be argued that even the loose debris which is geometrically trapped within the thin, conforming contact should not be included in wear quantitation. However, it was not possible to dismantle the brake discs from the test rig without loss of some loose material so the above procedure was adopted for consistency.

TABLE 2 Mean Wear Rates of Two Disc Specimens

Material	Wear Rate (x 10^{-5} mm^3/N m)			
	Air		Vacuum	
	Unslotted	Slotted	Unslotted	Slotted
Al_2O_3/SiC	--	0.06	11.5	12
Si_3N_4/SiC	1.15	1.30	0.46*	14
Si_3N_4/SiC/X	0.32	0.55	5.4	7.6
SiC/TiB_2	0.33	0.30	3.65	5.4
PEEK/GF	--	0.36	0.55	0.83

* Test run in Fig.3c where mostly low friction sliding. Wear rate
  was 5.3 in repeat test with ~ 50% high and low friction sliding.

The wear data may be compared with a value of ~ 1.5 x 10^{-5} mm^3/N m for undried asbestos/phenolic brake material sliding with high friction in vacuum. Present results are also in good agreement with comparable literature data on the wear, and friction, of ceramic composites in air (Mehrotra, 1983; Ishigaki & co-workers, 1988; Yust & co-workers, 1988) and of monolithic ceramics in vacuum (Sasaki, 1989; Semenov & Katsura, 1979; Shimura & Tsuya, 1977; Wayne & Buljan, 1988). The friction of ceramics is usually higher in vacuum than in air and this is often true also for wear (Tsuya, 1985; Wayne & Buljan, 1988). The results in Table 2 indicate that wear is about an order of magnitude higher in vacuum than in air for the ceramic composites which slide predominantly at high friction in vacuum. When friction is low in vacuum, wear rates are also lowered. Such a correlation suggests that interfacial wear debris layers strongly influence wear as well as friction in the present experiments. However, extensive wear debris coverage of surfaces sliding in air usually leads to reduced wear in both polymer based brake compositions (Anderson, 1980) and ceramics (Ajayi & Ludema, 1989). In the present experiments in high vacuum it is the materials which have less debris at the conforming contact interface which exhibit lower wear.

The small wear debris aggregates, or tongues, observed on worn surfaces which were sliding at high friction, Fig. 7a, appear similar to those reported on alumina/silicon carbide whisker composites slid in air at 425 C (Yust & co-workers, 1988) . These features were identified with a more severe, possibly abrasive, wear mode (wear rates 10^{-4}-10^{-5} mm^3/N m) than the very mild wear (rates 10^{-8}-10^{-9} mm^3/N m) found at room temperature. It may be that the similar layer of small, well dispersed debris features associated with the stable high friction, are more abrasive to the substrate in the vacuum environment than the much fewer, and larger, isolated debris islands.

The wear rates of the ceramic composites sliding under low severity conditions in vacuum are moderate rather than catastrophic. Even though their wear resistance is somewhat less than that of polymer based brake materials, these ceramic composites may still be attractive for use in space mechanisms because of their enduring frictional stability in the high vacuum environment.

CONCLUSIONS

From the experiments on four ceramic (and one polymer) composite materials sliding against themselves under low load and speed conditions in conforming contacts, the following conclusions are drawn:

1) All the materials exhibited high friction and moderate wear rates throughout extensive sliding in air.

2) Two of the ceramic composites, silicon carbide whisker reinforced silicon nitride and titanium diboride particle reinforced silicon carbide, can exhibit unstable friction when sliding in high vacuum.

3) The unstable friction behaviour of the ceramics is similar to that found for PEEK/glass fibre and other polymer composites.

4) The modified Si_3N_4/SiC and the silicon carbide whisker reinforced alumina composites exhibit stable friction and moderate wear rates when sliding in high vacuum.

5) The nature of wear debris generated at the sliding interface determines the tribological characteristics of the ceramic, and polymeric, composites investigated here, as in other tribosystems. In particular, the form of the debris structures as well as their properties in the local environment plays a major role in their friction and wear behaviour.

6) The stable high friction, and moderate wear, characteristics of the Al_2O_3/SiC and modified Si_3N_4/SiC composites in vacuum sliding indicates that they may be suitable materials for use in light severity, but long life critical, application in friction brakes on space mechanisms.

ACKNOWLEDGEMENTS

REFERENCES

Ajayi, O.O. & Ludema, K.C., (1989). Proc. Wear of Materials Conf., Denver, ASME, 349-359.
Anderson, A.E., (1980). In M.B.Peterson & W.O.Winer (Eds.), Wear Control Handbook. ASME.
Briscoe, B.J. & Tabor, D. (1980). In N.P.Suh & N Saka (Eds.), Fundamentals of Tribology, MIT Press.
Don, J. & Rigney, D.A. (1985). Proc. Wear of Materials Conf., Vancouver, ASME, 248-253.
Godet, M. (1984). Wear, 100, 437-452
Hawthorne, H.M. (1986). NRC/DME Technical Report CTR-TM-001.

Hawthorne, H.M. (1987). Proc. Wear of Materials Conf., Houston, ASME, 381-387.
Heilmann, P., Don, J., Sun, T.C., Glaeser, W.A. & Rigney, D.A. (1983). Wear, 91, 171-190.
Ishigaki, H., Nagata, R., Iwasa, M., Tamari, N. & Kondo, I. (1988). Trans. ASME, 110, 434-438.
Lancaster, J.K. (1973). Tribology, 6, 219-251.
Mehrotra, P.K. (1983). Proc. Wear of Materials Conf.,Reston, 194-201.
Rowson, D.H., (1978). Wear, 47, 315-321.
Sasaki, S. (1989). Proc. Wear of Materials Conf., Denver, ASME, 409-417.
Semenov, A.P. & Katsura, A.A. (1979). Proc. Wear of Materials Conf., Dearborn, ASME, 551-555.
Shimura, H. & Tsuya, Y., (1977). Proc. Wear of Materials Conf., St.Louis, ASME, 452-461.
Trenouth, J.M. & MacKenzie, C.W. (1986). Can. Aerospace J., 32, 205-213.
Tsuya, T. (1985). Proc. JSLE International Tribology Conf., Tokyo, 641-646
Wayne, S.F. & Buljan, S.T. (1988). Proc. SAE Ann. Mtg., Detroit, (SAE paper # 880676), 1-8.
Yust, C.S., Leitnaker, J.M. & Devore, C.E. (1988). Wear, 122, 151-164.

A study of the dry abrasion properties of zinc-aluminum matrix; Fe, Al, Al$_2$O$_3$ particles composites

J. Blain and J. Masounave
*Industrial Materials Research Institute, National Research Council Canada,
75 de Mortagne Blvd., Boucherville, Québec, Canada, J4B 6Y4*

ABSTRACT

Composite castings were prepared using commercial grade ZA27 as matrix material and either water atomized low carbon steel particles or air atomized aluminum particles. Ceramic particles such as alumina were also used in order to compare the behavior between metallic and ceramic particles. In order to compensate for matrix - particle density variations, rheocasting techniques were employed. These techniques produced castings with particle contents up to 20% vol.

Near net shape forming of the composites at elevated temperatures (semi solid state) eliminated the casting porosities and produced a cohesive bond between the matrix and the particles. X-ray probe analysis of the particle matrix interface were conducted.

Finally, a standard dry sand abrasion test was used to evaluate the strength of the particle - matrix interface and the increase in wear resistance that can be produced by adding particles to ZA27. Results show that even under severe mechanical solicitation, the particle-matrix bond held up. Furthermore, the use of large alumina particles produced a significant increase in wear resistance.

INTRODUCTION

Increasing demand for materials with better mechanical properties has lead material researchers to turn more and more towards composite materials as a possible solution. Because of the problems associated with the production of metal matrix - metal particle composites (Hosking, 1981; Hosking and co-workers, 1982), less work has been done in that field than in the field of metal matrix - ceramic particles composites. Most of the work being done right now is based on aluminum matrix composites. Numerous methods are used today in order to produce MMC: powder metallurgy followed by a consolidation step, infiltration during solidification (squeeze casting), die casting, stircasting in the liquid phase or semi-solid phase also with or without consolidation step in order to eliminate porosities. In this work, one of the cheapest road was followed: stircasting followed by a consolidation step in the semi-liquid phase. The main advantage of this technique is to eliminate porosities due to casting.

The zinc aluminum foundry alloys are gaining more and more relevance in today's modernizing casting industry. The main problems facing these alloys are an often low as cast ductility, low impact strength and poor resistance to abrasive wear. Since this alloy is used more and more as a bearing material because of its good lubricated wear behaviour, methods of increasing its dry abrasive wear resistance must be developed. Use of a reinforcing additive such as steel, aluminum or ceramic particles would be a possible alternative if production cost can be controlled. Furthermore, little MMC work has been done with zinc aluminum alloys as the matrix material The purpose of this paper is thus to investigate the potential benefits to be gained by the use of metal particles with coherent and non coherent bonding to the ZA matrix.

EXPERIMENTAL PROCEDURES

Alloy Preparation

The alloy used as matrix material in our composites was commercial grade ZA27. The nominal composition of ZA27 is: Al: 25-28%; Cu: 2-2.5%; Mg: 0.015%; Pb: 0.002%; Zn: bal.

Alloys were first melted in an electric furnace with a superheat of about 100°C. They were then poured in the stircaster crucible and allowed to cool slowly under a constant agitation of 800 RPM. Previous work (Lehuy, Masounave and Blain, 1985) has shown that under these conditions, it is possible to cast zinc aluminum alloys with fraction solids as high as 40%. Casting was done under a flow of argon to limit oxidation.

Powder Preparation

The powders used were of three types:

a)   Water atomized ferrous particles with a low carbon content and a mean diameter of 100 microns. These particles were degreased in acetone prior to being incorporated in the solution. No preheating of the particles was performed. The nominal composition of atomized Fe particles is: Fe: 99.935%; C: 0.06%; S: 0.005%.

b)   Air atomized aluminum particles with a mean diameter of 200 microns were also incorporated These gas atomized particles had a much less spherical shape and a wider dimensional scatter than the Fe particles. The particles were pure aluminum with traces of Fe (0.18%) and Si (0.12%)

c)   Two sizes of alumina particles were also used. The size of the larger particles was between 100 and 200 μm and the smaller particles were 14.5 μm wide.

Porosity Measurements

Composite casting porosities were measured using the standard flotation method. The actual particle content of each casting was evaluated by the standard surface ratio method. Each casting was examined at the top, the middle and the bottom. Results reported in this paper do not include casting with porosity or particle content variations greater than 5% between the top and the bottom of the ingot.

Composite Preparation

Casting was performed using a batch stircasting machine similar to that used by other groups (Flemmings, Mehrabian, 1974; Hosking and co-workers, 1982; Meharabian, Riek and Flemings, 1974). The temperature of the melt was maintained during agitation by inductive heating of the graphite crucible. Agitation was produced by a steel impeller coated with plasma sprayed alumina. Experimentation showed that sound composite casting could be produced by maintaining the agitation rate at 800 - 1000 RPM, and at temperatures ranging from 475°C to 490°C. Even with the presence of the Fe or Al particles, casting could be performed with matrix fraction solids as high 20%. Higher particle content lead to a slurry too viscous to be cast without any external applied pressure. Very high particle content also lead to rejection of the particles at the surface (Al_2O_3) or bottom (Fe) of the crucible. Composites with particle contents ranging from 0% vol. up to 25% vol. were produced.

Agitation was more critical in the case of the Fe and Al_2O_3 particles because they were not wetted by the melt and thus had a greater tendency to cluster or be expelled from the melt.

Composite Densification

As stated previously, as cast composites had varying degrees of porosity ranging from 1% up to 13% (see Table 1). The effect of the stircasting temperature is clearly seen. When the liquid fraction is too high, more gas is trapped during the stirring period.

In order to produce acceptable material, the stirring temperature has to be as low as possible. In order to obtain more reproducible results, the castings were then machined into cylinders 2.54 cm high with a 1.81 cm diameter. These cylinders were heated up to temperatures corresponding to fraction solids between 70% and 90% (Murray, 1983) and compressed into disks having a diameter of 3.81 cm. The load applied was 80 KN and compression of the specimen was done in 0.3 second. The compression chamber temperature was kept at between 300°C and 400°C. This insured a complete filling of the chamber without excessive liquid seapage out of the mold (Lehuy and co-workers, 1984). Porosity of the compressed specimen was low enough as to not be detectable even under SEM examination. Furthermore, Figures 1 and 2 show that the general aspect of the particle - matrix interface was influenced by the densification temperature in the case of the Fe composites.

TABLE 1 Variation of the Porosities of the As Cast Materials

Specimen	Density	% Porosity	Stircasting temp.
3	4.689	4.3	470°C
4	4.696	4.1	470°C
5	4.674	4.6	470°C
6	4.942	0.8	470°C
C	4.197	14.3	485°C
D	4.289	12.4	485°C
E	4.279	12.6	485°C
F	4.296	12.3	485°C
G	4.263	13.0	485°C
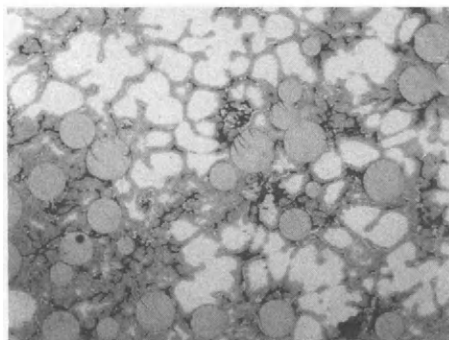
Fig. 1. As-cast apprearance of Fe particles composite, showing porosities formed during final solidification of the matrix. It should be noted that no particles are present in the aluminum rich (lighter) phase formed during stircasting (X70).
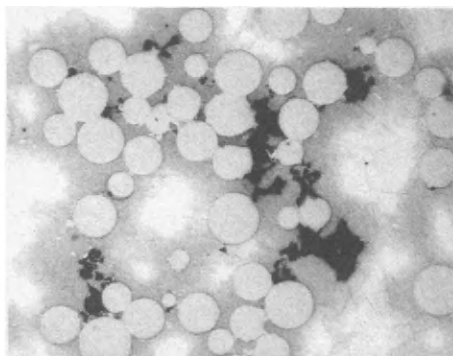
Fig. 2. Appearance of Fe particles composite after densification. The casting porosities have been eliminated. But a significant amount of intermetallic compounds has formed in the Zn rich phase (X70).

Dry Abrasion Tests

In order to evaluate the resistance of the composite, dry abrasion tests were performed on the densified composites. All tests were performed according to ASTM standard practice for conducting dry sand/rubber wheel abrasion tests (ASTM G65). Procedure D was used but because of the severity of these tests, only 2/3 of the normal duration of these test was used. The abrasion test conditions are:

6" rubber wheel; 257 RPM for 5140 turns; 10 pounds of normal load; 50 - 70 Ottawa silica sand flowing at 300 gr./min. Wear was measured by the weight loss during testing.

EXPERIMENTAL RESULTS

SEM Examinations

Metallic particles (Fe, Al). Figure 3 shows the typical aspects of the interface of our Fe composites after densification. In almost all cases, the interface between the matrix and the Fe particle was so narrow that it could not be observed even under high magnification. On the other hand, Al particles (Figure 4) were covered by degenerated dendrites that formed during primary solidification of our alloys during agitation. The exact boundary between particle and matrix is difficult to pinpoint in this case because of the smooth transition in aluminum content. Figure 2 shows the morphology before densification. Some very important features have to be pointed out. Porosities are formed during final solidification. The first solidified phase, rich in Zn is exempt of pores. Also, the iron particles are located in the porous regions. It is obvious that the solidification front rejects the particles regardless of their densities. This is an indication that particles are not wetted by the metallic liquid. This concentration of iron particles in the Al rich phase is detrimental to mechanical properties. In fact, each contact point between two particles is a weak point capable of initiating cracks.

The impact of Fe dissolution in the matrix is clearly evident. It is always associated with the presence of an aluminum rich dark phase as seen in Figure 3. This phase mainly formed when the casting temperature was raised above 490°C or the agitation period extended for more than 3 or 4 minutes. This dark phase is probably an Al, Fe intermetallic (Koster, Godecke, 1971).
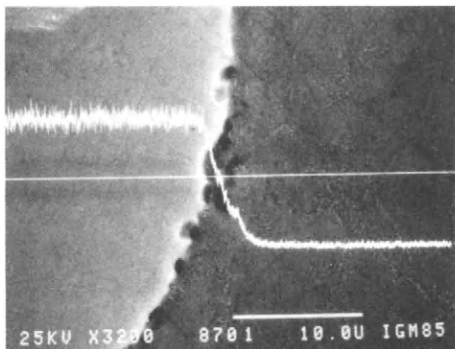
Fig. 3. X-ray probe analyses, showing Fe concentration variation across a Fe particules - ZA27 matrix interface. Dark intermetallic compounds can also be observed.
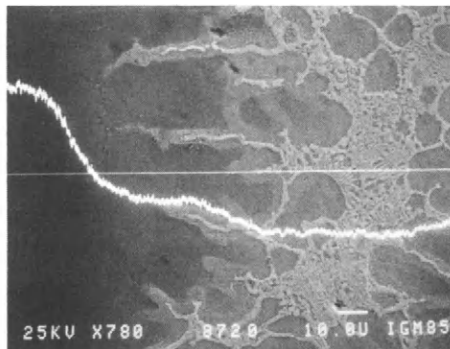
Fig. 4. X-ray probe analysis showing Al concentration variation across an Al particle - ZA27 matrix interface. A smooth transition is observed due to the formation and growth of degenerated dendrites on the particle during stircasting.

To facilitate SEM observation of the matrix-particle interface some of the composites were fractured at low temperature. Examination of the fractured surface revealed that in the case of our Fe composites, the incoherent interface ruptures easily leaving the surface covered by bear Fe particles. Figure 5 clearly shows this phenomenon. Furthermore, the interface between our Fe particles and the matrix seem to be discontinuous in nature and to only cover a small portion of the particle surface. On the other hand, ruptured Al composites show an interface which seems tougher than the matrix so that interface cracking was never clearly observed. However, cracks seem to be initiated in the zinc rich region that is found in between the degenerated dendrites formed at the surface of the particles during agitation (Figure 6).
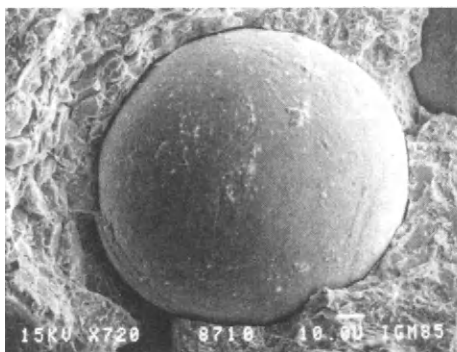
Fig. 5. Fractured Fe - ZA27 composite showing the limited amount of bonding between the Fe particles and the matrix.
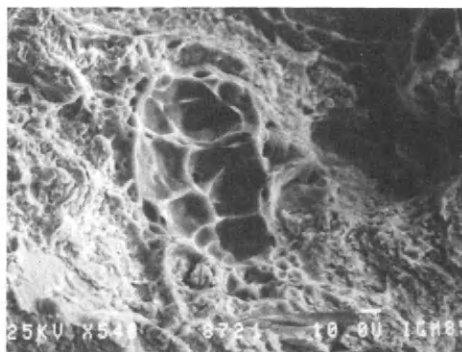
Fig. 6. Fractured Al - ZA27 composite showing the good cohesion between the particles and the matrix. The more ductile particles have a dimpeled surface.

Ceramic particle. Figure 7 shows a typical aspect of our MMC made of alumina particles. It is worthwhile to point out that the particles are also rejected by the solidification front. This is again a poor situation because these angular particles are touching. For wear applications, this configuration can be tolerated because the applied stresses are mainly in compression. No interface was observed between the ceramic and the matrix. Because of the differences in thermal expansion coefficients of ZA and Al_2O_3, large compressive residual stresses were probably developed during cooling. These stresses contribute to maintain the particles in the matrix. The effect of the stircasting temperature is also important on the clustering of alumina particles. A more uniform distribution of particles is observed when the melt fraction solid is increased. As is well known, the size of the particles plays an important role in the uniformity of their repartition. The tendancy to cluster increases when the size of the particles decreases. For smaller particles (14.5 µm), it is impossible to avoid clustering.

Wear Morphology

Metallic particles. The wear behavior of Fe particles and the matrix are different (Figure 8). More plowing is observed on the iron particles than in the matrix where more exfoliation can be seen. Iron particles wear slightly less than the matrix. This is due to the fact that iron particles have a hardness similar to the matrix (Table 2) but possess better ductility. Some material was moved from the matrix onto the Fe particles.

In all cases, no signs of particles being torn from the surface could be observed. Even with similar wear rates between the particle and the matrix, we would have expected to observe pores left behind by torn Fe particles.

TABLE 2 Microhardness Measurements of Fe Particles

1. As produced Fe particles	120	V
2. Standard ZA27 matrix	145	V
3. Standard ZA27 prim. part	168	V
4. Fe particle in composite	132	V
5. Matrix in composite	147	V
6. Prim. part. in composite	181	V

Ceramic particles. Two different mechanisms can take place depending on the size of the alumina particles. The larger particles (100 μm) bring a good protection to the matrix (Figure 9). Two reasons can explain this fact. First, the alumina particles are about the same size as the silica abrasive particles and the mean free path between particles is of the same order of magnitude than the abrasive size. In this case, abrasive particles always touch alumina particles which, hence, assures a good protection of the matrix. The protection is not efficient when the particles are much smaller than the abrasive (Figure 10). Plowing is observed in the matrix, and alumina particles are debonded from the matrix. Hence, small particles have a detrimental effect on the wear resistance. Clusters of small particles have highly negative effects on the protection of the matrix. They leave a hole in the matrix and the dislodged particles themselves participate in the abrasion, further increasing the wear rates.
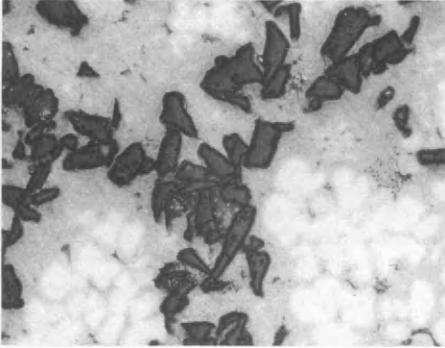
Fig. 7   Typical aspect of an Al_2O_3 - ZA27 composite in which particles clustering occurred. Again, all particles were rejected from the first solid phase formed during stircasting (X56).
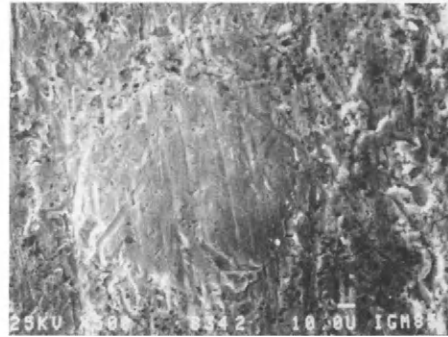
Fig. 8.   Typical aspect of a wear surface for a Fe - ZA27 composite. Although the wear rates are similar for the particles and matrix, the wear mechanisms are quite different.
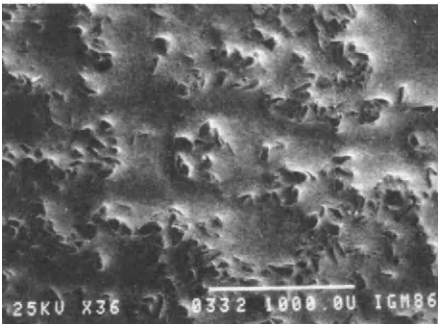
Fig. 9.   Wear surface for a 100 μm Al_2O_3 particle - ZA27 matrix which clearly shows the protection provided by the hard particles against the abrasive.
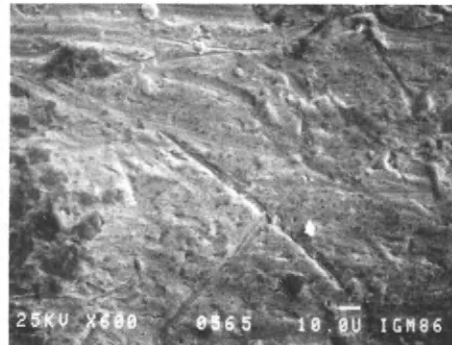
Fig. 10. When very small alumina particles are added to a ZA27 matrix, wear rates are increased. Because the particles themselves are gouged out of the matrix by the abrasive.

ABRASION TESTS RESULTS

Zinc aluminum alloys have good lubricated wear characteristics but very low resistance to dry abrasion tests. Figure 11 shows that abrasion resistance was improved by addition of the more ductile Fe particles. Furthermore, specimens densified at a higher temperature exhibited a slightly better wear resistance. This slight difference can be explained by an improvement in the compaction when the temperature is higher and also by the increased amount of hard intermetallic compounds produced in the matrix. In this case, the ZA matrix and the Fe particles have very similar hardness. However, the wear mechanisms are very different in both materials.

The improvement due to aluminum particles is very small (Figure 12). In one case, an attempt was done to control the repeatability of the wear test (experimental points around 25% or particles). The discrepancy is high. As shown aluminum particles have a beneficial effect on the wear of composite. Nevertheless, this effect is smaller than for Fe particles.

As anticipated, the improvement due to large alumina particles is higher than the two previous one (Figure 13). Alumina particles are obviously harder than iron or aluminum hence the protection is better. A strong limitation of this protection is shown on Figure 13. When the particles are too small, the behavior of the composite is worst than that of the pure matrix. Therefore, some caution has to be taken before selecting a specific composite. General selection rules will be shown in the next section.

Furthermore, tests performed on 1008 Fe steel show that the increase in wear resistance due to the presence of the Fe particles is significantly higher than that predicted by a linear rule of mixture law (Figure 14). In fact, the presence of 15% vol. Fe particles leads to a wear resistance that is equal to 80% of the resistance of 1008 steel.

DISCUSSION

As-cast Porosities

As indicated earlier, porosity was significant in our castings. Three different mechanisms are responsible:

1)   Gas can be entrapped in the semi solid slurry during agitation.
2)   Non wetting particles can cluster together and prevent liquid impregnation at the cluster center.
3)   Final solidification of the remaining liquid phase usually produces micropores.
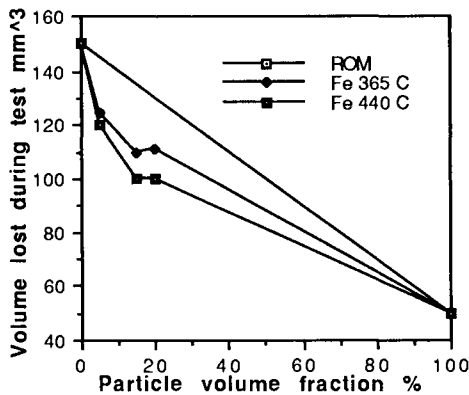
Fig. 11. Results of wear test on Fe - ZA27 composites densified at two different temperatures.
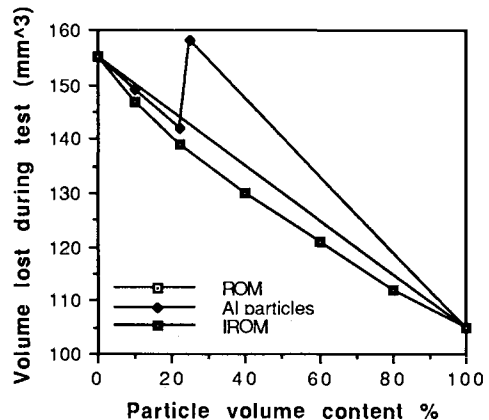
Fig. 12. Results of wear tests on Al - ZA27 composites.
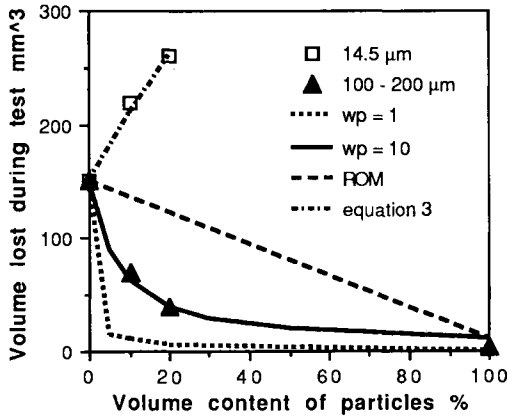
Fig. 13. Results of wear tests on Al_2O_3 - ZA27 composites showing the impact of Al_2O_3 particle size on the wear resistance.
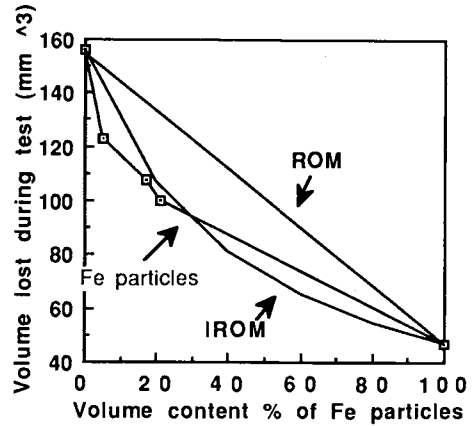
Fig. 14. The Fe particle composites give wear rates similar to those predicted by a standard IROM relation.

By carefully designing the impeller and by an accurate control of the agitation speed and temperature it is possible to control gas entrapment in the slurry during normal stircasting. This problem is more acute in the case of composites because the slurry solid content is significantly increased by addition of solid particles. In our case, gas entrapment during agitation and casting is the main source of porosity.

The second problem is impossible to eliminate unless the particle surfaces are treated to promote wetting. In our case, the problem occurred with Fe and alumina particles. Stircasting these composites is a good alternative to surface treatment of the particles (Levi, Abbaschian and Mehrabian, 1978). We have found that with our impellers, rotation speeds in excess of 600 RPM were sufficient to almost completely eliminate clustering.

The effect of Composite Morphology on Abrasion

For comparison purposes, the wear rate improvement, at volume fraction of 20% for our various composites are: Fe particles: 60%; Al: 5%; Al_2O_3 (large particles): 200%; Al_2O_3 (small particles): - 67%. As expected, large alumina particles give the best results, and the worst ones are for small alumina particles. These results relate well to the following quantitative models (Figure 15). Four cases can be distinguished:

1) When particles are harder or as hard as the abrasive, and the abrasive diameter is larger than the mean free path between the particles, the wear of composite is mainly controlled by the wear resistant phase (the harder one). If no interaction occurs between matrix and particles it is generally admitted that the standard inverse rule of mixture (IROM) should be used :

$$W^{-1} = \Sigma \left(V_i \cdot W_i^{-1} \right) \tag{1}$$

Where W_i is the wear rate of each specific phase and V_i their volume fraction. This type of wear behavior is observed for our Fe and large Al_2O_3 particles conposites.

If some interaction between matrix and particles exists, a modified relation was proposed:

$$W^{-1} = \Sigma \left(V_i^\gamma \cdot W_i^{-1} \right) \tag{2}$$

$$D < \lambda$$

$$W_1 < W_2$$

$$W^{-1} = \Sigma \left(V_i \cdot W_i^{-1} \right)$$

If interaction between phases:

$$W^{-1} = \Sigma \left(V_i^\gamma \cdot W_i^{-1} \right)$$

$$D \gg \lambda$$

$$W = \alpha\, V_p\, W_p + (1 - V_p)\, W_M$$

$$D > \lambda,\ W_1 \sim W_2$$

$$W = \Sigma V_i \cdot W_i$$
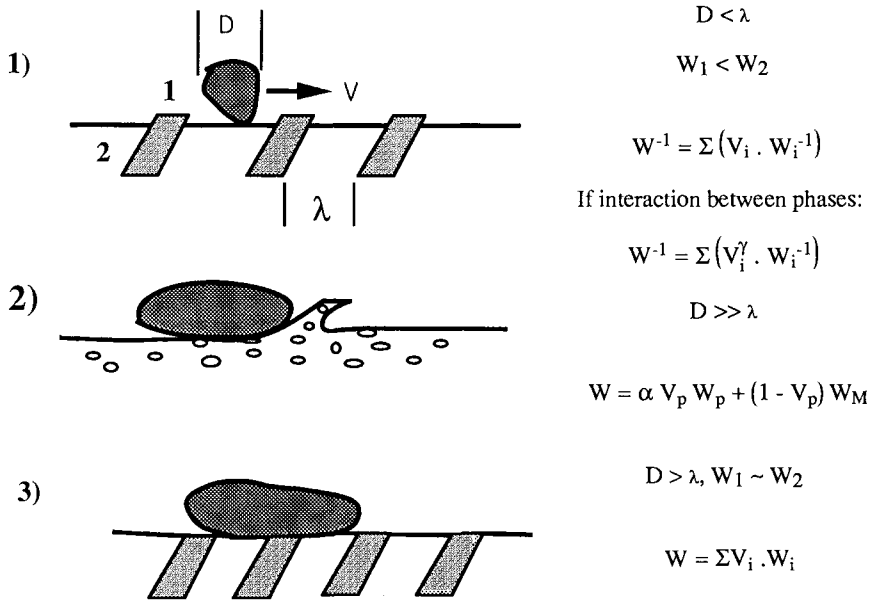
Fig. 15. Illustration of the typical wear mechanisms observed in our composites.

This relation was verified by (Zum Gahr) for white iron ($\gamma = 2$). For our composites such a behavior was not observed even in the case of Fe particles where significant transfer of material from the matrix onto the Fe phase was present.

For Fe particles composite, Figure 14 shows a very reasonnable agreement between the IROM relation and the experimental results. In this case, the wear rate of pure 1008 specimens was directly measured from experimental wear tests.

Figure 13 shows corresponding results for large Al_2O_3 particles. Since the wear rate of pure Al_2O_3 is impossible to measure, the best value was obtained from curve fit ($Wp = 10$). This value is probably higher than the real one. As an example of the influence of Wp on the total wear rate, the curve for $Wp = 1$ is also shown.

2)   When the hard particles are really smaller than the abrasive one, they contribute to the wear rate. In other words, if the volume fraction of particles is increased, the wear rate of the composite is also increased. In order to take care of this negative effect of the particles, the volume fraction efficiency has to be artificially increased. A coefficient α is thus introduced in the ROM wear relation. This coefficient of efficieny is valid only for small concentration of particles:

$$W = \alpha\, V_p\, W_p + (1 - V_p)\, W_M \tag{3}$$

Figure 13 shows experimental results and a line corresponding to relation (3) with $\alpha = 75$ and $Wp = 10$.

3)   For aluminum particles, the wear rates observed are comparable to that of the matrix. In this case, the standard rule of mixture (ROM) should apply :

$$W = \Sigma V_i \cdot W_i \tag{4}$$

It is difficult to reach a conclusion in the case of aluminum particles composite because the wear rate of aluminum is close to that of the matrix. In this case, both relations (1) and (4) can be applied (see Figure 12) with equal validity.

CONCLUSION

1) Stircasting is an effective method of producing zinc-aluminum matrix composites
2) Aluminum particles do not significantly improve the wear resistance of the matrix.
3) The use of Fe particles, even at volume fraction of 20%, can increase the wear resistance of the matrix by 60%.
4) Alumina particles, if they are large enough, can improve the wear rates by 200 to 300%.
5) For abrasive applications, where the applied load is in compression, the interface toughness does not seem to play an important role.
6) A modification to the ROM model is proposed in order to take into account the undesirable effect of small alumina particles.
7) The inverse rule of mixture (ASTM G65-81) is generally in good agreement with our experimental data (aluminum, iron, large alumina).

REFERENCES

1) ASTM standard practice for conducting dry sand/rubber wheel abrasion tests. Designation G65-81.
2) Flemmings M.C., R. Mehrabian (1974). Casting semi-solid metals. United States exchange paper to 40th Internationl Foundry Congress, Moscow.
3) Hosking, F.M. (1981). Compocasting of an aluminum alloy composite containing B4C particulage. NTIS DE81, 028185, 28 p.
4) Hosking, F.M., F.Portillo Folgar, R. Wunderlin, R. Mehrabian (1982). Composites of aluminium alloys: fabrication and wear behaviour. Journal of Materials Science, 17, pp. 477-498.
5) Koster, W., T. Godecke (1971). The iron-aluminum-zinc ternary system. 9th International Conference on Hot Dip Galvinizing, Dusseldorf, London, June 1970, Industrial New Papers Ltd, pp. 128-139.
6) Lehuy, H., J. Masounave, J. Blain (1985). Rheological behaviour of stir-casting zinc-aluminum alloys. Journal of Material Science, 20, pp. 105-113.
7) Lehuy, H., J. Blain, G.L. Bata, J. Masounave (1984). Compression of semi-solid dendritic and non dendritic Zn-Al alloy at low strain rates. Materials Science and Engineering, 67, L29-L32.
8) Levi, C.G., G.J. Abbaschian, R. Mehrabian (1978). Interface interactions during fabrication of aluminum alloy-alumina fiber composites. Metallurgical Transactions A, vol. 9A, pp. 697-711.
9) Meharabian R., R.I. Riek, M.C. Flemings (1974). Preparation and casting of metal-particulate non-metal composites. Metallurgical Transactions, vol. 5, pp. 1899-1905.
10) Murray J.L. (1983). The Al-Zn (Aluminum-Zinc) system. Bulletin of alloy phase diagrams, vol. 4, no 1.
11) Zum Gahr, K.H (1981). Proceedings of the Int. Conf. on Wear, Vancouver, pp. 33-47.

AUTHOR INDEX

SUBJECT INDEX